

N O T I C E

THIS DOCUMENT HAS BEEN REPRODUCED FROM
MICROFICHE. ALTHOUGH IT IS RECOGNIZED THAT
CERTAIN PORTIONS ARE ILLEGIBLE, IT IS BEING RELEASED
IN THE INTEREST OF MAKING AVAILABLE AS MUCH
INFORMATION AS POSSIBLE

NASA Contractor Report 152224

(M. Falcowski)

(NASA-CR-152224) TRAILING EDGE WAKE FLOW
CHARACTERISTICS OF UPPER SURFACE BLOWN
CONFIGURATIONS Final Report, Aug. 1977 -
Dec. 1978 (Lockheed-Georgia Co., Marietta.)
435 p HC A19/MF A01

N81-23028

Unclas
23847

CSSL 01A G3/02

TRAILING EDGE WAKE FLOW CHARACTERISTICS OF UPPER SURFACE BLOWN CONFIGURATIONS

N. N. Reddy and W. H. Brown

LOCKHEED-GEORGIA COMPANY
Marietta, GA 30063

CONTRACT NAS2-9615
December 1978



NASA

National Aeronautics and
Space Administration

Ames Research Center
Moffett Field, California 94035

NASA Contractor Report 152224

**TRAILING EDGE WAKE FLOW CHARACTERISTICS
OF UPPER SURFACE BLOWN CONFIGURATIONS**

N. N. Reddy and W. H. Brown

**LOCKHEED-GEORGIA COMPANY
Marietta, GA 30063**

**CONTRACT NAS2-9615
December 1978**



**National Aeronautics and
Space Administration**

**Ames Research Center
Moffett Field, California 94035**

CONTENTS

	Page
SUMMARY	1
1. INTRODUCTION	2
2. EXPERIMENTAL PROGRAM	2
2.1 Model Description	3
2.2 Propulsive Performance Measurements	9
2.3 Acoustic Measurements	14
2.4 Flow Measurements	29
3. ANALYTICAL PROGRAM	51
3.1 Parametric Effects	54
3.2 Flow Characteristics	86
3.3 Comparison of Measured Data with Prediction	98
4. CONCLUSIONS	103
REFERENCES	105
APPENDICES	A-i
A. Wake Flow Properties	A-1
B. Wake Flow Space-Time Correlations	B-1
C. Wake Flow Cross Power Spectra	C-1
D. Near-Field Noise Spectra	D-1

TRAILING EDGE WAKE FLOW CHARACTERISTICS OF UPPER SURFACE BLOWN CONFIGURATION

N. N. Reddy and W. H. Brown
Lockheed-Georgia Company, Marietta, Ga.

SUMMARY

Detailed flow measurements in the near wake region of an upper surface blown flap were made using a small-scale model with a D-shaped jet nozzle. The test model was selected from existing USB models based on previous aircraft integration studies. To ascertain that the selected model configuration would provide the required performance characteristics, static propulsive performance tests were conducted in the low-speed wind tunnel. Acoustic tests were conducted in an anechoic room to measure far-field noise characteristics. Flow and near-field noise tests were conducted in the Lockheed-Georgia Aeroacoustics Flow Facility. The wake flow measurements include mean velocity and turbulence intensity profiles and space-time correlations of the fluctuating velocities. A hot-wire system was used extensively in these flow measurements; but to evaluate the feasibility of using a laser velocimeter system for the blown flap measurements, limited tests were conducted using an existing four-channel laser velocimeter. Near-field noise and correlations between the near-field noise and the two orthogonal fluctuating velocity components in the wake were measured to evaluate the relative importance of these two velocity components. In all these tests, the jet velocity, the initial turbulence in the jet flow, and the flap deflection angle were varied to study their effects on noise and wake flow characteristics. The measured radiated noise is compared with that predicted by an existing empirical prediction method. The wake flow properties are compared with the results of an analytical model assumed in the existing USB wake flow noise generation theory. Modifications to the assumed model and further studies to understand blown-flap noise generation and reduction are suggested.

1. INTRODUCTION

The additional lift augmentation required for the operation of future jet-powered short-haul aircraft is generally obtained with an integrated powered-lift system. The upper surface blown flap (USB) concept is one of the leading candidates among the integrated powered-lift systems. In this concept, the jet exhaust is discharged on the upper surface of the wing and is turned along the deflected flaps. One of the primary concerns with this type of aircraft is community noise. During the last few years, extensive investigations to understand the noise-generating mechanisms and to determine the effect of various geometric and operational parameters on USB noise characteristics have been performed. These studies indicate that the most significant noise source is located near the flap trailing edge. The actual noise generating mechanism appears to be the turbulence generation in the shear layer downstream of the trailing edge where mixing between the entrained flow and the jet leaving the trailing edge takes place. To verify this fact and to help develop analytical methods for noise predictions, the flow properties in the trailing edge wake were studied. The static propulsive performance, radiated noise characteristics, and correlations between the in-flow and radiated noise were also investigated in this program.

2. EXPERIMENTAL PROGRAM

Experiments were conducted to measure the following properties of USB: (1) static lift and drag, (2) radiated sound field, (3) mean and fluctuating velocity distributions, (4) space-time correlations of fluctuating velocities, (5) near-field sound, and (6) correlation between turbulence and near-field noise. The experimental model was selected based on previous studies (ref. 1) to be compatible with a practical USB configuration and small-scale models existing at Lockheed-Georgia. Tests were conducted in three different facilities; the load (lift and thrust) measurements were obtained in the low-speed wind tunnel, the flow characteristics and the near-field noise were obtained in the flow facility, and the far-field sound was measured in the

anechoic room. The same model was used in all the experiments. The model description and the various measurements in different facilities are discussed in this section.

2.1 Model Description

The low-speed performance of upper surface blown flap configuration improves as the flow spreading and turning (without separating from the surface) increases. One of the ways of increasing the flow spreading is to use a nozzle with a large effective aspect ratio. The upper limit of aspect ratio, however, is limited by the duct transition requirements and nacelle afterbody angles that would cause excessive performance losses with fuel consumption penalties for cruise operation. Compatibility studies (ref. 2) indicate that the D-shaped nozzle offers a good compromise between cruise, low speed, and noise performance requirements. Thus, a D-shaped nozzle which was already available (fig. 1) at Lockheed-Georgia was used in these experiments.

The wing/flap consisted of three basic elements; the wing, the curved surface with constant radius of curvature, and the straight trailing edge element. The wing was two-dimensional with 50.8 cm span. The nozzle was located at the mid-span position. The dimensions and other description of the USB configuration tested are shown in figure 2 and the critical dimensions are given below.

Nozzle

Aspect ratio, AR	3.25	--
Height, h	2.25 cm	(0.886 in.)
Width, w	5.74 cm	(2.26 in.)
Area, A_N	10.12 cm ²	(1.57 in. ²)
Nozzle angle with reference to the wing surface, θ_N	20°	--
Nozzle chordwise location on wing	20% nominal chord	

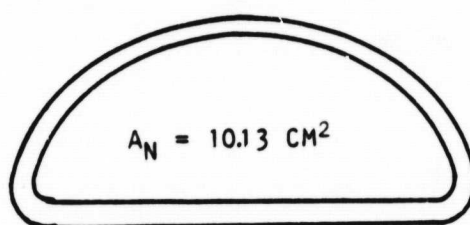
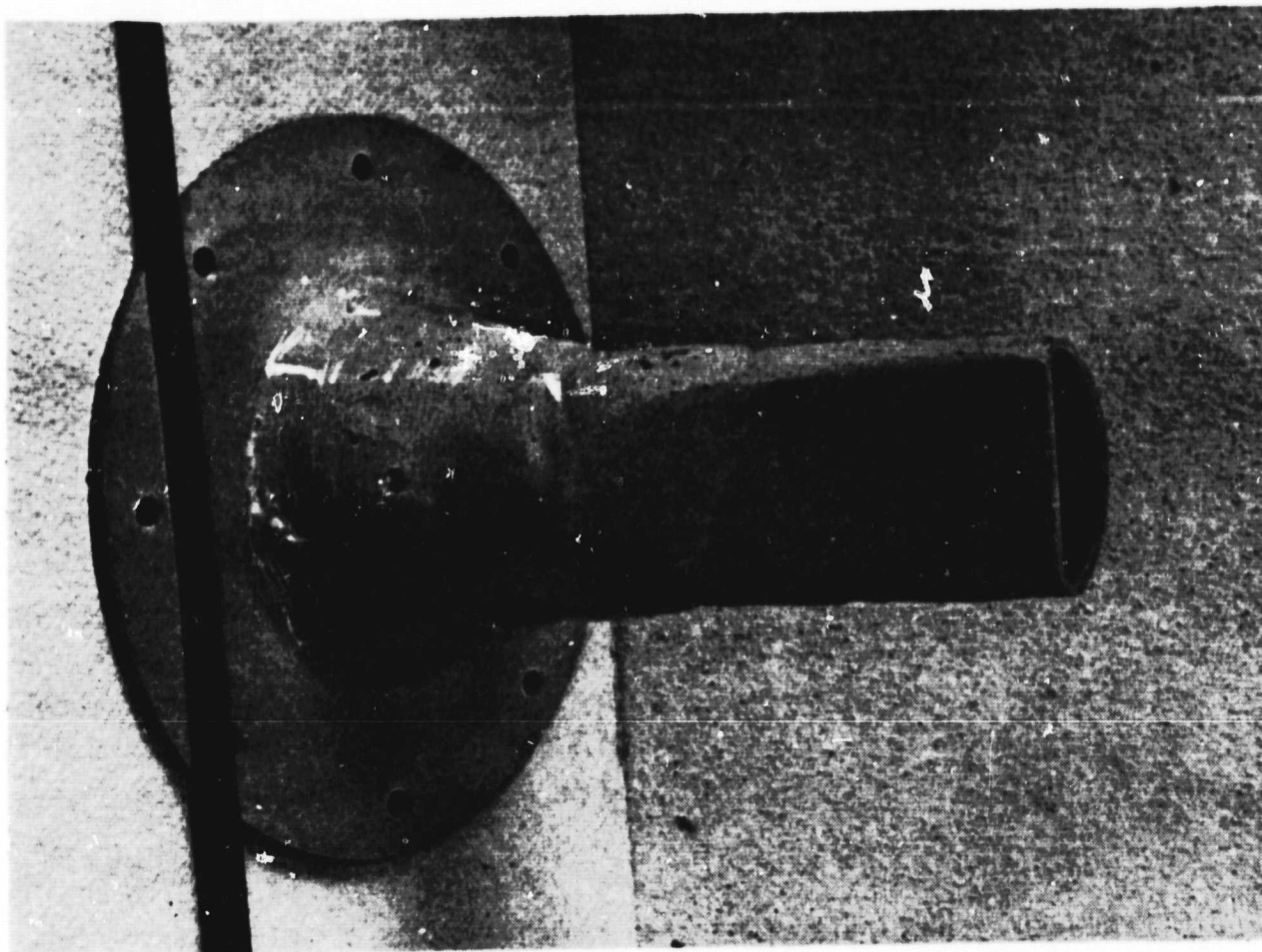


FIGURE 1. NOZZLE SHAPE

ORIGINAL PAGE IS
OF POOR QUALITY

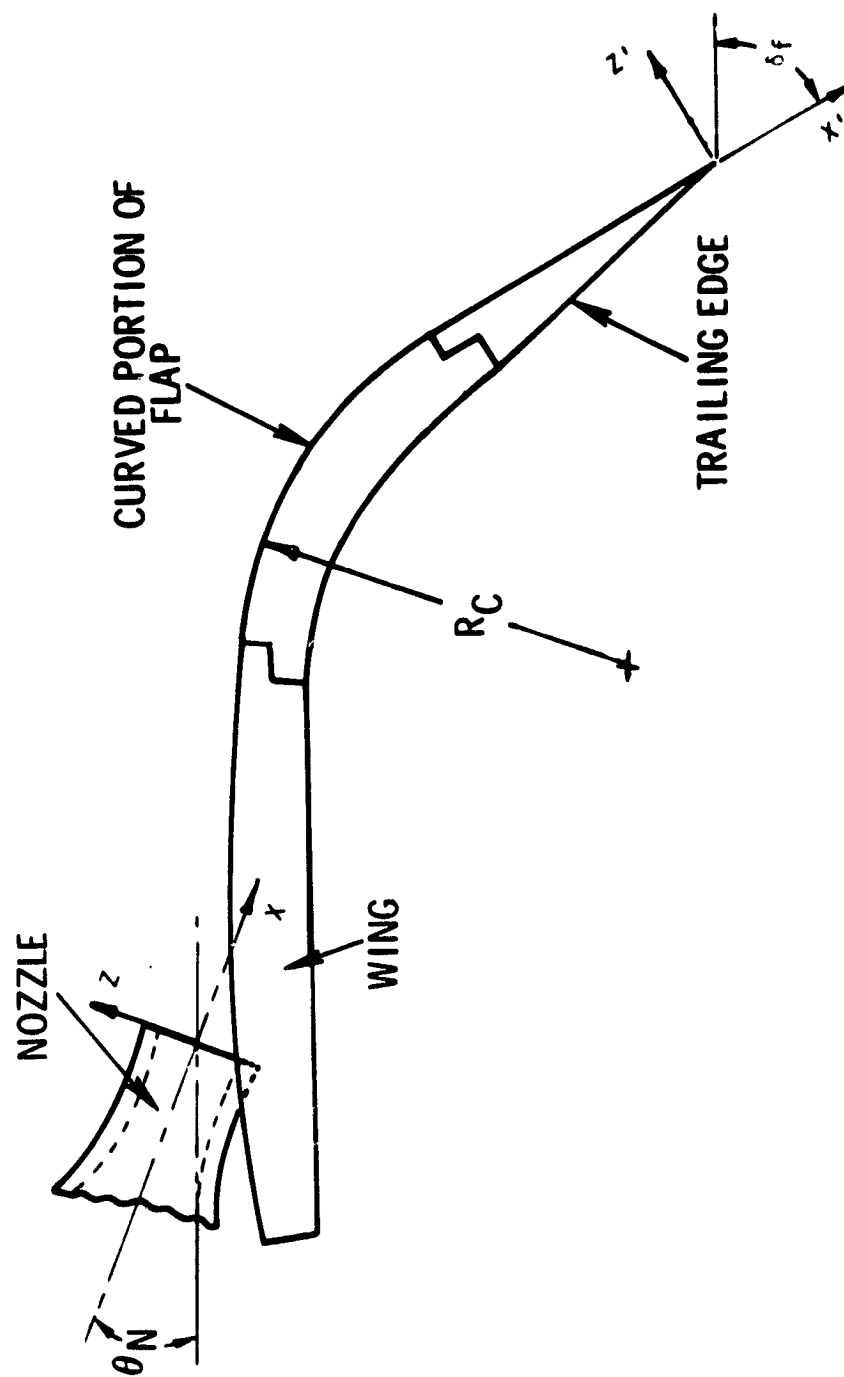


Figure 2 Model Schematic and Coordinate System

Basic Wing

Span	50.4 cm (20 in.)
Chord	15.24 cm (6 in.)
Flow length (from nozzle exit to start of curvature), L_w	8.05 cm (3.17 in.)

Curved Flap

Radius of curvature, R_c	7.62 cm (3.17 in.)
Flow length, L_{cf}	
30° Flap	3.25 cm (1.28 in.)
60° Flap	7.25 cm (2.85 in.)

Trailing Edge

Flow length, L_{te}	
30° Flap	10.46 cm (4.12 in.)
60° Flap	6.47 cm (2.55 in.)
Nominal chord length of wing/flap, C	15.24 cm (6 in.)

The flap angle was varied by changing the curved surface and the flap trailing edge simultaneously so that the total flow length, L_f , defined as the length along the surface from the nozzle exit to the trailing edge was constant at 21.77 cm (8.57 in.). Most of the tests were conducted with 30° flap angle, although 60° flap angle was used to evaluate the flap angle effect. The nozzle, nozzle location, and the wing elements can all be seen in figure 3, which shows the installation with the LV system. Another view, which shows the near-field microphone location and the nozzle with the screen at the nozzle exit, is shown in Figure 4.

Jet flow. The jet flow was provided by an air supply system consisting of a remote compressor and storage tank which can deliver clean, dry air at ambient temperature continuously up to 9.1 kg per second at a pressure of 2.1×10^6 N/m² through a 15.24 cm diameter line to the various test facilities. From this supply line, the air was supplied to the nozzle through regulators, plenum chambers and screens. Jet exit velocity was varied in these tests from 150 m/s. But most of the trailing edge wake flow measurements were obtained



Figure 3. Model Installation in LV Facility.

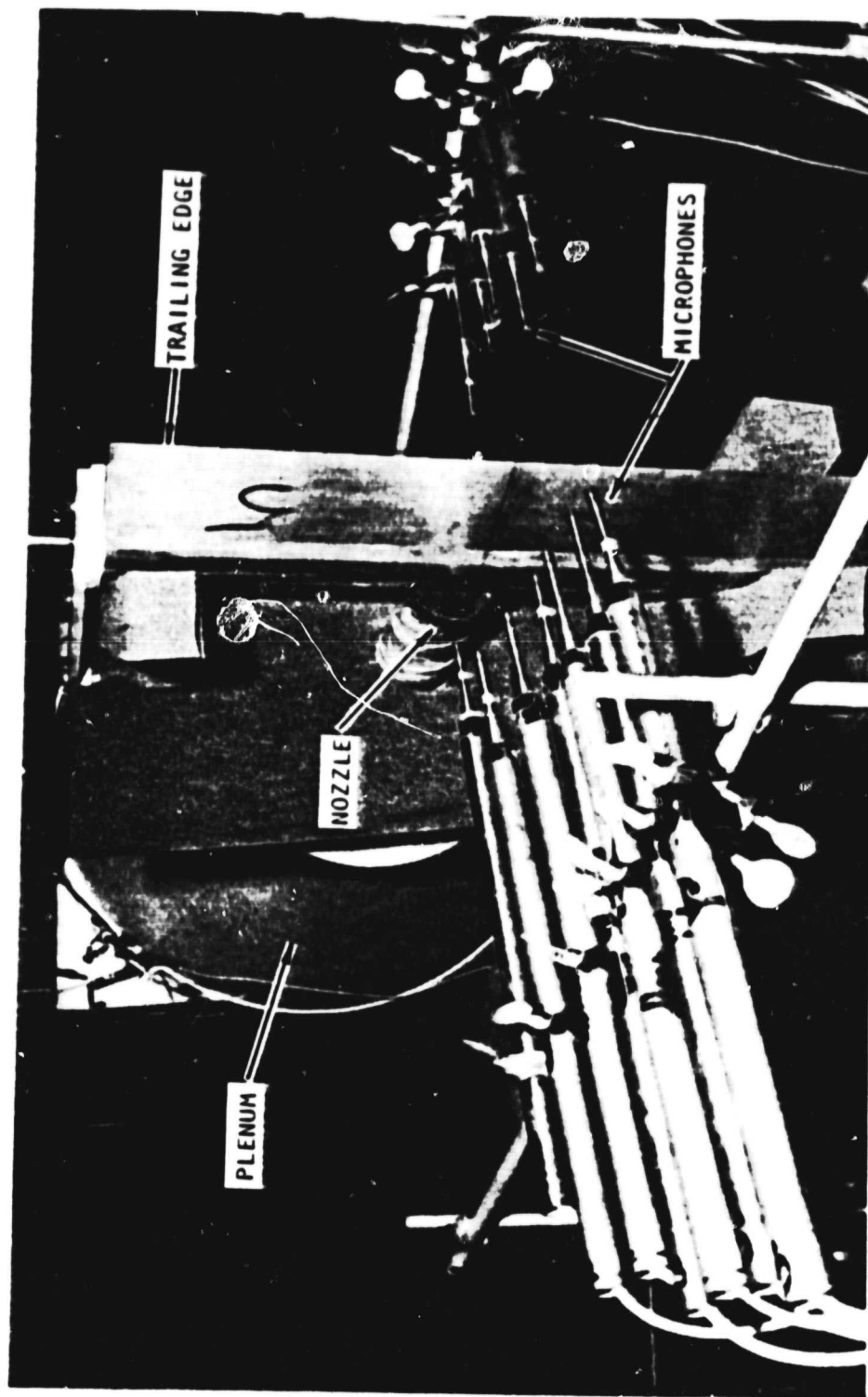


Figure 4 Model Installation with Near-Field Microphones

at a jet velocity of 180 m/sec, because this is the typical velocity of short-haul aircraft during takeoff and landing.

2.2 Propulsive Performance Measurements

The closed-circuit low speed wind tunnel located in the Lockheed-Georgia Research Laboratory was used to obtain the static propulsive performance data. The wind tunnel is shown schematically in Figure 5. The test section was approximately 0.76 m \times 1.09 m with a length of 1.22 m.

A three-component external strain-gauge balance installed below the tunnel floor was used to measure the USB model loads under static conditions. The balance was capable of measuring the longitudinal force (thrust or drag), transverse force (lift) and the pitching moment. The load capacity of the balance was adequate to measure the loads encountered by the blown-flap model.

The air jet to the nozzle was provided through a square plenum chamber of 22.86 cm \times 22.86 cm \times 90 cm attached directly to the nozzle as illustrated in figure 6. The air supply to the plenum chamber was through a 7.62 cm diameter trapeze just upstream of the balance. The downstream end of the trapeze was rigidly connected to the balance base. From this end of the pipe, the air was supplied to the plenum chamber through a 5.1 cm diameter flexible hose. The jet velocity was controlled by using a 5.1 cm automatically controlled valve. The air supplied to the nozzle exhausted on the wing surface down the center of the wind tunnel test section.

To measure the loads of the total system, the wing and plenum chamber were mounted vertically on the balance through the tunnel floor cutout. Loads of the nozzle alone (without wing/flap) were measured by removing the wing and flap from the tunnel.

The force data was acquired through an eight-channel data system controlled by the MAC-16 computer. The data was printed out in digital form

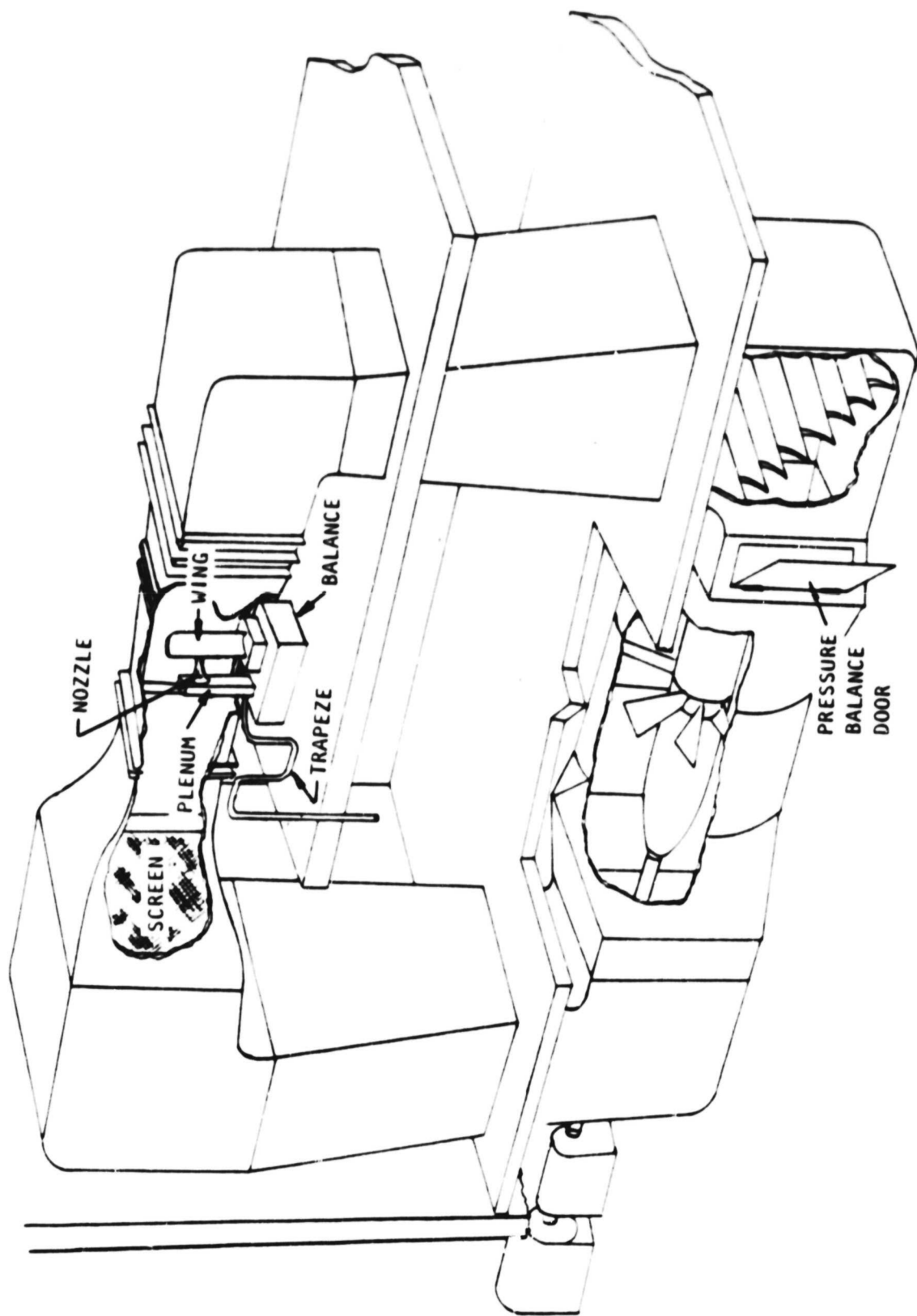


Figure 5. Schematic of Low-Speed Wind Tunnel

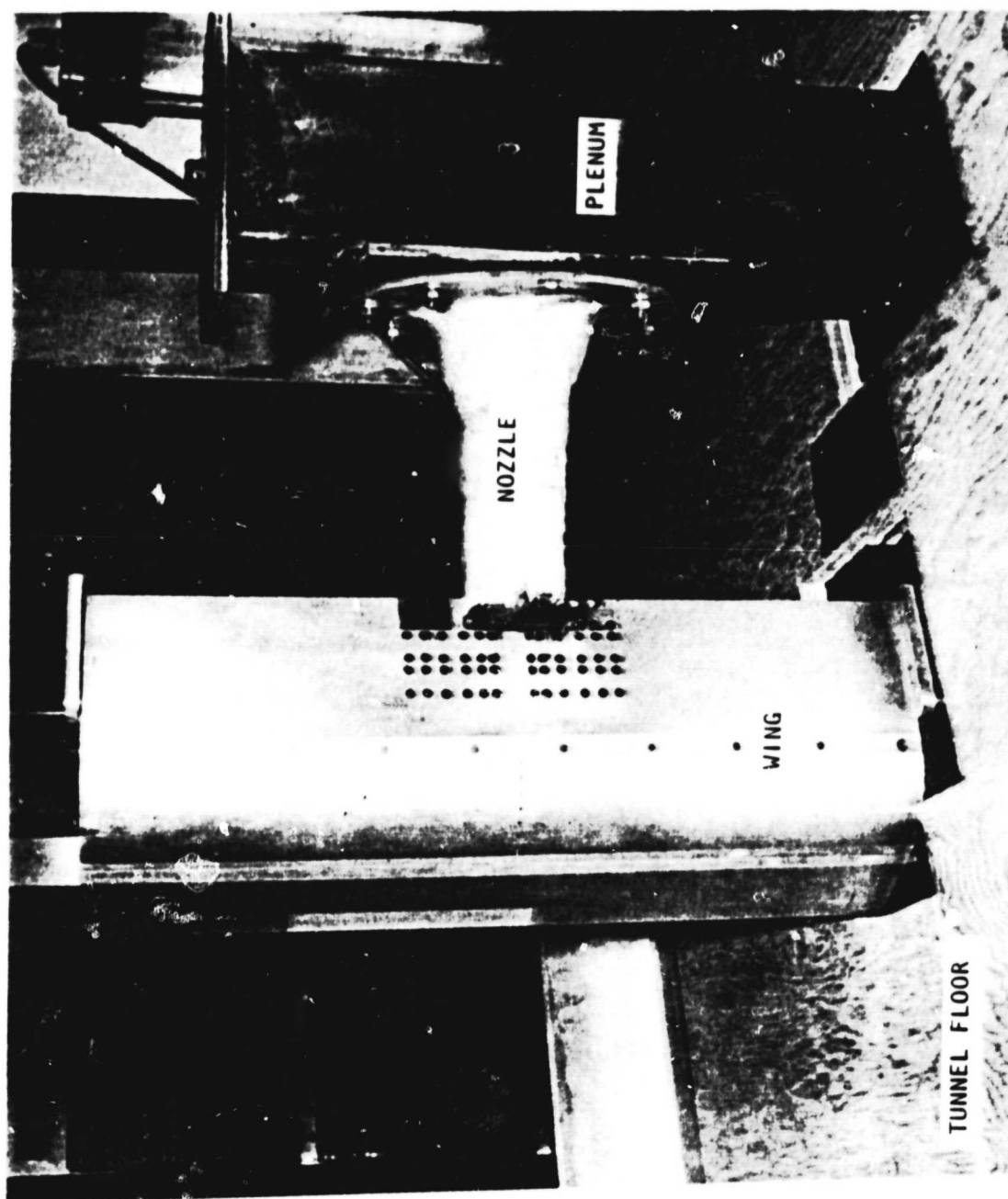


Figure 6. Model Installation in Wind Tunnel.

through a teletype printer and were reduced into lift and drag forces with the use of a desk calculator.

The total static force of the integrated USB system is generally less than the force generated by the nozzle alone due to the losses by surface friction and other effects. Thus, the propulsive efficiency, η , is defined as the ratio of the total force of the integrated system to the nozzle-alone force. This is given by

$$\eta = \frac{\sqrt{L_T^2 + D_T^2}}{\sqrt{L_N^2 + D_N^2}}$$

where L_T and D_T are the lift and drag forces of the integrated USB configuration and L_N and D_N are the lift and drag forces of the nozzle alone.

The flow-turning angle, δ_j , is defined as the angle between the drag force (thrust) and the total force of the USB system. This turning angle is calculated by using the following equation:

$$\delta_j = \tan^{-1} \frac{L_T}{D_T}.$$

The lift force, drag force, efficiency, and flow turning angles for different nozzle pressure ratios and flap angles are summarized in Table 1. Figure 7 is a polar plot illustrating the efficiency and turning angle for the USB configuration. These results indicate that the flow is turning along the surface fairly well. The efficiency increases as the jet velocity increases. In the operating velocity range of about 215 m/s, the efficiency is about 0.8, which is acceptable for the USB configuration.

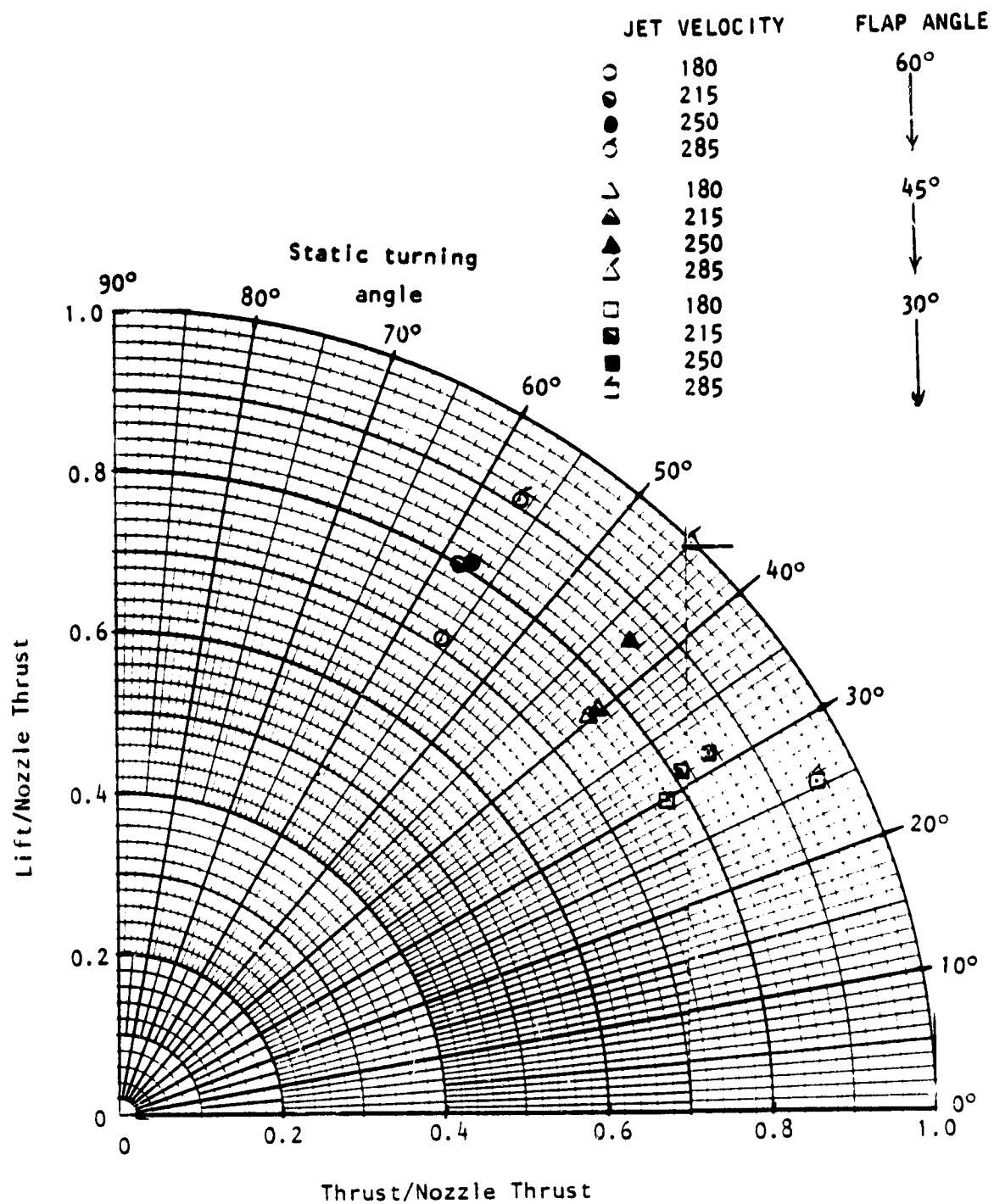


Figure 7. Static Propulsion Efficiency of the USB Model.

TABLE 1. STATIC PERFORMANCE OF USB MODEL

NPR H/P	Flap Angle, δ_f , Deg.	Lift, L N (lbs)	Thrust, T N (lbs)	Prop Efficiency η	Flow Def. Angle, δ_f , Deg.
1.22	--	14.1 (3.17)	35.8 (8.05)	Nozzle Alone	--
1.32	--	19.7 (4.42)	51.4 (11.55)		--
1.48	--	29.3 (6.58)	88.9 (15.48)		--
1.67	--	40.7 (9.15)	76.7 (17.25)		--
1.22	60	22.9 (5.15)	15.37 (3.46)	0.72	56.1
1.32	↓	37.5 (8.42)	23.0 (5.18)	0.80	58.4
1.48		51.4 (11.55)	32.8 (7.37)	0.81	57.4
1.67		68.2 (15.34)	44.3 (9.96)	0.93	57.0
1.22	45	20.0 (4.49)	21.7 (4.87)	0.76	42.6
1.32	↓	28.7 (6.45)	31.8 (7.14)	0.77	42.1
1.48		42.7 (9.59)	45.5 (10.24)	0.86	43.1
1.67		62.1 (13.97)	62.0 (13.93)	1.00	45.0
1.22	30	15.1 (3.39)	26.1 (5.87)	0.78	30.0
1.32	↓	23.4 (5.26)	38.1 (8.56)	0.81	31.6
1.48		33.6 (7.55)	54.1 (12.16)	0.85	31.8
1.67		34.8 (7.82)	69.5 (15.62)	0.95	25.8

2.3 Acoustic Measurements

Acoustic tests were conducted to study the variation of magnitude, spectra, and directivity of radiated sound with jet exit velocity and flap angle. Near-field noise was measured with microphones located just outside the flow in the Aeroacoustic Flow Facility. Far-field noise was measured in the anechoic room. The details of the facilities and of the measurements are given in this section.

Far-field noise measurements. The far-field noise was measured in the Lockheed-Georgia anechoic room shown in figure 8. The walls of this anechoic room are covered with specially designed acoustic wedges to provide an anechoic environment at all frequencies above 200 Hz. The dimensions of the anechoic room are 6.71 m \times 6.10 m \times 8.53 m high, giving a free-field volume of 265 m³. A "cherry picker" crane in the room provides access to the instrumentation and to the test installation. The crane is stowed under an acoustically treated shelter during testing. The air supply is the same as that described before. The plenum chamber between the nozzle and the air supply pipe was extended to the center of the room to allow noise measurements to be made in the forward and aft quadrants. This plenum was wrapped with acoustic foam to prevent noise reflections by the pipe and the external transmission of upstream noise through the plenum walls.

Six B&K 0.635 cm (1/4 inch) free-field microphones (Model 4135) with protective grids and B&K Model 2619 preamplifiers were used to measure far-field sound. These microphones were mounted on a 2.44 m (8 ft.) radius arch at 15° intervals as shown in figure 9. The microphones cover a polar angle between 60° and 135° from the nozzle inlet axis. All the microphones were frequency calibrated using an electrostatic-actuator calibrator swept through the entire frequency range of interest (from 50 Hz to 80 KHz).

The microphone signals were analyzed in real time as one-third octave band spectra using a General Radio Model 1921 Real-Time Analyzer and recorded in digital form on a magnetic tape by a Kennedy incremental tape recorder. This data was further reduced using a digital computer whereby appropriate microphone corrections and atmospheric attenuation were incorporated. The microphone corrections include the free-field corrections, the pressure response correction, and the daily piston phone calibration corrections. To obtain "lossless" acoustic data, the atmospheric attenuation due to the propagation from the source to the microphone was removed. The complete data acquisition and reduction systems are illustrated schematically in figure 10.

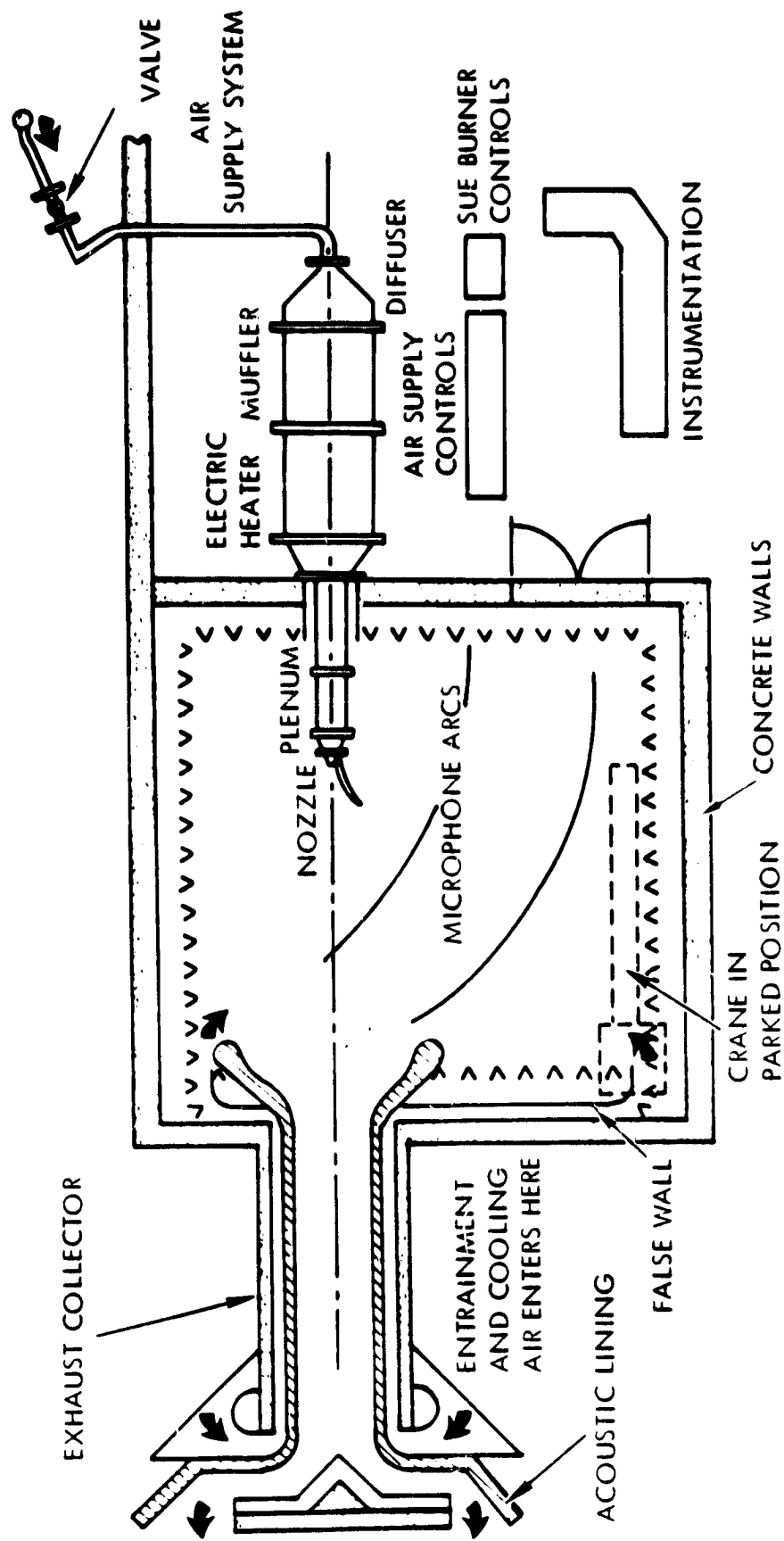


FIGURE 8(A). ANECHOIC ROOM SCHEMATIC



FIGURE 8(B). ANECHOIC ROOM FACILITY

RECEIVED 10/28/52
OF POOR QUALITY

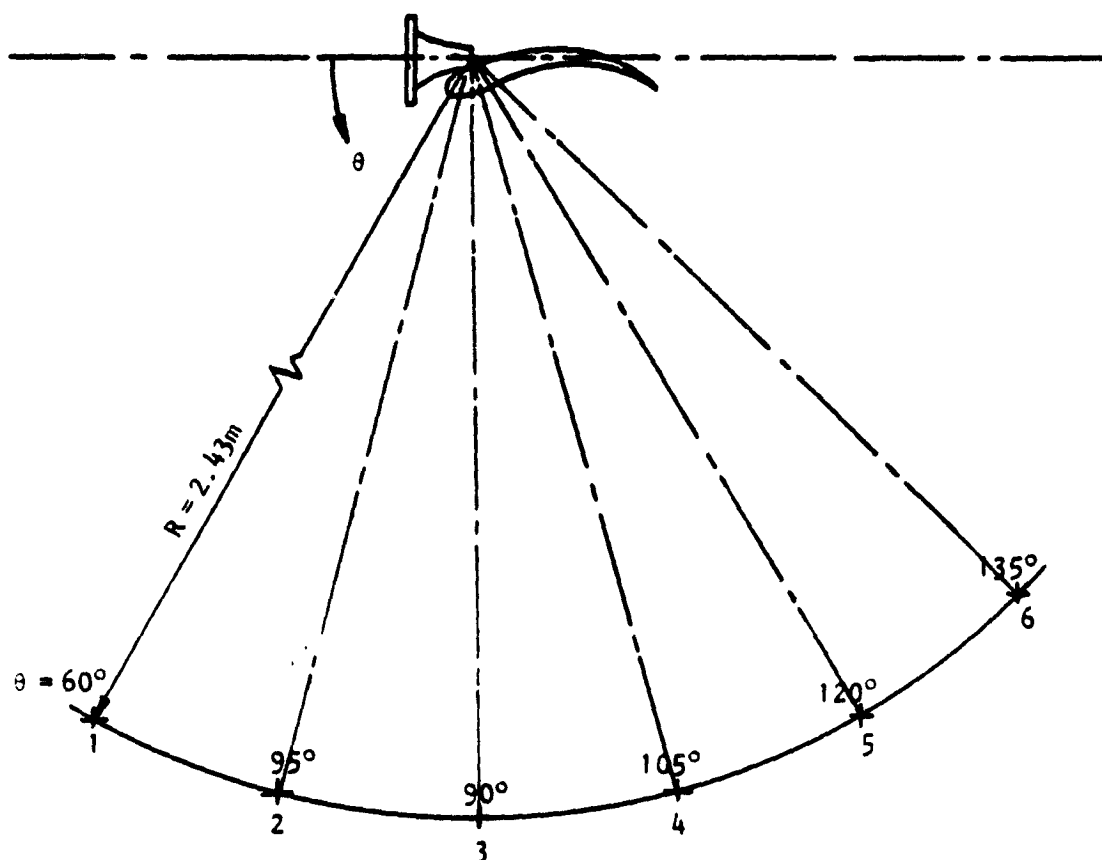


Figure 9. Microphone Locations for Far-Field Noise Measurements.

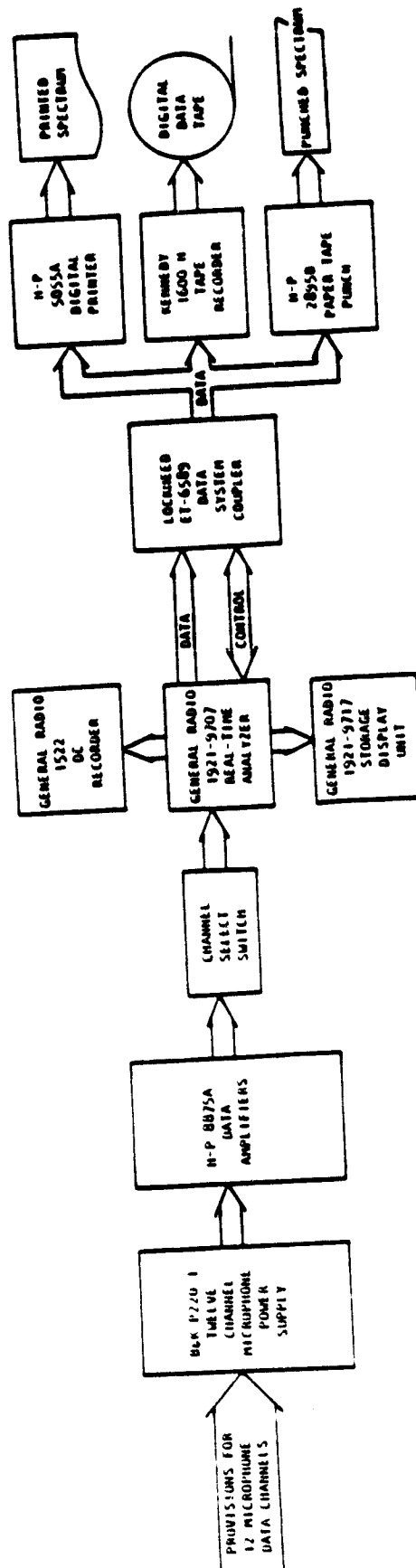


FIGURE 10(a). ACOUSTIC DATA ACQUISITION SYSTEM

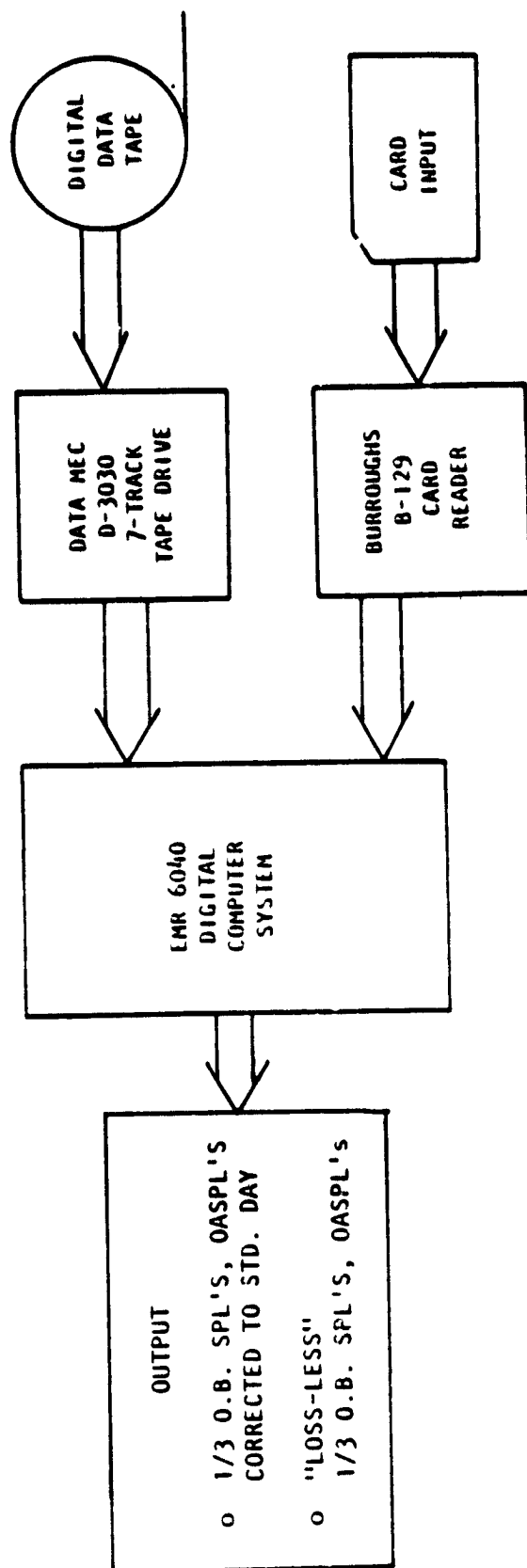


Figure 10(b). Acoustic Data Reduction System.

The following parameters were varied in the far-field acoustic tests:
 (a) flap deflection angle, (b) jet exit velocity, (c) azimuthal angle, and
 (d) jet flow turbulence. The test configurations are tabulated in Table 2.

TABLE 2 ACOUSTIC TEST CONFIGURATIONS

δ_f	Nom. Jet Velocity (m/s)	Mic. Arch Angle (Azimuthal Angle)	Remarks
30°	180, 215, 250, 285	90° (Flyover)	Screen was installed between the flanges of nozzle and plenum chamber
↓	↓	60°	
		30°	
		0° (Wing Plane)	
		90°	
		30°	
45°		90°	
↓		30°	
60°		90°	
↓	↓	30°	

Flap deflection angle was varied by replacing the curved part and the flat trailing edge segment of the wing. These two parts of the wing were manipulated to keep the radius of curvature and the total flow length (length between the nozzle exit to the flap trailing edge measured along the wing surface) constant for all flap angles.

Jet exit velocity was varied by changing the nozzle pressure ratio with an air supply control valve upstream of plenum chamber.

The azimuthal angle was varied by rotating the model about the nozzle axis.

Jet turbulence was varied by introducing a wire mesh between the nozzle flange and the plenum downstream flange. The change in the flow turbulence due to the introduction of the screen in the nozzle, however, was found to be negligible as discussed in the later sections.

The variation of OASPL with jet exit velocity, the directivity of the OASPL, and the one-third octave band spectra of the far-field noise are shown in figures 11 - 13. The effects of the screen and the flap angle on OASPL in the flyover plane are negligible as illustrated in figure 11. The directivity of OASPL in any given azimuthal plane is independent of polar angle for low jet velocity, but for higher jet exit velocities, the OASPL increases as the polar angle increases. This is illustrated in figure 12. The one-third octave band spectra in figure 13 illustrates that only the high frequency SPL varies as the polar angle varies. These results are discussed further in the analysis section.

Near-field noise measurements. Near-field noise was measured in the Aeroacoustic Flow Facility located in the Lockheed-Georgia Research Laboratory. This facility was developed to measure the detailed flow properties of small-scale static blown-flap models. Air to the plenum is supplied through a 5.08 cm regulating valve and a calibrated nozzle flow meter. The plenum contains an end-baffled perforated tube inlet, a 15.24 cm thick honeycomb baffle and two smooth conical transitions, the last of which matches the inside of the nozzle. A static pressure tap and a thermometer are provided for measurement of plenum conditions.

Twelve 0.635 cm (1/4 in.) B&K microphones (Model 4136), six below and six above the wing, mounted in the mid-span plane just outside the flow, were used to measure the near-field noise. The microphone positions with respect to the wing and flap are shown in figure 14. The exact locations of the microphones are given in Table 3. A photograph showing the model with microphones is shown in figure 4. The microphone system was calibrated with a piston phone before each day's testing.

TABLE 3 MICROPHONE LOCATIONS FOR NEAR-FIELD
PRESSURE SPECTRA MEASUREMENTS

δf	Initial Turbulence	Microphone	X'	Z'
30°	No Screen	1	NOZ.	2.54*
		2	-15.24	6.35*
		3	- 1.27	8.89
		4	1.91	10.00
		5	7.62	11.43
		6	11.43	12.70
		7	- 7.62	- 2.54**
		8	- 1.27	- 2.54
		9	1.91	- 2.06
		10	7.62	- 5.24
		11	15.24	- 7.30
		12	- 7.62	7.14
30°	Screen	1	NOZ.	2.54*
		2	-15.24	6.35*
		3	- 1.26	7.78
		4	1.91	10.00
		5	7.62	11.43
		6	11.43	12.70
		7	- 7.62	- 2.54*
		8	- 1.27	- 2.54
		9	1.91	- 2.06
		10	7.62	- 5.24
		11	15.24	- 7.30
		12	- 7.62	7.14
60°	No Screen	1	NOZ.	2.54*
		2	-13.72	5.08**
		3	- 1.27	8.26
		4	1.91	13.34
		5	7.62	16.19
		6	11.43	18.42
		7	- 7.62	- 2.54**
		8	- 1.27	- 2.54**
		9	1.91	- 2.54
		10	7.62	- 5.56
		11	11.43	- 7.30
		12	- 6.48	8.41
		1A	30.48	28.73
		2A	15.24	20.00
		6A	22.86	22.70
		7A	30.48	-17.78
		10A	15.24	-10.32
		11A	22.86	-13.34

*Measured from the nozzle lip. **Measured normal to the surface.

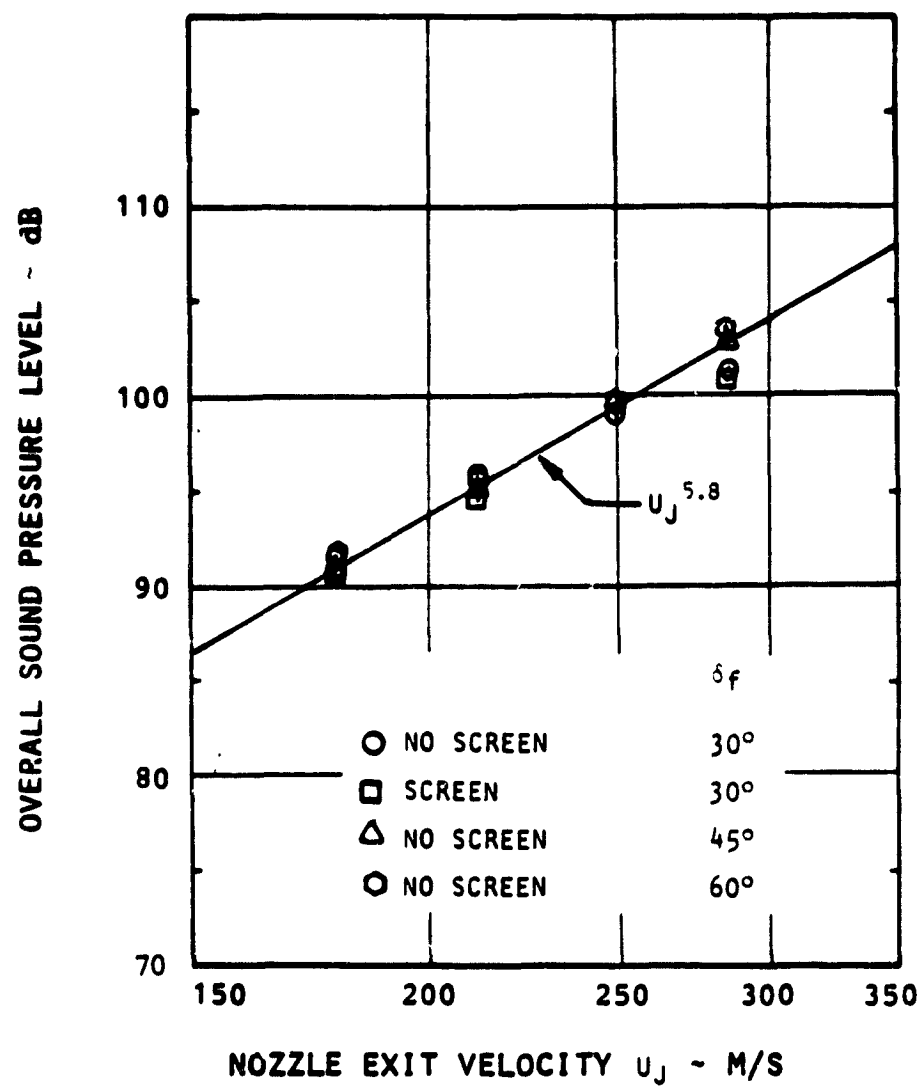


Figure 11. Variation of OASPL with Jet Velocity
 $\phi = 90^\circ$, $\theta = 60^\circ$, Radius = 2.4 m.

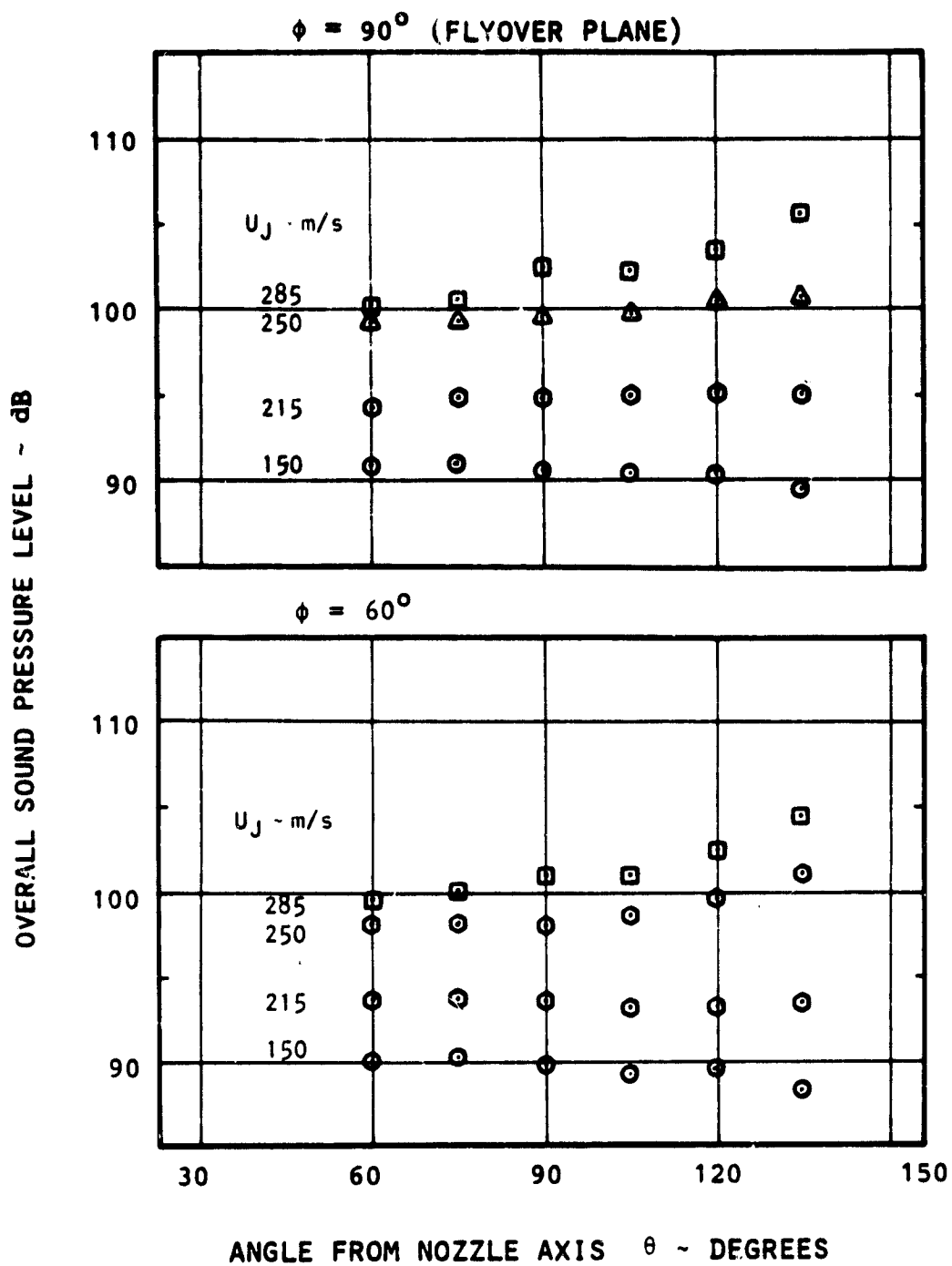


Figure 12. Variation of OASPL with Polar Angle, $\delta_f = 30^\circ$.

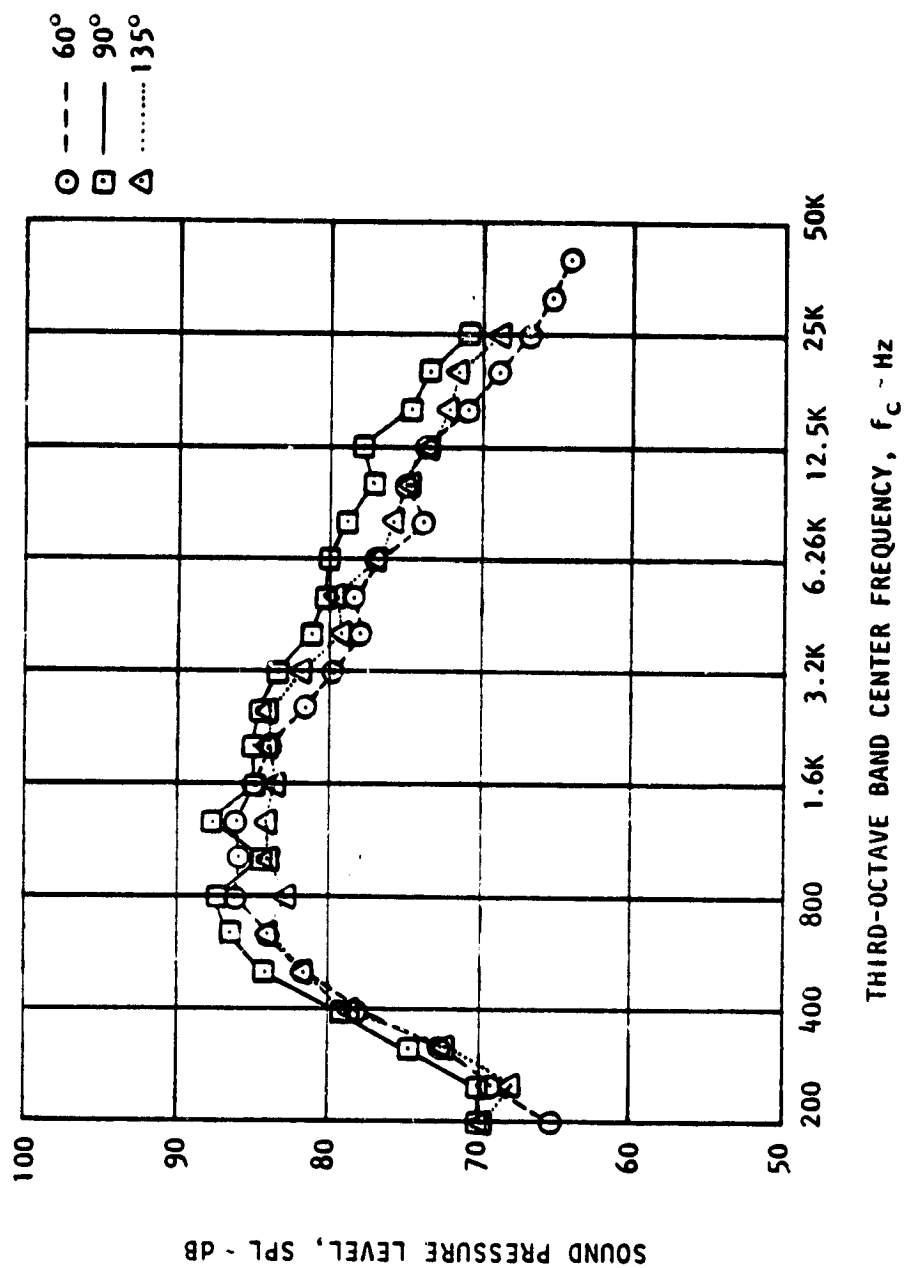


Figure 13. Spectral Distribution of Radiated Noise;
 $U_J = 212$ m/s, $\delta f = 30^\circ$, $\phi = 90^\circ$.

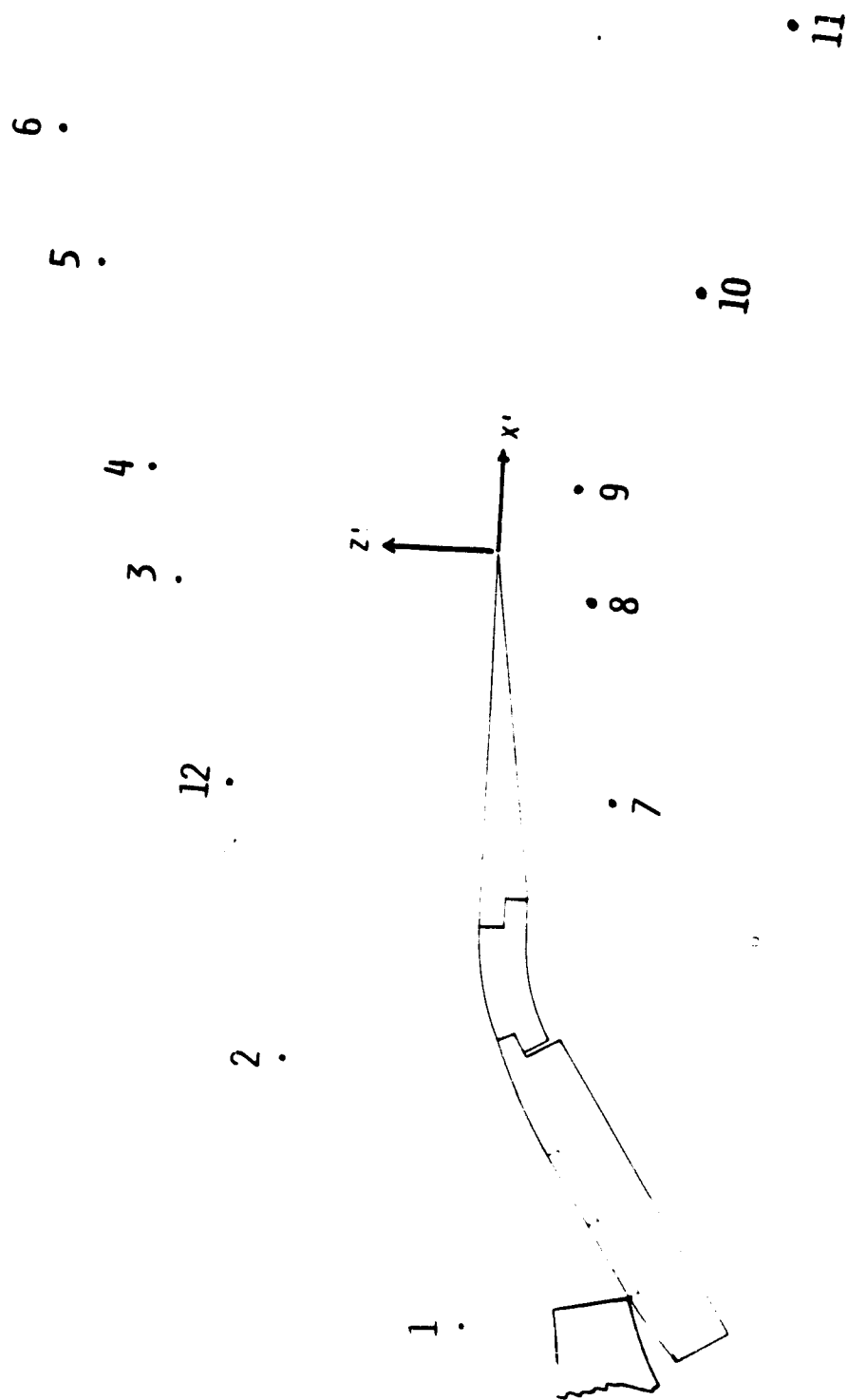


Figure 14. Near-Field Microphone Layout.
(a) 30° Flap Angle.

1A

6A

2A

6

5

4

3

12



9

8

7

10

11

10A

11A

Figure 14. Near-Field Microphone Layout.
(b) 60° Flap Angle.

7A

The noise data from the microphones, after signal level adjustments through the attenuators, were recorded on magnetic tape in the FM mode at 152.4 cm/sec. (60 ips). The near-field noise data acquisition system is shown in the block diagram of figure 15.

The recorded data was analyzed as one-third octave spectra using General Radio Real Time Analyzer (Model 1921) and a D.C. Recorder (Model GR1522). The block diagram of the data reduction system is shown in figure 16.

Effects of flap angle and initial flow turbulence (screen at the nozzle exit) are in the high frequencies as shown in figure 17. The complete discussion is provided in the analysis section.

2.4 Flow Measurements

Trailing edge wake flow characteristics were measured in the aero-acoustic flow facilities where the near-field noise was measured. The measurements consisted of mean and fluctuating velocity profiles and space-time correlations of fluctuating velocities. Most of the measurements were for 180 m/sec. jet velocity and 30° flap angle. However, the jet velocity, jet turbulence, and flap angle on the wake flow characteristics were also investigated. Hot-wire anemometry was used extensively; but the laser velocimeter (LV) was also used to obtain some flow profiles and correlations to evaluate the relative merits of the LV and hot-wire systems for measurement of the flow properties of blown flap configurations.

Hot-wire measurements. The basic system of hot-wire anemometry used in measuring the flow characteristics consisted of one-, two-, or four-channel linearized constant temperature anemometers with appropriate five-micron diameter gold plated wire probes of miniature configuration. A single hot-wire (one-channel system) measures the sum of two orthogonal velocity components. Since the mean velocity in the lateral (y) and transverse (z) directions is small compared to the velocity in the longitudinal (x) direction, a single wire oriented parallel to the trailing edge is used to

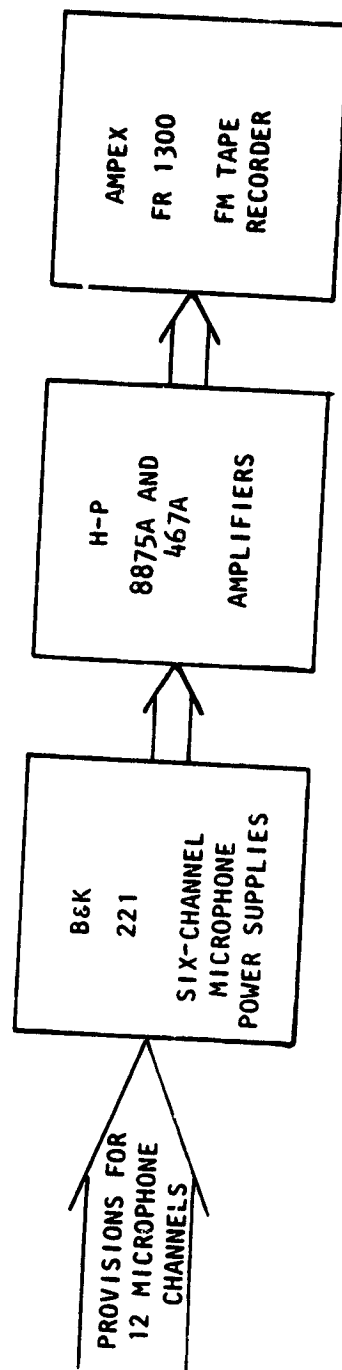


FIGURE 15. NEAR-FIELD PRESSURE DATA ACQUISITION SYSTEM.

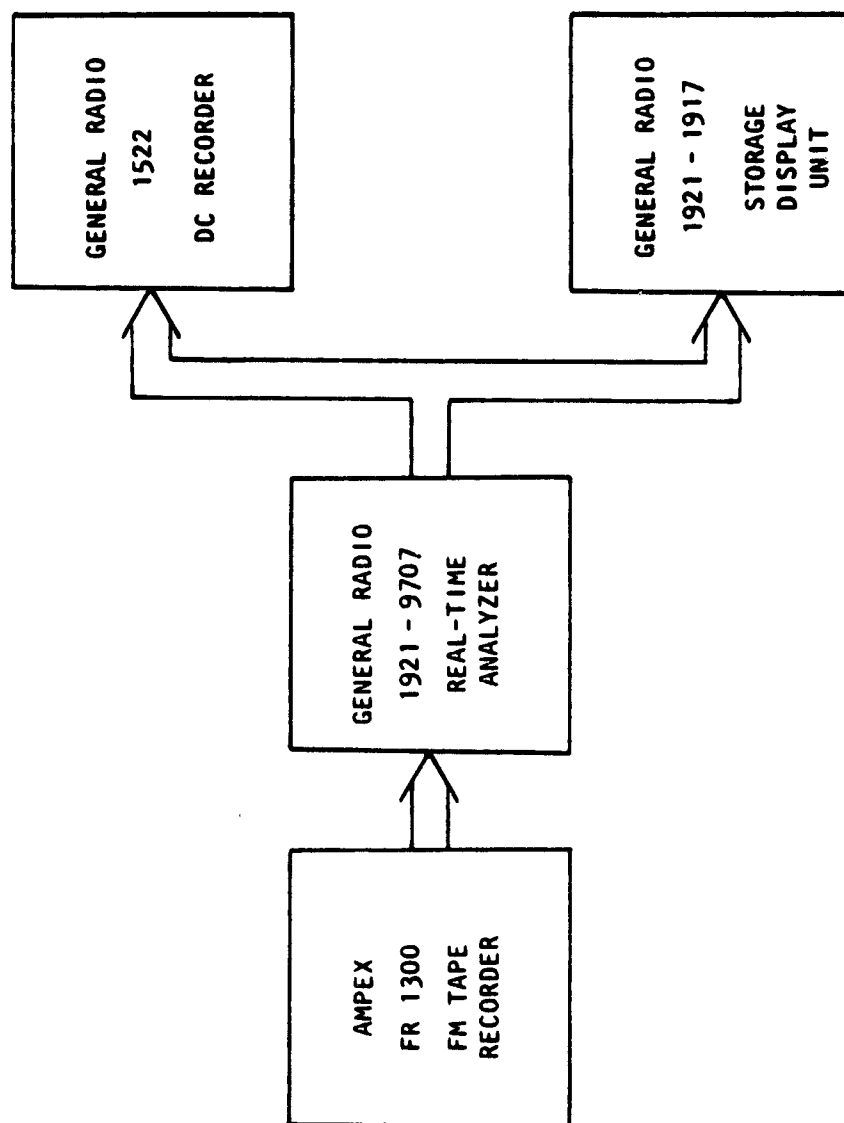


FIGURE 16. NEAR-FIELD PRESSURE SPECTRUM DATA PROCESSING SYSTEM.

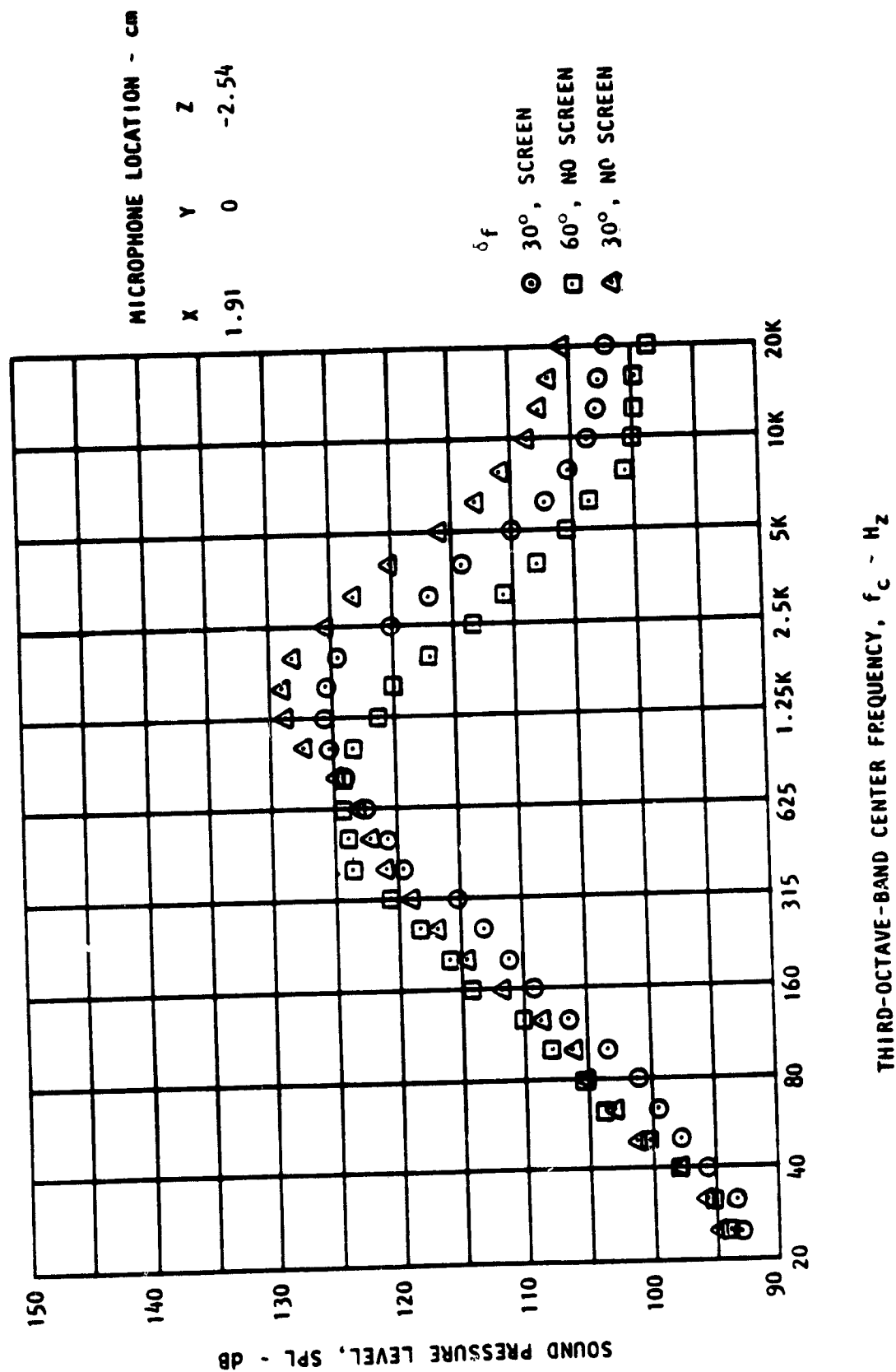
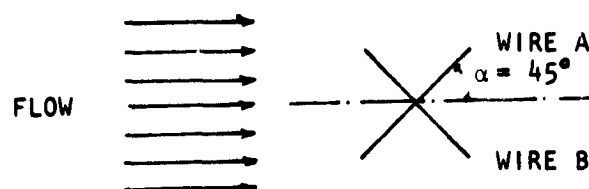


Figure 17. Typical Near-Field Noise Spectra.

measure the velocity profiles. A cross hot-wire (two wires oriented appropriately) with an analog adder and subtractor was used to resolve the two orthogonal velocity components. Single-wire data were compared with the cross-wire data to evaluate the relative magnitude of the velocity components and to determine if a single-wire would be acceptable. Space-time correlations of longitudinal and transverse velocity components were measured using a four-channel system with two crossed wires at two locations. The lateral velocity component, v , is not used in correlations, since this (v) is very small compared to u and w .

Calibration. Each day's testing was started with a system calibration and calibration checks were made during the day when it was deemed necessary. The calibrations were made in a uniform flow field (core flow) of a separate calibration jet of known velocity. The plenum pressure and the temperature of the jet were monitored during calibration and temperature corrections were applied.

The probe was aligned in the calibration flow as it would be in the test flow; single wires were normal to the flow, and cross-wire probes were oriented with the plane of the wires parallel to the flow and with each wire at 45° to the mean flow direction as shown in the sketch below.



Assuming the typical yaw function, $f(\alpha) = \cos \alpha$, yields a simple sum and difference solution for the velocity components (ref. 3).

$$U(t) = \frac{V_{oA}(t) + V_{oB}(t)}{2 \cos 45^\circ} = \frac{V_{oA}(t) + V_{oB}(t)}{\sqrt{2}}$$

$$W(t) = \frac{V_{0B}(t) - V_{0A}(t)}{2 \sin 45^\circ} = \frac{V_{0B}(t) - V_{0A}(t)}{\sqrt{2}}$$

A simple analog adder and subtractor built at Lockheed was used to extract the velocity components from the cross-wire signals as indicated above. By rotating the plane of the wire by 90° about the mean flow axis, the lateral component $V(t)$ was obtained in the place of $W(t)$. Linearization of the hot-wire system was accomplished by trial and error in the manner recommended by DISA Electronics.

Positioning. To position and align the probe accurately in the steep velocity gradients of the wake flow and to move the probe in the longitudinal and transverse directions, a mount consisting of two orthogonal lathe beds was used. The screw drives of the lathes provided accurate measures of position changes relative to the trailing edge in the midspan plane. Accurate remote or automatic positioning would be prohibitively expensive and therefore the positioning was done manually. Care was taken to preclude the adverse effects of backlash.

Transverse movements for cross-correlations were made using a micrometer drive from a microscope stage. Other, less critical, lateral positioning was accomplished by clamping the probe holder on the lateral probe support at the required position; adjustment was provided simply by movement of the clamp.

Mean and fluctuating velocity profiles. Figure 18 shows a schematic diagram of the instrumentation used to acquire the velocity and the turbulence intensity profile data. DISA 55M-System anemometers with DISA 55M25 Linearizers were used in obtaining the mean and fluctuating components sensed by the hot-wire probes. When cross-wires were used, a signal processor (adder and subtractor) was used as shown in figure 18 to resolve the orthogonal velocity components. Linearizer output gain was adjusted during calibration to obtain convenient signal levels. Mean velocity and turbulence intensity profile data were manually recorded from voltmeters. The data were corrected

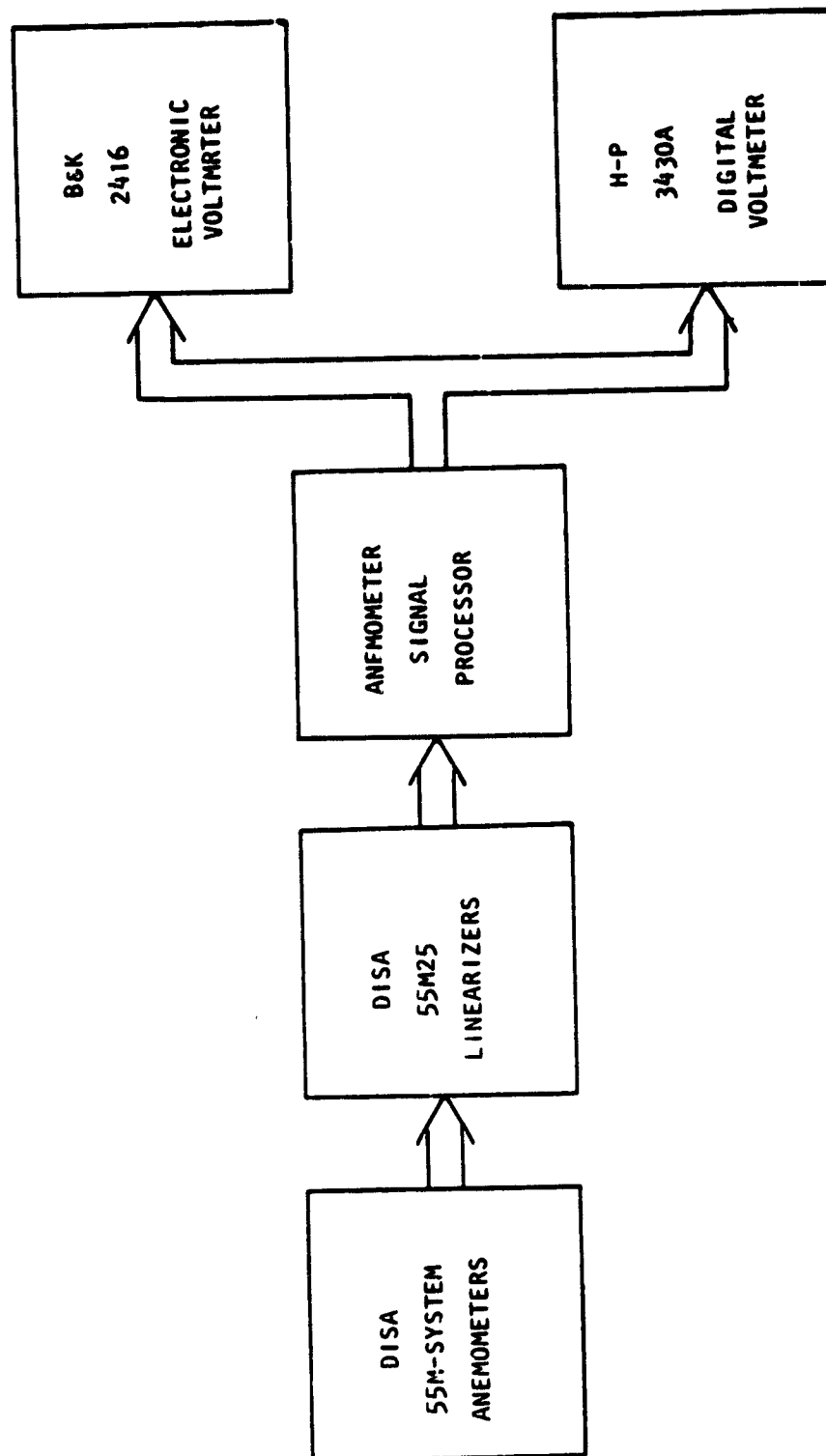


FIGURE 18. VELOCITY PROFILE DATA ACQUISITION SYSTEM, HOT-WIRE.

for flow temperature variations using the method described in reference 3. The measurement locations for the flow profiles are shown in Table 4.

Mean velocity and turbulence intensity profiles obtained from a single hot-wire were compared with the longitudinal velocity component measured from a cross-wire probe in figure 19. The mean velocity profiles are very similar as can be seen in figure 19(a). The difference in the turbulence intensities, however, as measured by the two probes is clear in figure 19(b). This illustrates that the traverse component of fluctuating velocity is also important, and therefore the cross-wire probe was used to measure the turbulence structure in the wake.

To vary initial jet turbulence, preliminary tests were conducted by introducing a screen mesh between the nozzle flange (inlet) and plenum flange. As illustrated in figure 20, jet Mach number, wake mean velocity profile, and wake turbulence intensity profile were not affected by the presence of the screen. This is due to negligible flow velocity at the nozzle entrance where the screen was located. Therefore, the screen was installed at the nozzle exit to study the effects of initial turbulence on wake flow characteristics.

Fluctuating velocity correlations. Space-time correlations of the fluctuating velocities in the trailing edge wake were measured using two cross-wires with two two-channel anemometer and linearizer systems, as shown schematically in figure 21(a). In addition to the use of DISA 55M-55M25 system used in the velocity profile measurements, a DISA 55D01 anemometer with a DISA 55D10 linearizer was used as a second two-channel system. These two different systems were used primarily because of their availability. Even though these are different models, their performance characteristics are essentially the same. However, potential phasing difficulties between the two models were eliminated by overall system calibration. Phasing calibration was done by firing a pistol at a location equally distant from the two cross-wires which were oriented to sense the shock. The resulting impulse responses were recorded on the tape and read from the tape into the Spectral Dynamics SD360 Digital Signal Processor for evaluation of the overall system

TABLE 4 MEAN AND FLUCTUATING VELOCITY MEASUREMENTS

Flap Angle δ_f	Jet Velocity U_j (m/sec)	Initial Turbulence	Hot-Wire Location (cm)			
			x	y	z	
30°	180	No Screen	1.91	0	0 - 12	Single Wire
			7.62	0		
			1.91	5.08		
			1.91	0		Cross Wire
			7.62	0		
			1.91	2.0		
			-1.27	0		Cross Wire
			3.82	0		
			7.62	0		
			11.43	0		
15.24	0					
1.91	1.91	Cross Wire				
1.91	3.81					
	5.08					
			7.62			
	180					
	150			0		
	215	No Screen			Effect of Jet Velocity, Initial Turbulence, and Flap Angle	
30°	180	Screen	1.91			
60°		No Screen	-1.27			
			1.91			
			3.81			
60	180	No Screen	7.62	0	0 - 12	

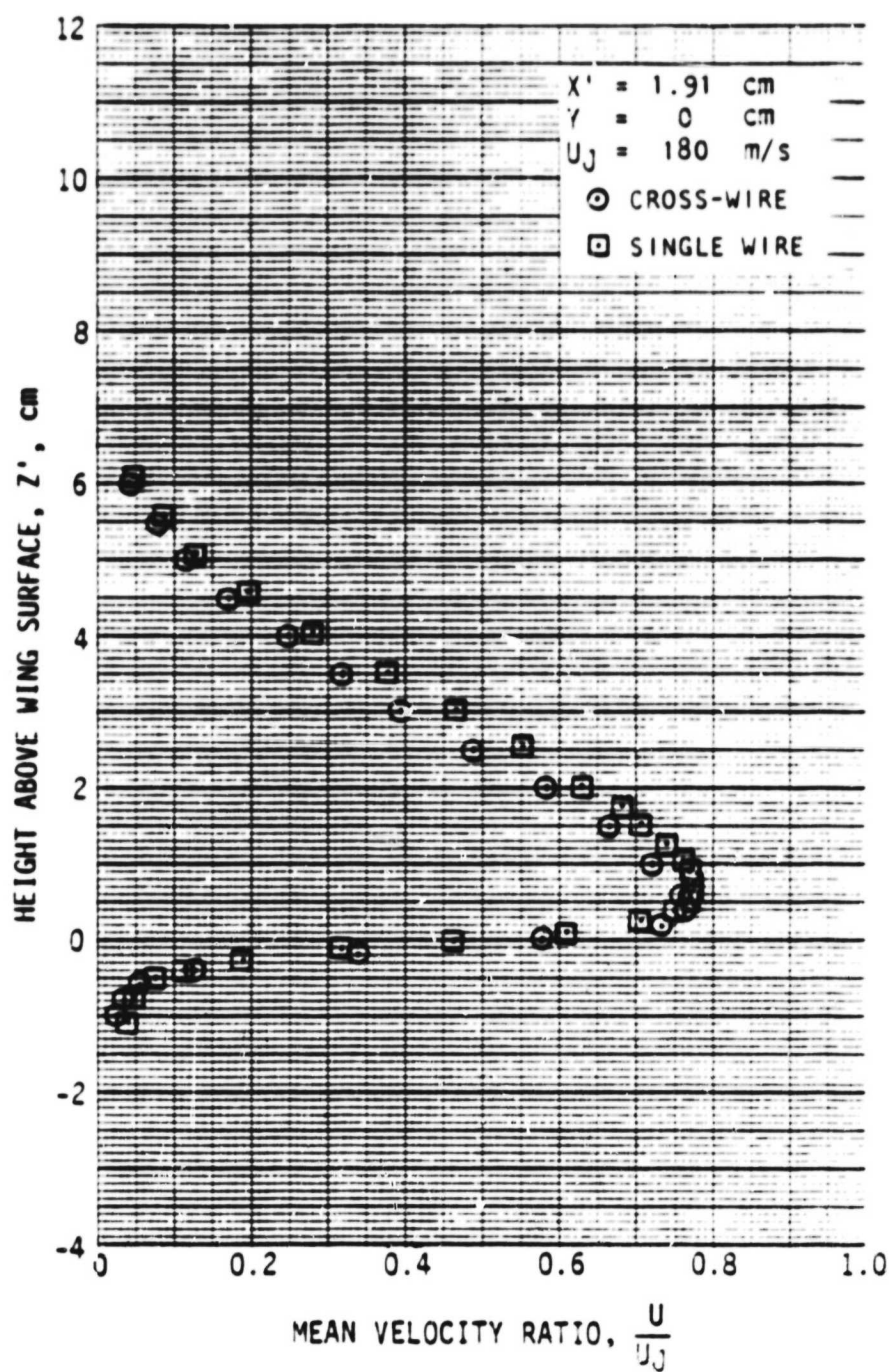


Figure 19. Comparison of Single-Wire and Cross-Wire Data.
 (a) Mean Velocity, Longitudinal Component.

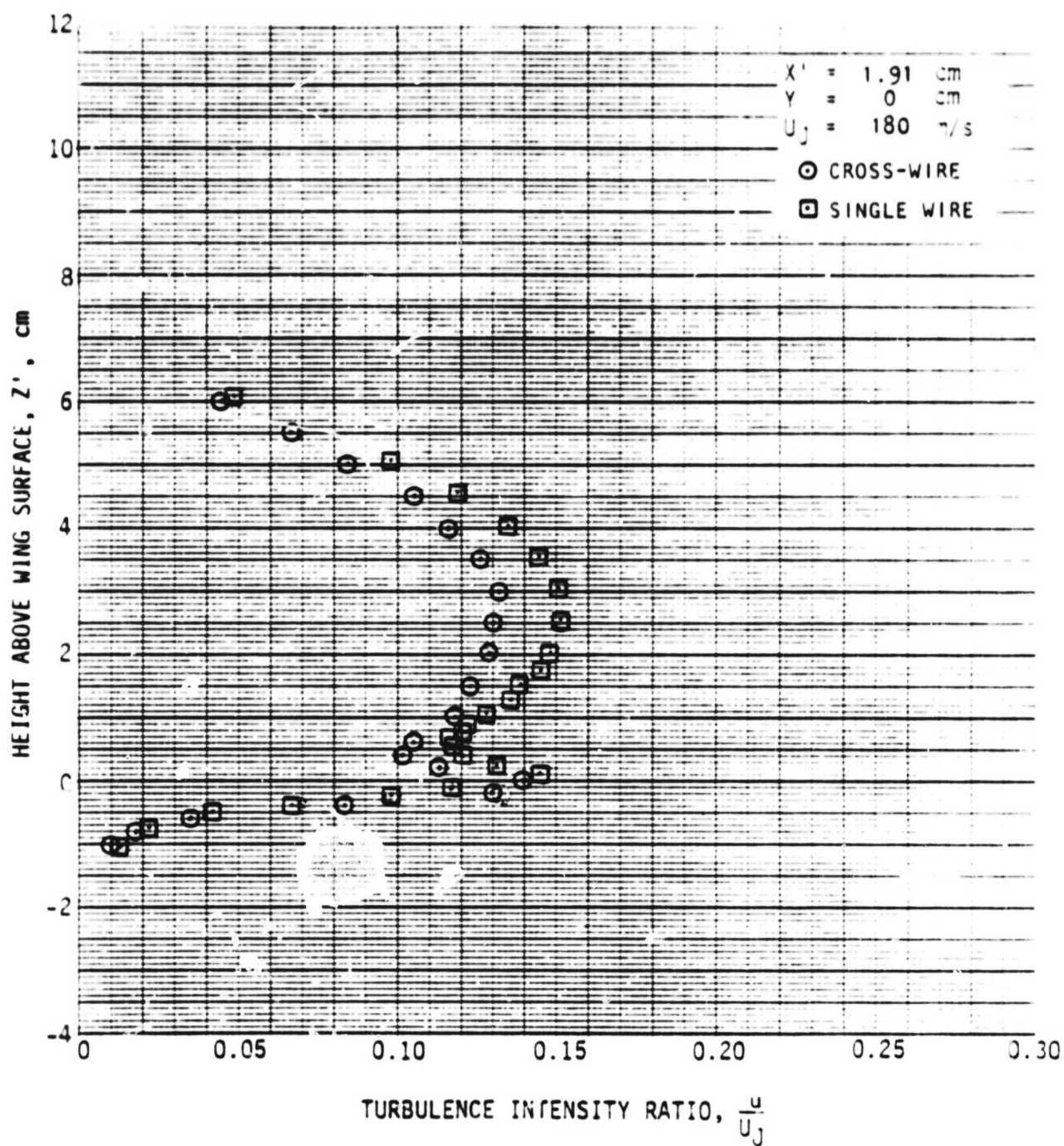
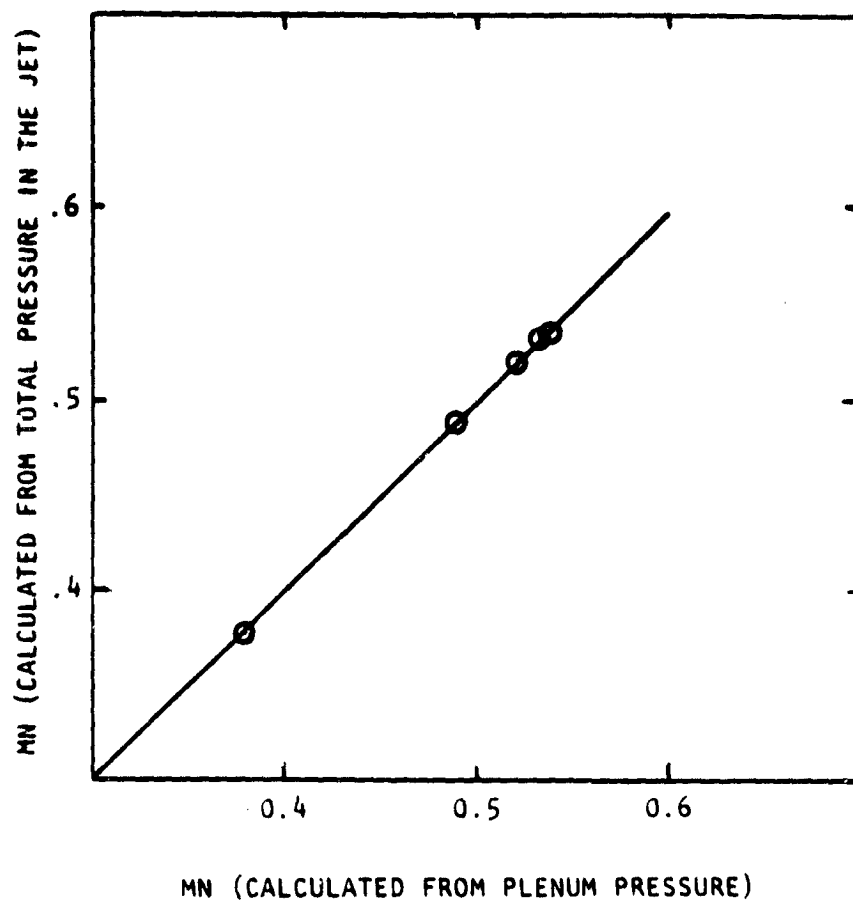
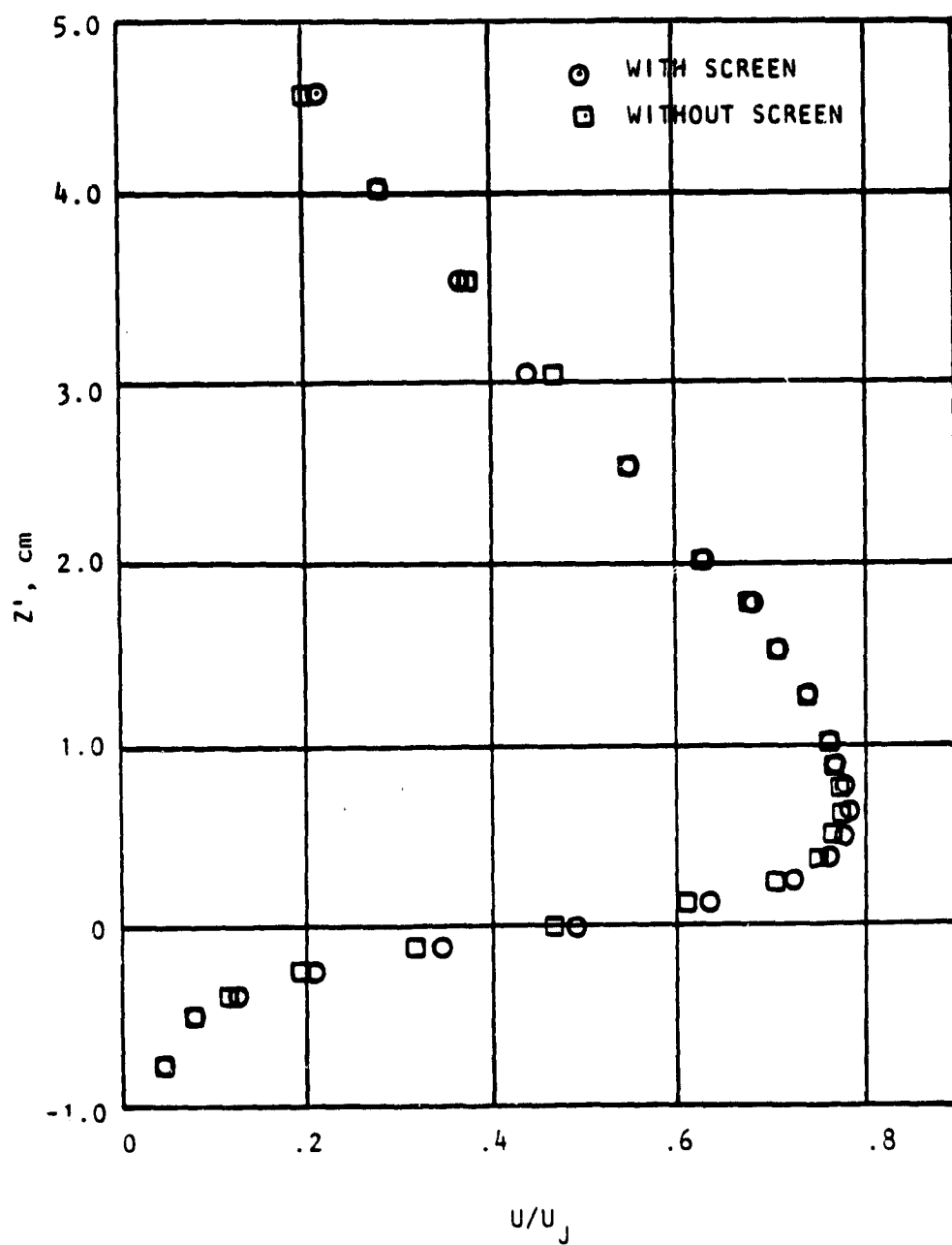


Figure 19. Comparison of Single-Wire and Cross-Wire Data.
 (b) Turbulence Intensity, Longitudinal Component.



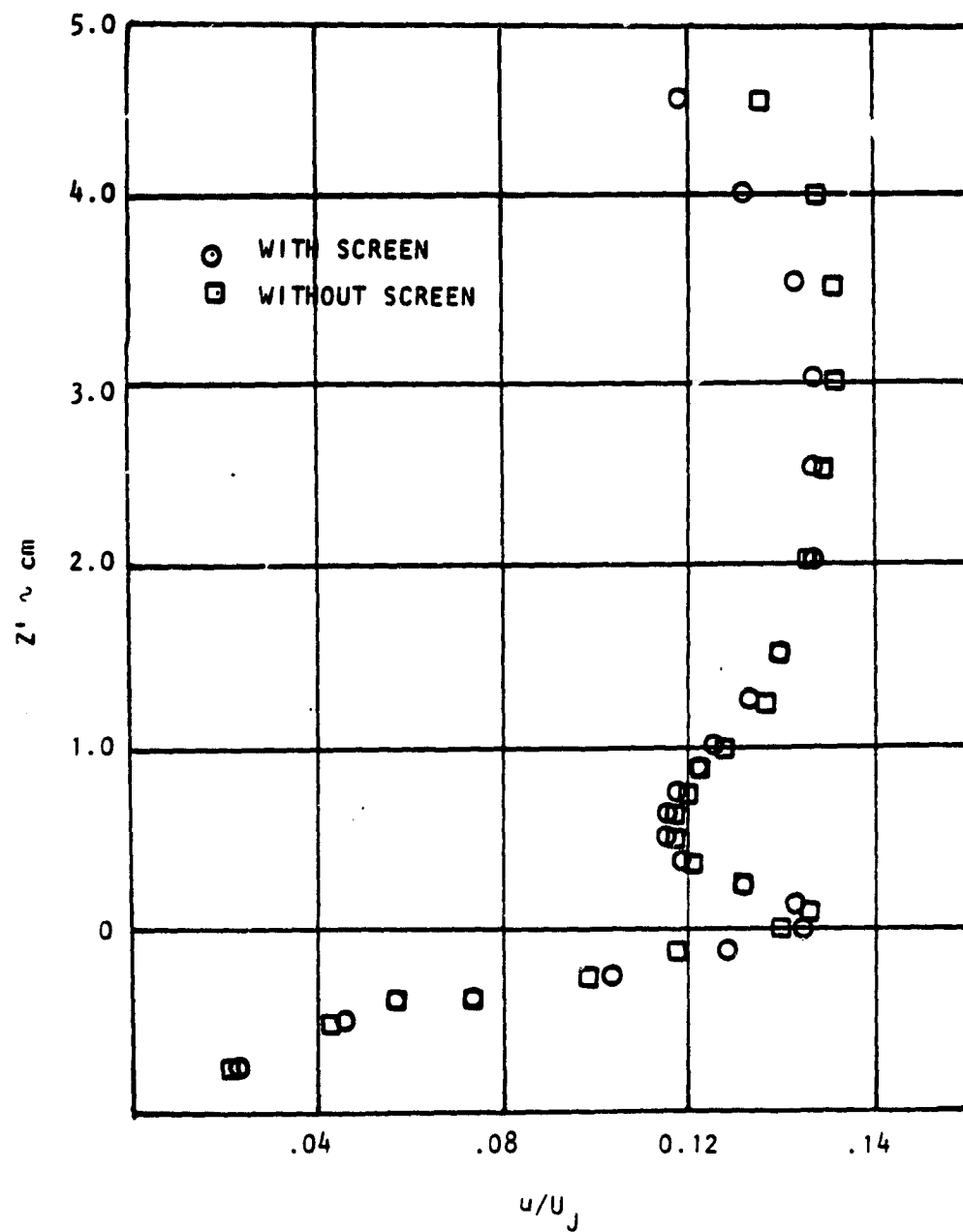
(a) JET MACH NUMBER

Figure 20. The Effect of Screen at the Nozzle Entrance



(b) WAKE MEAN VELOCITY PROFILE
 ($x' = 1.91 \text{ cm}$, $y' = 0$)

Figure 20. Contd.



(c) TURBULENCE INTENSITY PROFILE

Figure 20. Concluded.

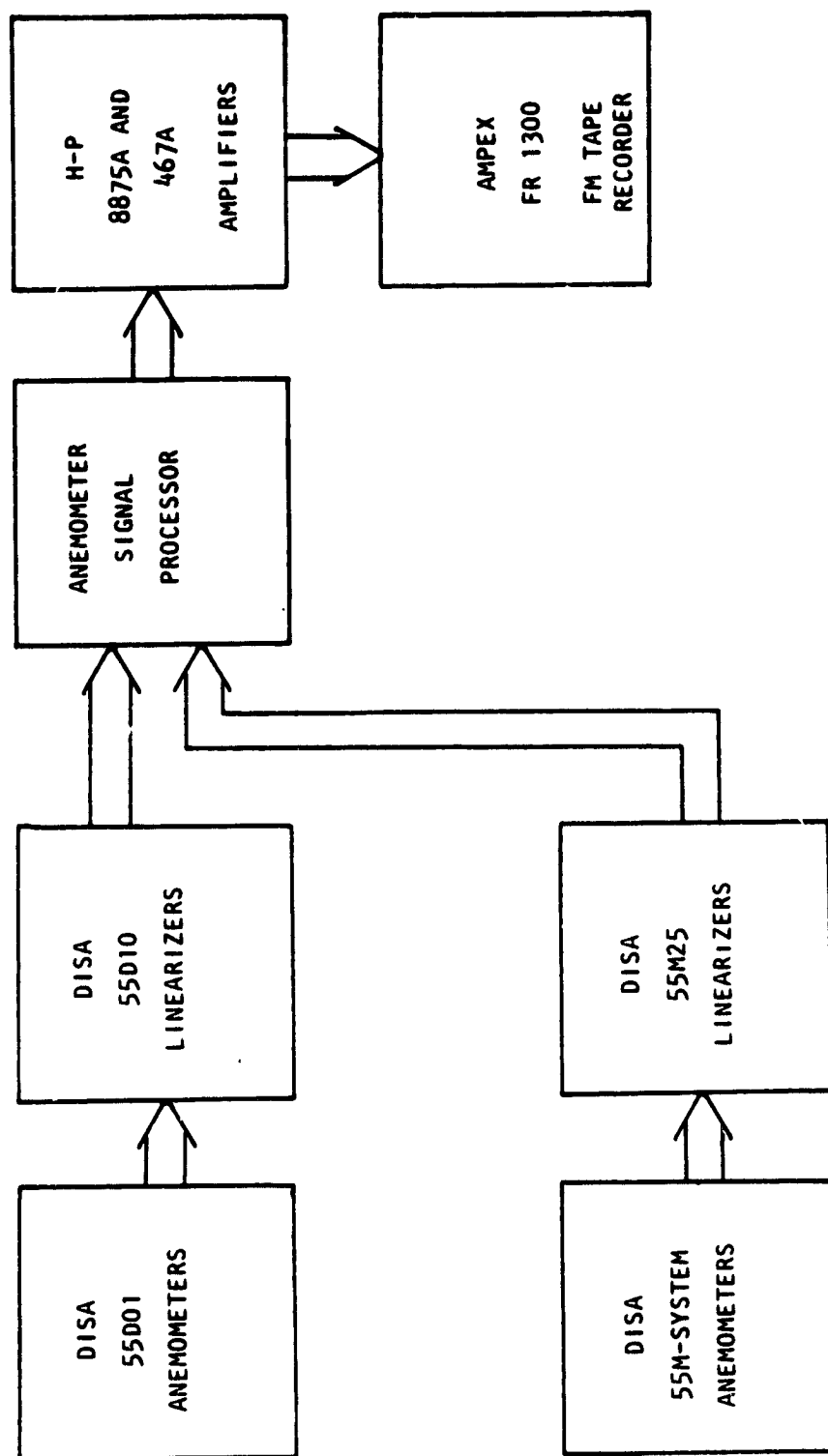


Figure 21. Velocity Cross-Correlation Data Acquisition and Reduction System.
(A) Data Acquisition.

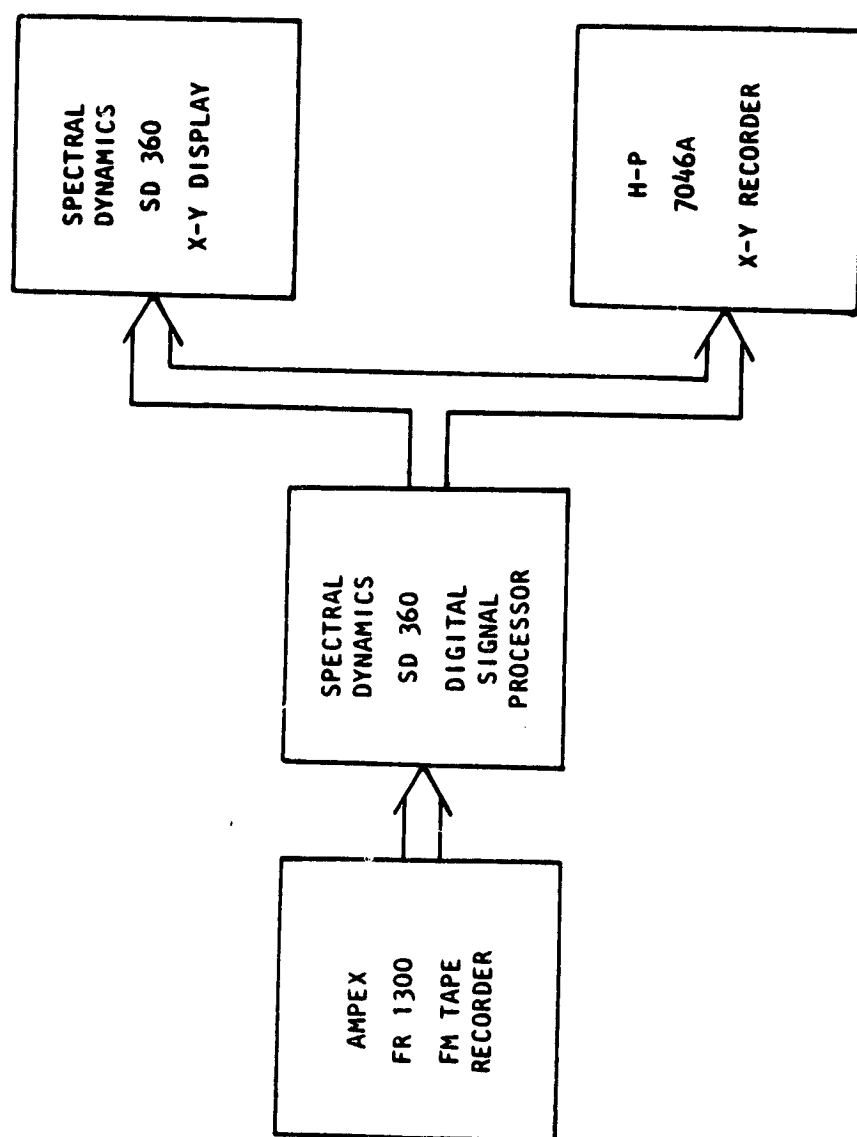


Figure 21. Concluded.
(B) Data Reduction.

calibration. The anemometers were also tuned as described in the DISA manual to obtain high frequency response with minimum danger of ringing.

Velocity components were extracted by the anemometer signal processor (analog adder and subtractor) from the two cross-wire signals. The linearized output of each velocity component was amplified through an amplifier system and simultaneously recorded on magnetic tape in the FM mode at a tape speed of 152.4 cm/sec. (60 ips) to obtain a frequency response of up to 20 KHz.

Fluctuating velocity measurements for correlations were obtained at several locations as indicated in Table 4 for 30° flap deflection, jet velocity of 180 m/s, without the screen at the nozzle exit. Space-time correlations and the power spectra of the fluctuating velocities were obtained by playing back the recorded magnetic tape and analyzing the data using the Spectral Dynamics Digital Signal Processor, SD360, as shown schematically in figure 21(b).

The single channel (for auto-correlations) or the two channels (for cross-correlations) were read from the FM tape into the SD360 memory. Then the histories were correlated and the correlograms were plotted on the X-Y recorder. The power spectra were also obtained from the SD360 and were plotted similarly. A typical correlation function and power spectrum is shown in figure 22.

LV system. A small measuring volume, an accurate sense of direction, and noninterference of the probe in the flow are the desirable characteristics of the LV system used to measure the fluctuating velocities. The system used here was a four-channel system developed by Lockheed and ordinarily used to measure two components of velocity at each of two positions. Figure 23 shows a one-point two-channel LV system complete with data processing equipment.

The LV facility is located in a small building between the anechoic room and the aeroacoustic flow facility. The control system for the LV facility is located in the acoustics laboratory. Air is supplied to the jet from the main supply through a conditioning system which controls pressure

VEL. COMP.	U_j m/s	INIT. TURB.	θ_f	X' cm	$\Delta X'$ cm	Y cm	ΔY cm	Z' cm	$\Delta Z'$ cm
U	180.	LOW	30°	1.91	0	0	0	0	0

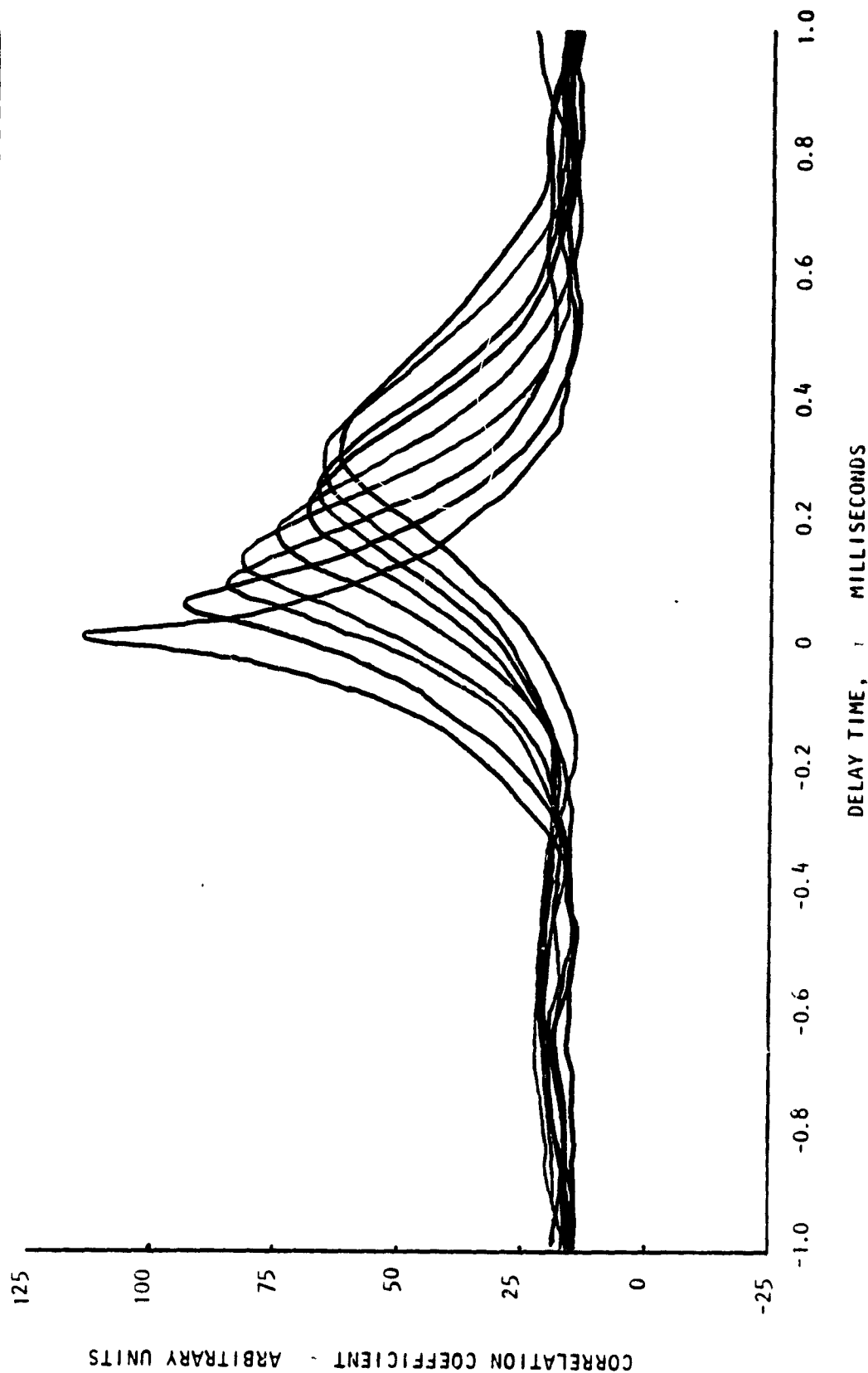


Figure 22. Typical Correlation and Spectrum of Fluctuating Velocities in the Wake.

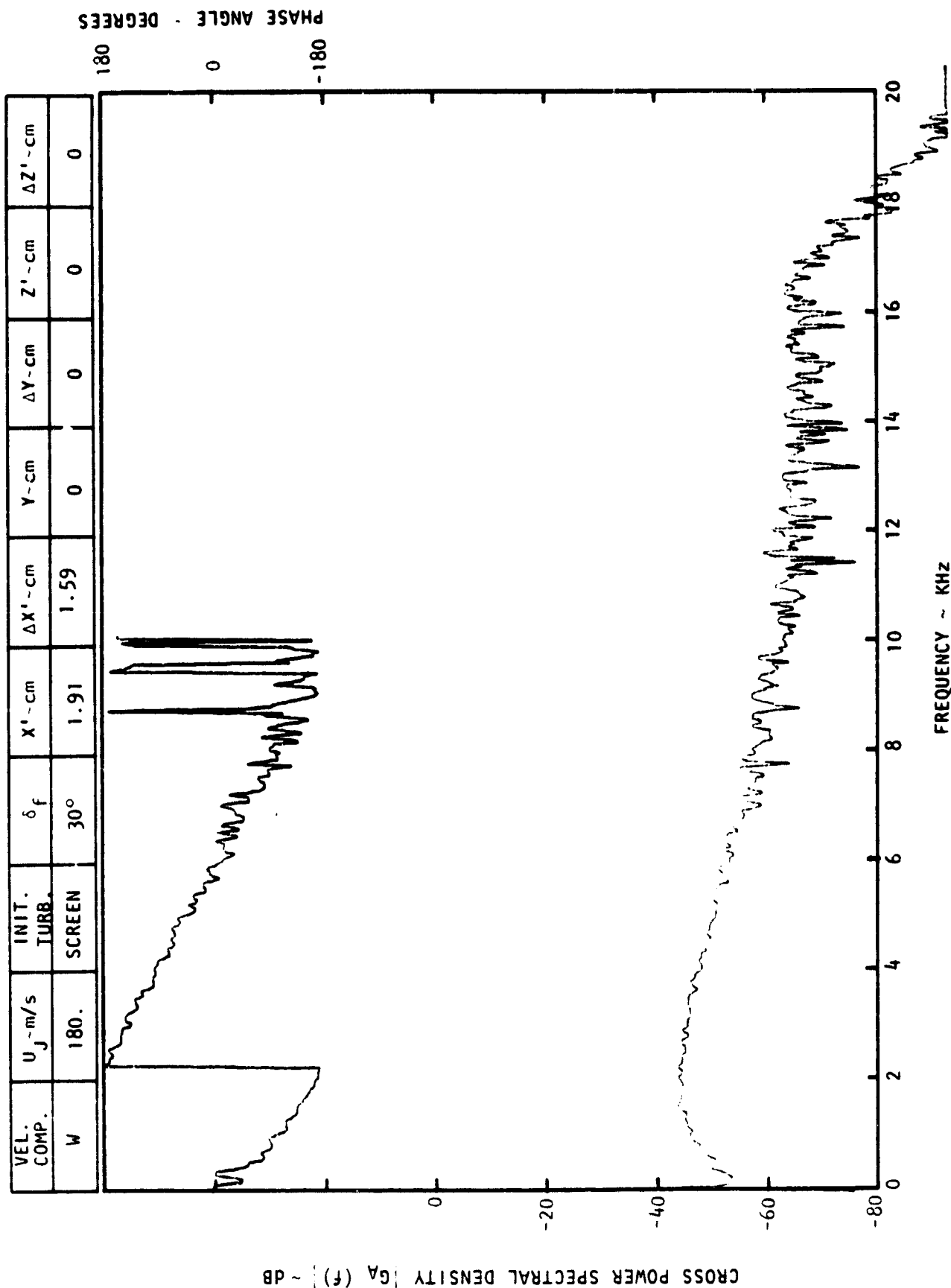


Figure 22. Concluded. (B) Cross Power Spectrum.

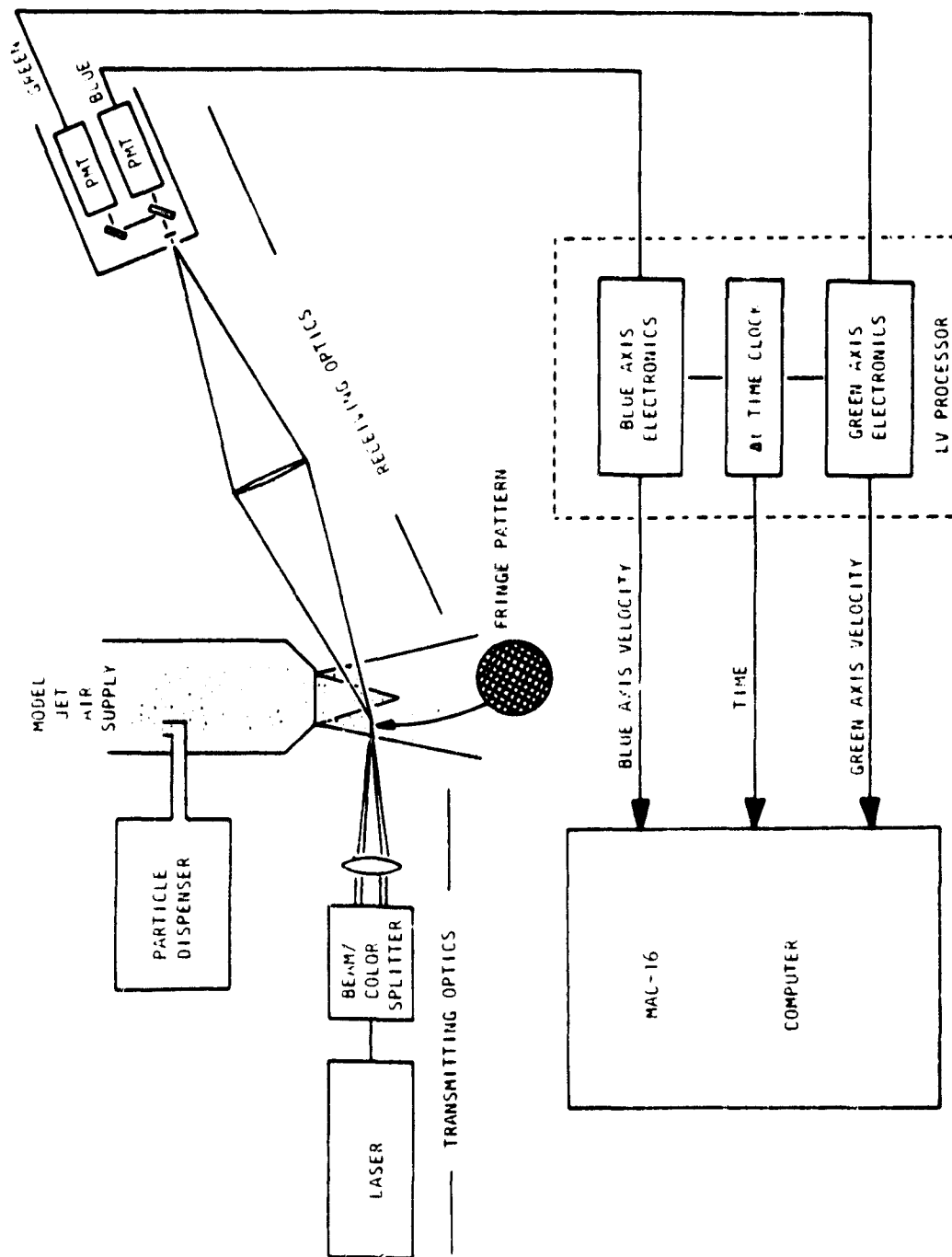


FIGURE 23. TWO AXIS LASER VELOCIMETER

and temperature in two independently regulated plenum chambers which are coannularly arranged. The primary flow system, with a 25.4 cm diameter flange was used in these tests. After a conical contraction, the plenum is terminated in a 10.16 cm diameter flange. An adapter was used between the flange and nozzle to align the wing surface with the optical axis of the LV.

All the LV experiments were conducted using 30° flap angle and jet velocity of 180 m/sec. The measurement locations and the configuration for the LV measurements is shown in Table 5. The LV data is compared with the hot-wire data in the next section under Analysis.

TABLE 5 LV MEASUREMENTS

Flap Angle δ_f	Jet Velocity U_j (m/sec)	Jet Turbulence Intensity	Measurement Locations (cm)		
			x_1	y_1	z_1
30	185	Minimum	0.75	0	0 - 7.0
30	185	Minimum	1.5	0	0 - 7.0
30	185	Minimum	3.0	0	0 - 7.0

Turbulence/near-field noise correlations. To establish the significance of the trailing edge wake turbulence to the noise, correlations between the fluctuating velocities in the wake and fluctuating pressures just outside the flow were measured. These experiments were conducted in the aeroacoustic flow facility for 30° flap angle, jet velocity of 180 m/sec. and without screen at the nozzle.

Fluctuating velocities were measured using a crossed hot-wire with two-channel system and fluctuating pressures were measured using eight microphones (four above the wing and four below the wing) as shown in figure 24. All the microphones and the hot wire were in the midspan of the wing/flap. The hot-wire system and microphone system used in these tests were the same as those used in the flow and near-field measurements.

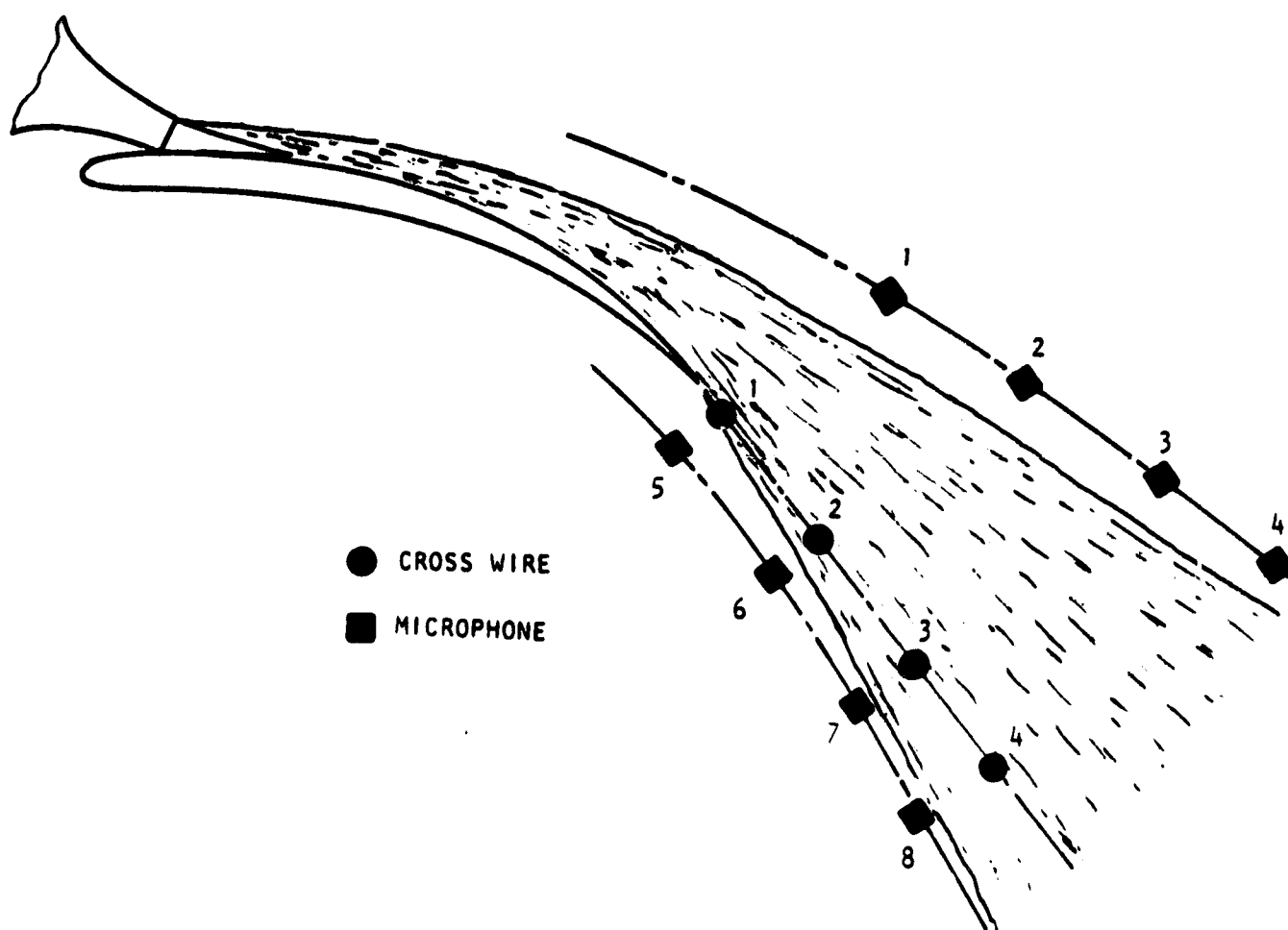


Figure 24. Hot-Wire and Microphone Locations for Correlations

The data from the hot-wire and microphones were recorded simultaneously on a magnetic tape using a 14-channel tape recorder as illustrated in the block diagram of figure 25. The hot-wire data was passed through a signal processor (adder and subtractor) where the orthogonal velocity components were resolved. These two velocity components and the two signals sensed by the cross-wires (without resolving) were recorded on four channels of the tape recorder. The unresolved hot-wire signals were also recorded on the other channels of the tape so that this data could be used later. The data system (both fluctuating velocities and pressures) was calibrated in the same way as described before. The phase angle calibration was conducted by placing the hot-wire adjacent to a microphone so that their sensing elements were equally distant from the impulse pressure from the pistol firing. The responses to the impulse were recorded on the respective channels of the tape.

The correlations between the various microphones and the hot-wire positions were obtained by reducing the taped data through the Digital Signal Processor, SD360. Correlations shown in figure 26 indicate that the correlation of fluctuating velocity and the pressure at microphone position 6 is smaller than that of between velocity and microphone position 5. These are further discussed in the next section.

3. ANALYTICAL PROGRAM

The experimental data discussed in the previous section are analyzed to evaluate the effect of jet velocity, initial turbulence, and flap angle on the noise and flow characteristics of USB configuration. The turbulence data are analyzed to derive the turbulence properties such as convection velocity, turbulence decay rate, integral length scales and power spectra. The measured radiated noise is compared with the noise predicted by the empirical method given in reference 2; the measured turbulence is compared with that predicted by the analytical model also given in reference 2.

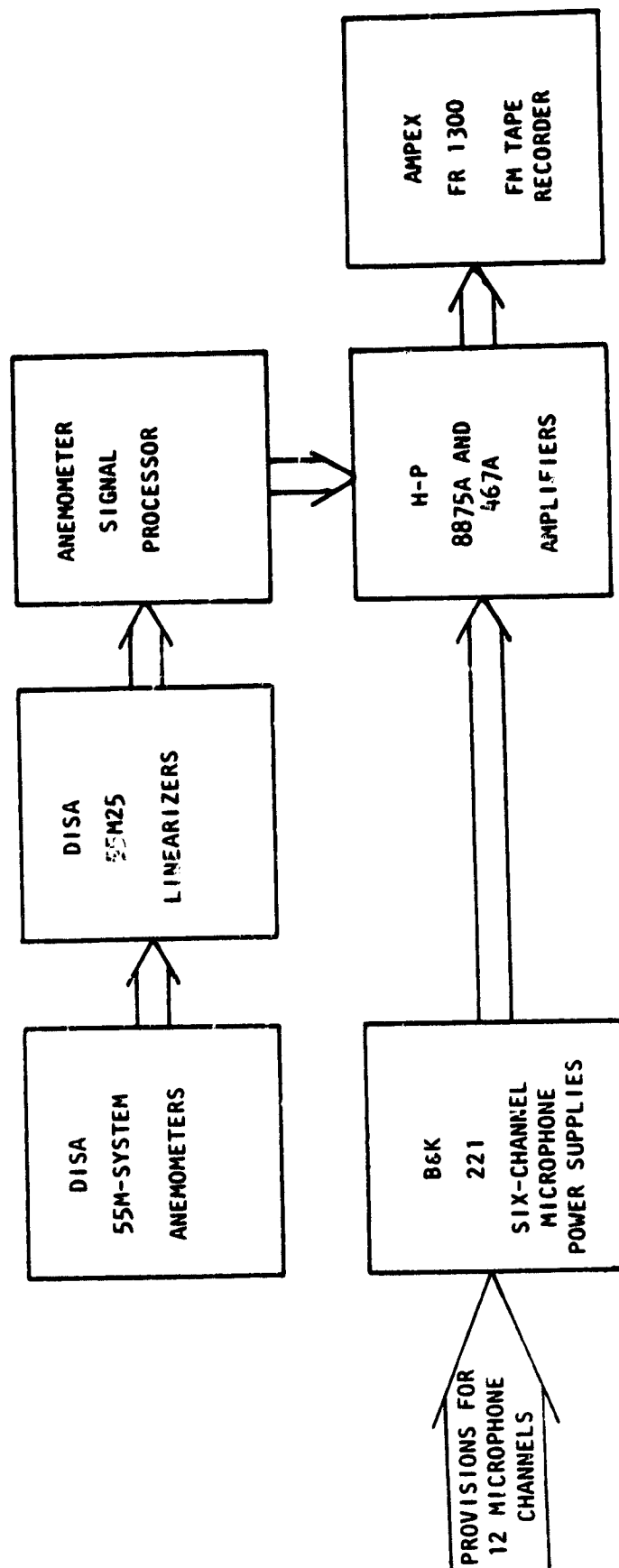


FIGURE 25. IN-FLOW VELOCITY/NEAR-FIELD PRESSURE CROSS-CORRELATION DATA ACQUISITION SYSTEM.

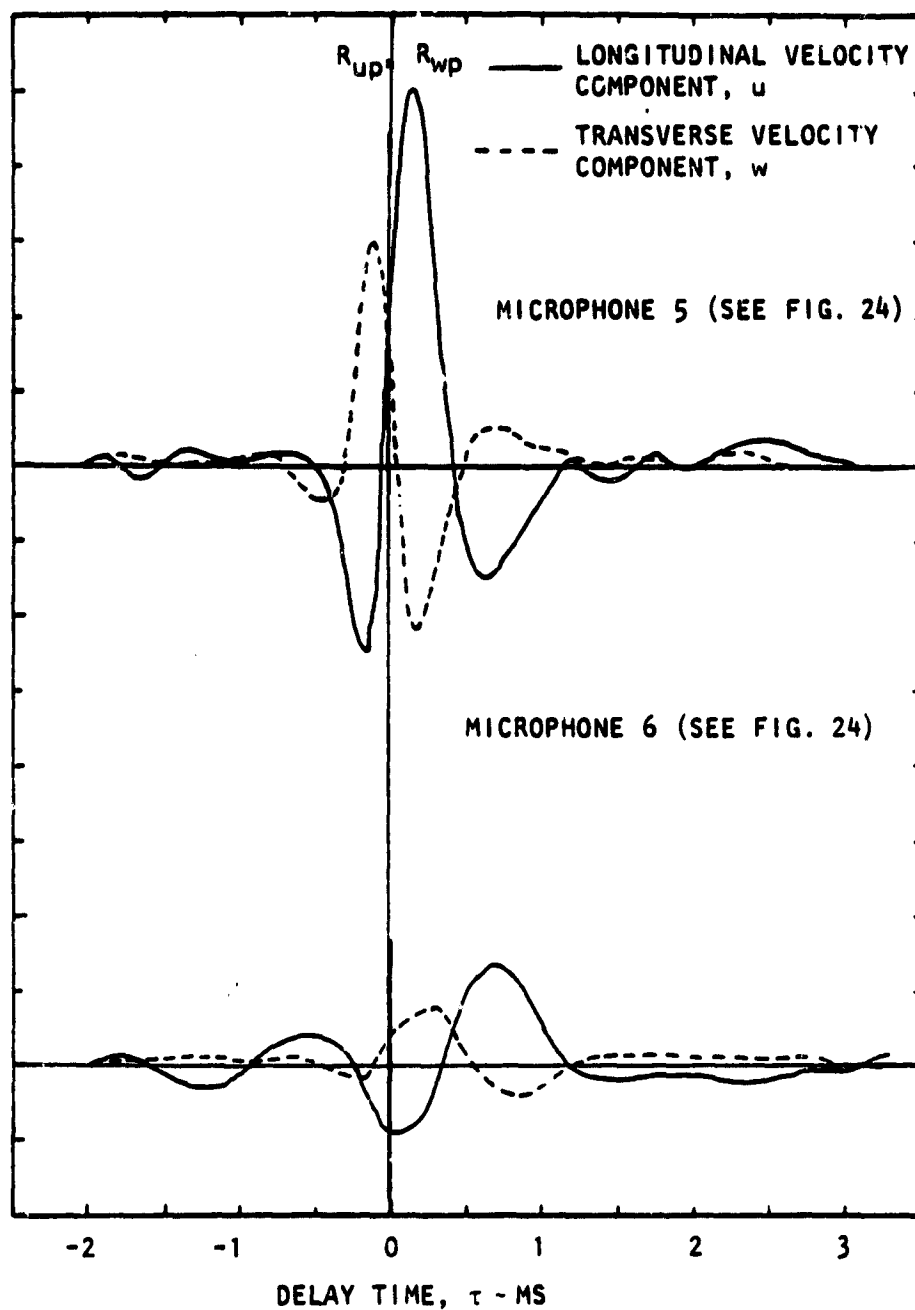


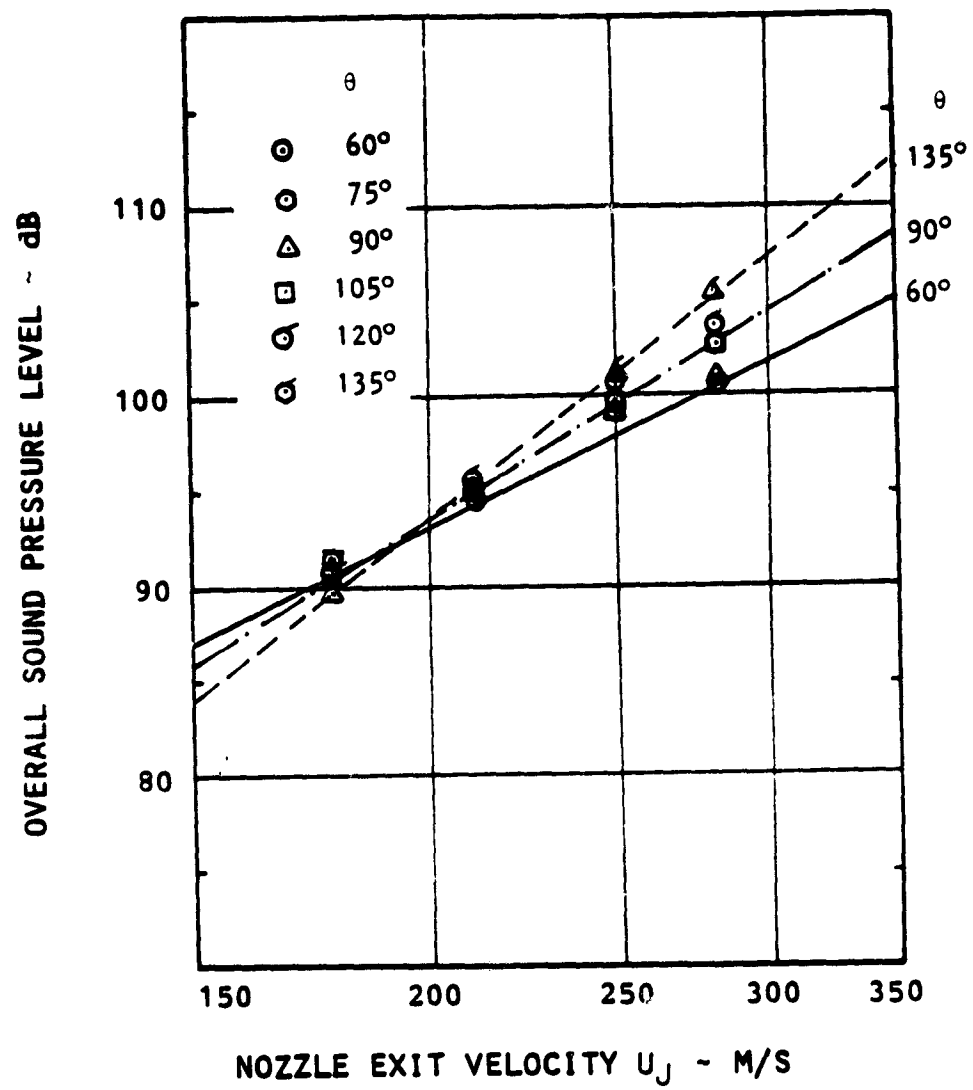
Figure 26. Correlation of Fluctuating Velocities With Near-Field Noise.

3.1 Parametric Effects

Radiated sound field. The acoustic characteristics of USB configurations are studied by observing: (1) the variation of OASPL with jet velocity, (2) the directivity, and (3) the spectral distribution. Unfortunately, these three properties are interdependent, and therefore it is not possible to study them independently. This interdependency and the lack of axisymmetry of USB model make it very difficult to define USB noise characteristics. In this report, however, a simplified approach is taken by observing the variation of OASPL with jet exit velocity for various azimuthal and polar angles, the directivity of OASPL as a function of polar angle in the various azimuthal planes ($\phi = \text{constant}$), and the one-third octave spectral distribution for selected velocity and direction.

Effect of jet velocity. The variation of OASPL with jet exit velocity is shown in figure 27 for a flap angle of 30° , and azimuthal angles, $\phi = 90^\circ$, 60° , 30° and 0° ($\phi = 90^\circ$ corresponds to the flyover plane and $\phi = 0^\circ$ corresponds to the wing plane). The effect of polar angle on OASPL is also shown in this figure by plotting OASPL for polar angles, $\theta = 60^\circ$, 75° , 90° , 105° , 120° , and 135° in each azimuthal angle plane. The overall sound pressure increases as the jet exit velocity is raised to the power n . This velocity exponent, n , varies from about 5 for $\theta = 60^\circ$ to about 8 for $\theta = 135^\circ$ in the azimuthal planes $\phi = 90^\circ$, 60° , and 30° (figures 27a, b, c). But in the azimuthal plane, $\phi = 0^\circ$ (figure 27d), the velocity exponent is approximately constant at 8 for all polar angles. This variation of velocity exponent as a function of azimuthal and polar angles is summarized in figure 28. From these results, it may be concluded that only in the wing plane ($\phi = 0^\circ$) does the OASPL vary with jet velocity in the same way as jet noise.

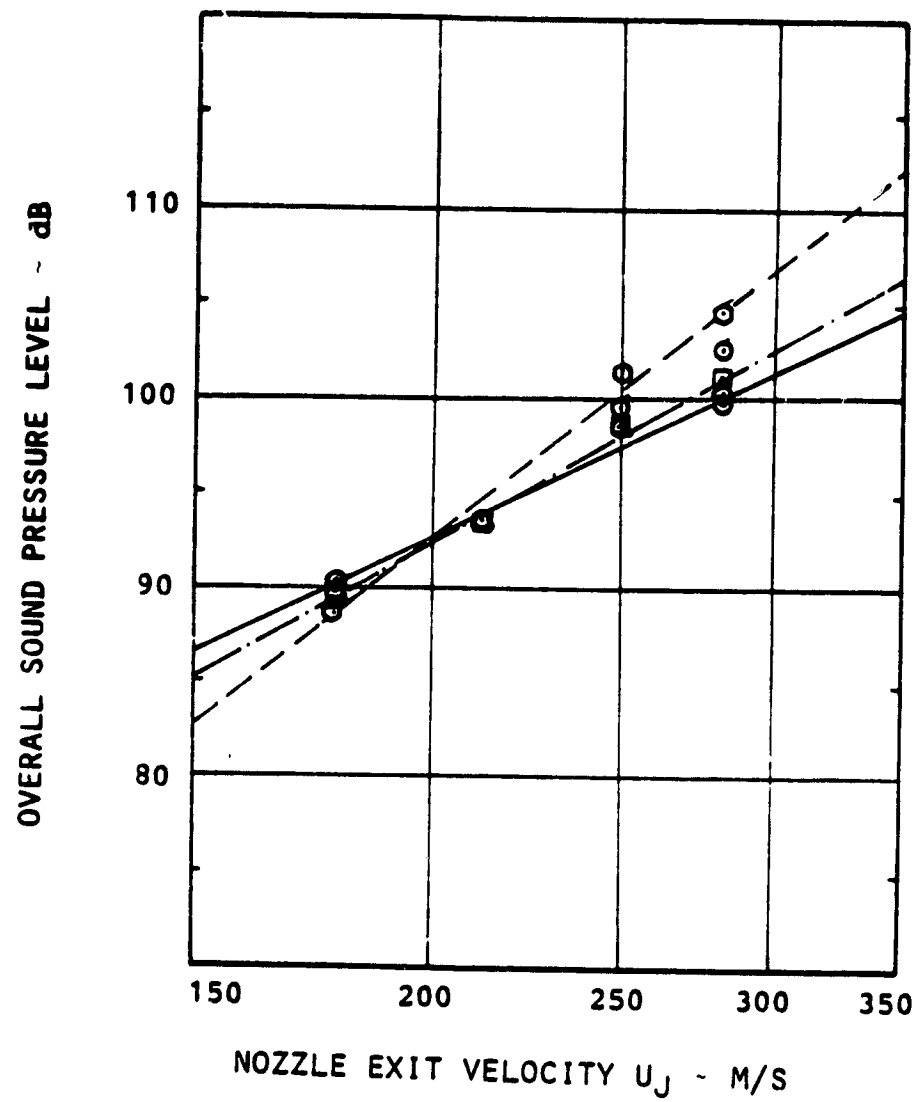
The effects of the screen mesh in the nozzle entrance and of the flap angle on OASPL are illustrated in figure 29. Comparison of OASPL with and without the screen for the 30° flap angle and at four jet velocities as shown in this figure indicates that the effect on noise of the screen is negligible. This is because the screen at the nozzle entrance does not influence the turbulence and mean flow properties of the jet as discussed previously.



(a) $\phi = 90^\circ$

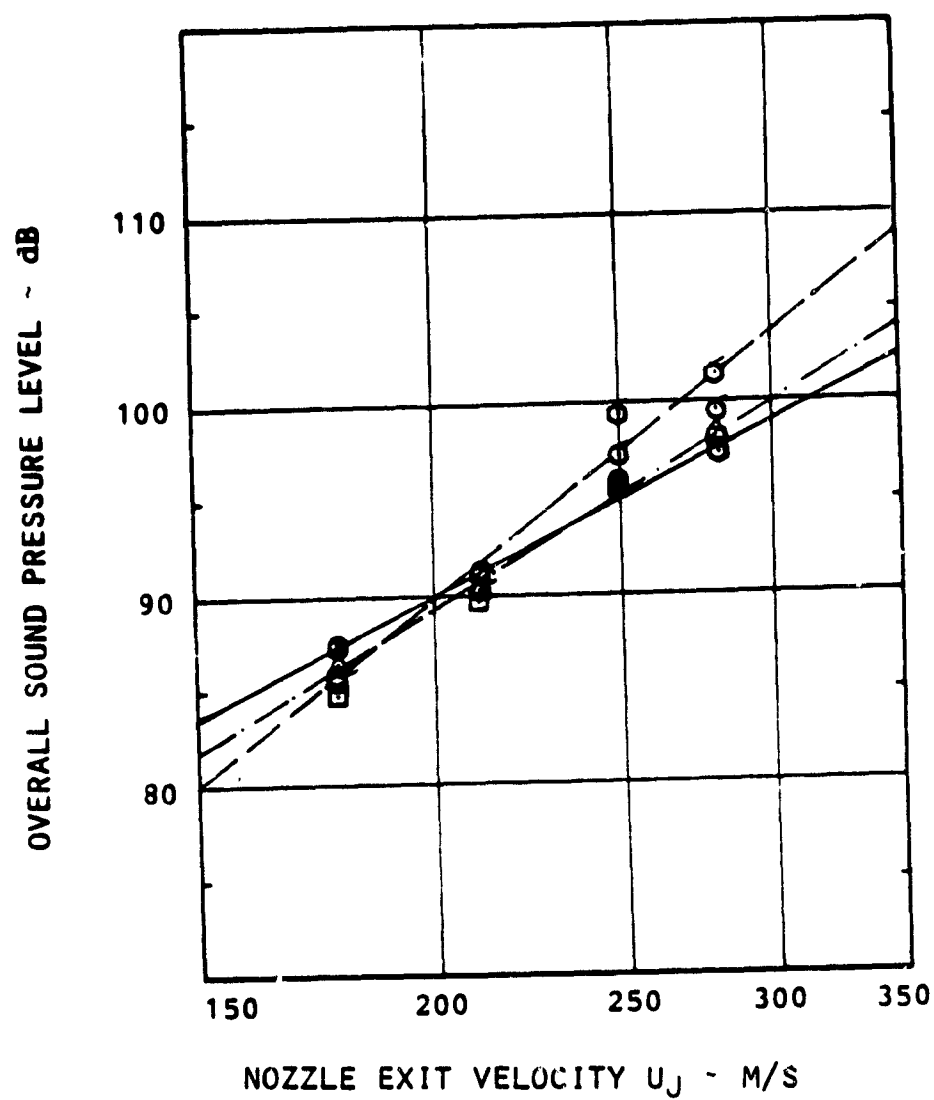
Figure 27. Variation of OASPL with Jet Velocity

$\delta f = 30^\circ$



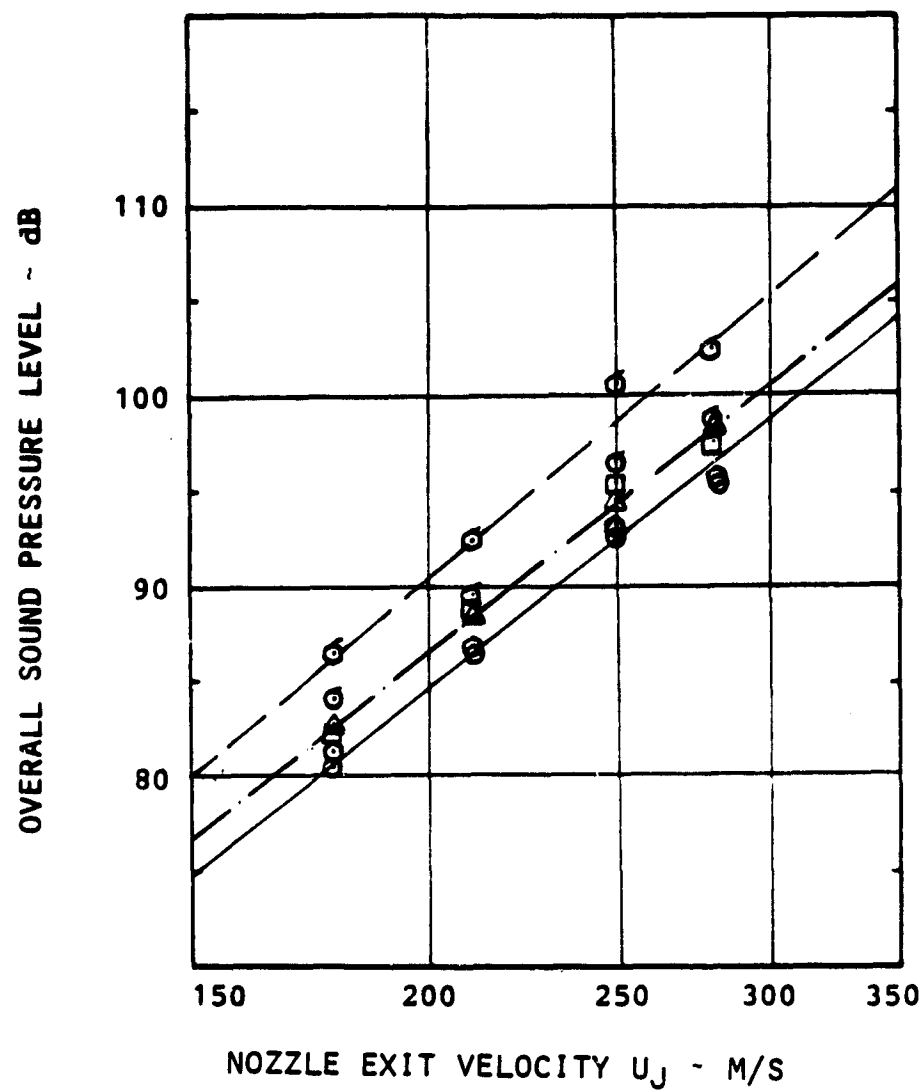
(b) $\phi = 60^\circ$

Figure 27. Continued.



(c) $\phi = 30^\circ$

Figure 27. Continued.



(d) $\phi = 0^\circ$

Figure 27. Concluded.

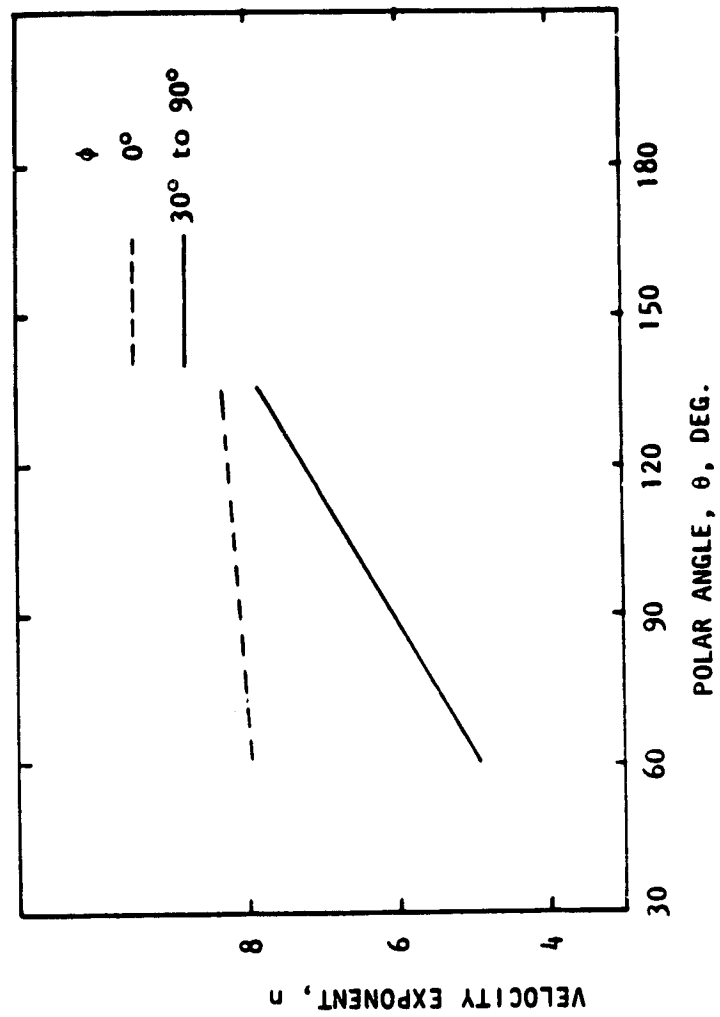


Figure 28. Velocity Exponent as a Function of Azimuthal Angle and Polar Angle.

The effect of the flap angle on noise is studied by comparing the OASPL for the three flap angles in the flyover plane, for the polar angle $\theta = 90^\circ$ at four jet velocities (fig. 29). It is clear in this figure that the effect of flap angle on noise is negligible. In the previous studies (ref. 2), it was found that USB noise is independent of flap angle provided the upper surface of the flap at the trailing edge is used as the reference plane.

Directivity. The directivity (variation of OASPL with polar angle, θ) is shown in figure 30 for several velocities and azimuthal angles. It may be observed that for low velocities the OASPL is approximately independent of polar angle, but for higher velocities the OASPL increases as the polar angle increases. In the wing plane ($\phi = 0^\circ$), however, the OASPL increases with polar angle for all jet velocities.

Spectral distribution. The spectral shape of the radiated noise and the variation of spectra with directivity (polar and azimuthal angles) can be investigated by observing the data for a velocity where OASPL is independent of polar angle. From the results of figure 27, it was observed that the OASPL is independent of polar angle at a jet velocity of about 200 m/sec. The velocity close to the 200 m/sec. for which the noise data is available is 215 m/sec.; and therefore, the spectral data at a velocity of 215 m/sec. are studied. Figure 31 shows one-third octave-band spectra as functions of polar angle and azimuthal angle. It may be observed in this figure that for all azimuthal angles except $\phi = 0^\circ$ (wing plane), the low frequency spectra are independent of polar angle, whereas the SPL in the high frequencies increases slightly as the polar angle increases. In the wing plane, the noise levels increase at all frequencies as the polar angle increases.

Flow profiles. The effect of jet velocity, initial turbulence, and flap angle on the trailing edge wake flow characteristics were determined by analyzing the mean velocity and turbulence intensity profiles.

Effect of jet velocity. The effect of jet velocity on mean and fluctuating velocity profiles are shown in figure 32. There are no startling effects of jet velocity on profiles of the longitudinal component of mean and

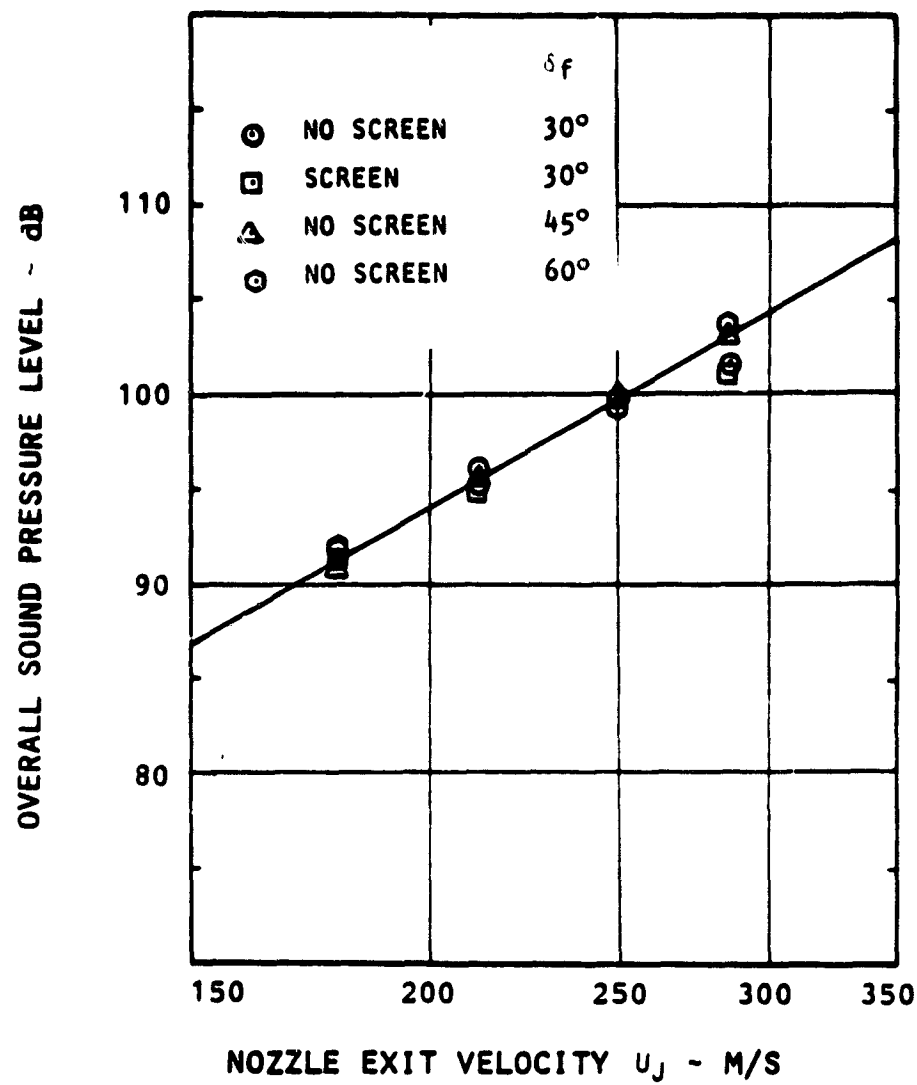


Figure 29. Effect of Screen and Flap Angle on OASPL.

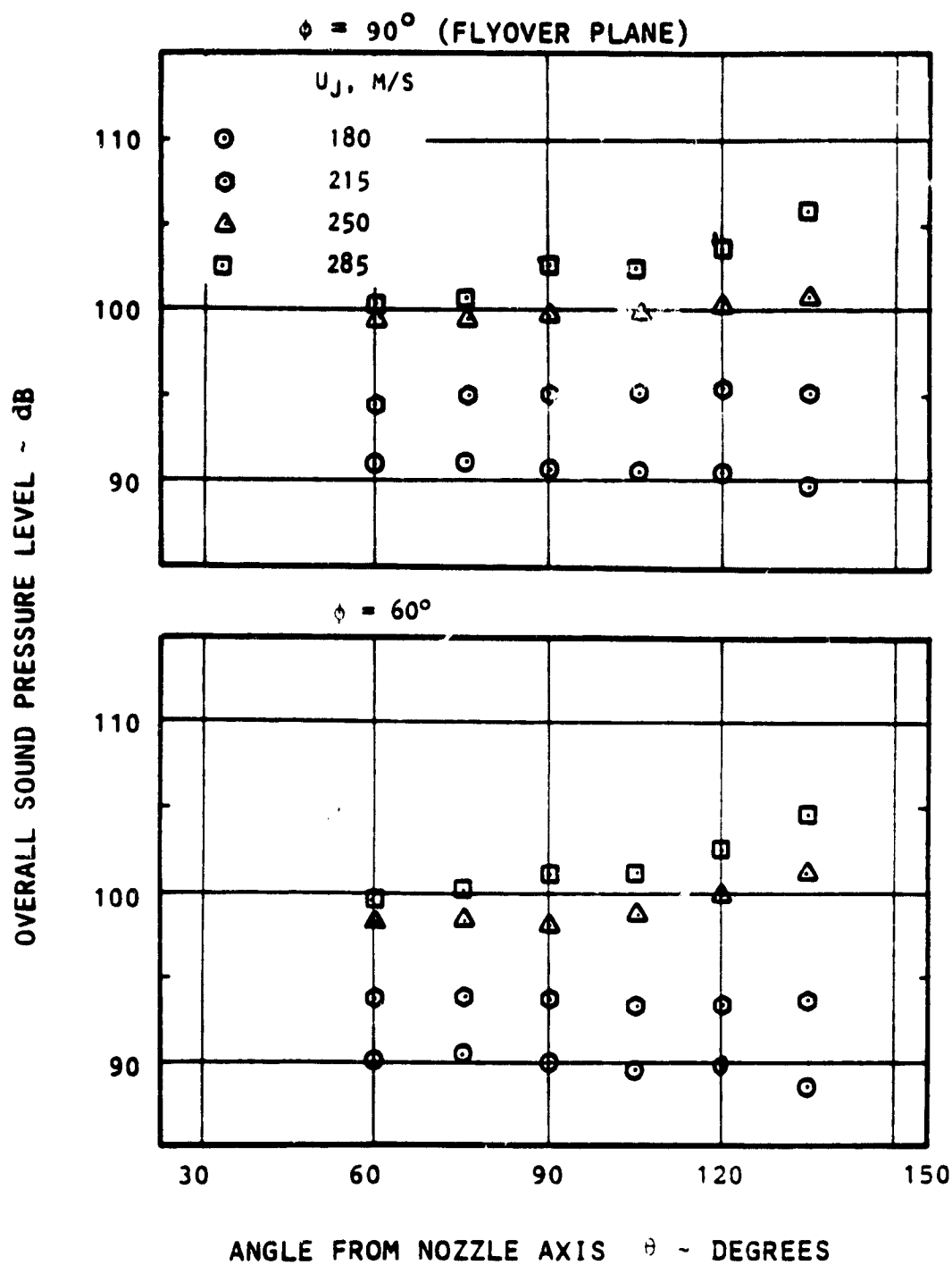


Figure 30. Variation of OASPL With Polar Angle, θ .

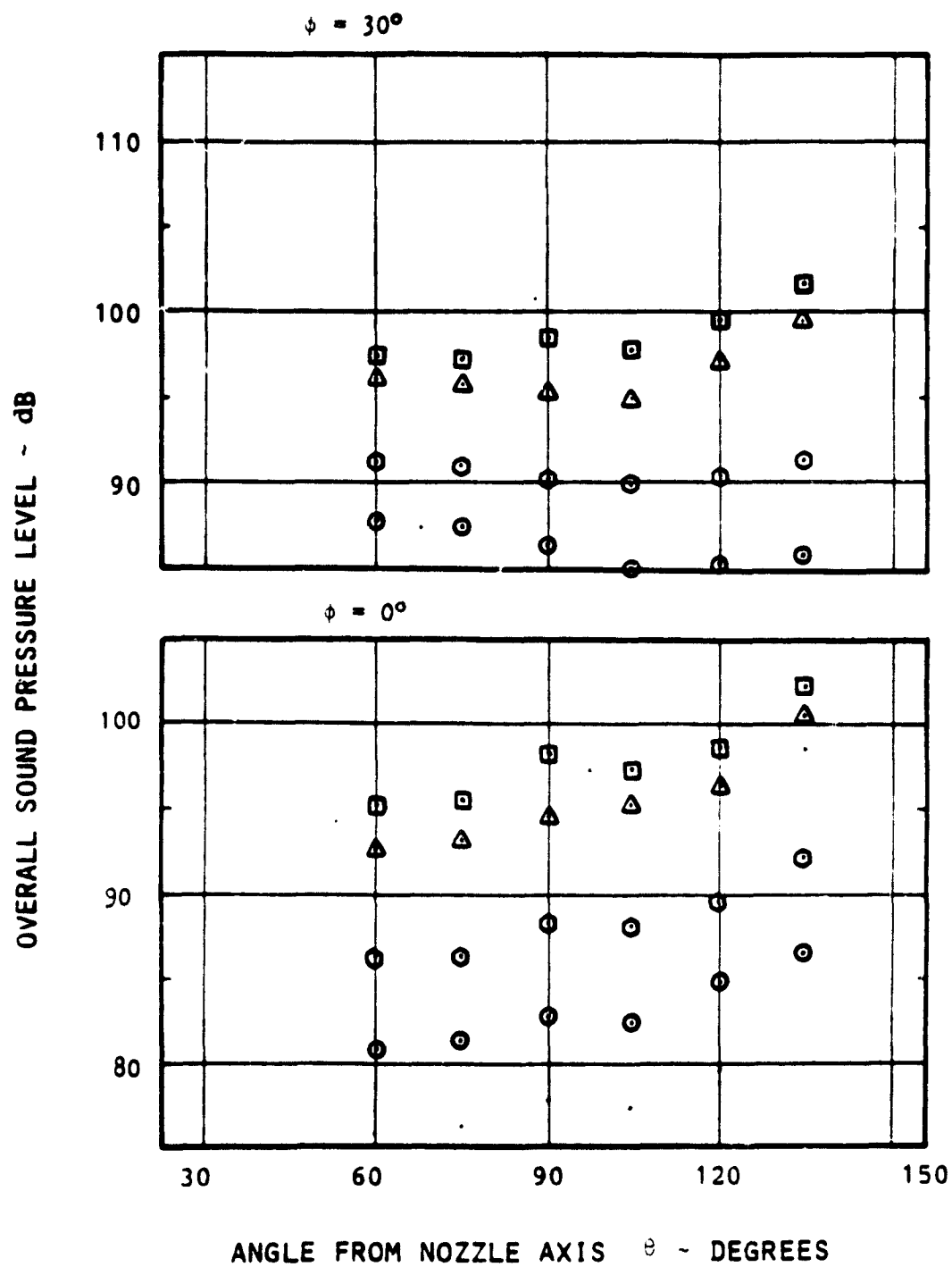


Figure 30. Concluded.

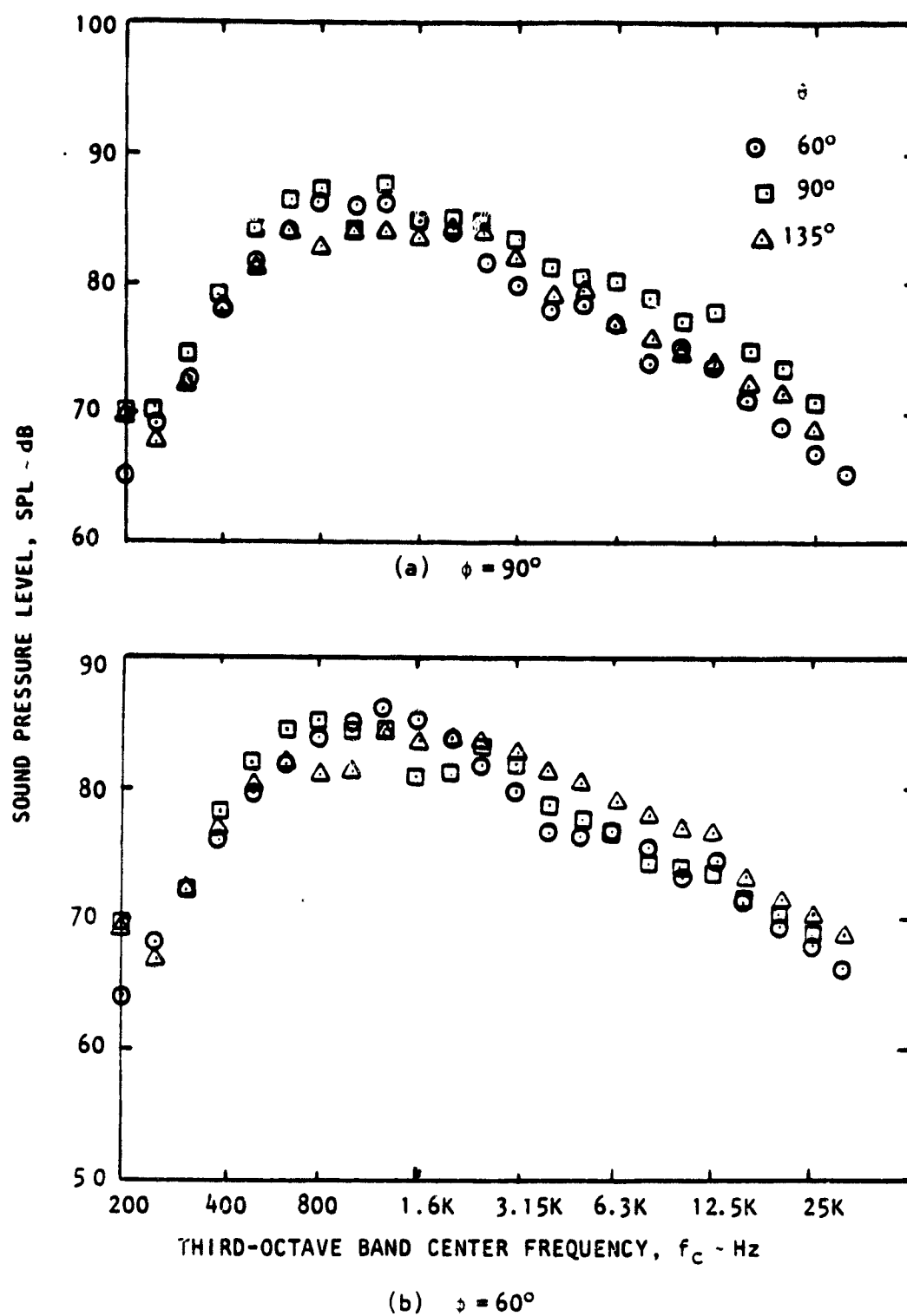


Figure 31. Spectral Distribution of Radiated Noise.

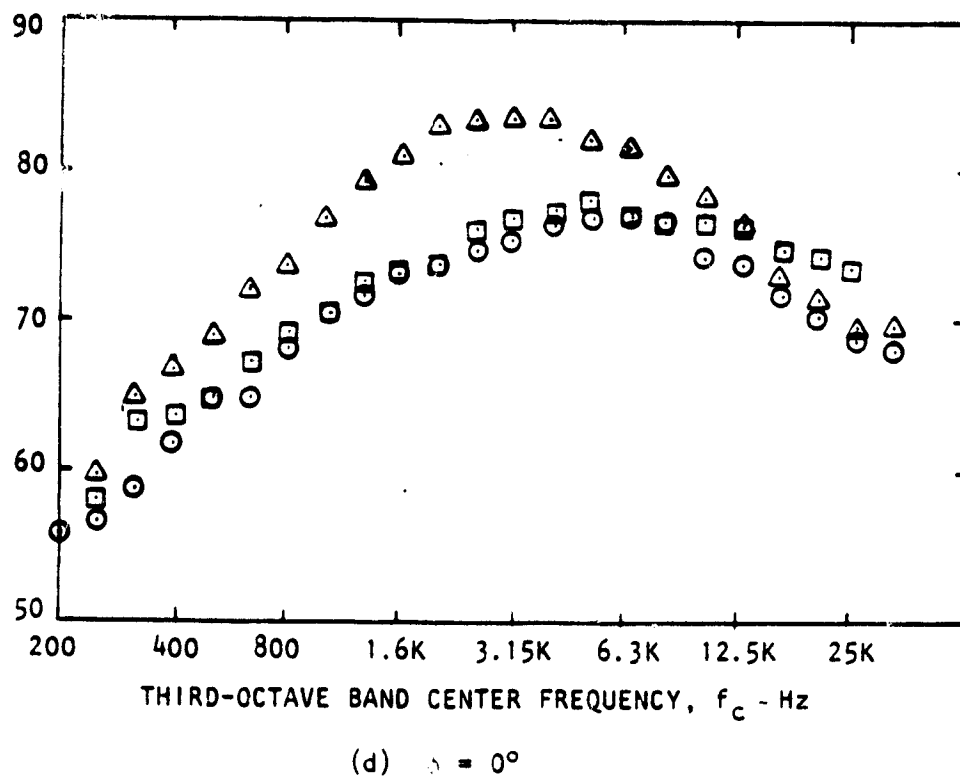
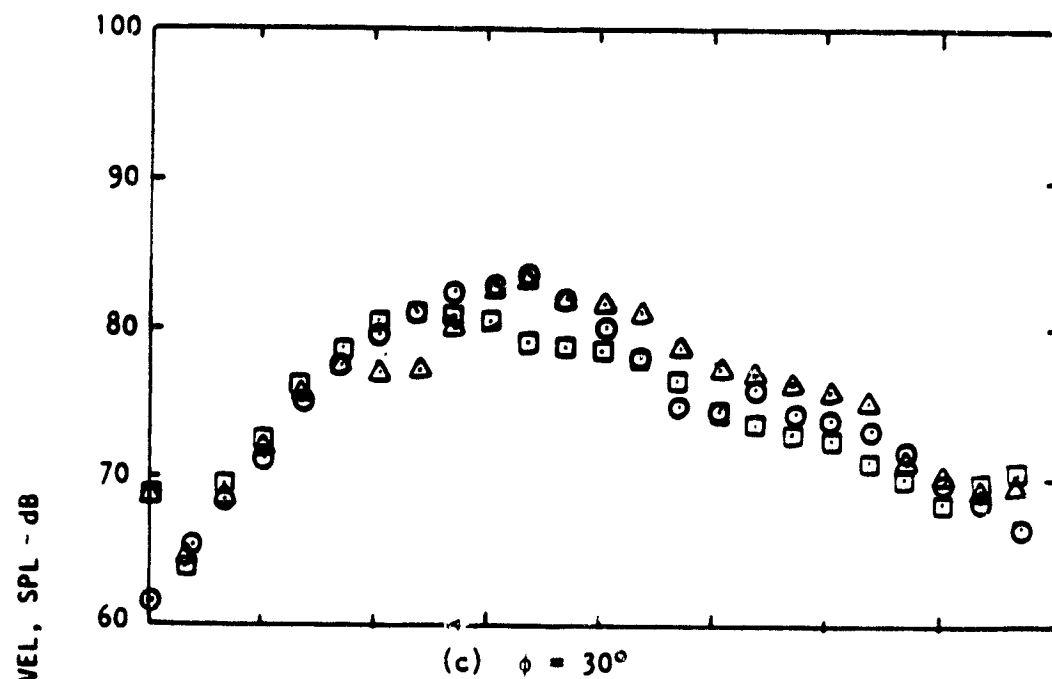


Figure 31. Concluded.

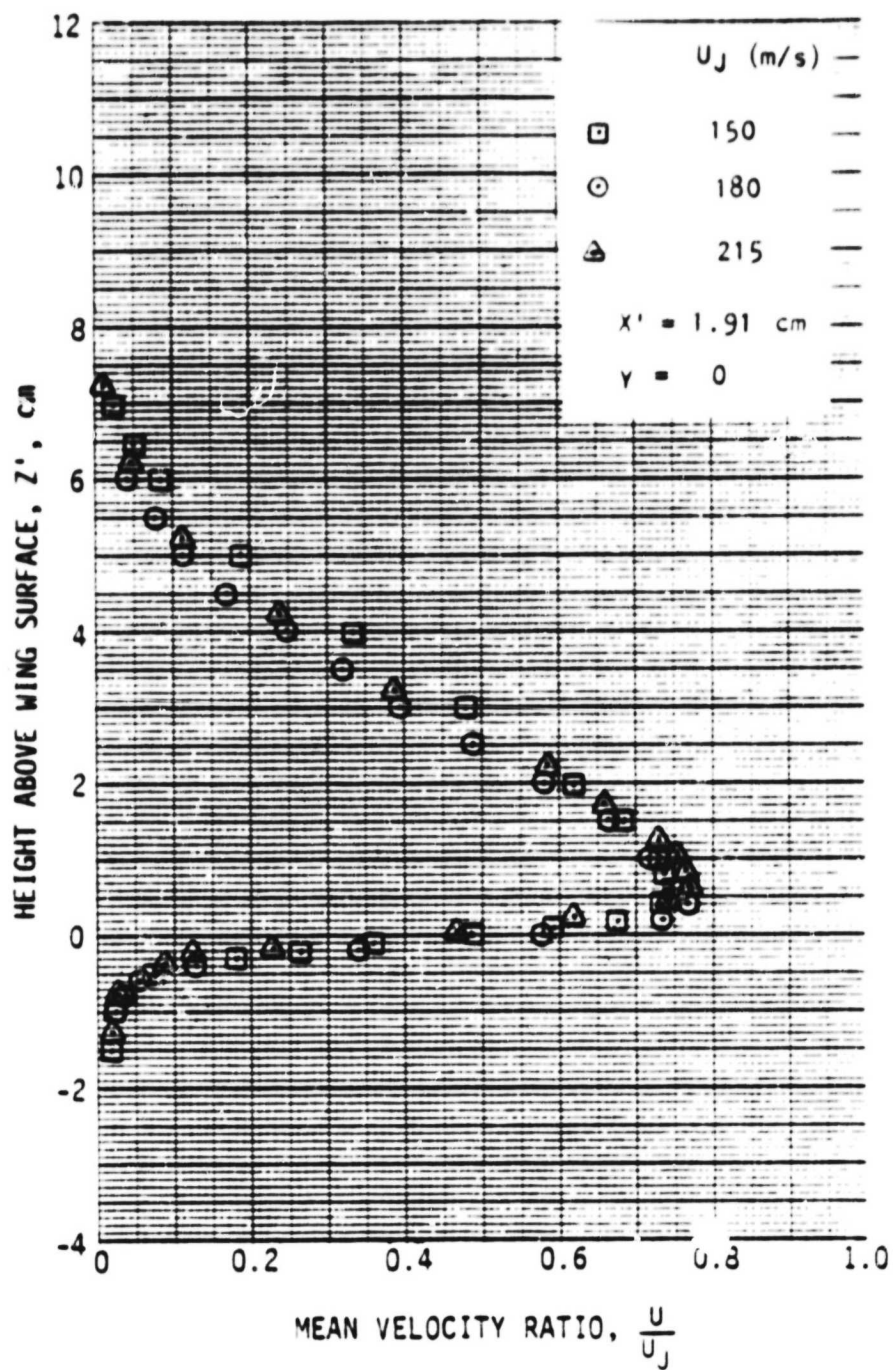


Figure 32. Effect of Jet Velocity on Wake Flow Characteristics.
(A) Mean Velocity, Longitudinal Component.

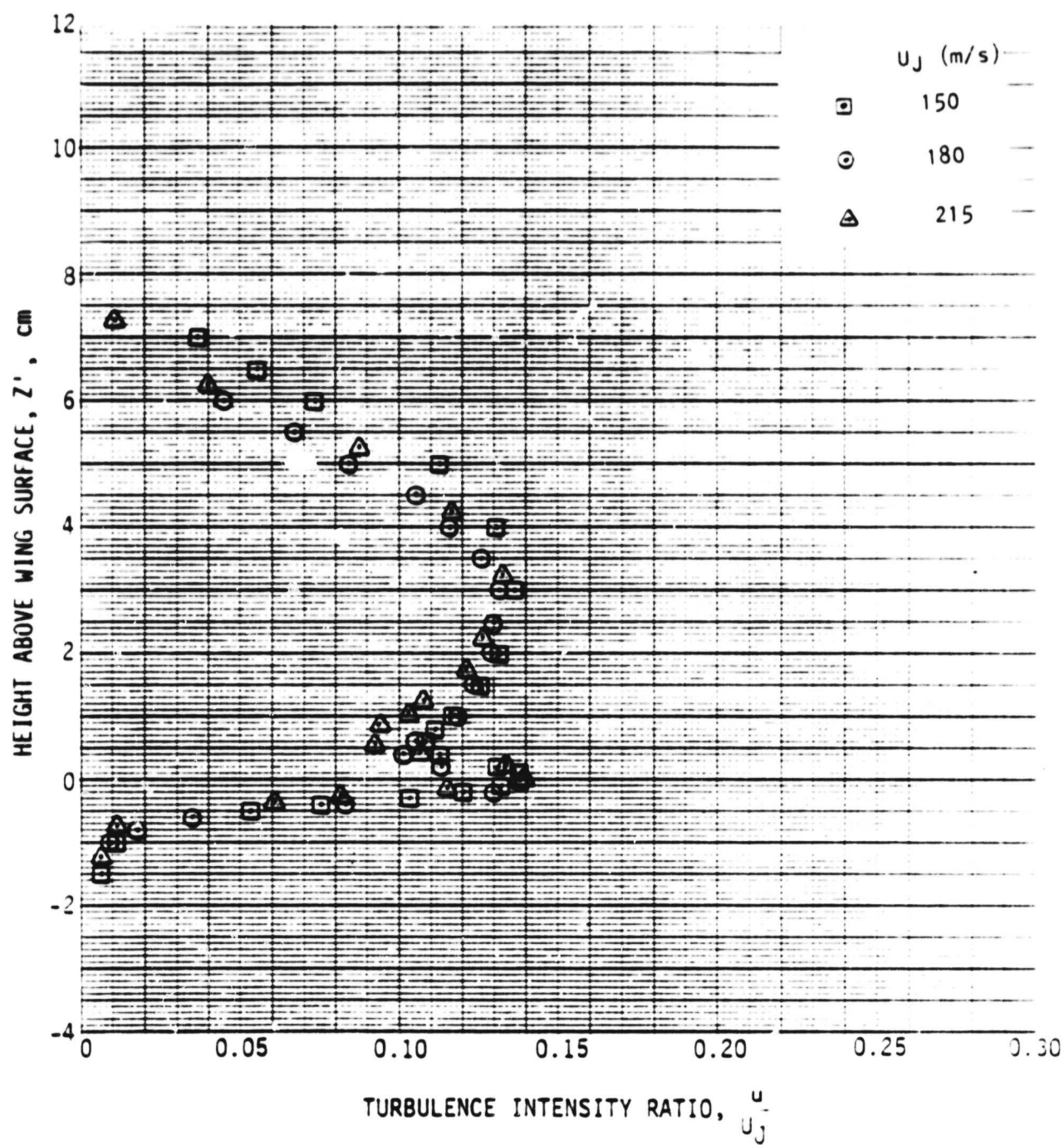


Figure 32. Continued. (B) Turbulence Intensity, Longitudinal Component.

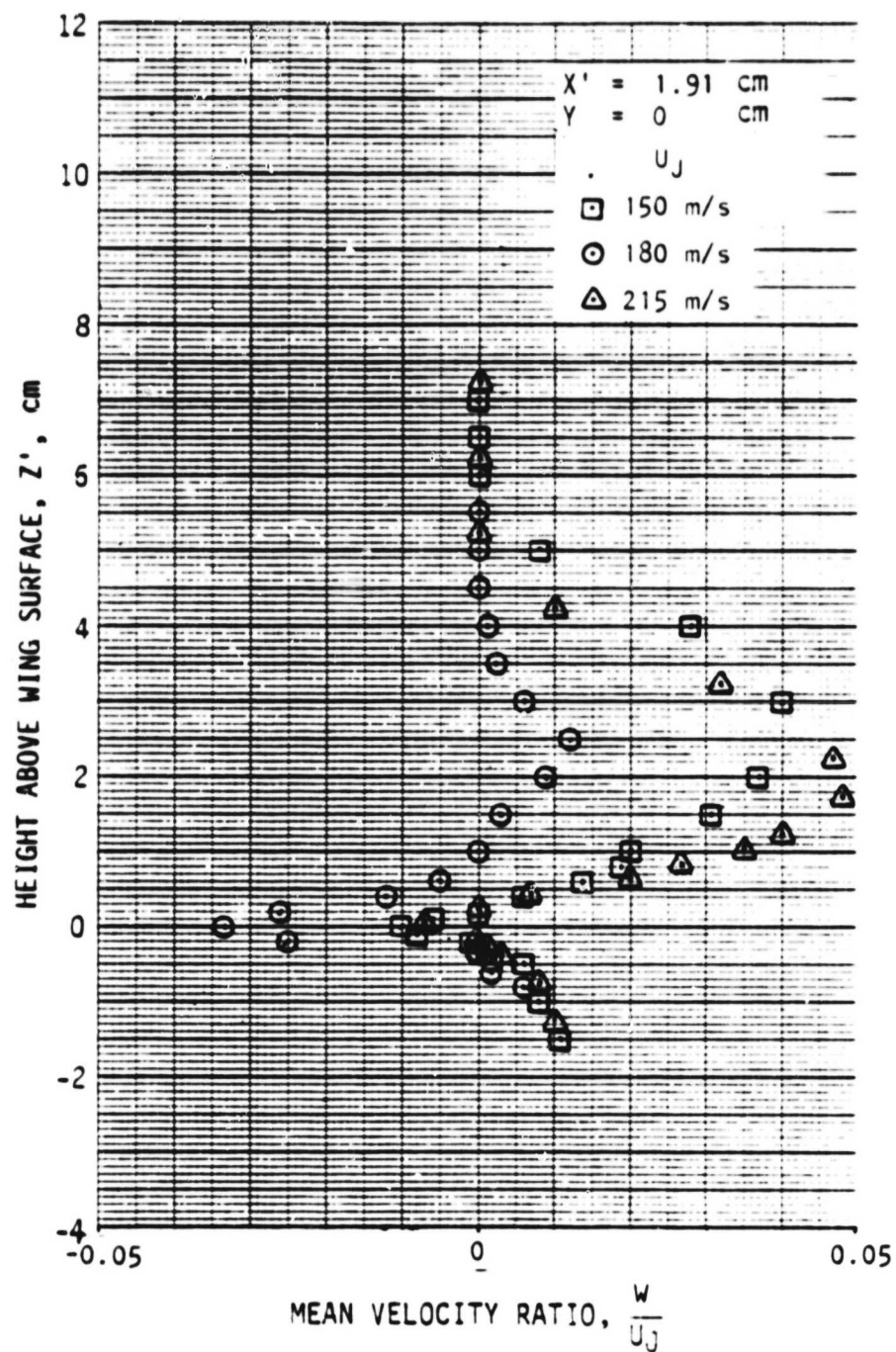


Figure 32. Continued. (C) Mean Velocity, Transverse Component.

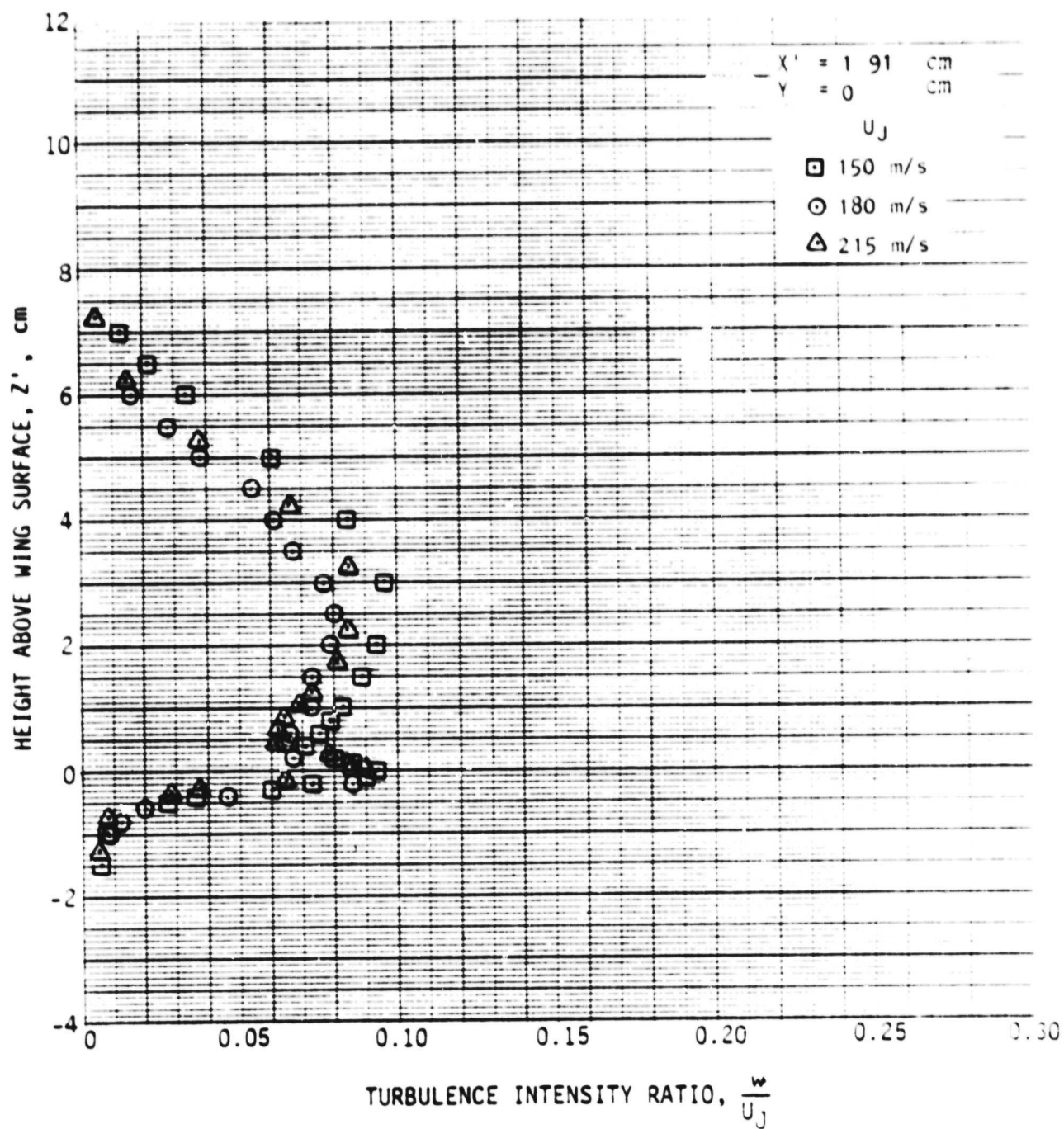


Figure 32. Concluded. (D) Turbulence Intensity, Transverse Component.

fluctuating velocities as illustrated in figures 32(a) and (b). The variation of the transverse velocity component (W, w) with jet velocity is not consistent as is shown in figures 32(c) and (d). It should be noted that the transverse velocity component is a very small percentage of jet velocity and is derived from the difference between two relatively large signals of cross hot-wire as discussed previously under the hot-wire measurement section. Therefore, these transverse component data are more vulnerable to errors due to calibration shifts, probe yaw, and probe positioning than are longitudinal data. These are probable reasons for the observed inconsistency of the variation of w with jet velocity.

The velocity gradient in the lower shear layer (secondary mixing region) of the trailing edge wake measured at a location where the peak turbulence is shown in figure 33 for three jet velocities. It can be seen that the effect of jet velocity on the velocity gradient is small.

Effect of initial turbulence. An examination of the velocity profiles in the trailing edge wake taken with and without the screen at the nozzle exit shows that the peak velocities (and therefore velocity potentials) are greater with the screen than without it. It may be hypothesized that the screen tends to establish turbulence of smaller scale than would otherwise occur. This small-scale turbulence is less effective in smoothing the velocity profile than is large-scale mixing. Figure 34 shows the effect of initial turbulence (screen) on the velocity gradient in the lower shear layer. At the location close to the trailing edge, the velocity gradient is larger with the screen than that of without the screen. But, as the longitudinal distance increases the difference between these two gradients reduces as illustrated in this figure.

Effect of flap deflection. Increasing flap deflection from 30° to 60° considerably thickens the flow profile as can be seen in Figure 35(a). A reduction in U/U_j from 0.765 to 0.615 and a very significant reduction in velocity gradient accompany the broadening of the profile. However, there is little change in the longitudinal component of the fluctuating velocity, u , except the loss of the well-defined second peak as shown in figure 35(b).

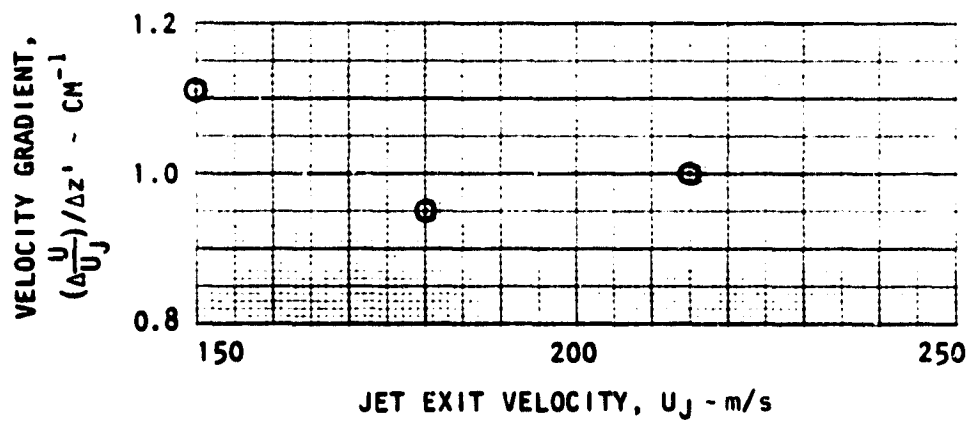


Figure 33. Effect of Jet Exit Velocity on Wake Velocity Gradients.

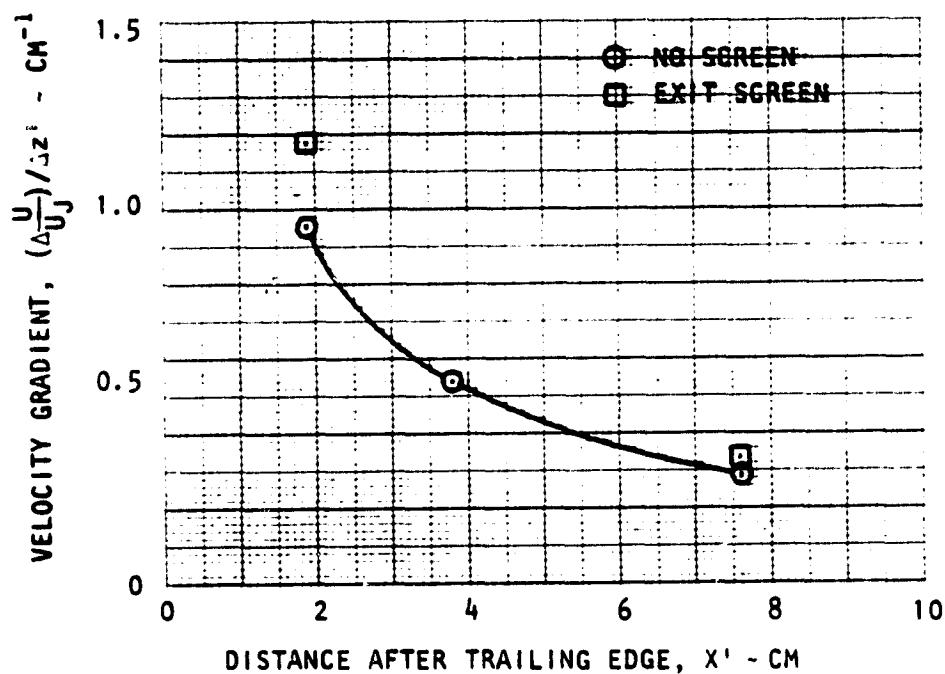


Figure 34. Effect of Nozzle Exit Screen on Wake Velocity Gradients.

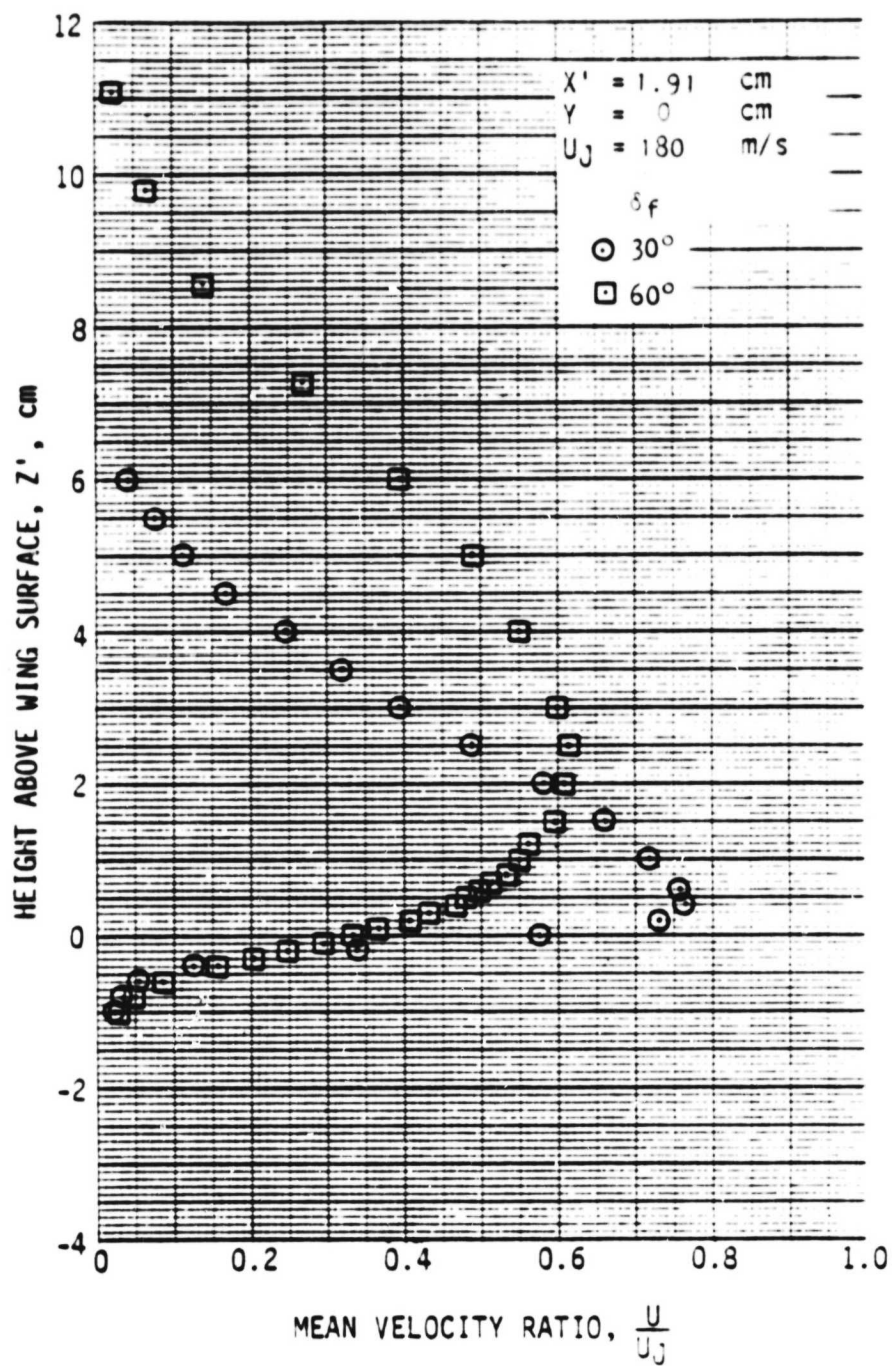


Figure 35. Effect of Flap Deflection on Wake Flow Characteristics. (A) Mean Velocity, Longitudinal Component.

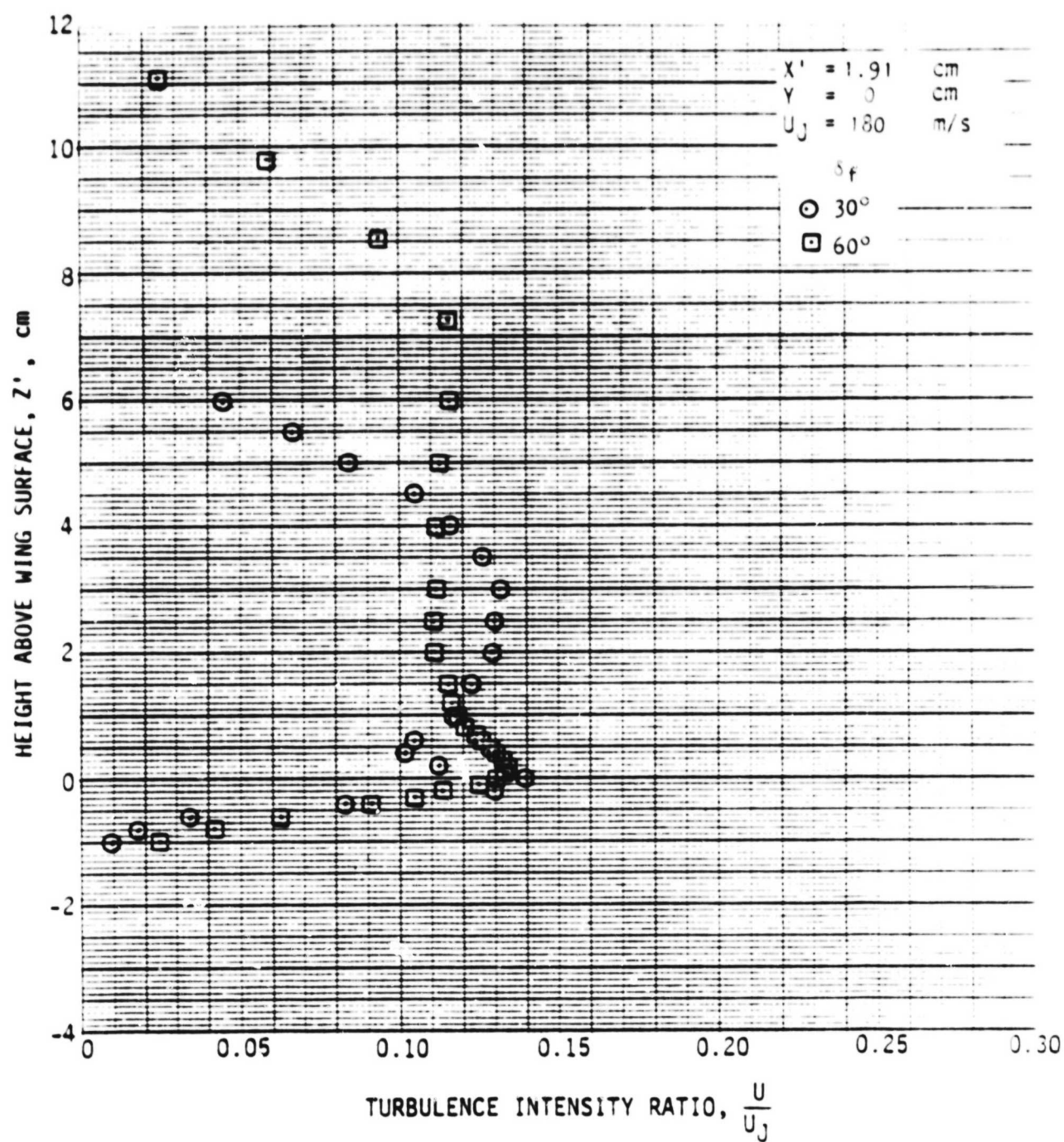
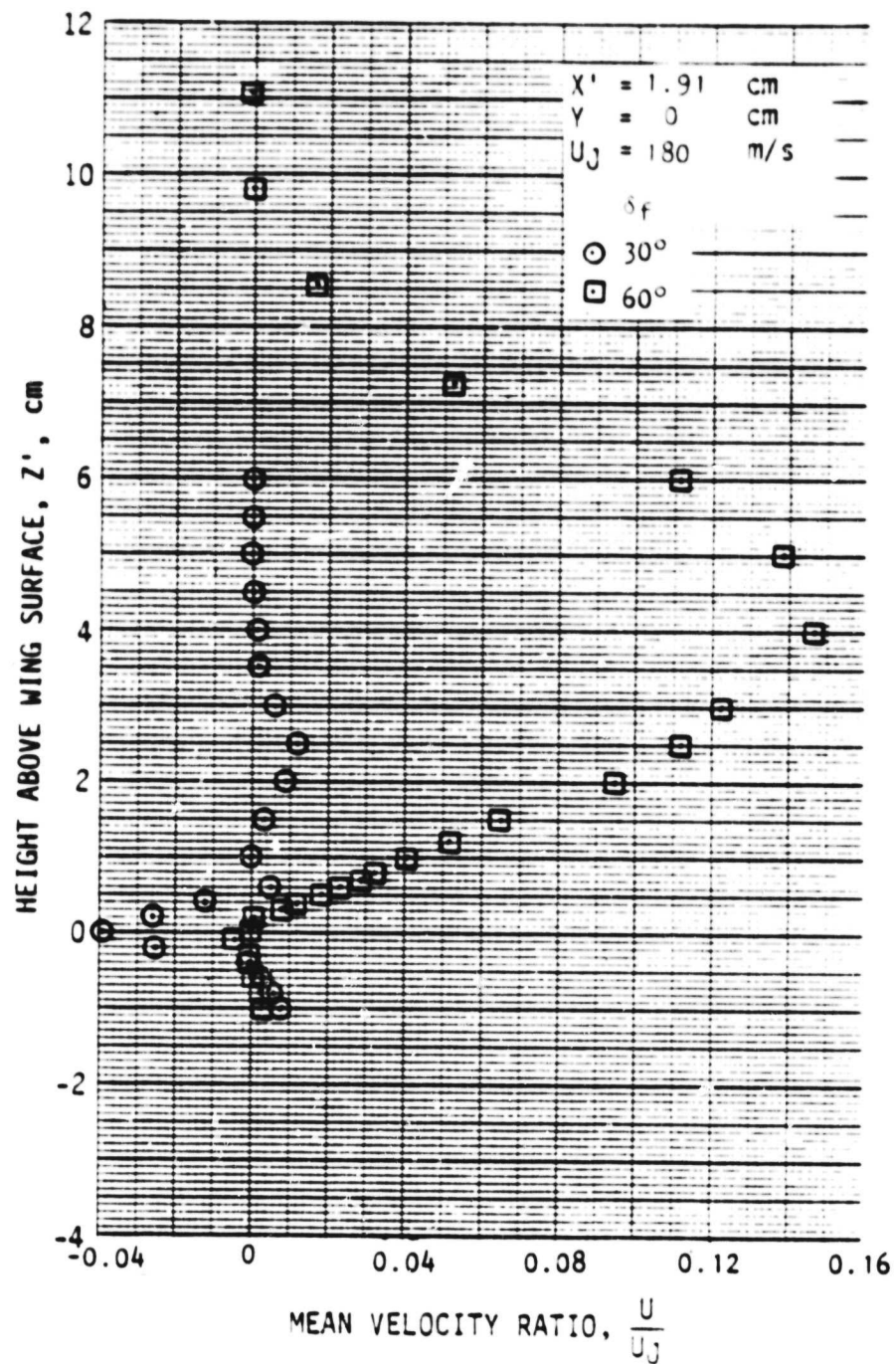


Figure 35. Continued. (B) Turbulence Intensity, Longitudinal Component.



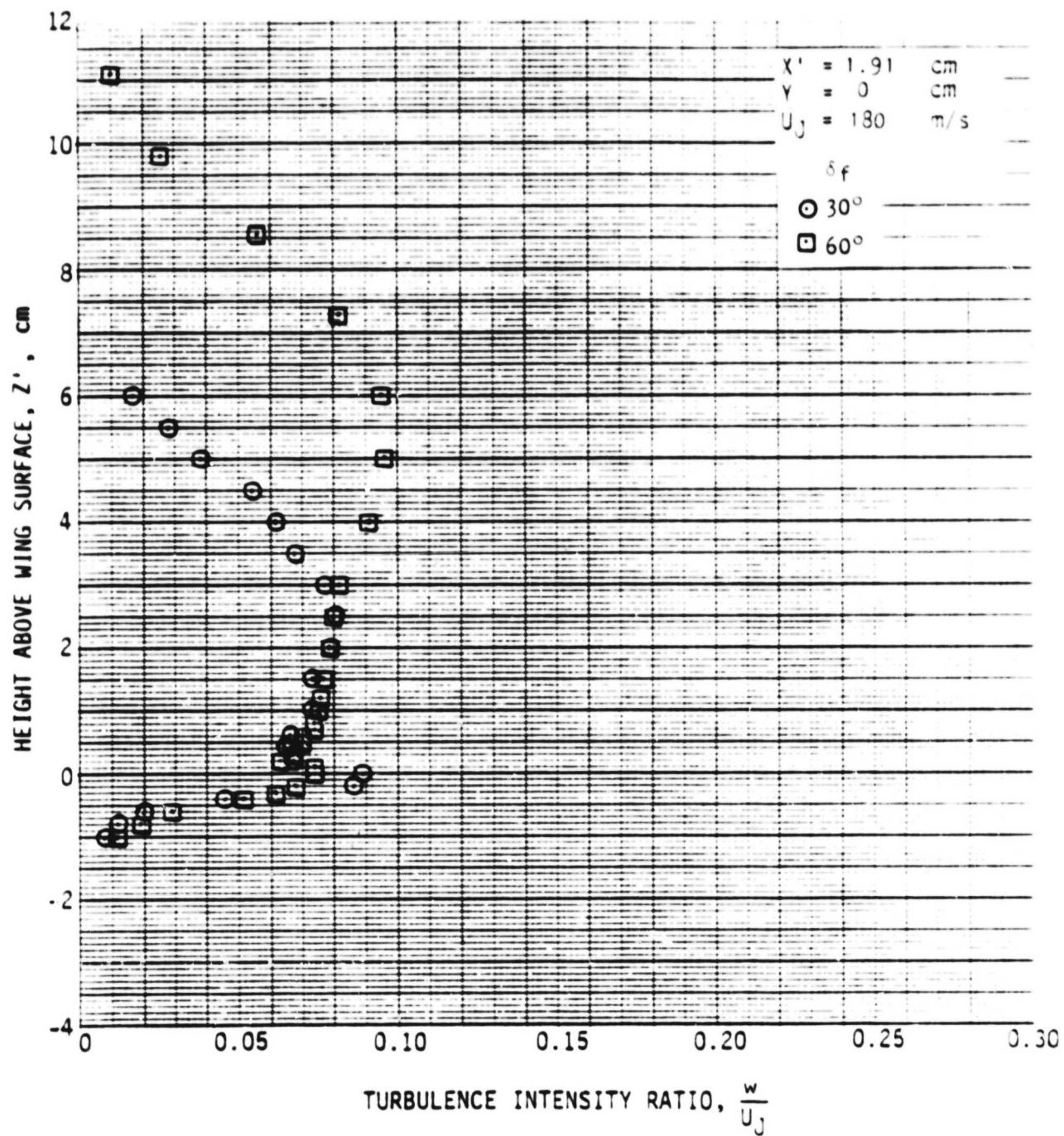


Figure 35. Concluded. (D) Turbulence Intensity, Transverse Component.

There is considerable increase in the transverse velocity, W , as flap deflection is increased. As shown in figure 35(c), W is increased from -4% to +15%. That increase is accompanied by a considerable broadening of the fluctuating velocity (w) profile and an increase in peak turbulence intensity level in the outer mixing layer as shown in Figure 35(d). Flow turning and increased outer layer mixing diminish the maximum velocity in the jet and create a thick boundary layer so that much less velocity gradient exists for the generation of turbulence.

The effect of flap angle on the velocity gradient is shown directly in Figure 36. It may be observed that the velocity gradient is smaller for 60° flap angle than for the 30° flap angle. This figure also illustrates that the velocity gradient diminishes rapidly with distance behind the trailing edge.

The test data of mean and fluctuating velocity profiles at different locations of the trailing edge are presented in the Appendix.

Near-field noise. The near-field fluctuating pressures were measured in the vicinity of the wing/flap surface just outside the flow as discussed previously. The effects of the jet velocity, the initial turbulence, and the flap angle on the near-field pressure spectra are discussed in the following paragraphs. The complete near-field pressure data are presented in the appendix.

Effect of jet velocity. Figure 37 shows one-third octave spectra measured near the flap trailing edge and below the wing for four jet velocities. These spectra exhibit a maximum SPL at a well defined peak frequency. It may be observed in this figure that the peak frequency and the SPL increase as the jet exit velocity increases. The line drawn through the peak SPL's in this figure indicates that the peak frequency increases linearly with jet velocity. Since the total fluctuating pressures are proportional to peak SPL's, the variation of the pressure magnitude with jet velocity may be studied by observing the effect of jet velocity on the peak pressures of the spectra as shown in figure 38. The fluctuating pressures vary as jet velocity raised to the power 4.3. The longitudinal component of the

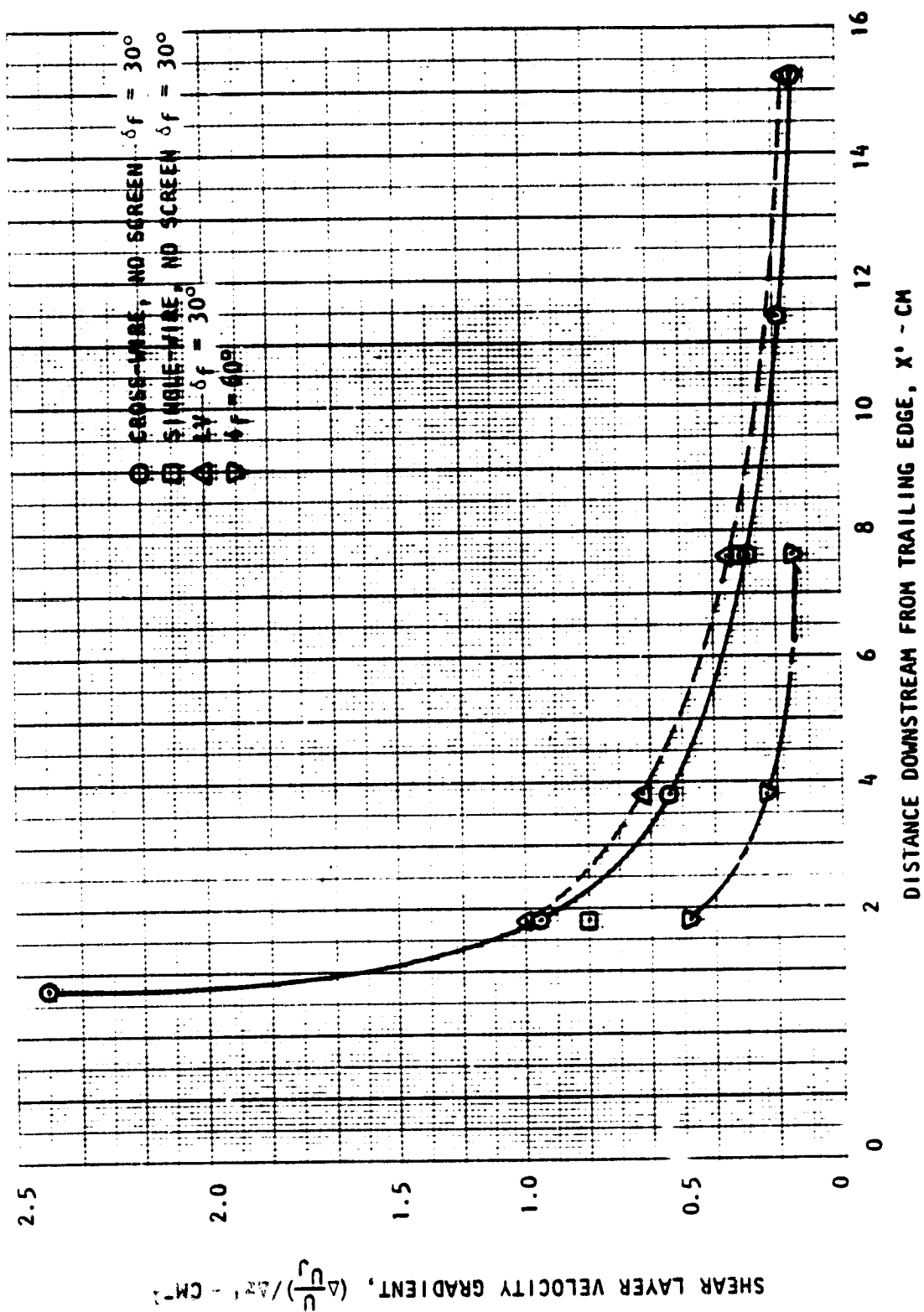


Figure 36. Shear Layer Velocity Gradients in the Wake;
 $U_J = 180$ m/s (160 m/s for LV), $\delta f = 30^\circ$, $\gamma = 0$.

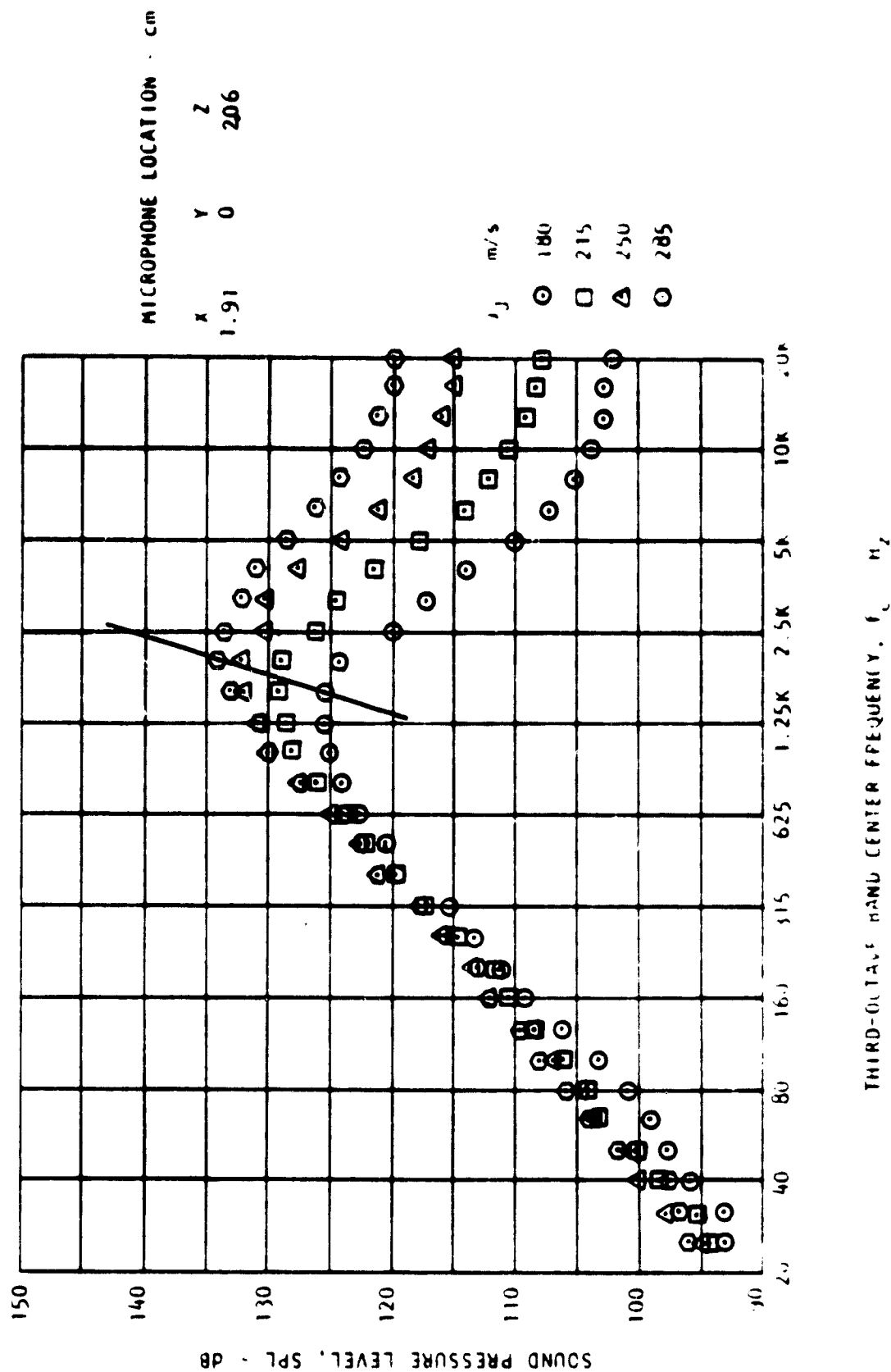


Figure 37. One-Third Octave Band Spectra of Near-Field Noise
 $\delta_f = 30^\circ$ Microphone No. 9 (see fig. 14)

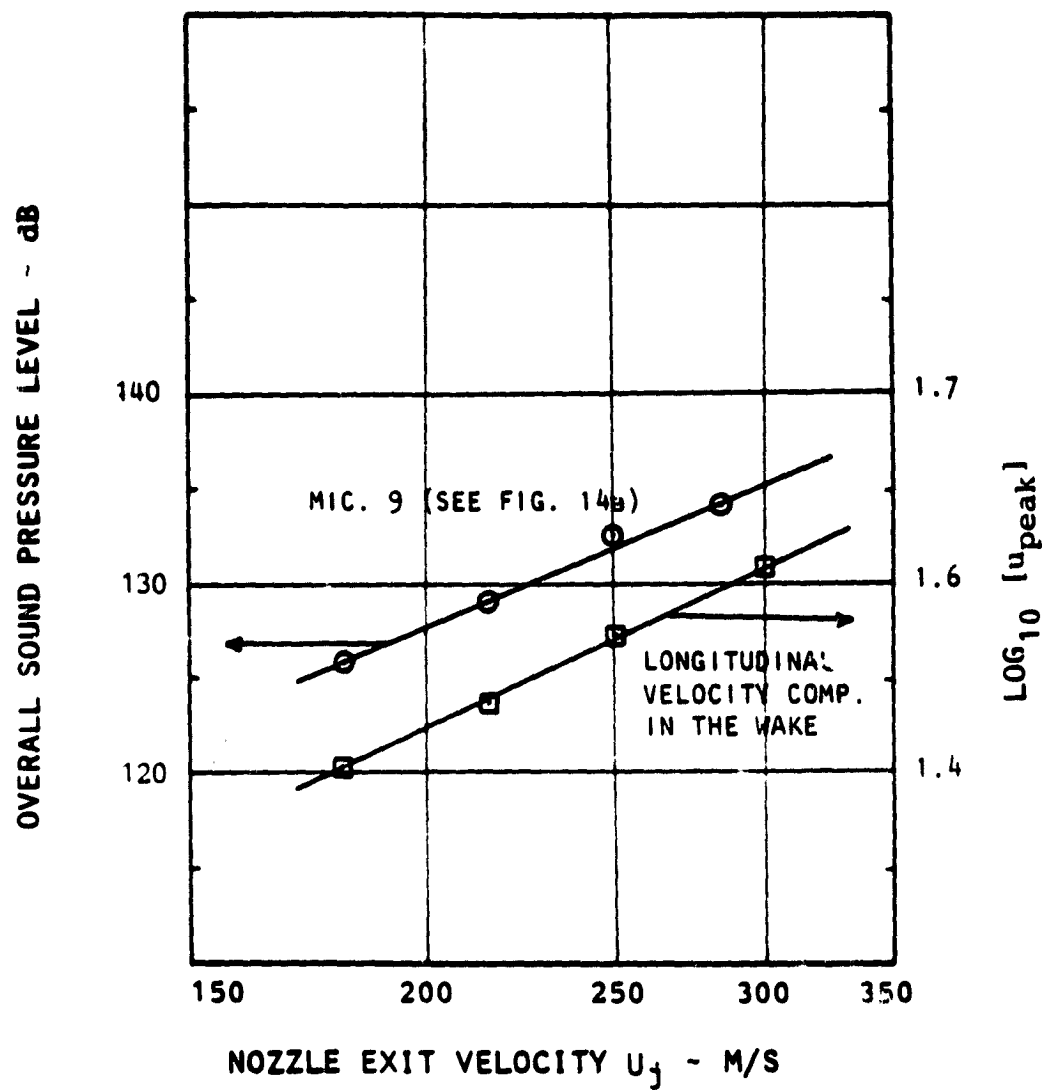


Figure 38. Effect of Jet Velocity on Fluctuating Pressures and Turbulence Velocity.

fluctuating velocity also varies in the same proportion as the fluctuating pressures. From these observations, it may be hypothesized that the cause of these fluctuating pressures is the turbulence generation in the trailing edge wake. Figure 39 shows the variation of near-field noise spectra measured at a location above the wing with jet velocity. For each velocity, there are two well-defined peak pressure levels in this figure. In the same way at a location below the wing (fig. 37), both peak SPL and peak frequency increase as the velocity increases. The high-frequency peak is attributed to the secondary mixing region (close to the trailing edge), and the low frequency peak is attributed to the primary mixing region (away from the surface). Effect of the primary mixing region is not seen at the measurement location below the wing (fig. 37).

Effect of initial turbulence. The effect of initial turbulence (nozzle exit screen) on the near-field fluctuating pressures is shown in figure 40. Increase in initial turbulence (screen at the nozzle exit) increases the sound pressure levels in all frequencies in the direction below the wing as shown in figure 40(a). The SPL increase in the high-frequency range, however, is slightly larger than that of the low frequency range. In the direction above the wing the increase in sound pressure levels due to the screen is primarily in the mid- and high-frequency ranges [fig. 40(b)]. It may also be observed in these figures that the screen at the nozzle exit shifts the spectrum toward higher frequencies. The same trends were observed at all the other locations in the direction above the wing (see Appendix D for the spectra in the other locations). Therefore, it may be concluded that the screen produces a small-scale turbulence structure which dominates the high-frequency fluctuating pressures.

Effect of flap angle. The effect of flap angle on the near-field noise is studied by comparing the one-third octave band spectra for flap angles of 30° and 60° at locations below the wing and above the wing near the trailing edge. These results are shown in figure 41. It may be observed in this figure that by increasing the flap angle from 30° to 60° , the spectra below the wing shifts towards lower frequencies [fig. 41(a)]. But the magnitude at this location (below the wing) is not affected by the flap angle. At the

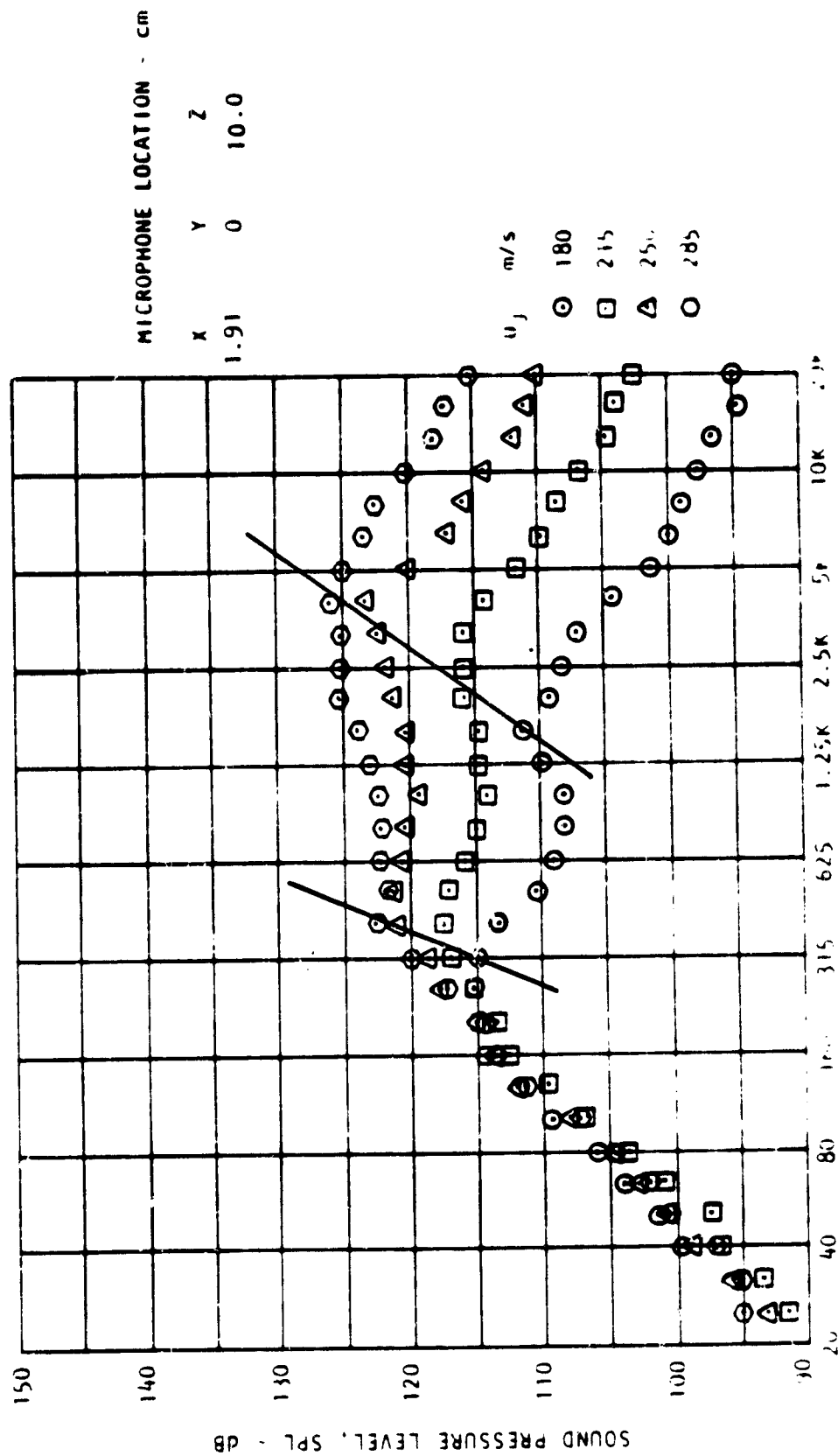
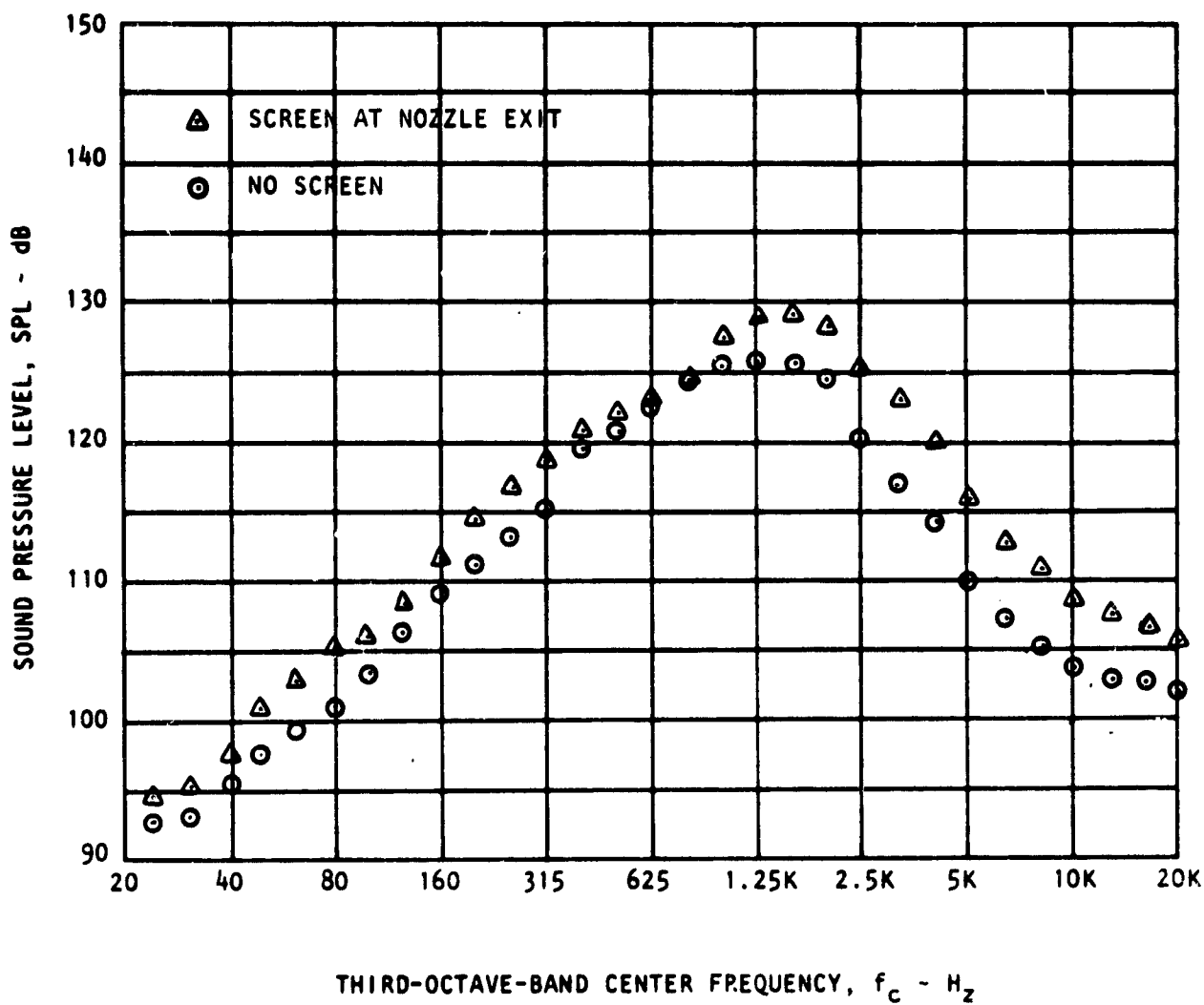
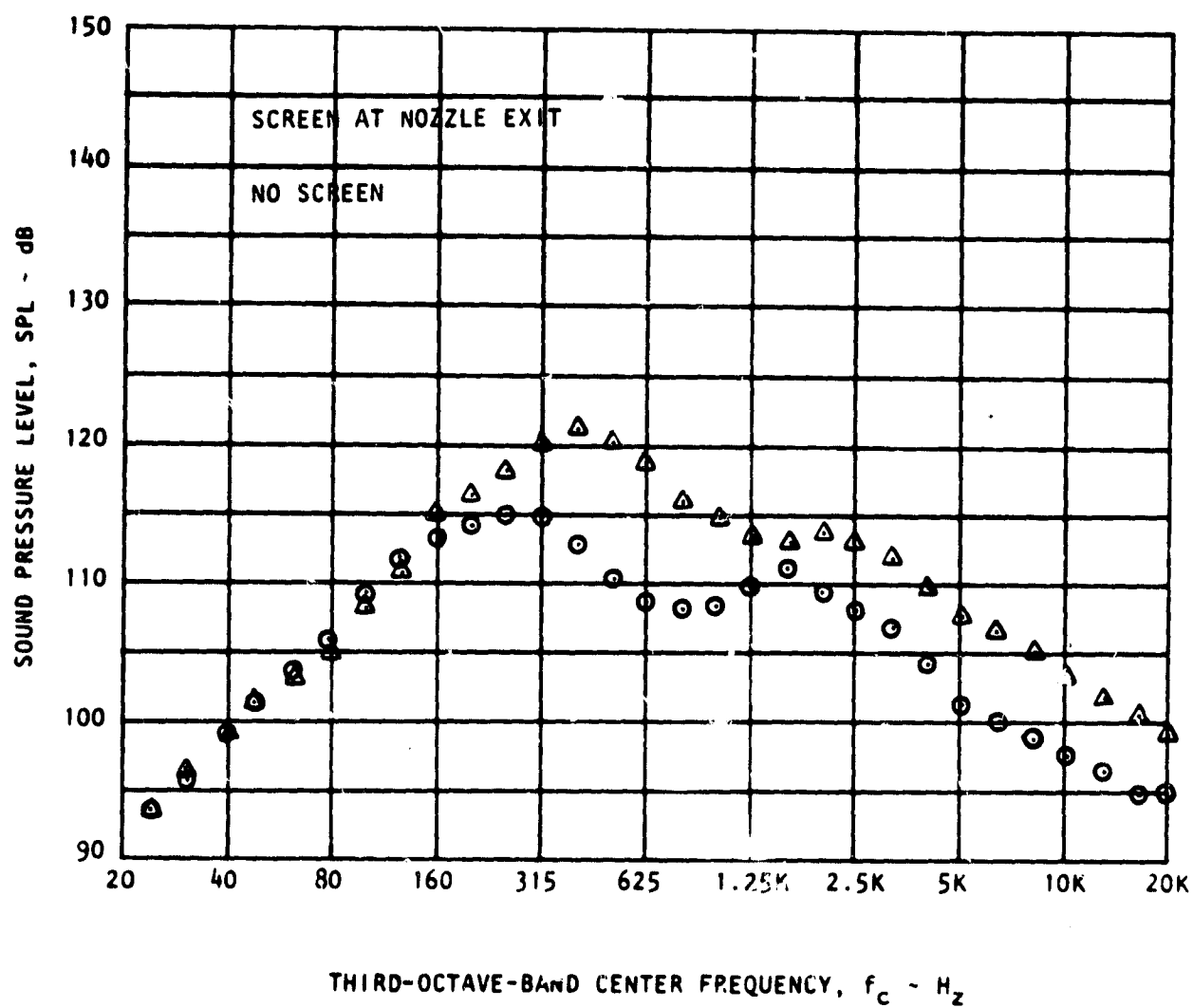


Figure 39. One-Third Octave Band Spectra of Near-Field Noise
 $\delta_f = 30$. Microphone No. 4 (see fig. 14)



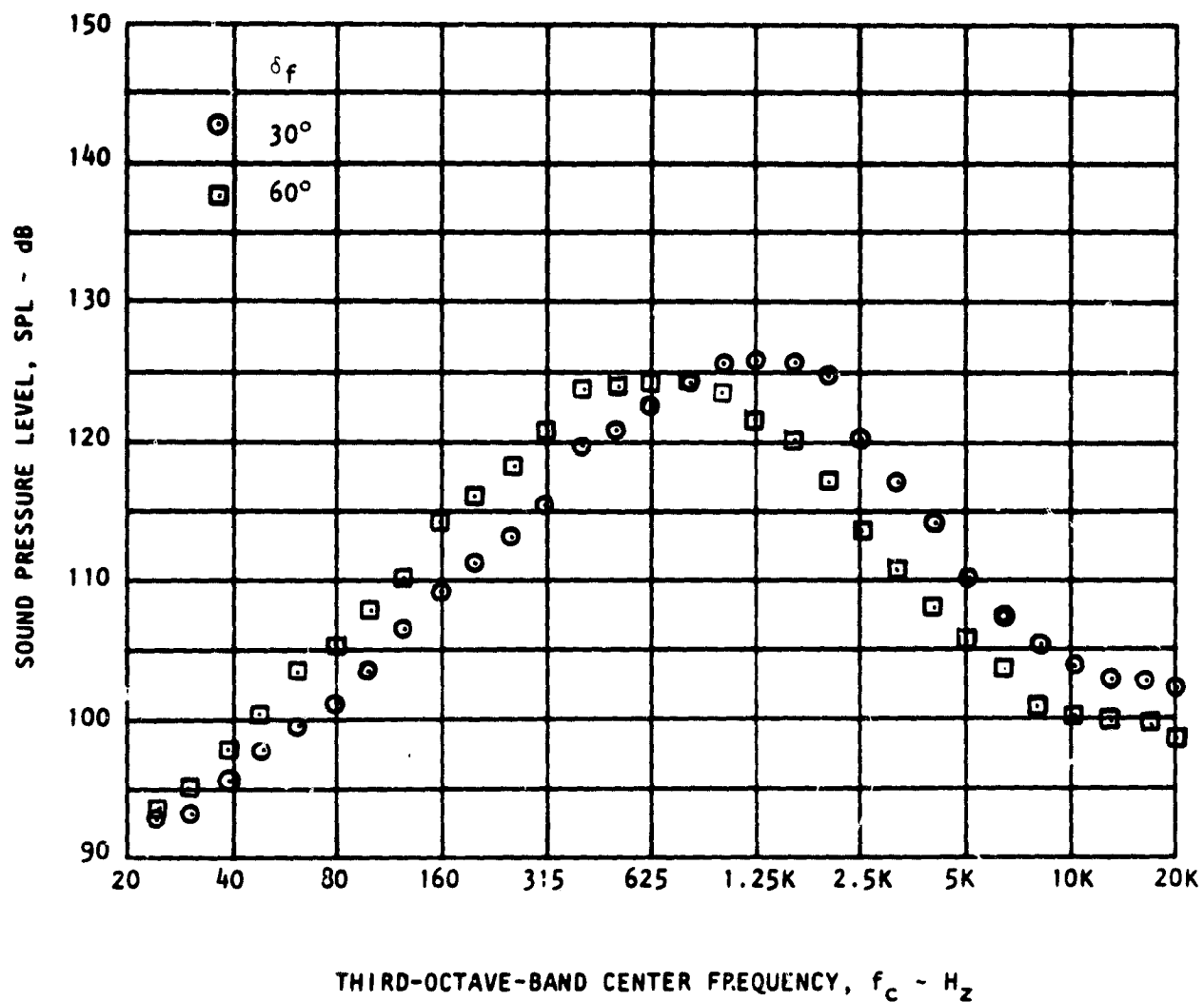
(a) Microphone 9 (See Fig. 14)

Figure 40. Effect of Screen on Near-Field Noise,
 $U_j = 180$ m/sec., $\delta_f = 30^\circ$



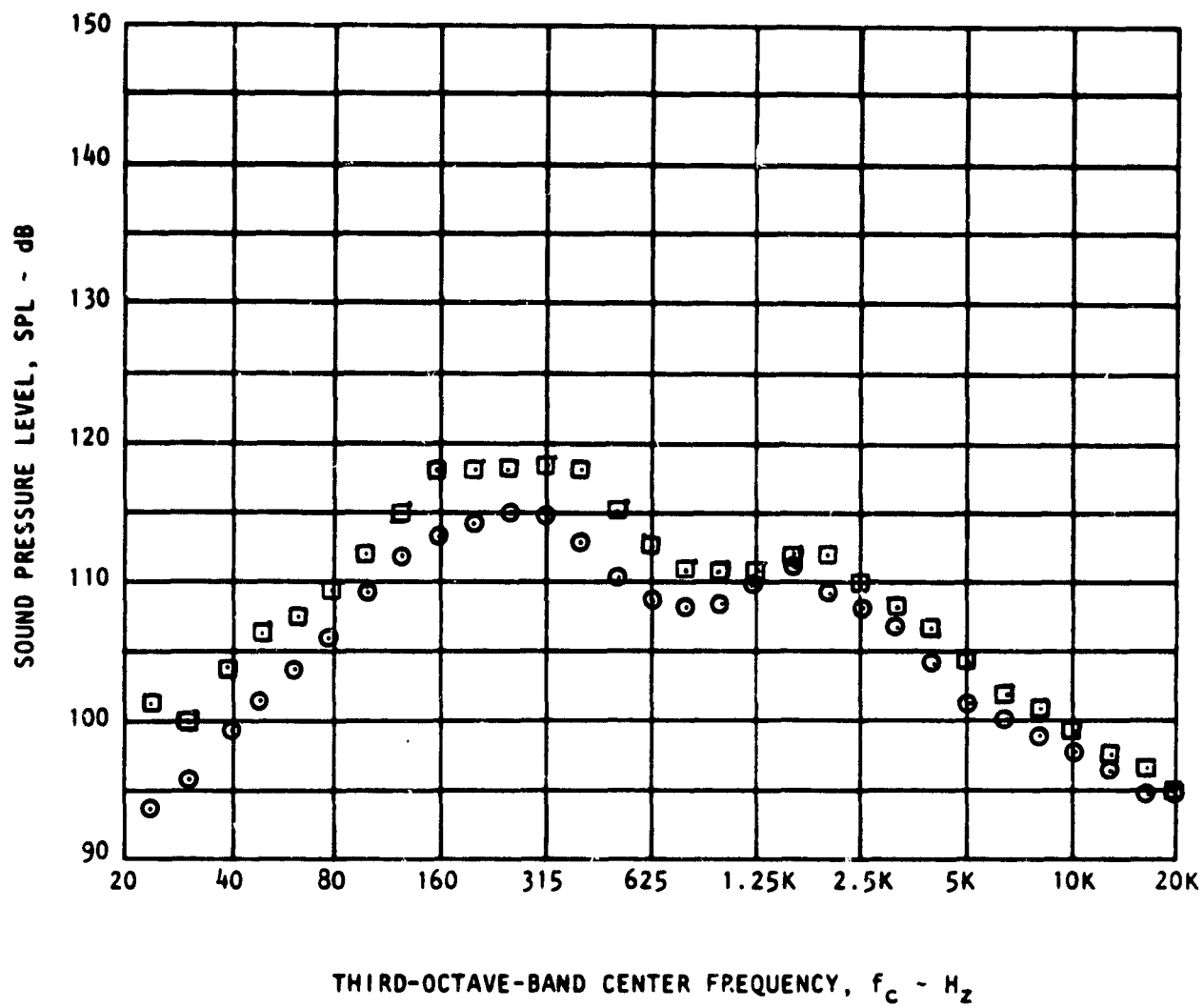
(b) Microphone 4 (See Fig. 14)

Figure 40. Concluded.



(a) Microphone 9 (See Fig. 4)

Figure 41. Effect of Flap Angle on Near-Field Noise,
 $U_j = 180$ m/sec, No Screen.



(b) Microphone 4 (See Fig. 14)

Figure 41. Concluded.

location above the wing the change in peak frequency due to flap angle is negligible [fig. 41(b)], but the magnitude is increased. This is due to increase in turbulence intensity of the primary mixing region of the jet flow.

3.2 Flow Characteristics

As discussed previously, the mean velocities and the turbulence intensities in the trailing edge wake were measured using single hot-wire, cross hot-wire and laser velocimeter (LV) systems. These detailed measurements were obtained without a screen at the nozzle exit, for the 30° flap configuration, and at a jet velocity of 180 m/sec. The single hot-wire data are compared with the cross hot-wire data to evaluate the relative magnitude of the velocity components, u , v , w and to assess the adequacy of the single-wire measurements to represent the flow characteristics. The LV data are compared with the hot-wire data to evaluate the relative merits of the LV and hot-wire systems to measure the flow characteristics of blown flap configuration. The detailed turbulence structure is studied from the measured data.

Comparison of single hot-wire data with cross hot-wire data and LV data.

Mean velocity and turbulence intensity profiles in the trailing edge wake obtained from single hot-wire, cross hot-wire and LV systems are compared with each other in figure 42. The single wire data was measured with the wire parallel to the trailing edge to obtain the resultant of longitudinal and transverse velocity components. The cross wire and LV data presented in this figure are the longitudinal components alone derived from the two signals as discussed previously. One would expect that single hot-wire data should be of larger magnitude than the cross wire data or LV data because single-wire measures some of the two components. From the results in this figure, however, it is clear that the mean velocities obtained by the three systems do not differ from each other [fig. 42(a)]. But the turbulence intensity measured by the LV and the single wire are slightly higher than the cross-wire data [fig. 42(b)]. For the LV measurements the seeding was introduced into the flow upstream of the nozzle and the seeding in the outer entrained flow was sparser than that in the region of higher velocity. This phenomena of bias

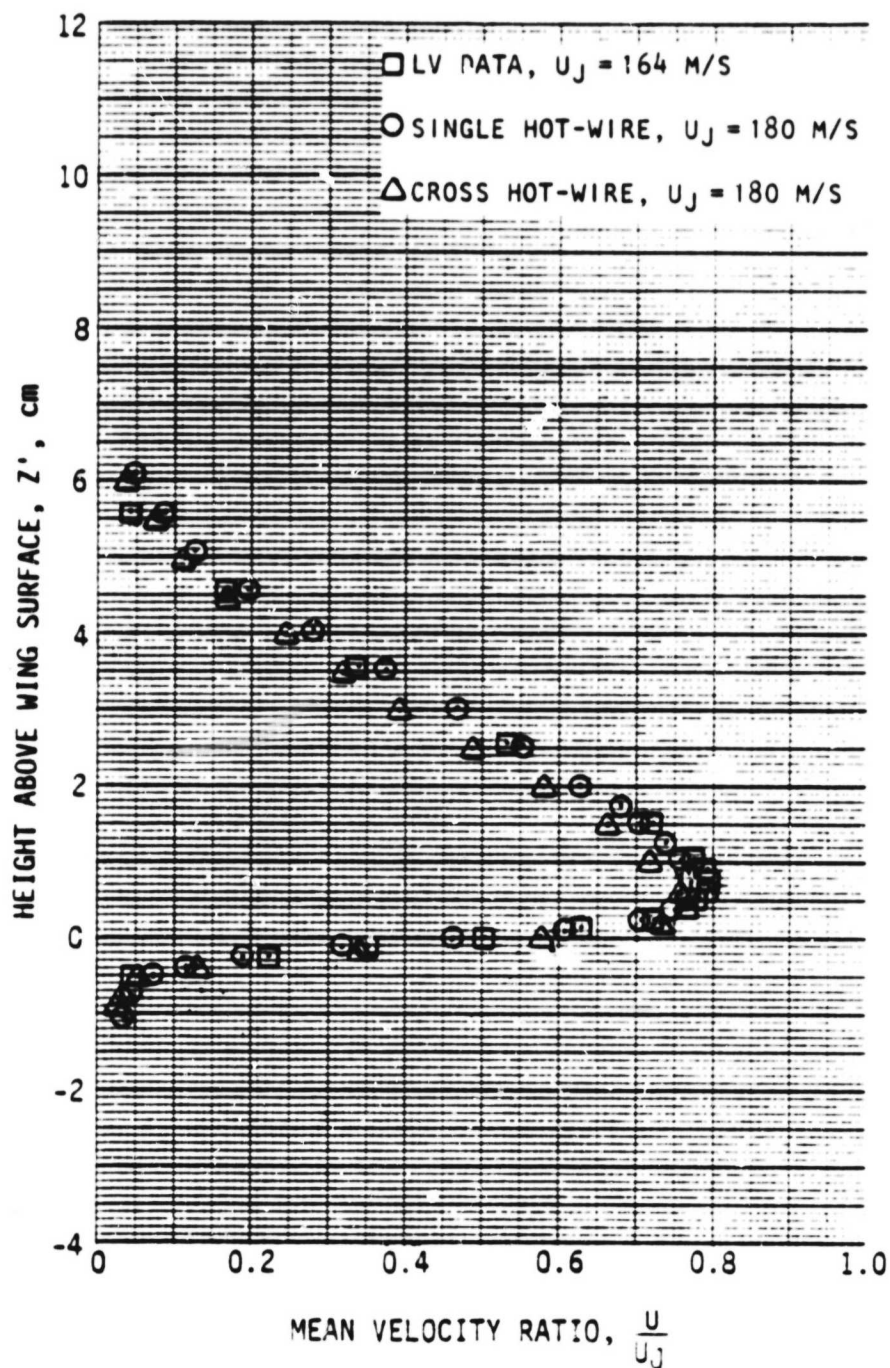


Figure 42. Comparison of LV Data With Hot-Wire Data Just Downstream of the Trailing Edge. $X' = 1.91$ cm, $Y = 0$. (A) Mean Velocity Profile.

ORIGINAL PAGE IS
OF POOR QUALITY

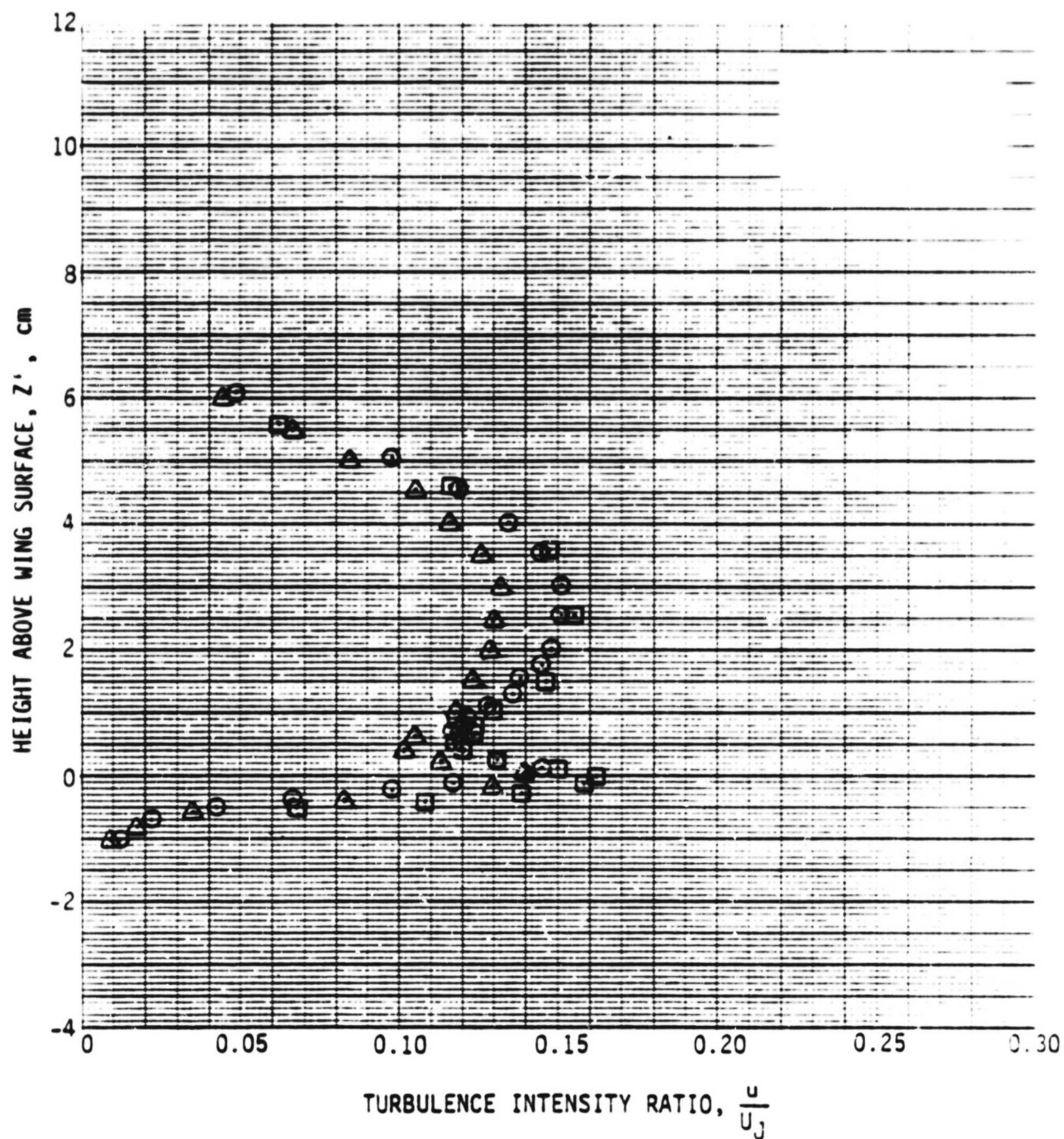


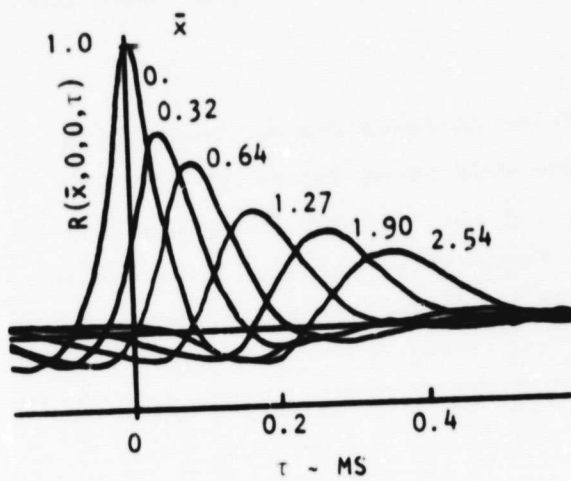
Figure 42. Concluded. (B) Turbulence Intensity Profile.

in the LV measurements is a probable cause for measuring the higher magnitude of fluctuating velocity.

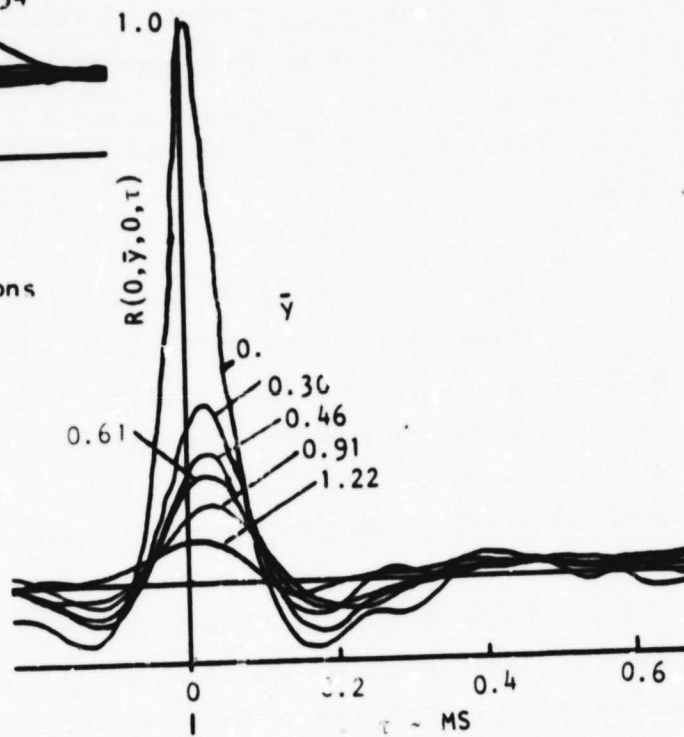
Turbulent structure. Two-point space-time correlations of fluctuating velocities were measured in the trailing edge wake using two cross hot-wire probes, with four-channel system. The longitudinal, lateral and transverse correlations of the transverse component of fluctuating velocity measured in the trailing edge wake are shown in figure 43. Several important turbulence characteristics such as eddy convection velocity, longitudinal, spanwise, and lateral turbulence scales are deduced from these correlation measurements as discussed below.

Convection velocity. The convection velocity, U_c , characterizes the gross motion of turbulence in the longitudinal direction. A signal of fluctuating velocity at one measurement position is received at a second position, distance x_1 , downstream of the position of time τ_1 later. For a frozen pattern of turbulence, the convection velocity, U_c , is defined as the ratio of the distance travelled by the eddy per unit time. This convection velocity can be evaluated from the longitudinal space-time correlations as $U_c = x_1/\tau$, where x_1 is the fixed separation distance and τ is the delay time at $\partial R(x_1, \tau)/\partial \tau = 0$. Observation of the space-time correlation function indicates that the peak value of correlation function occurs where $\partial R(x_1, \tau)/\partial \tau = 0$. The convection velocity, therefore, is determined by taking the slope of a curve, hot-wire separation distance vs. the delay time for maximum correlation function as shown in figure 44. From this figure, U_c is calculated as 81 m/sec. for 30° flap and 60 m/sec. for 60° flap. These convection velocities are approximately 0.6 times the maximum peak velocity in the trailing edge wake.

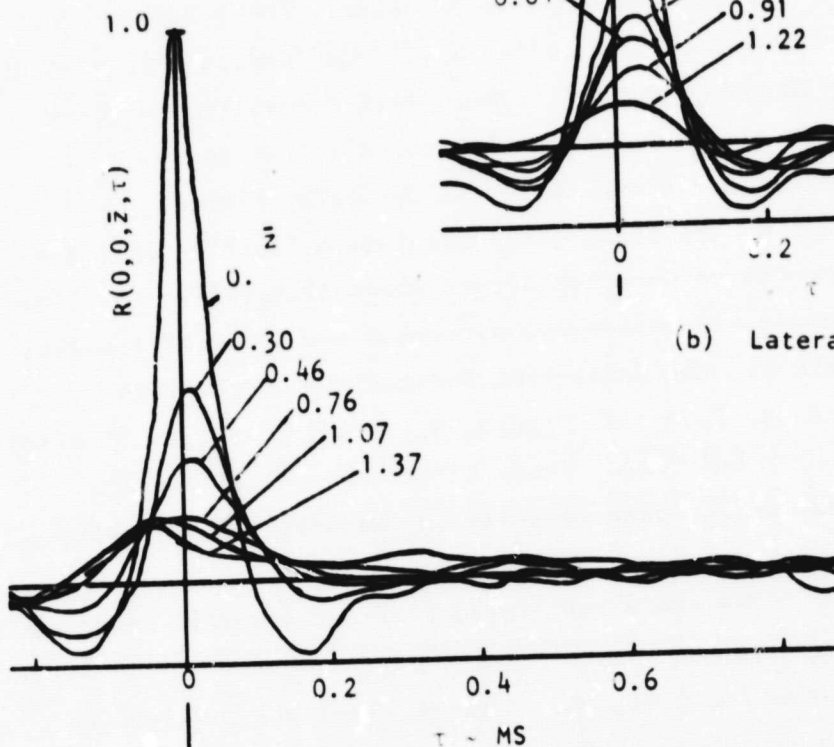
Integral length scales. The space correlations of longitudinal velocity fluctuations in the longitudinal and lateral (x,y) directions are given in figure 45. These are obtained from the space-time correlations plotted for zero time delay. The fixed wire for these measurements was located at $x'_0 = 1.91$ cm, $y'_0 = 0$, and $z'_0 = 0$. These correlations provide a measure of the size of turbulent eddies (or coherent region). The length scale in these directions are defined as



(a) Longitudinal correlations



(b) Lateral correlations



(c) Transverse correlations

Figure 43. Space-Time Correlation Functions of Transverse Velocity Component. $U_j = 180$ m/s, $\delta_f = 30^\circ$, $(x' = 1.91$ cm, $y' = 0$, $z' = 0)$.

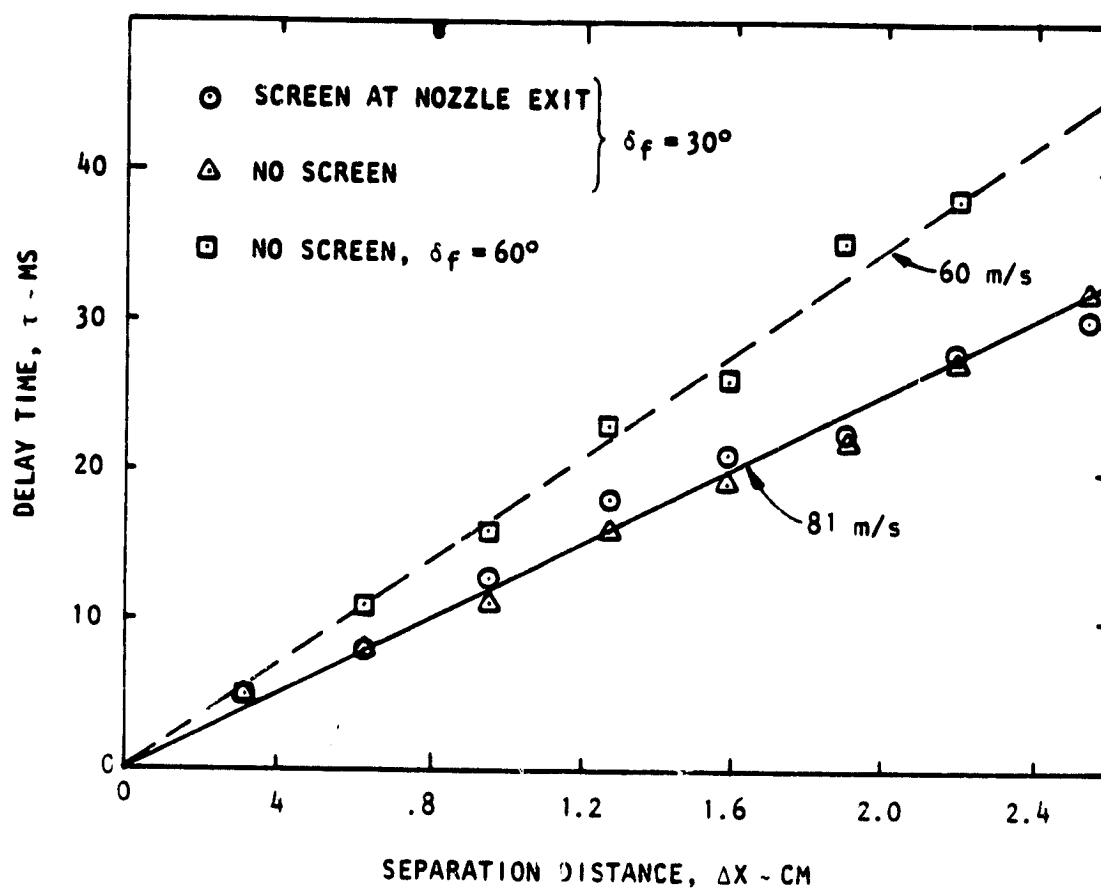
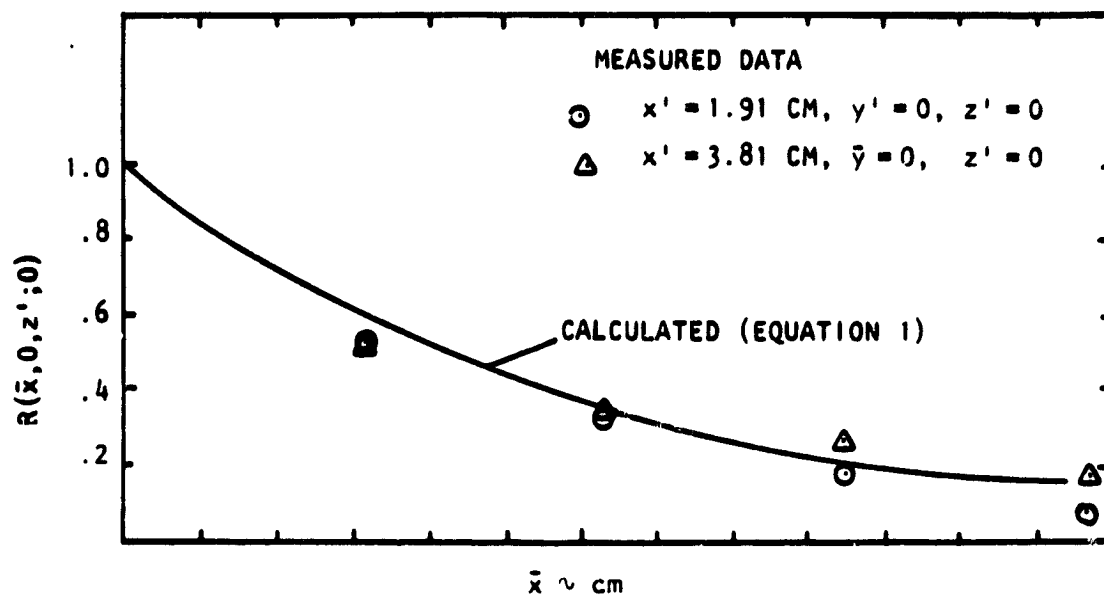
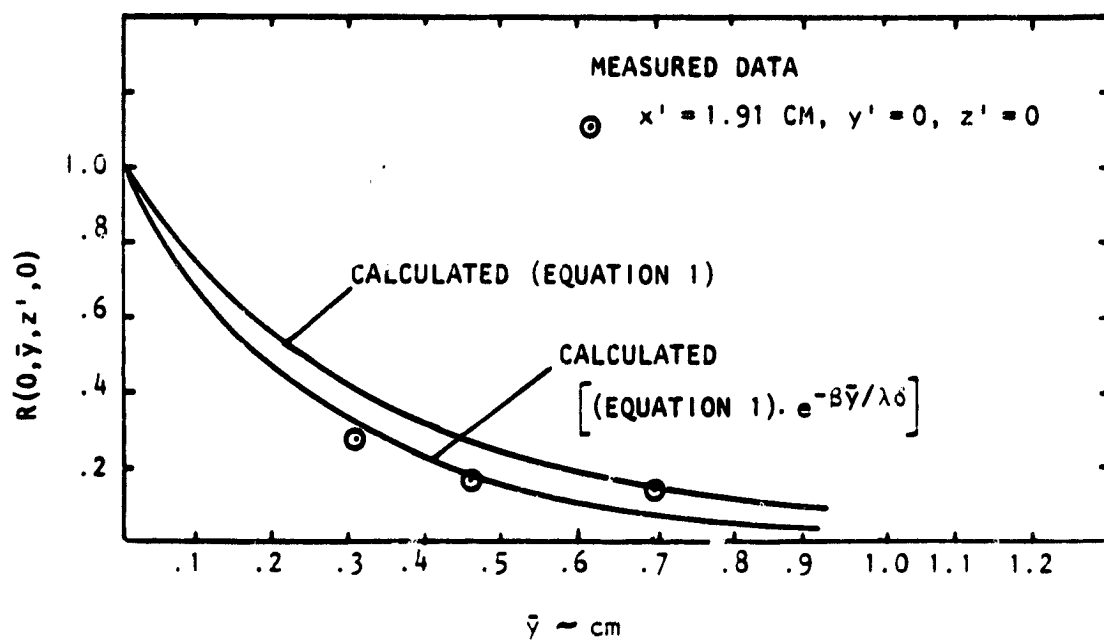


Figure 44. Variation of Peak Correlation Time With Separation Distance, $U_j = 180$ m/s.



(a) LONGITUDINAL CORRELATION



(b) LATERAL CORRELATION

Figure 45. Space Correlation Function of Wake Turbulence
 $\delta_f \approx 30^\circ, U_j = 180 \text{ m/s}$

$$L_x = \int_0^{\infty} R(\bar{x}, 0, 0, 0) d\bar{x} ,$$

$$L_y = \int_0^{\infty} R(0, \bar{y}, 0, 0) d\bar{y} ,$$

$$L_z = \int_0^{\infty} R(0, 0, \bar{z}, 0) d\bar{z} .$$

The scale of anisotropy is defined as the ratio of streamwise to spanwise length scales. From figure 45 it is found that $L_x = 0.625$ cm, $L_y = 0.27$ cm. This gives a scale of anisotropy, $\beta = L_x/L_y = 2.3$. This value is comparable to that measured in the initial mixing layer of turbulent jets (ref. 4) and the trailing edge wake shear layer of similar configuration (ref. 2). Generally the length scales are inversely proportional to the velocity. But the scale of anisotropy is not a function of velocity.

Longitudinal decay rate. Turbulence structure (eddy) will lose its coherence after traveling a certain distance downstream. This characteristic length can be estimated from the spatial envelope of the space-time correlation function. The variation of the peak correlation function with the longitudinal distance is shown in figure 46. The equation of the form, $R(x) = e^{-x/\lambda\delta}$ is derived from the experimental data. The longitudinal decay rate of the correlation function, $\lambda\delta$ is found to be 1.44, where δ is the shear layer thickness.

Power spectra. Cross power spectra of the fluctuating velocities of the trailing edge wake in the longitudinal, lateral, and transverse directions are shown in figure 47. The variation of the power spectral density and the phase angle with the frequency are shown in these figures. The longitudinal cross-power spectral density [fig. 47(a)] shows that as the frequency increases the phase angle decreases from 0° to -180° at a constant rate. The

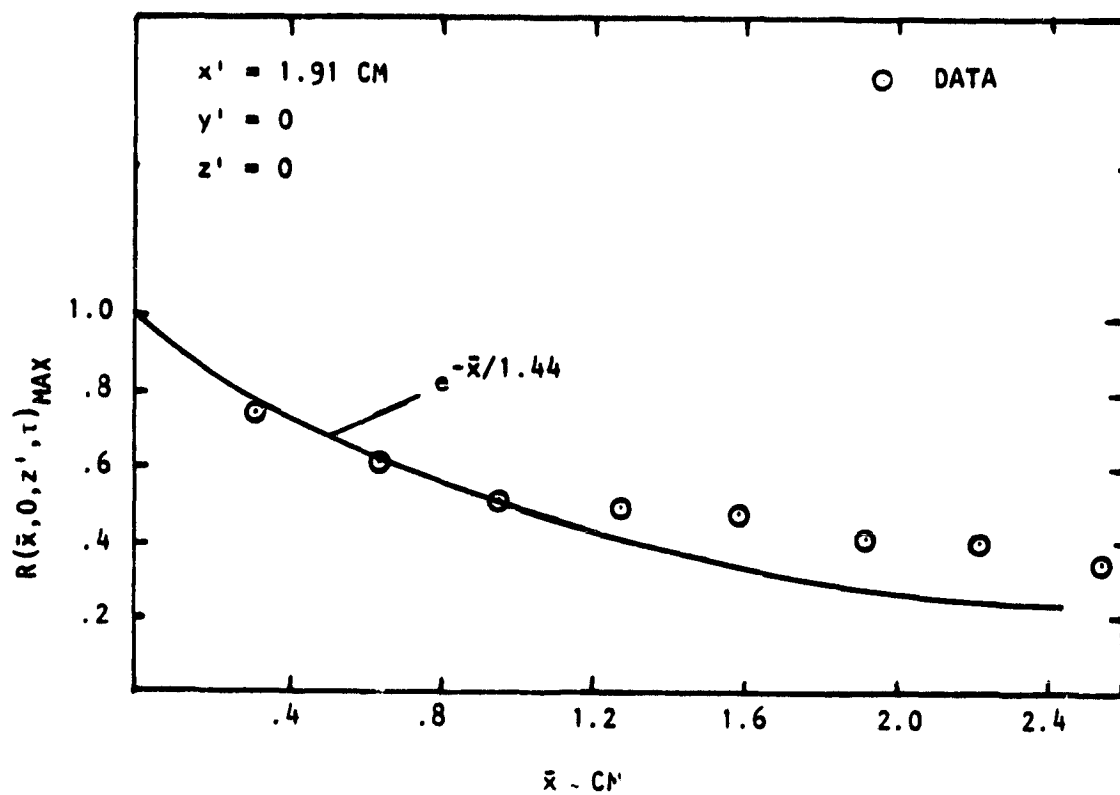


Figure 46. Longitudinal Decay of u Correlation Function.
 $U_j = 180 \text{ m/s}$, $\delta_f = 30^\circ$.

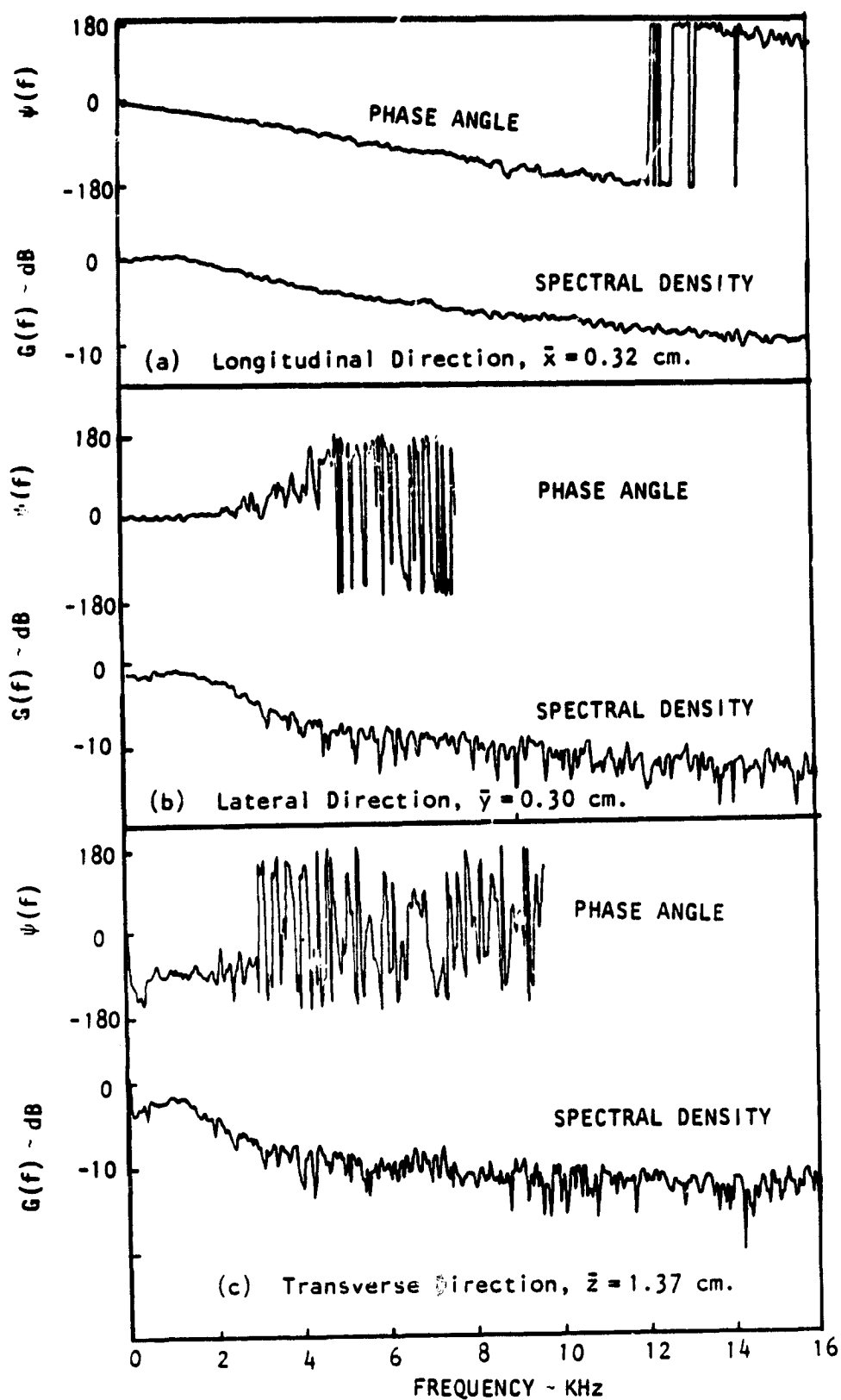


Figure 47. Cross Power Spectral Density and Phase Angle of Longitudinal Velocity Component. $U_j = 180$ m/s, $\delta_f = 30^\circ$, $(x' = 1.91 \text{ cm}, y' = 0, z' = 0)$.

rate of change or the slope of this phase angle with frequency is about 1° per 68 Hz. The convection velocity which may be assumed to be the same as the phase velocity of the turbulence in the longitudinal direction is calculated as

$$U_c = 2\pi f \cdot \frac{\bar{x}}{\theta} = 78.4 \text{ m/sec.}$$

This value is the same order of magnitude as obtained from the cross correlations (81 m/sec). Since the variation of the phase angle with the frequency is constant throughout the frequency range, it is concluded that the convection velocity in the trailing edge wake is independent of frequency. Comparing the cross-power spectra in the longitudinal direction with those of lateral and transverse directions [fig. 47(b) and (c)], it is apparent that the spectral density drops faster with frequency in the lateral and transverse directions than in the longitudinal direction. The lateral and the transverse phase angles vary randomly for frequencies greater than about 3000 Hz. The phase angle in the lateral direction [fig. 47(b)] increases with frequency (between 3000 to 5000 Hz) indicating the negative convection velocity. If the flow is completely two dimensional, the convection velocity with lateral direction should be zero. Since the convection velocity is not zero, it may be suspected that the flow is not completely two dimensional.

Correlation between turbulence and near-field noise. The correlations of the fluctuating velocities, u, w , with the near-field noise are shown in figure 48. The fluctuating velocity is measured in the mid-span plane at $x' = 1.9 \text{ cm}$, $y' = 0$, $z' = 0$, and the near-field noise is measured at $x' = 1.91 \text{ cm}$, $y' = 0$, $z' = 1.91 \text{ cm}$. The correlation functions in this figure are normalized with respect to the product of the mean square values of the velocity and pressure measured in their respective locations.

The curve $R_{up}(\tau)$ shown in figure 48 indicates that u and p are in quadrature as discussed in reference 5. The first positive peak occurs at positive time delay, τ , indicating that the longitudinal component of velocity, u , leads the pressure by about 90° . This implies the presence of

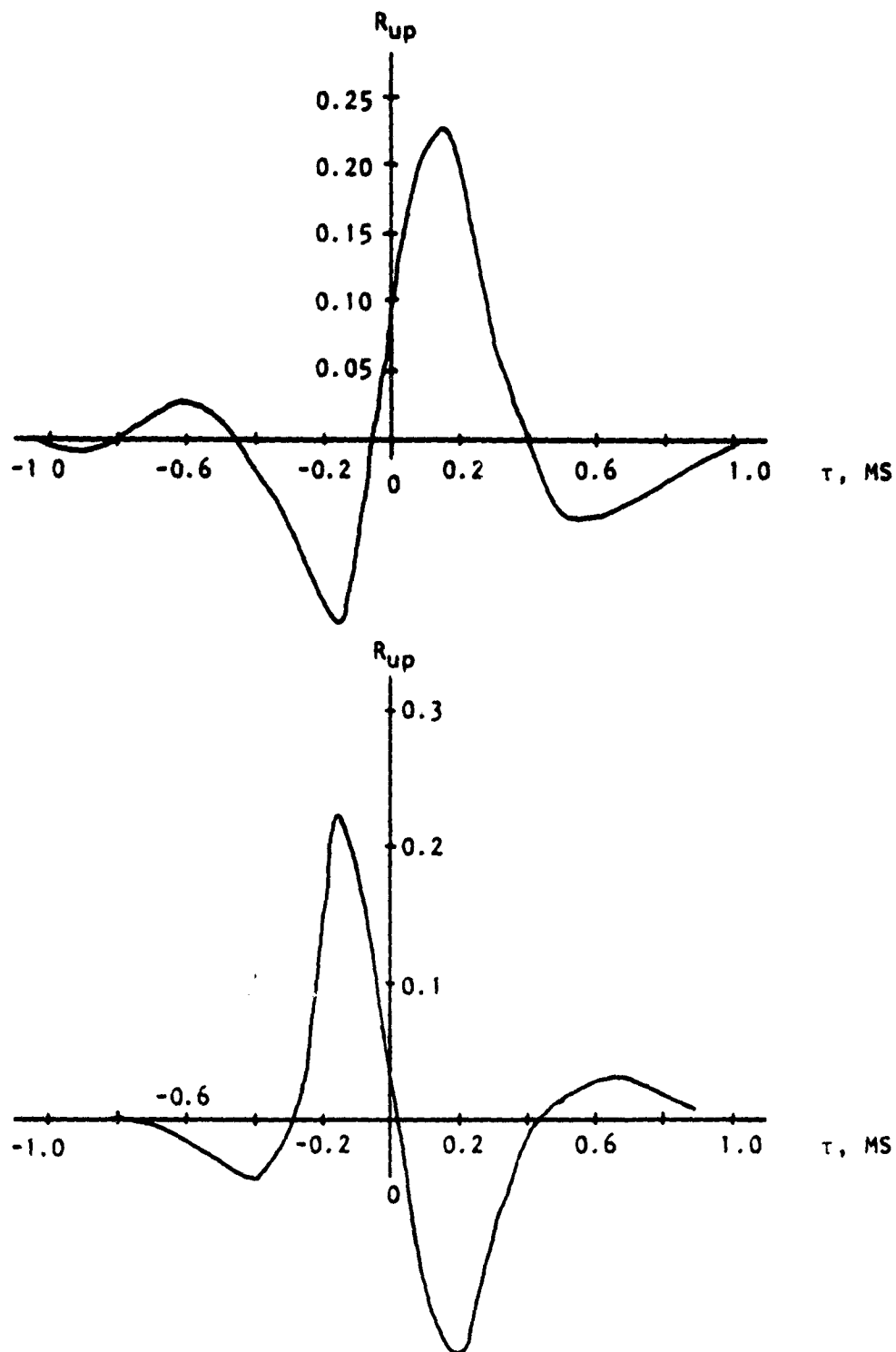


Figure 48. Fluctuating Velocity-Near-Field Noise Correlation Coefficient as a Function of Time Delay τ ; Microphone 2 and Hot-Wire 1 (See Figure 24).

vortex flow in the shear layer as in the jet mixing layer (ref. 5). The maximum value of R_{up} occurs at a time delay of about 145 microseconds and has a value of 0.227. The maximum value of R_{wp} occurs at time delay of about -150 microseconds and has a value of 0.223. This indicates that the transverse velocity component, w , lags the pressures by about 90° . Both correlation functions, R_{up} and R_{wp} are of the same order of magnitude. However, the magnitude of the transverse velocity component is about 0.6 times the longitudinal component. Thus, even though both u and w correlates equally well with the pressure signal, it may be concluded that the contribution of the longitudinal velocity component to the near-field pressure is more than the contribution of transverse velocity component.

3.3 Comparison of Measured Data With Prediction

An empirical noise prediction model for USB configurations and an analytical model for trailing edge wake turbulence were developed in reference 2. The radiated sound and the wake flow turbulence of USB configurations measured in the present tests are compared with the results predicted by the respective analytical models of reference 2.

Radiated sound field. Before we compare the measured noise with the predicted data, the noise spectral data measured under this program is compared in figure 49 with the data given in reference 1 for the same configuration. It is in this figure that the difference between the two sets of data is shown to be within the scatter of test data (± 0.5 dB). In the same figure, the predicted noise spectra is shown as a solid line. The measured OASPL directivity in the flyover plane ($\phi = 90^\circ$) is compared with the prediction in figure 50. These comparisons of spectra and directivity indicate that the measured data is higher than the prediction by about 2 dB at the low velocity ($V_J = 180$ m/sec) and approaches the prediction as the velocity increases.

Turbulence properties. Turbulence structure in the trailing edge wake of one-sided flow (typical USB configuration) was mathematically modeled in

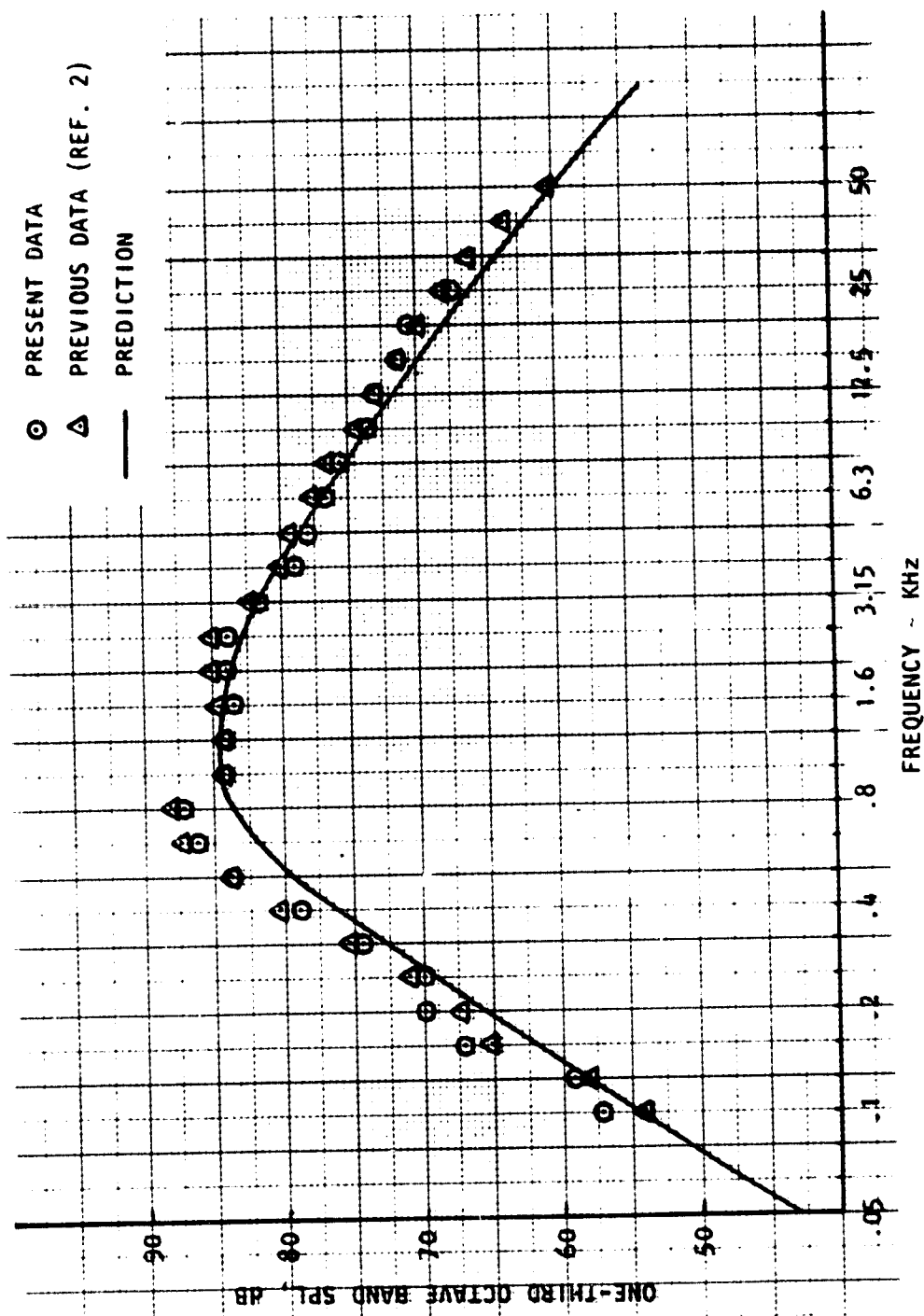


Figure 49. Comparison of Prediction with Measurements
 (D-Nozzle, $A_N = 10.13 \text{ cm}^2$, $\delta_f = 30^\circ$, $\theta = 90^\circ$,
 Flyover Plane, $V_j = 215 \text{ m/s}$)

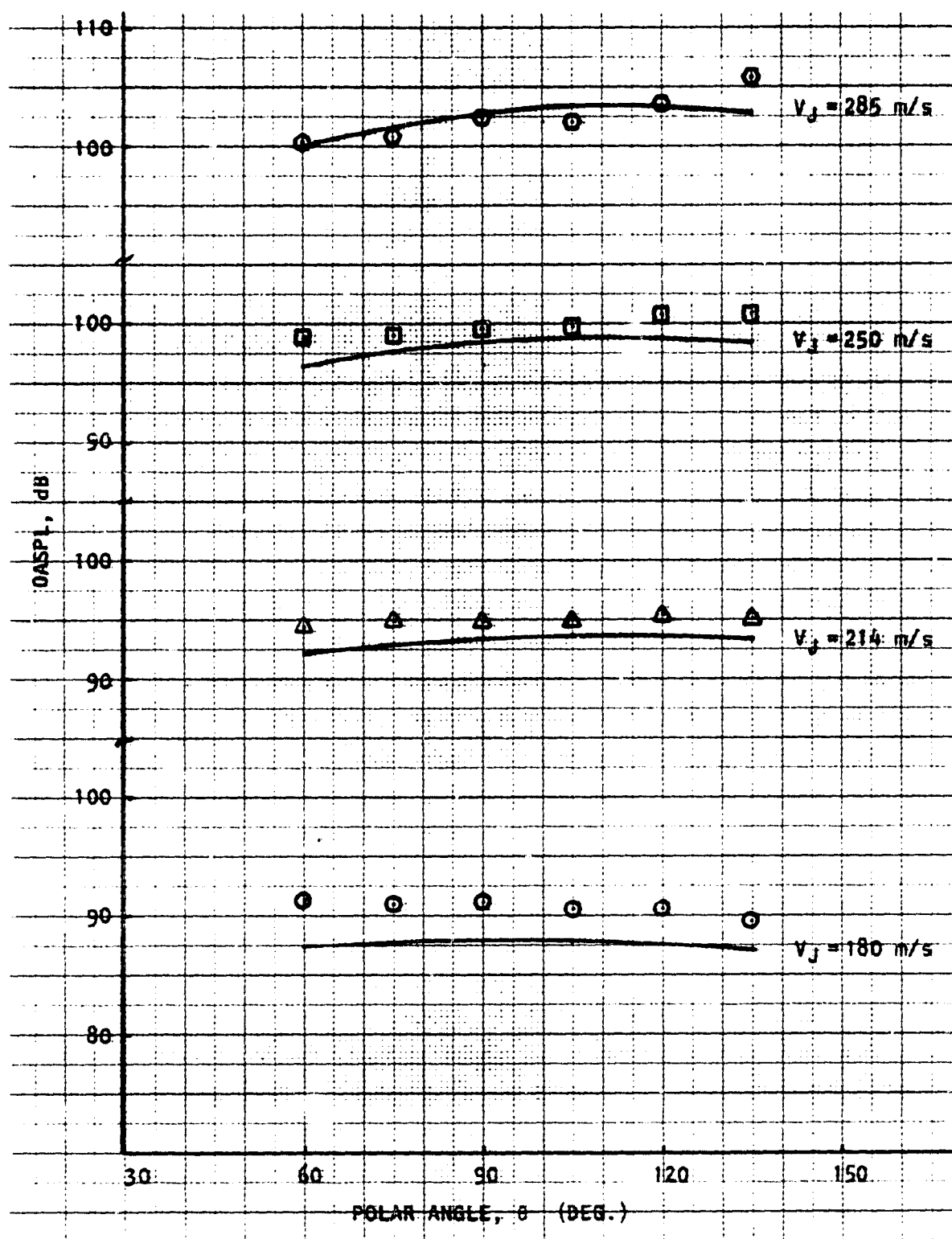


Figure 50. Directivity in the Flyover Plane (Comparison of Measured Data with Prediction)

reference 2 by depicting the space-time correlation function in the following form:

$$R(\bar{x}, \bar{y}, z'z'', \tau) = G(z'z'') e^{-\frac{\bar{x}}{\lambda\delta}} \frac{\sum_{i=1}^n \frac{\alpha_i A_i}{\alpha_i^2 + (\frac{U}{U_c\delta})^2 [(\bar{x} - U_c\tau)^2 + \beta^2 \bar{y}^2]}}{\sum_{i=1}^n \frac{A_i}{\alpha_i}} \quad (1)$$

where $G(z'z'')$ = transverse correlation function of zero time delay
 λ = longitudinal decay rate
 α and A = constants
 U_c = convection velocity
 β = scale of anisotropy
 δ = shear layer thickness
 \bar{x}, \bar{y} = separation distances in the longitudinal and lateral directions.

The following values of the constants were established in reference 2: $n=3$, $A_1=0.7$, $A_2=6.3$, $A_3=3.0$, $\alpha_1\delta=0.256$ cm; $\alpha_2\delta=1.12$ cm; $\alpha_3\delta=16.0$ cm; $U_c=0.7 U$, $\lambda\delta=2.84$ cm, and $\beta=2.3$.

It is assumed in this formulation that the turbulence is spatially homogeneous with respect to any plane parallel to the shear layer. Therefore, the space correlation function is a function of hot-wire separation distance in the longitudinal and lateral directions (\bar{x}, \bar{y}) . The turbulence is generally inhomogeneous in the transverse plane, and thus R is a function of transverse coordinates (z', z'') rather than just the separation distance, \bar{z} . In order to establish the dependence of the correlation function, R , on the transverse coordinates, extensive correlation measurements are required. In figure 51, an attempt was made to study the variation of correlation as a function of separation distance, \bar{z} . The transverse correlation data for the two fixed wire positions are presented in this figure. A curve, $R(\bar{z}) = e^{-1.4\bar{z}}$ approximates the data very well. The data taken from reference 1 for slightly different configuration appears to fit the curve $e^{-1.9\bar{z}}$ as shown in this figure.

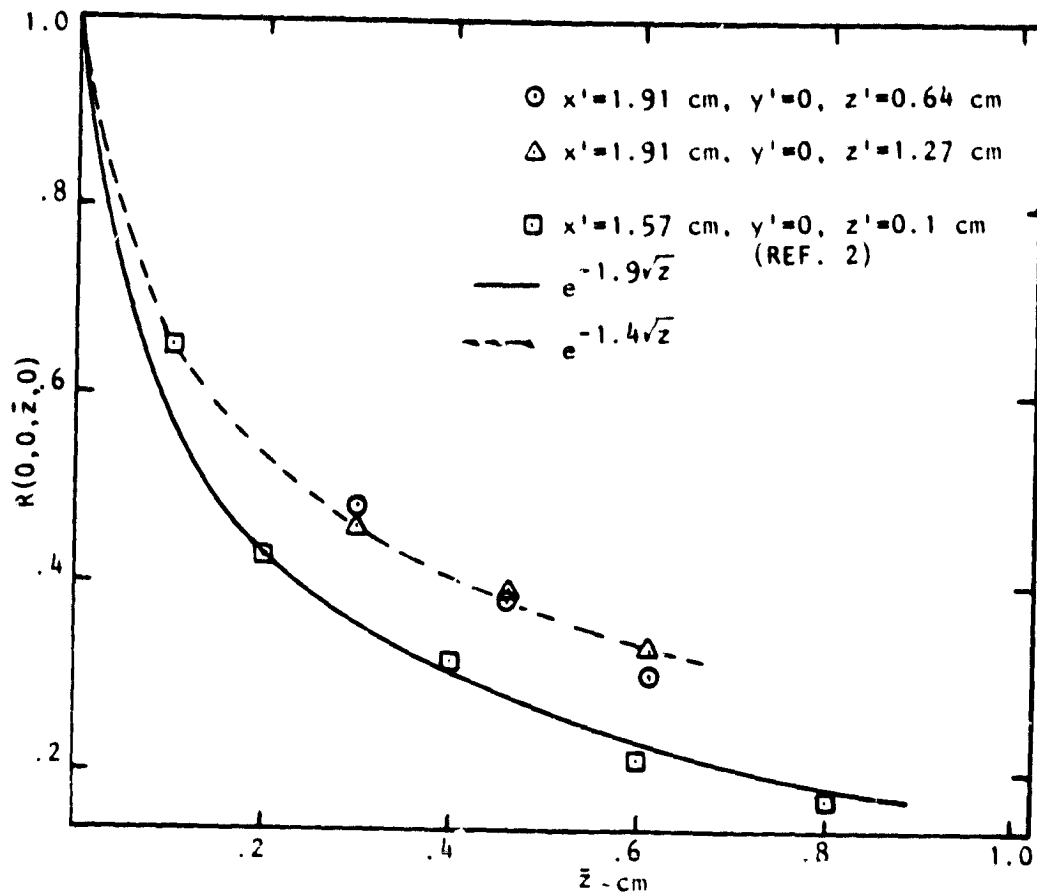


Figure 51. Transverse Correlation Function

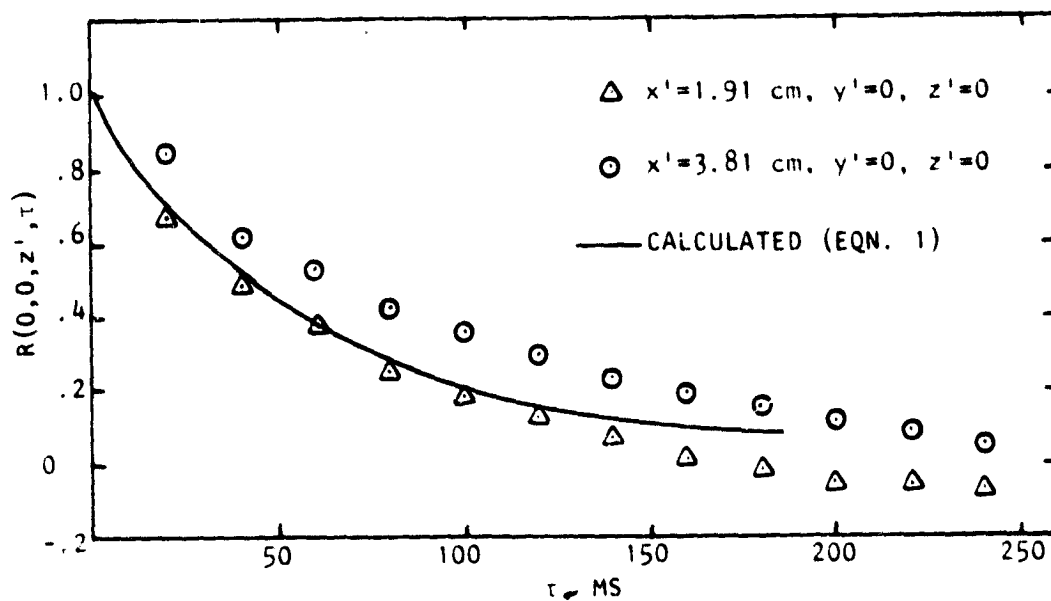


Figure 52. Comparison of Measured and Calculated Autocorrelation.

Auto-correlation function measured at two longitudinal locations ($x_0' = 1.91$ cm, and 3.82 cm) is compared with the calculated values from the above-mentioned equation in figure 52. It can be seen that the calculated values agree well with the measured data for $x_0 = 1.91$ cm. But for $x_0 = 3.81$ cm, the measured values are higher than the calculated values.

The space correlations in longitudinal (x) and lateral (y) directions for zero delay time are shown in figure 45. The agreement between the calculated and measured data is very favorable in the longitudinal direction. In the lateral direction, however, the formula (equation 1) overpredicts the correlations. But with a modifier decay term, $e^{-\beta \bar{y}/\lambda \delta}$, the agreement between the calculations and the measurements is improved for small values of \bar{y} .

4. CONCLUSIONS

(1) Jet exit velocity is the most important operating parameter that controls the USB noise.

(2) Flap deflection angle has least influence on the magnitude of the noise produced in the shear layer of the trailing edge wake, provided the jet flow is attached to the surface and spreads over the surface before leaving the trailing edge. However, increase in the flap angle increases the shear layer thickness, thus causing the radiated noise spectra to shift to lower frequencies.

(3) Trailing edge wake flow characteristics were not influenced greatly by the initial turbulence of the flow (screen mesh at the nozzle exit). Therefore, noise generated in the shear layer of the wake is not affected by initial turbulence. It should be noted that the increase in initial turbulence increases the noise generated in the jet flow upstream of the trailing edge and at the trailing edge, but not in the wake.

(4) Transverse and longitudinal components of the fluctuating velocities in the wake are equally important in noise generation.

(5) The existing analytical model (ref. 2) for the fluctuating velocities in the trailing edge wake has to be modified by considering the longitudinal and transverse velocity components separately. This may be achieved by analyzing the detailed data provided. The modified turbulence model must be used to predict the noise levels from the wake shear layer.

(6) The near-field noise data given in Appendix D can be used to estimate the acoustic loading on structural elements in the vicinity of the jet exhaust.

(7) To reduce the noise levels generated in the wake, the magnitude of both the longitudinal and transverse components of the fluctuating velocities must be reduced. Noise generated at the trailing edge by the turbulence convected past the trailing edge must also be reduced in order to reduce the total USB noise. The actual method of noise reduction in a practical USB configuration should be studied further.

(8) The effect of forward speed on the wake shear layer must be investigated by conducting experiments either in the anechoic free-jet facility, or in the wind tunnel. Particularly, the influence of forward speed on the wake flow characteristics should be investigated.

REFERENCES

1. Brown, W. H.; Searle, N.; Blakney, D. F.; Pennock, A. P.; and Gibson, J.S.: "Noise Characteristics of Upper Surface Blown Configurations; Experimental Program and Results." NASA CR-145143, October 1977.
2. Reddy, N. N.; Pennock, A. P.; Tibbetts, J. G. and Tam, C. K. W.: "Noise Characteristics of Upper Surface Blown Configurations - Analytical Studies." NASA CR-2812, March 1978.
3. Brunn, H. H.: "Interpretation of Cross Hot-Wire Signals." DISA Information No. 18, Sept. 1975.
4. Laurence, J. C.: "Intensity, Scale, and Spectra of Turbulence in Mixing Region of Free Subsonic Jet." NACA Report 1292, 1966.
5. Lau, J. C.; Fisher, M. J.; and Fuchs, H. V.: "The Intrinsic Structure of Turbulent Jets." *Journal of Sound and Vibration* (1972) 22(4), 379-406.

APPENDICES

The four appendices which follow contain the detailed data which were used in the evaluation of parametric effects and in the development of the analytical model of USB wake flow and noise characteristics. The appendices are:

- o Appendix A - Wake Flow Profiles
- o Appendix B - Wake Flow Space-Time Correlations
- o Appendix C - Wake Flow Cross Power Spectra
- o Appendix D - Near-field Noise Third Octave Band Spectra

Each appendix contains an introductory statement which identifies the data included. Refer to Section 2 for descriptions of the model and of the data acquisition and data reduction systems.

APPENDIX A

WAKE FLOW PROFILES

This section contains mean velocity and turbulence intensity profiles measured in the wake of a USB model. Most of the data are from a cross hot-wire probe; laser velocimeter and single hot-wire data are included. All parameter variations are made from the following condition:

$$U_j = 180 \text{ m/s}$$

No Screen

$$\delta_f = 30^\circ$$

$$X' = 1.91 \text{ cm}$$

$$Y = 0$$

The general arrangement of the data is shown in Table A-1. Each line in the table for Figures A-1 through A-5 represents five plots arranged. U , u , W , w , and w/u . Figure A-6, single-wire data, has only U and u plots; and Figure A-7, LV data, has U , u , W , and w plots.

TABLE A-1 DATA CONTENTS

Figure	U_j - m/s	Initial Turbulence	δf	$X' - \text{cm}$	Y	Instrumentation
A-1	180	No Screen	30°	-1.27 0.75 1.91 3.81 7.62 11.43 15.24	0	Cross-Wire
A-2	180	No Screen	30°	1.91	1.91 3.81 5.08 7.62	Cross-Wire
A-3	180	No Screen	60°	-1.27 1.91 3.81 7.62	0	Cross-Wire
A-4	180	Screen	30°	1.91 7.62 1.91	0 5.08	Cross-Wire
A-5	150 215	No Screen	30°	1.91	0	Cross-Wire
A-6	180	No Screen	30°	1.91 7.62 1.91	0 5.08	Single-Wire
A-7	164 211	No Screen	30°	1.91 3.81 7.62 15.24 1.91	0	LV

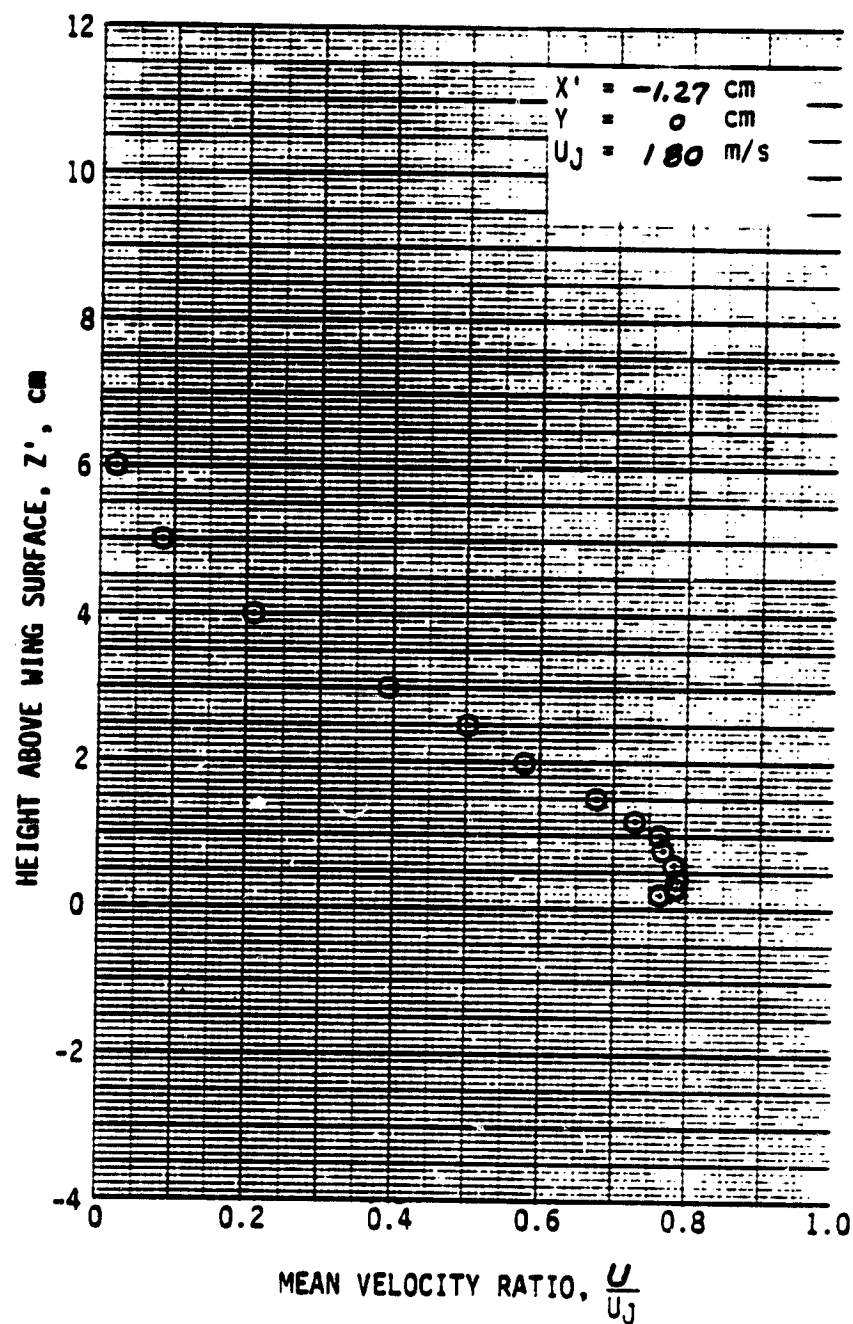


Figure A-1. Wake Flow Profiles by Cross Hot-Wire; $\delta_f = 30^\circ$, No Screen, X' Variations.

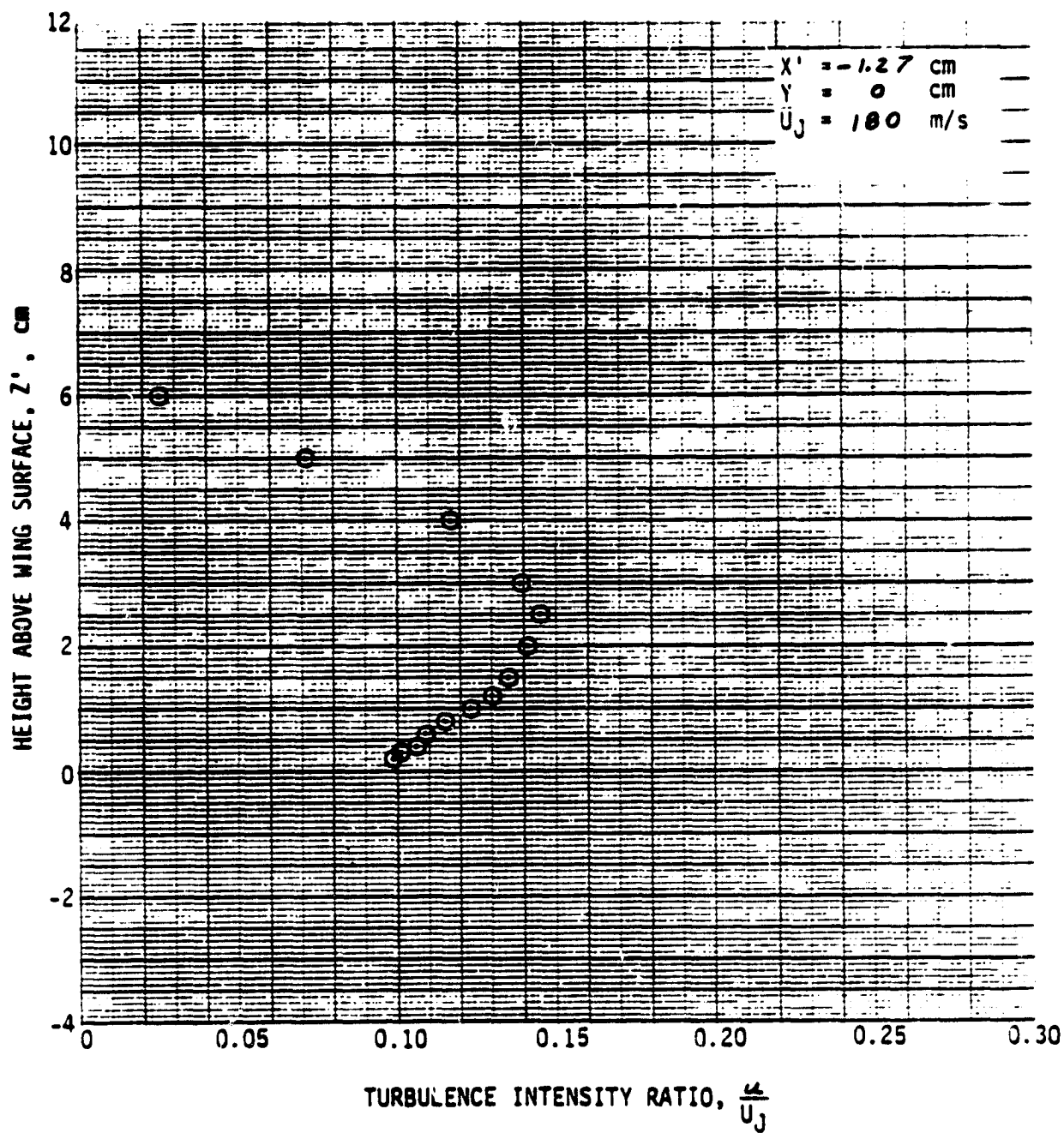


Figure A-1. Continued.

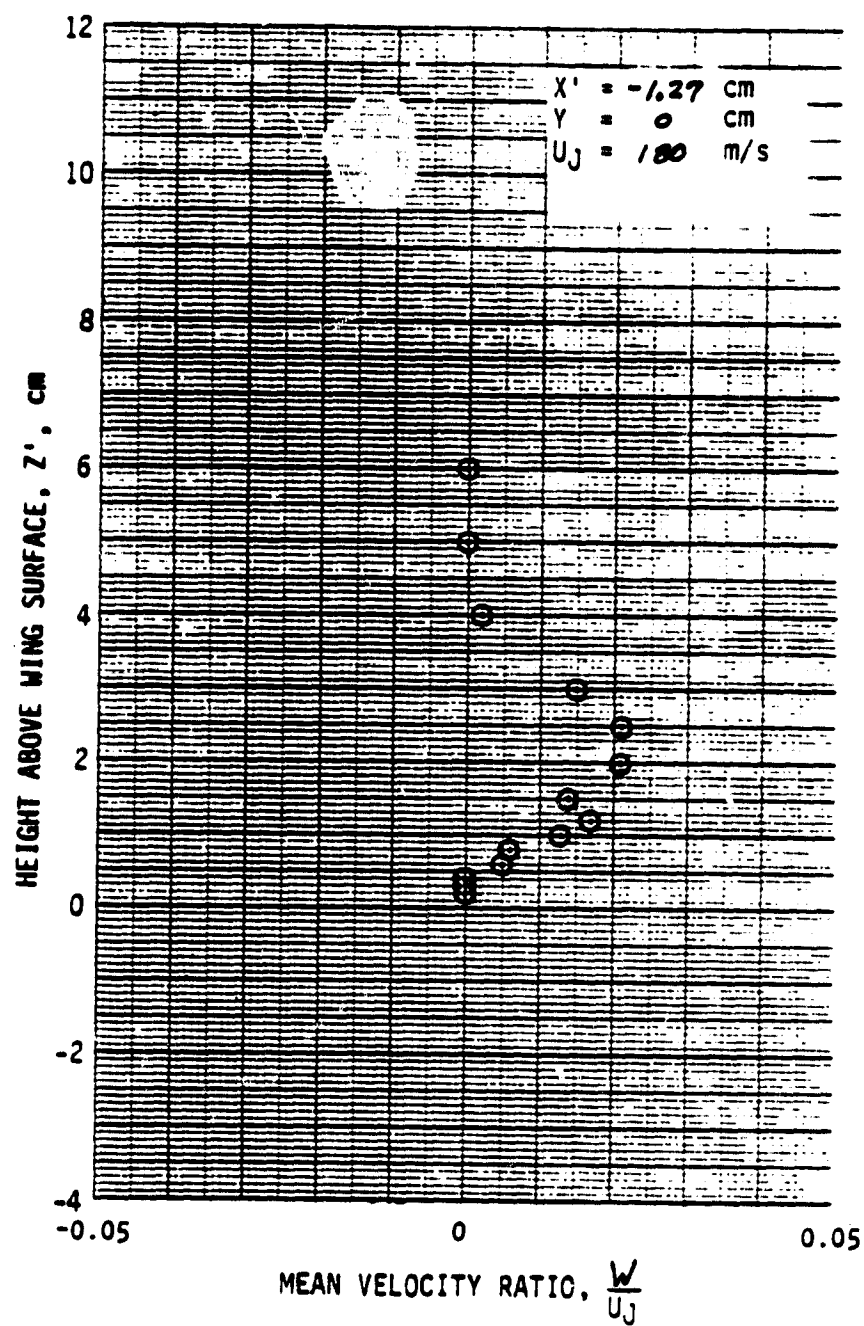


Figure A-1. Continued.

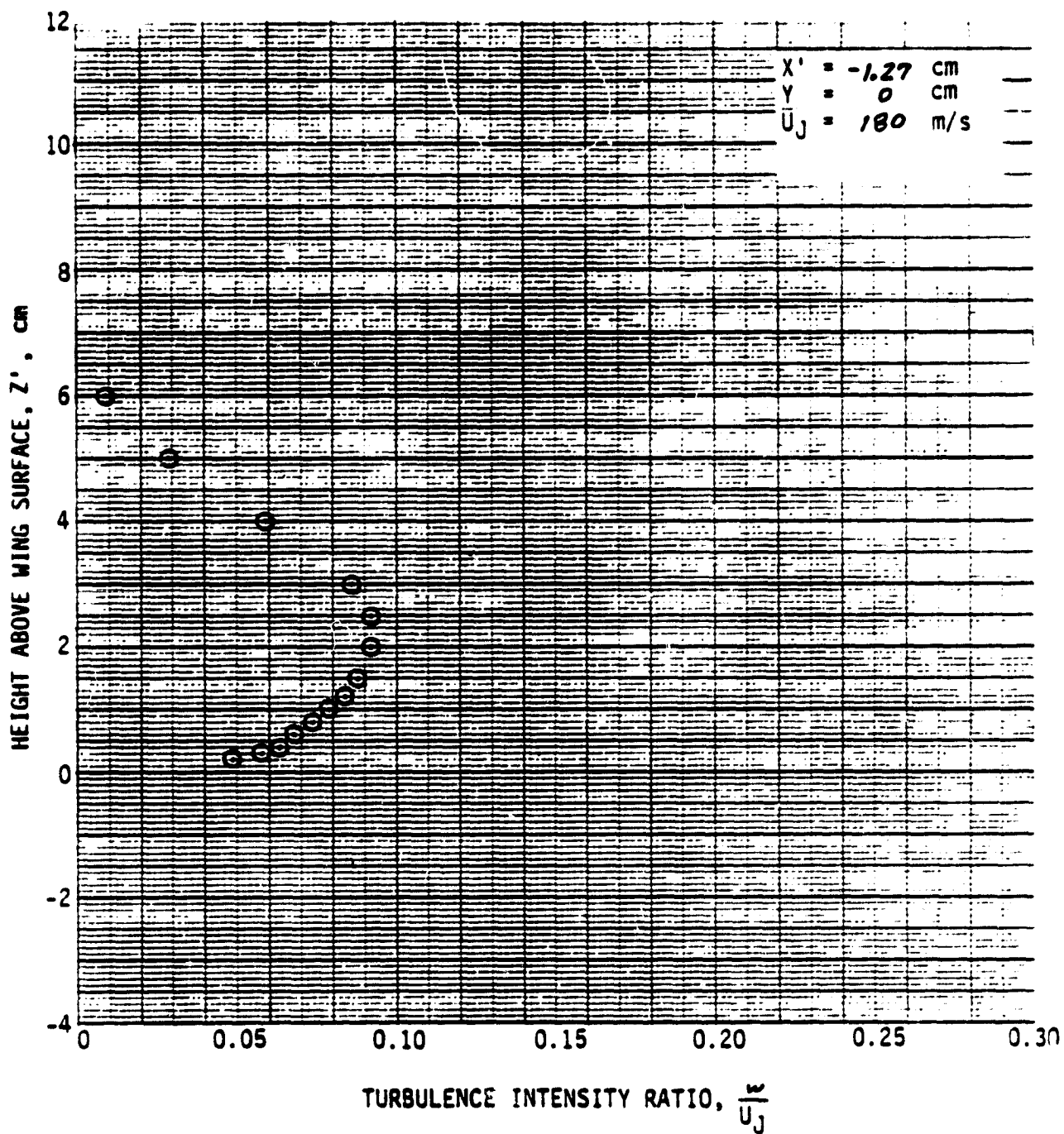


Figure A-1. Continued.

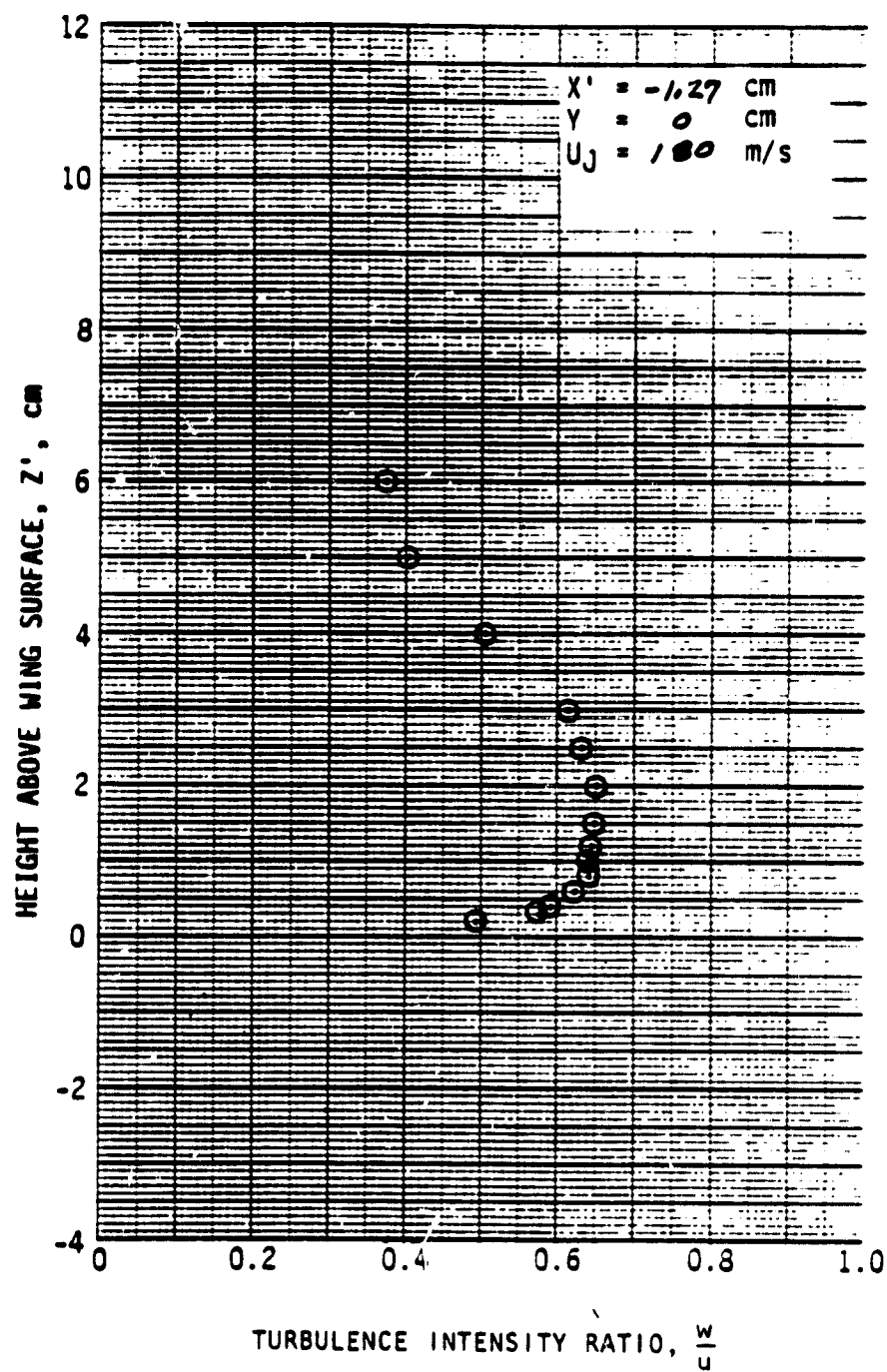


Figure A-1. Continued.

ORIGINAL PAGE IS
OF POOR QUALITY

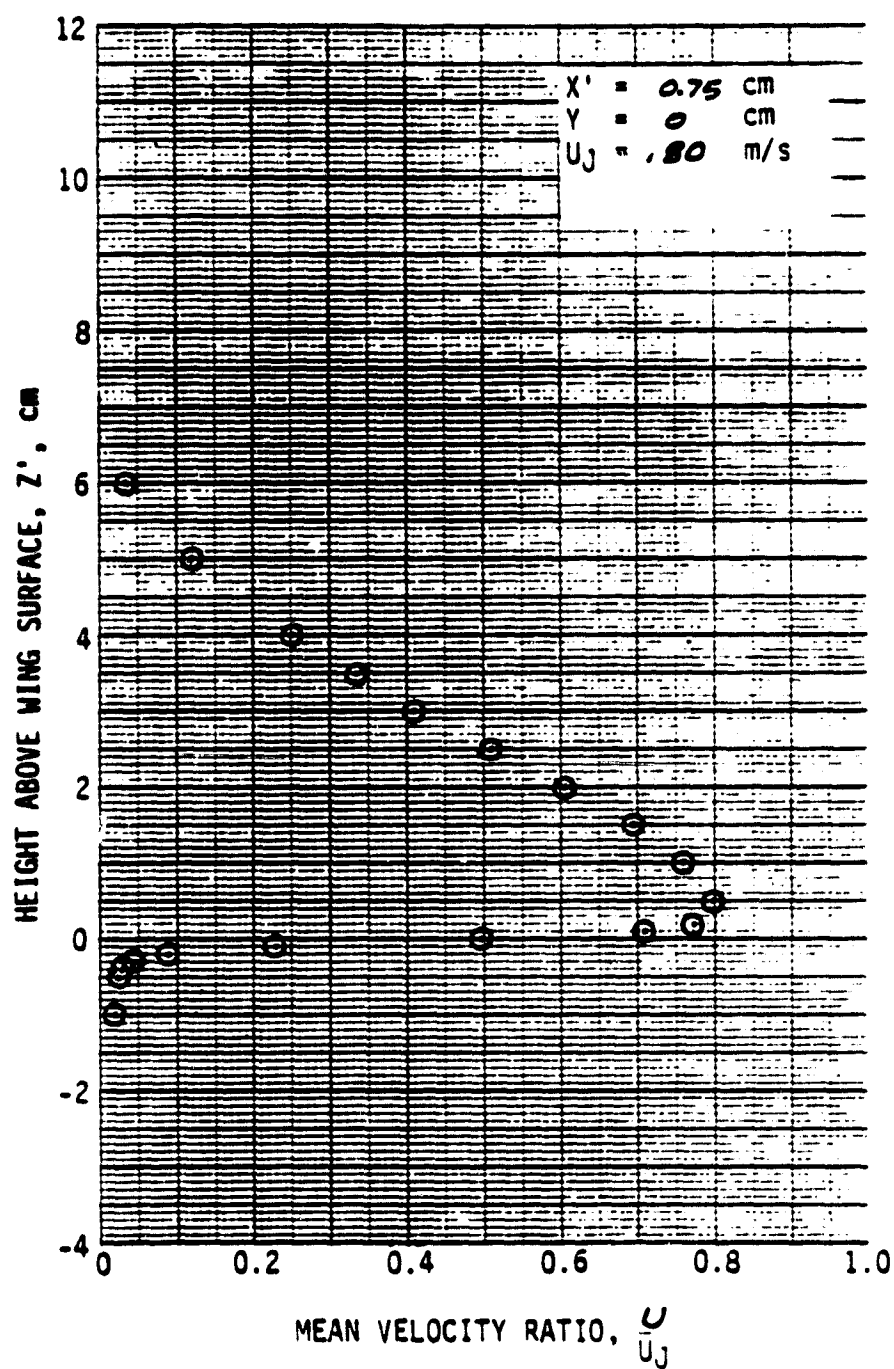


Figure A-1. Continued.

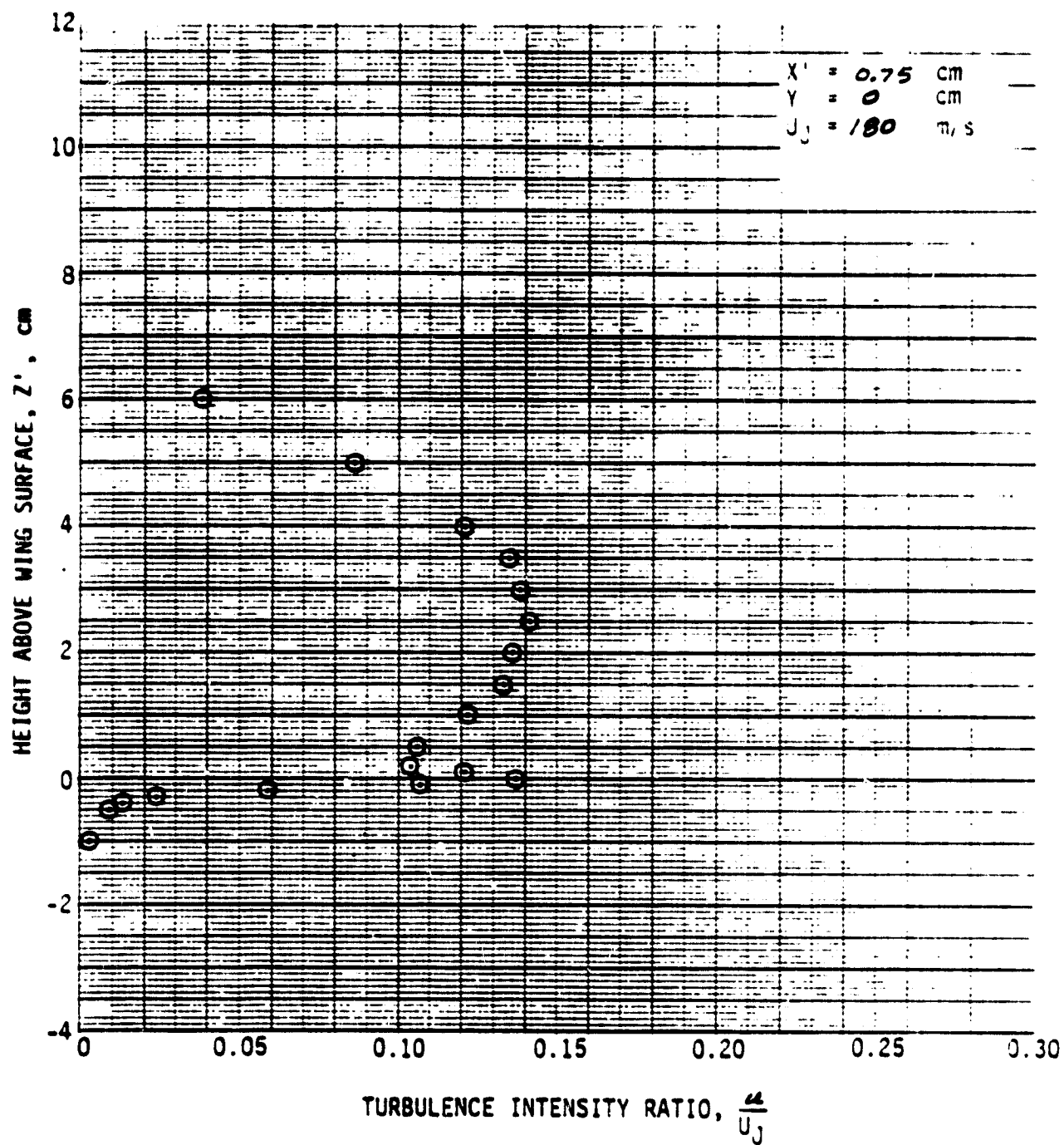


Figure A-1. Continued.

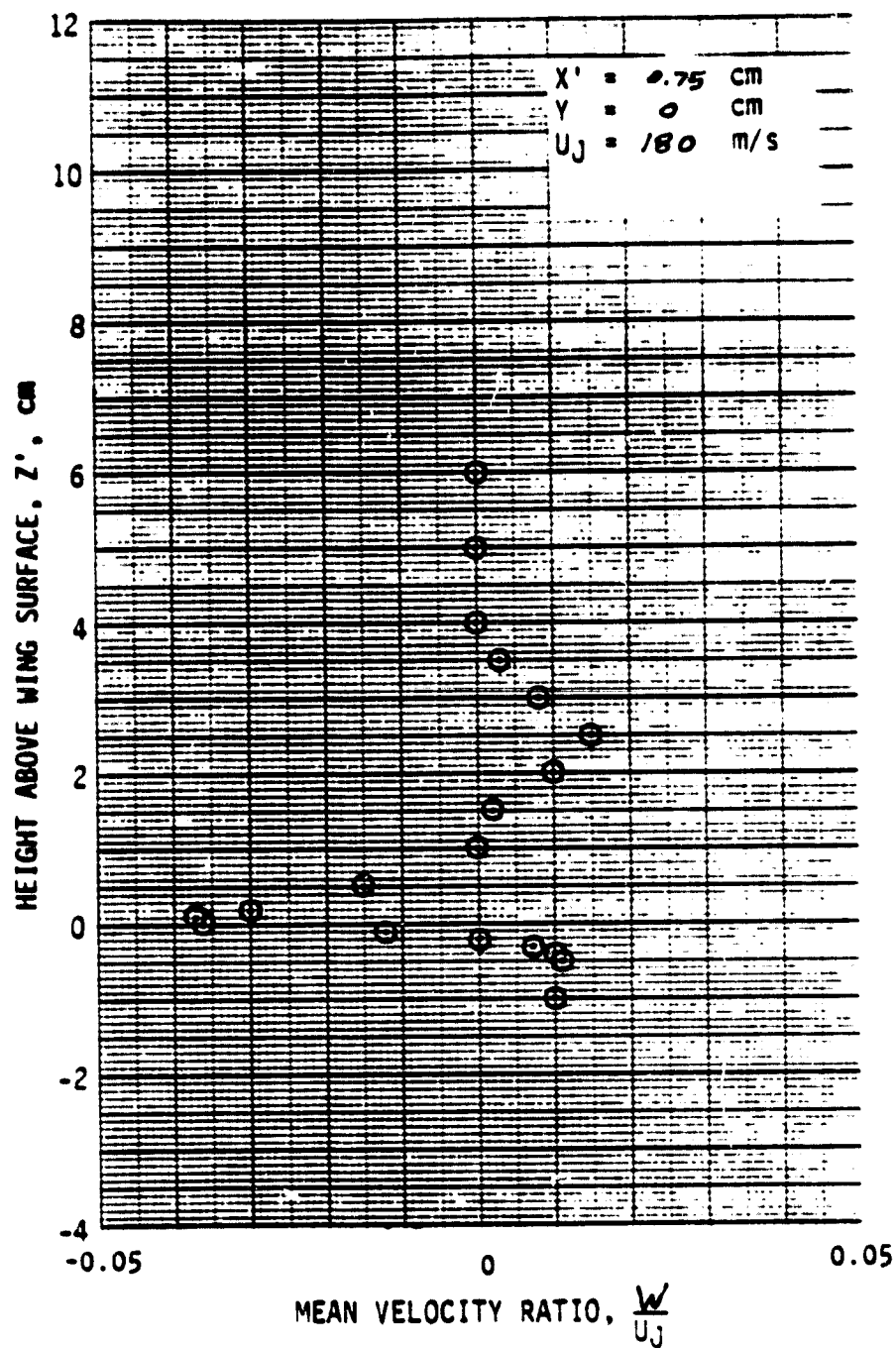


Figure A-1. Continued.

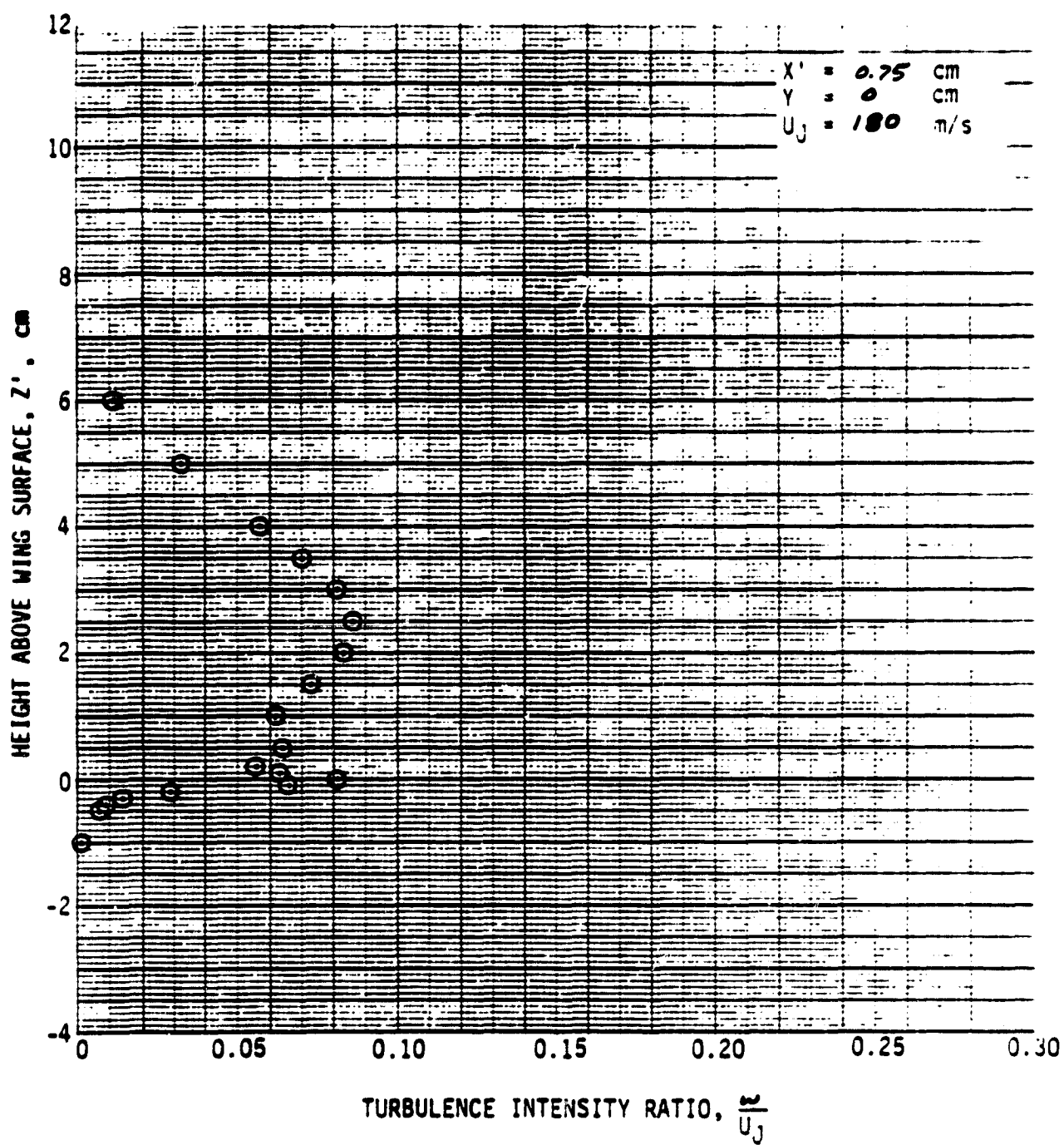


Figure A-1. Continued.

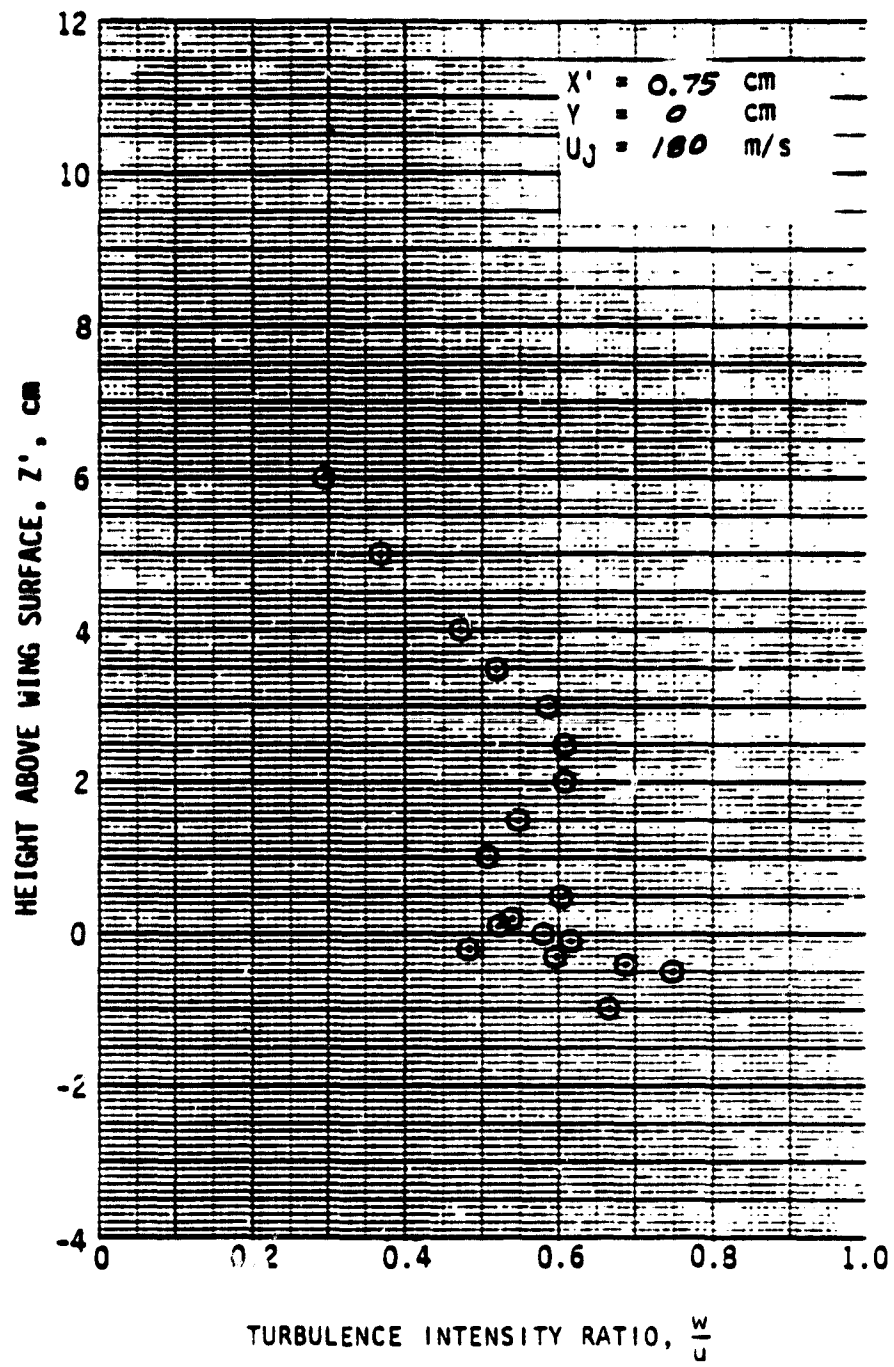


Figure A-1. Continued.

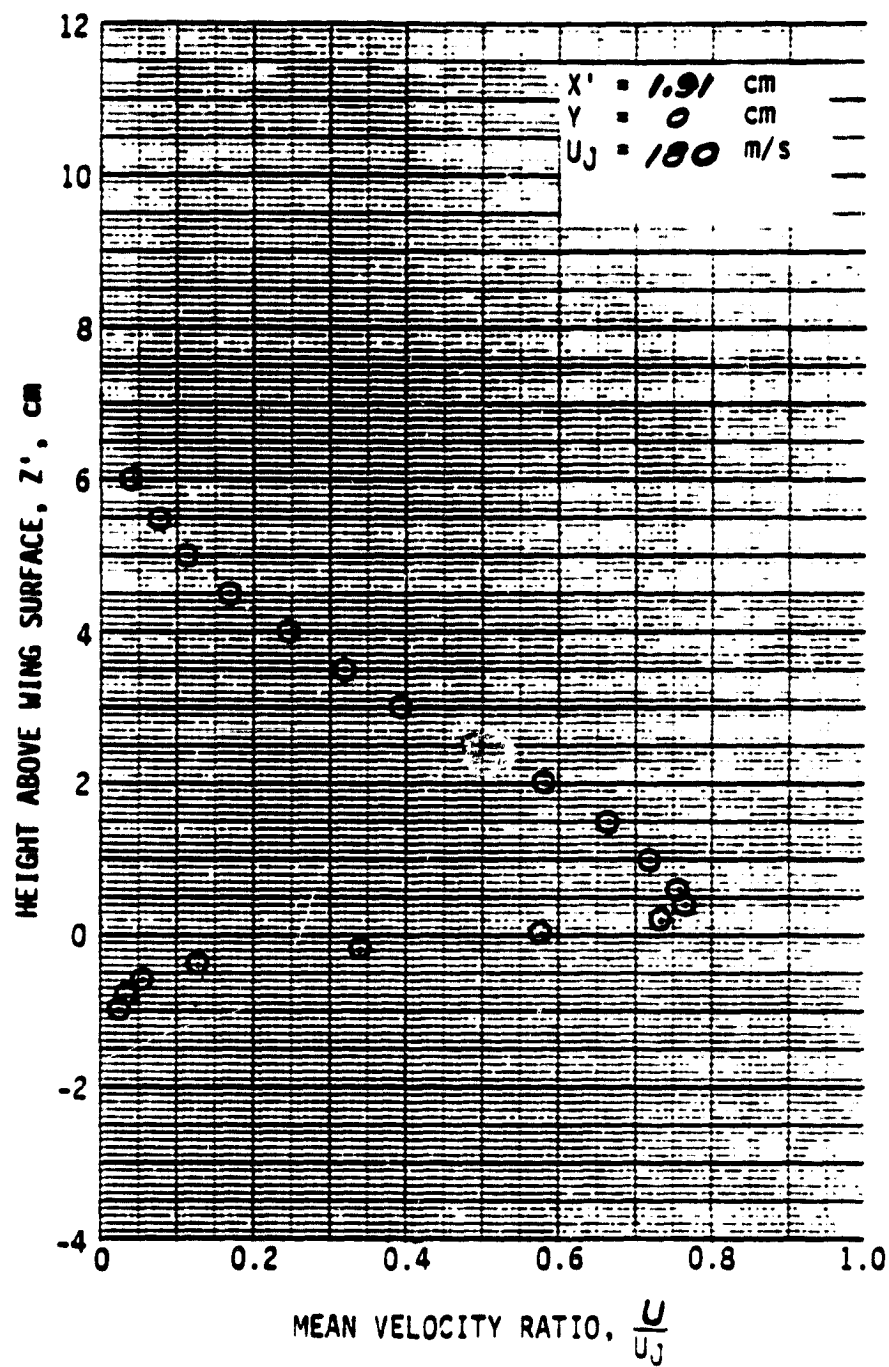


Figure A-1. Continued.

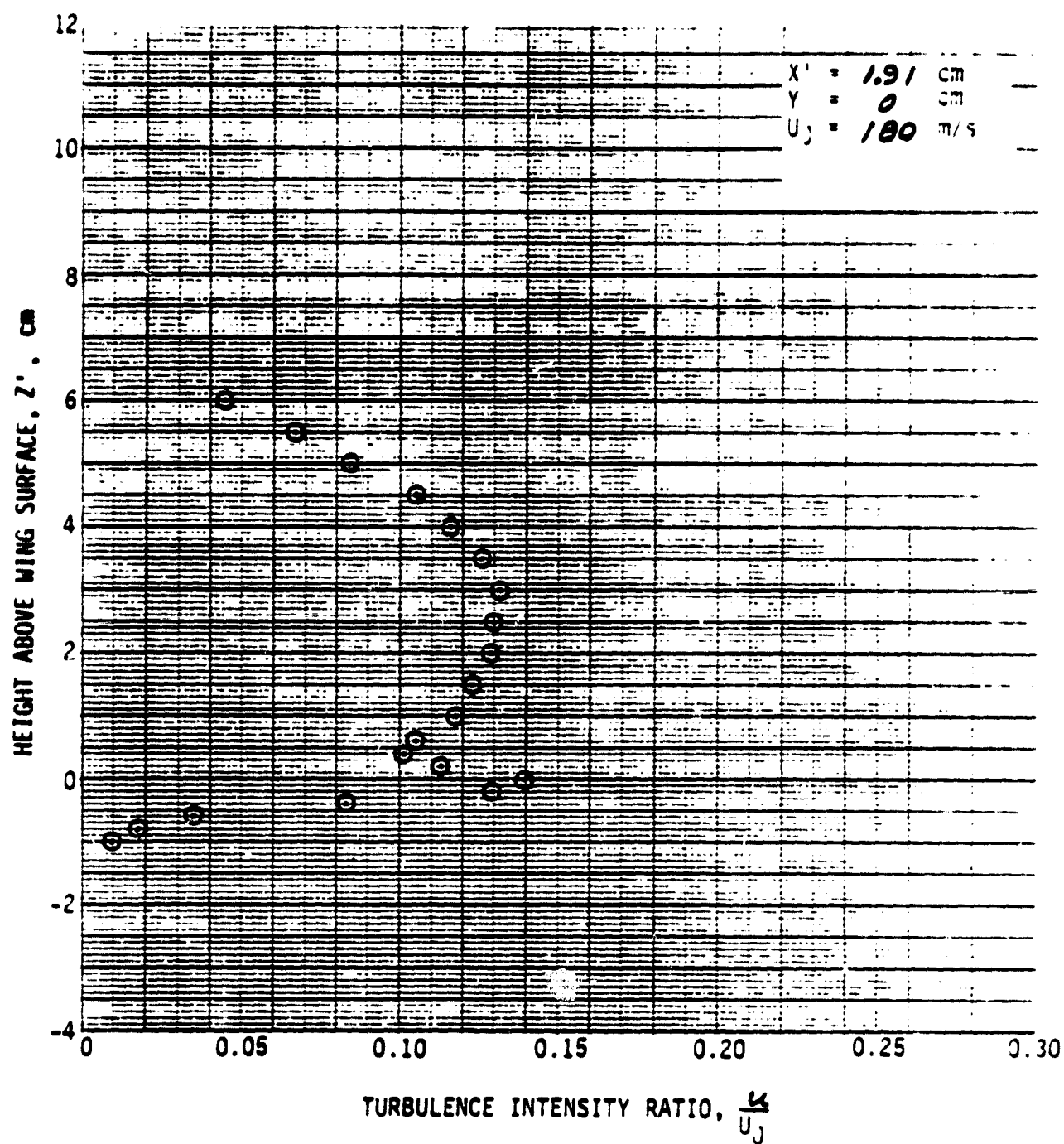


Figure A-1. Continued.

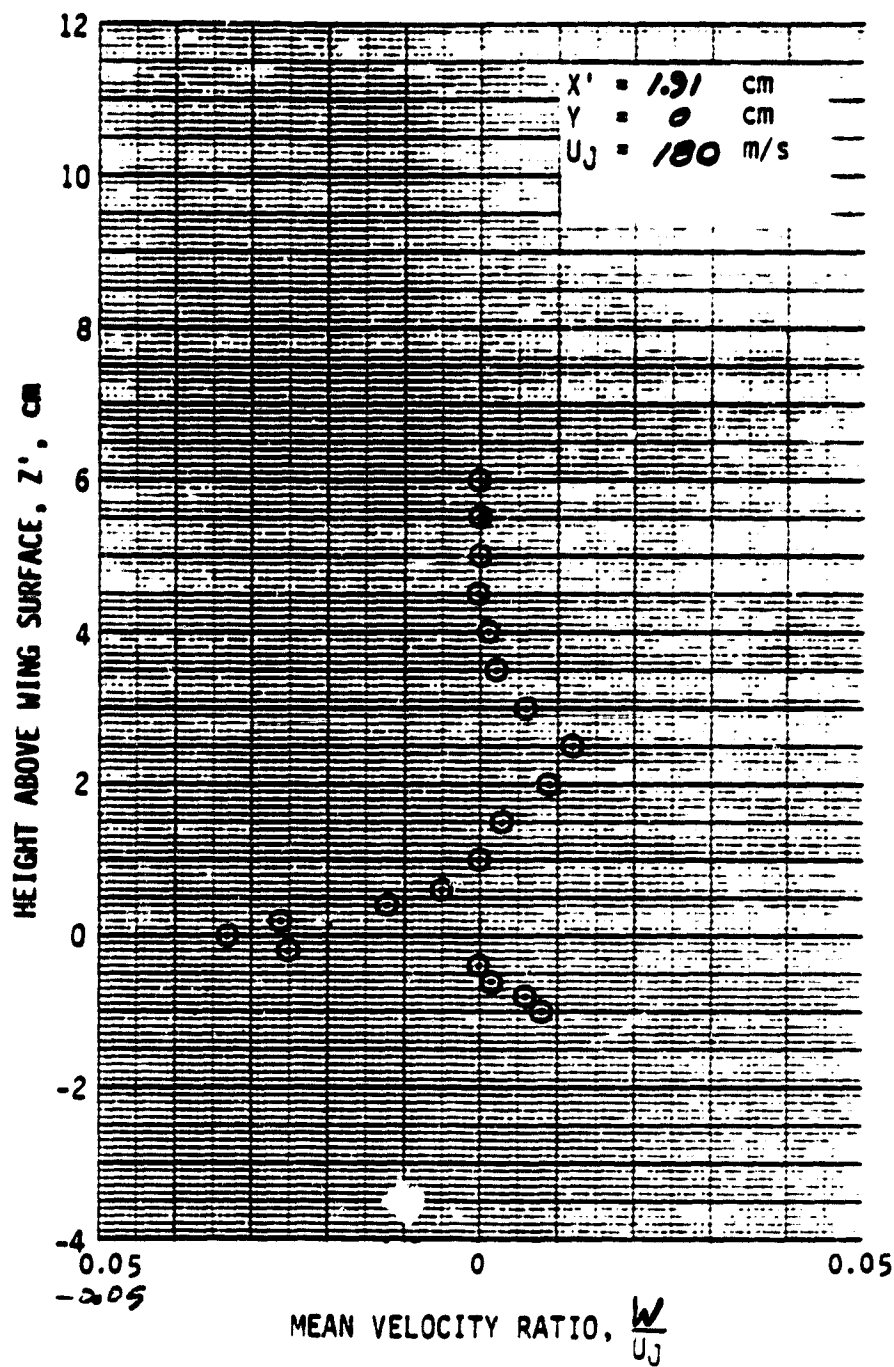


Figure A-1. Continued.

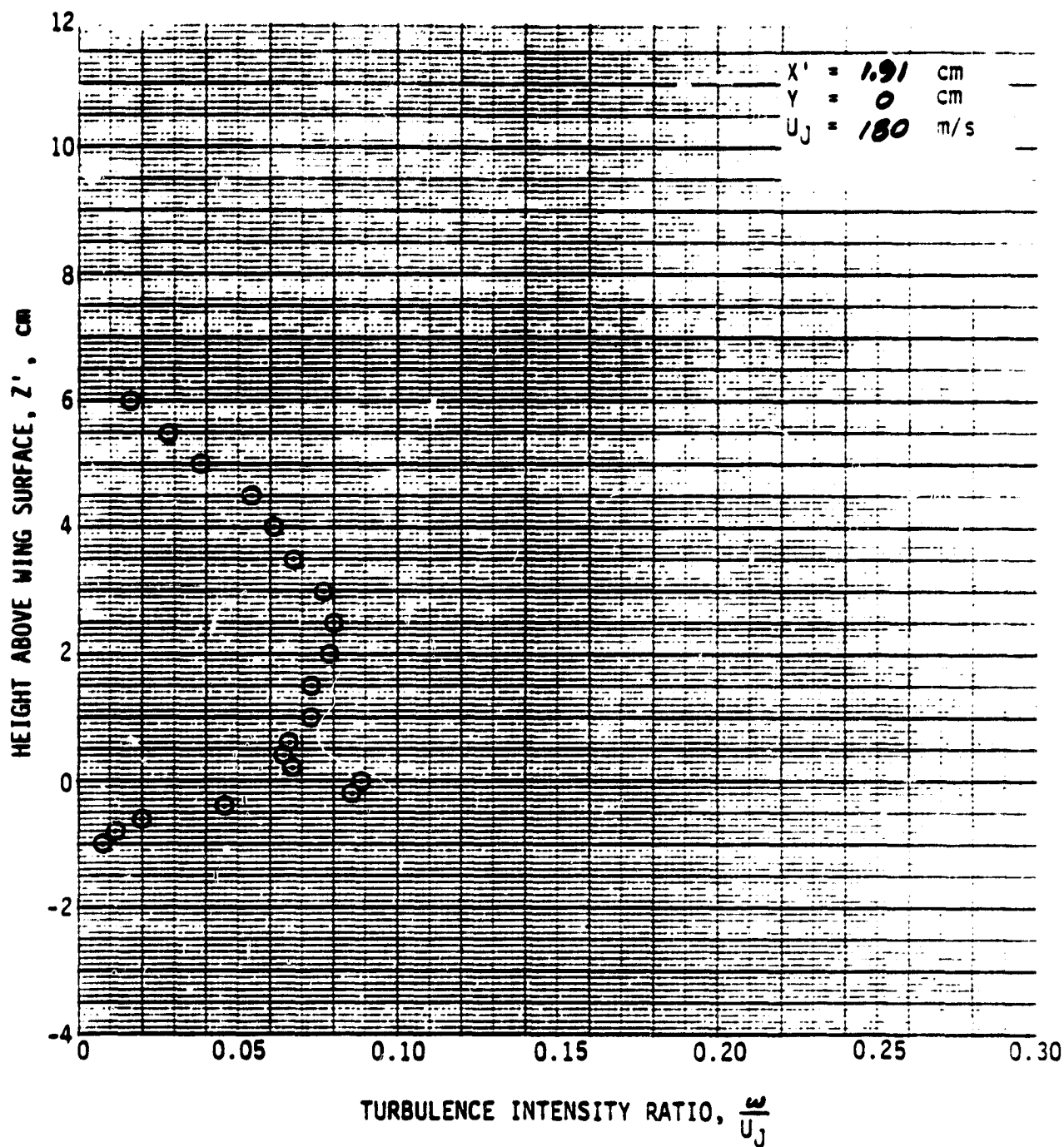


Figure A-1. Continued.

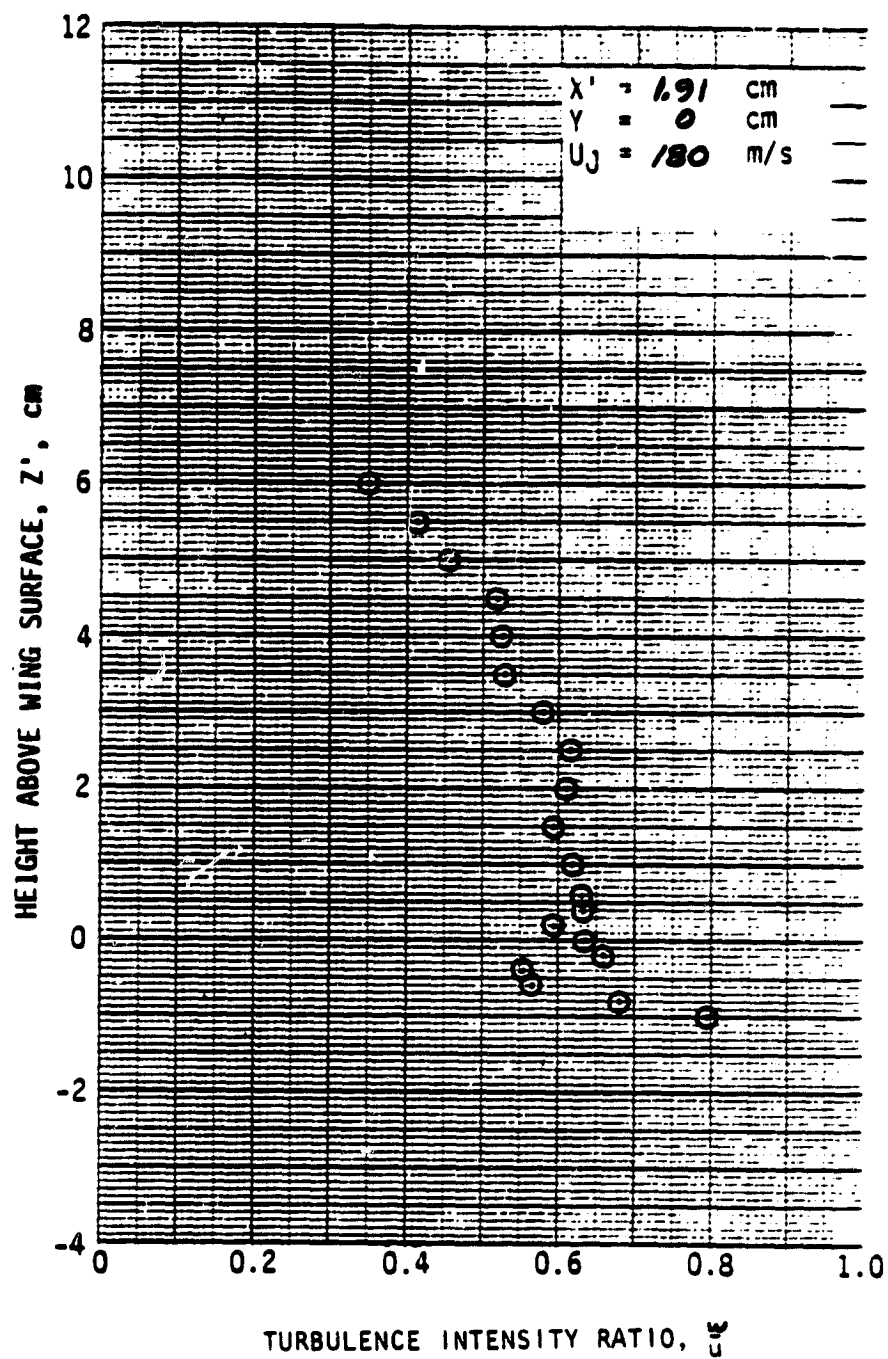


Figure A-1. Continued.

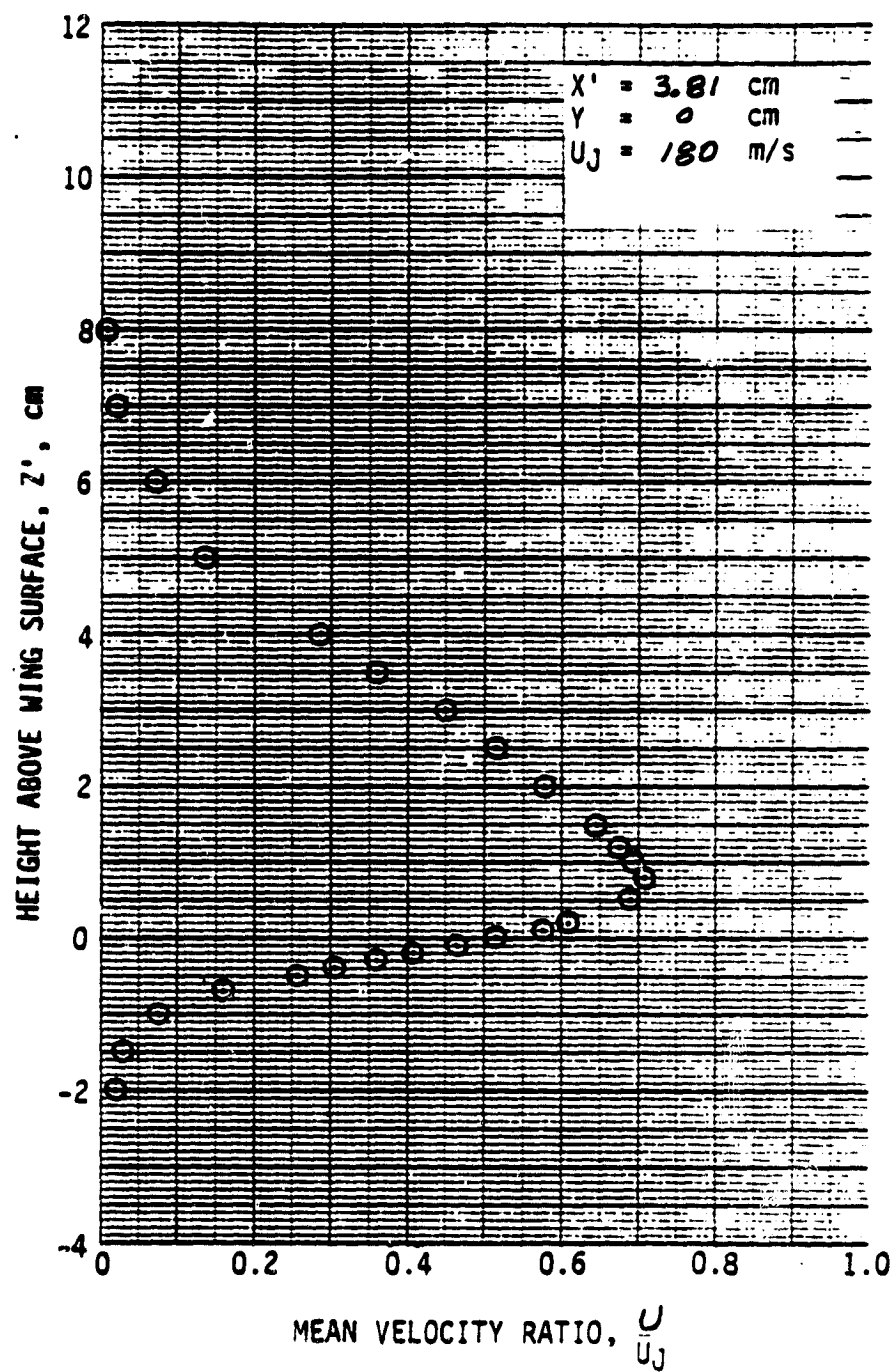


Figure A-1. Continued.

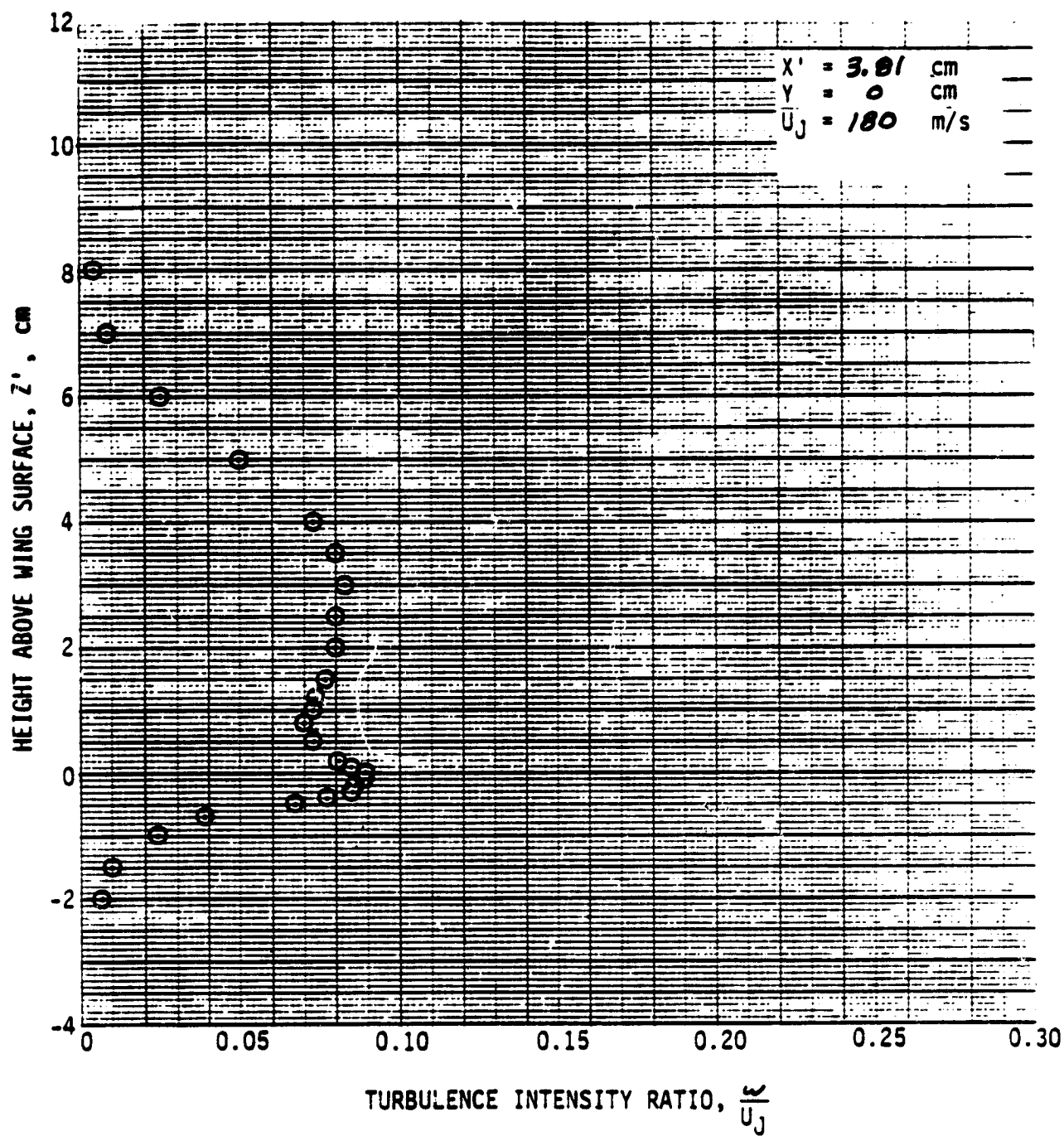


Figure A-1. Continued.

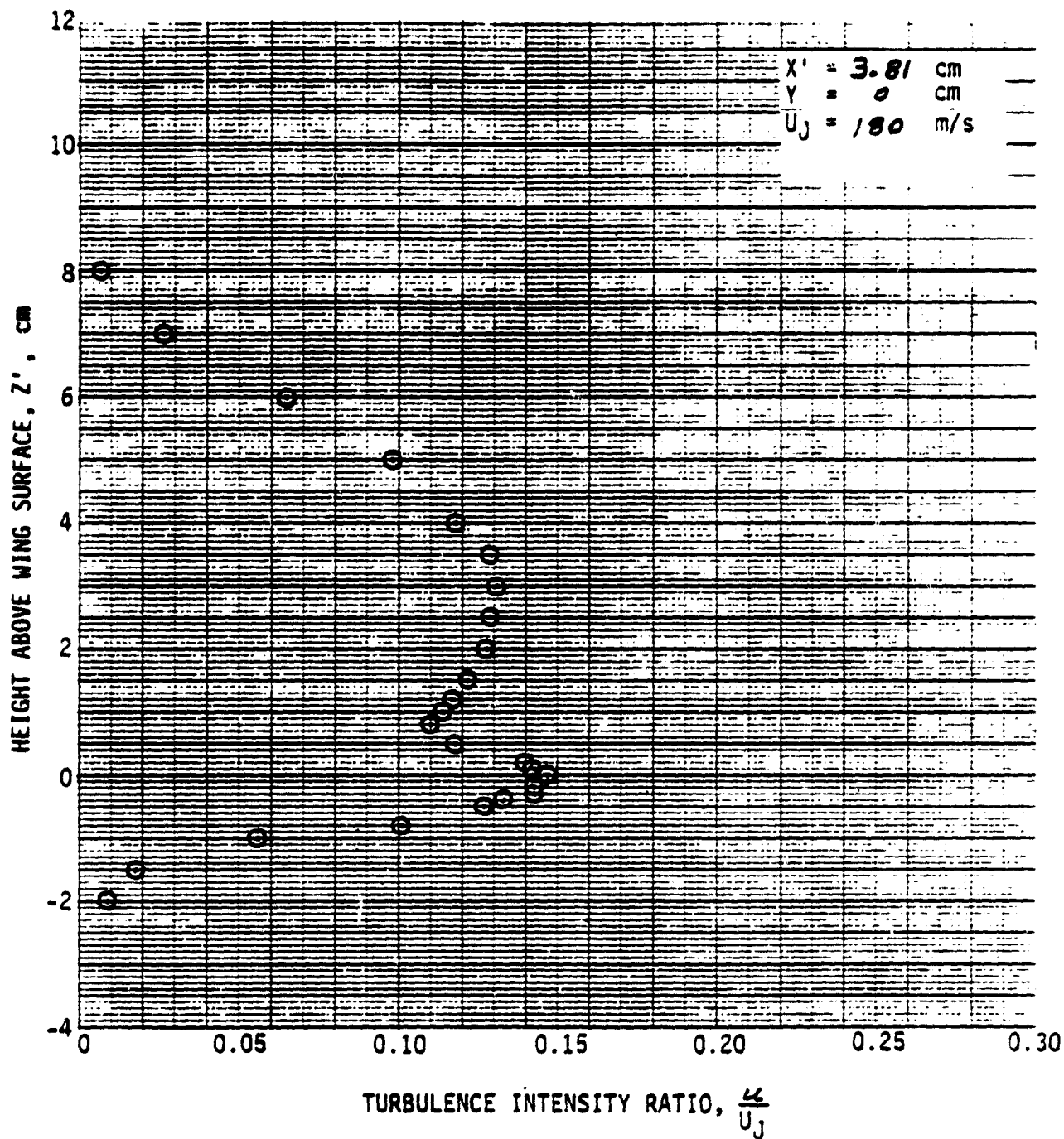


Figure A-1. Continued.

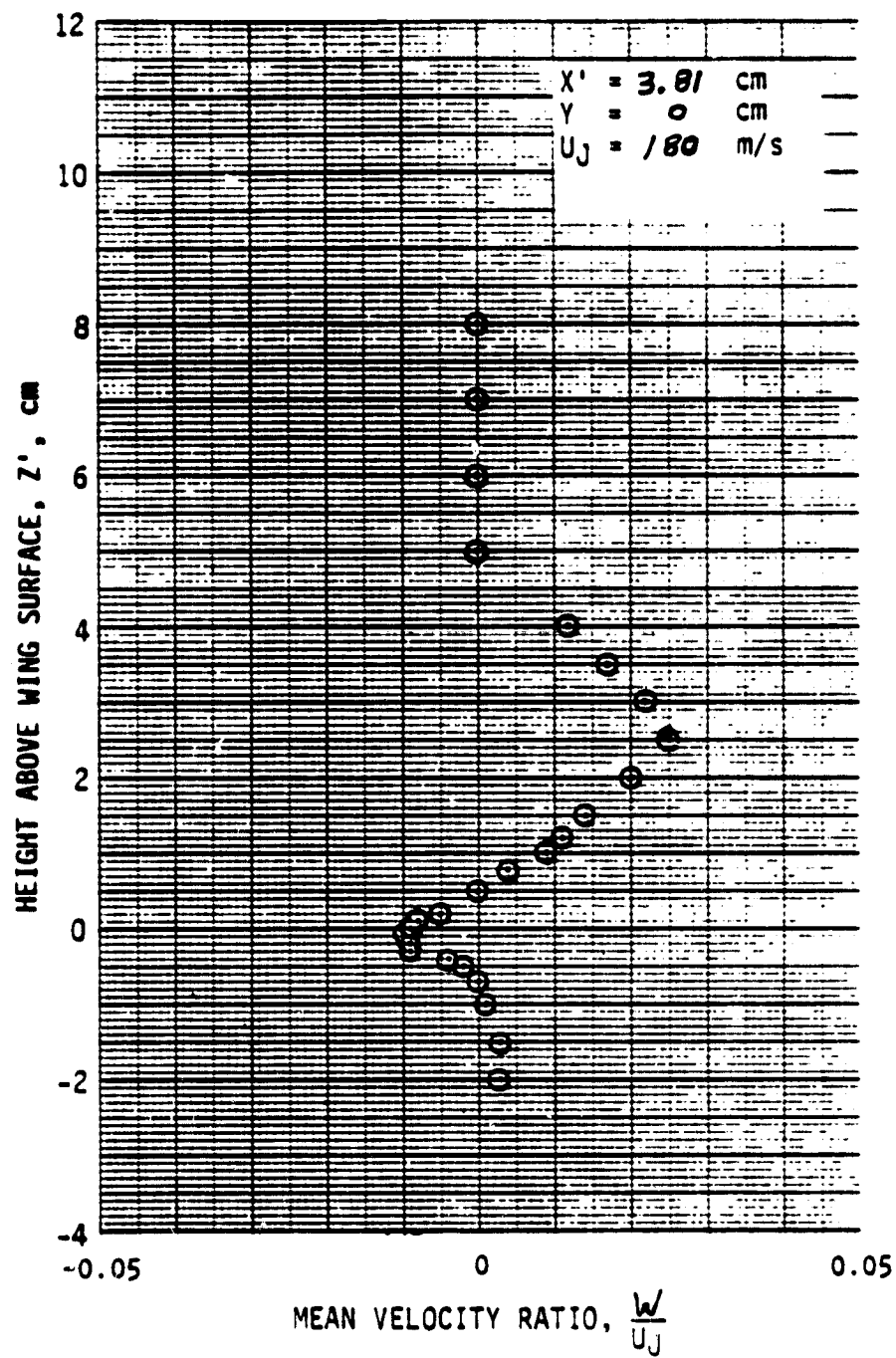


Figure A-1. Continued.

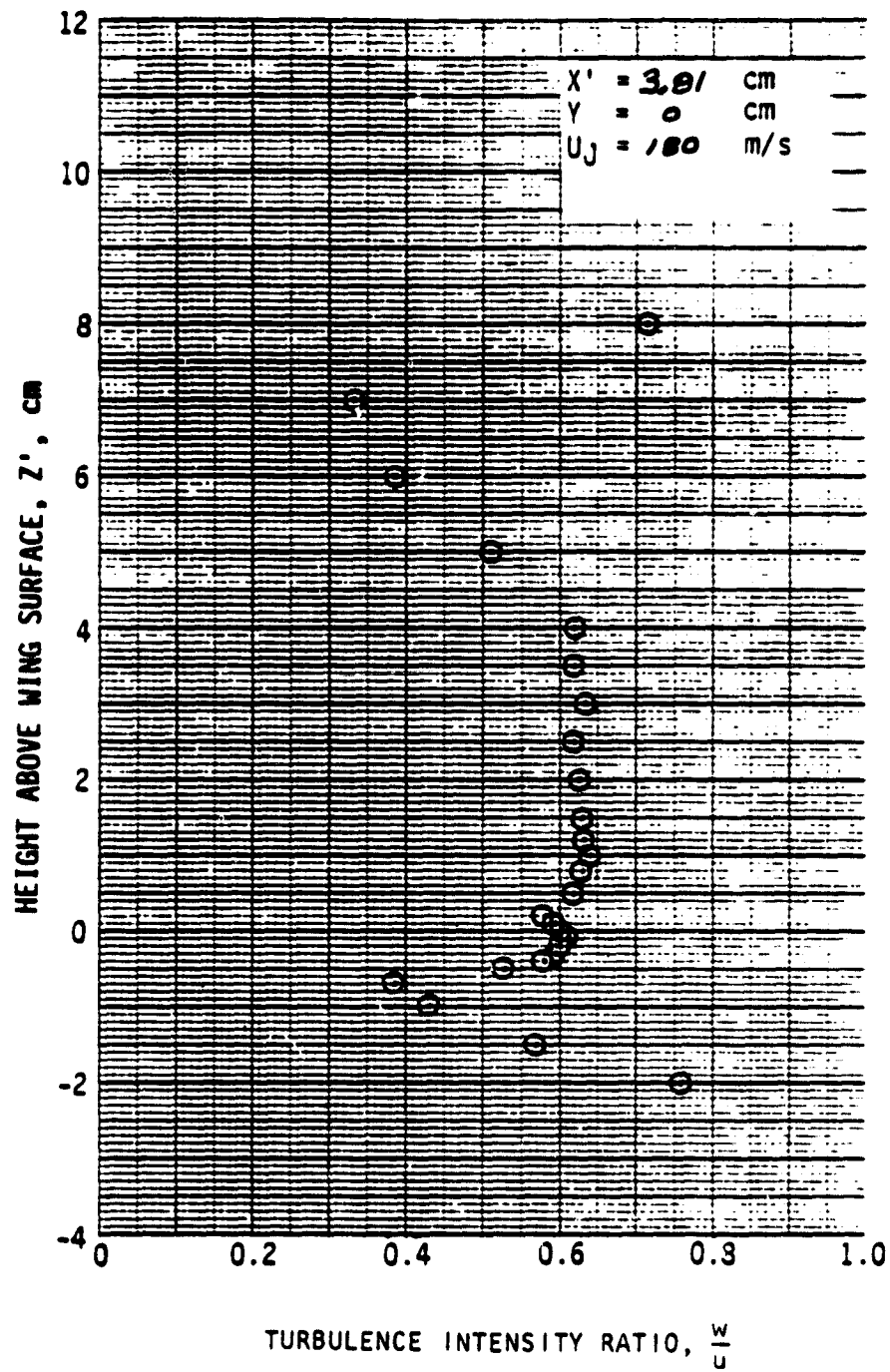


Figure A-1. Continued.

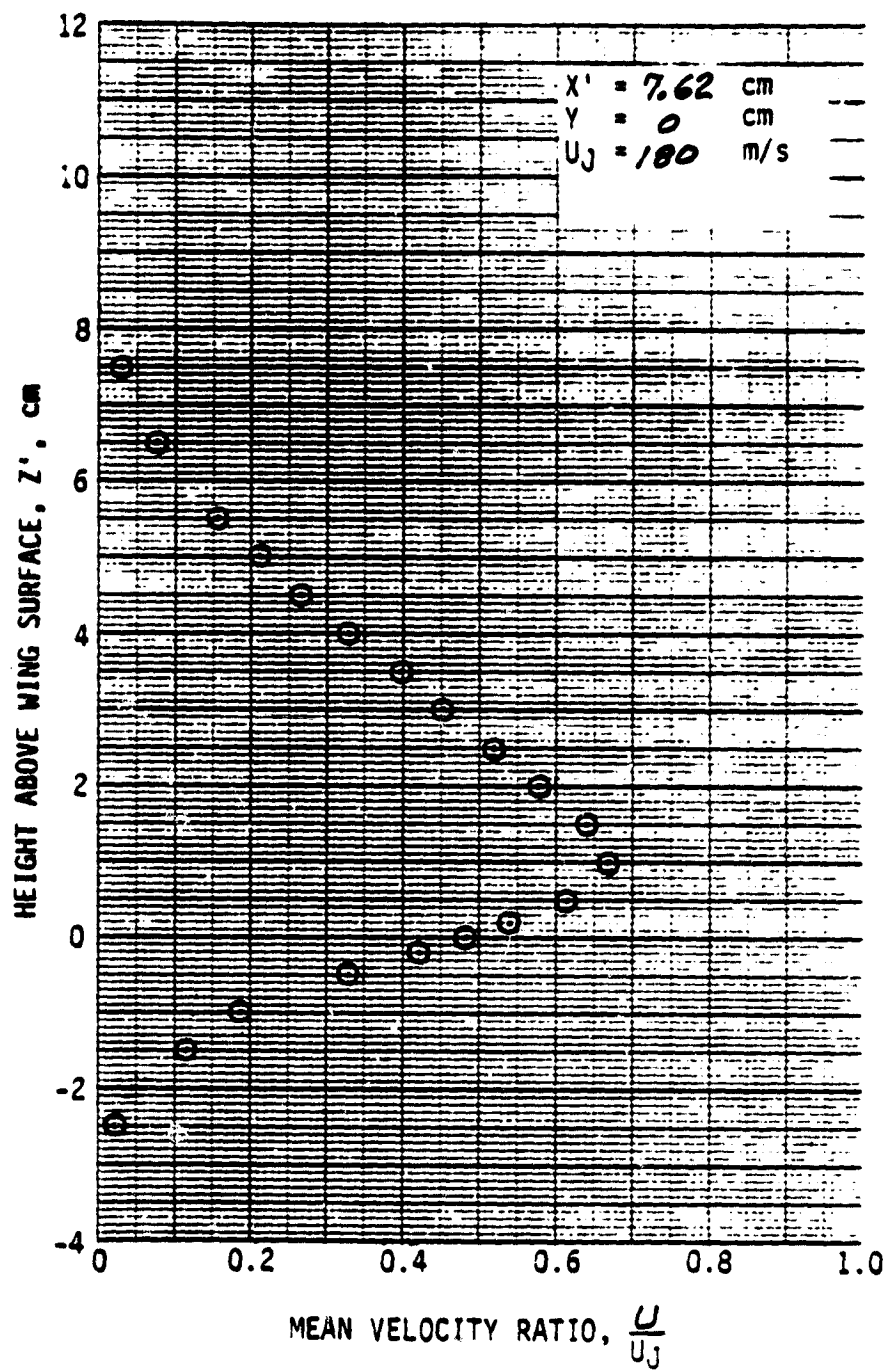


Figure A-1. Continued.

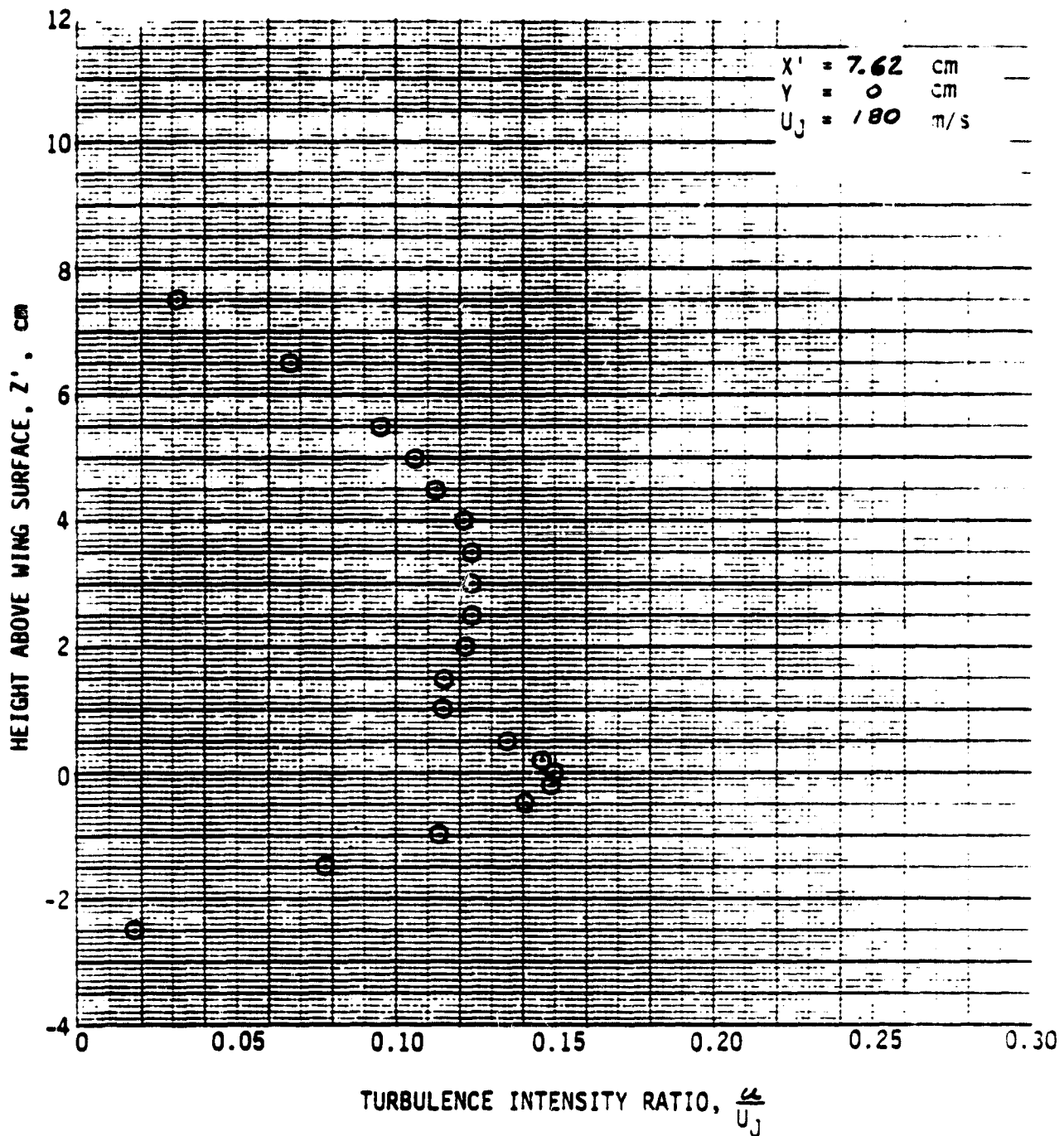


Figure A-1. Continued.

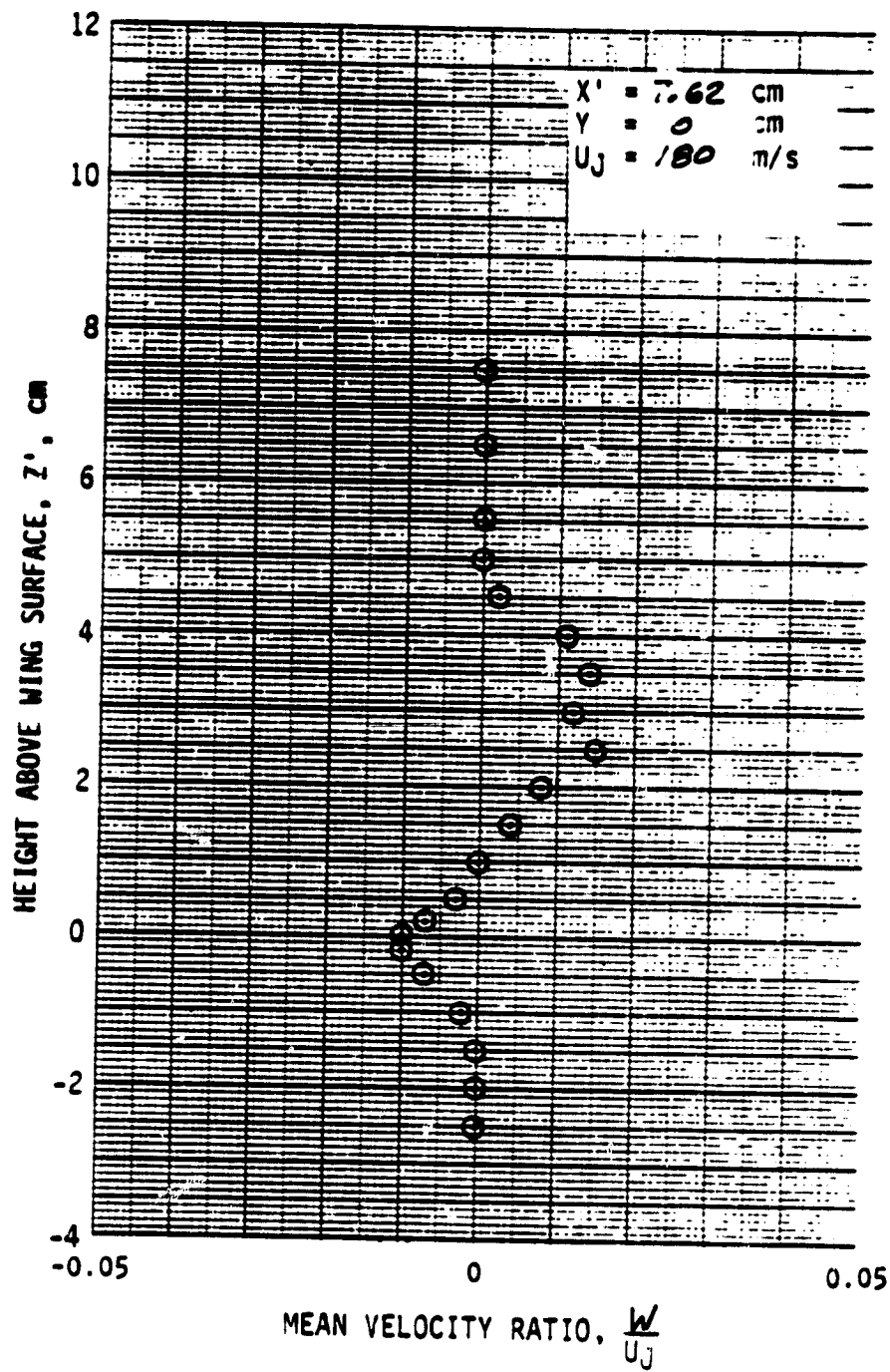


Figure A-1. Continued.

ORIGINAL PAGE IS
OF POOR QUALITY

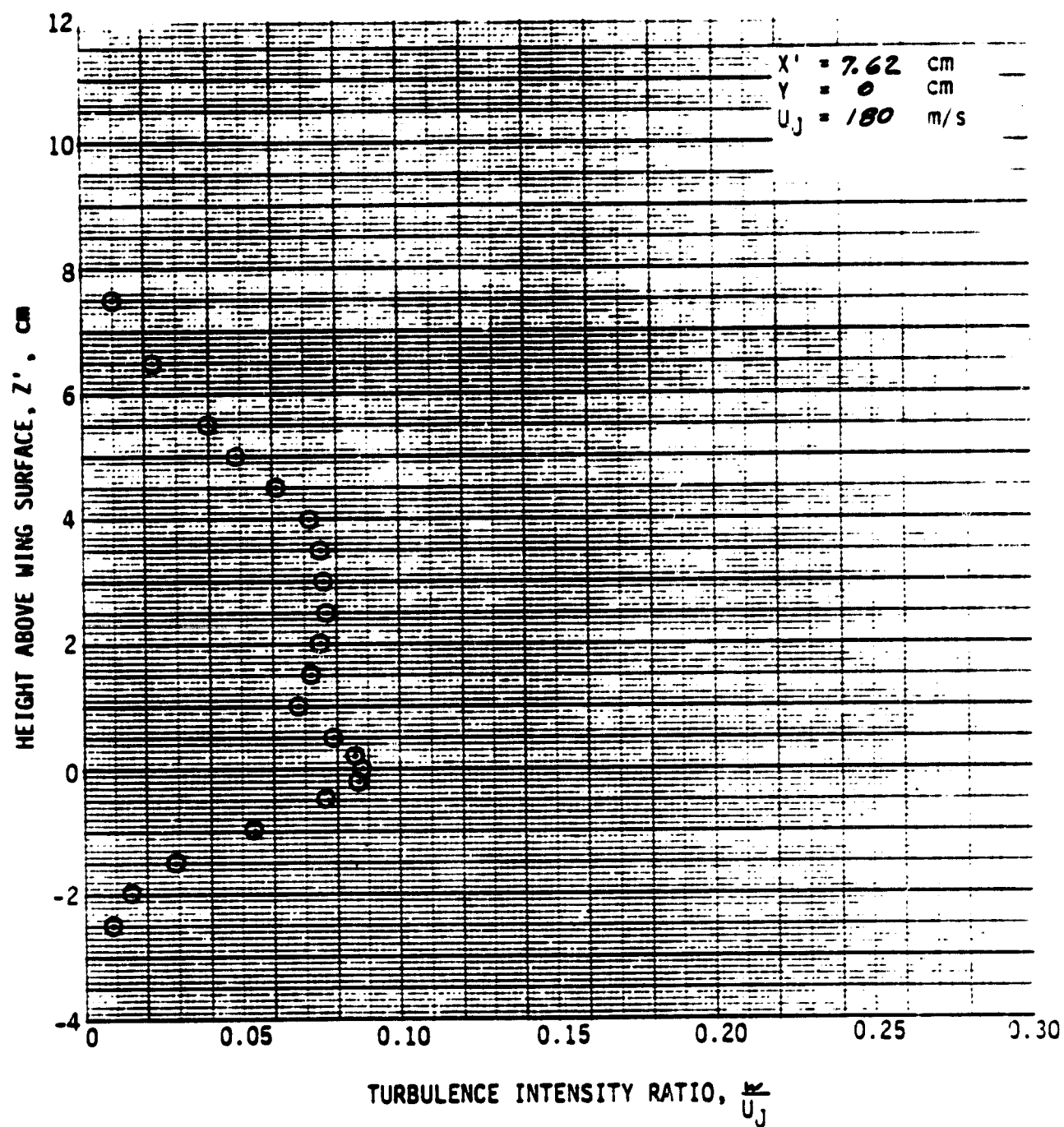


Figure A-1. Continued.

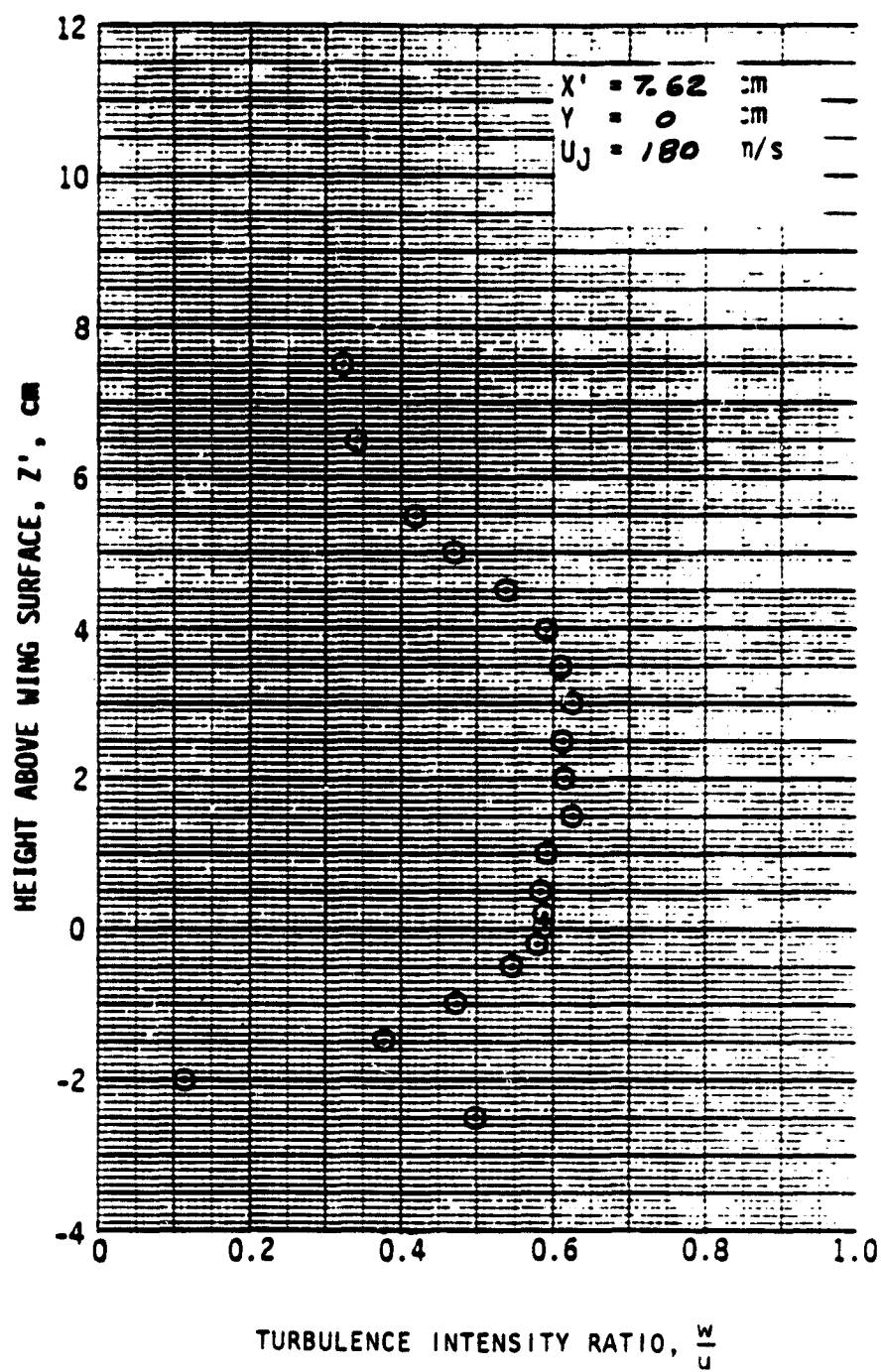


Figure A-1. Continued.

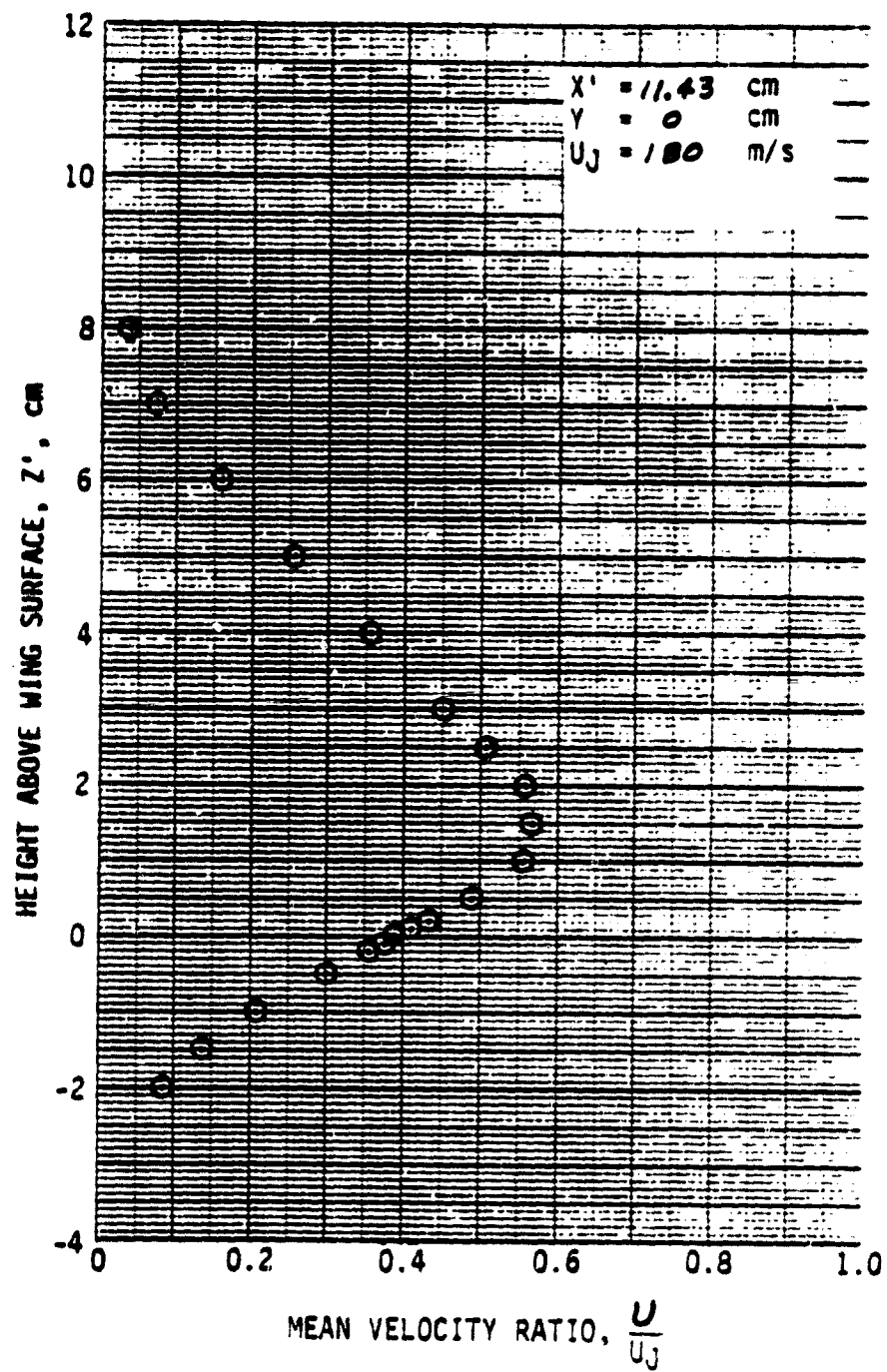


Figure A-1. Continued.

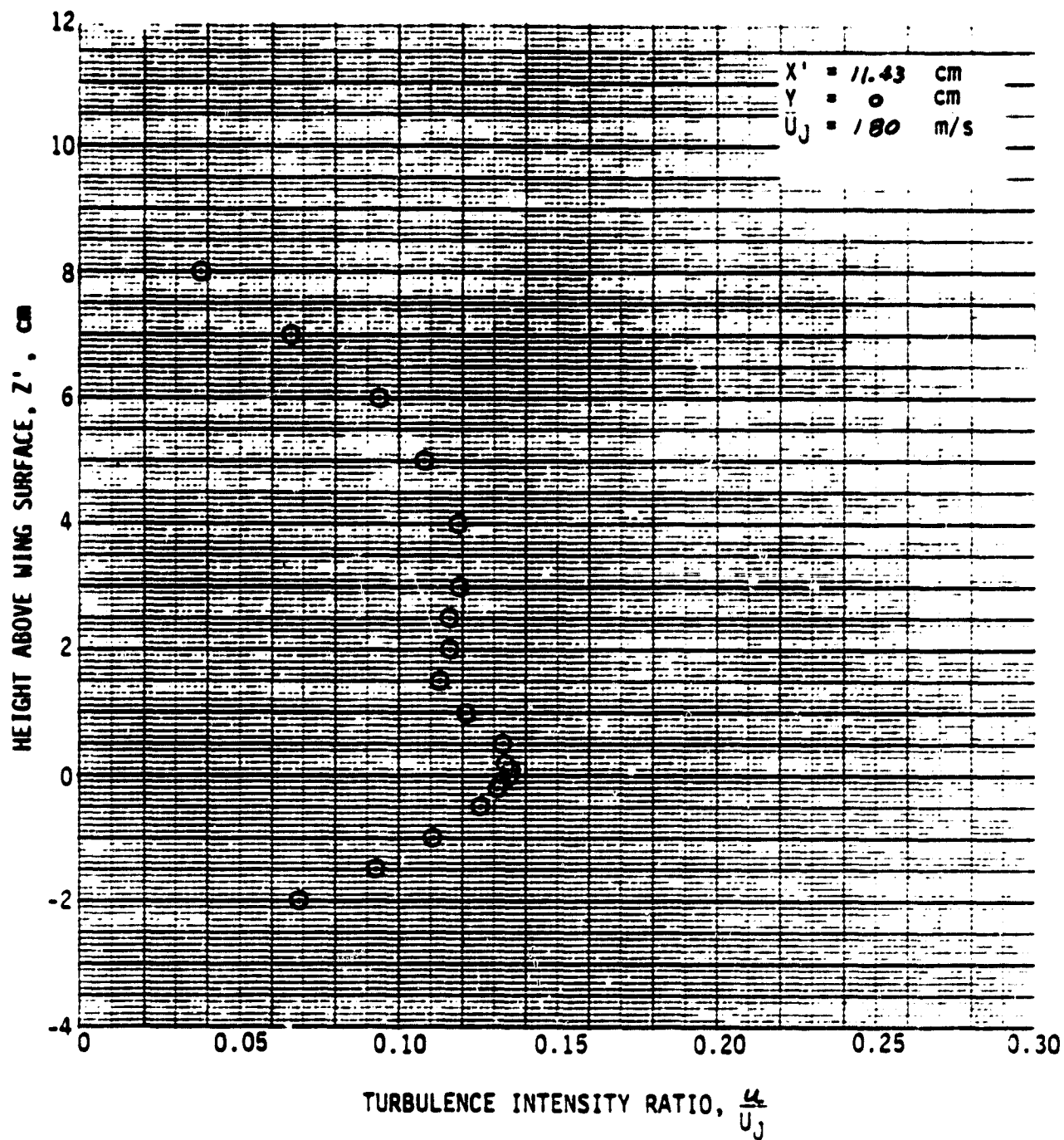


Figure A-1. Continued.

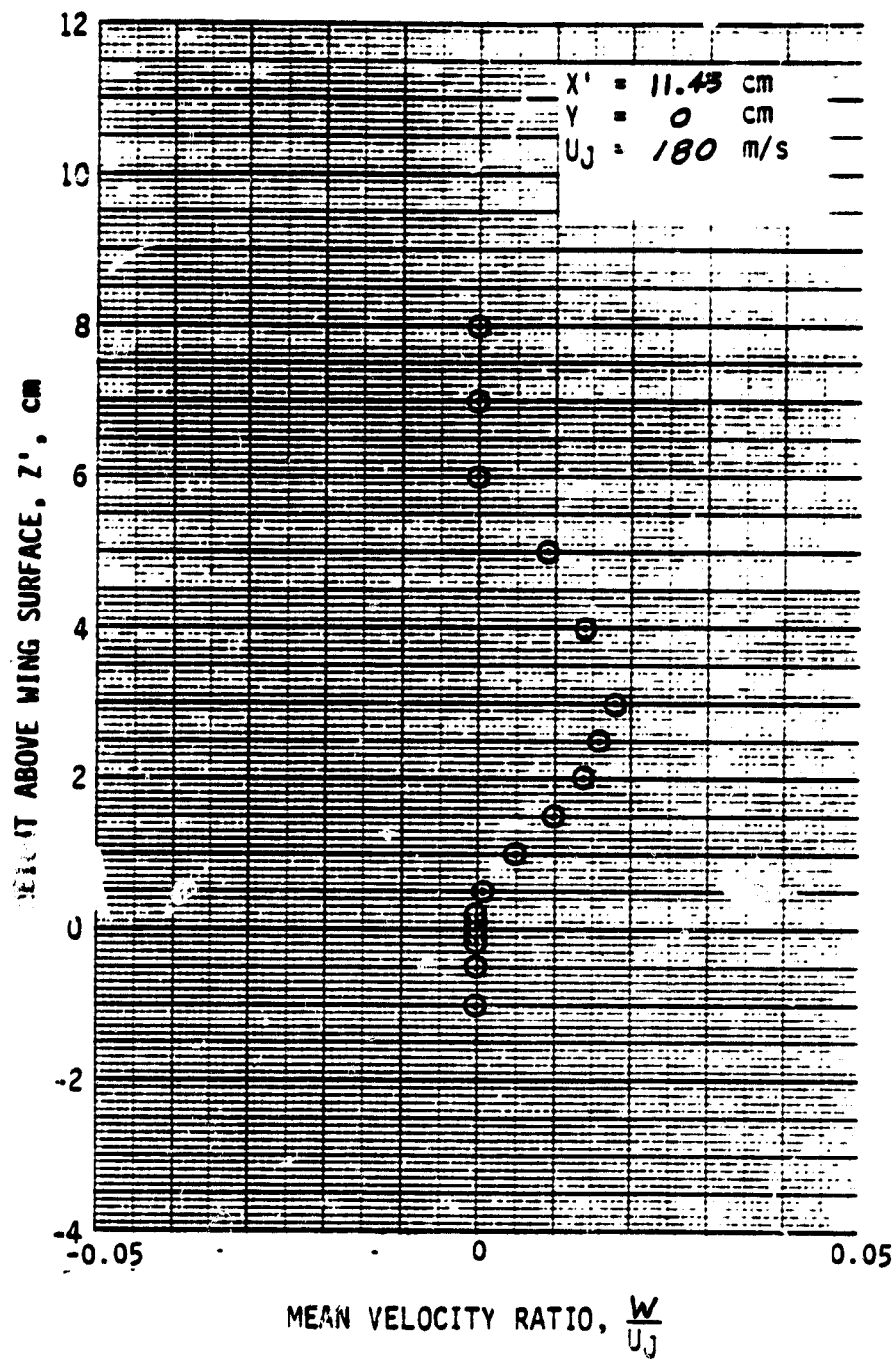


Figure A-1. Continued.

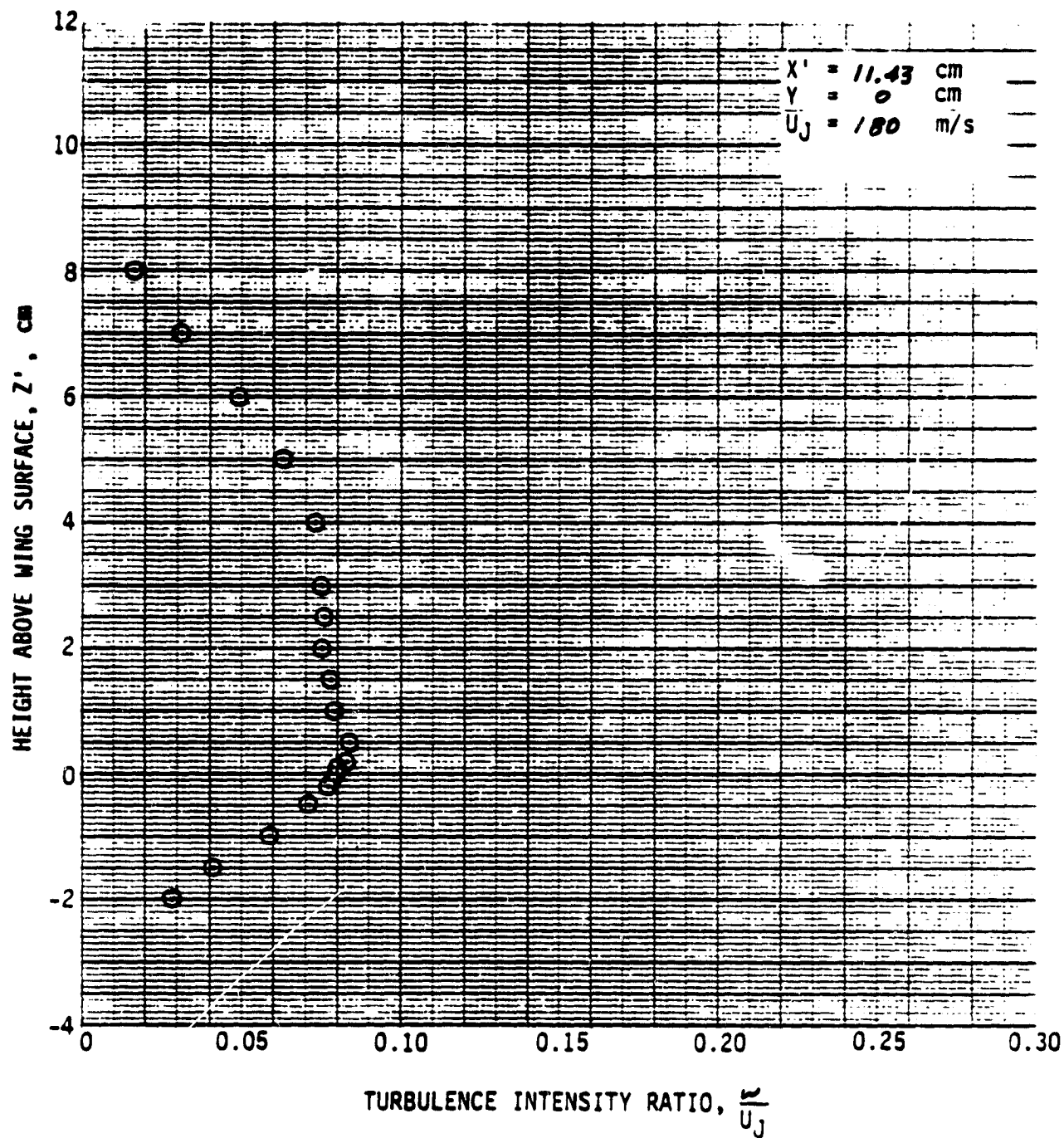


Figure A-1. Continued.

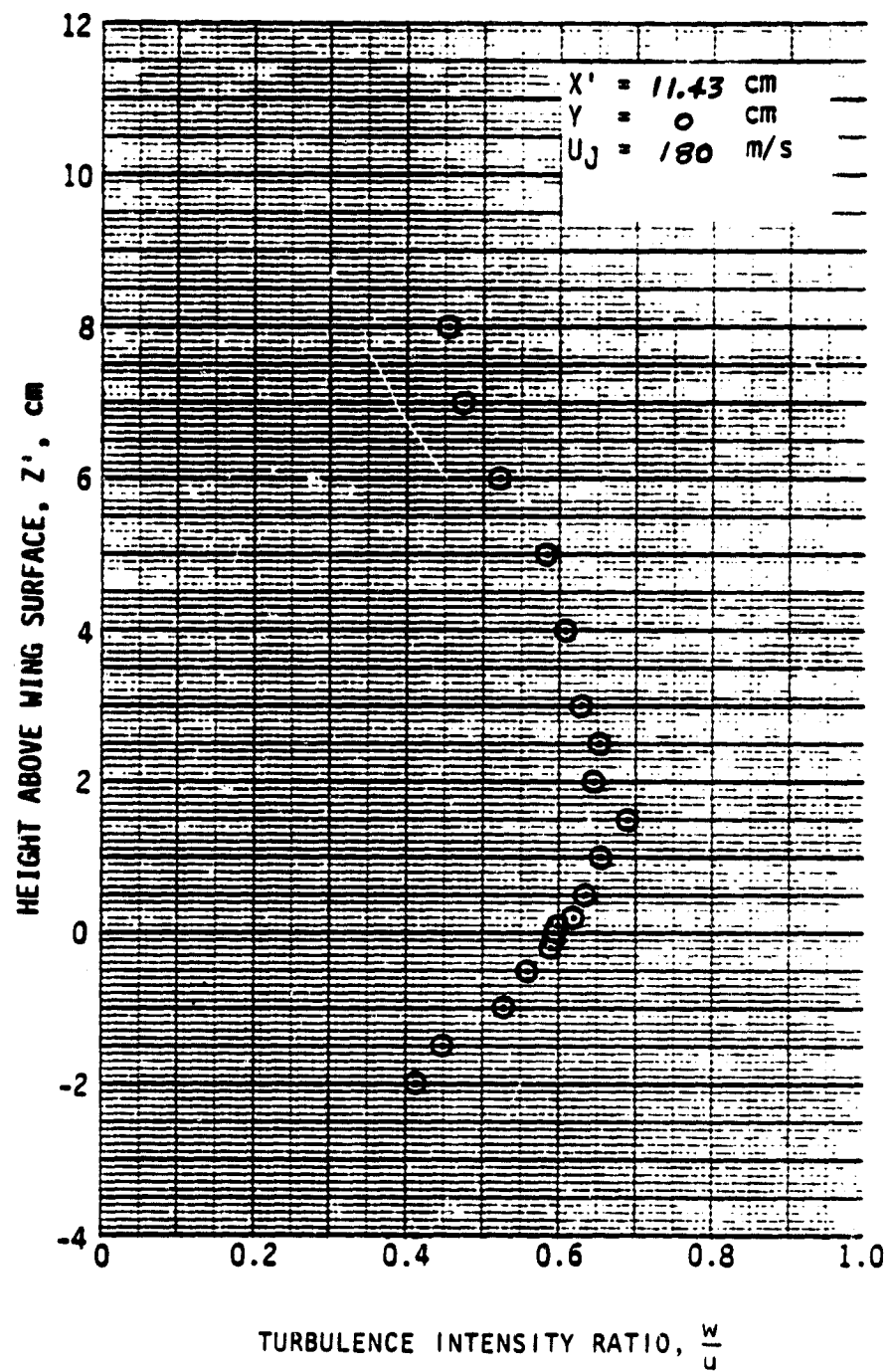


Figure A-1. Continued.

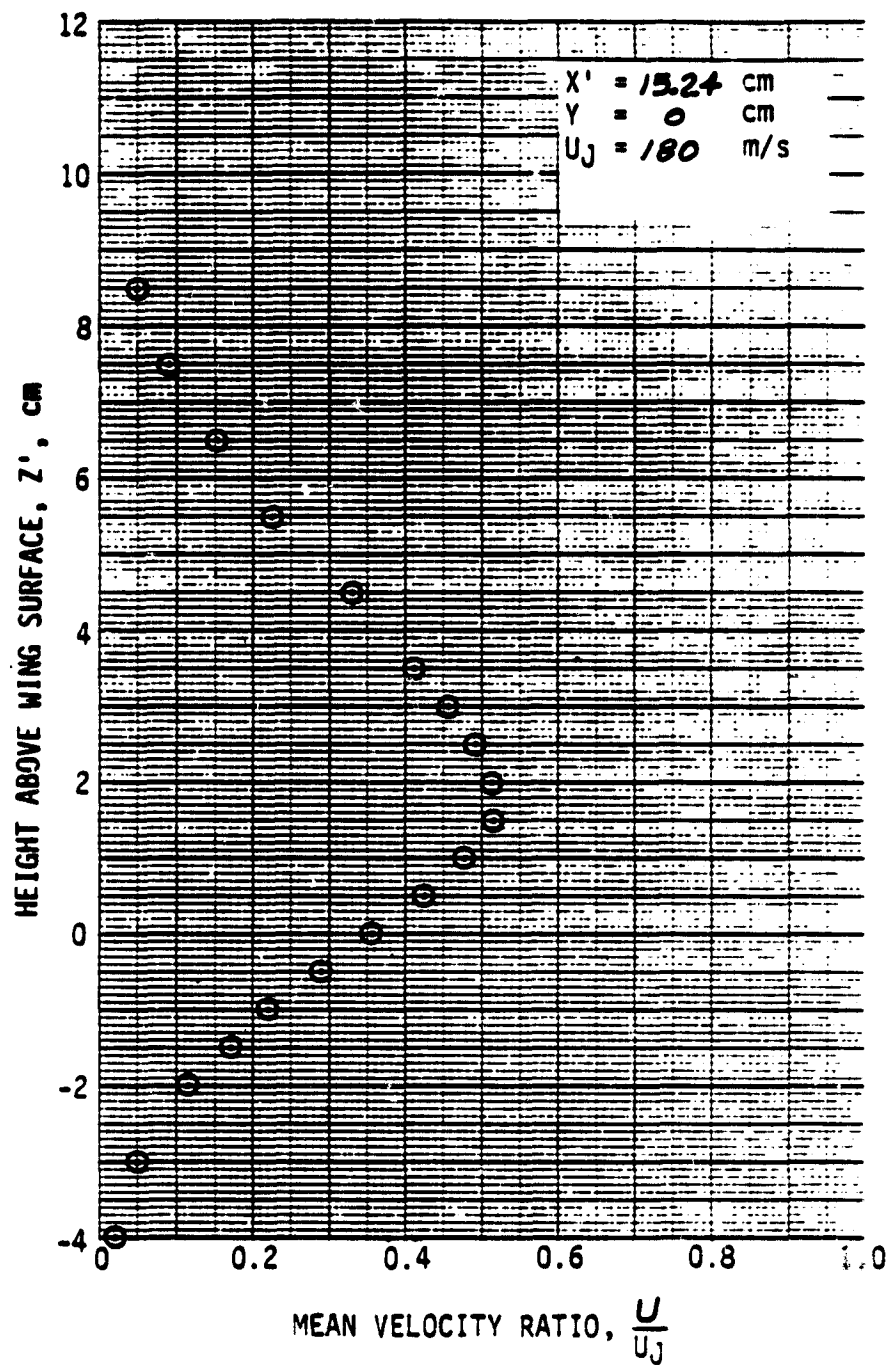


Figure A-1. Continued.

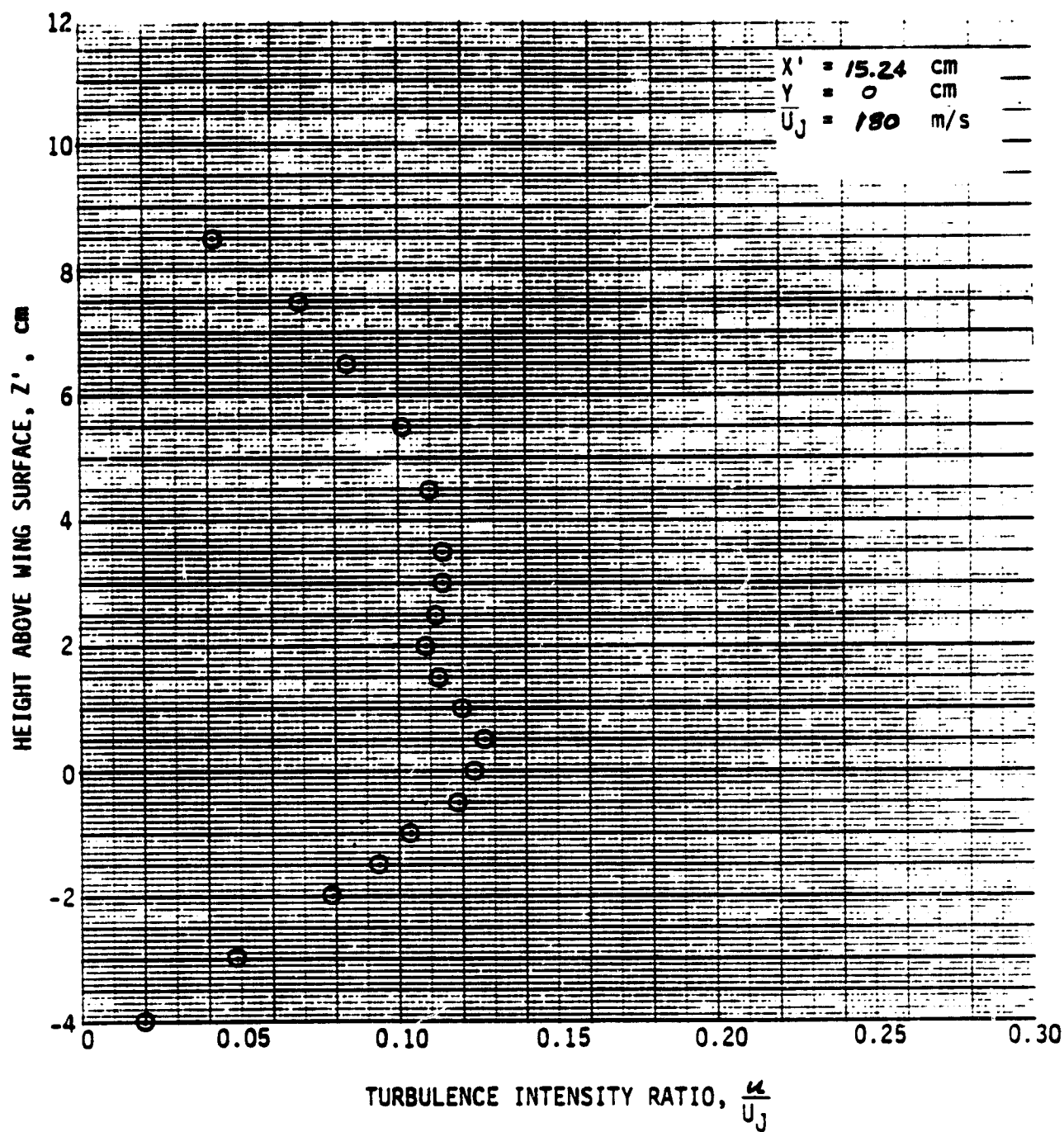


Figure A-1. Continued.

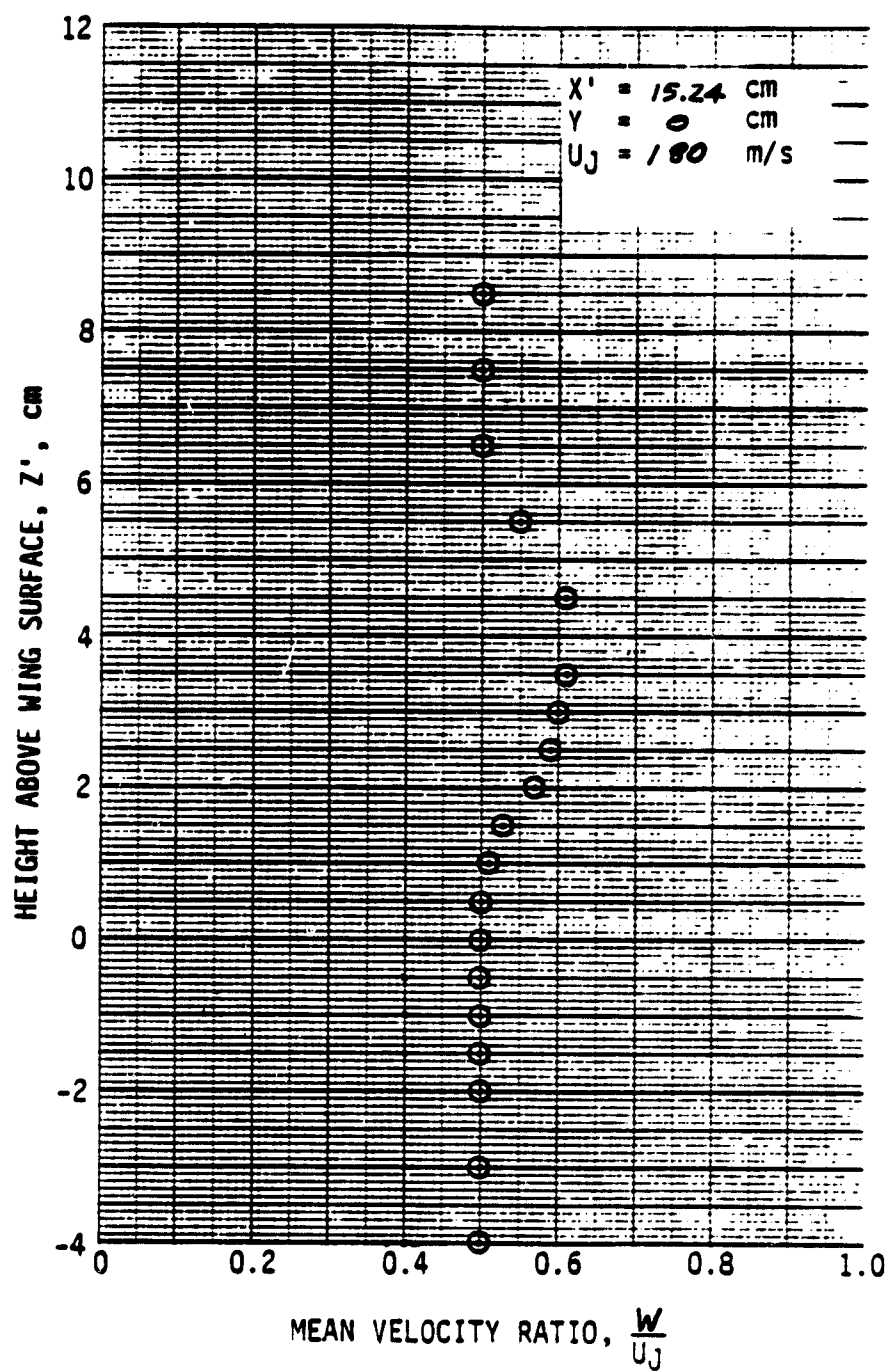


Figure A-1. Continued.

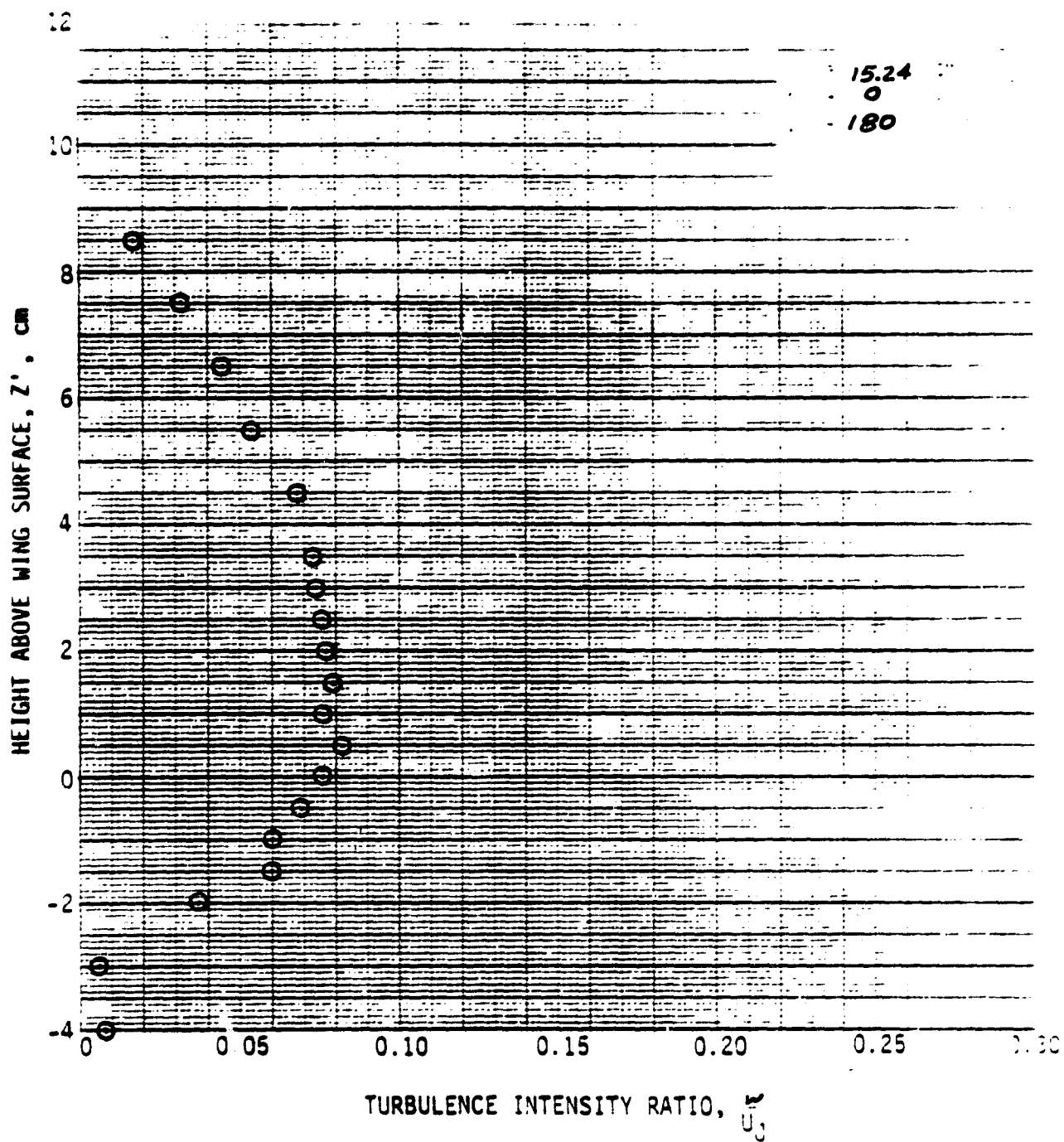


Figure A-1. Continued.

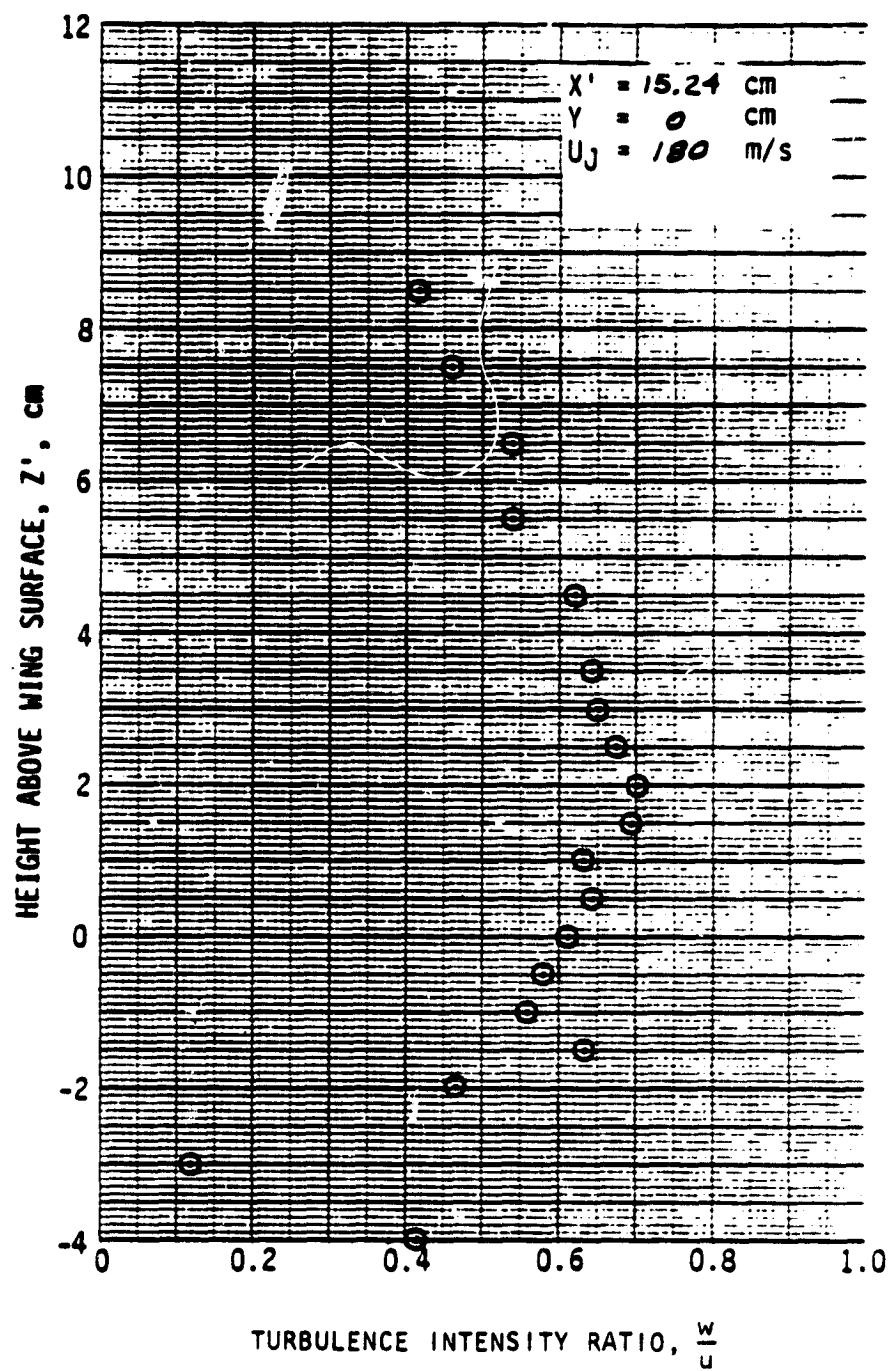


Figure A-1. Concluded.

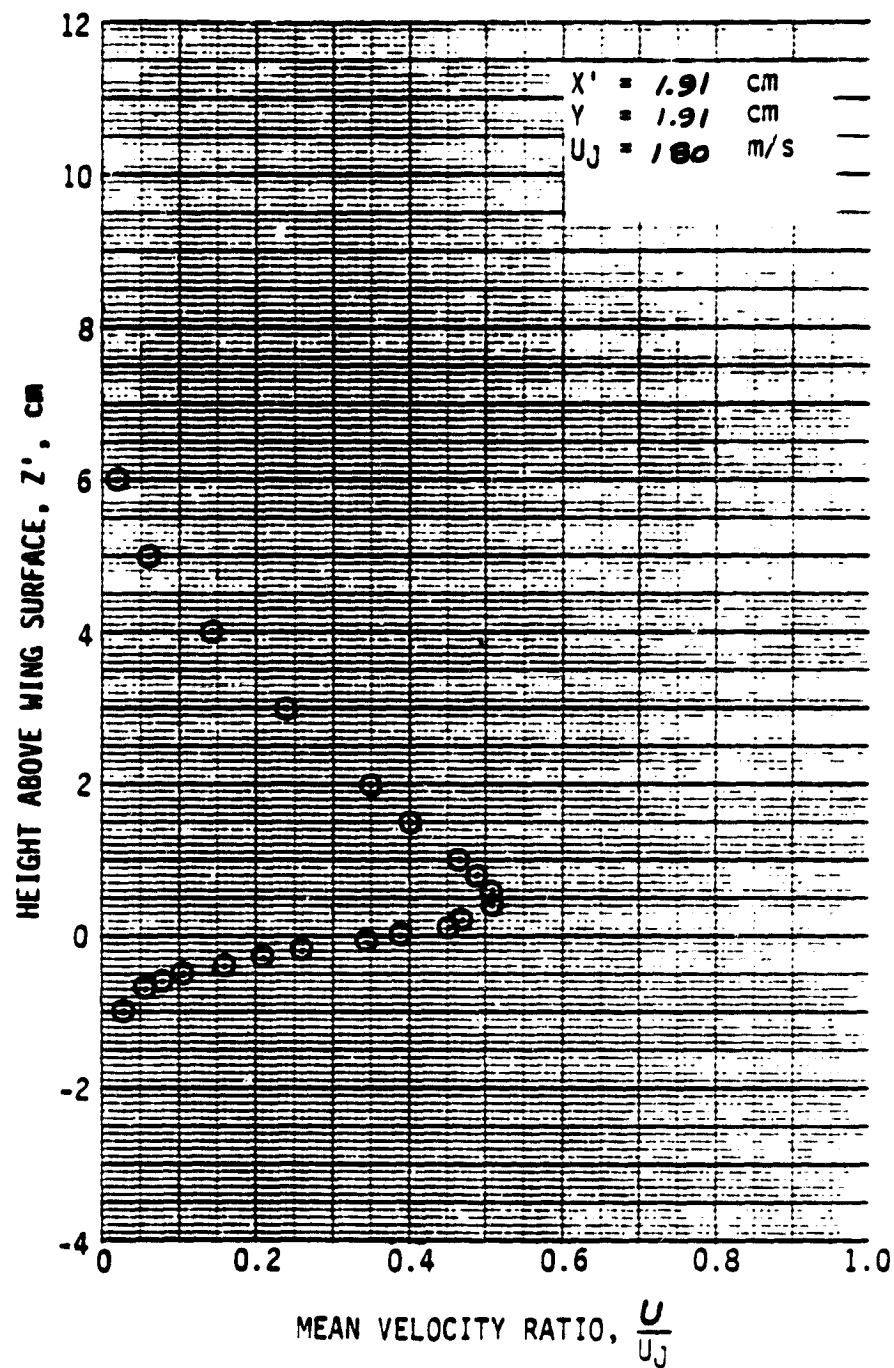


Figure A-2. Wake Flow Profiles by Cross Hot-Wire; $\delta_f = 30^\circ$, No Screen, Y Variations.

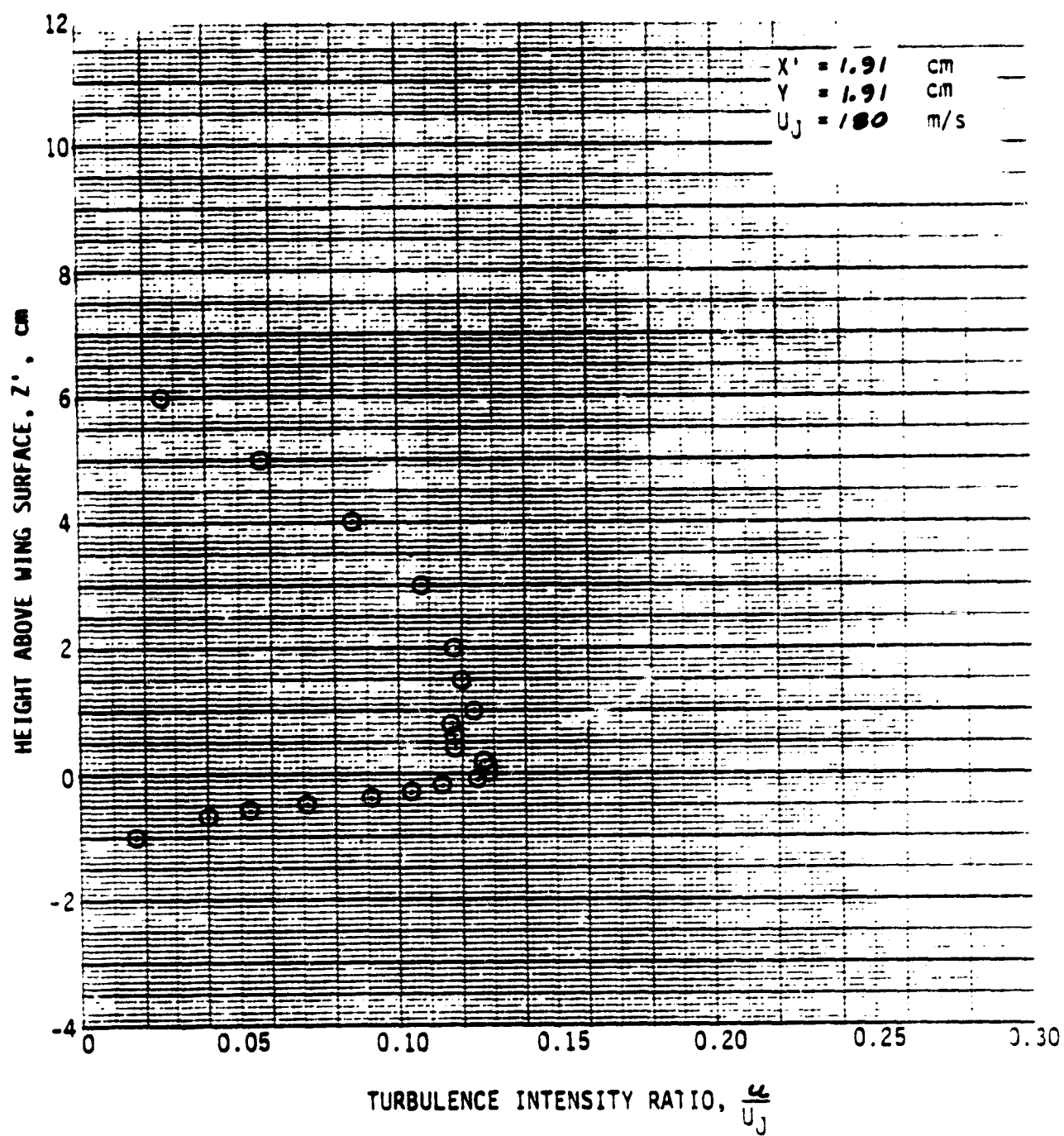


Figure A-2. Continued.

ORIGINAL PAGE IS
OF POOR QUALITY

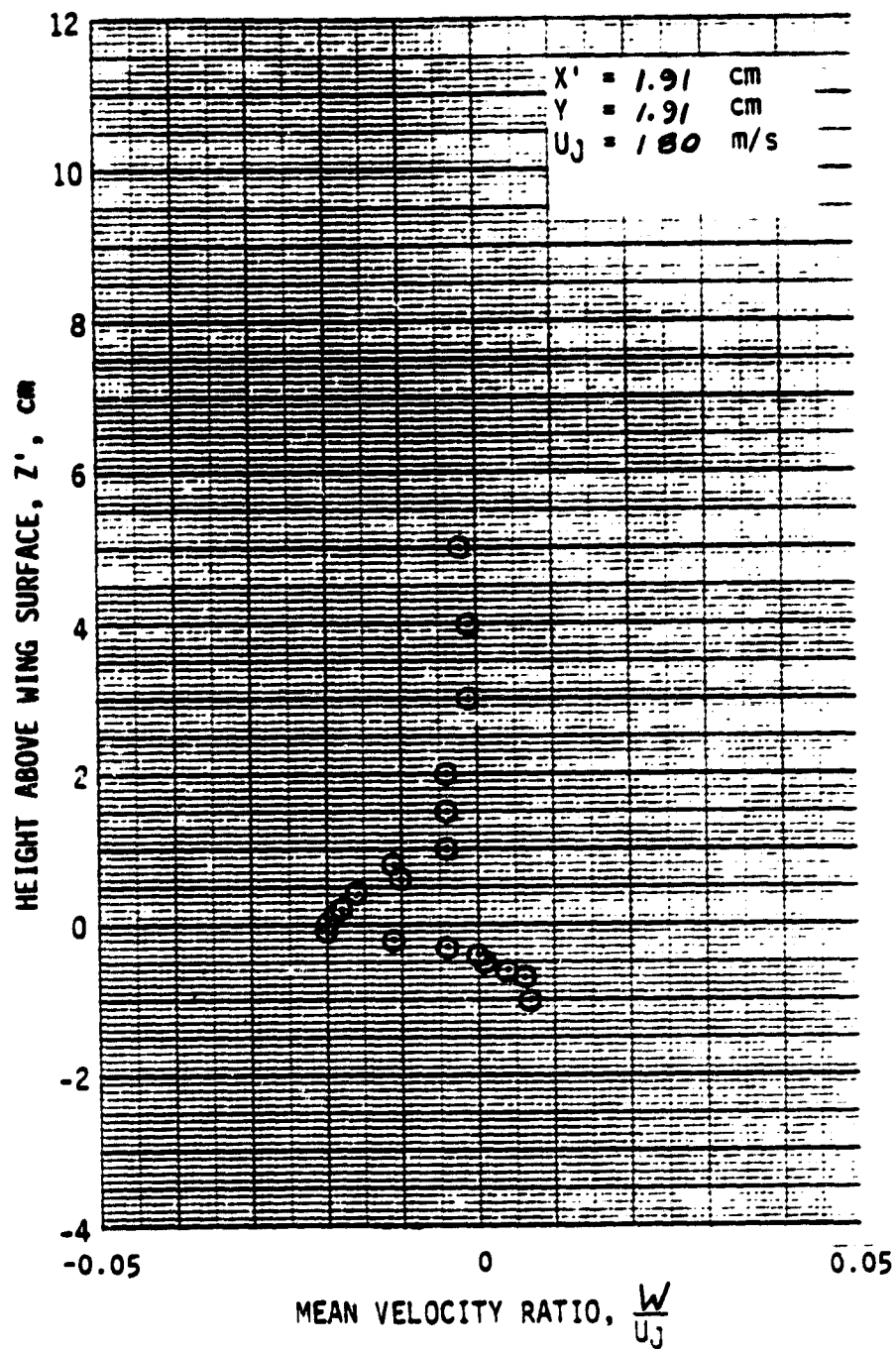


Figure A-2. Continued.

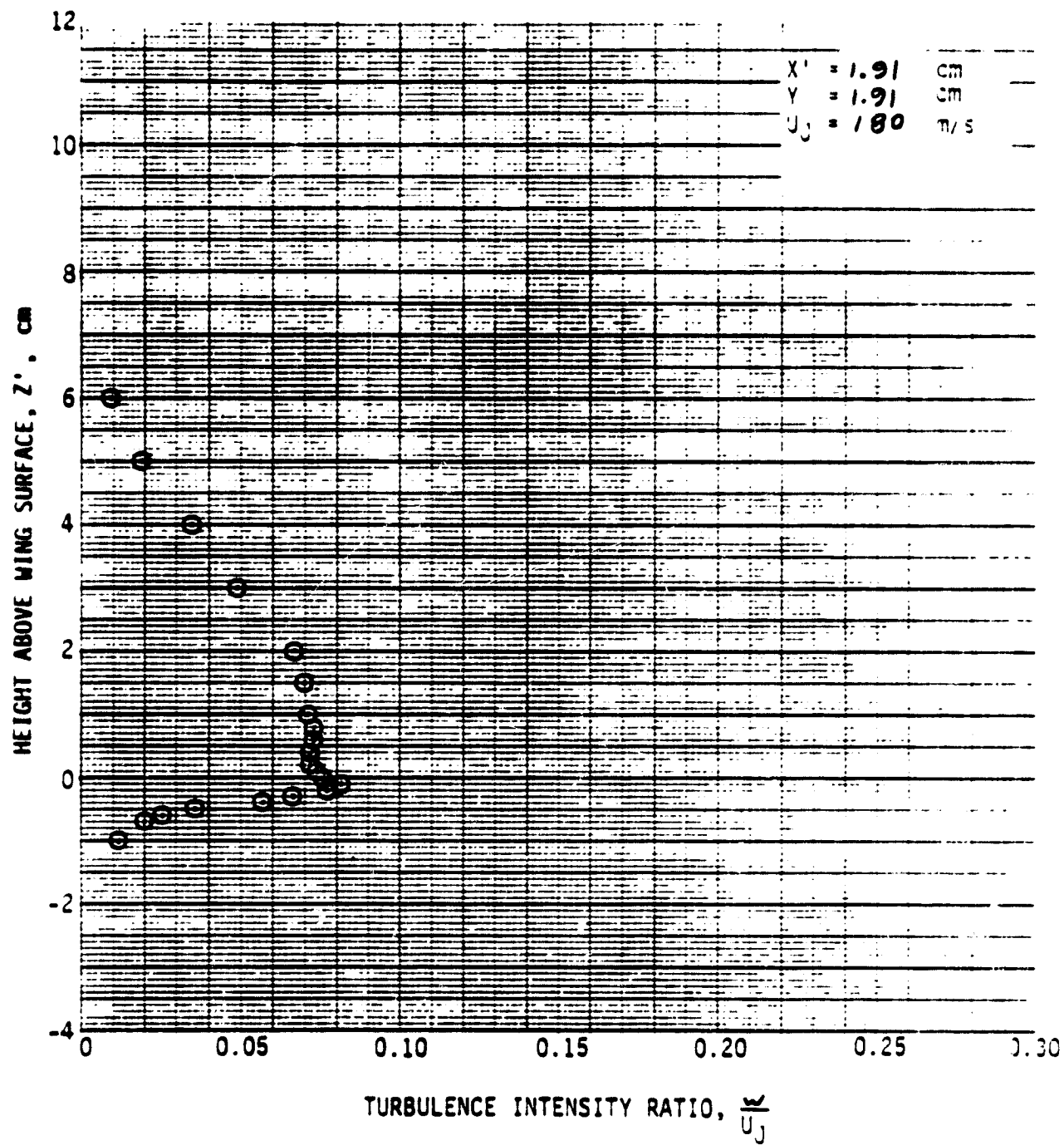


Figure A-2. Continued.

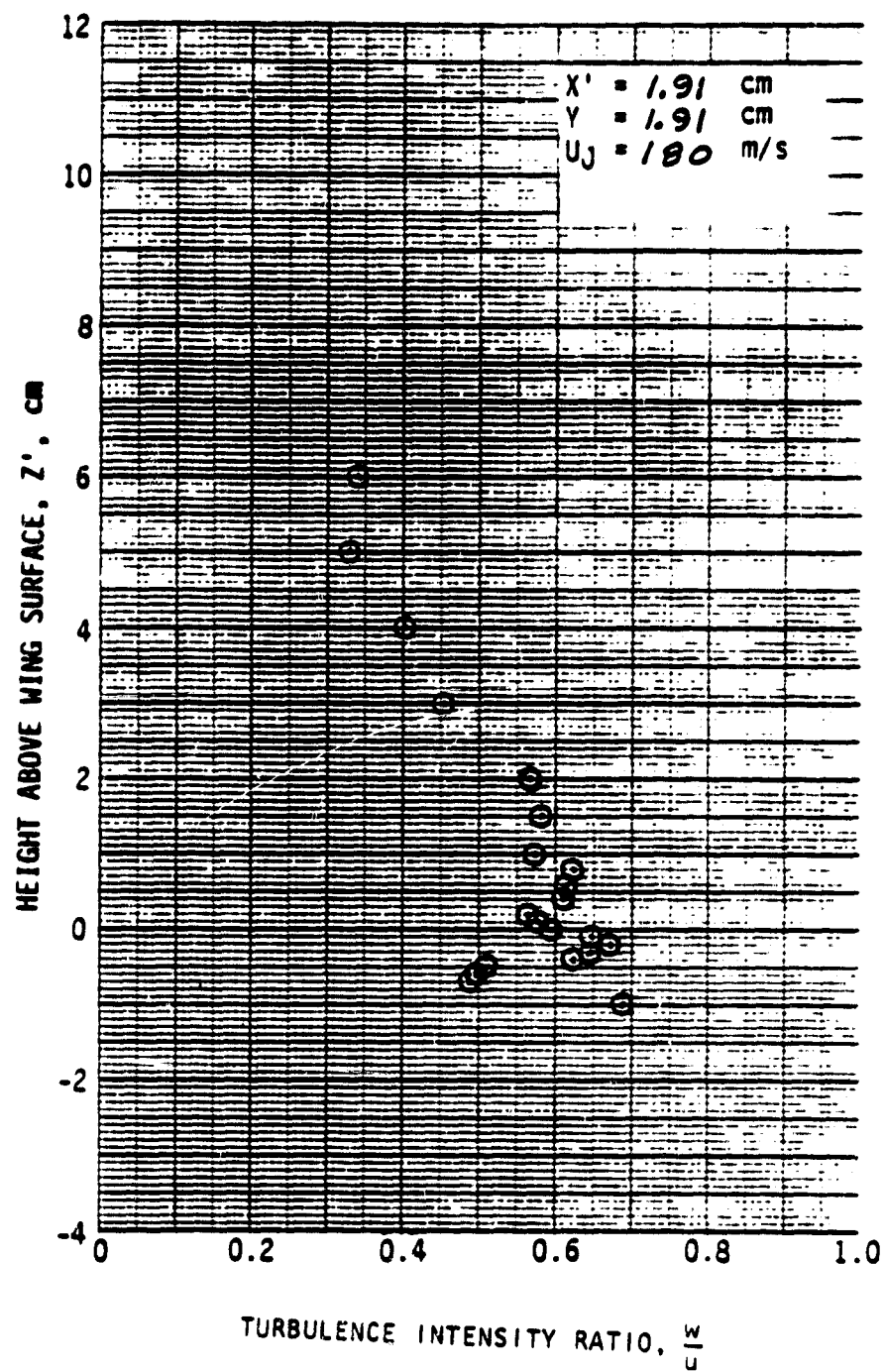


Figure A-2. Continued.

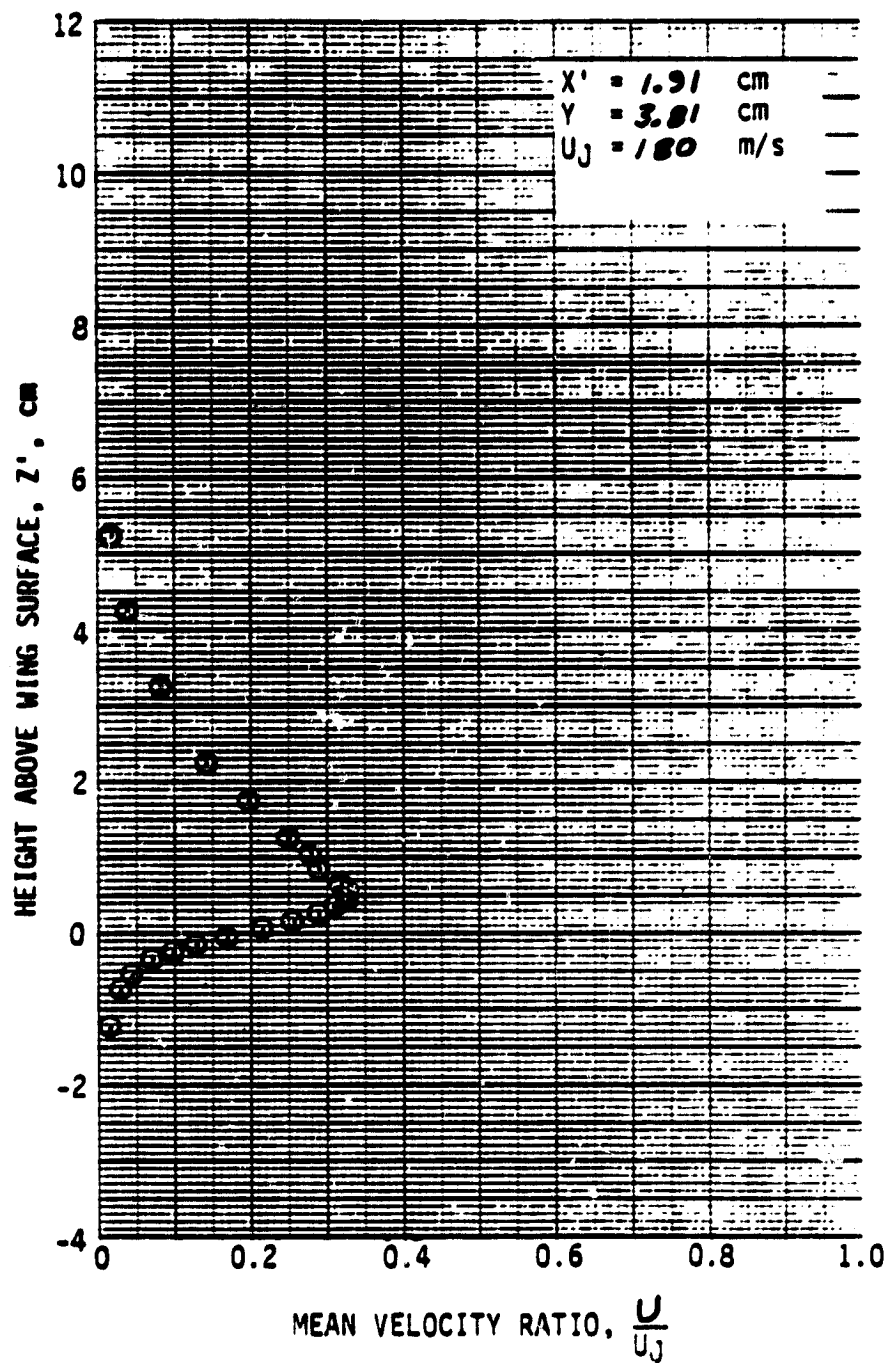
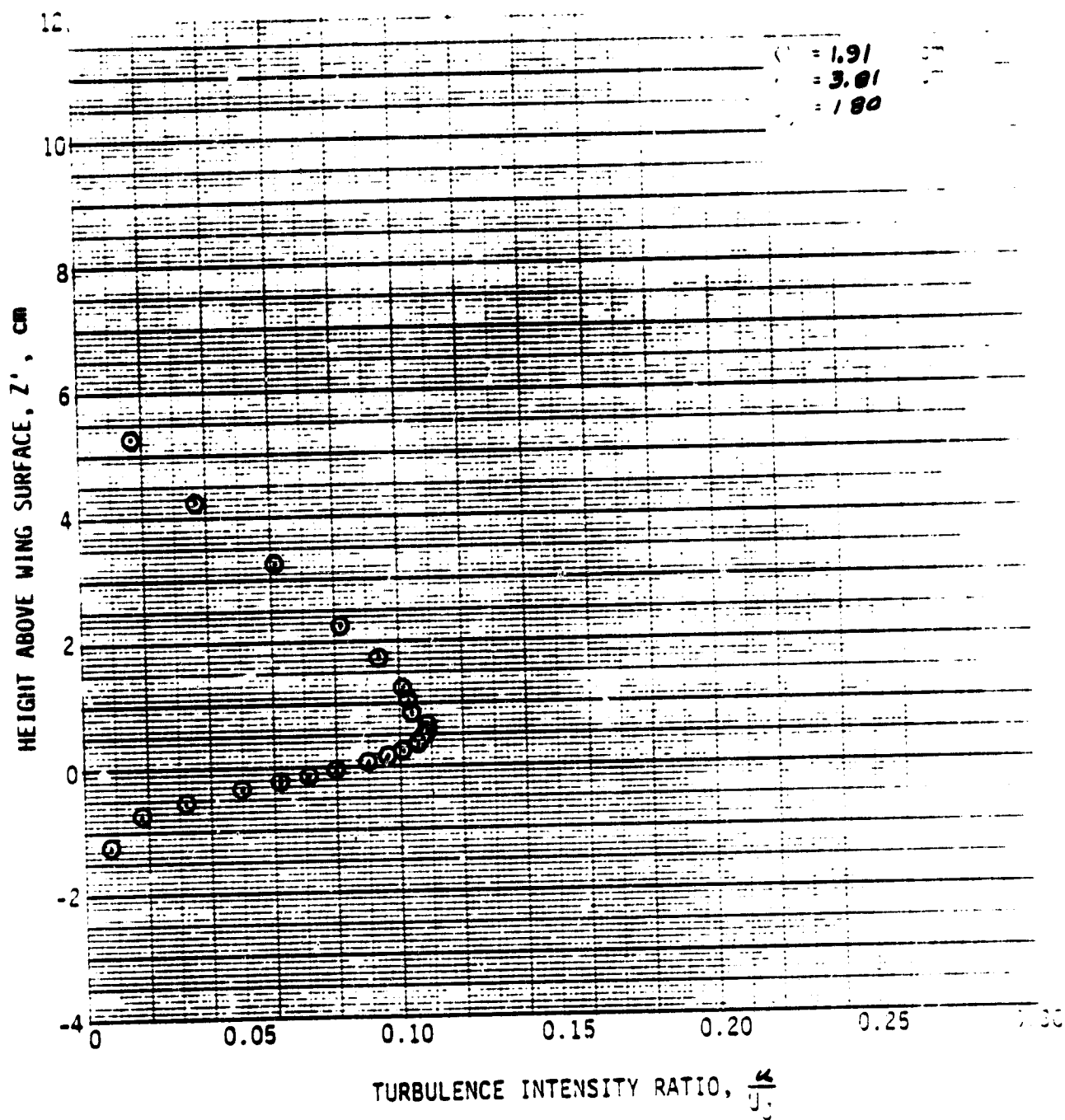


Figure A-2. Continued.



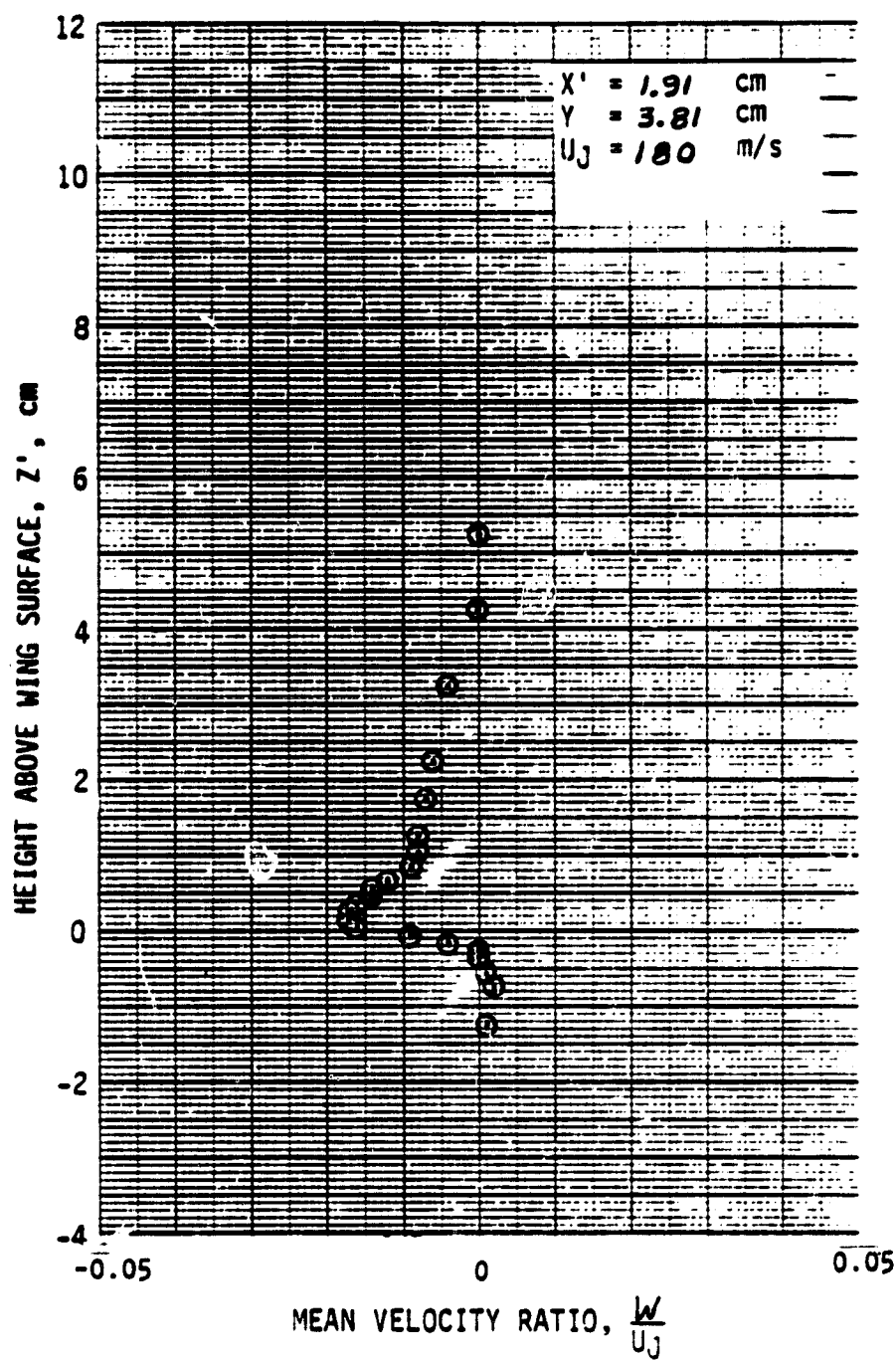


Figure A-2. Continued.

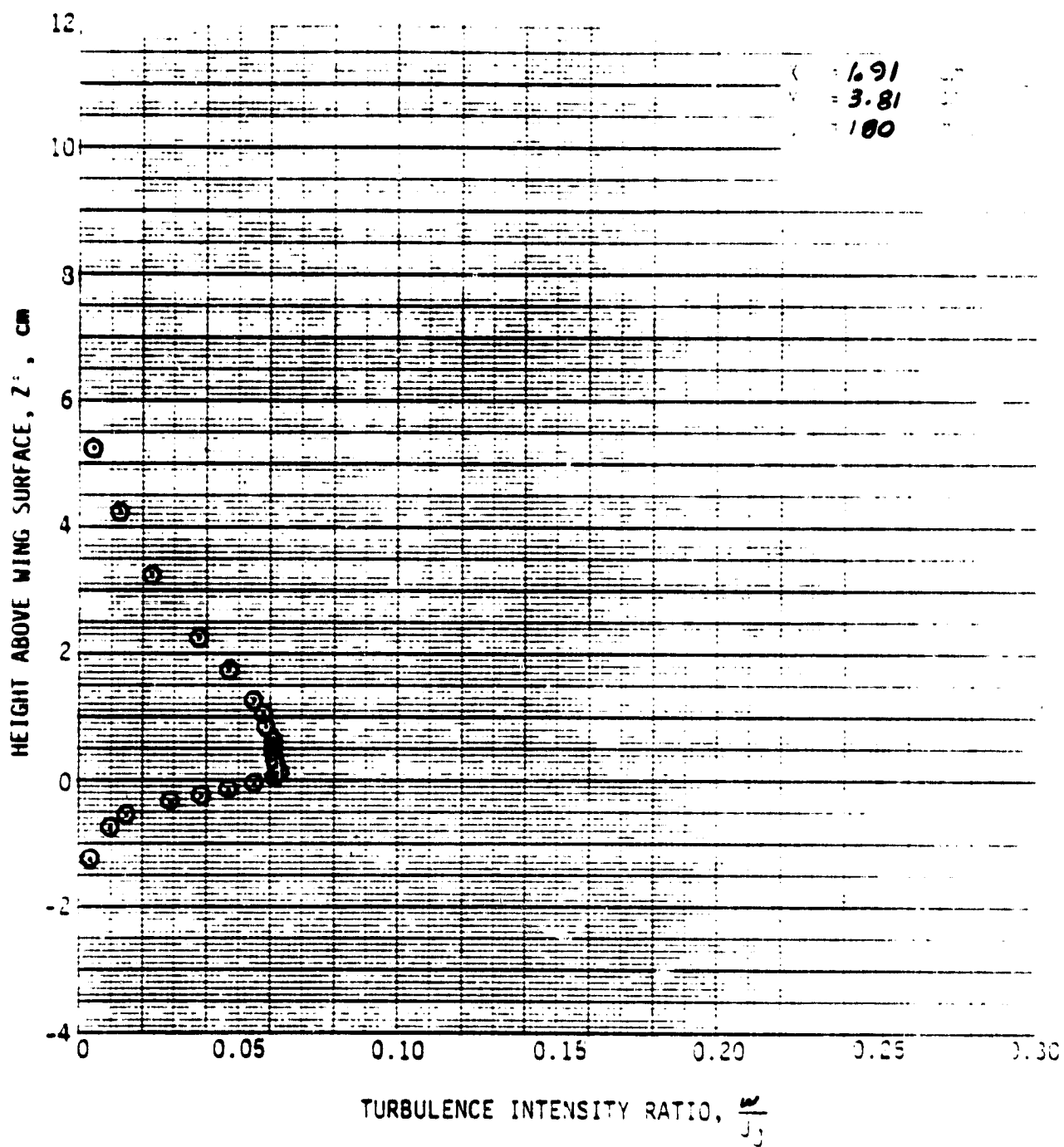


Figure A-2. Continued.

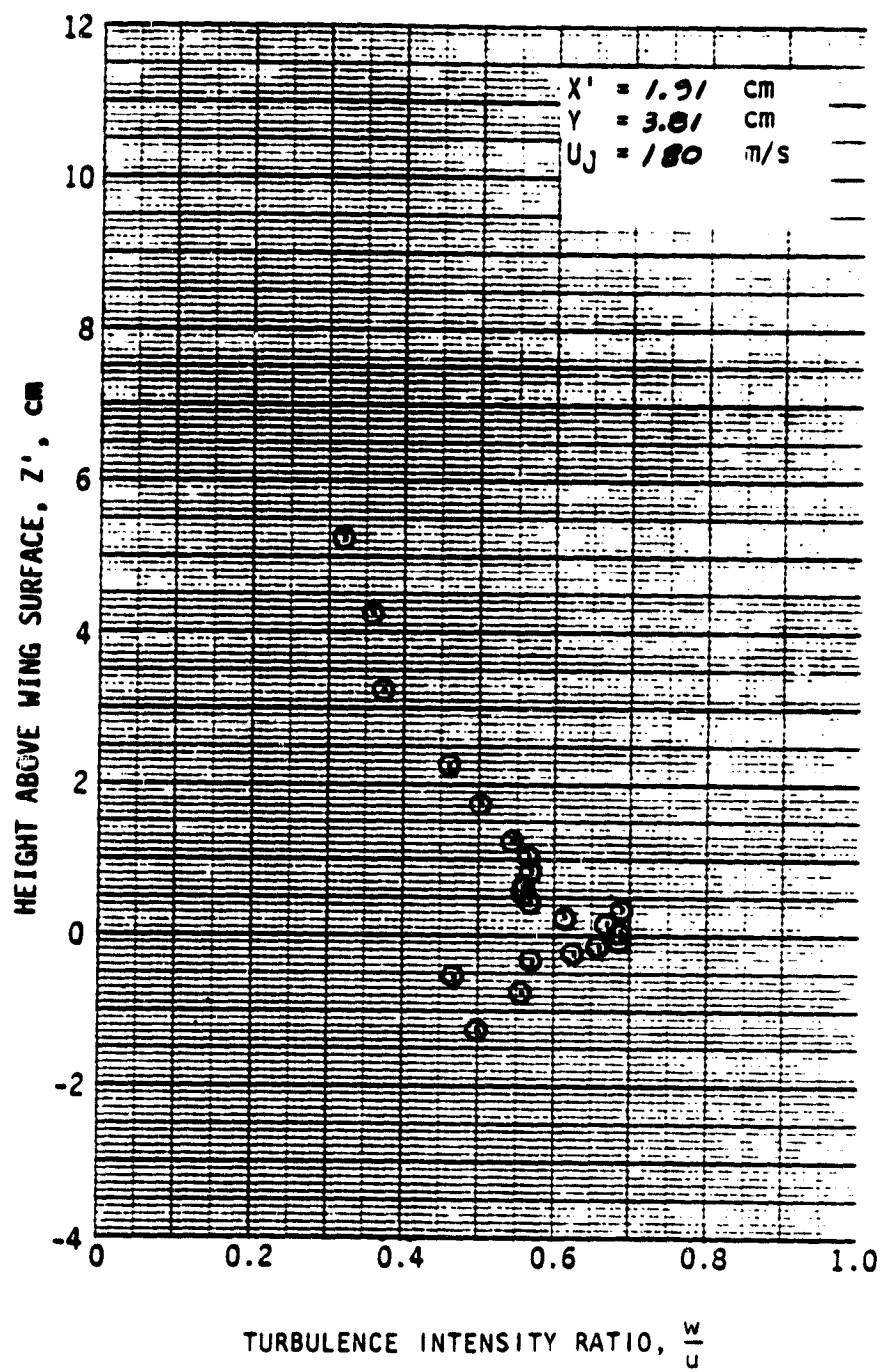


Figure A-2. Continued.

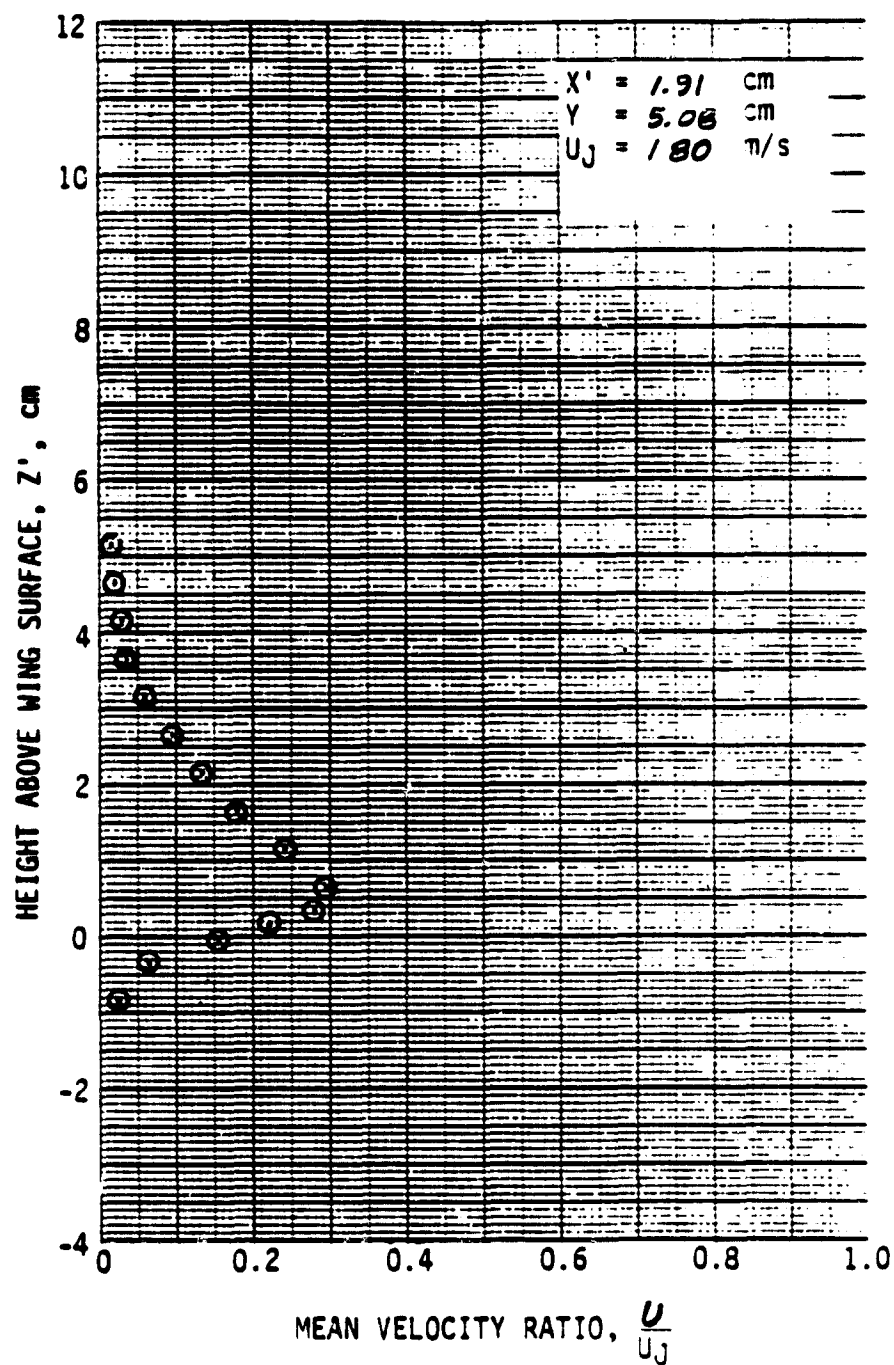


Figure A-2. Continued.

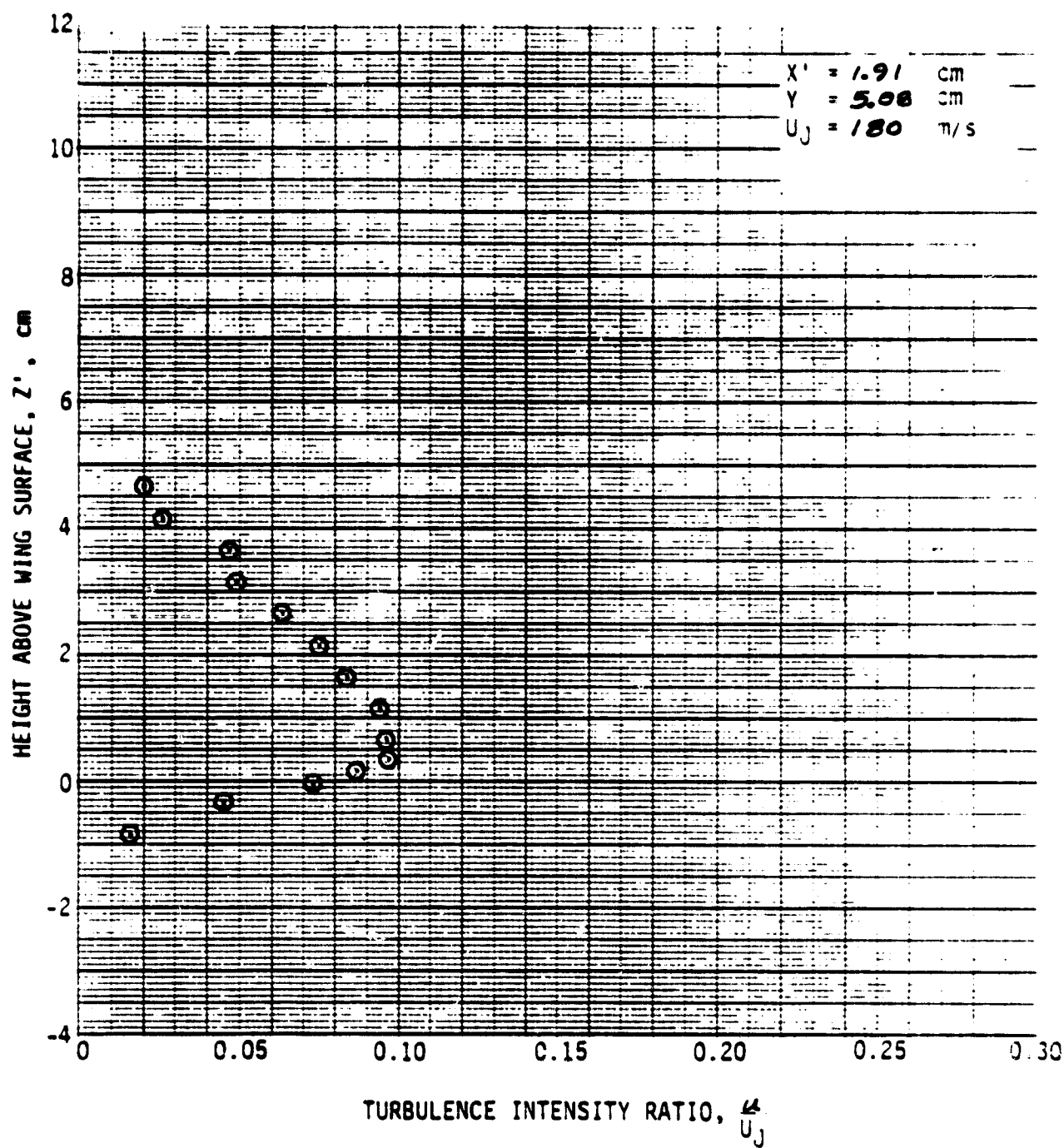


Figure A-2 Continued.

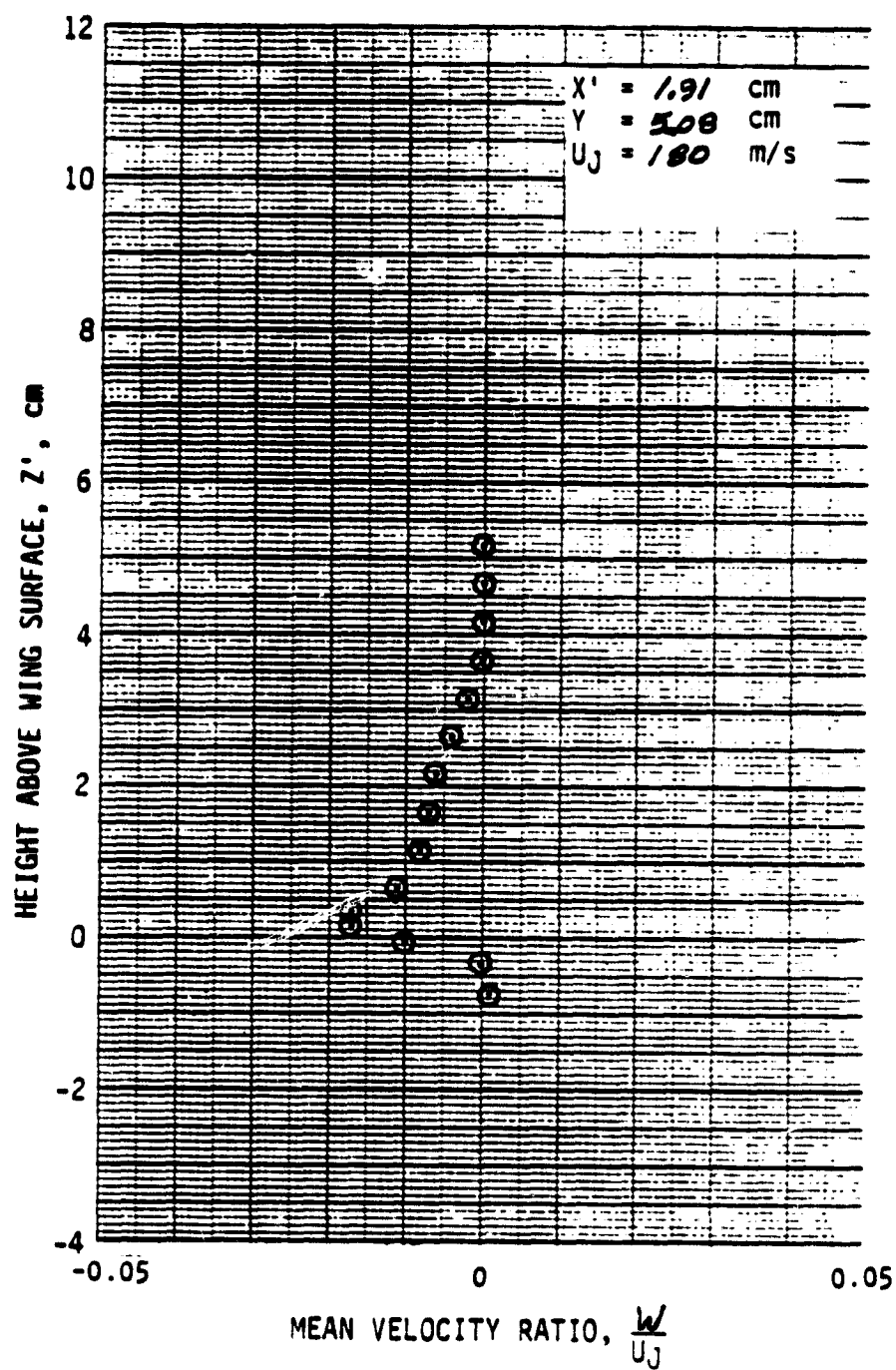


Figure A-2. Continued.

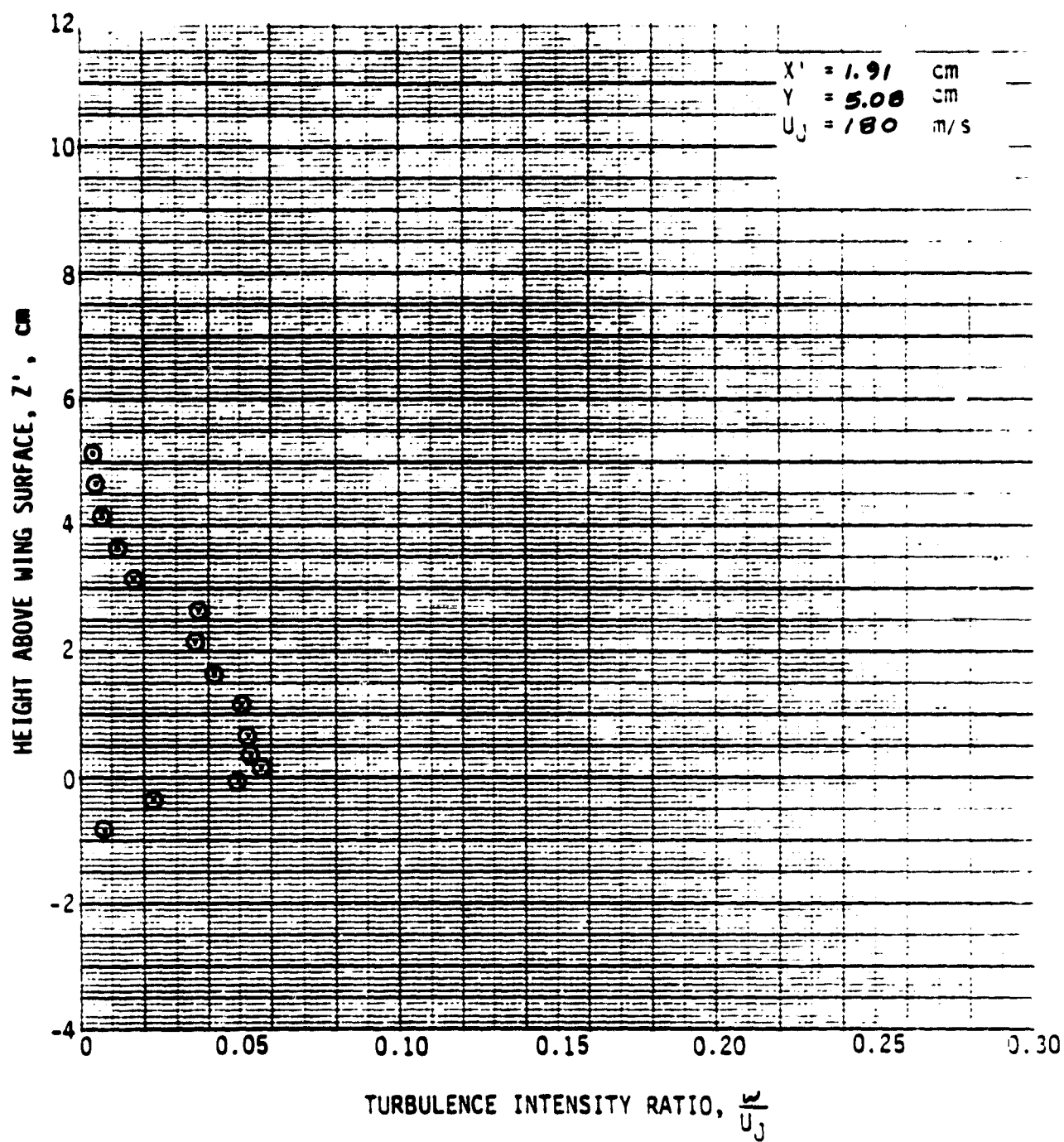


Figure A-2. Continued.

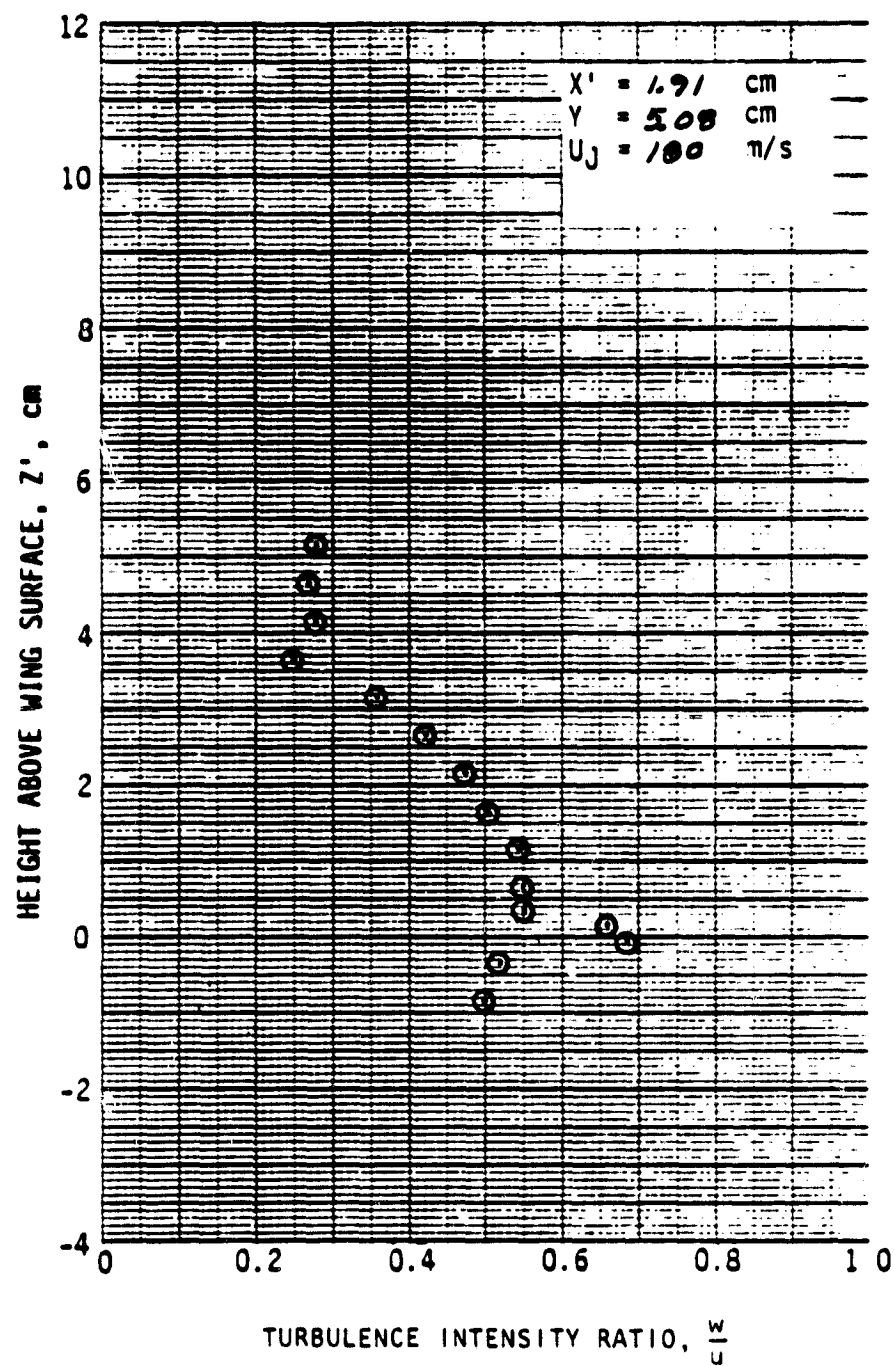


Figure A-2. Continued.

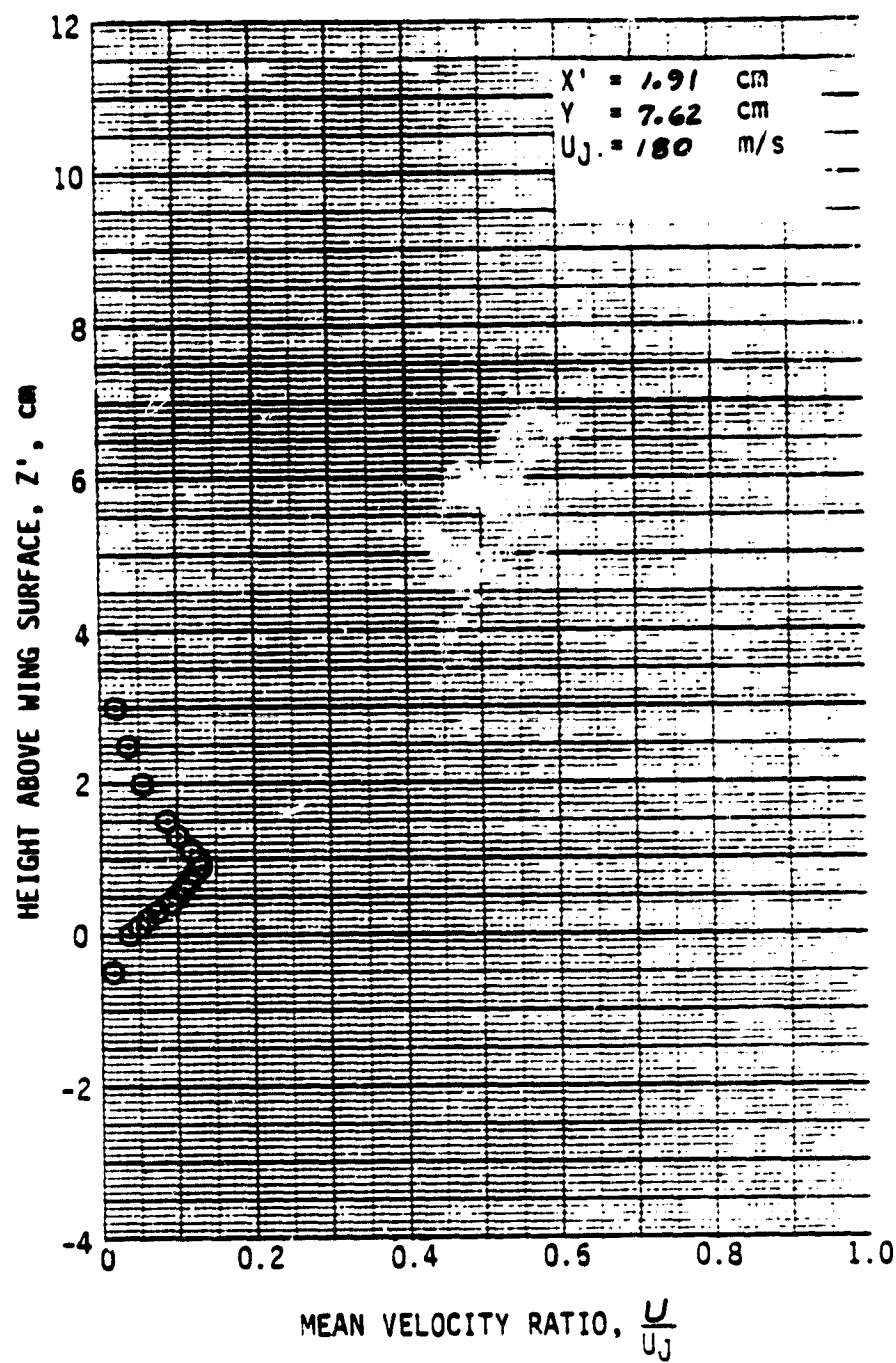


Figure A-2. Continued.

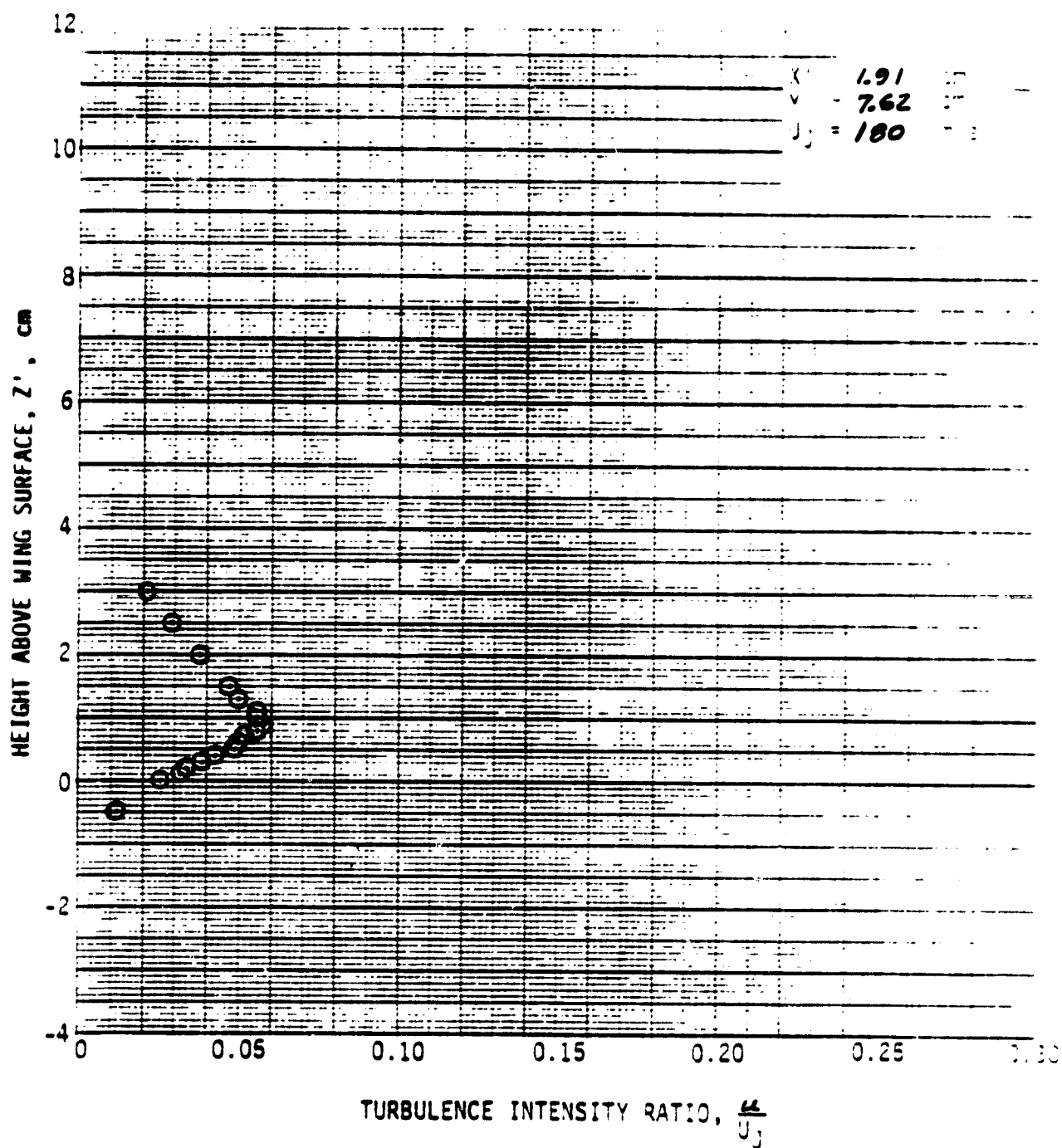


Figure A-2. Continued.

ORIGINAL PAGE IS
OF POOR QUALITY

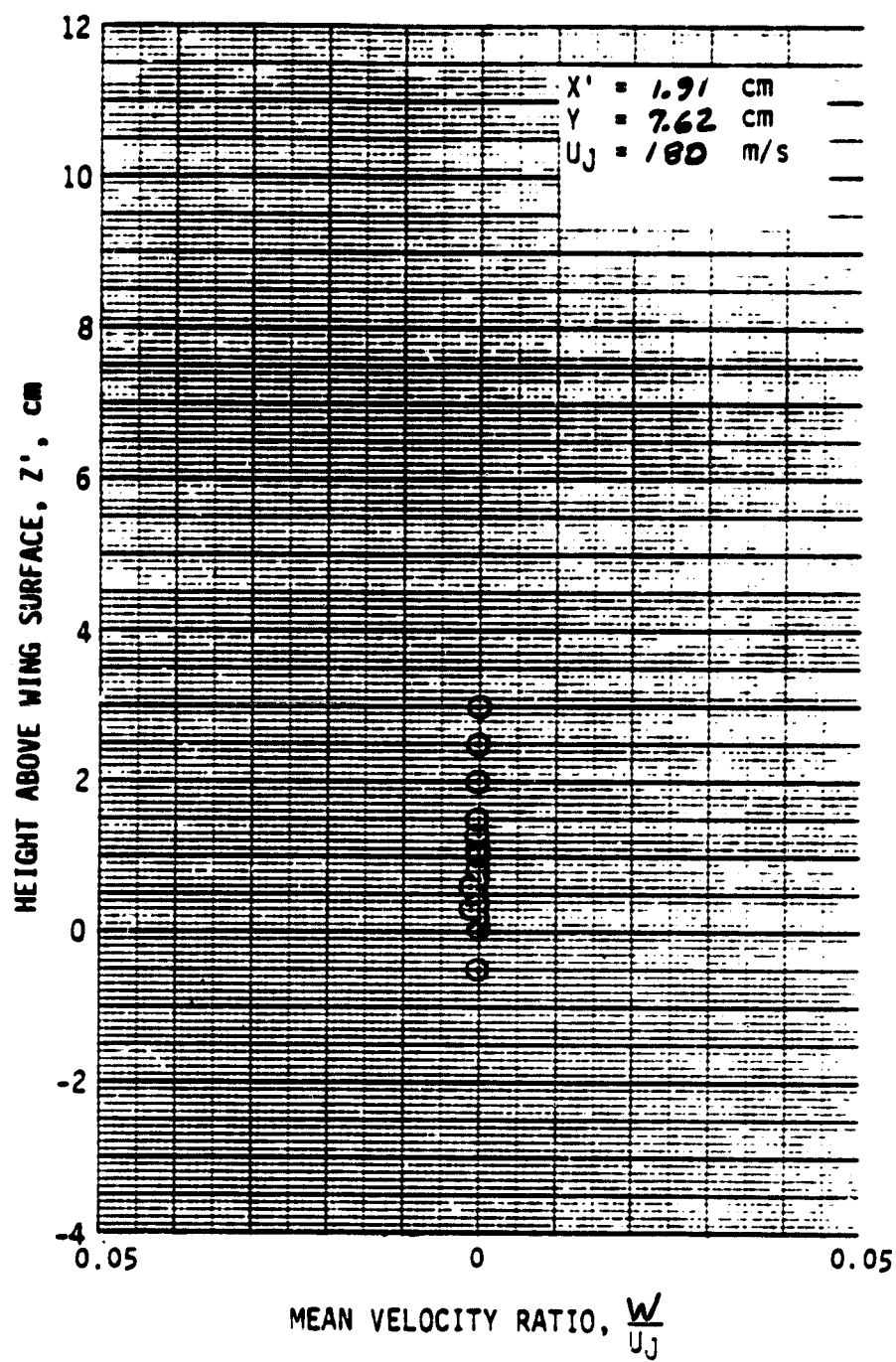


Figure A-2. Continued.

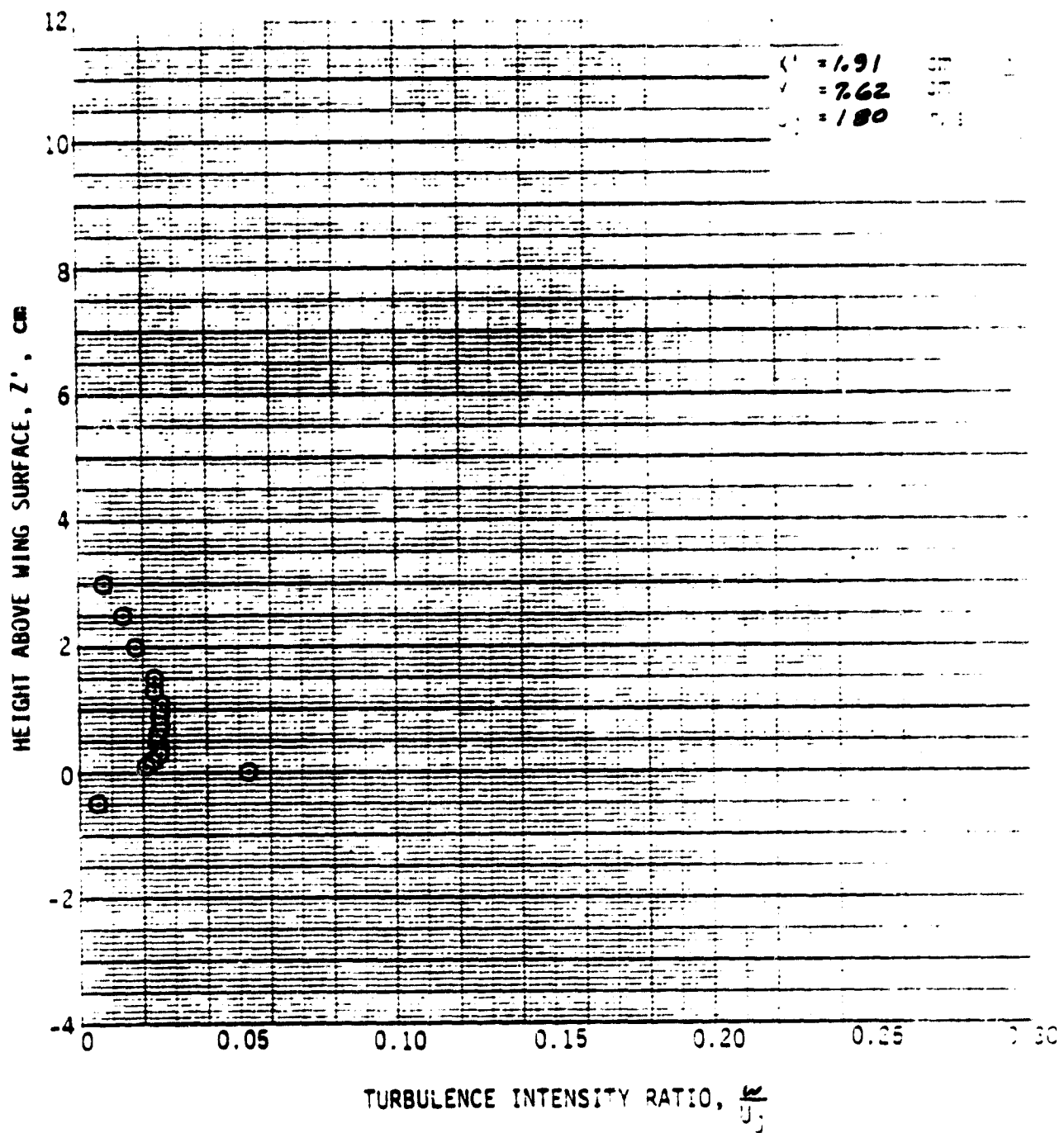


Figure A-2. Continued.

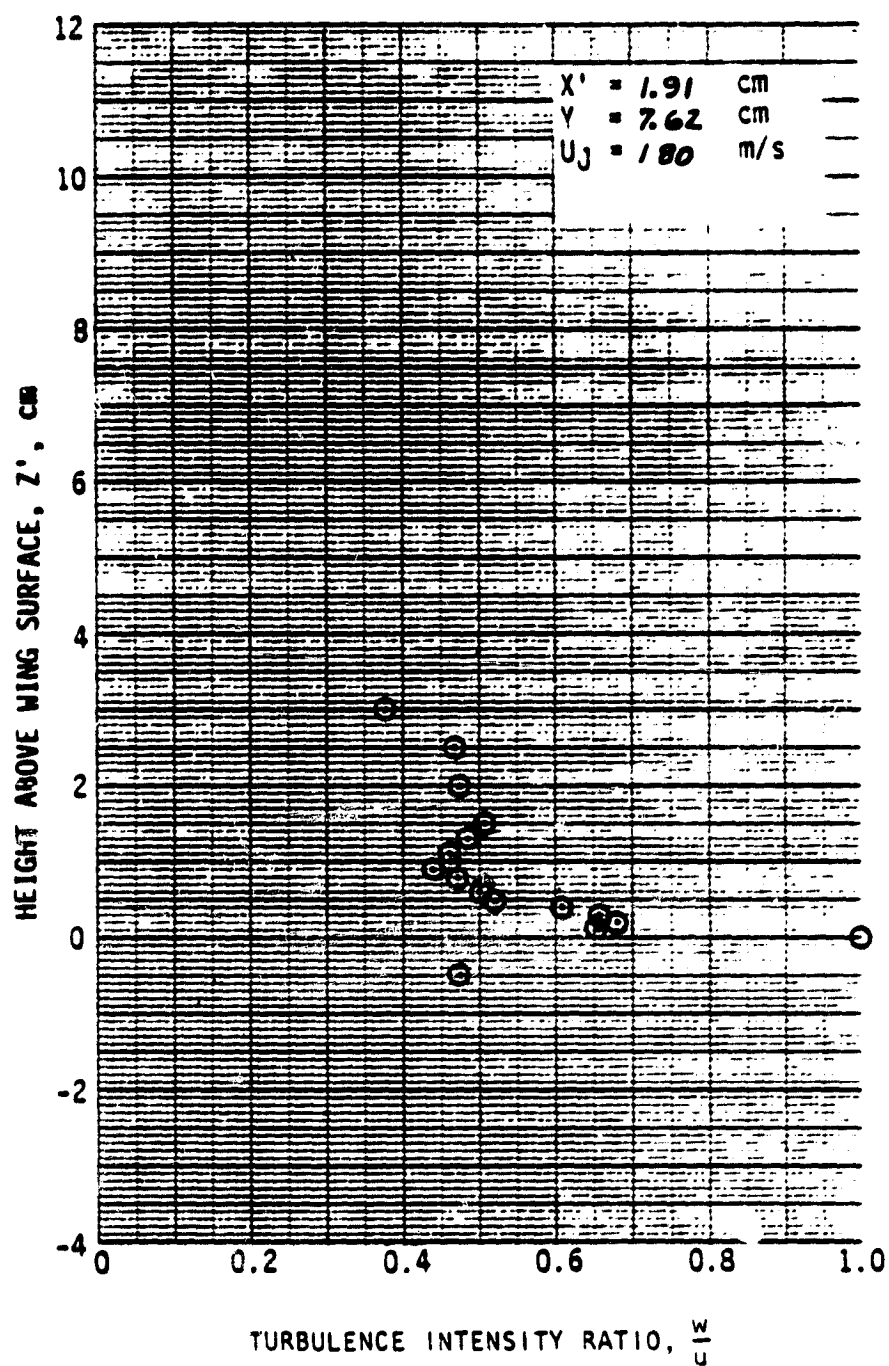


Figure A-2. Concluded.

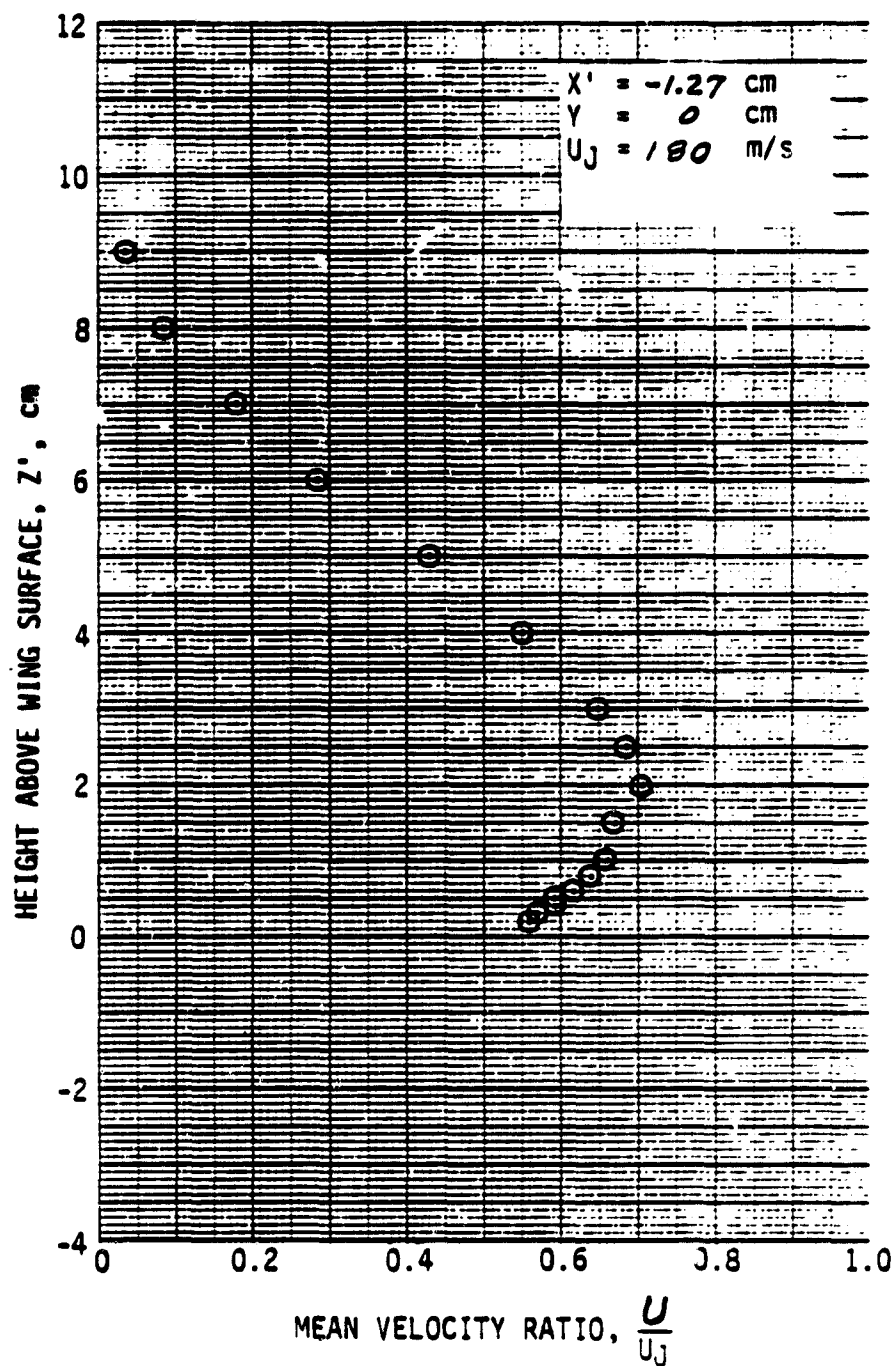


Figure A-3. Wake Flow Profiles by Cross Hot-Wire; $\delta_f = 60^\circ$, No Screen.

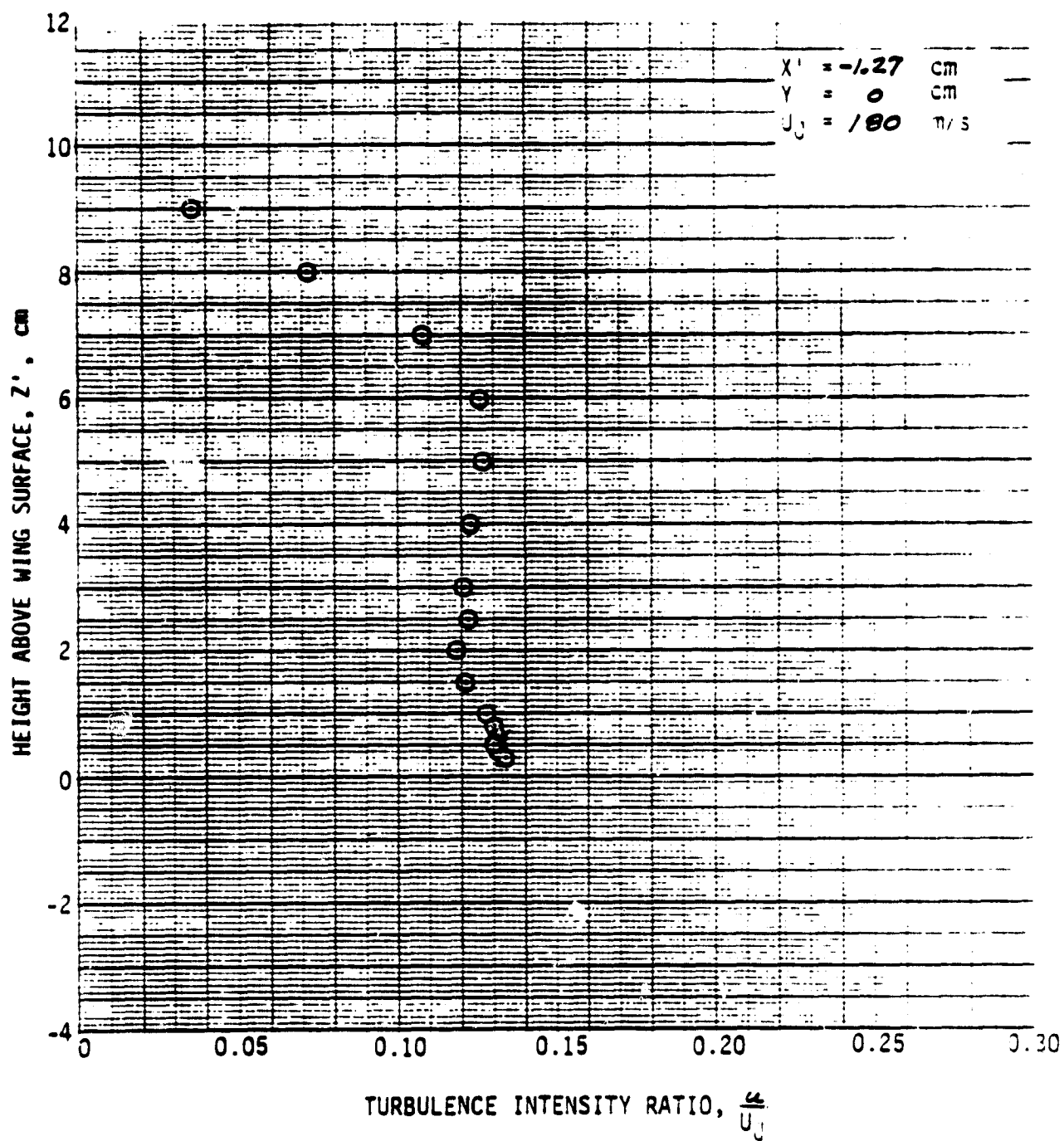


Figure A-3. Continued.

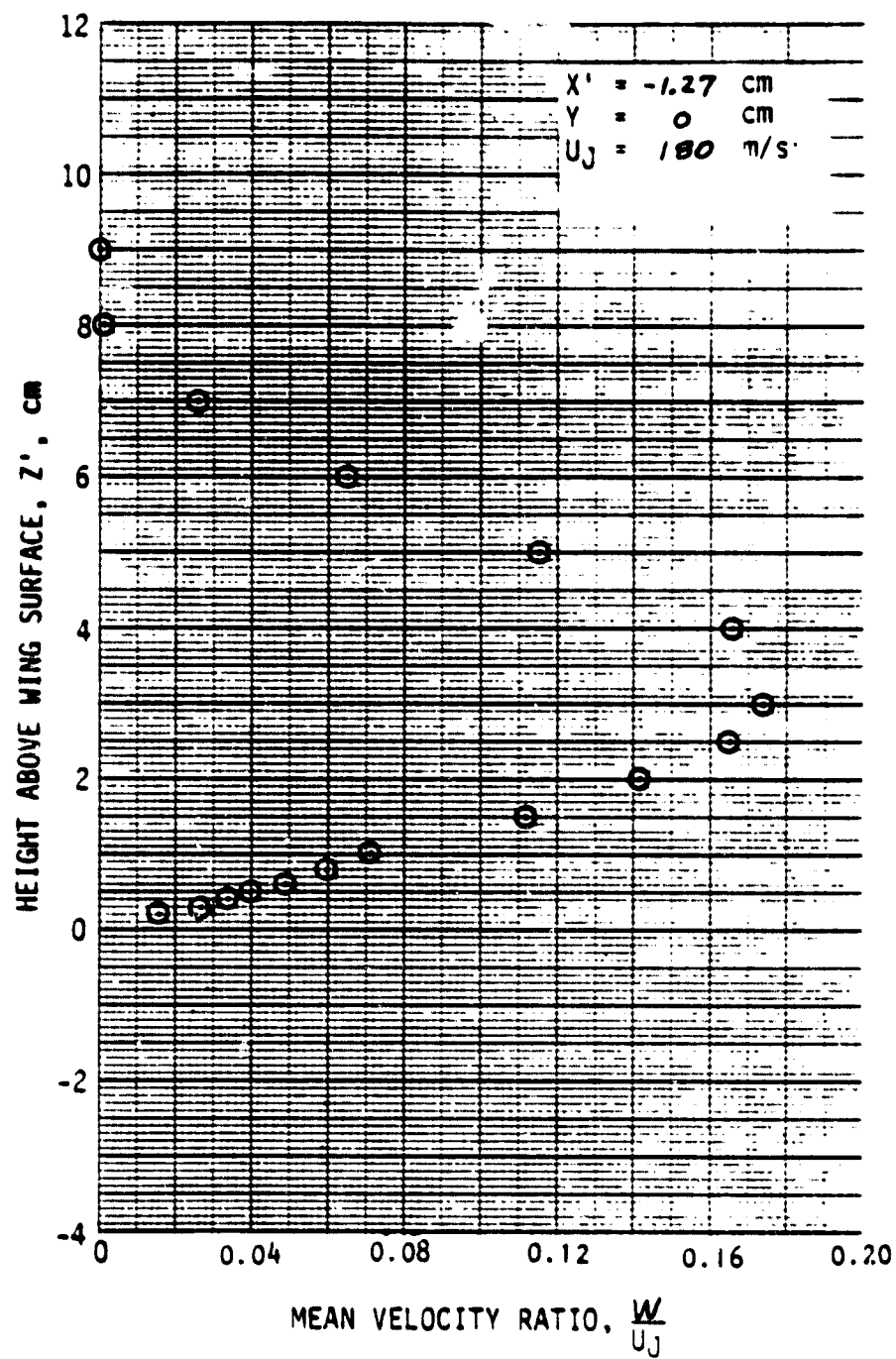


Figure A-3. Continued.

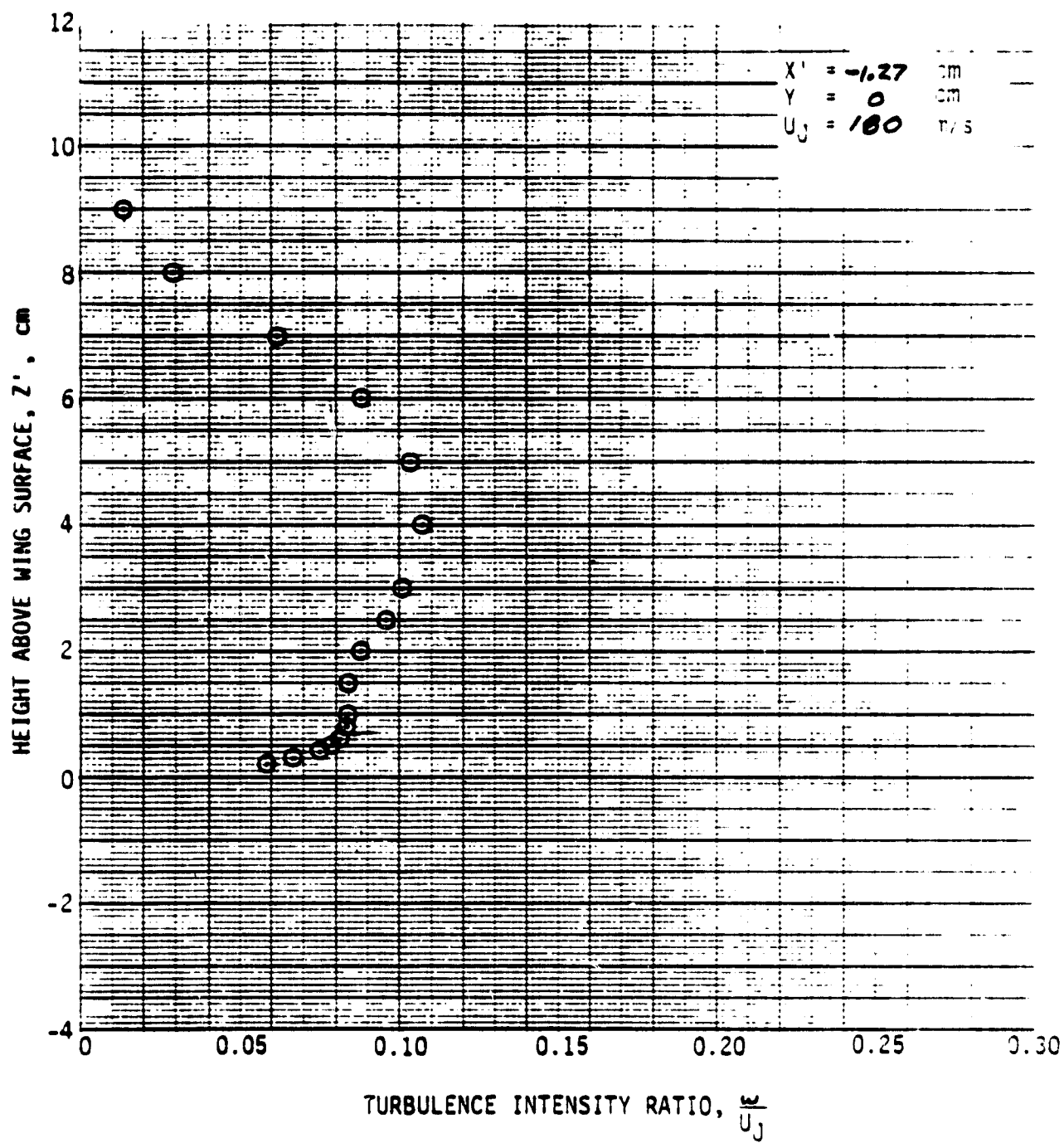


Figure A-3. Continued.

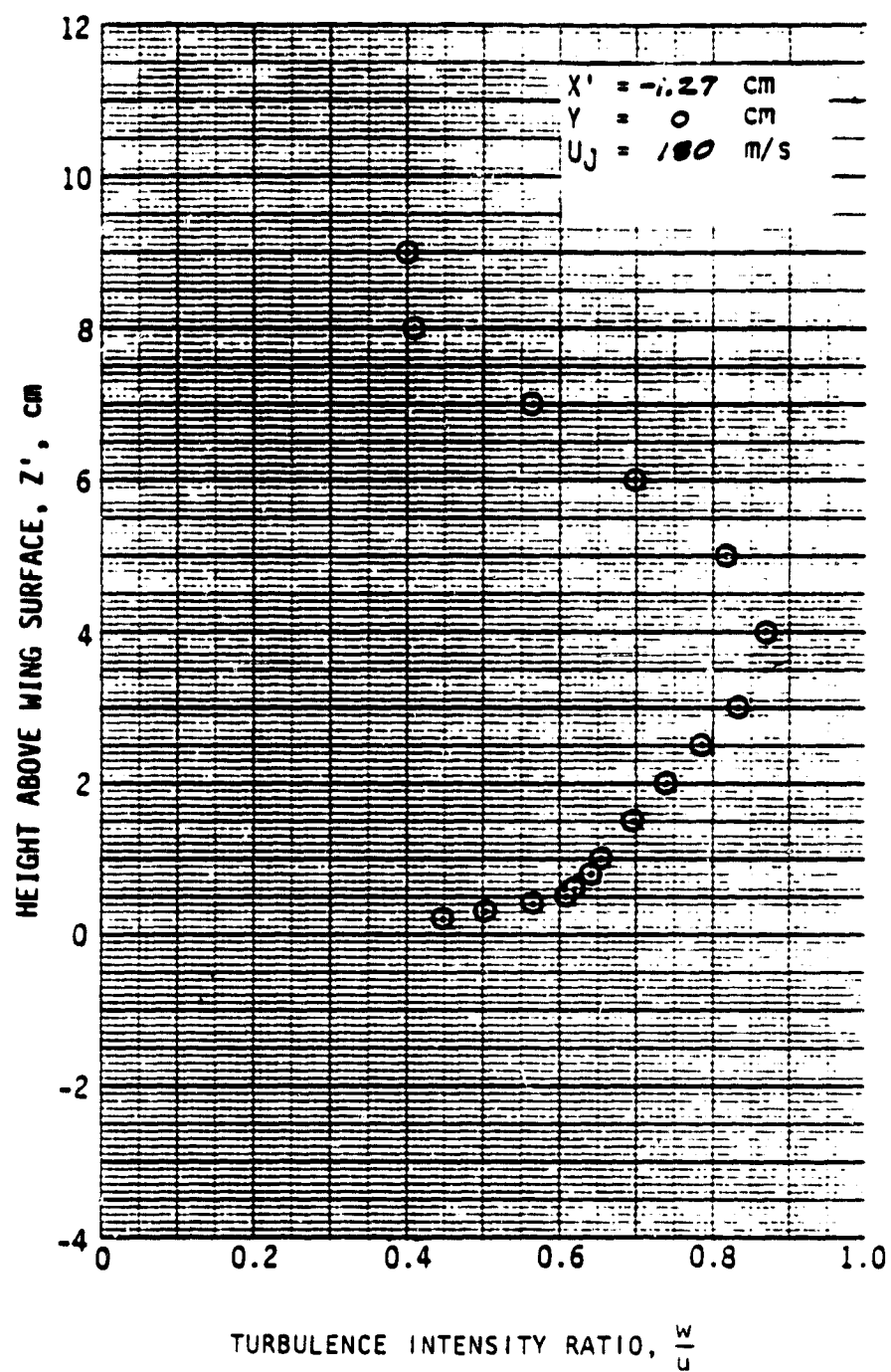


Figure A-3. Continued.

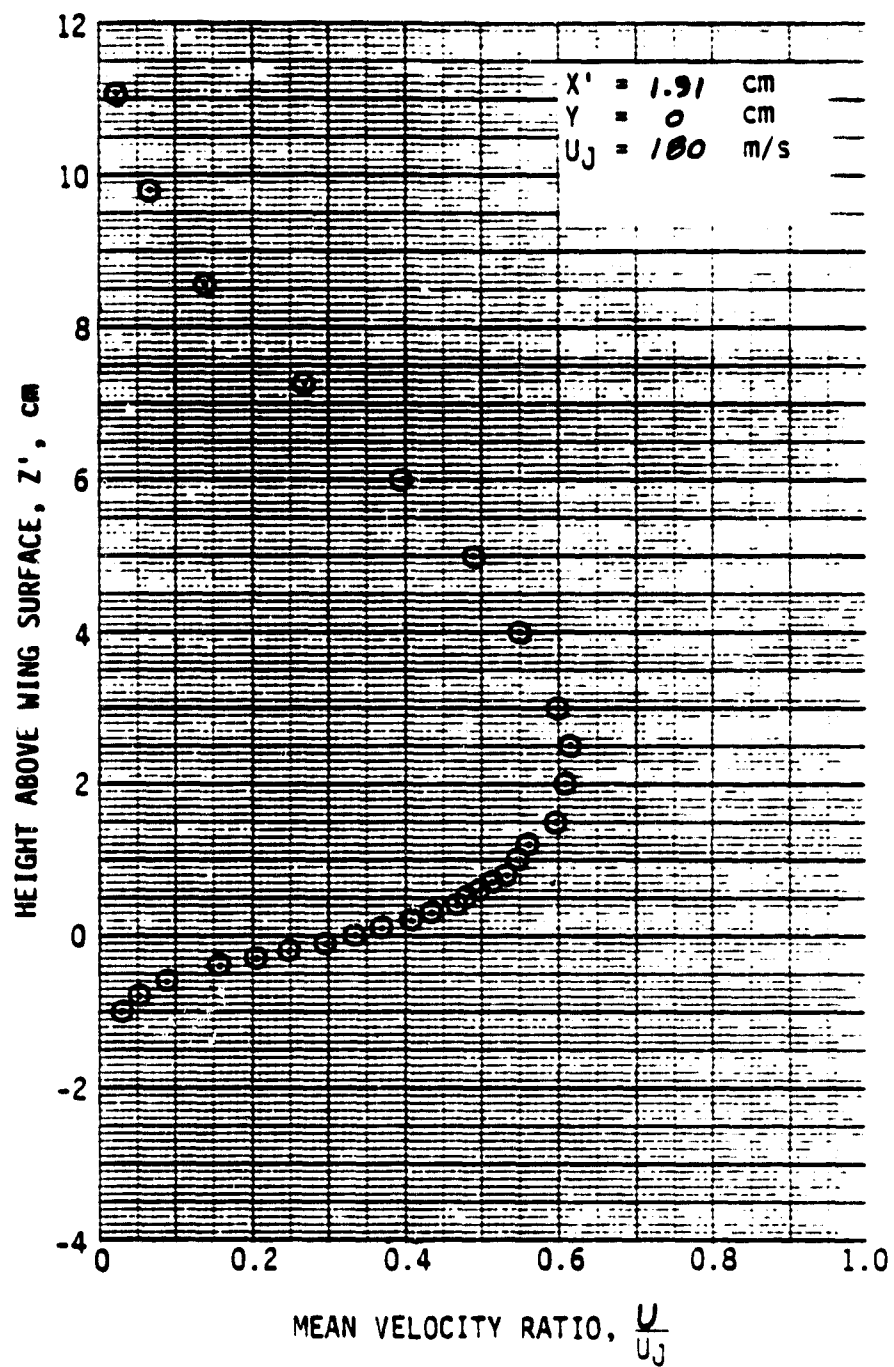


Figure A-3. Continued.

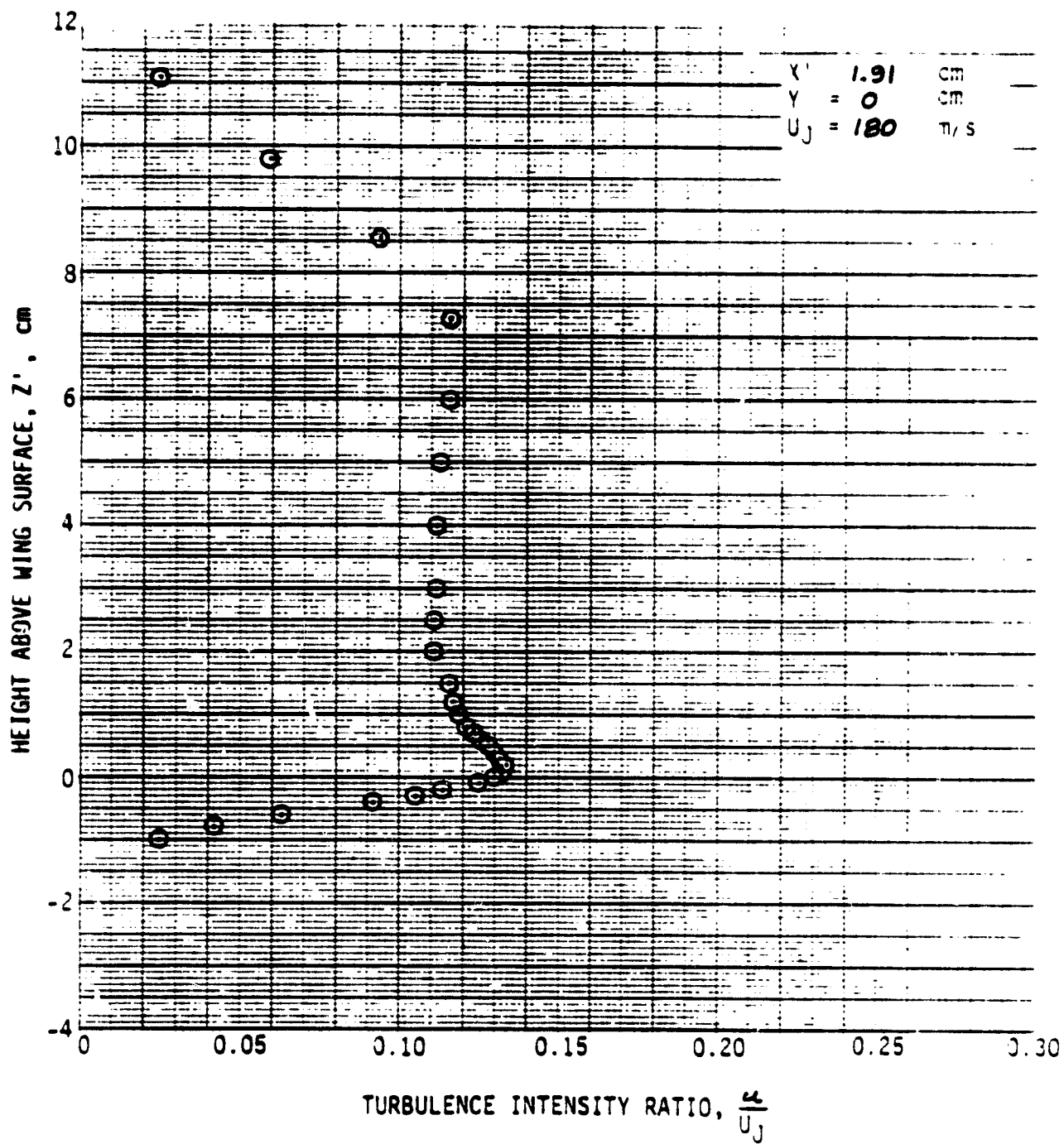


Figure A-3. Continued.

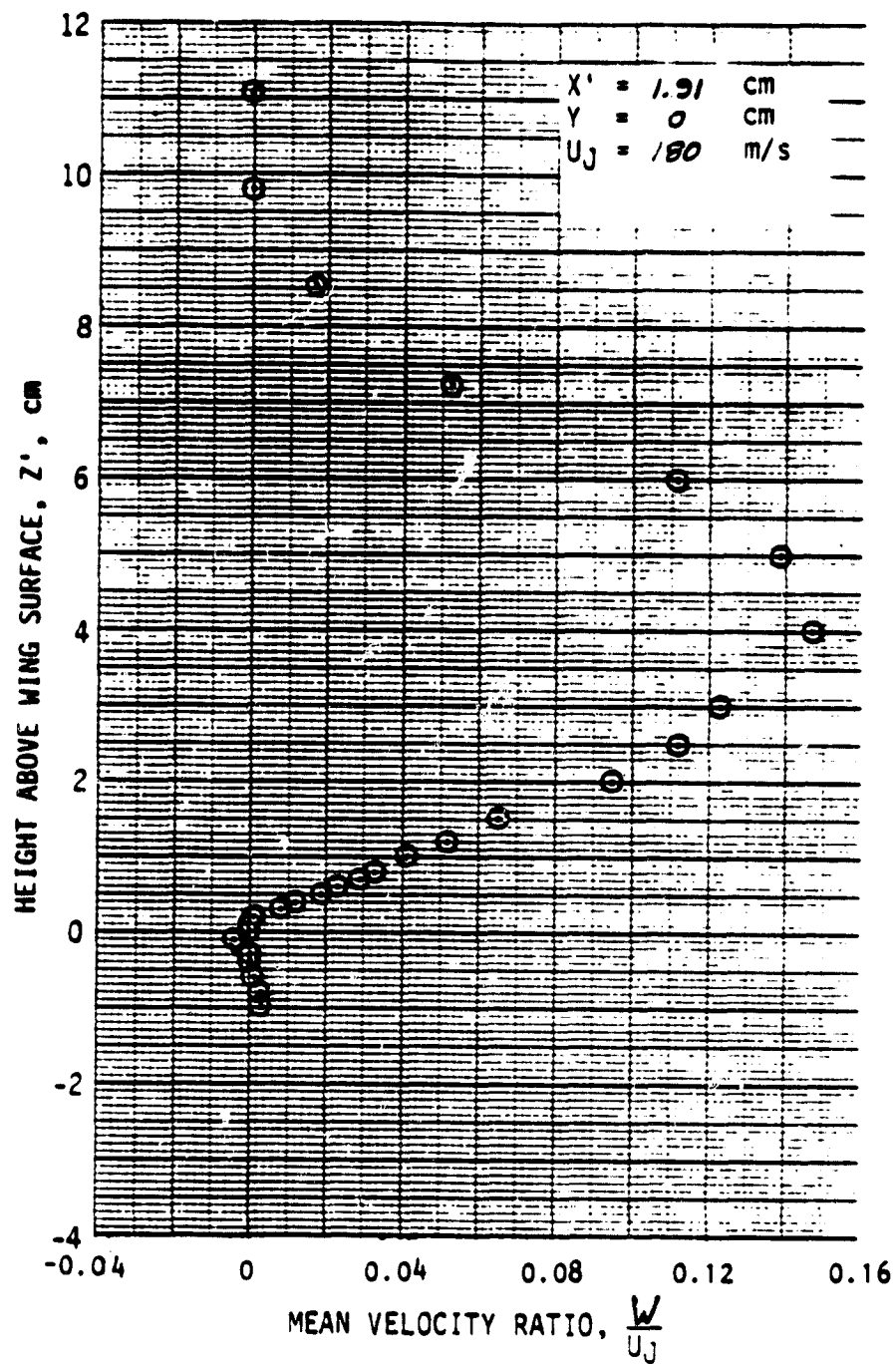


Figure A-3. Continued.

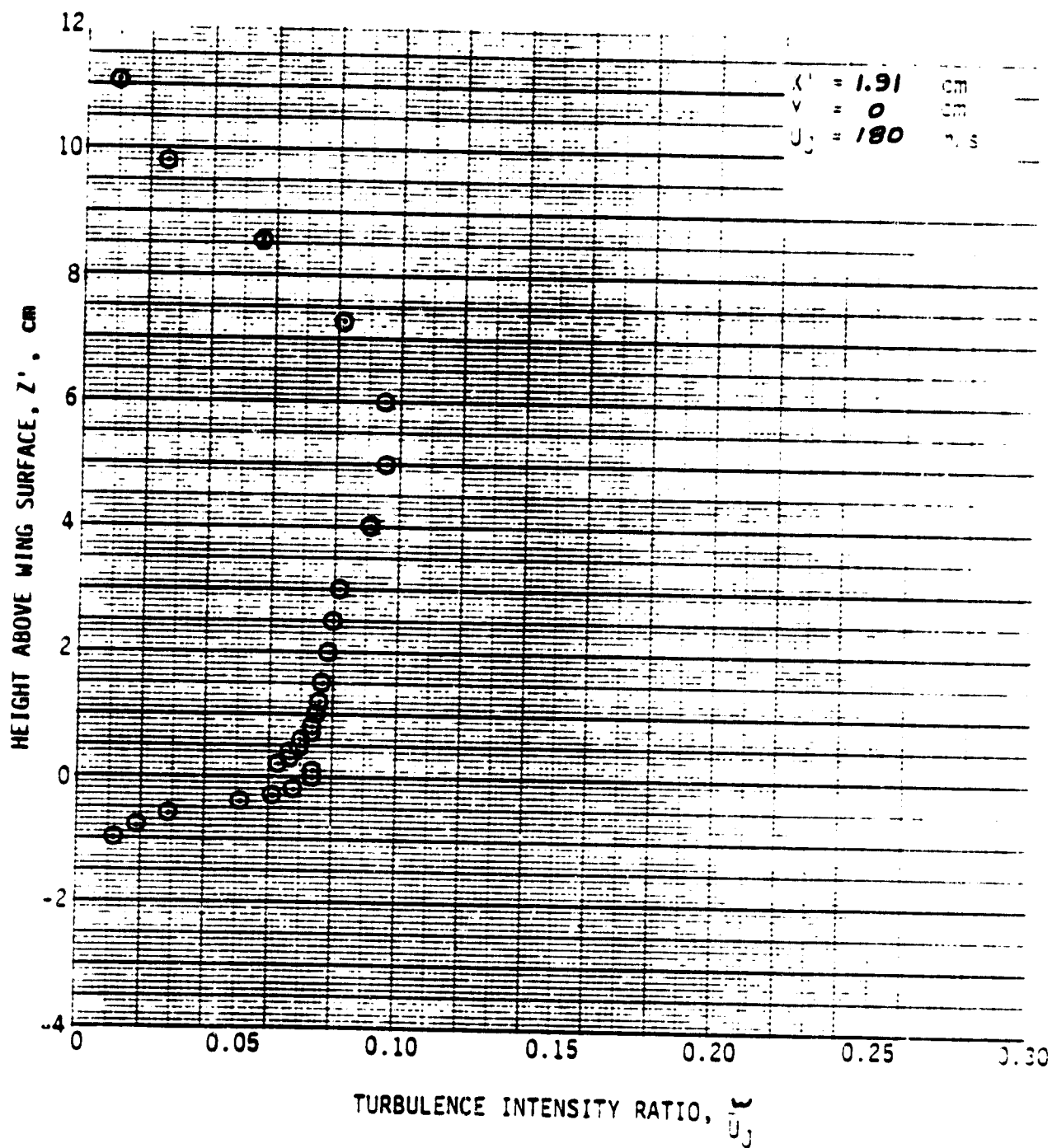


Figure A-3. Continued.

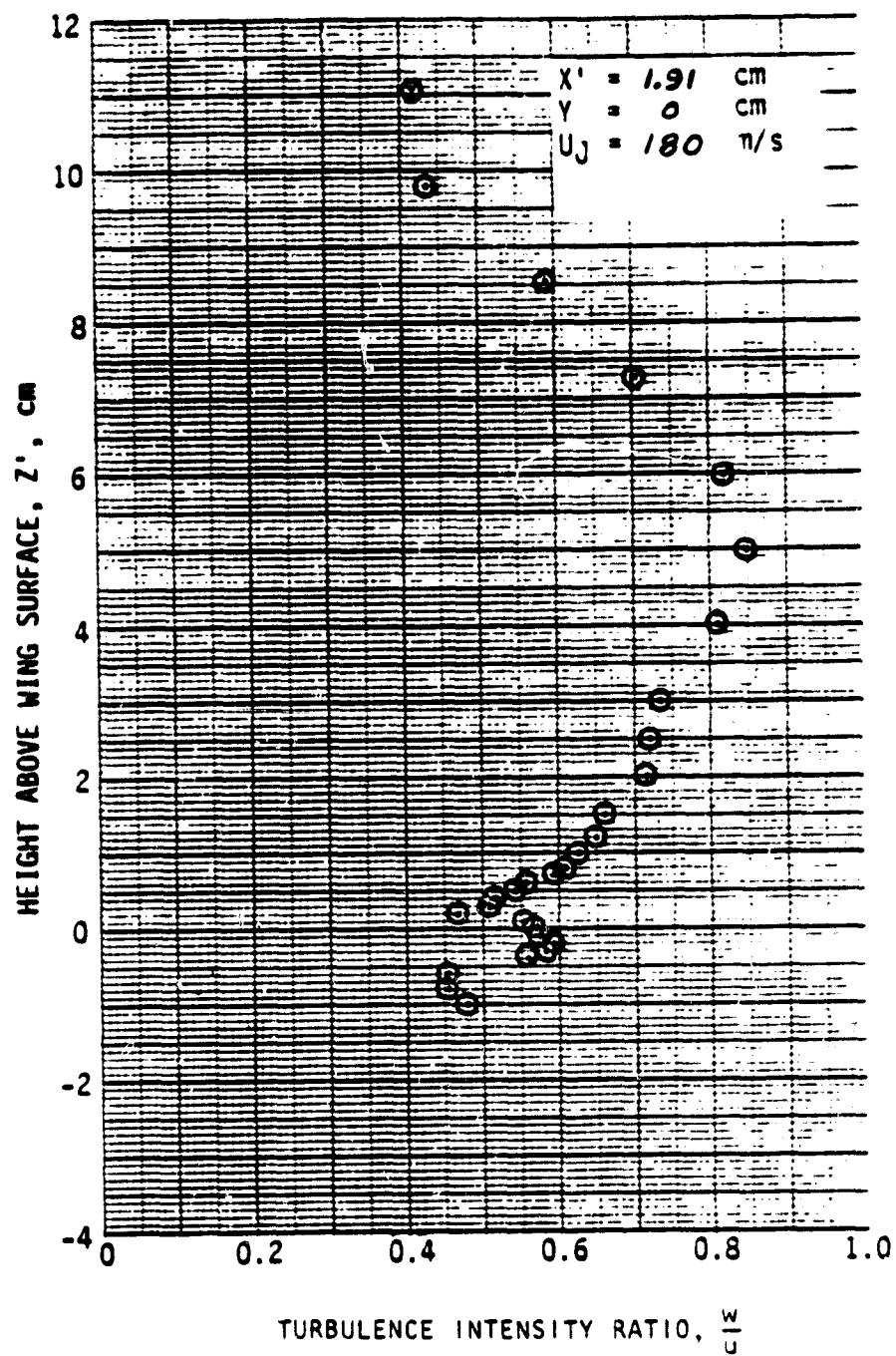


Figure A-3. Continued.

ORIGINAL PAGE IS
 OF POOR QUALITY

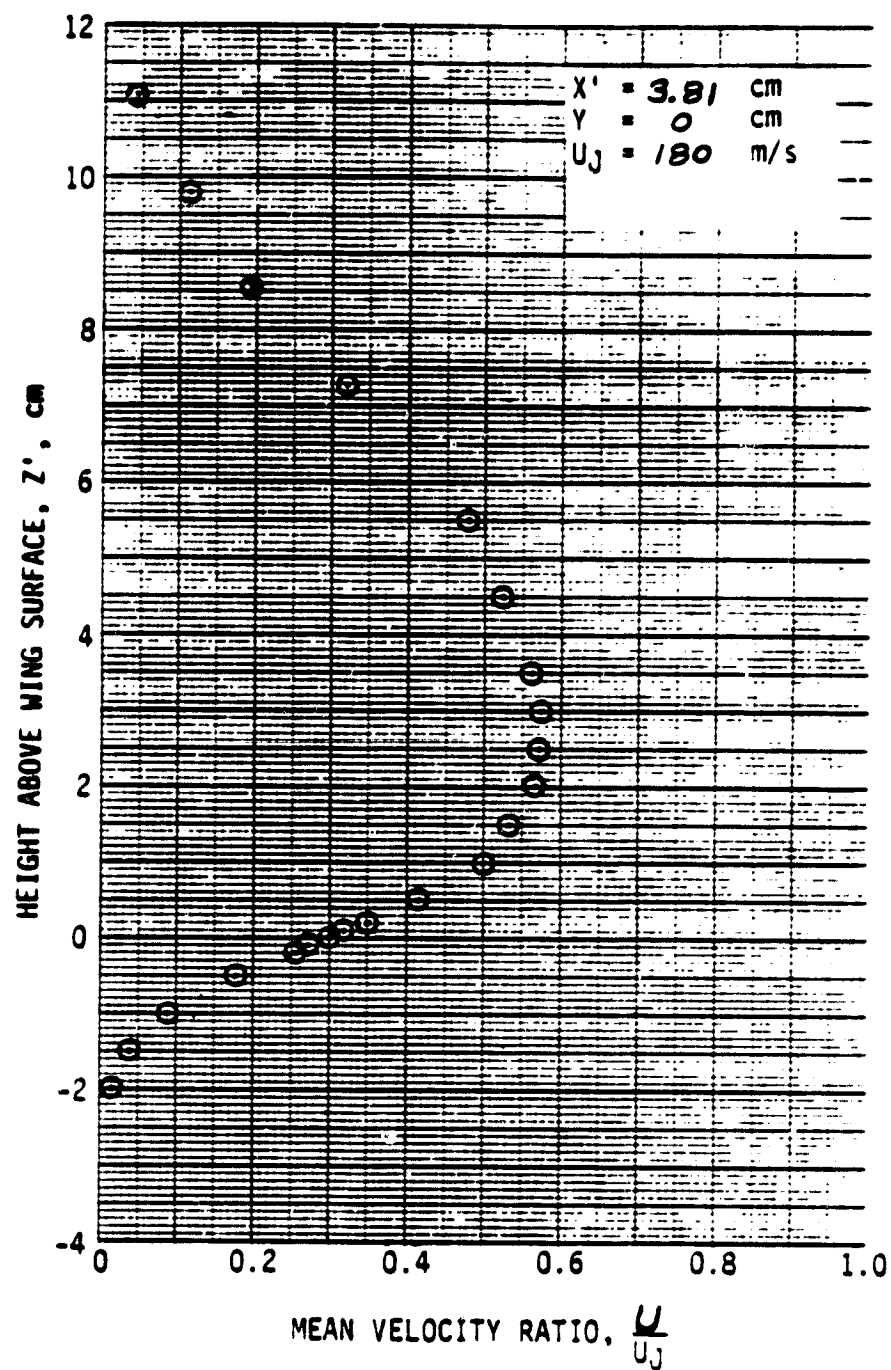


Figure A-3. Continued.

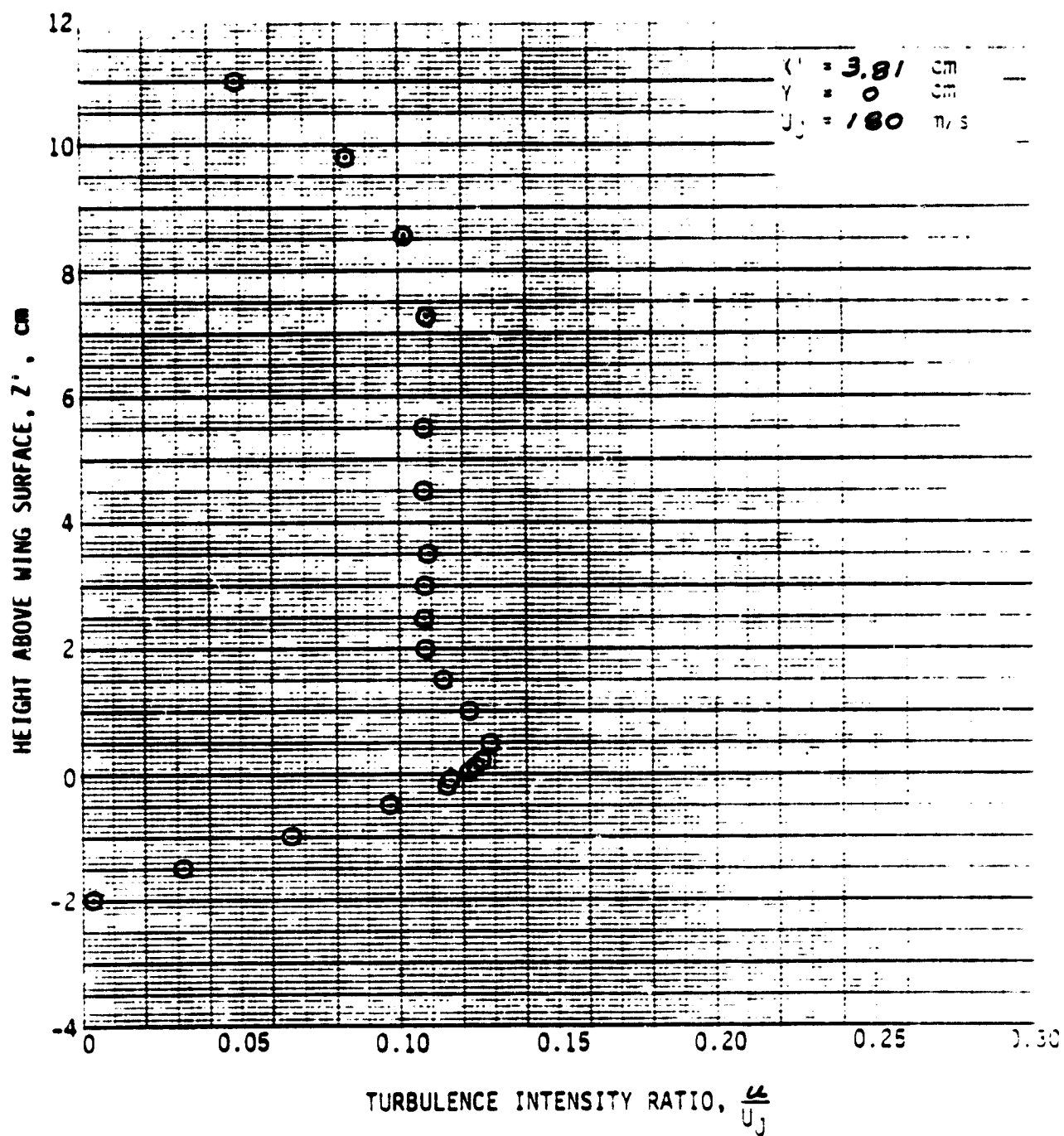
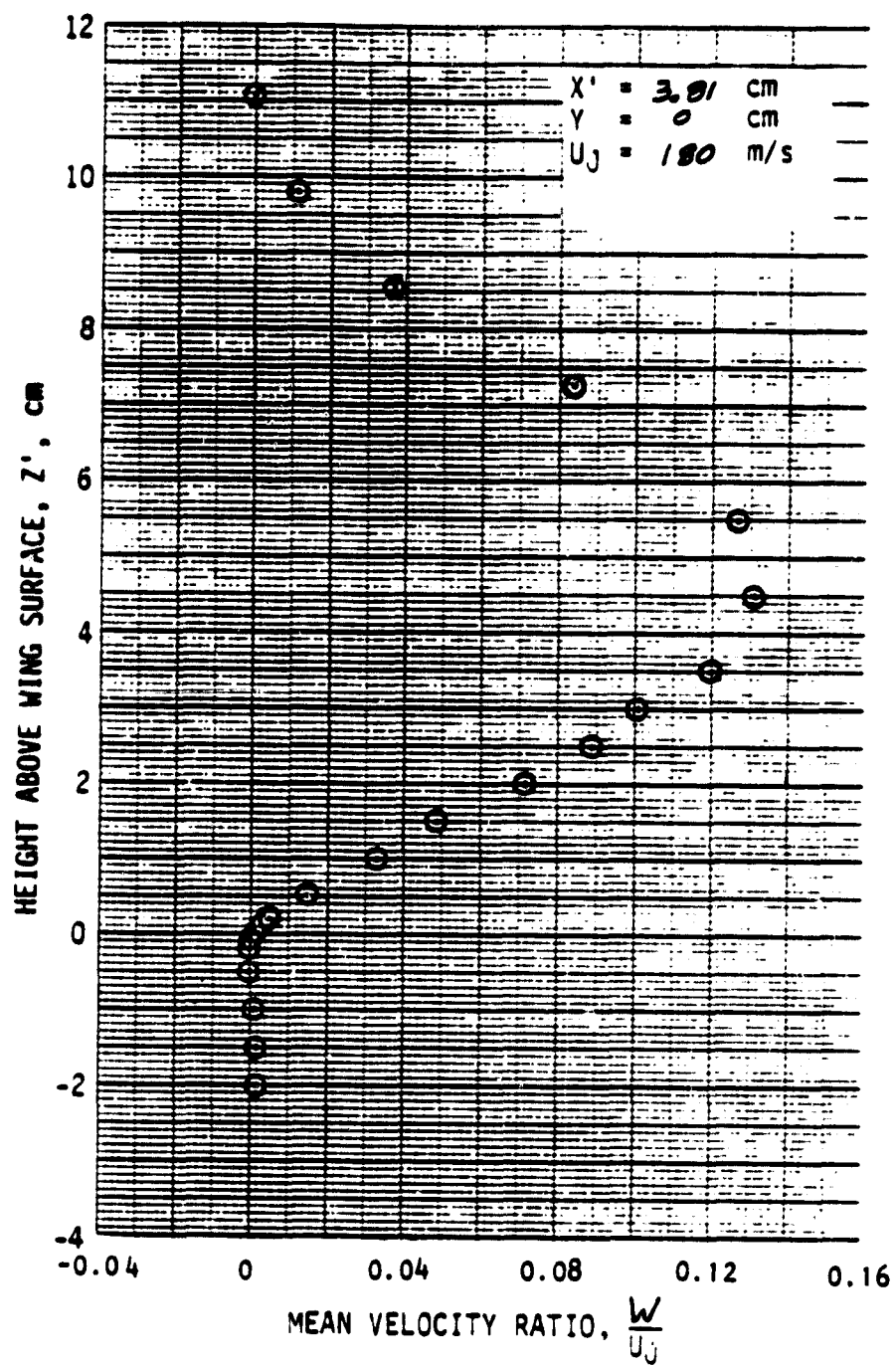


Figure A-3. Continued.



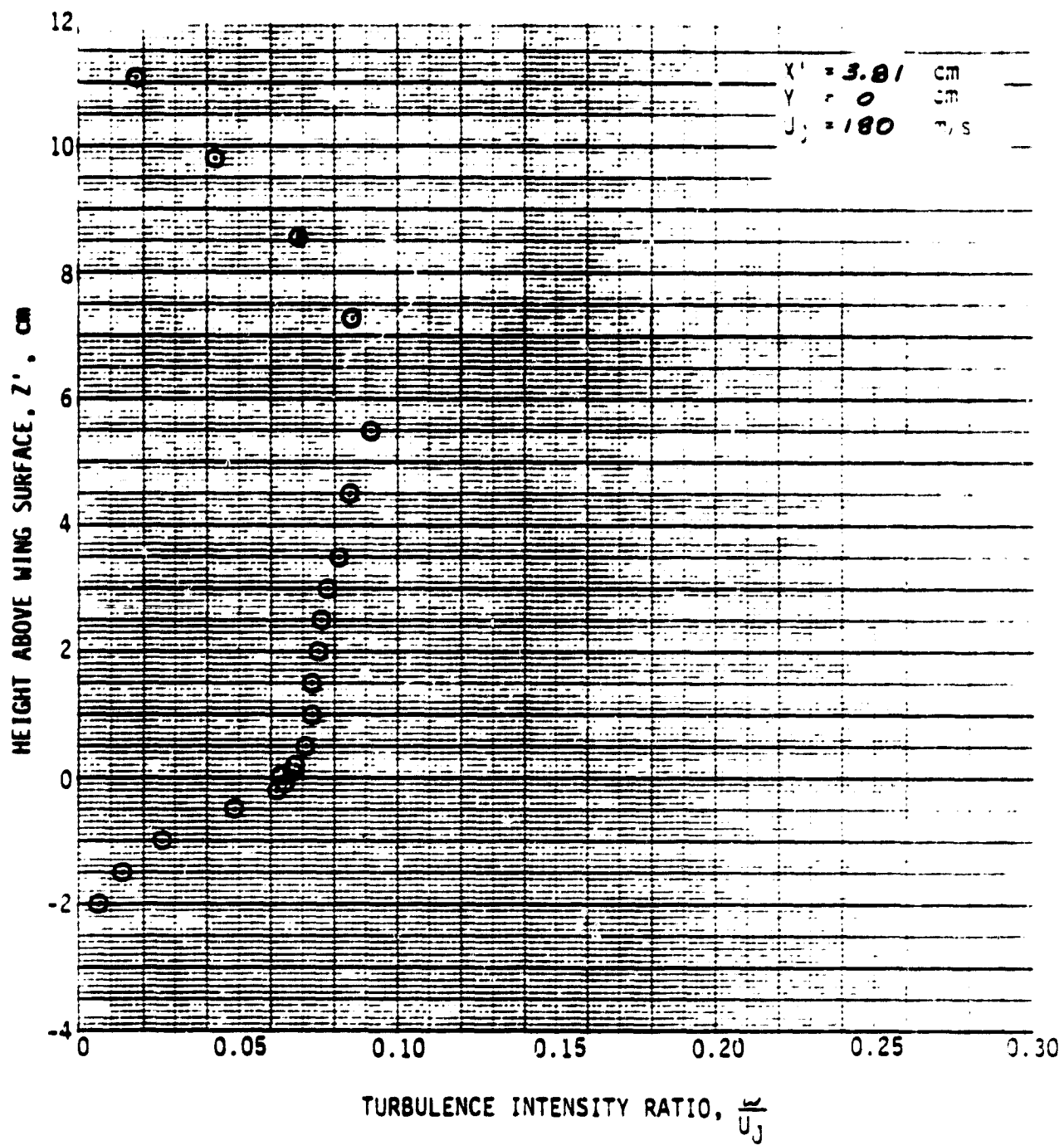


Figure A-3. Continued.

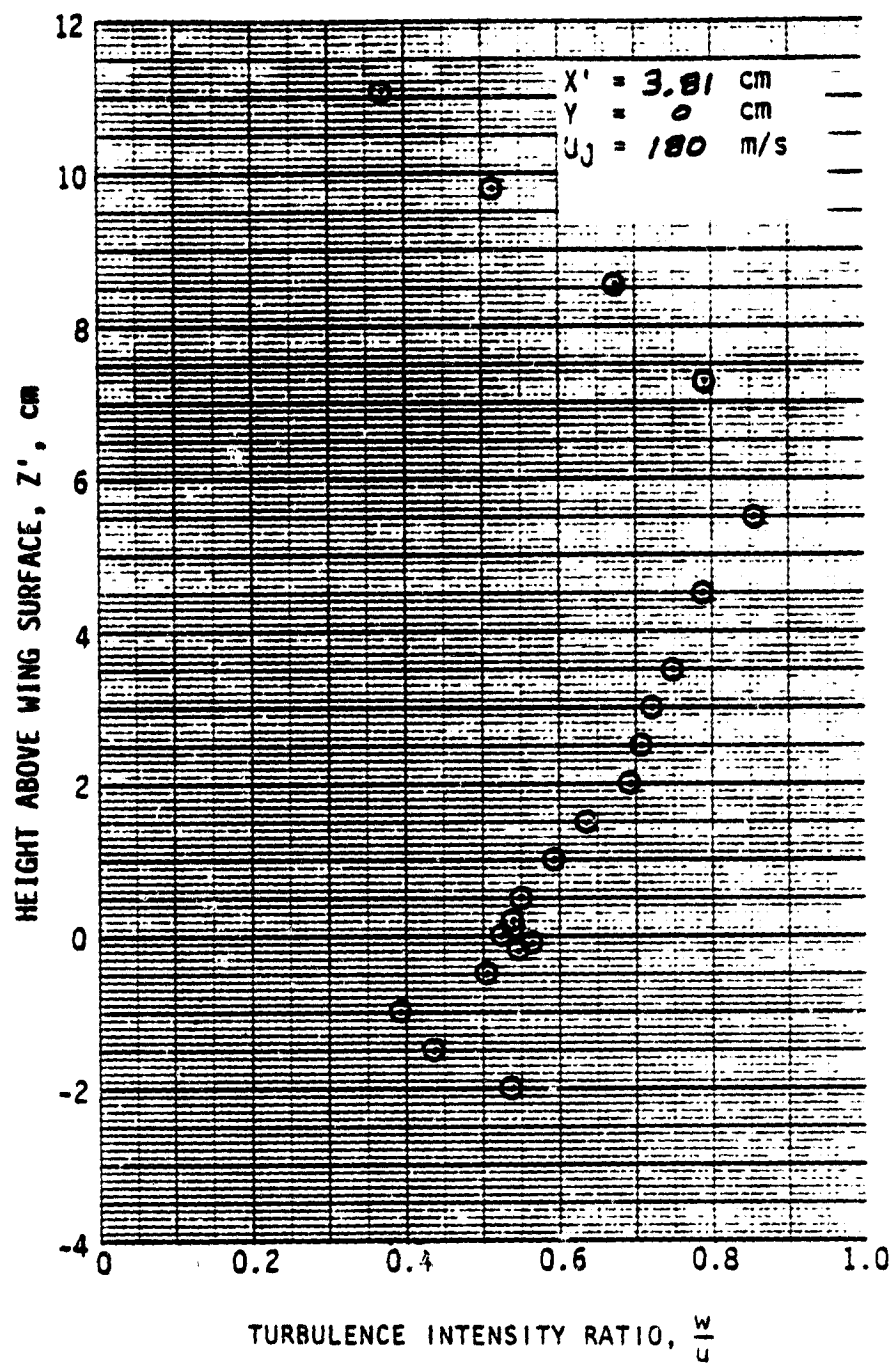


Figure A-3. Continued.

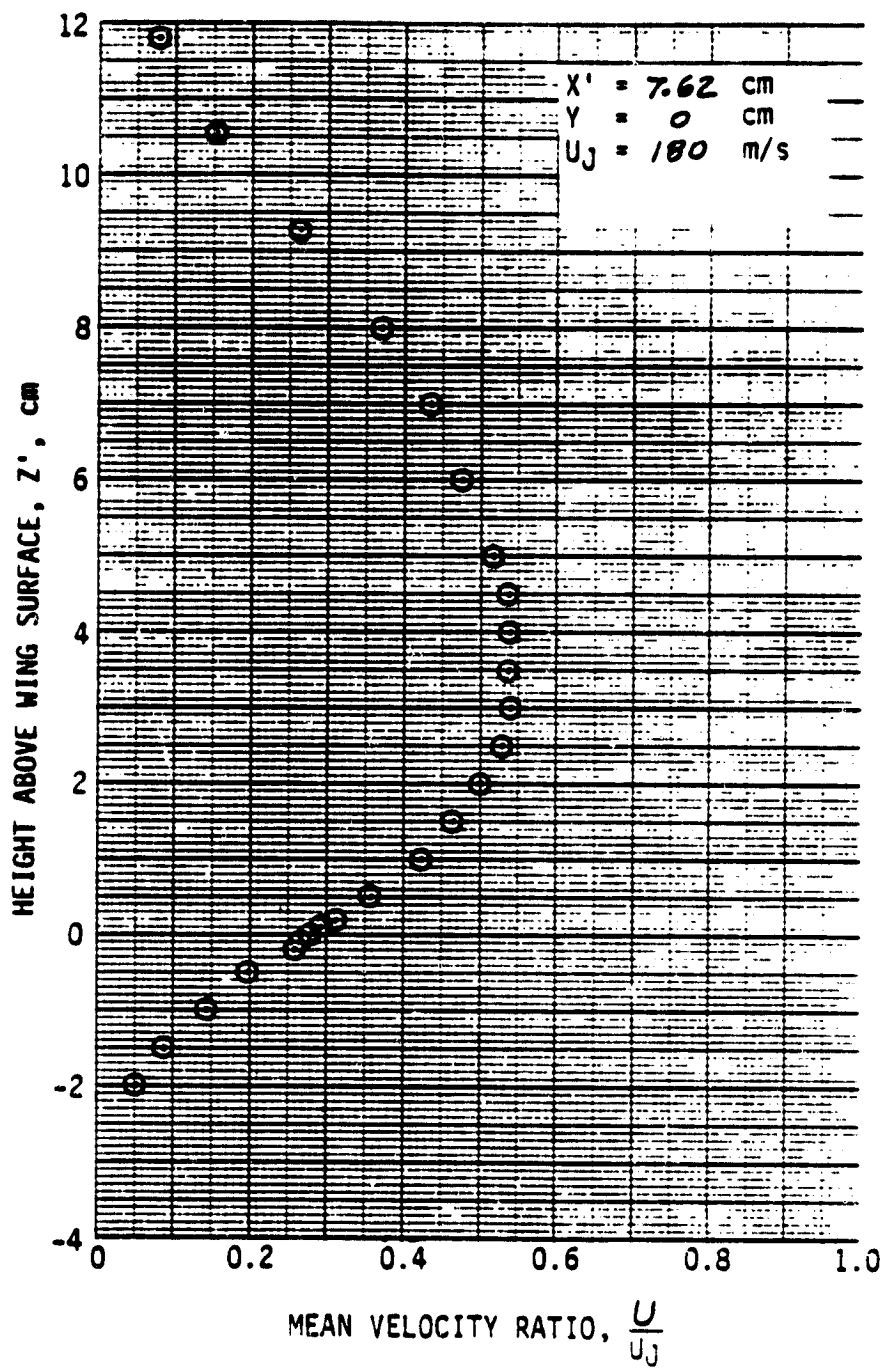


Figure A-3. Continued.

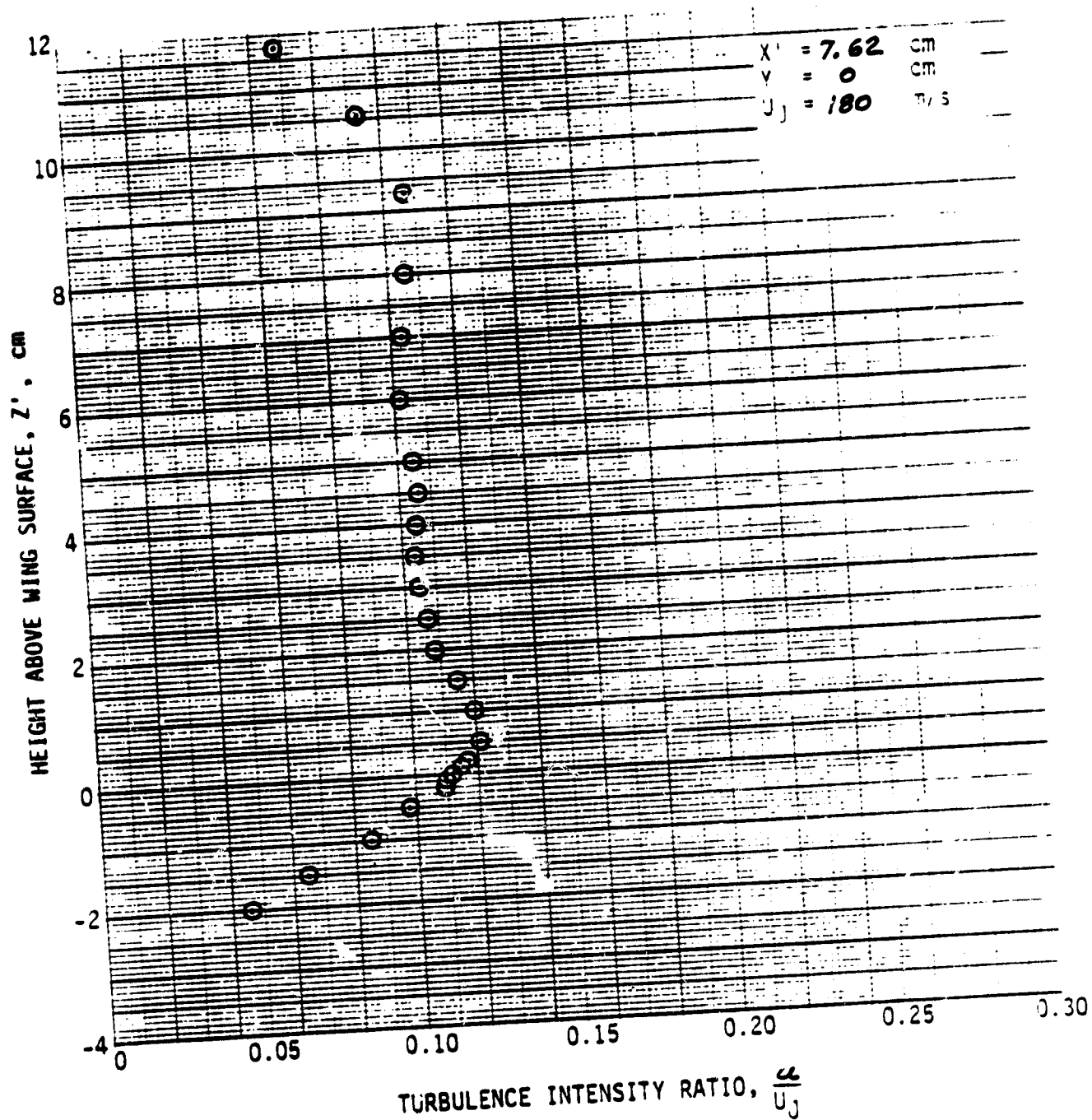


Figure A-3. Continued.

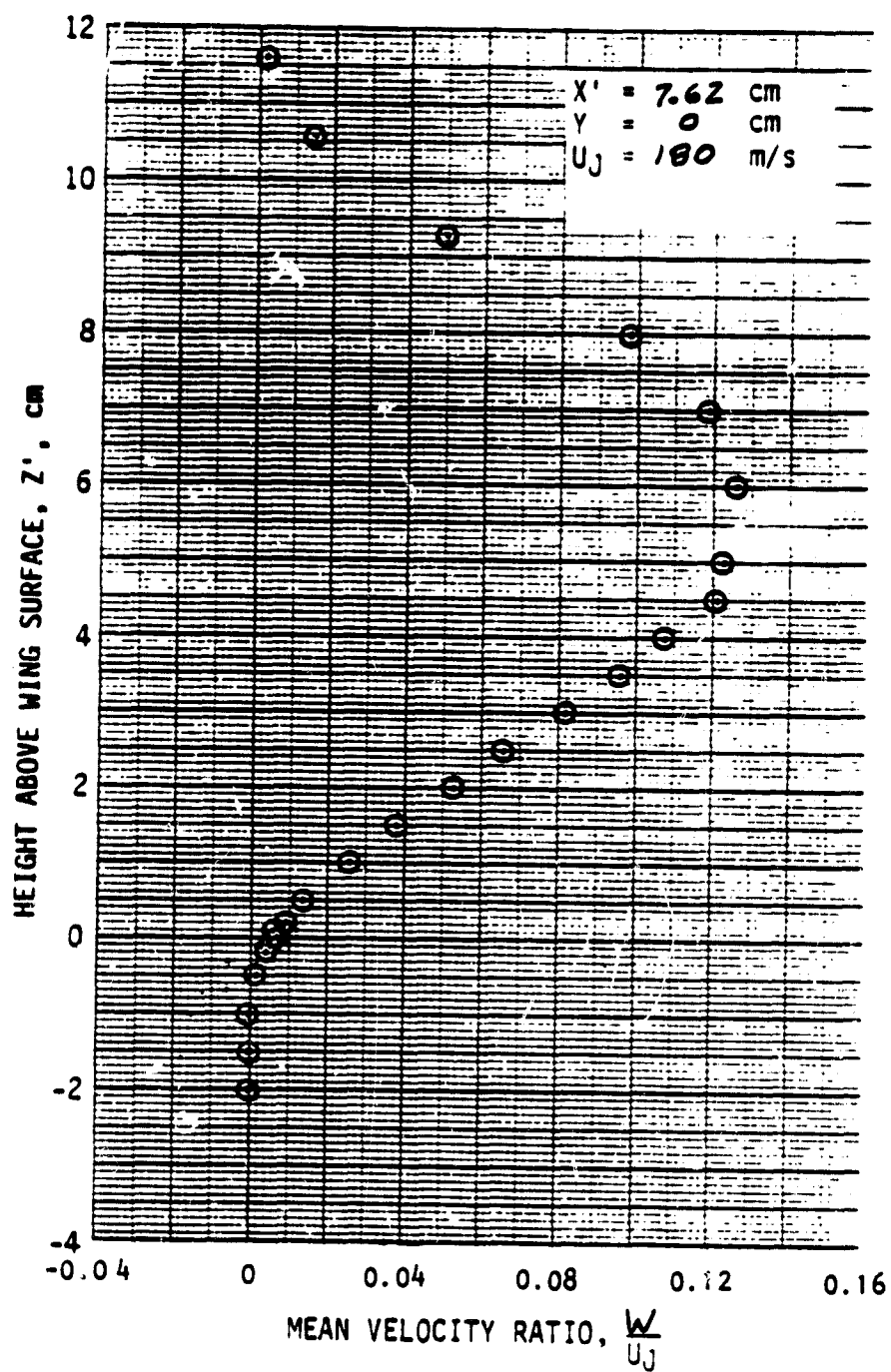


Figure A-3. Continued.

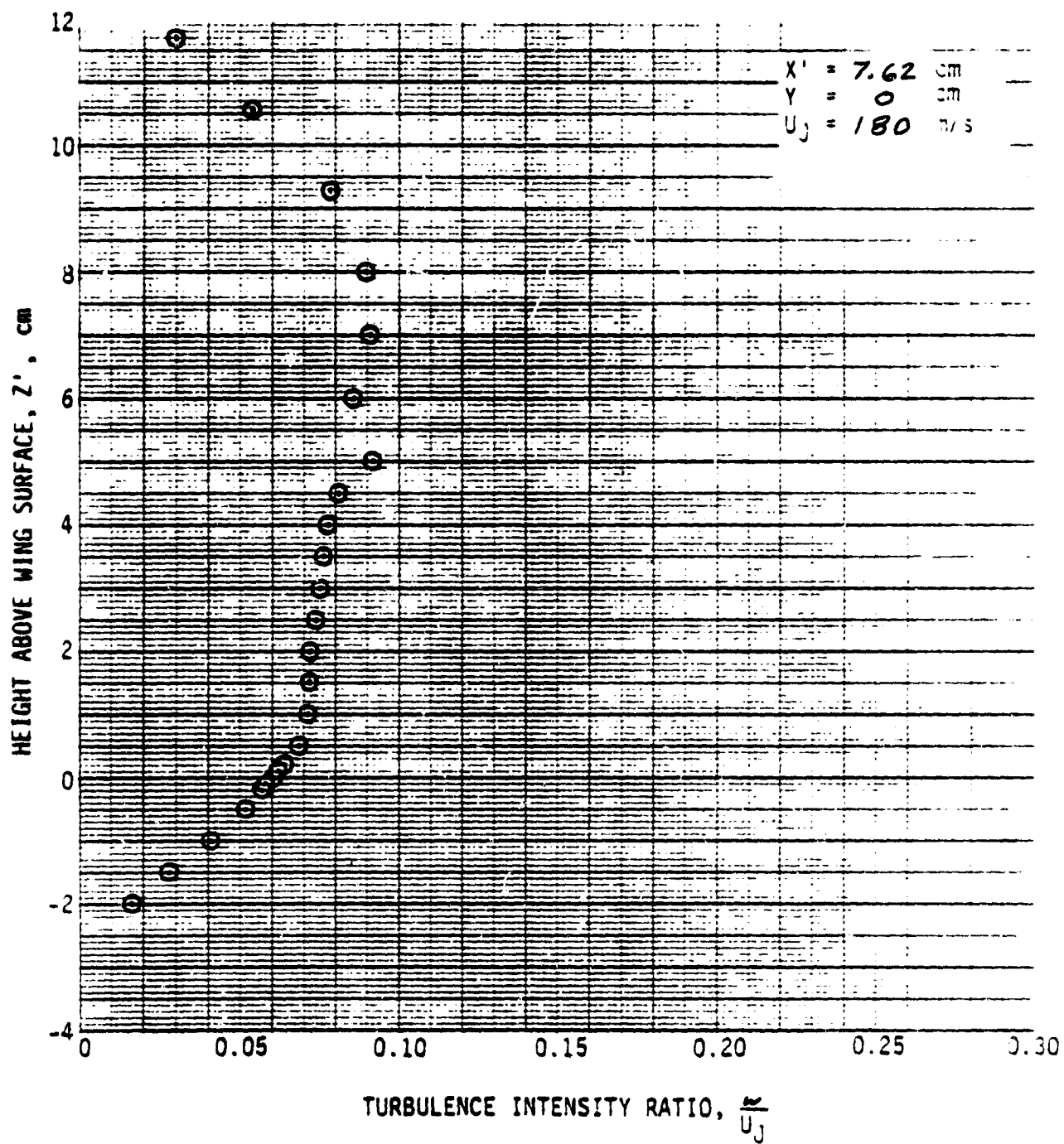


Figure A-3. Continued.

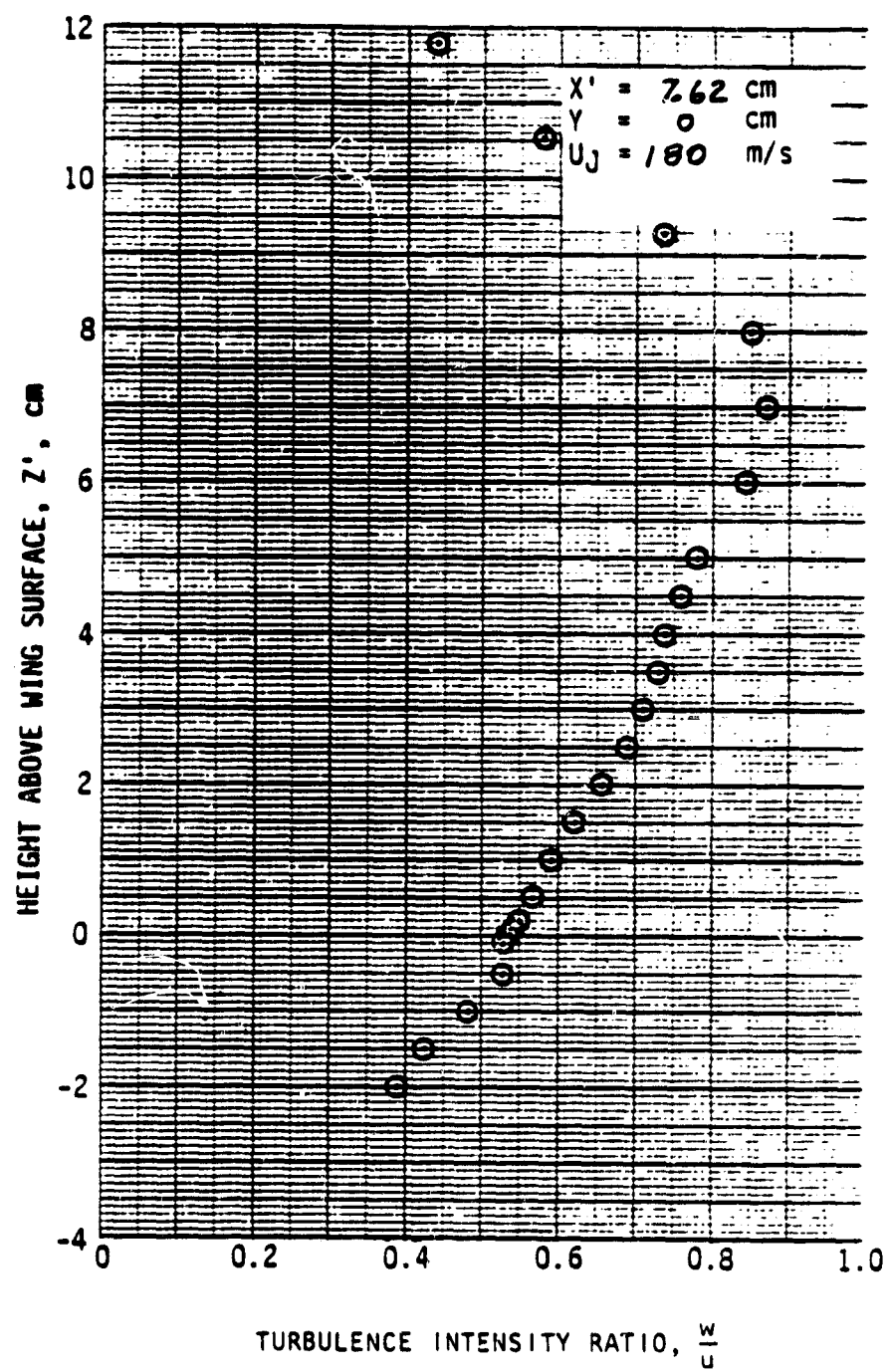


Figure A-3. Concluded.

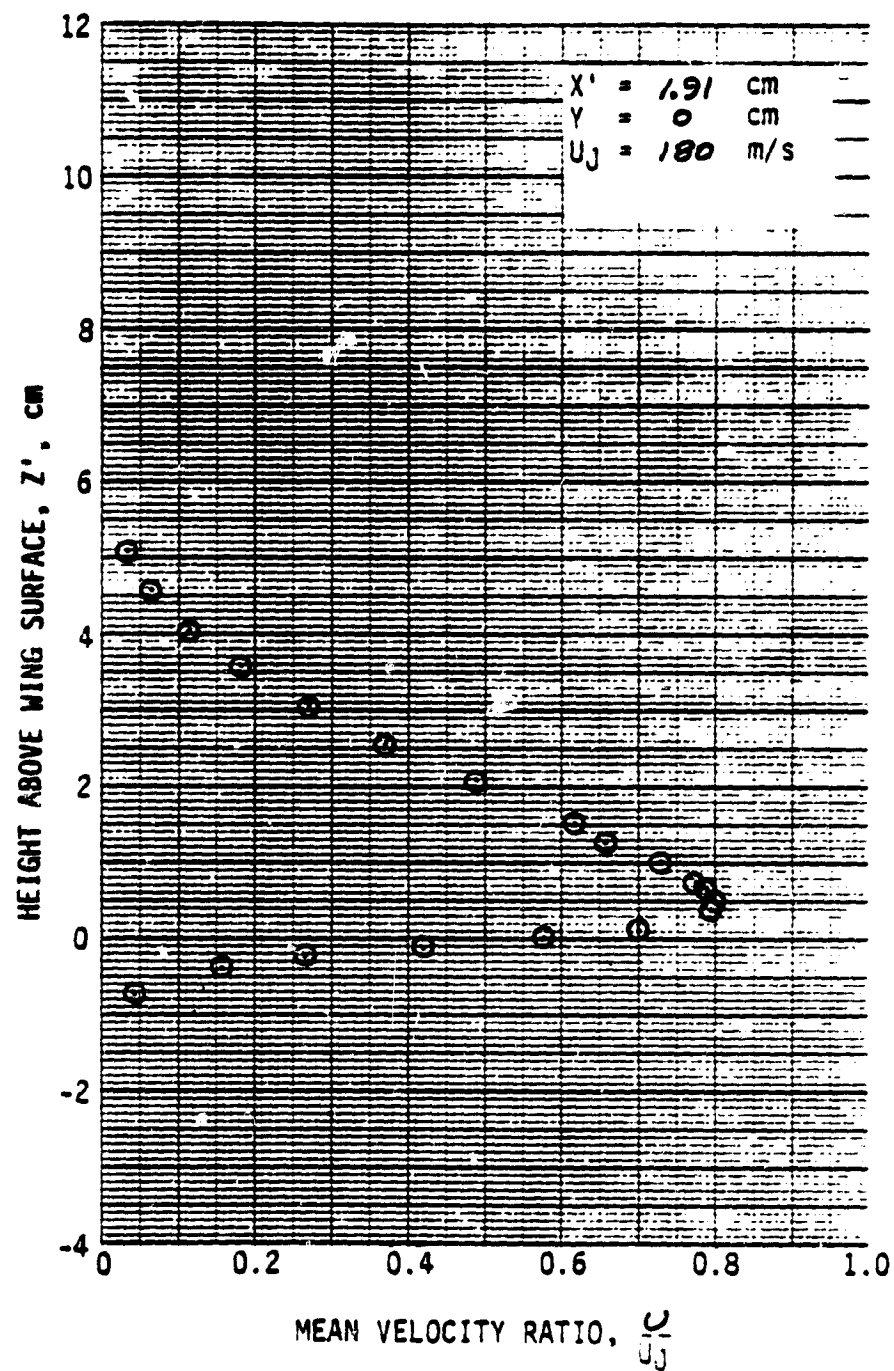


Figure A-4. Wake Flow Profiles by Cross Hot-Wire; $\delta_f = 30^\circ$, Screen.

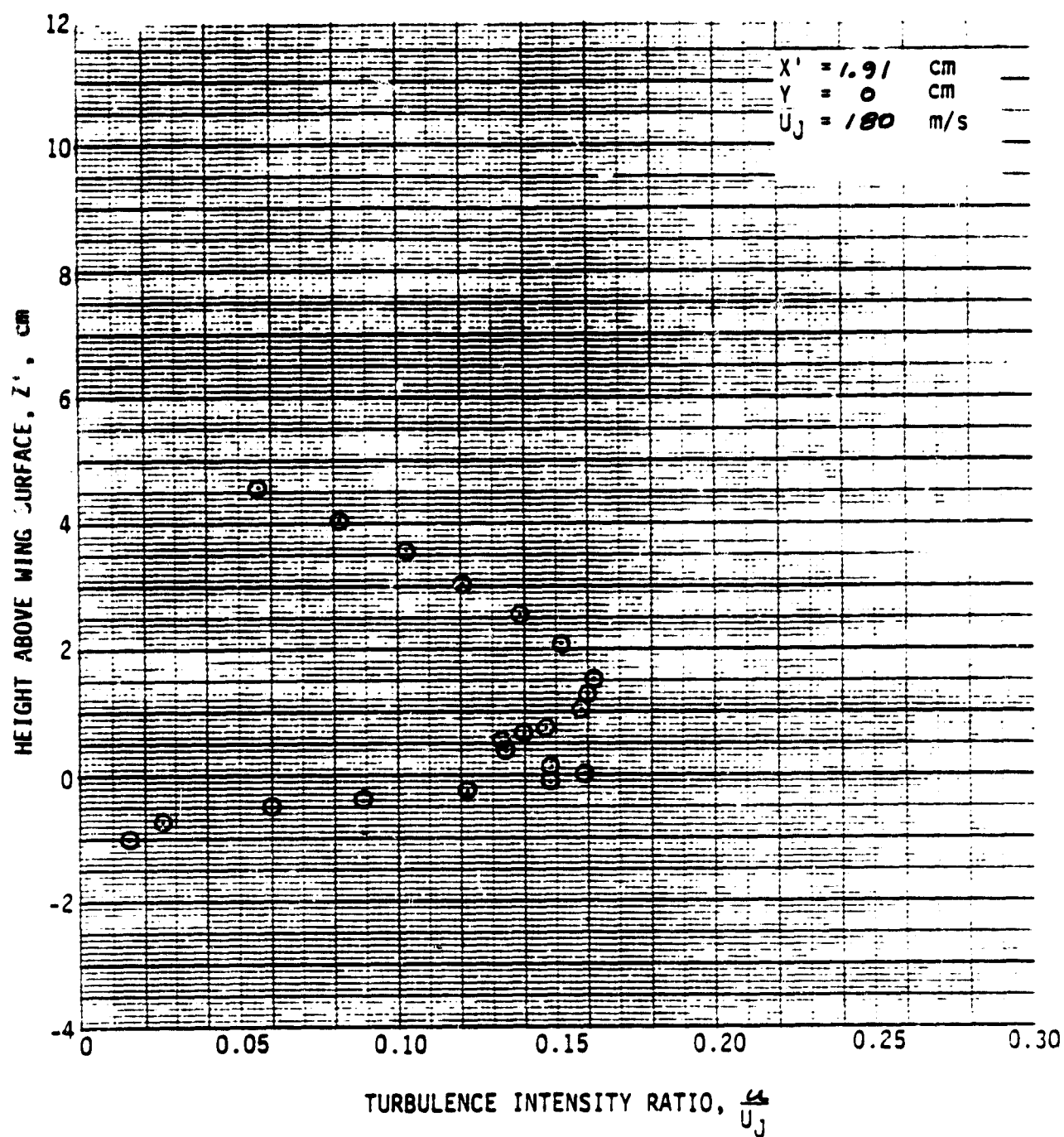


Figure A-4. Continued.

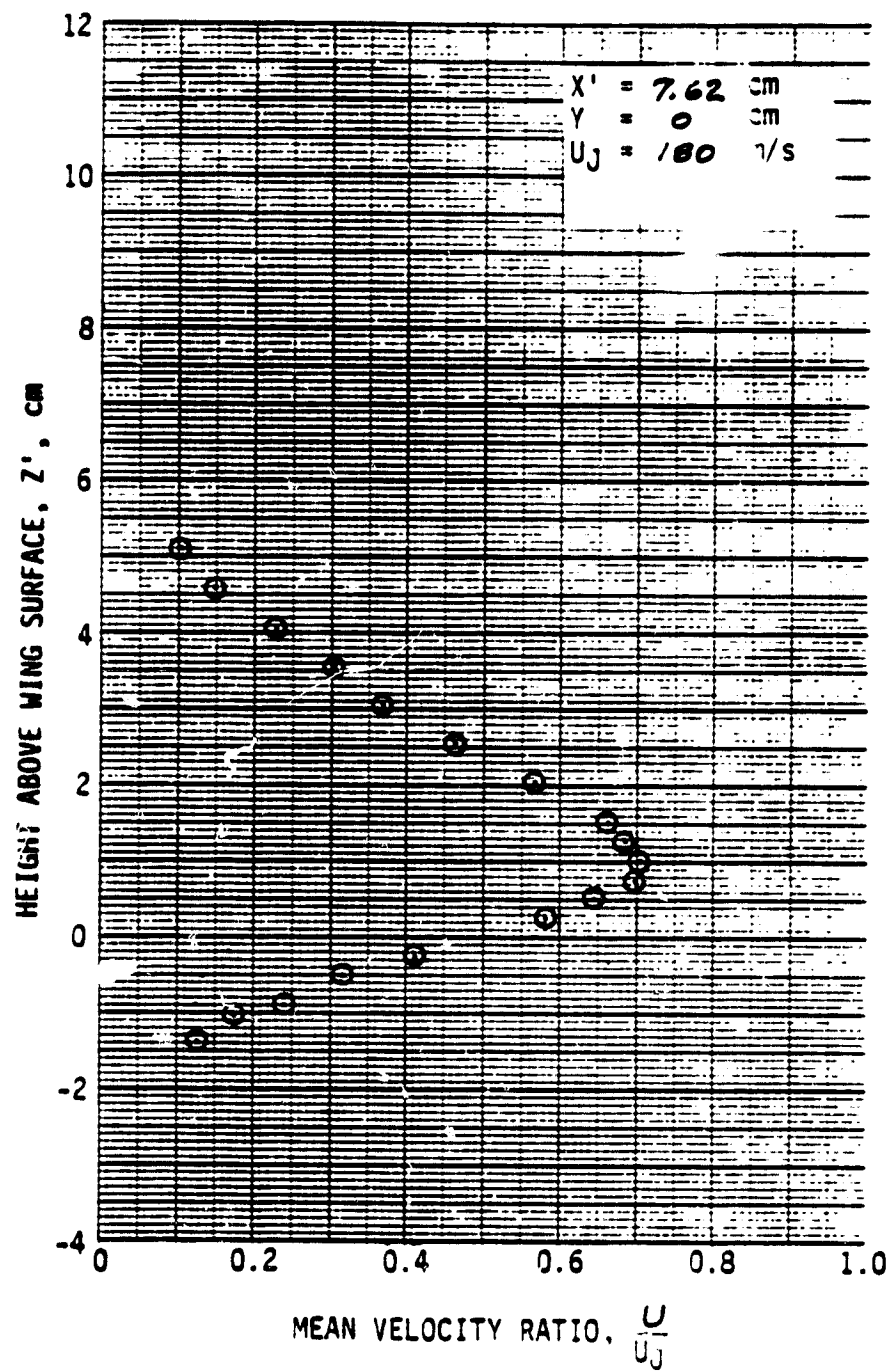


Figure A-4. Continued.

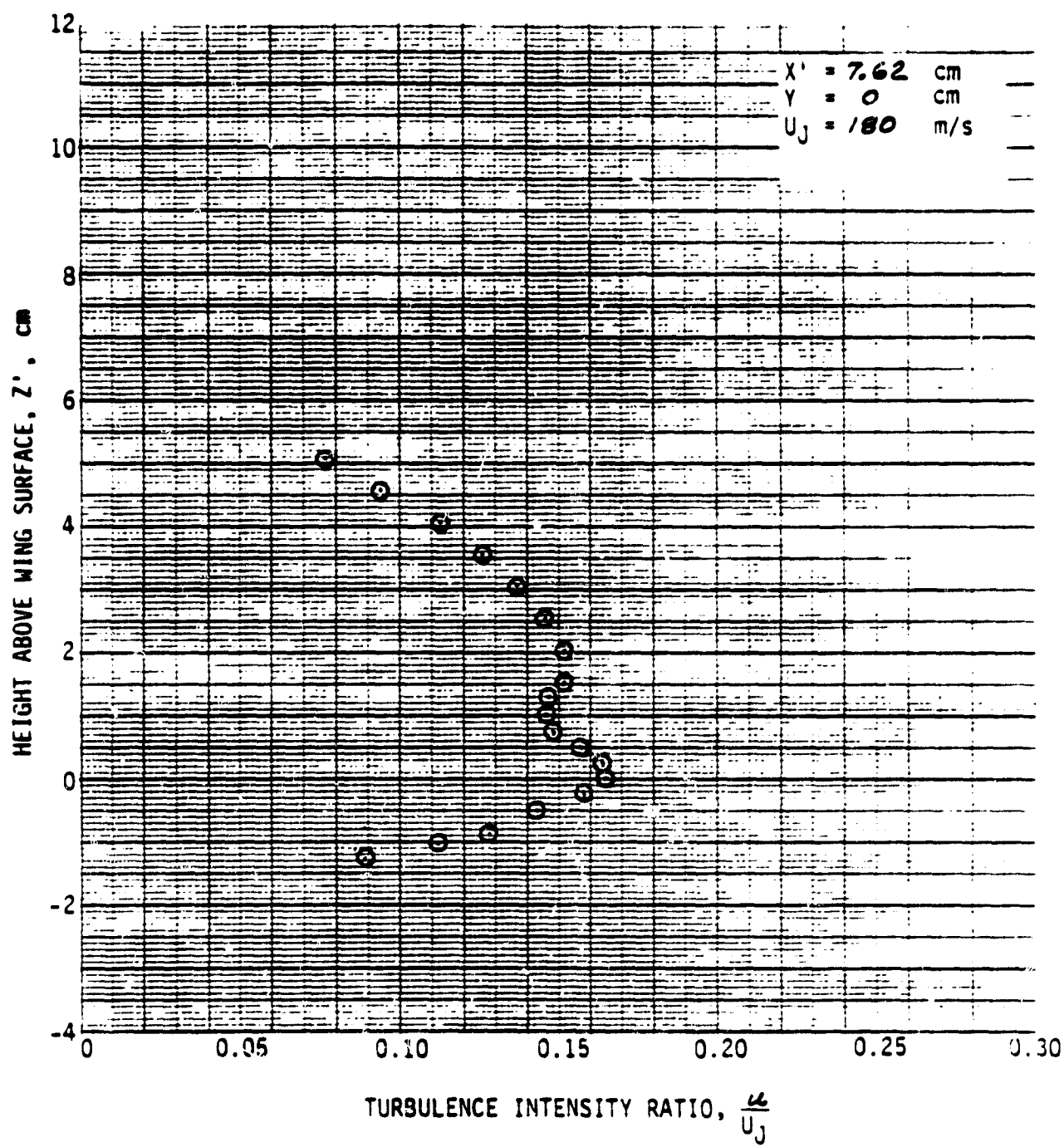


Figure A-4. Continued.

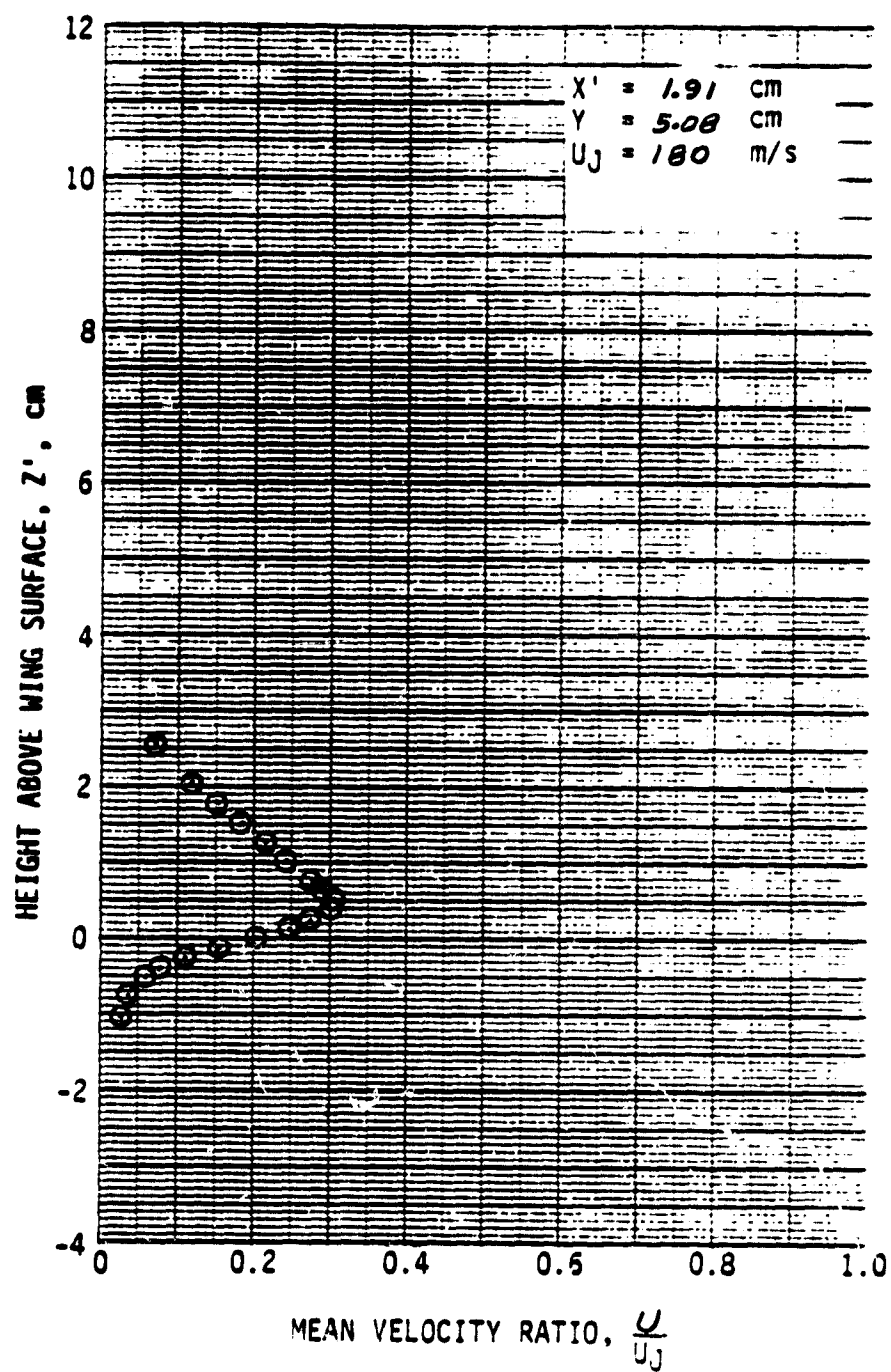


Figure A-4. Continued.

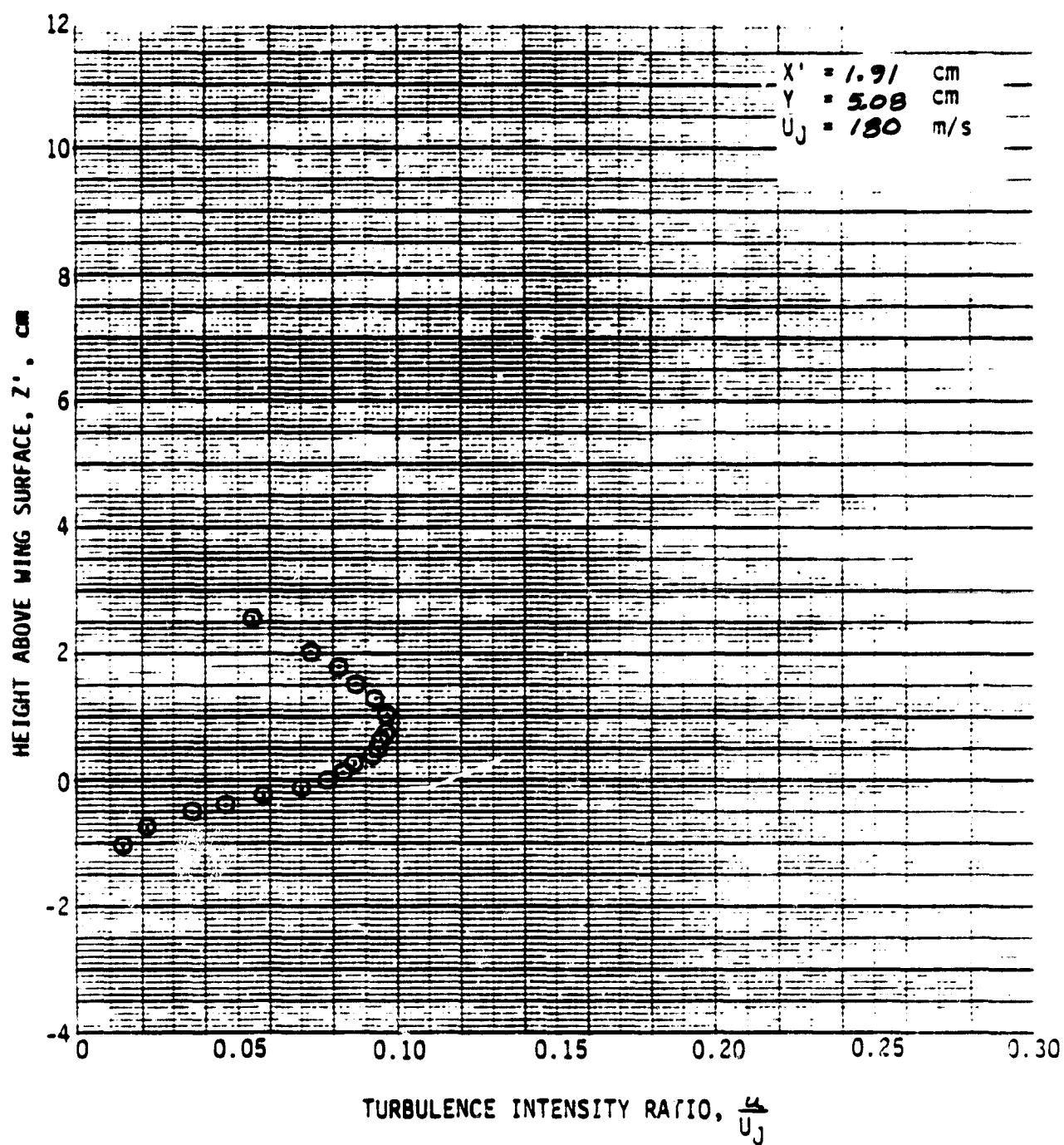


Figure A-4. Concluded.

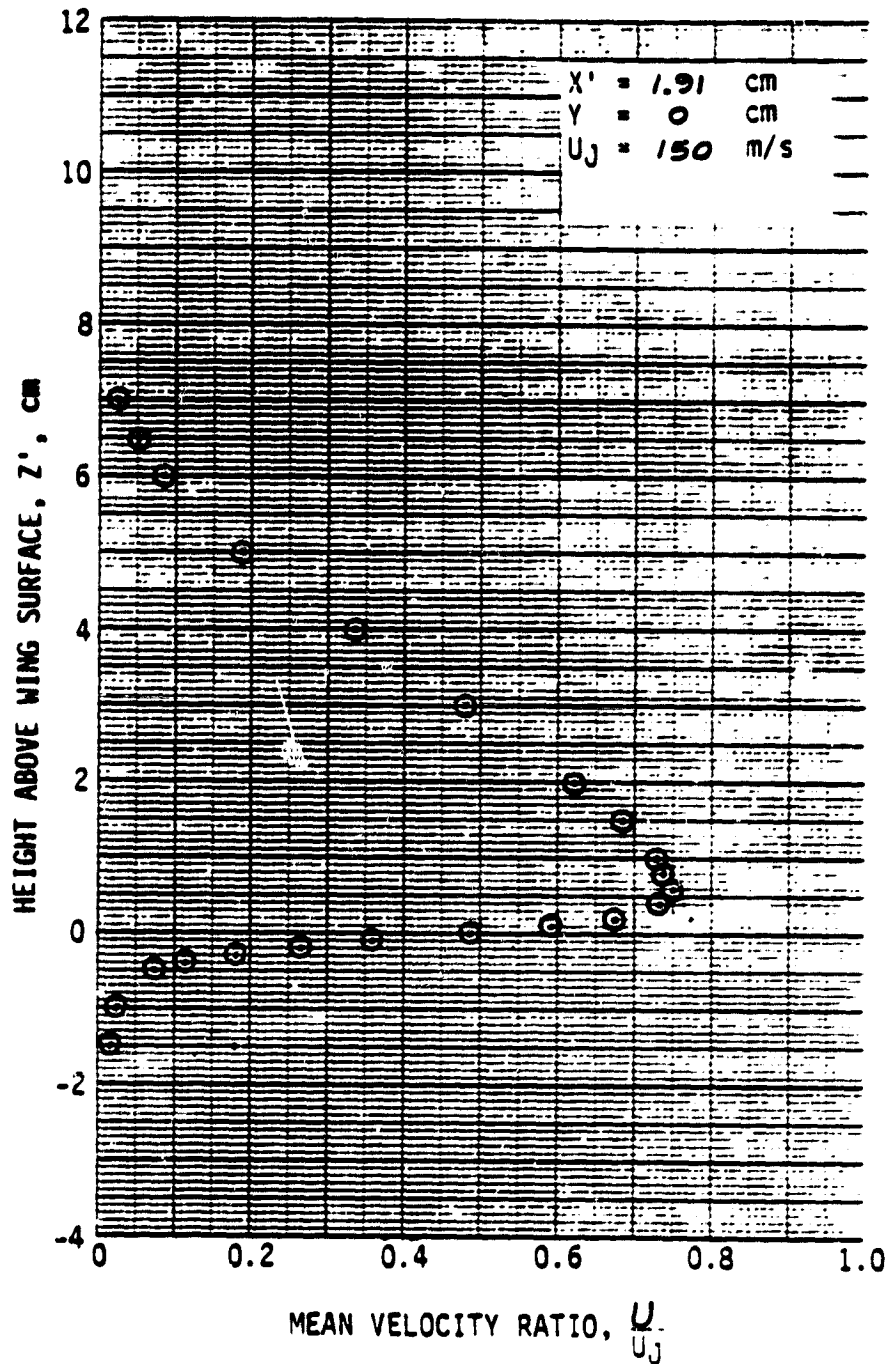


Figure A-5 Wake Flow Profiles by Cross Hot-Wire; $\delta_f = 30^\circ$, No Screen, Velocity Variations.

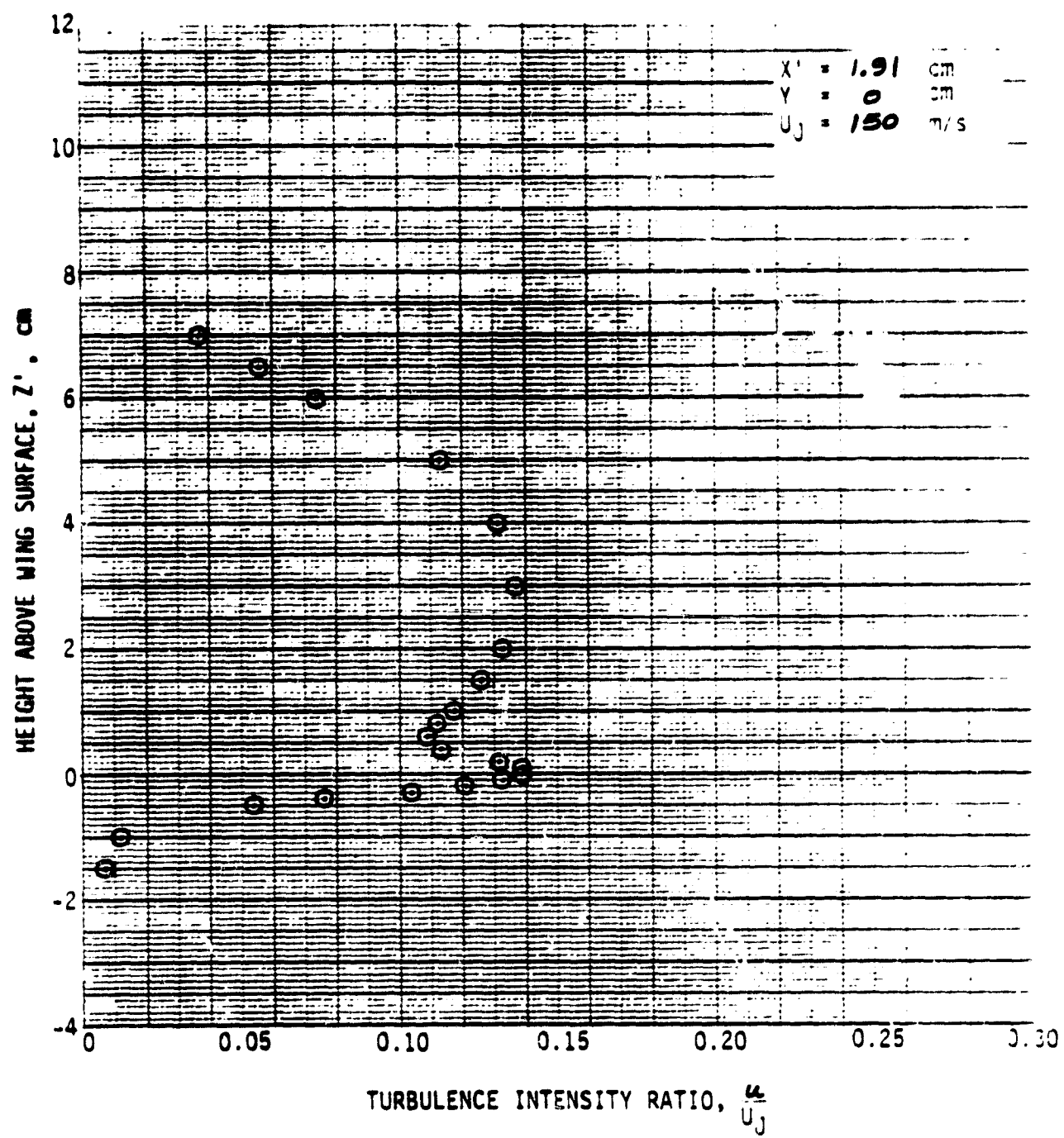


Figure A-5. Continued.

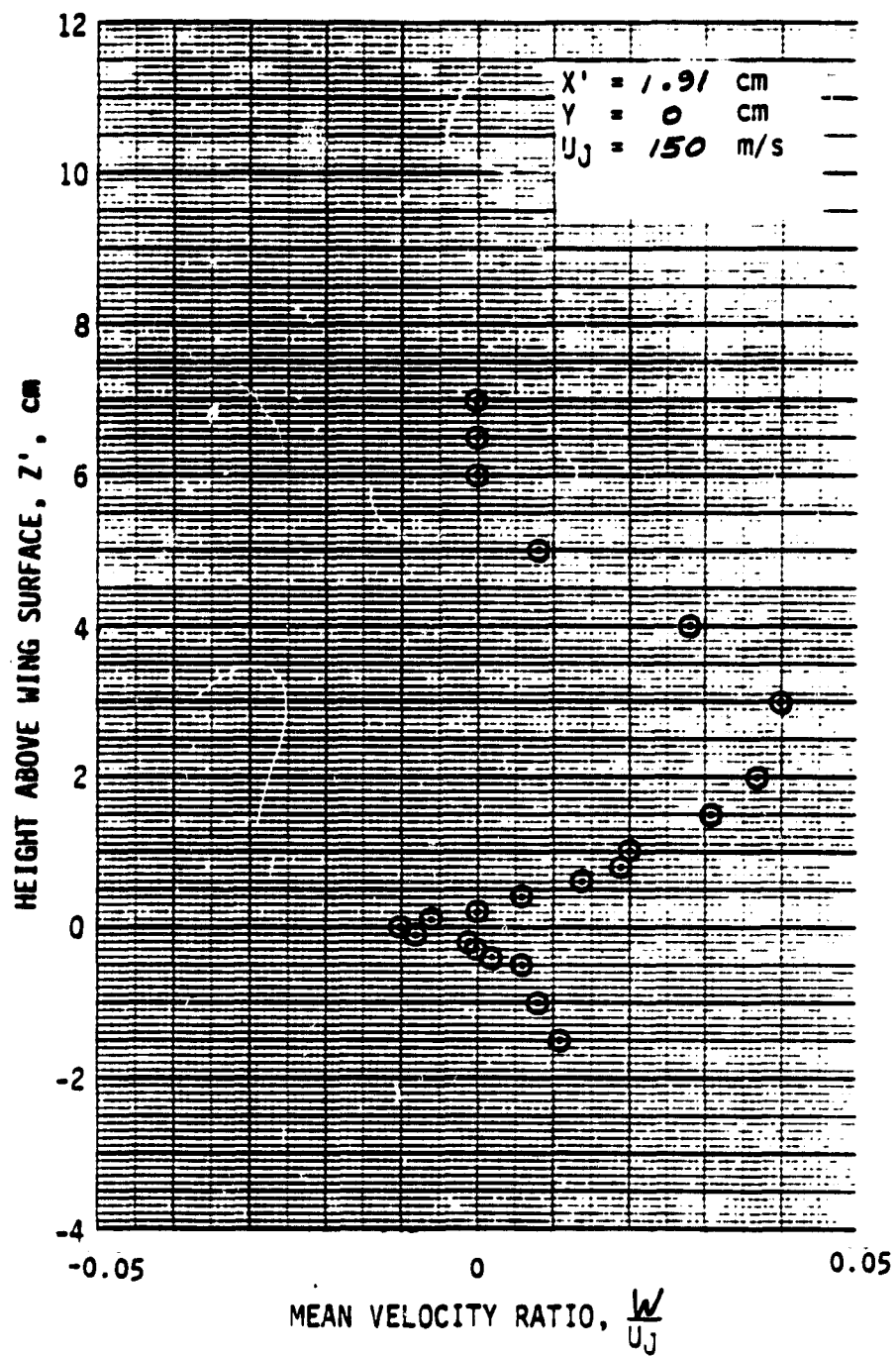


Figure A-5. Continued.

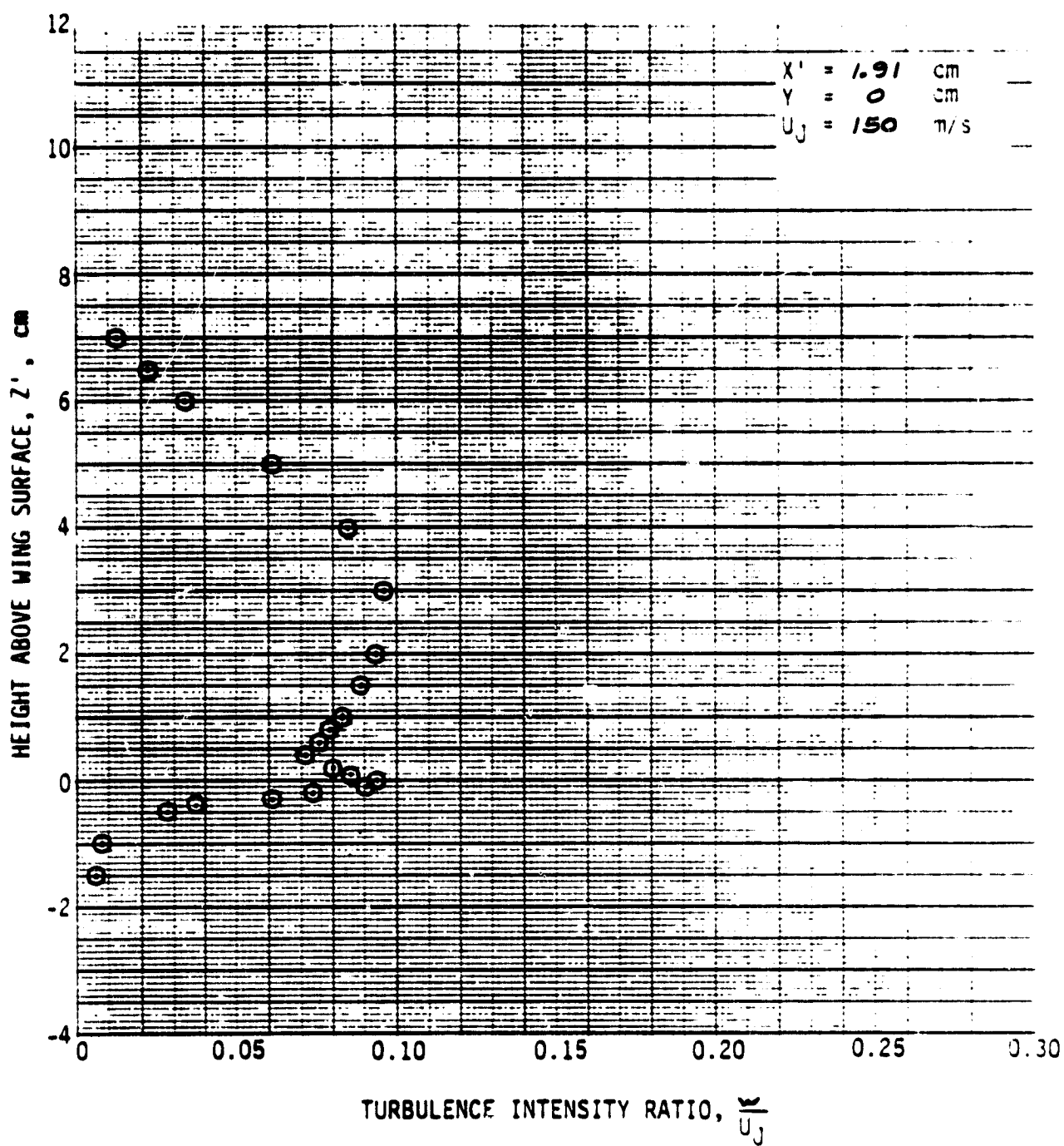


Figure A-5. Continued.

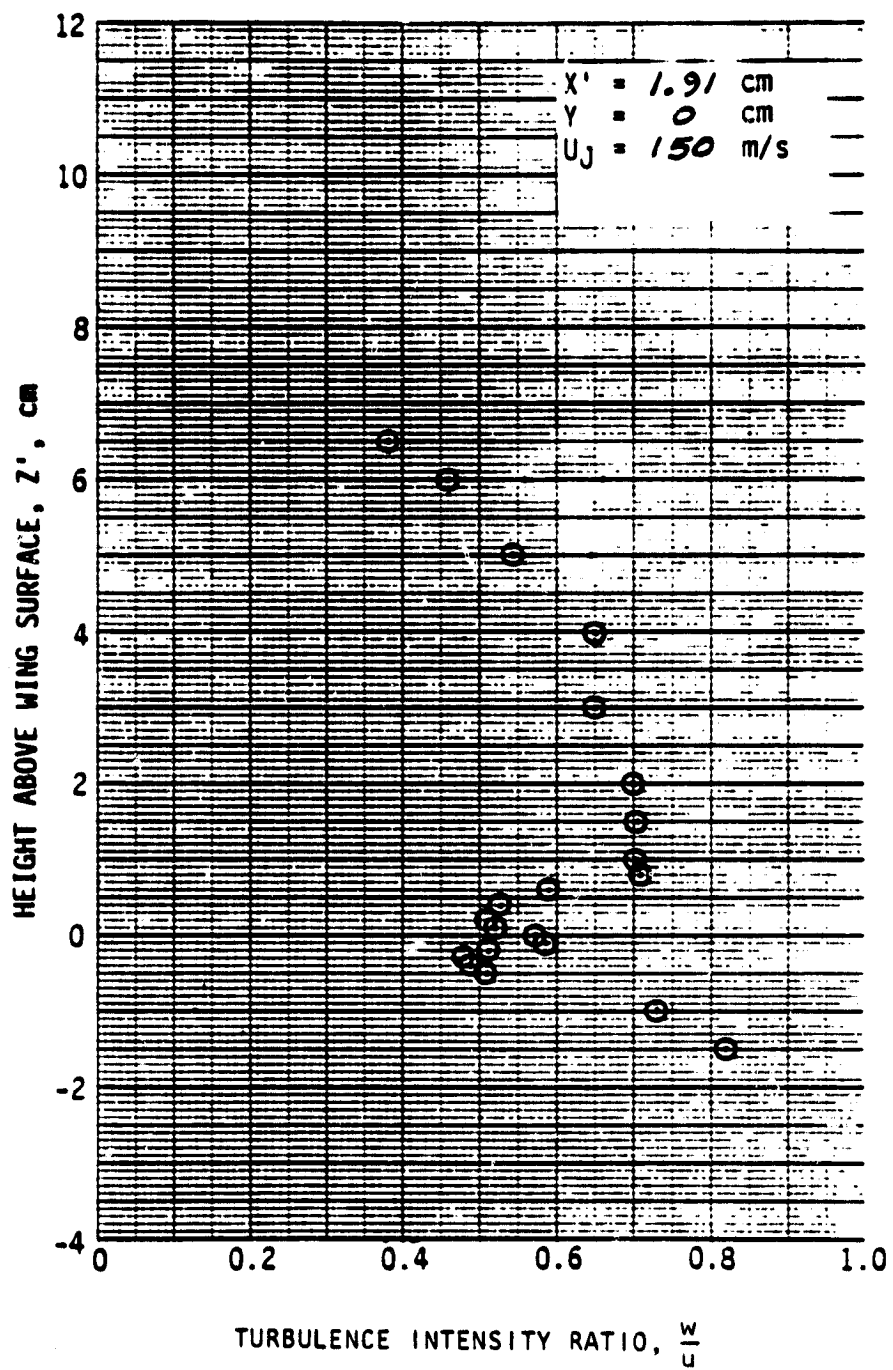


Figure A-5. Continued.

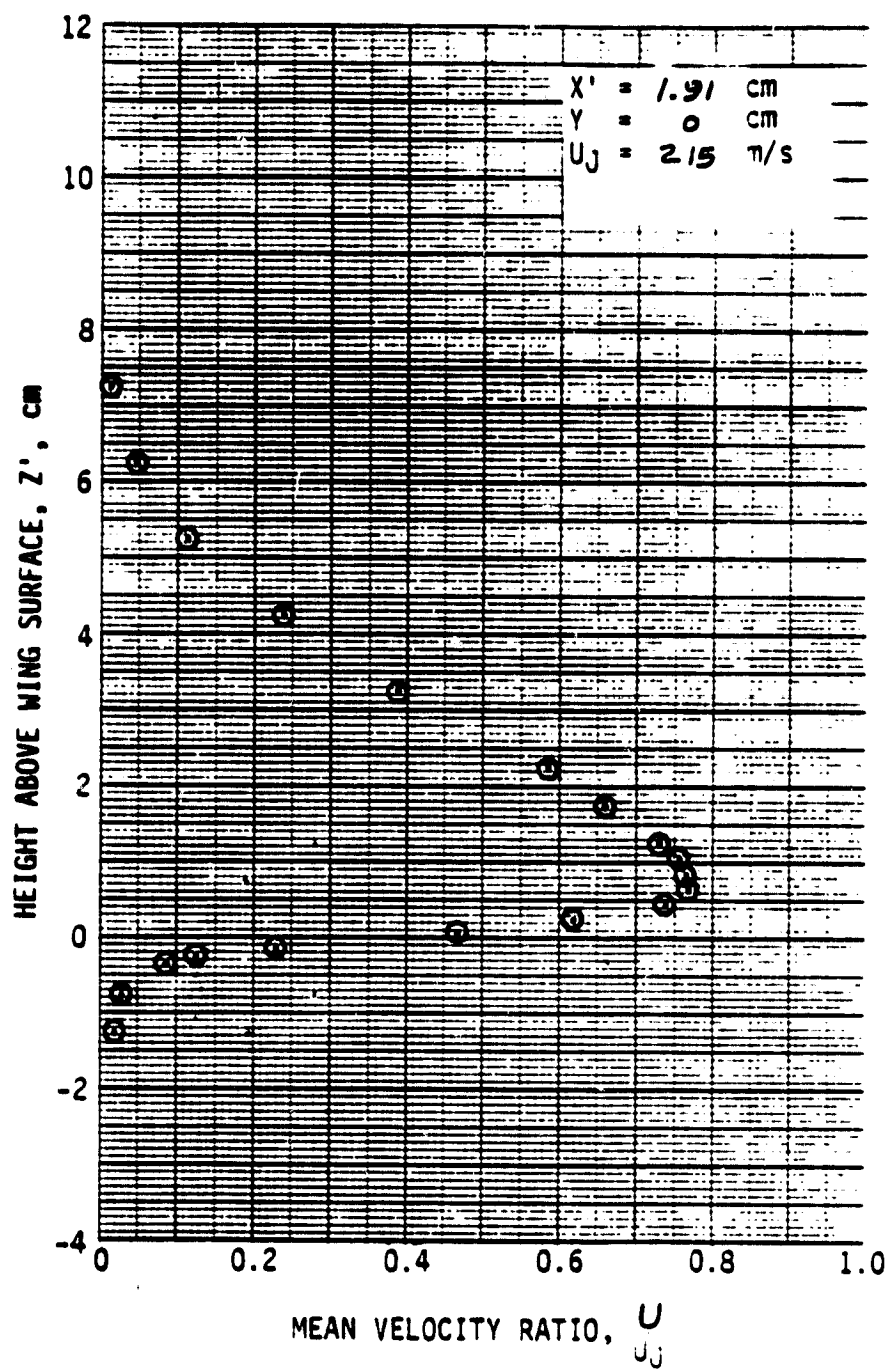


Figure A-5. Continued.

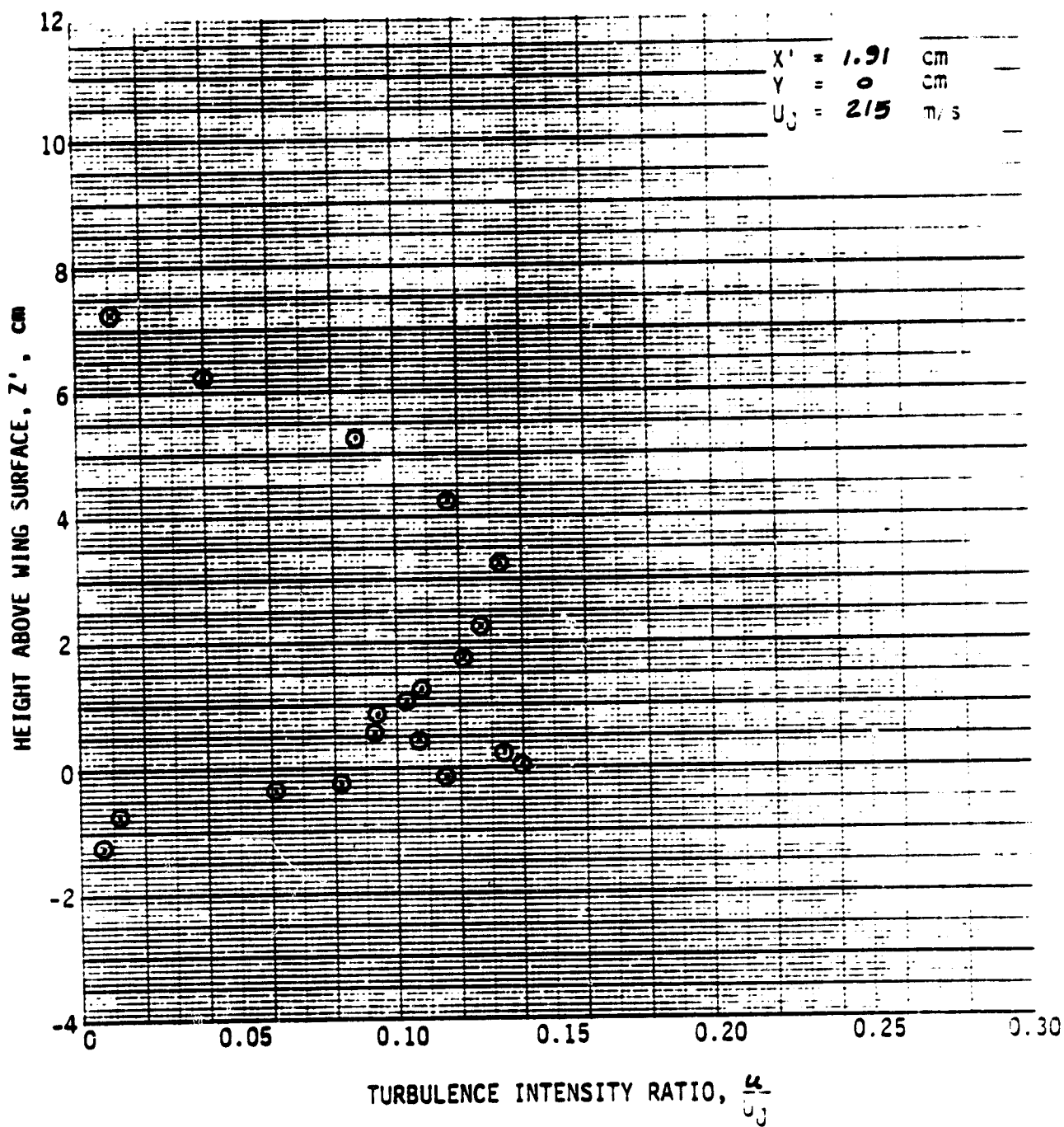


Figure A-5. Continued.

ORIGINAL PAGE IS
OF POOR QUALITY

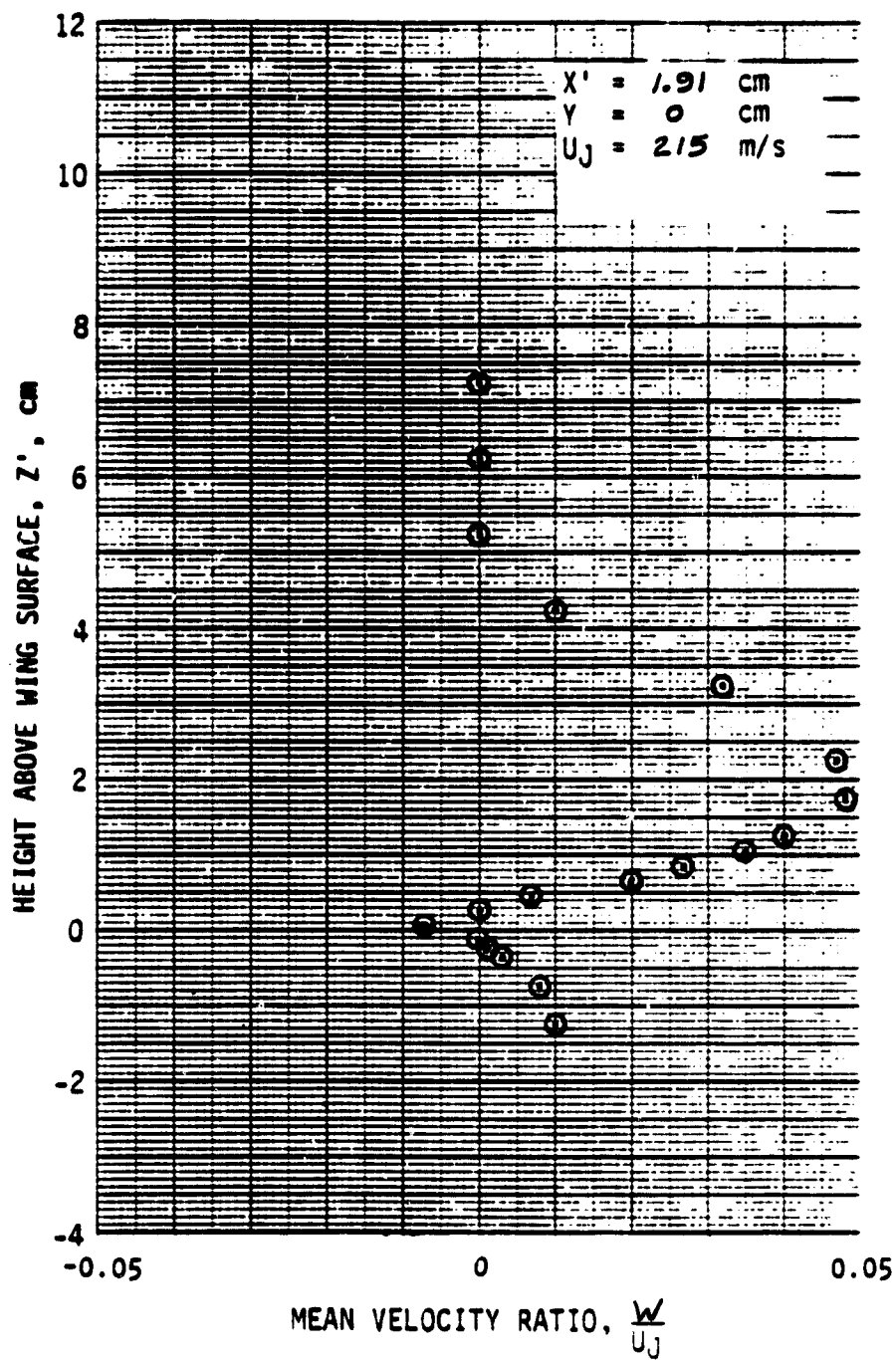


Figure A-5. Continued.

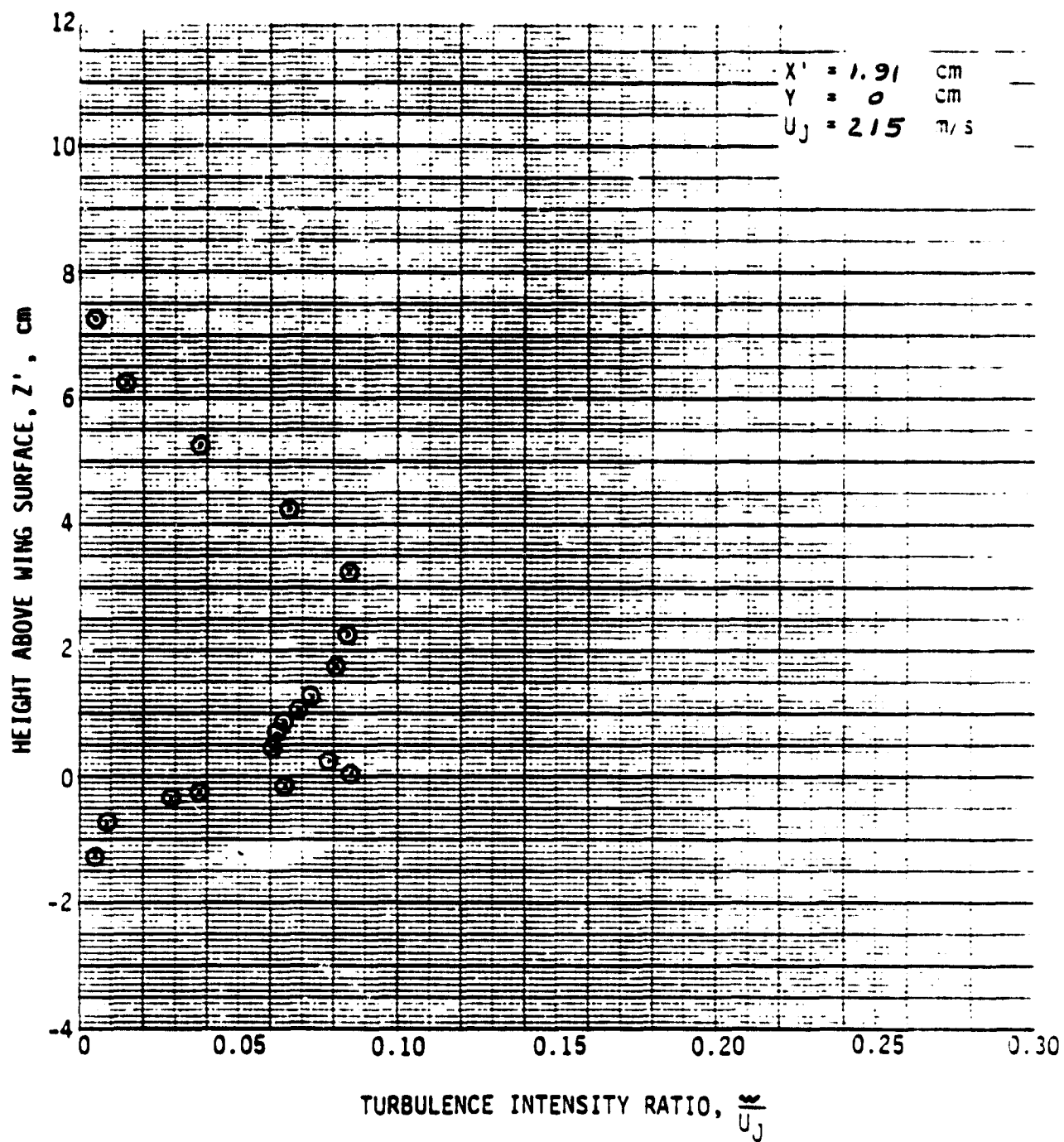


Figure A-5. Continued.

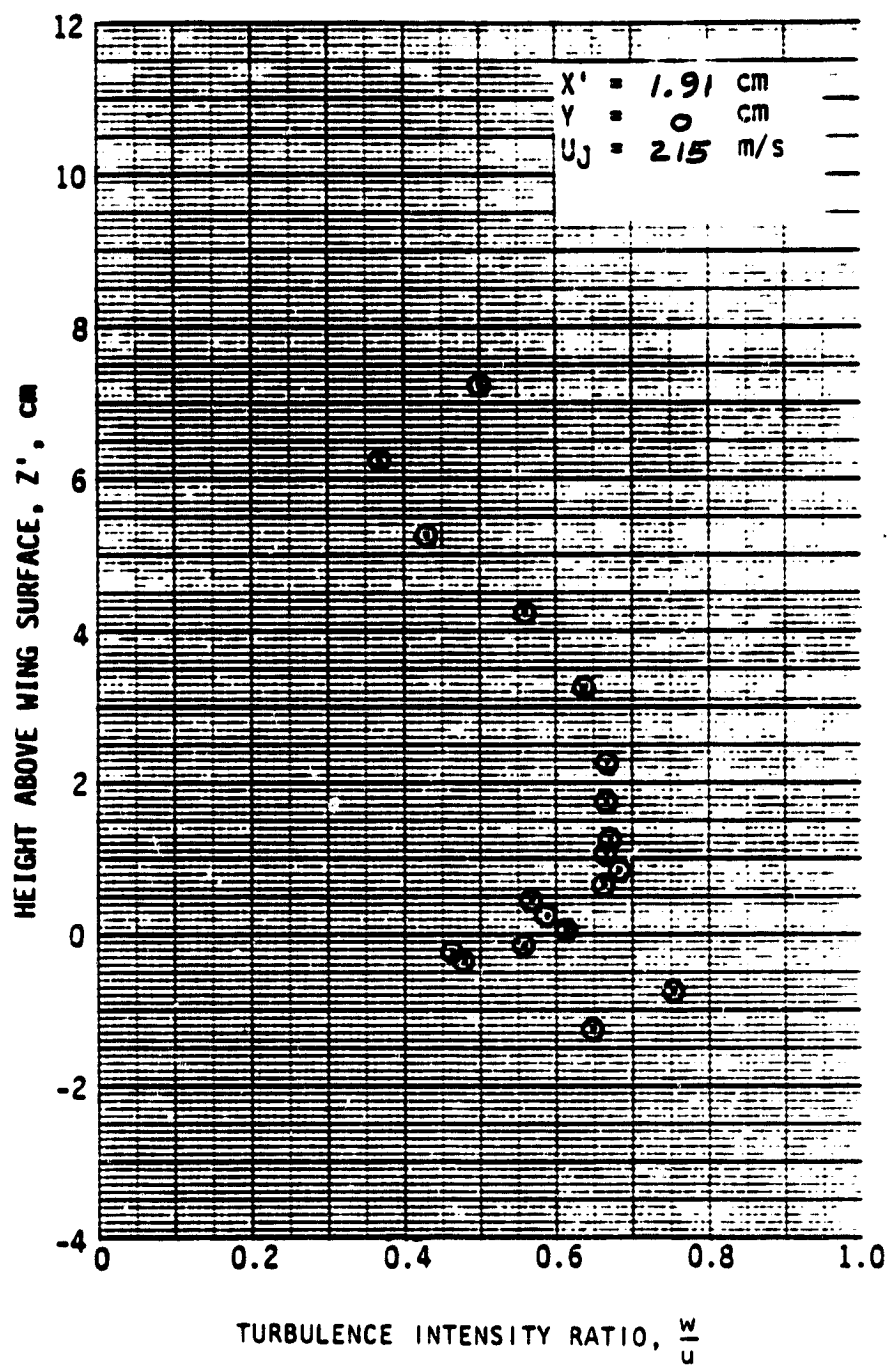


Figure A-5. Concluded.

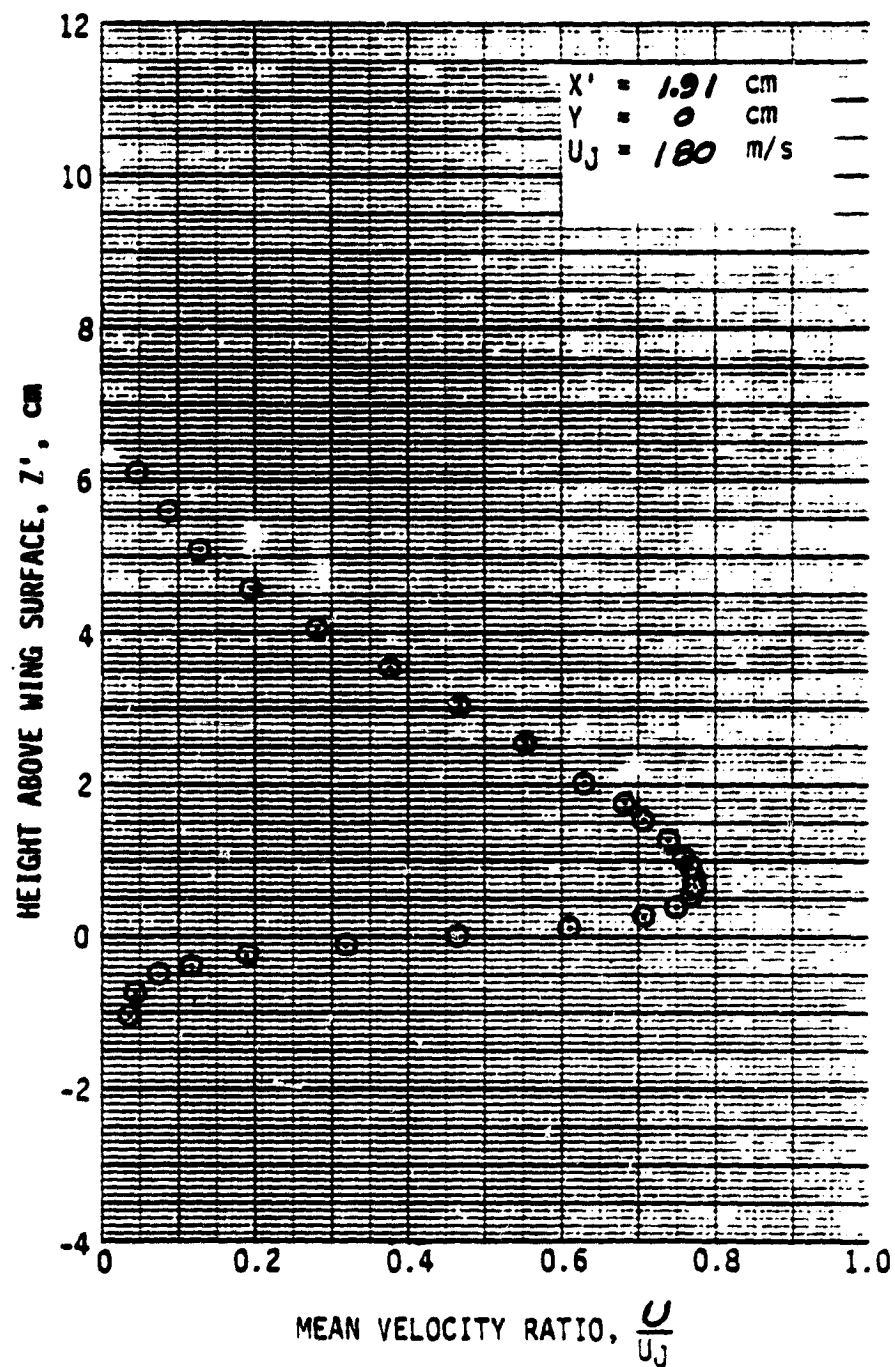


Figure A-6. Wake Flow Profiles by Single Hot-Wire; $\delta_f = 30^\circ$, No Screen.

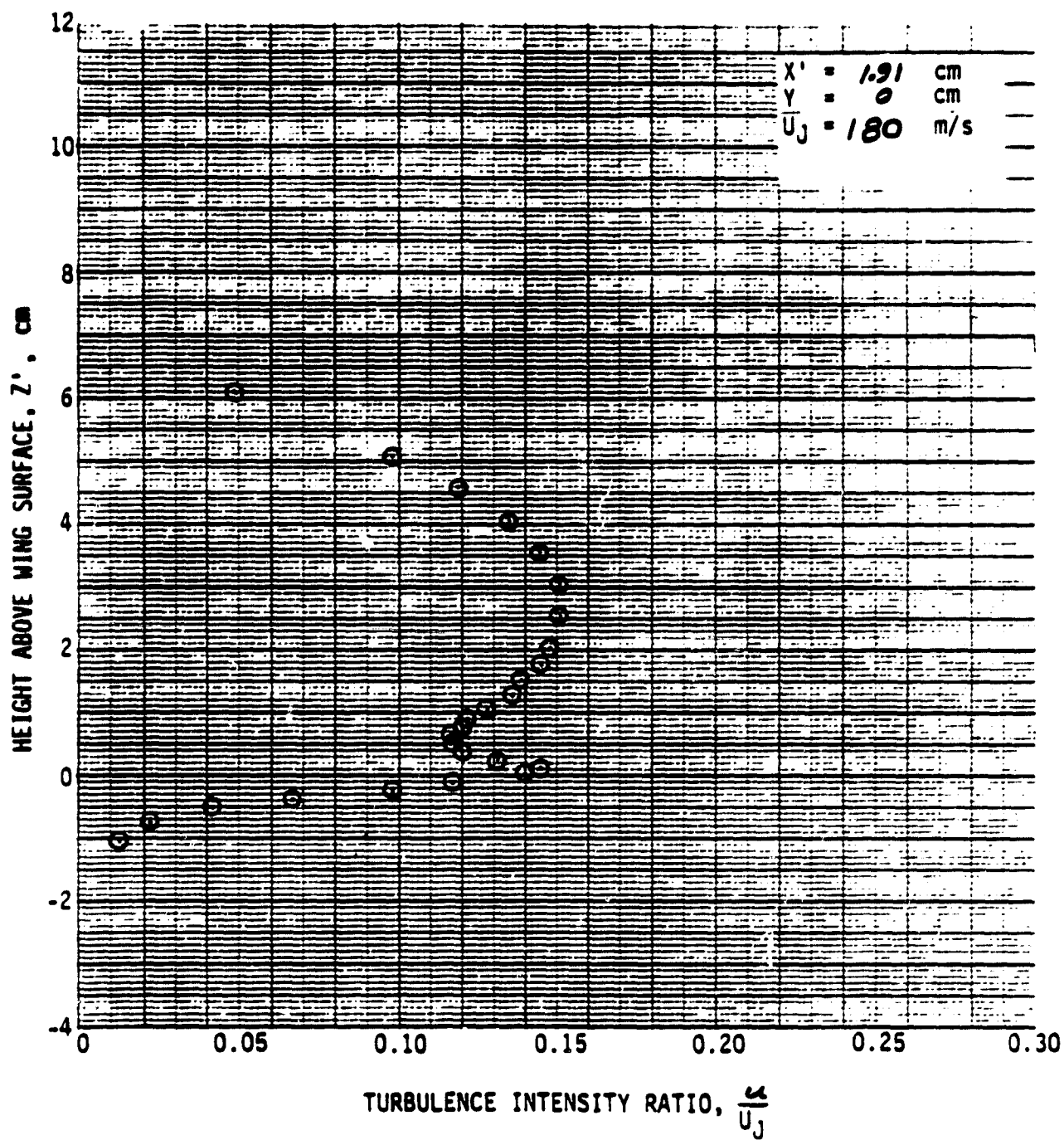


Figure A-6. Continued.

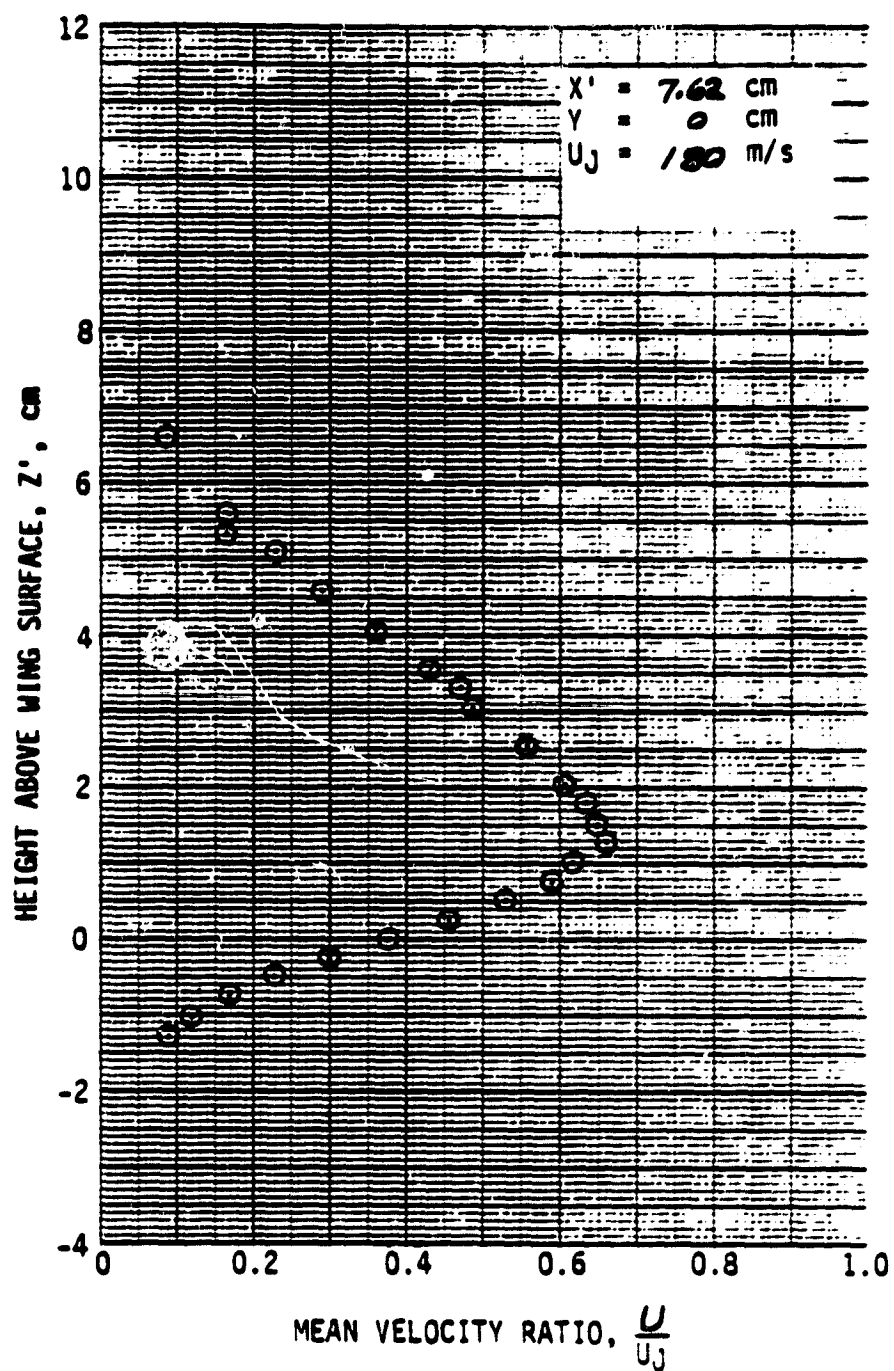


Figure A-6. Continued.

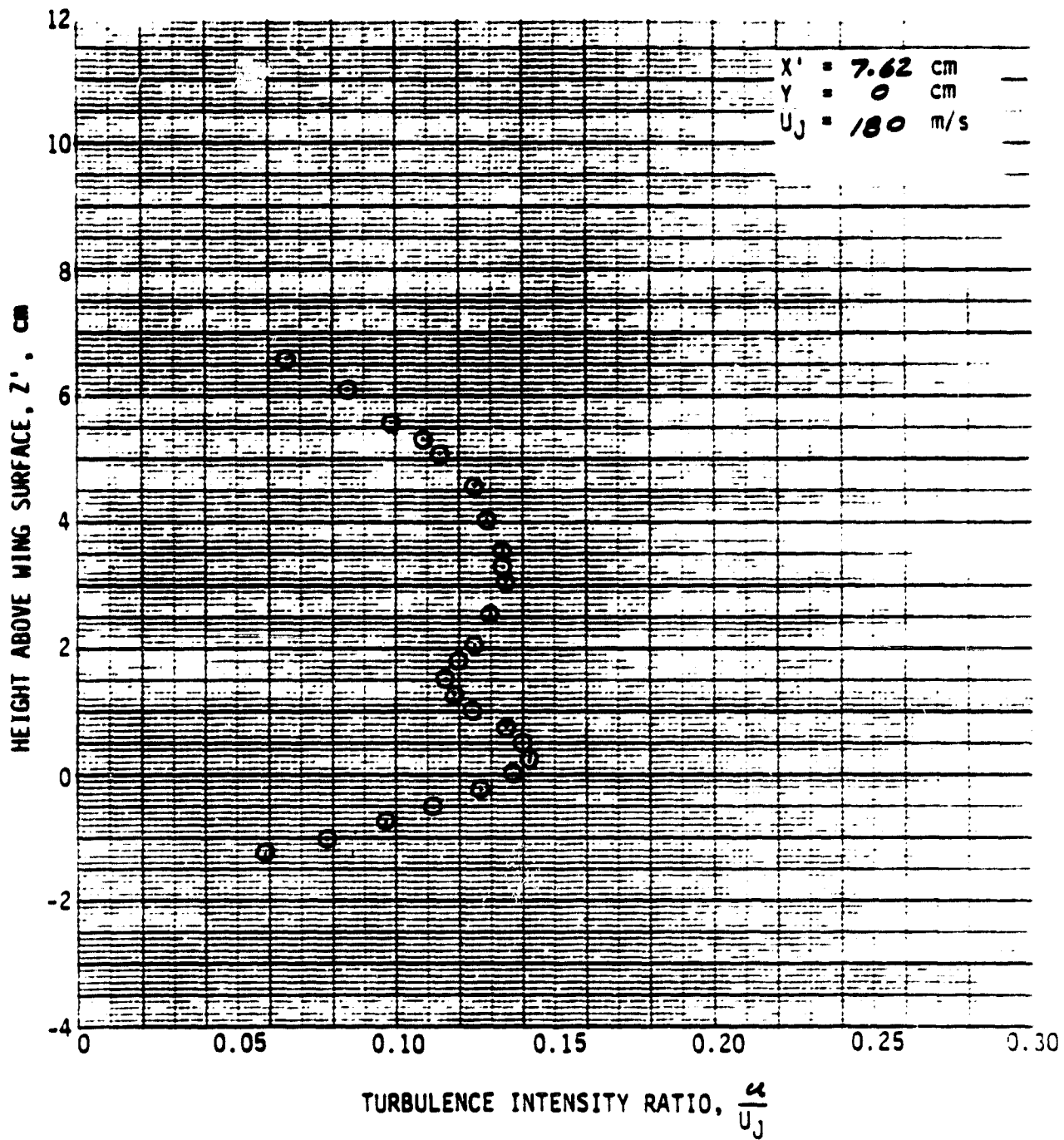


Figure A-6. Continued.

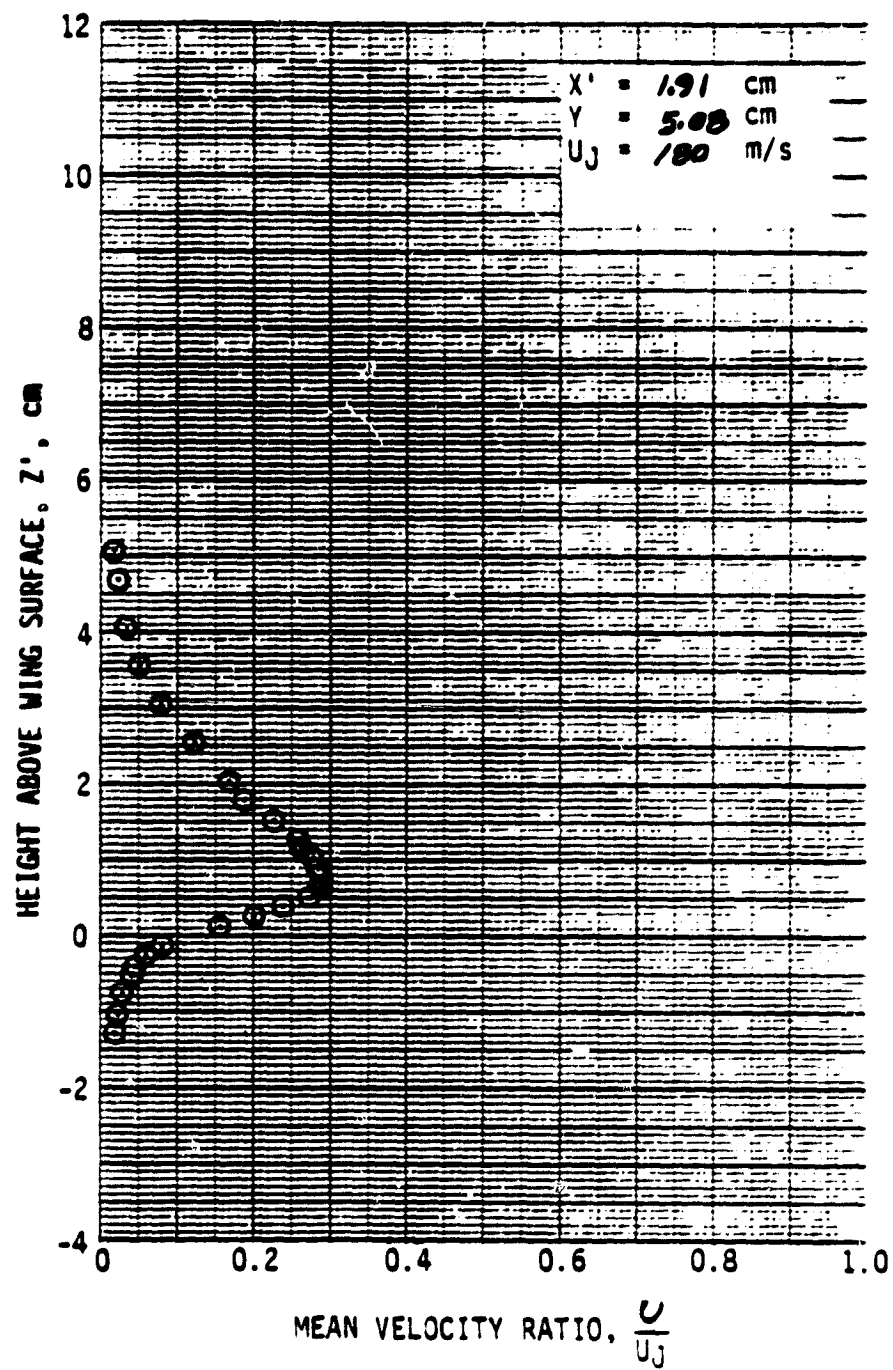


Figure A-6. Continued.

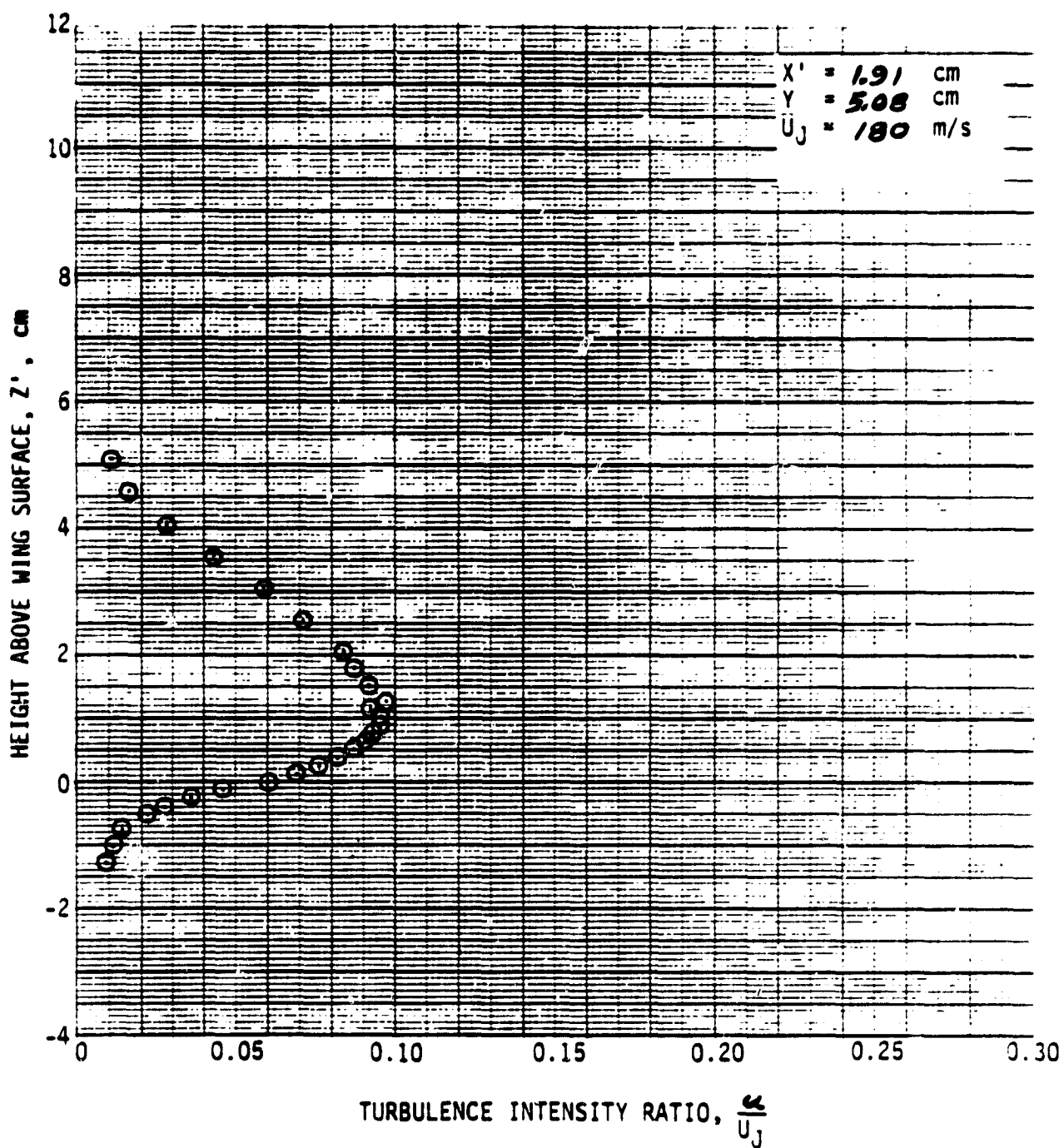


Figure A-6. Concluded.

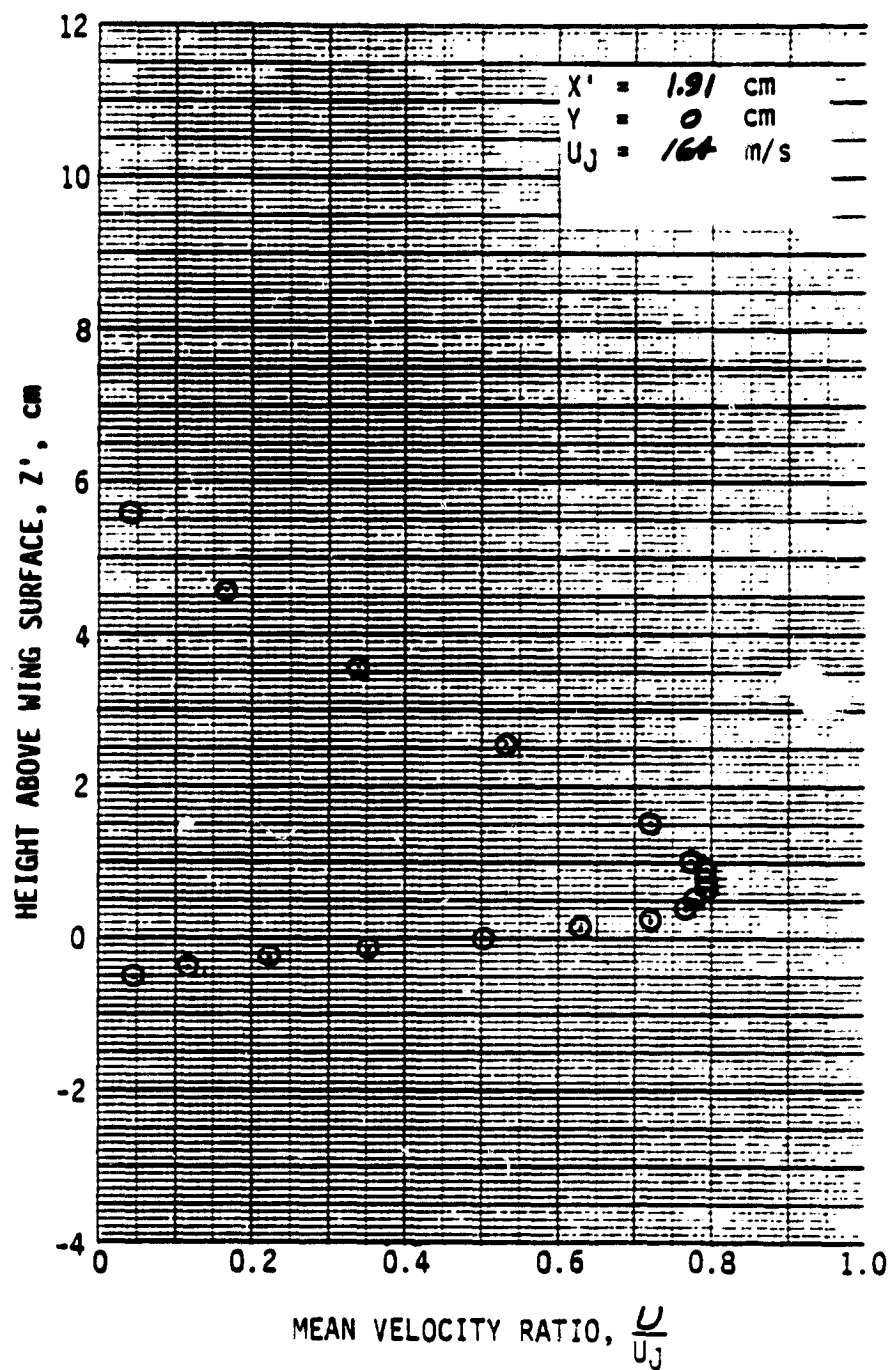


Figure A-7. Wake Flow Profiles by Laser Velocimeter, $\delta_f = 30^\circ$, No Screens.

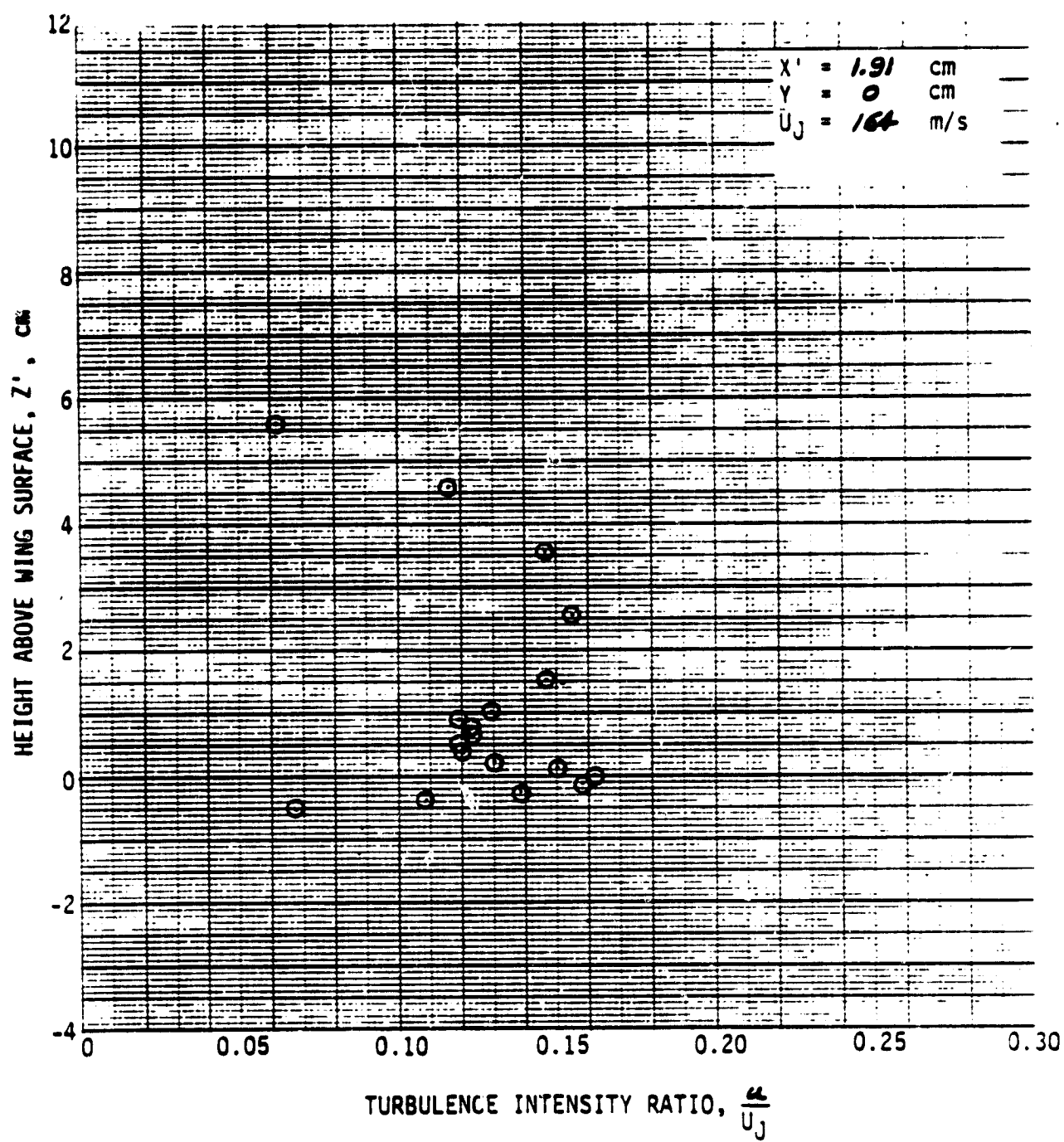


Figure A-7. Continued.

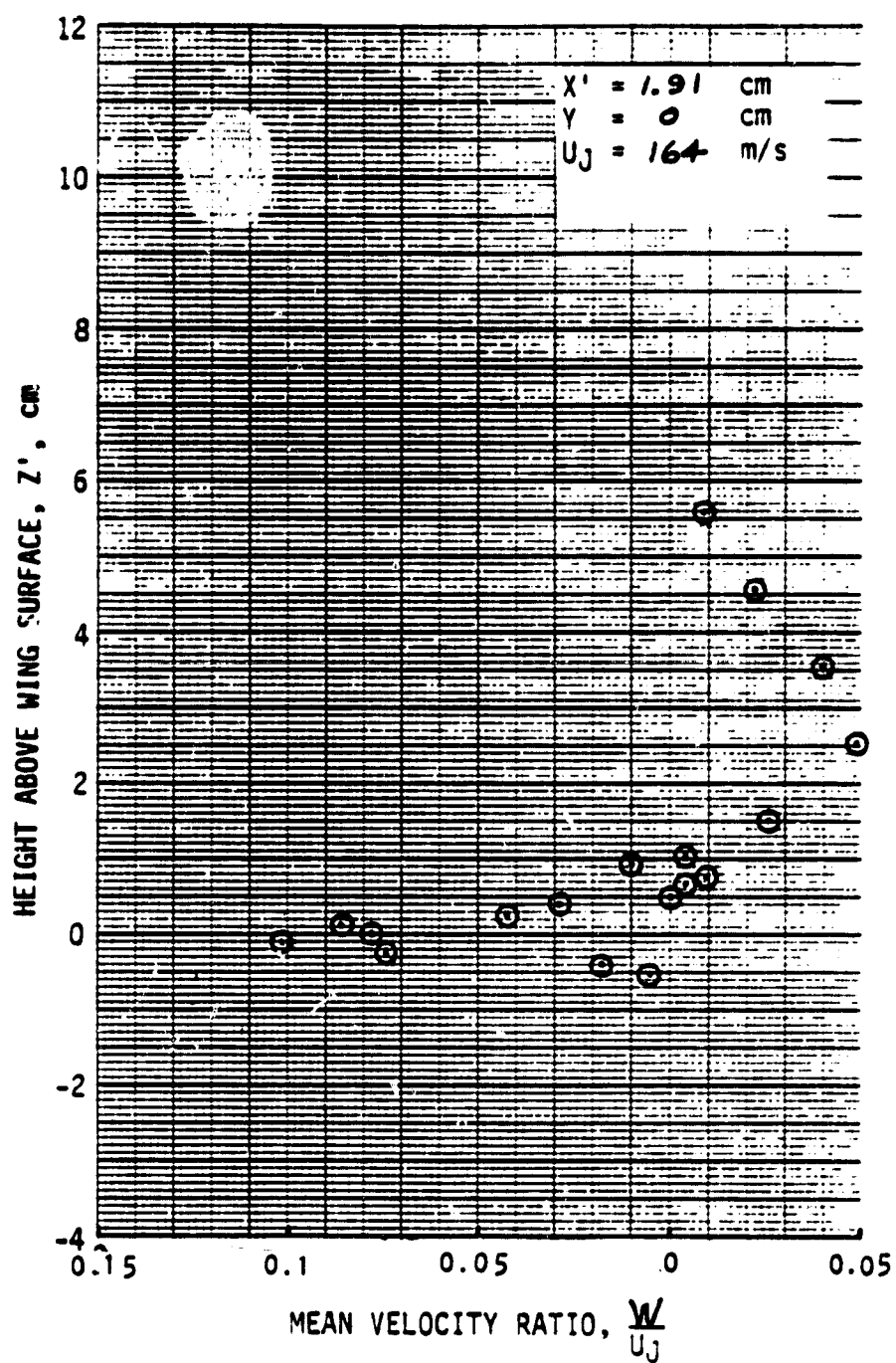


Figure A-7. Continued.

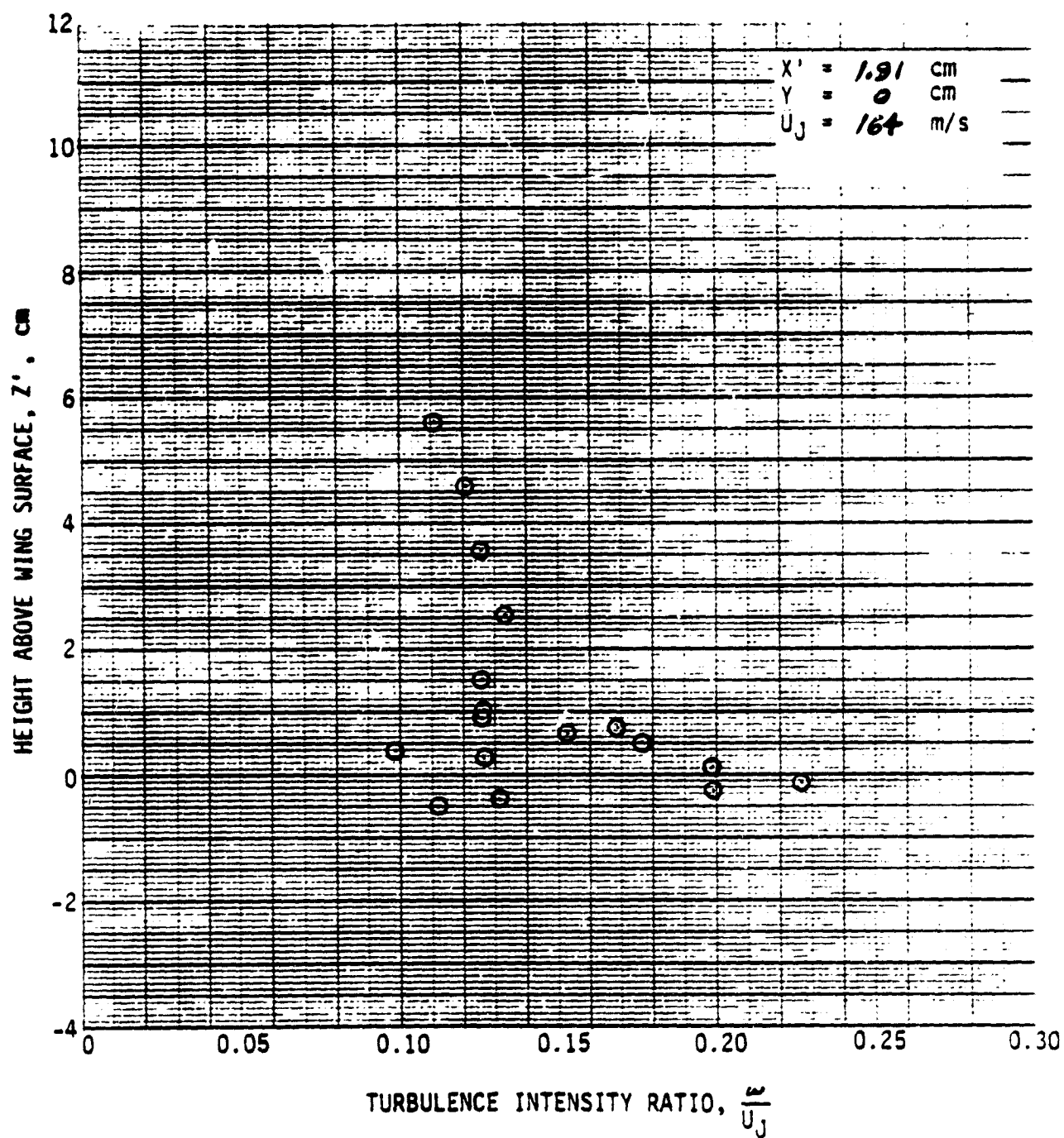


Figure A-7. Continued.

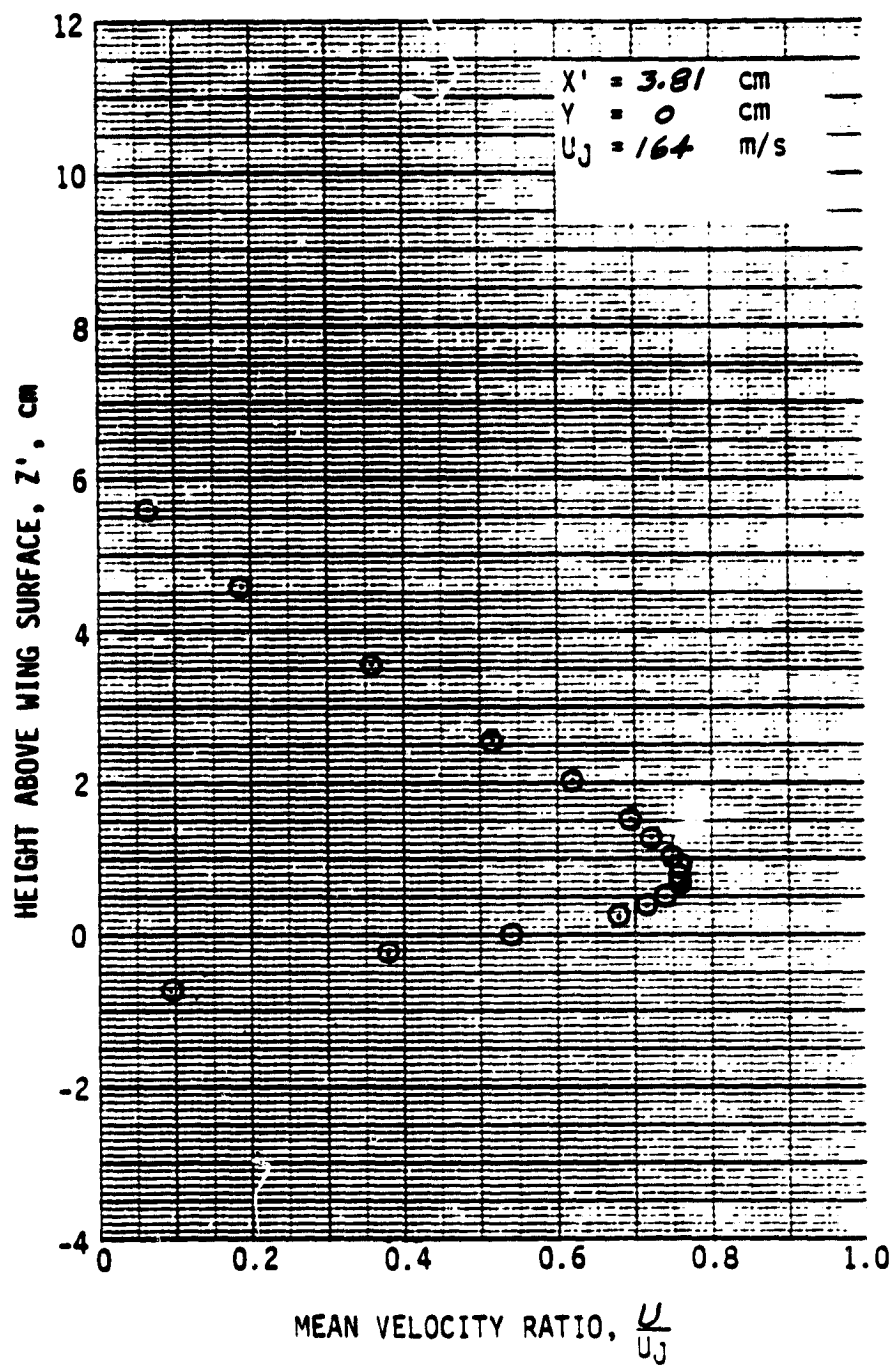


Figure A-7. Continued.

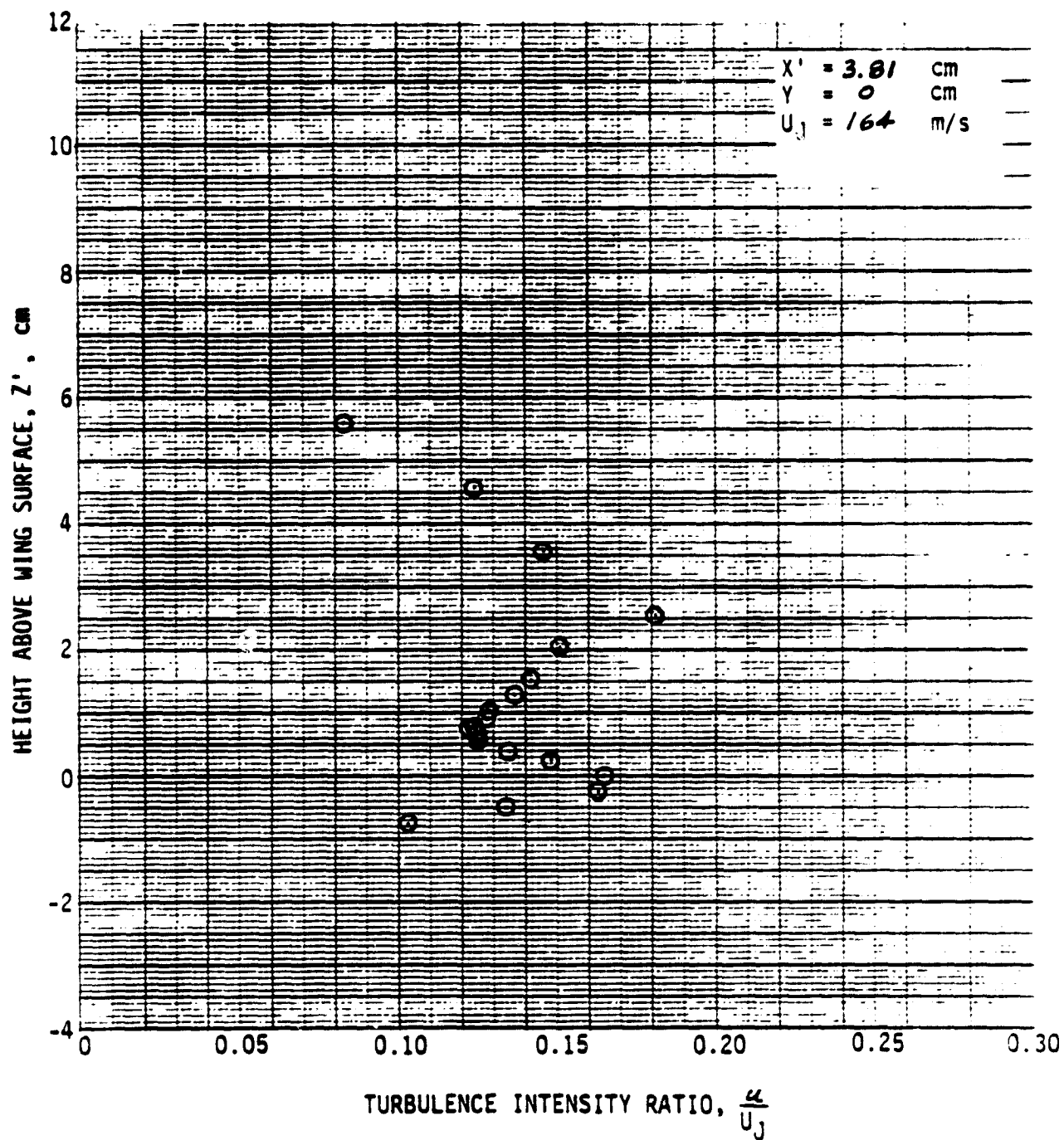


Figure A-7. Continued.

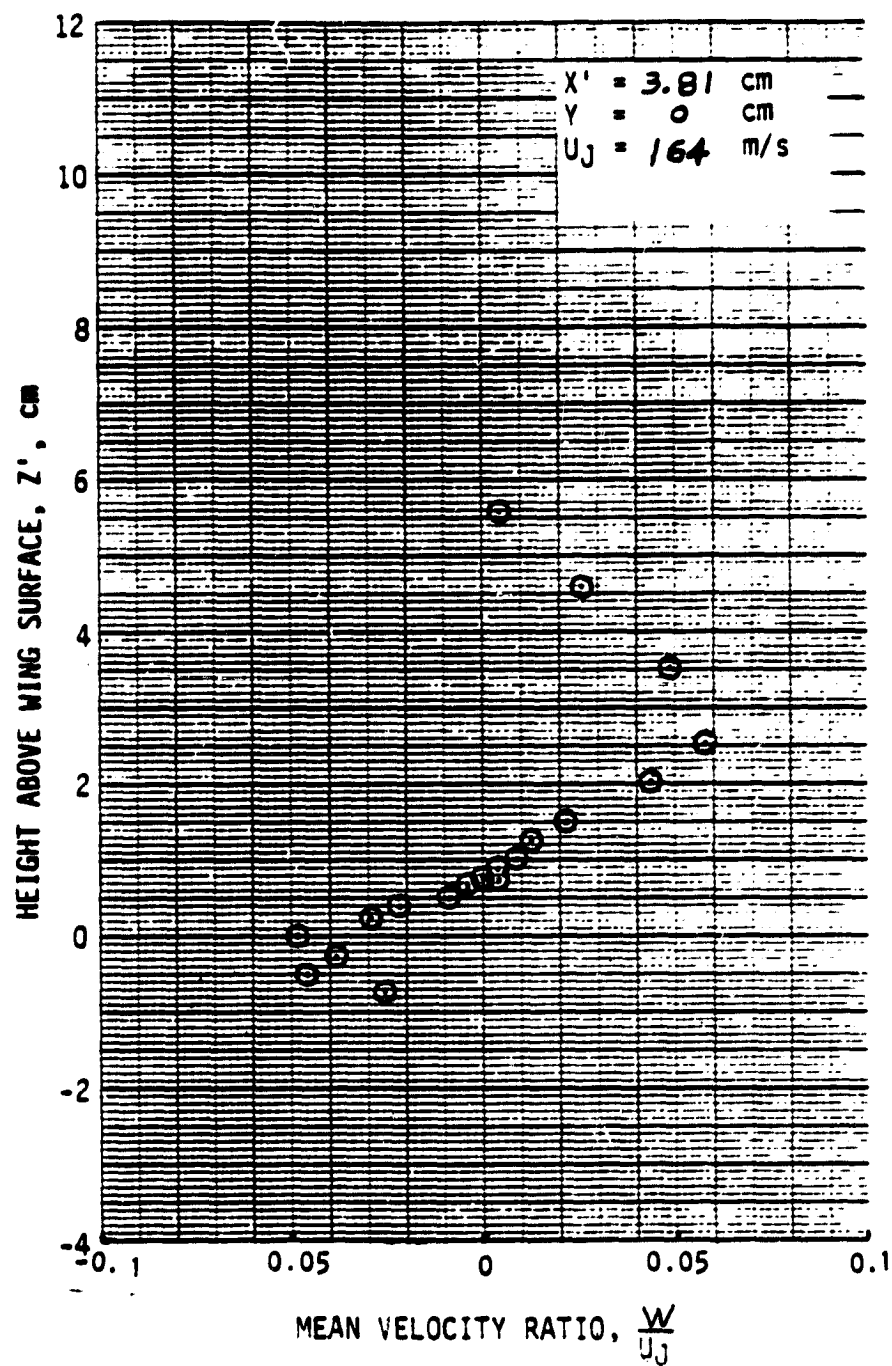


Figure A-7. Continued.

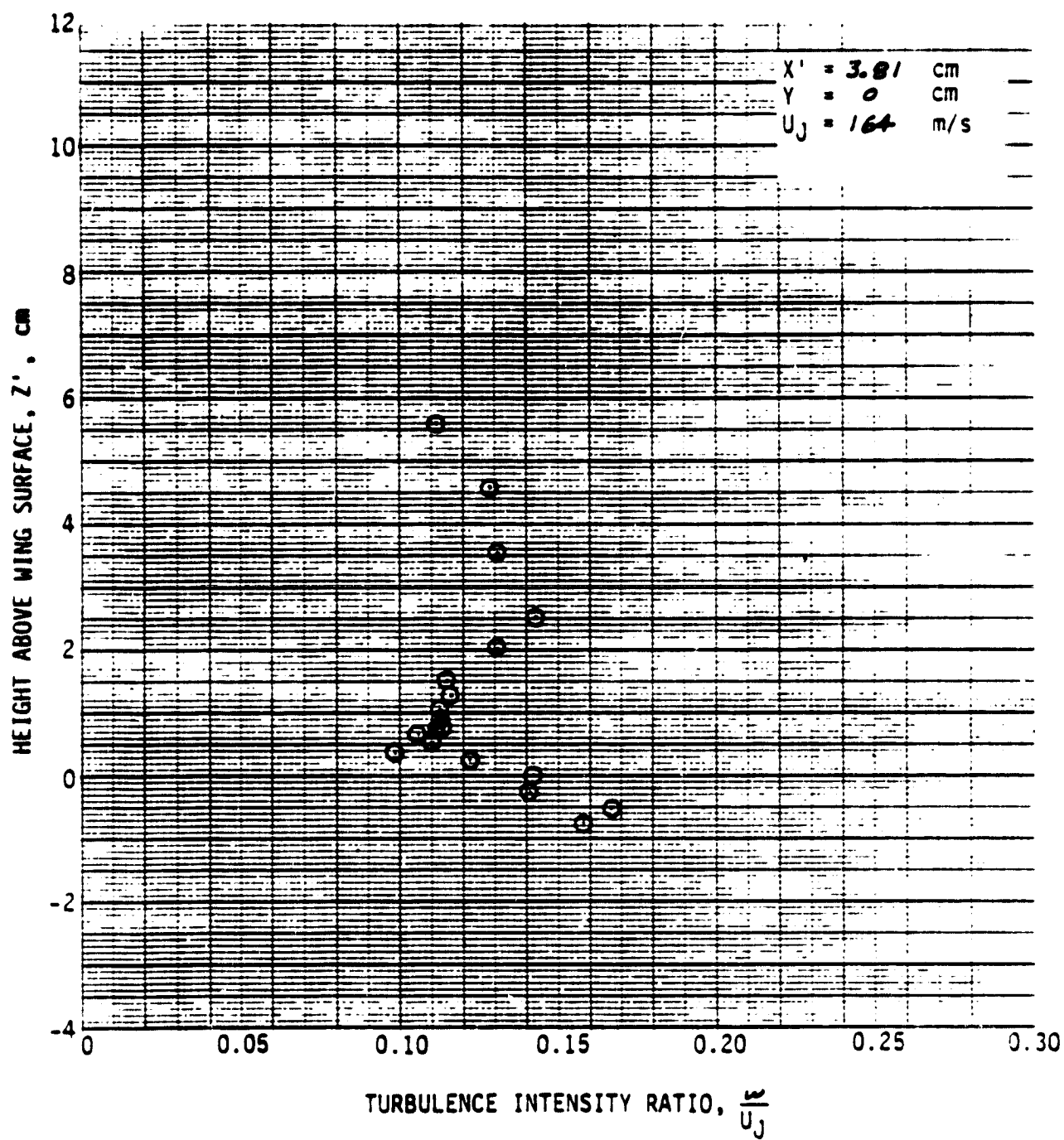


Figure A-7. Continued.

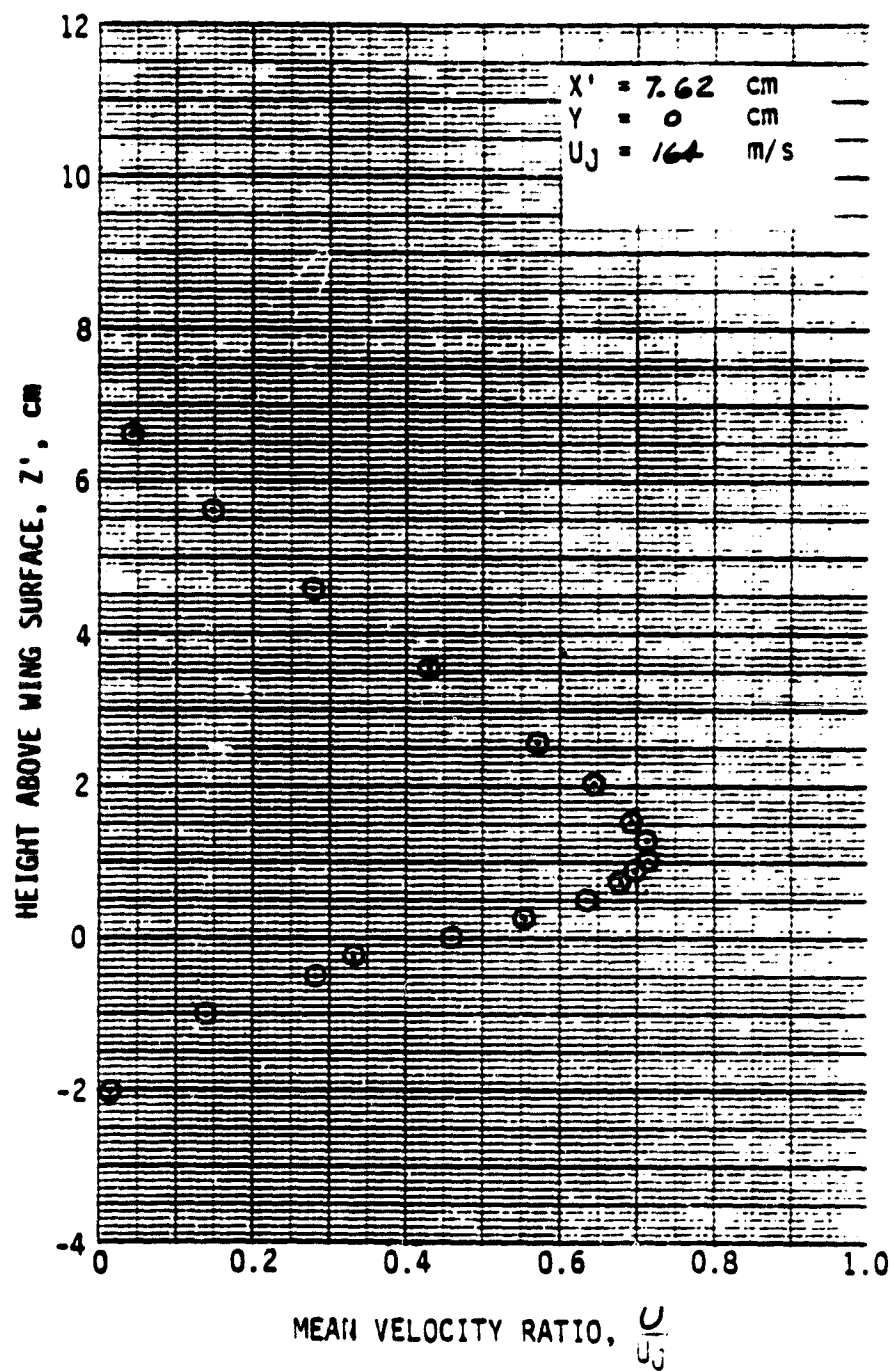


Figure A-7. Continued.

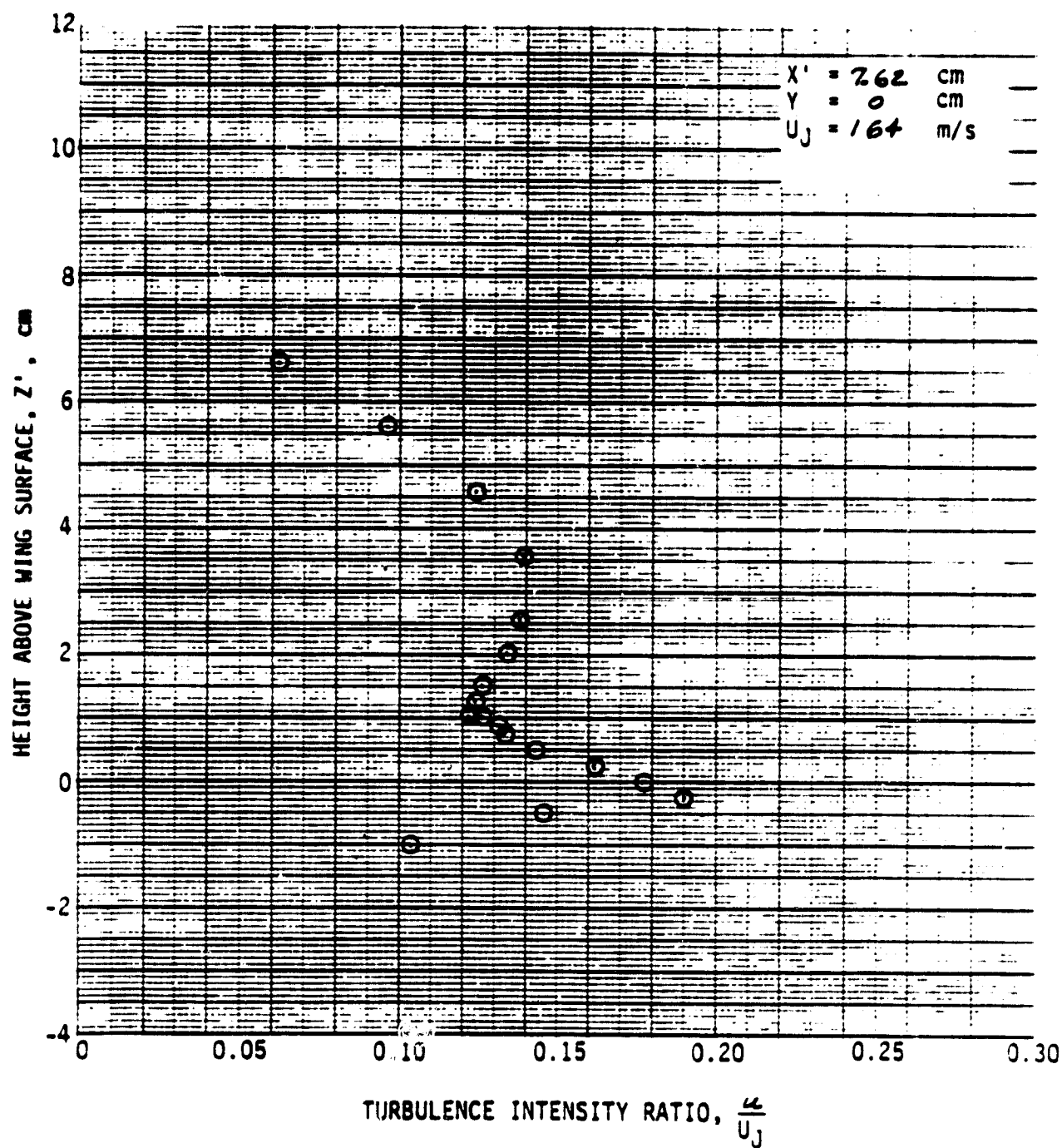


Figure A-7. Continued.

ORIGINAL PAGE IS
OF POOR QUALITY

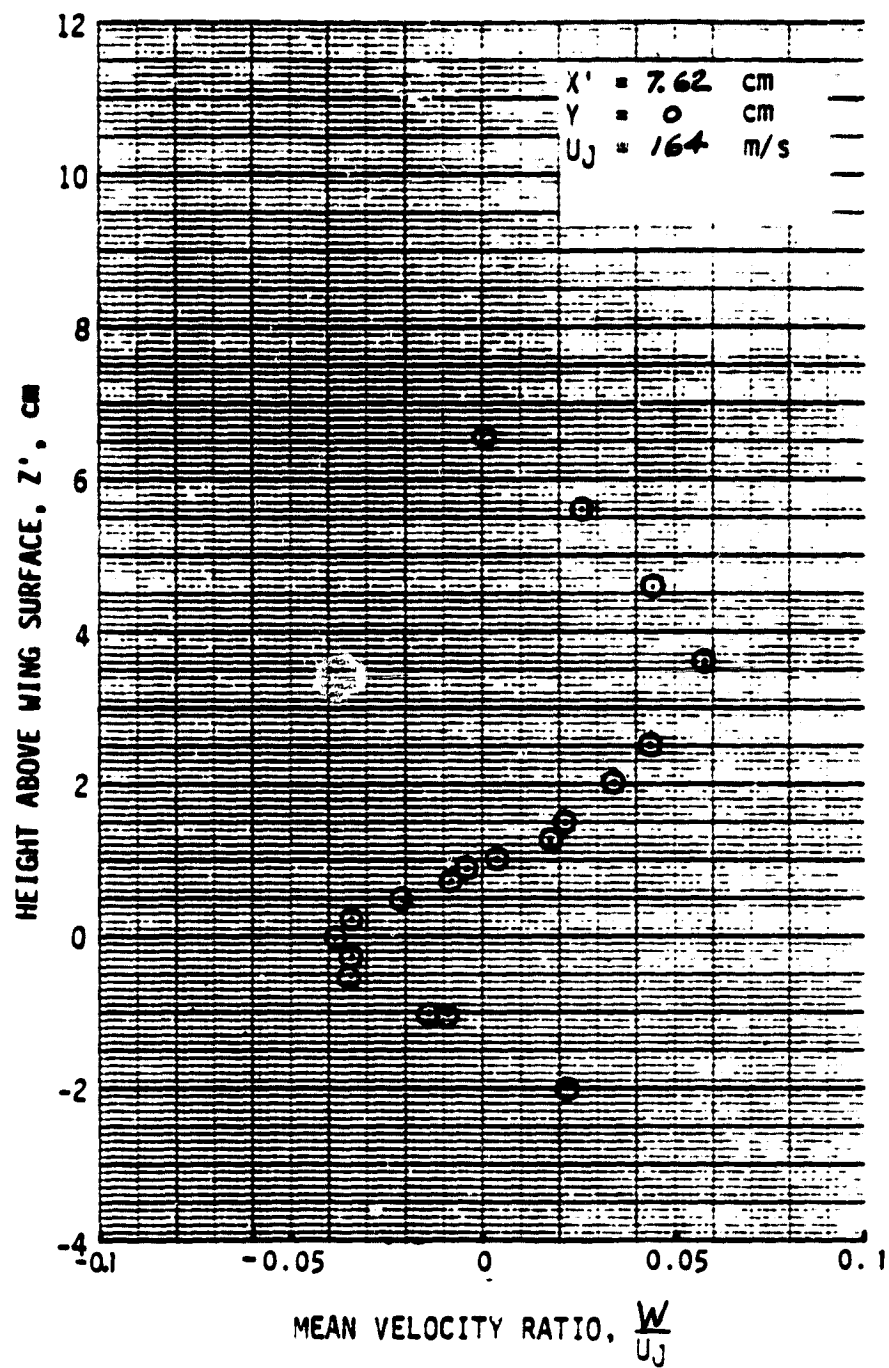


Figure A-7. Continued.

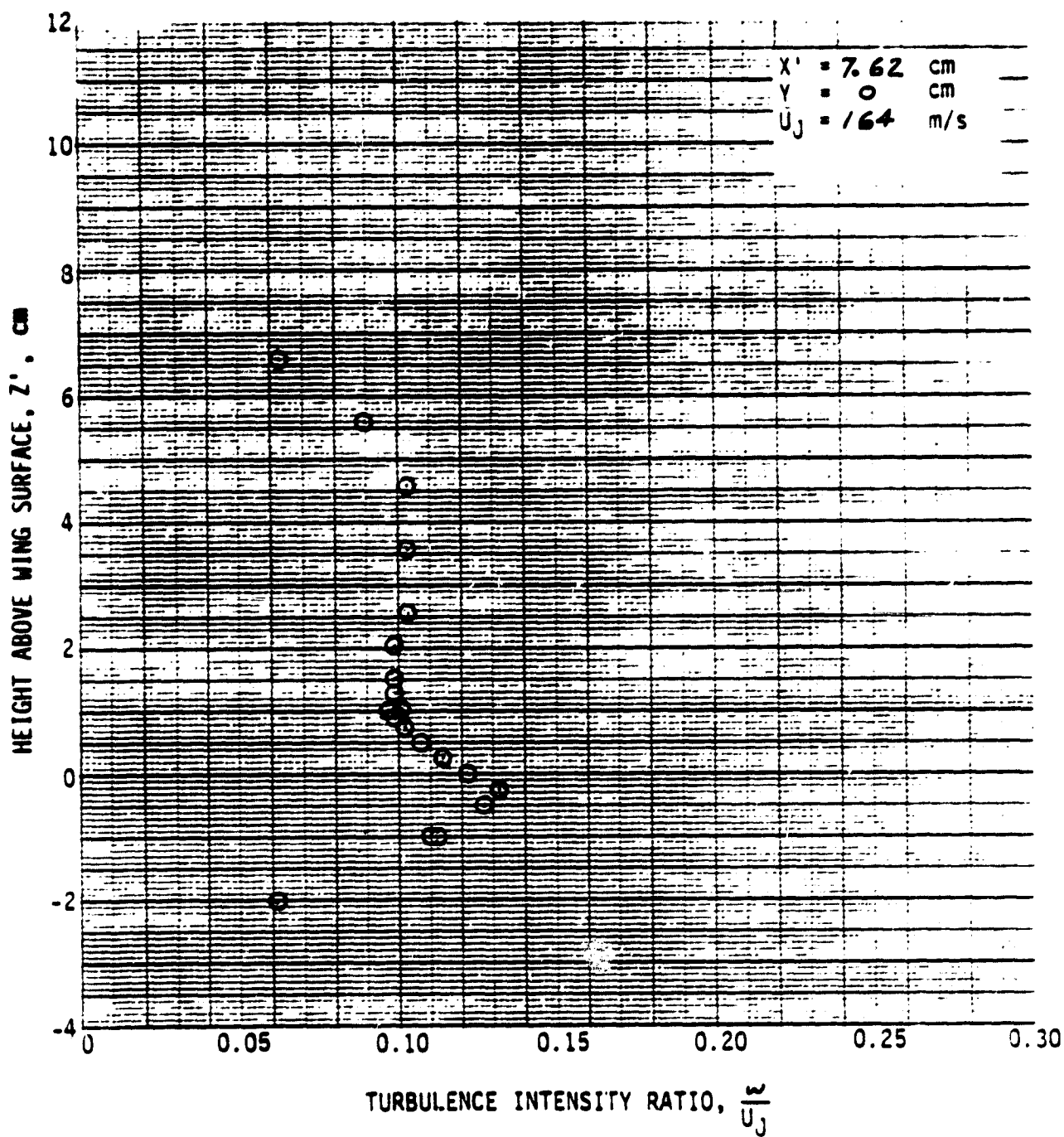


Figure A-7. Continued.

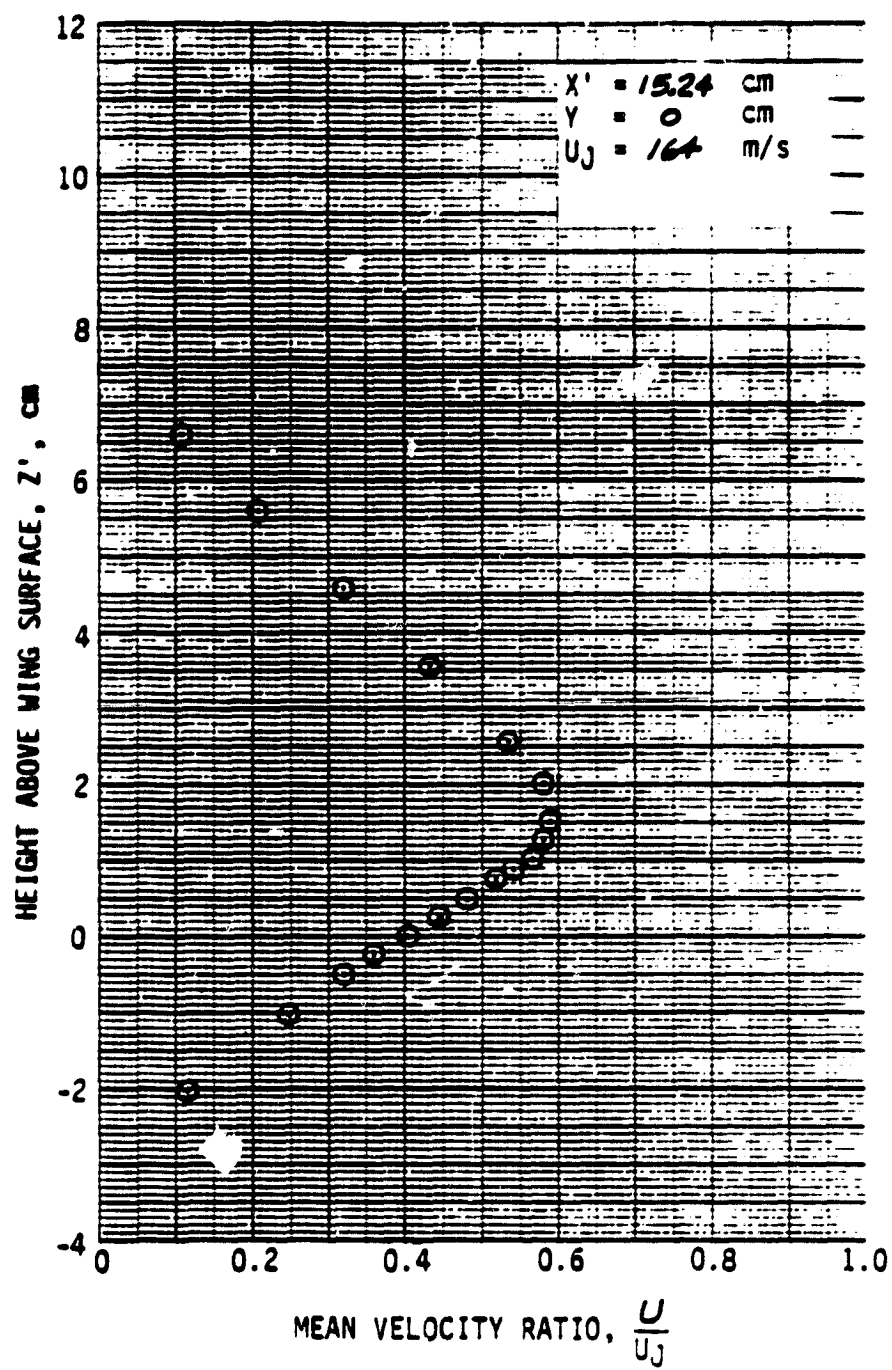


Figure A-7. Continued.

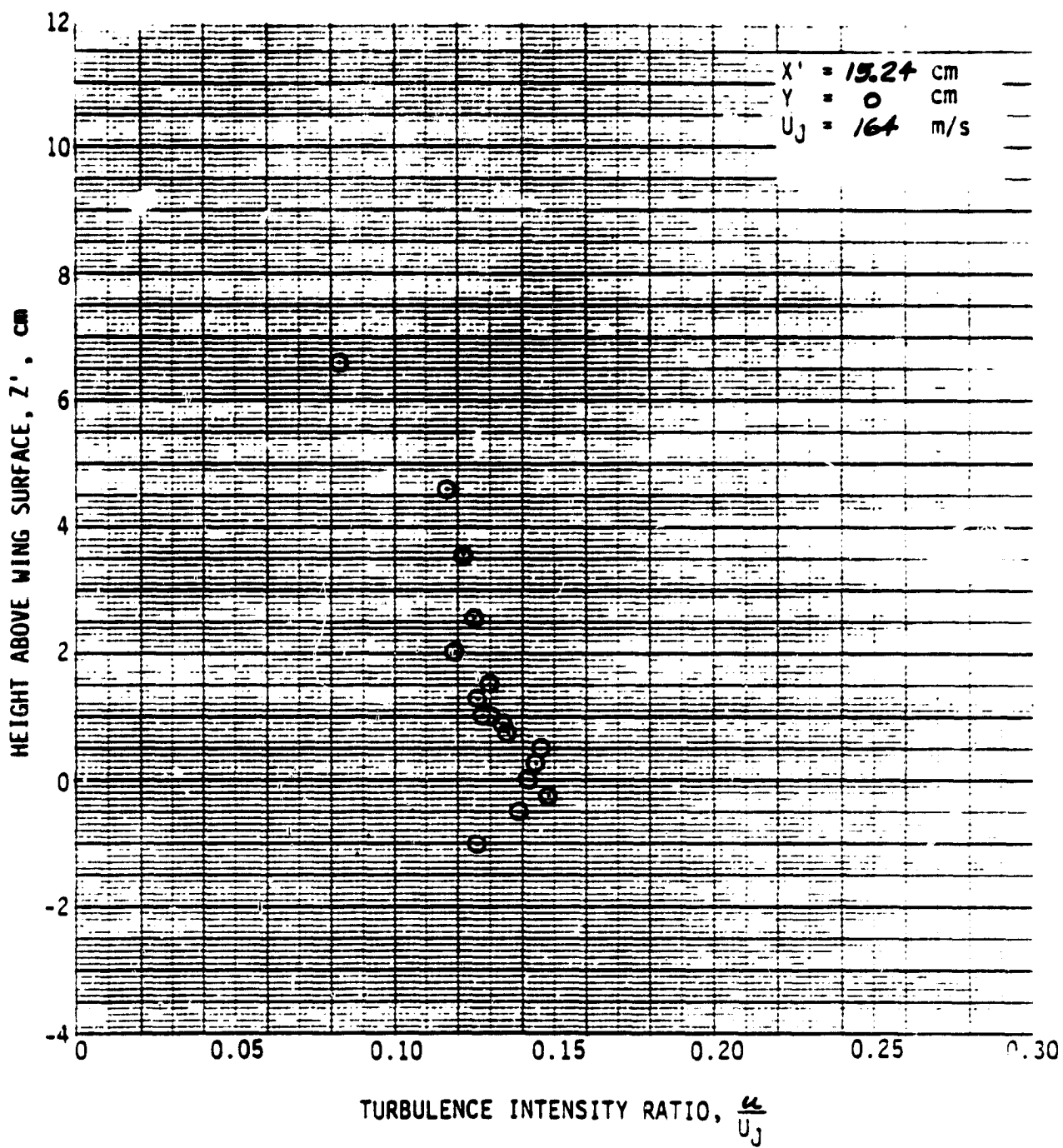


Figure A-7. Continued.

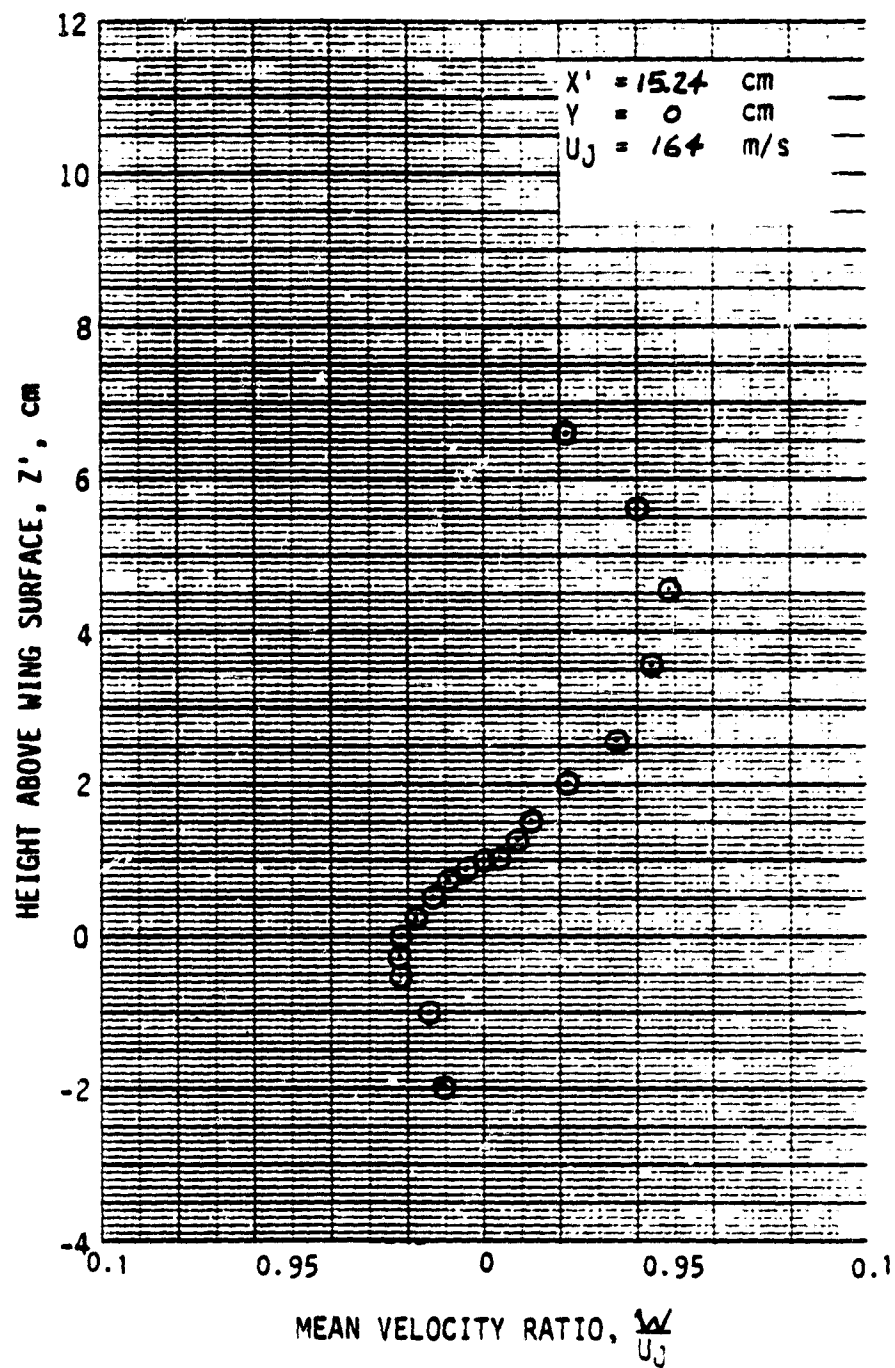


Figure A-7. Continued.

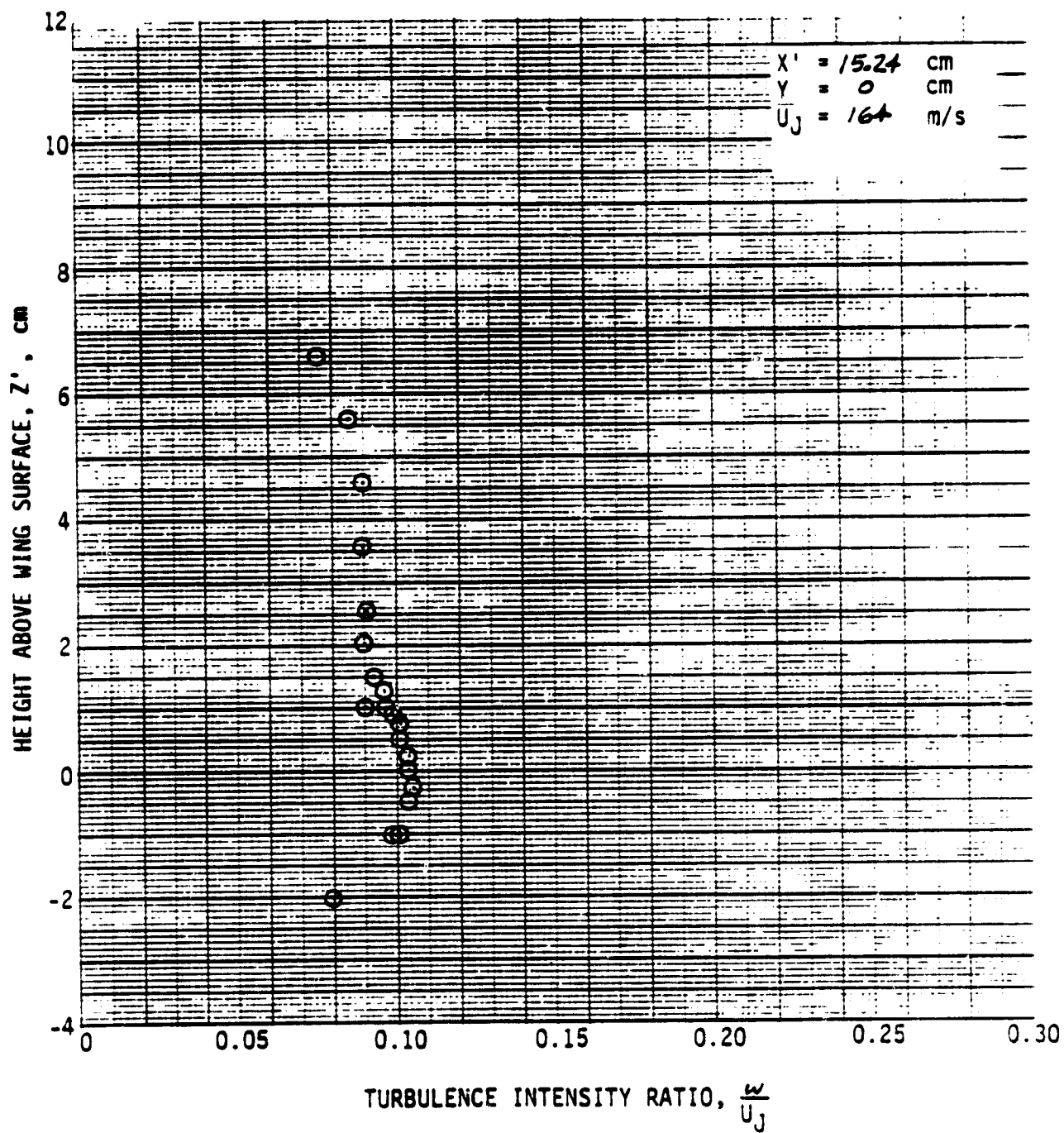


Figure A-7. Continued.

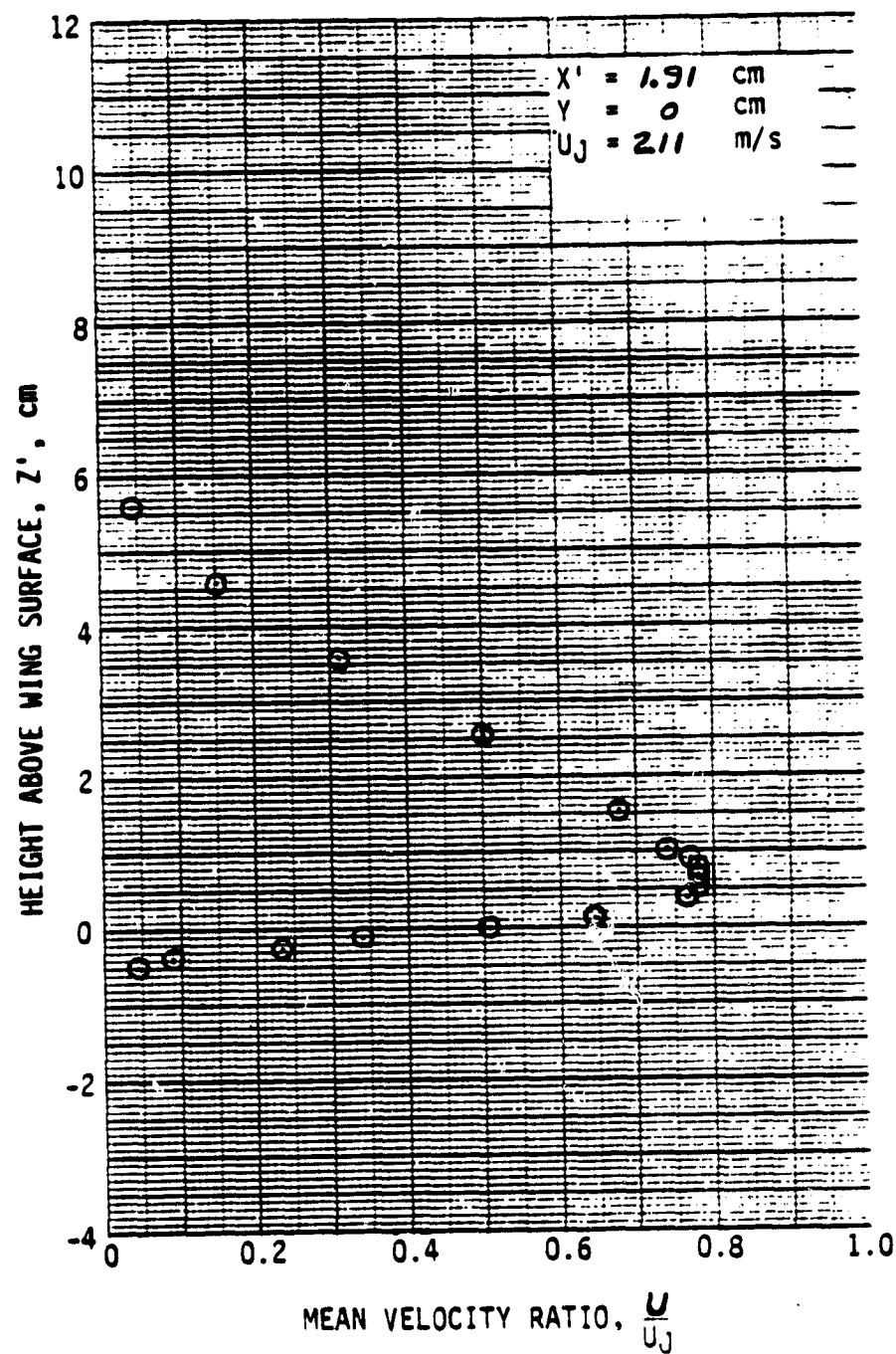


Figure A-7. Continued.

ORIGINAL PAGE IS
OF POOR QUALITY

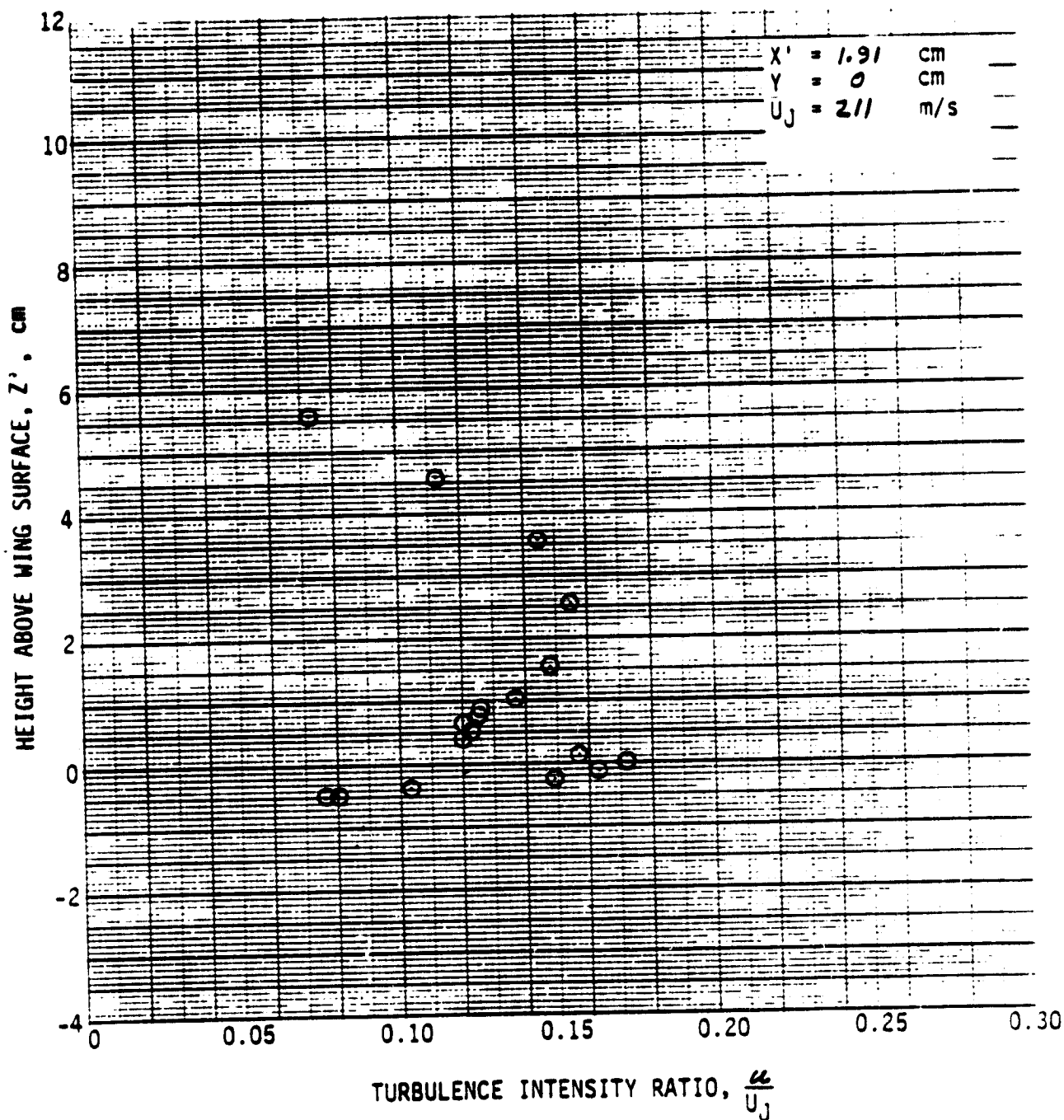


Figure A-7. Continued.

ORIGINAL PAGE IS
OF POOR QUALITY

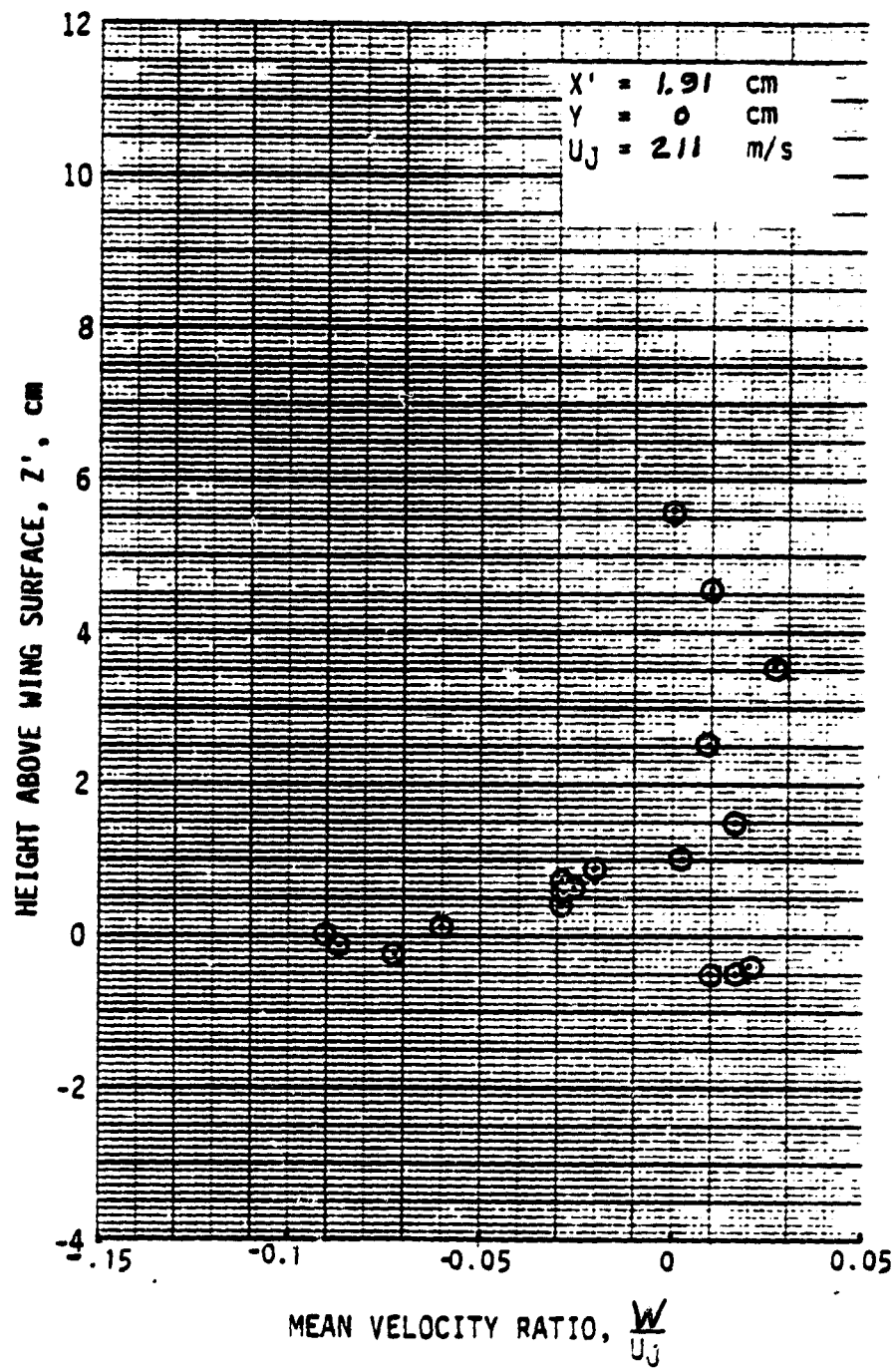


Figure A-7. Continued.

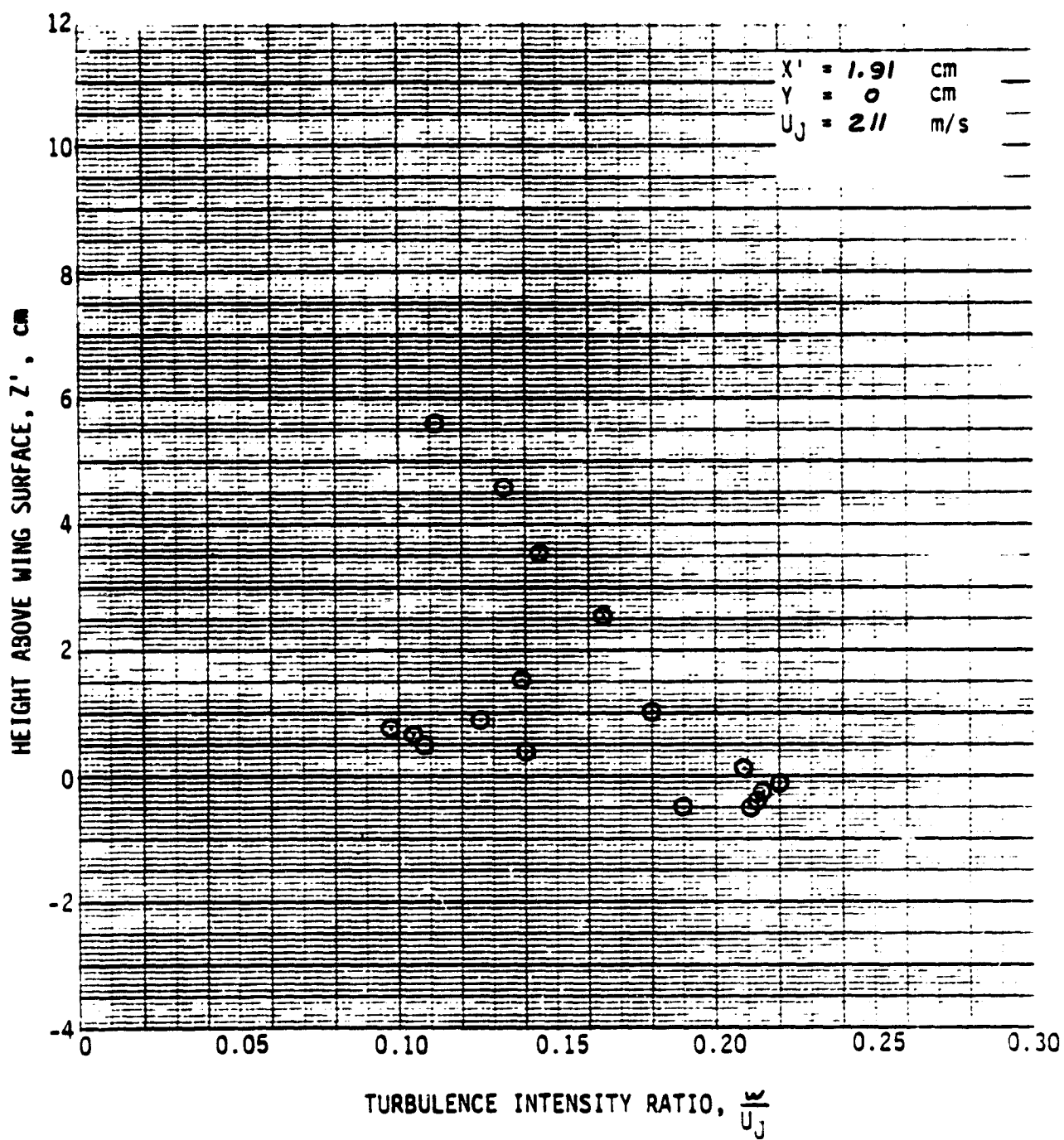


Figure A-7. Concluded.

APPENDIX B

WAKE FLOW SPACE-TIME CORRELATIONS

This appendix contains two-point correlation data obtained from two cross-wire probes located in the flow. Auto-correlations and cross-correlations are presented for separations in the X' , Y , and Z' directions. Included are variations in flap angle and in initial turbulence conditions. All variations are made from the following condition:

$$U_j = 180 \text{ m/s}$$

No Screen

$$\delta_f = 30^\circ$$

$$X' = 1.91 \text{ cm}$$

$$Y = 0$$

The data are arranged as shown in Table B-1 where each line represents two plots - one for each velocity component, U and W .

TABLE B-1 DATA CONTENTS

Figure	Initial Turbulence	δ_f	$X' - \text{cm}$	$Y - \text{cm}$	$Z' - \text{cm}$	Separation Direction
B-1 ↓	No Screen ↓	30° ↓	1.91 3.81	0 ↓	0 ↓	X' ↓
B-2	No Screen	30°	1.91	0	0	Y'
B-3 ↓	No Screen ↓	30° ↓	1.91 ↓	0 ↓	0 0.64 1.27 1.91 2.54	Z' ↓
B-4	No Screen	60°	1.91	0	0	X'
B-5 ↓	Screen ↓	30° ↓	1.91 ↓	0 ↓	0 ↓	X' Y Z'

VEL. COMP.	U_j m/s	INIT. TURB.	Δf	$X' - \text{cm}$	$\Delta X' - \text{cm}$	$Y - \text{cm}$	$\Delta Y - \text{cm}$	$Z' - \text{cm}$	$\Delta Z' - \text{cm}$
U	180.	NO SCREEN	30°	1.91	NOTED	0	0	0	0

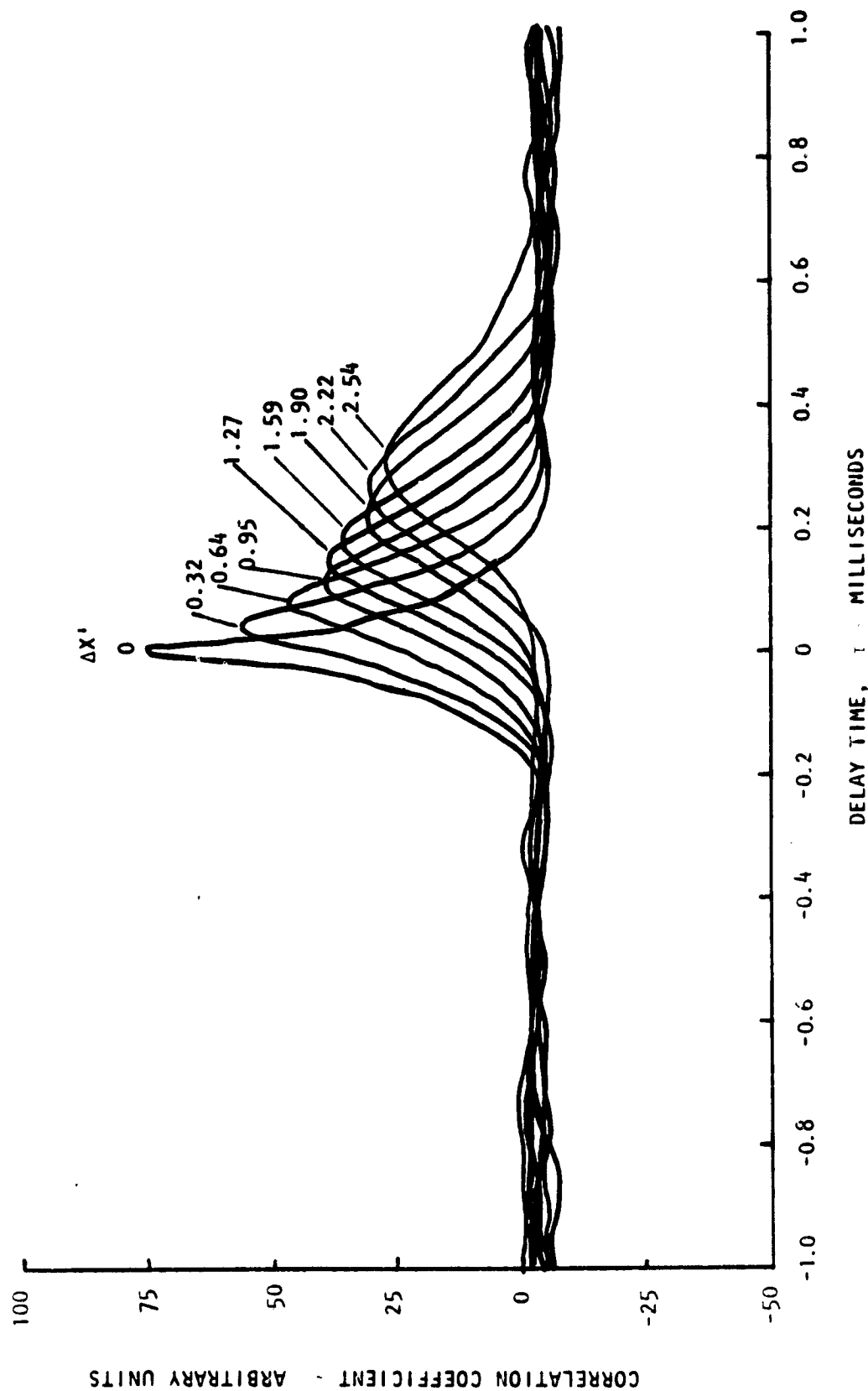


Figure B-1. Space-Time Correlation Function

VEL. COMP.	U_j m/s	INIT. TURB.	θ_f	X' cm	$\Delta X'$ cm	Y cm	ΔY cm	Z' cm	$\Delta Z'$ cm
W	180.	NO SCREEN	30"	1.91	NOTED	0	0	0	0

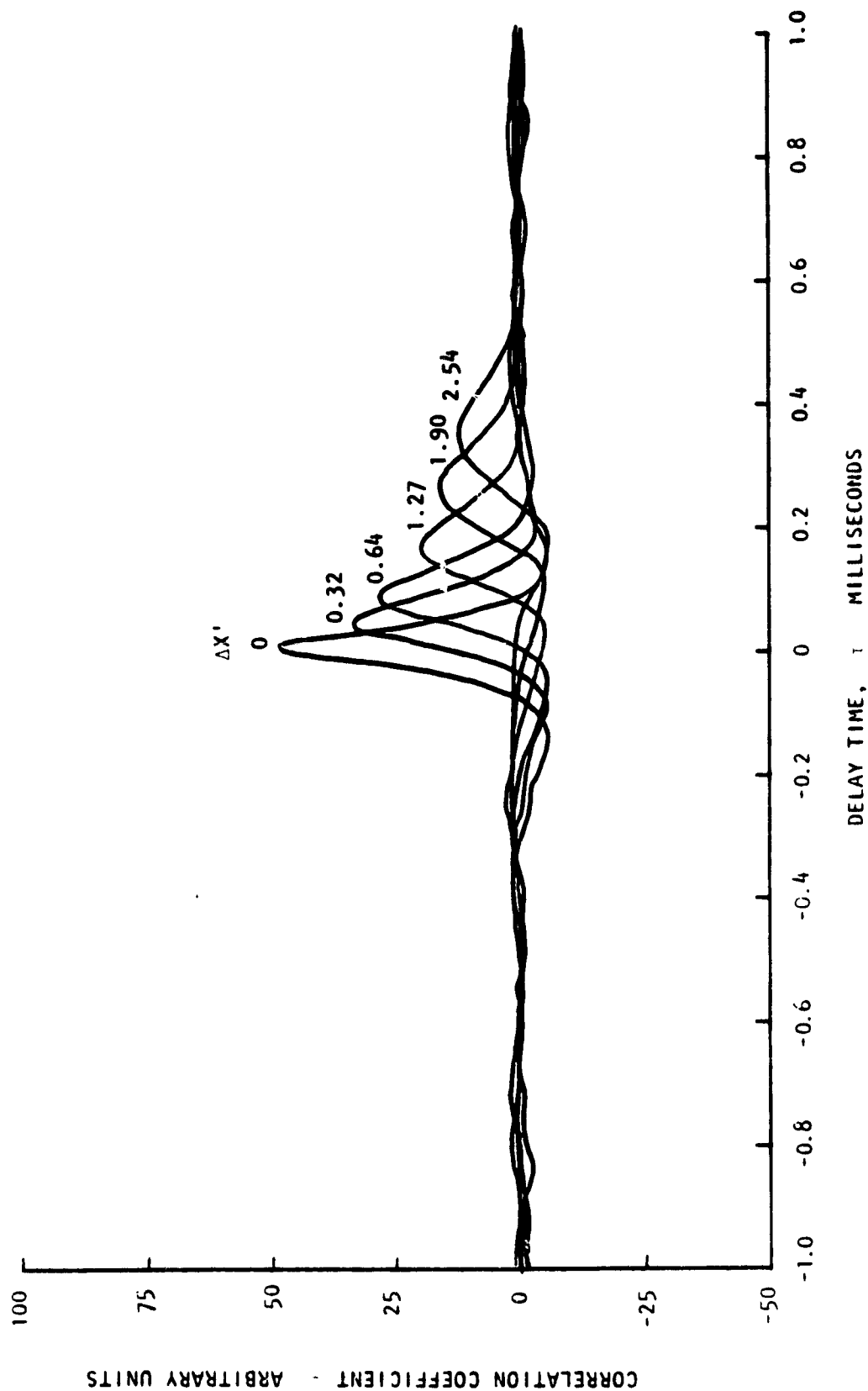


Figure B-1. Space-Time Correlation Function
(B) X' Variations

VEL. COMP.	U_j m/s	INIT. TURB.	θ	X' cm	$\Delta X'$ cm	Y cm	ΔY cm	Z' cm	$\Delta Z'$ cm
U	180.	NO SCREEN	30°	3.81	NOTED	0	0	0	0

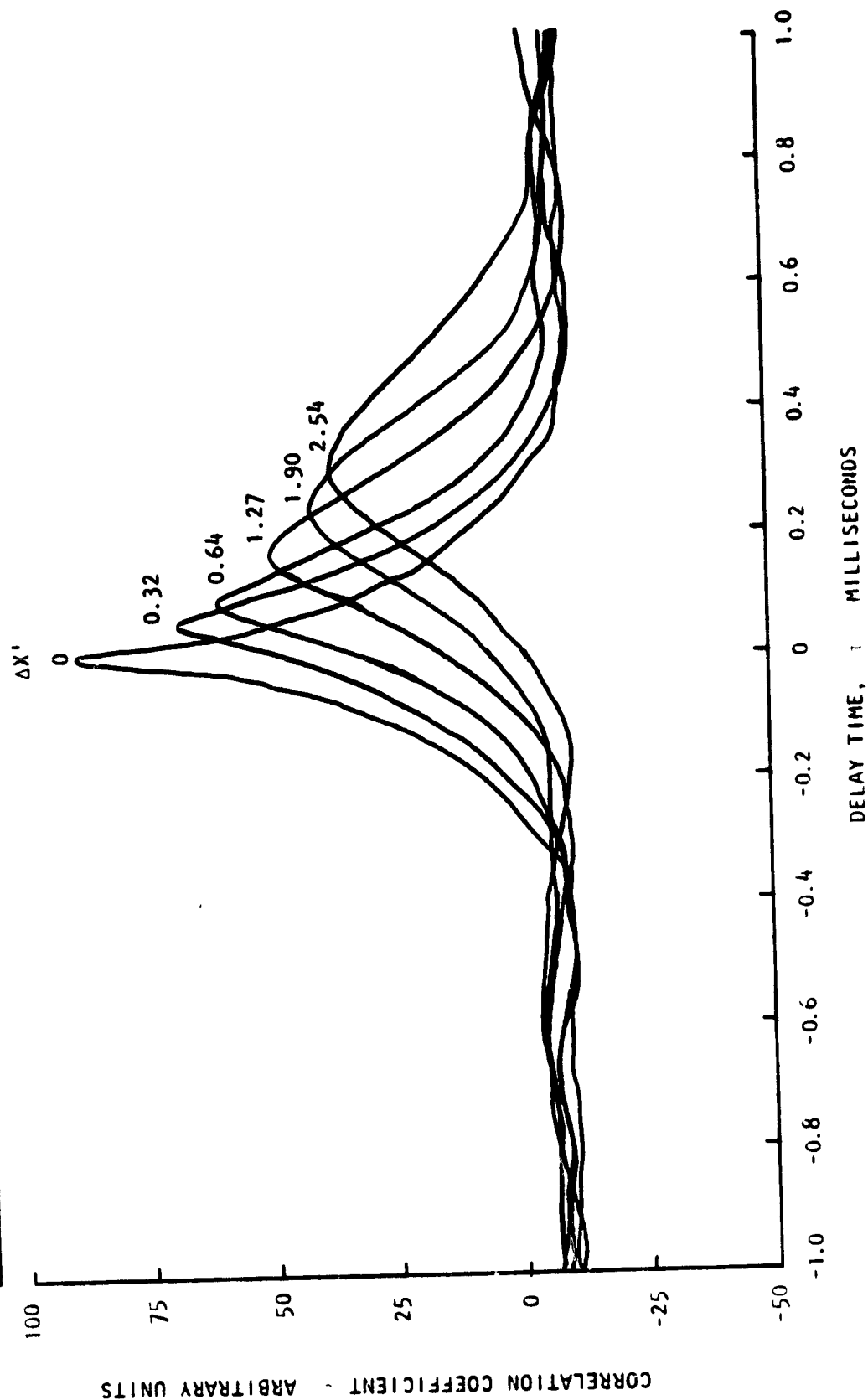


Figure B-1. Space-Time Correlation Function

VEL. COMP.	U_j m/s	INIT. TURB.	τ_f	X' cm	$\Delta X'$ cm	Y cm	ΔY cm	Z' cm	$\Delta Z'$ cm
W	180.	NO SCREEN	30'	3.81	NOTED	0	0	0	0

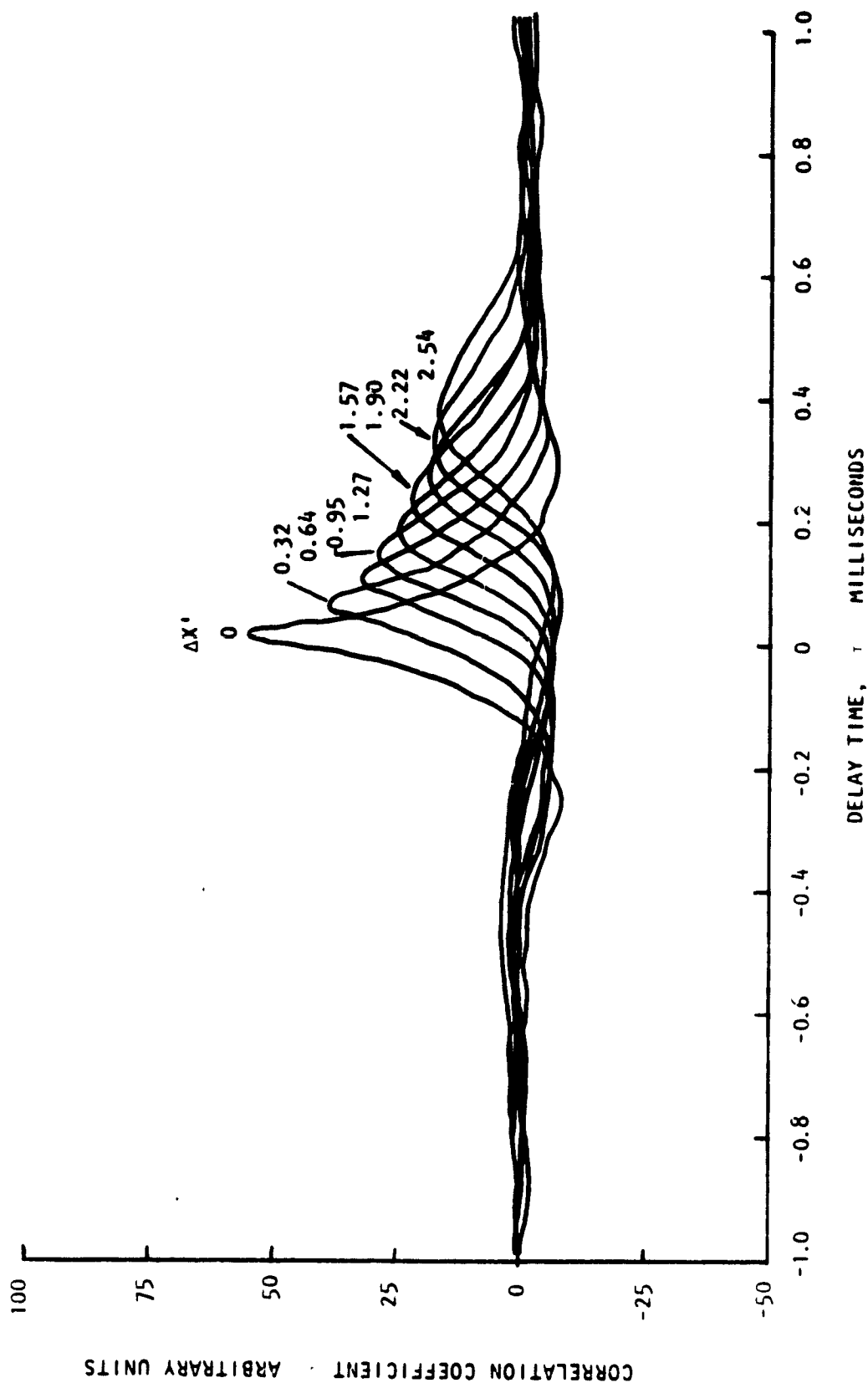


Figure B-1. Space-Time Correlation Function
(D) X' Variations

VEL. COMP.	U_j m/s	INIT. TURB.	α_j	X' cm	$\Delta X'$ cm	Y cm	ΔY cm	Z' cm	$\Delta Z'$ cm
U	180.	NO SCREEN	30°	1.91	0	0	NOTED	0	0

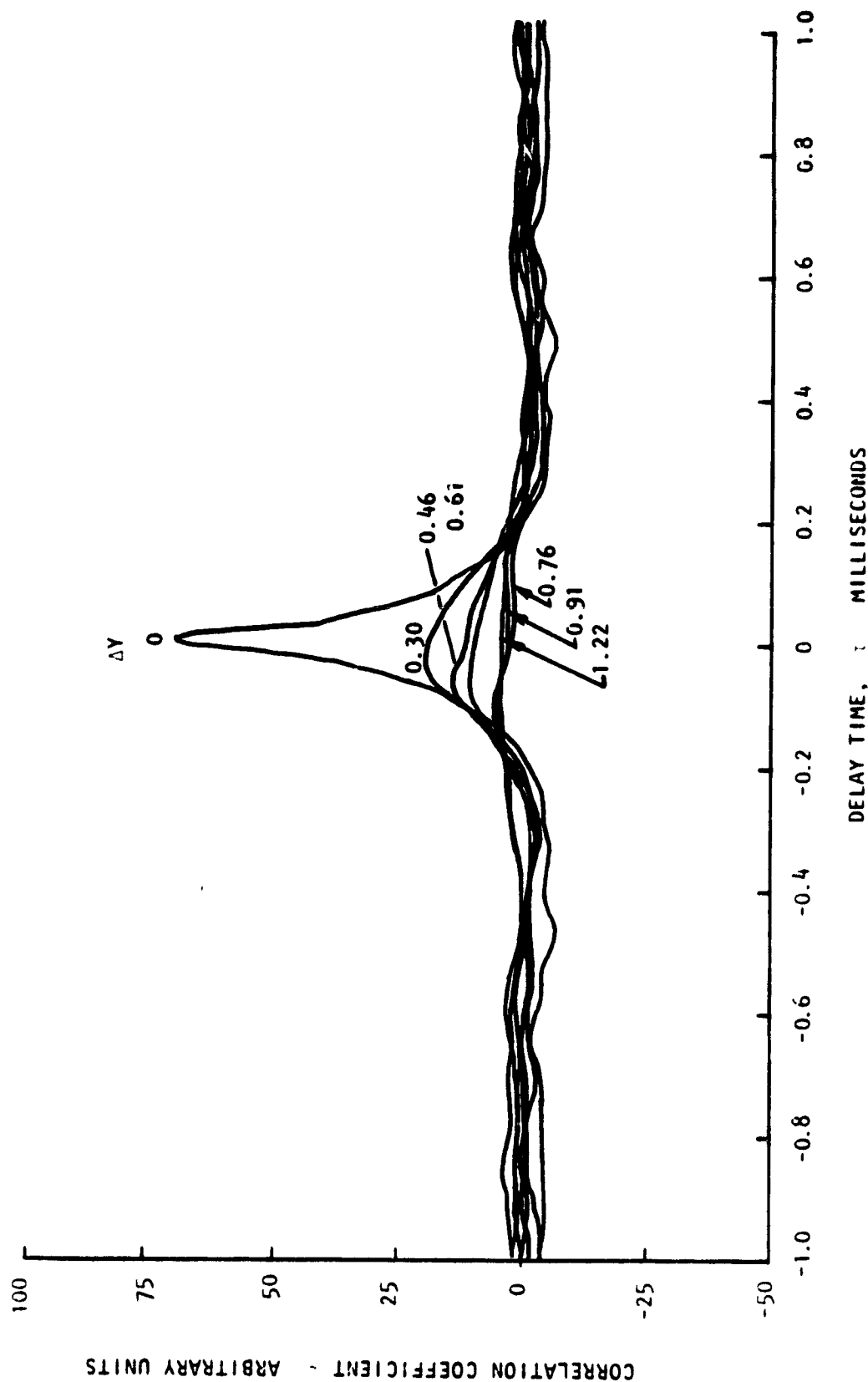


Figure B-2. Space-Time Correlation Function

(A) V. V. V. V. V.

VEL. COMP.	U_j m/s	INIT. TURB.	θ	X' cm	$\Delta X'$ cm	Y cm	ΔY cm	Z' cm	$\Delta Z'$ cm
W	180.	NO SCREEN	30"	1.91	0	0	NOTED	0	0

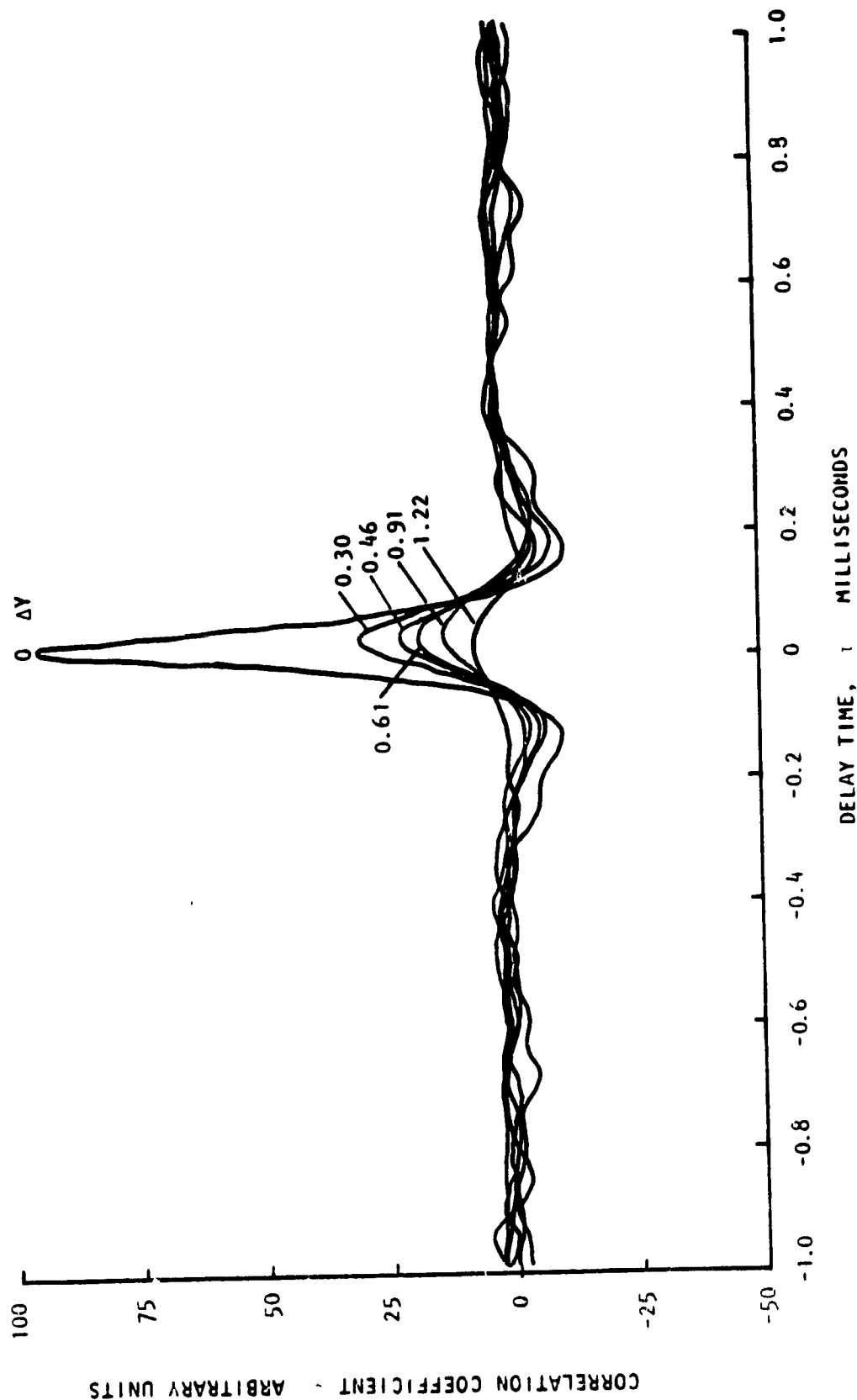


Figure B-2. Space-Time Correlation Function
(B) Y Variations

VEL. COMP.	U_j m/s	INIT. TURB.	f	X^1 - cm	ΔX^1 - cm	Y - cm	ΔY - cm	Z^1 - cm	ΔZ^1 - cm
U	180.	NO SCREEN	3)	1.91	0	0	0	0	NOTED

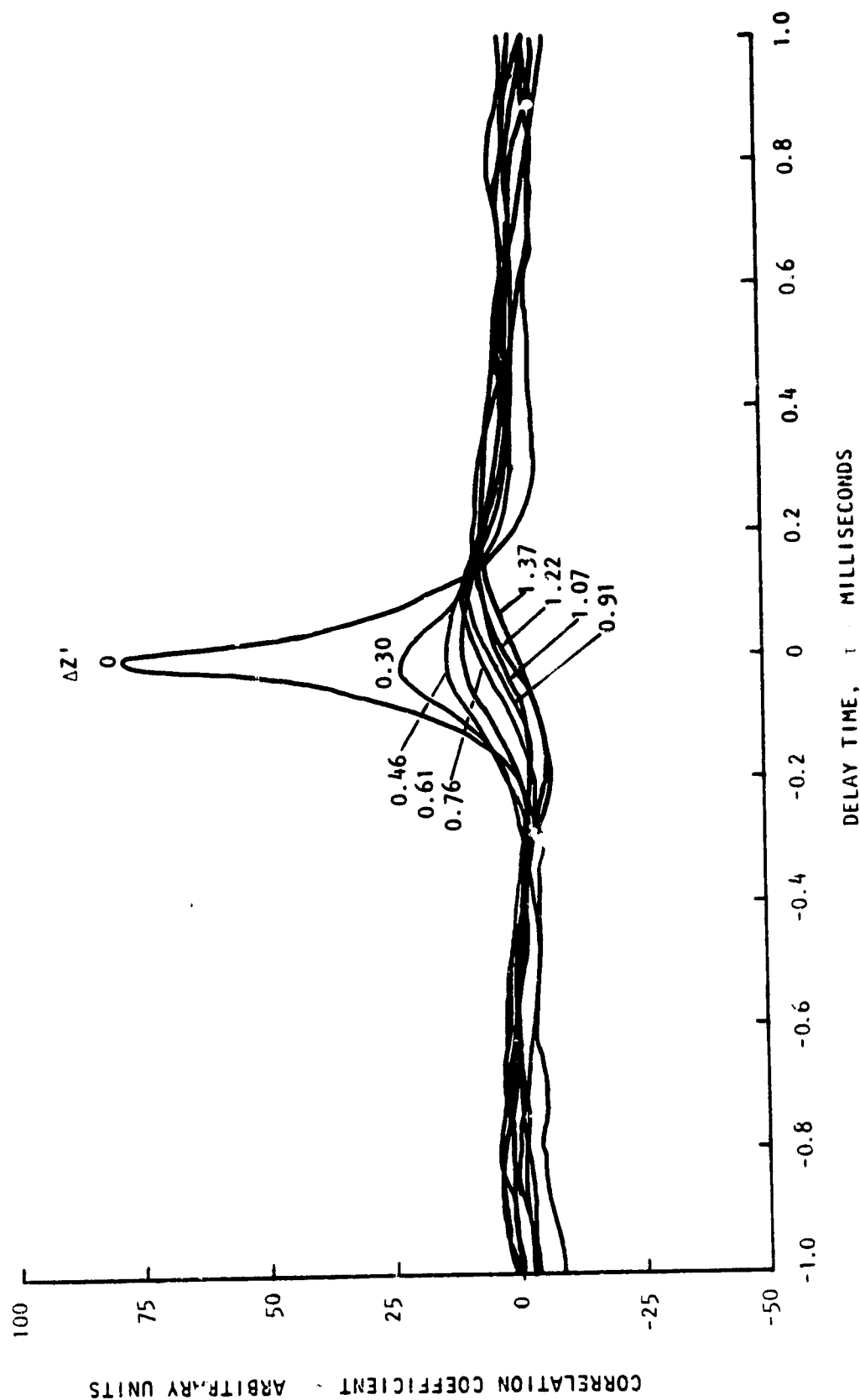


Figure B-3. Space-Time Correlation Function

REL. COMP.	U_J m/s	INIT. TURB.	θ_f	$X' - \text{cm}$	$\Delta X' - \text{cm}$	$Y - \text{cm}$	$\Delta Y - \text{cm}$	$Z' - \text{cm}$	$\Delta Z' - \text{cm}$
W	180.	NO SCREEN	30''	1.91	0	0	0	0	NOTED

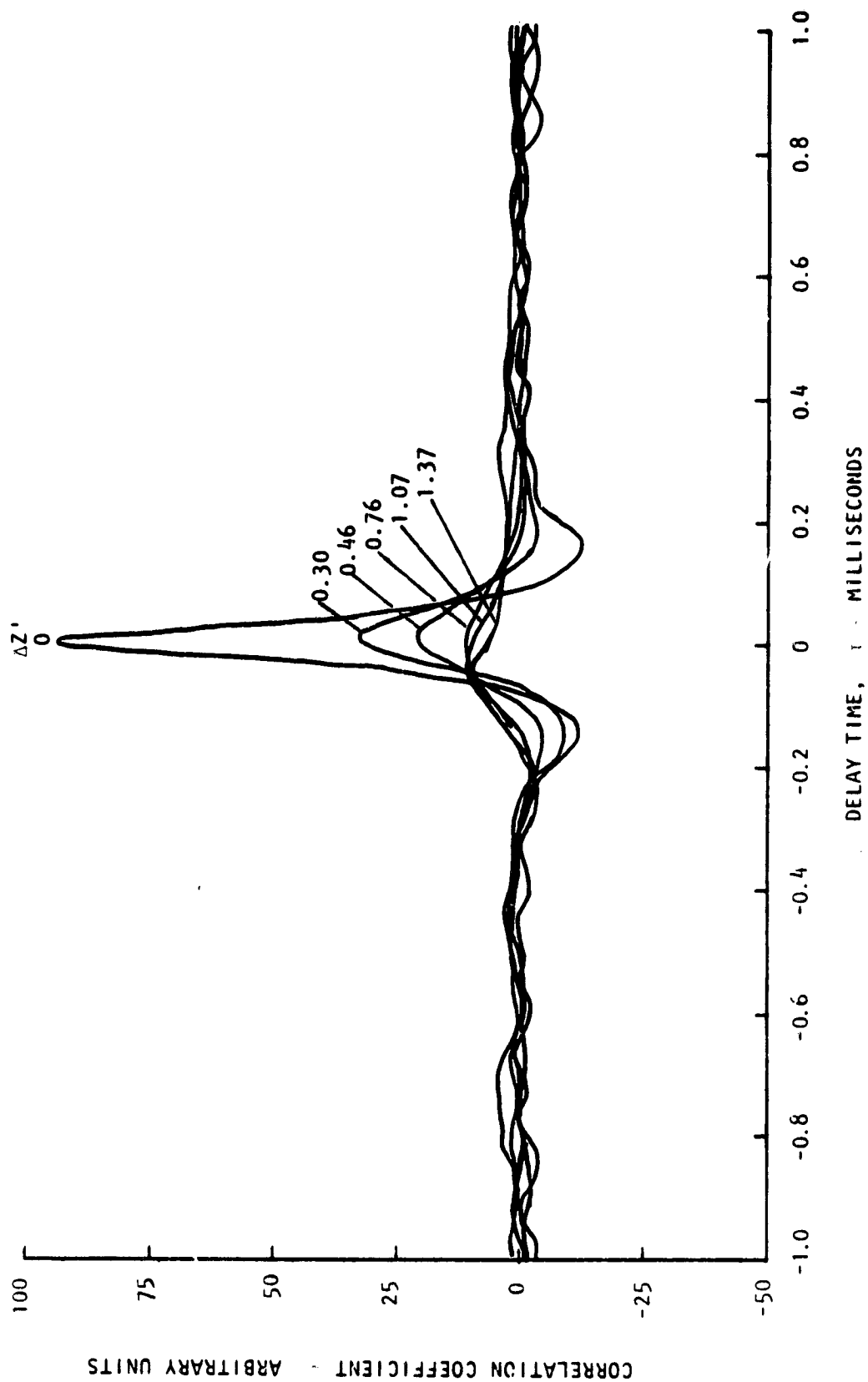


Figure B-3. Space-Time Correlation Function
(B) Z' Variations

VEL. COMP.	U_j m/s	INIT. TURB.	θ_f	X' cm	$\Delta X'$ cm	Y' cm	$\Delta Y'$ cm	Z' cm	$\Delta Z'$ cm
U	180.	NO SCREEN	30"	1.91	0	0	0	0.64	NOTED

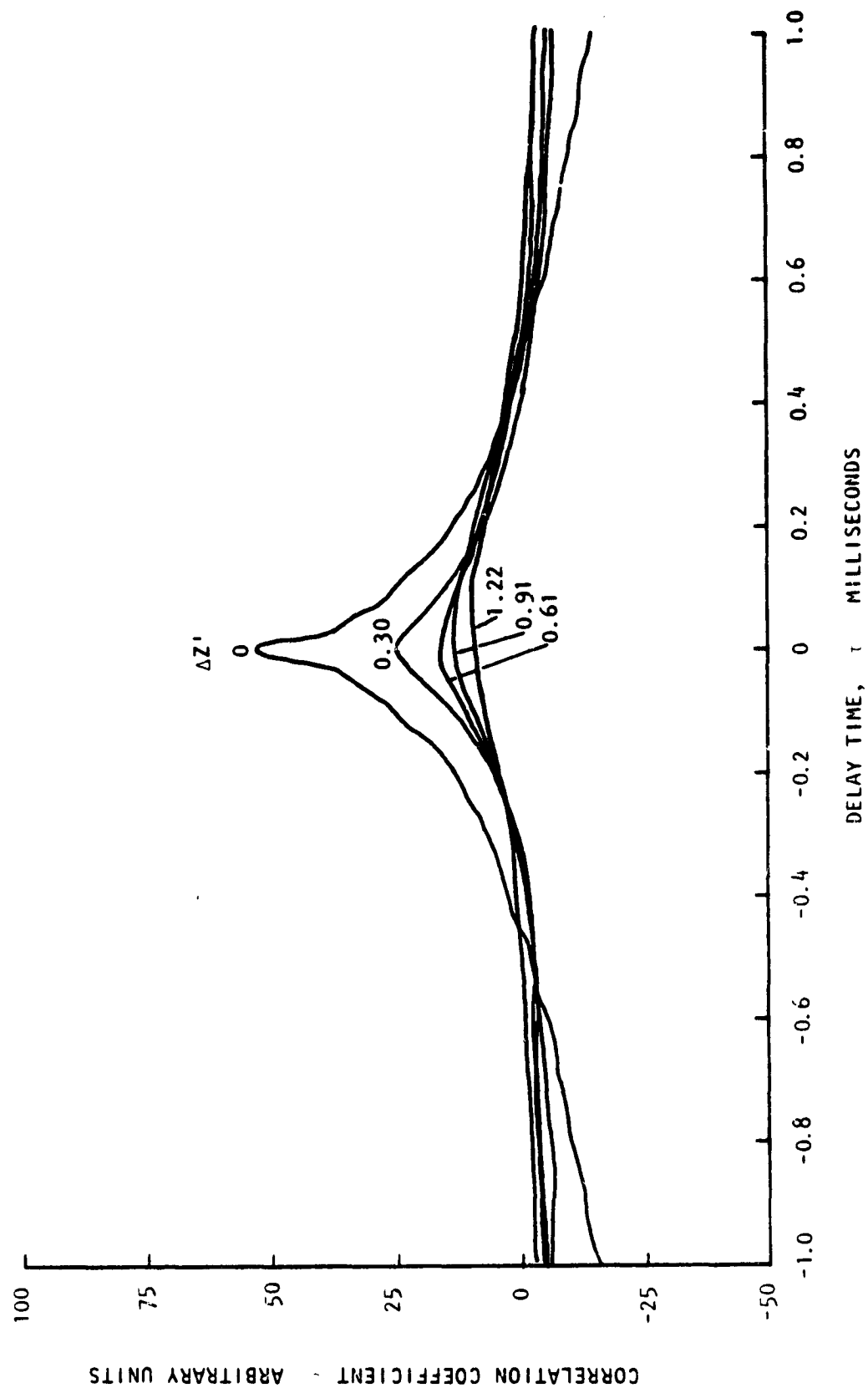


Figure B-3. Space-Time Correlation Function
(c) Z' Variations

VEL. COMP.	U_J m/s	INIT. TURB.	f	X' cm	$\Delta X'$ cm	Y cm	ΔY cm	Z' cm	$\Delta Z'$ cm
W	180.	NO SCREEN	30'	1.91	0	0	0	0.64	NOTED

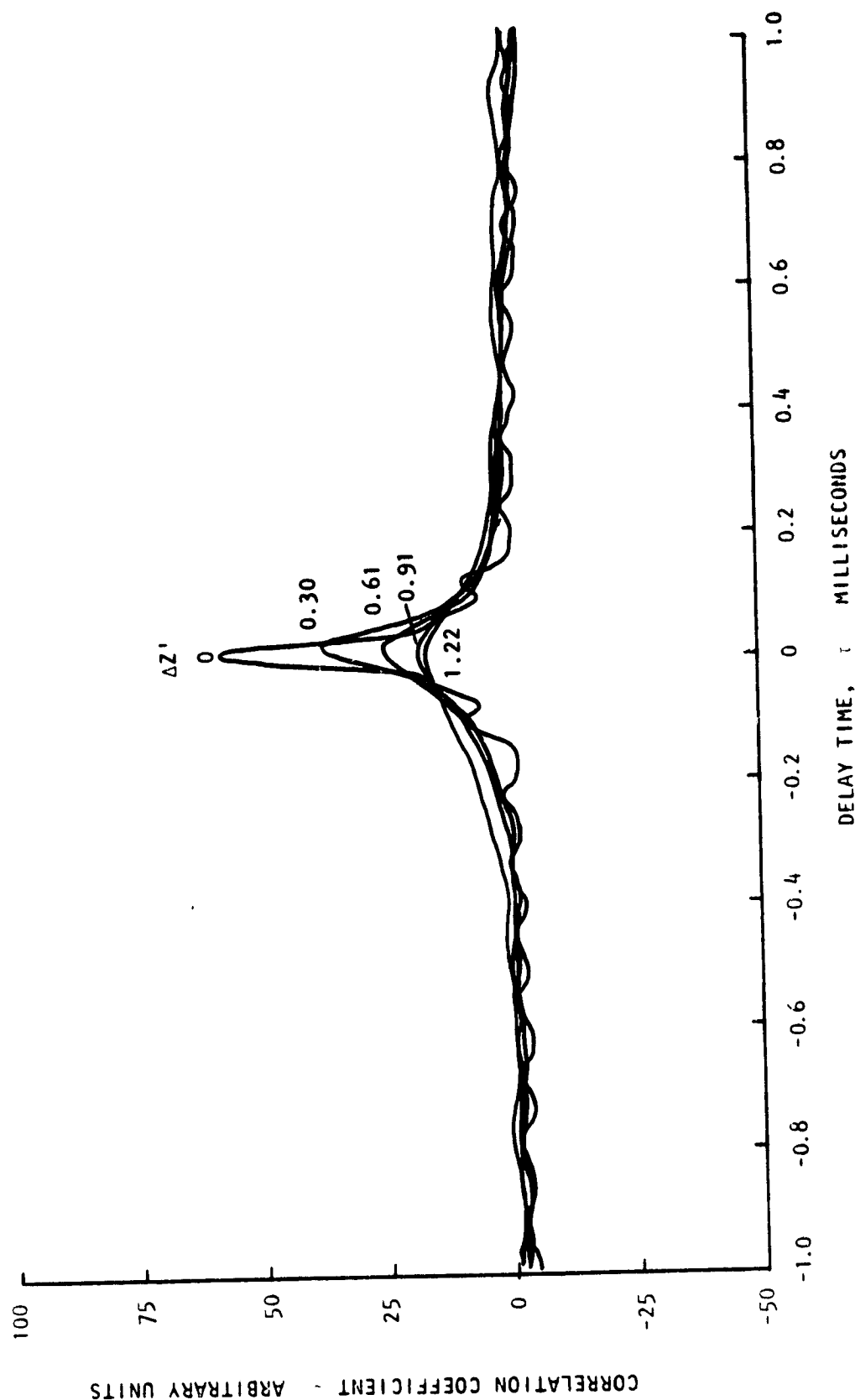


Figure B-3. Space-Time Correlation Function
(D) Z' Variations

VEL. COMP.	U_j m/s	INIT. TURB.	θ	X' cm	$\Delta X'$ cm	Y cm	ΔY cm	Z' cm	$\Delta Z'$ cm
U	180.	NO SCREEN	30°	1.91	0	0	0	1.27	NOTED

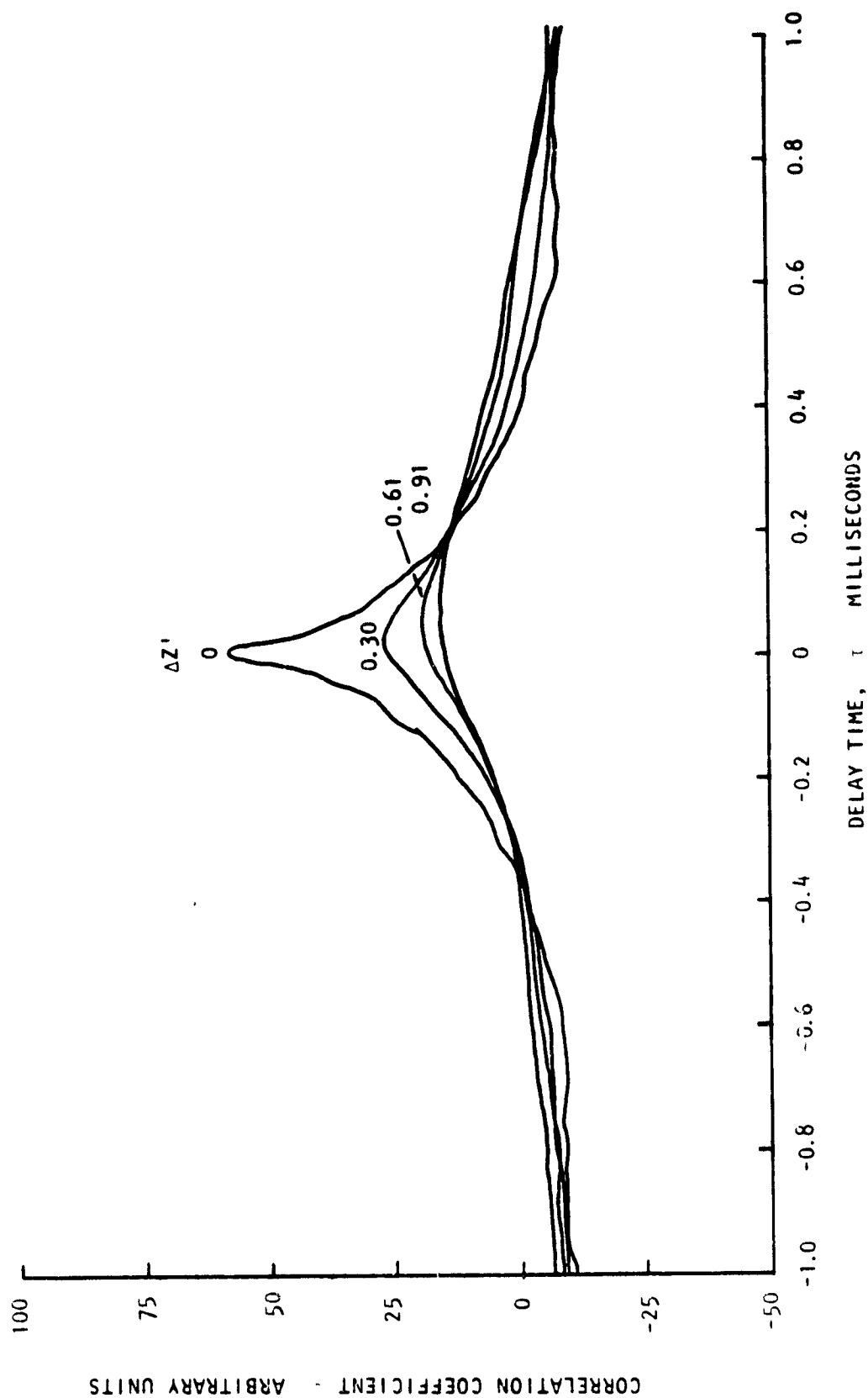


Figure B-3. Space-Time Correlation Function
(E) Z' Variations

VEL. COMP.	U_j m/s	INIT. TURB.	θ_f	X' cm	$\Delta X'$ cm	Y cm	ΔY cm	Z' cm	$\Delta Z'$ cm
W	180.	NO SCREEN	30°	1.91	0	0	0	1.27	NOTED

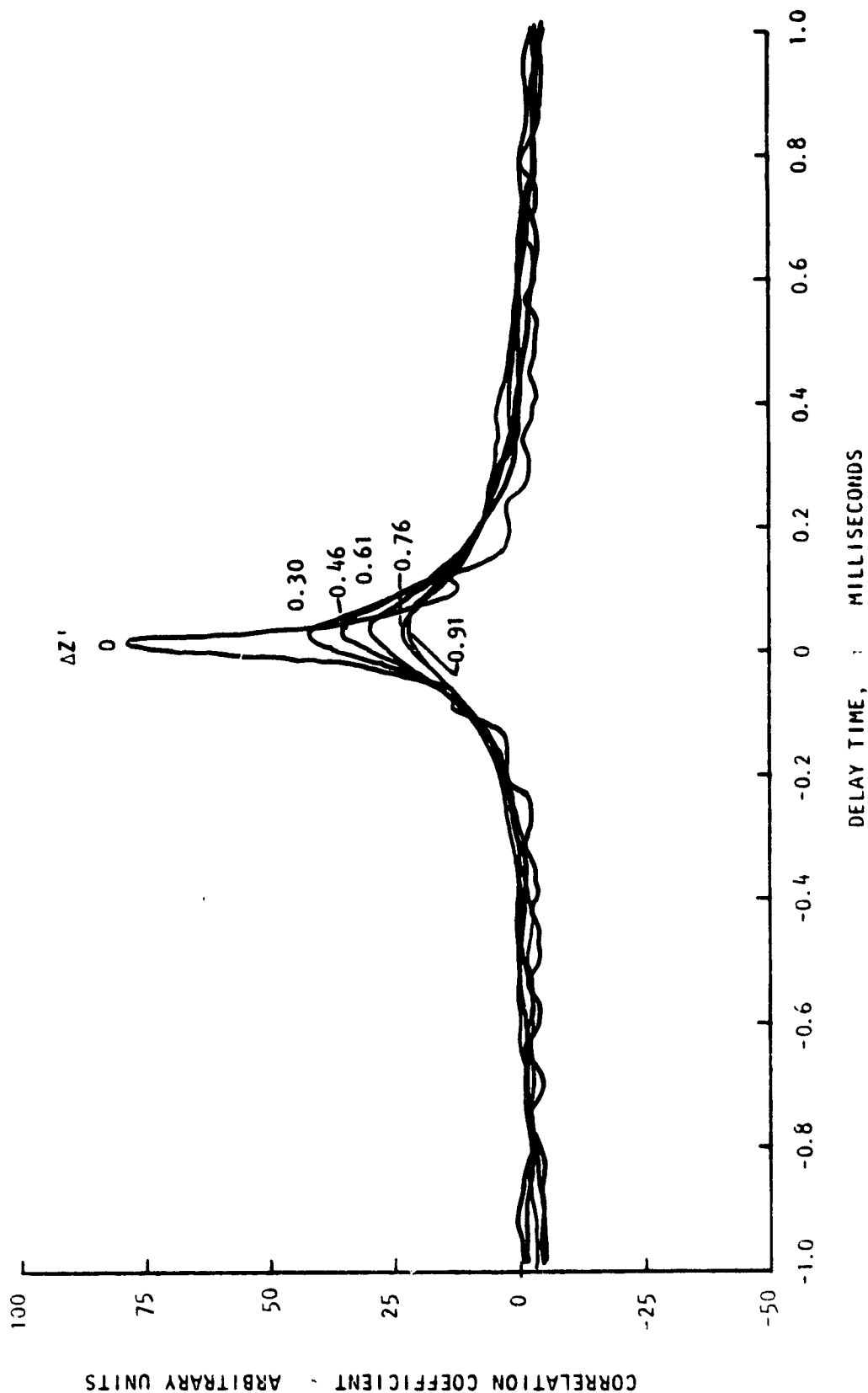


Figure B-3. Space-Time Correlation Function
(F) Z' Variations

VEL. COMP.	U_j m/s	INIT. TURB.	ϕ_f	$X' - \text{cm}$	$\Delta X' - \text{cm}$	$Y - \text{cm}$	$\Delta Y - \text{cm}$	$Z' - \text{cm}$	$\Delta Z' - \text{cm}$
U	180.	NO SCREEN	30°	1.91	0	0	0	1.91	NOTED

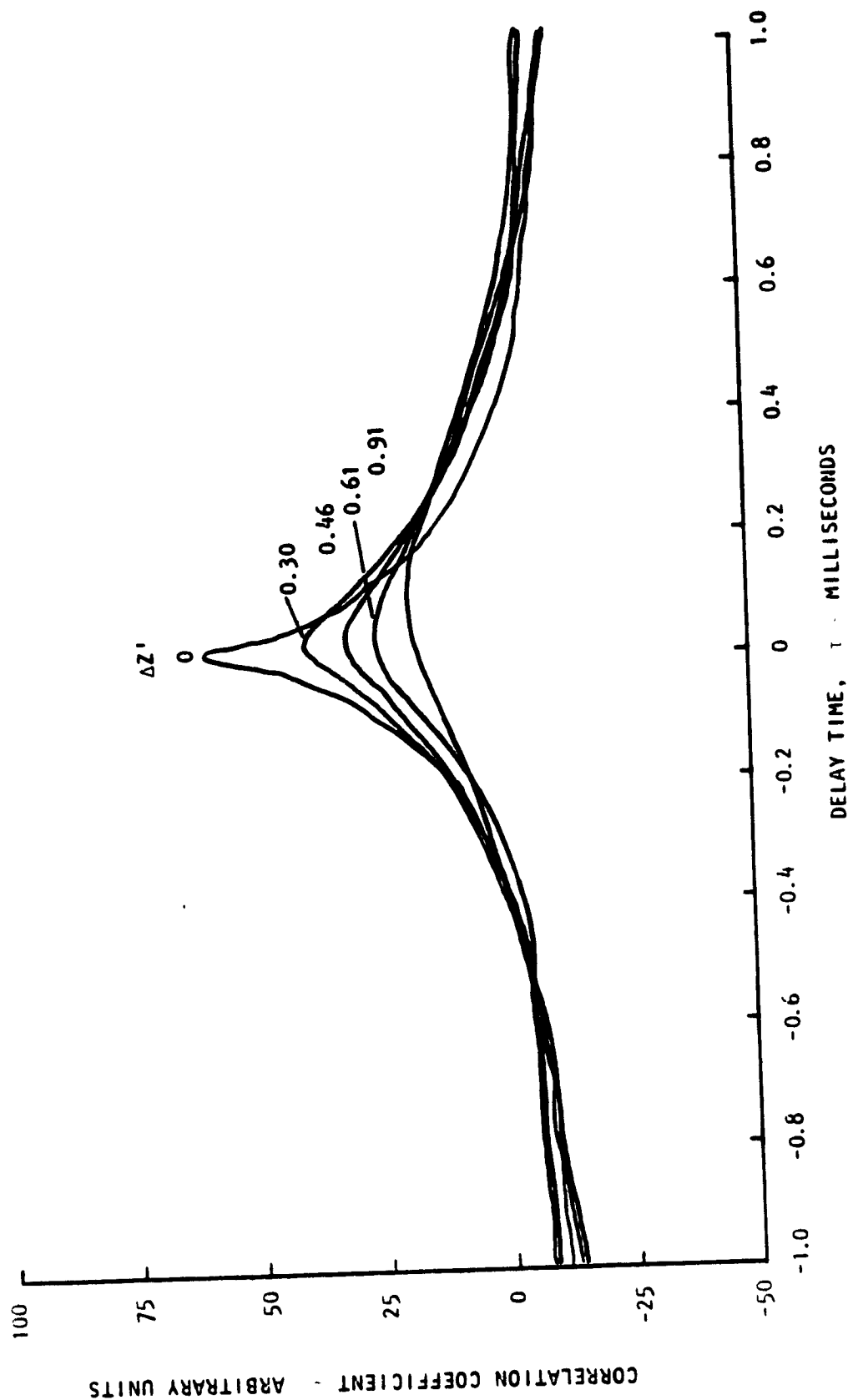


Figure B-3. Space-Time Correlation Function
(G) Z' Variations

VEL. COMP.	U_j m/s	INIT. TURB.	θ	X' cm	$\Delta X'$ cm	Y cm	ΔY cm	Z' cm	$\Delta Z'$ cm
W	180.	NO SCREEN	30°	1.91	0	0	0	1.91	NOTED

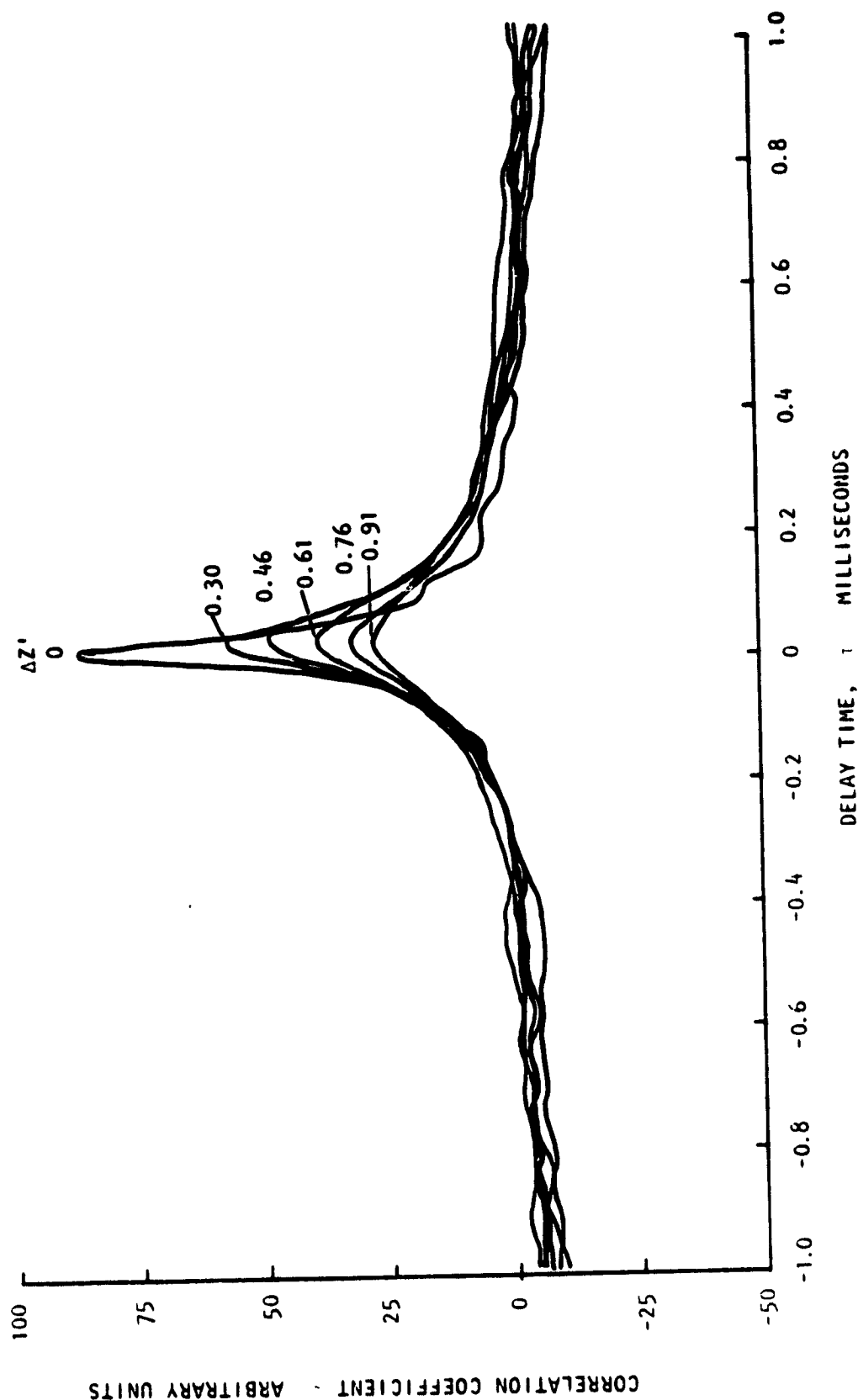


Figure B-3. Space-Time Correlation Function
(H) Z' Variations

VEL. COMP.	U_j m/s	INIT. TURB.	θ_f	X' cm	$\Delta X'$ cm	Y cm	ΔY cm	Z' cm	$\Delta Z'$ cm
U	180.	NO SCREEN	30°	1.91	0	0	0	2.54	NOTED

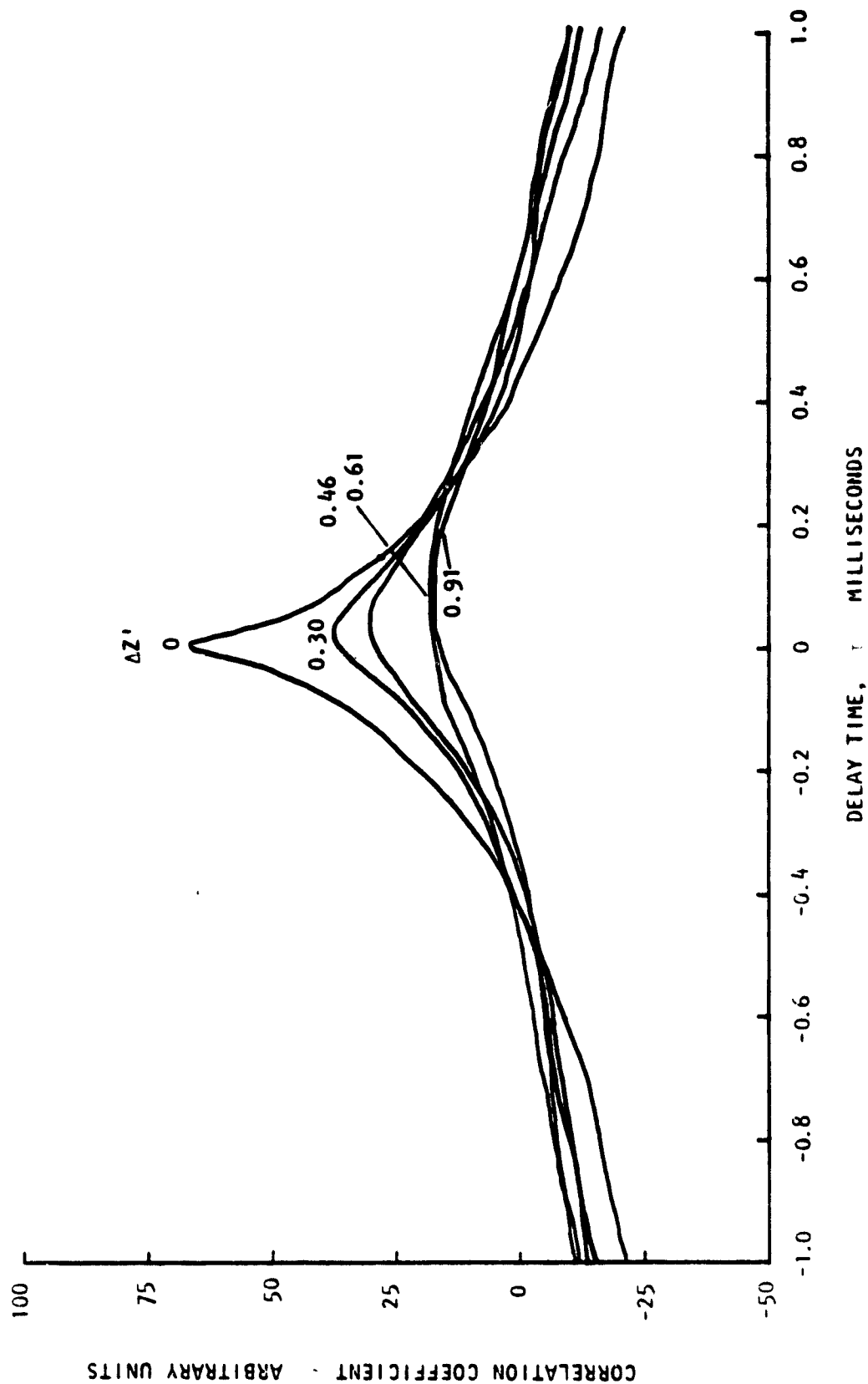


Figure B-3. Space-Time Correlation Function
(1) Z' Variations

VEL. COMP.	U_j m/s	INIT. TURB.	θ	X' - cm	$\Delta X'$ - cm	Y - cm	ΔY - cm	Z' - cm	$\Delta Z'$ - cm
W	180.	NO SCREEN	30°	1.91	0	0	0	2.54	NOTED

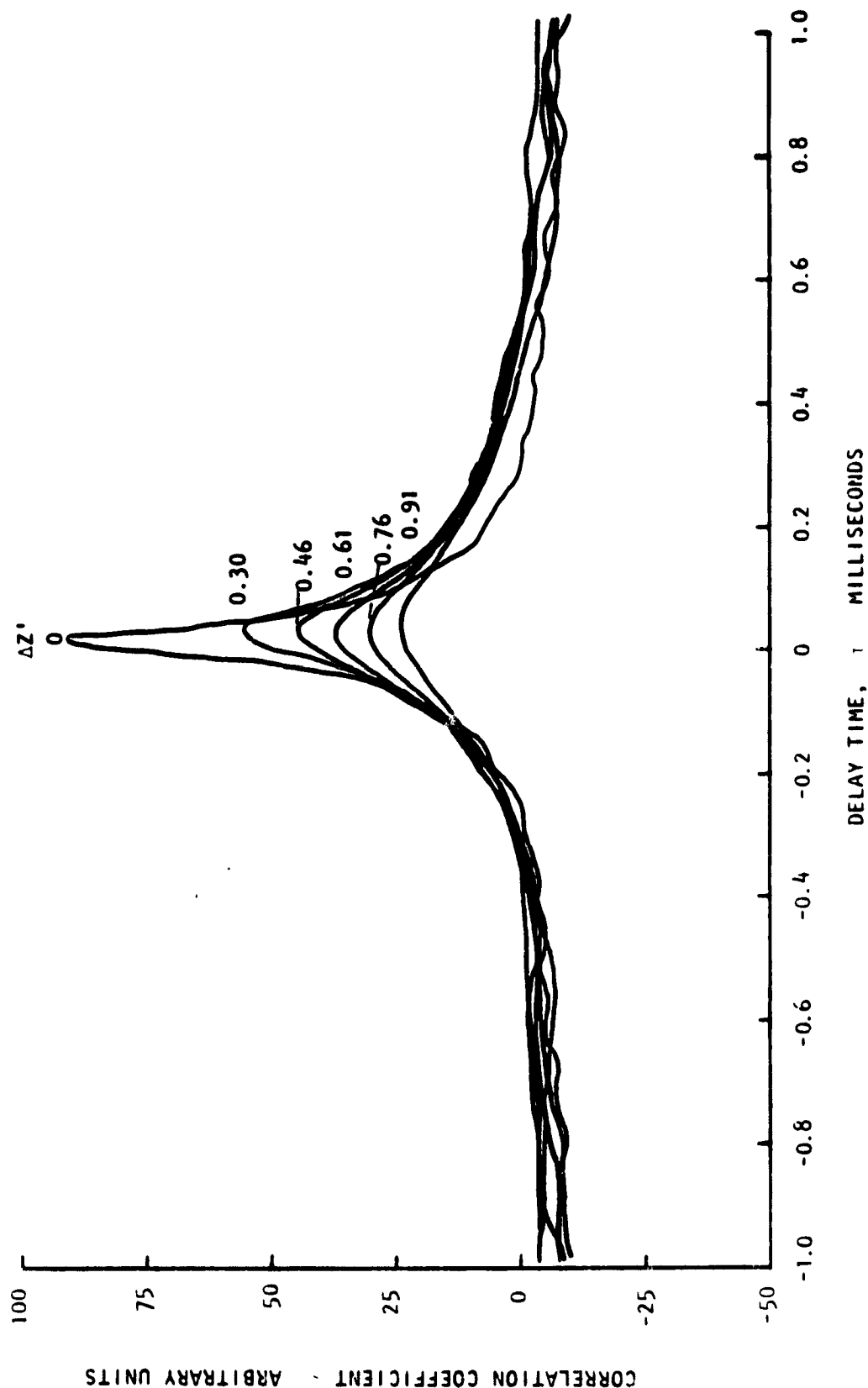


Figure B-3. Space-Time Correlation Function
(J) Z' Variations

VEL. COMP.	U_j m/s	INIT. TURB.	θ_f	X' - cm	$\Delta X'$ - cm	Y - cm	ΔY - cm	Z' - cm	$\Delta Z'$ - cm
U	180.	NG SCREEN	60°	1.91	NOTED	0	0	0	0

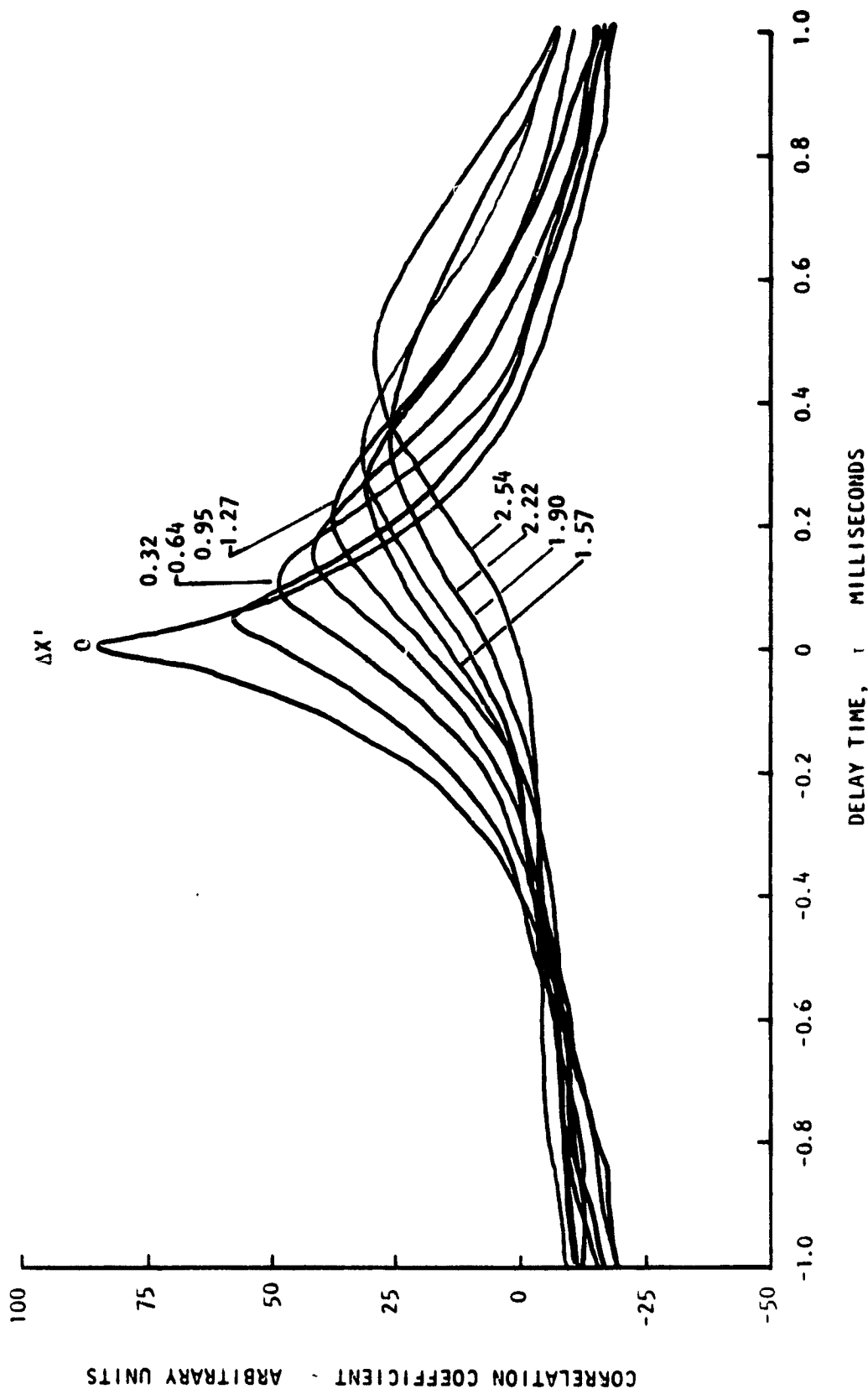


Figure B-4. Space-Time Correlation Function
(A) 60° Flap

VEL. COMP.	U_j m/s	INIT. TURB.	θ_f	X^+ cm	ΔX^+ cm	Y cm	ΔY cm	Z^+ cm	ΔZ^+ cm
W	180.	NO SCREEN	60°	1.91	NOTED	0	0	0	0

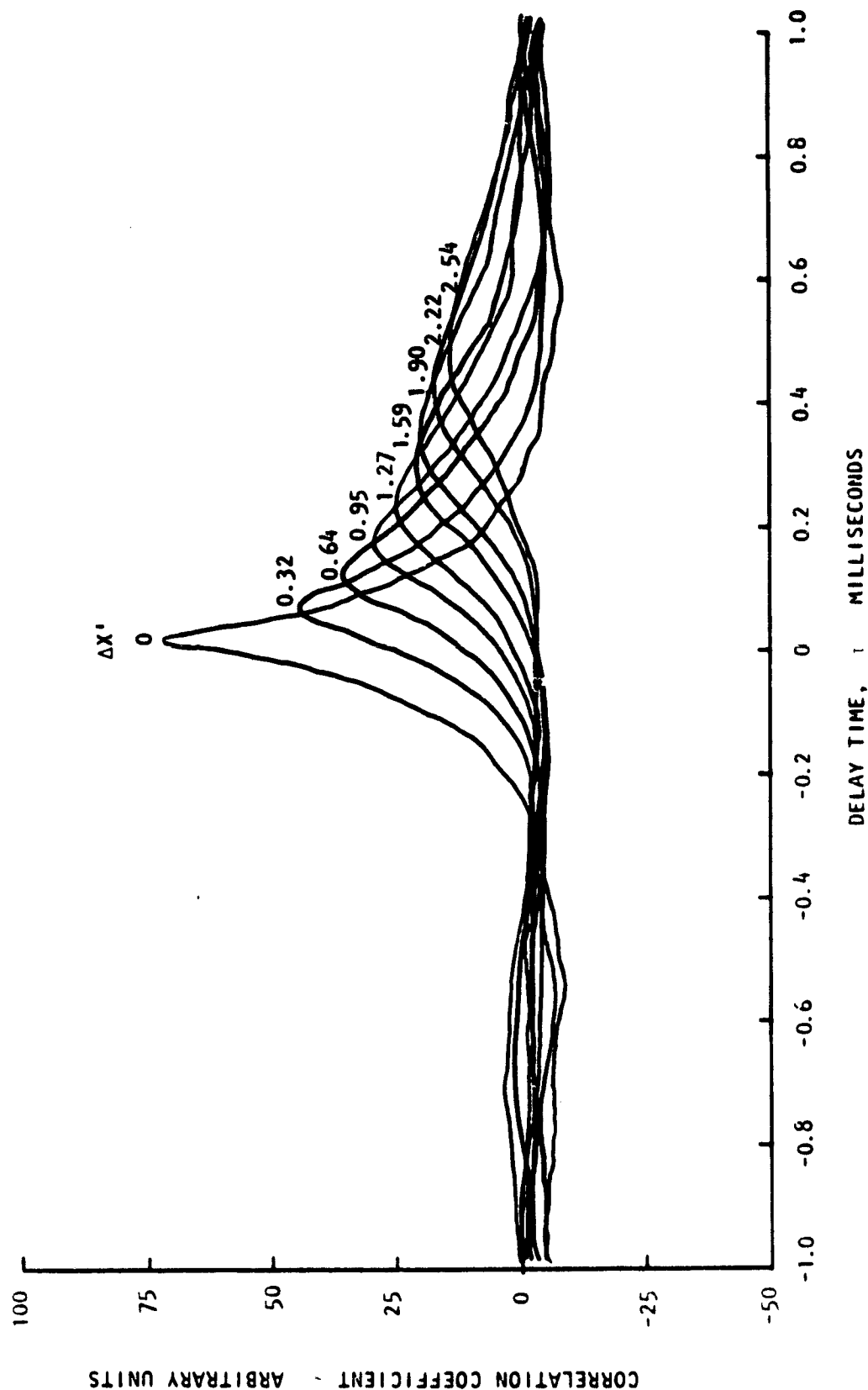


Figure B-4. Space-Time Correlation Function
(B) 60° Flap

VEL. COMP.	U_j m/s	INIT. TURB.	θ_f	x' cm	$\Delta x'$ cm	y cm	Δy cm	z' cm	$\Delta z'$ cm
U	180.	SCREEN	30°	1.91	NOTED	0	0	0	0

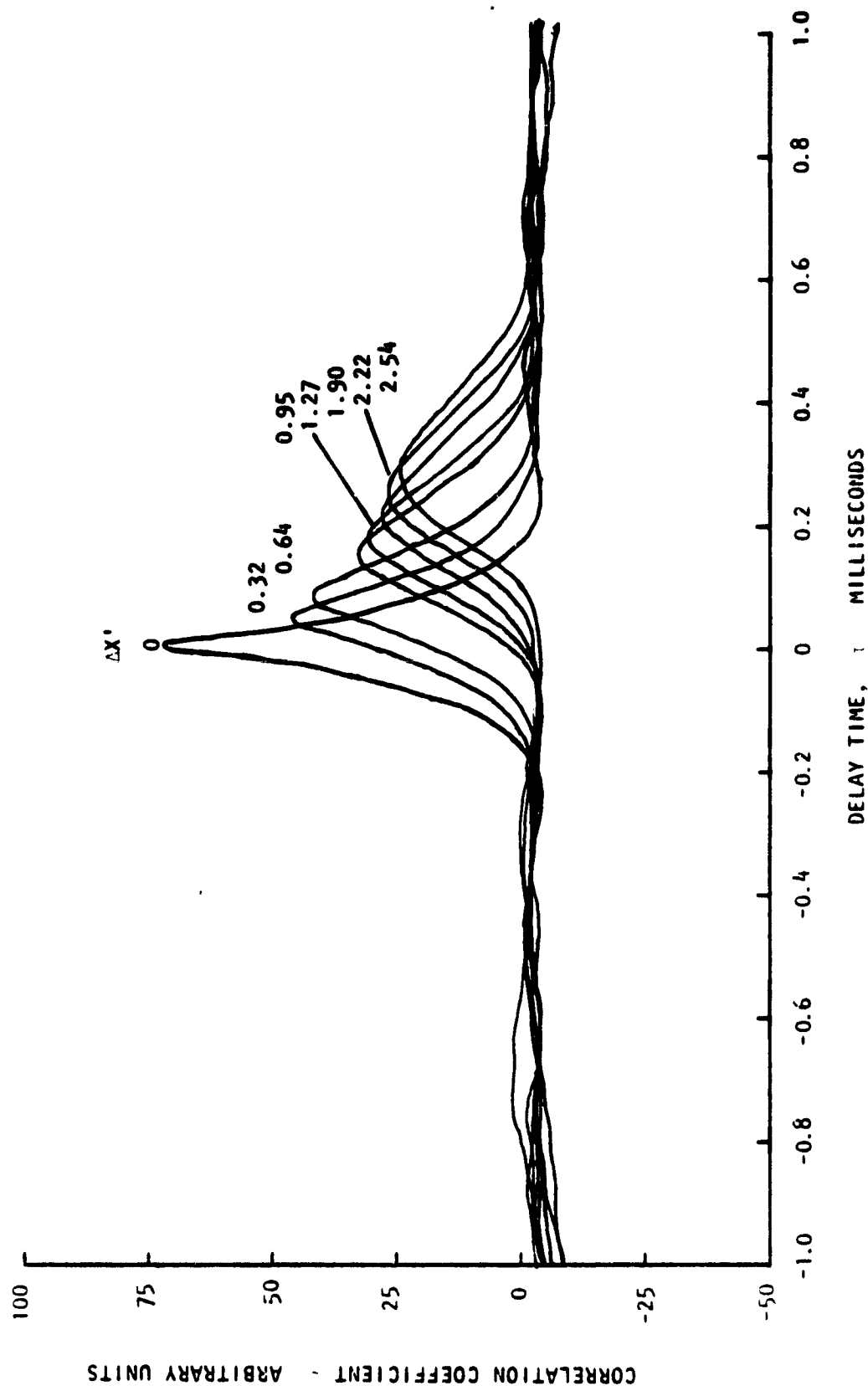


Figure B-5. Space-Time Correlation Function
(A) Nozzle Exit Screen

VEL. COMP.	U_J m/s	INIT. TURB.	θ_f	X' cm	$\Delta X'$ cm	Y cm	ΔY cm	Z' cm	$\Delta Z'$ cm
W	180.	SCREEN	30°	1.91	NOTED	0	0	0	0

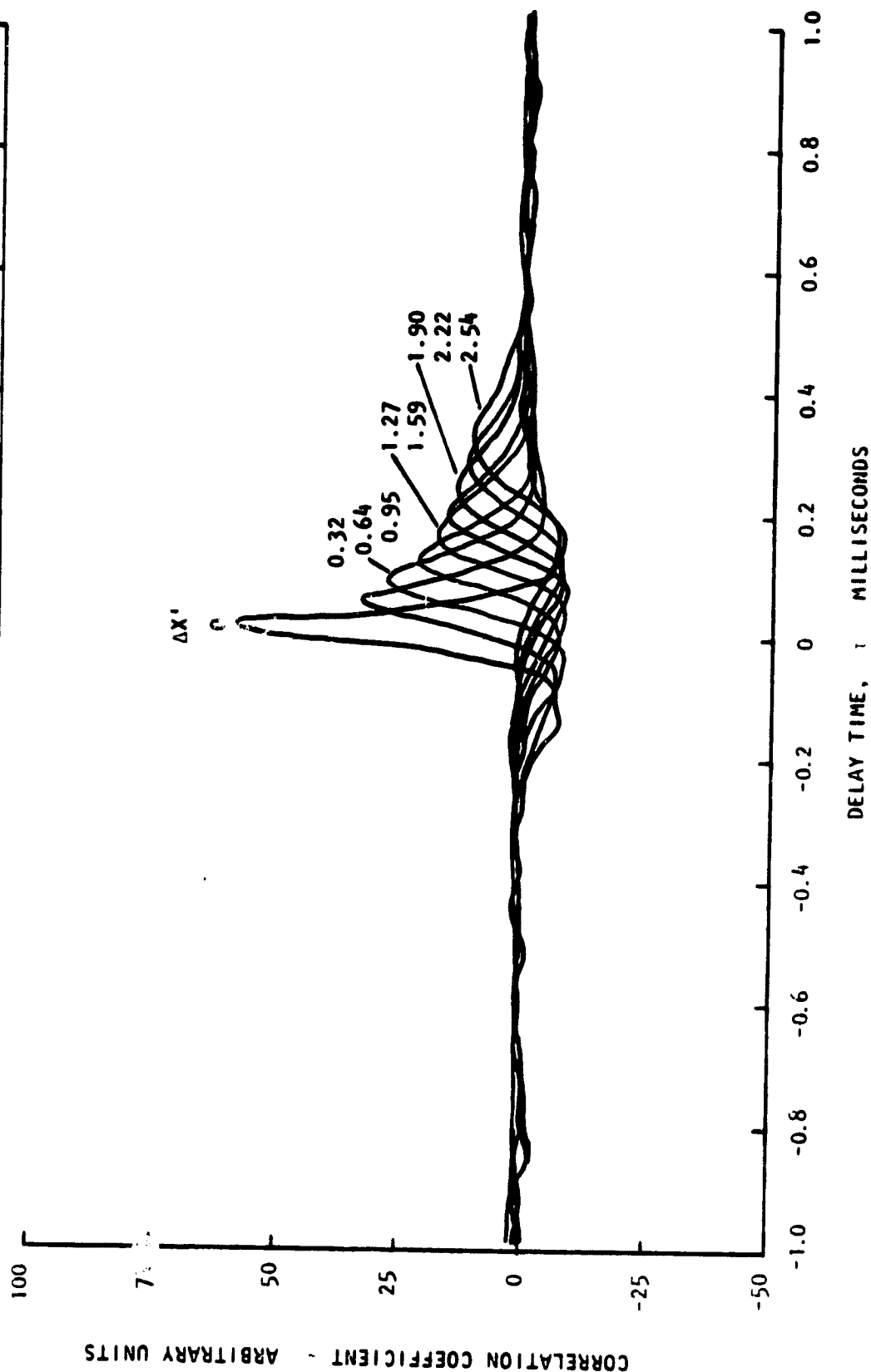


Figure B-5. Space-Time Correlation Function
(B) Nozzle Exit Screen

VEL. COMP.	U_j m/s	INIT. TURB.	ϕ_f	X^1 - cm	ΔX^1 - cm	V - cm	ΔV - cm	Z^1 - cm	ΔZ^1 - cm
U	180.	SCREEN	30°	1.91	0	0	NOTED	0	0

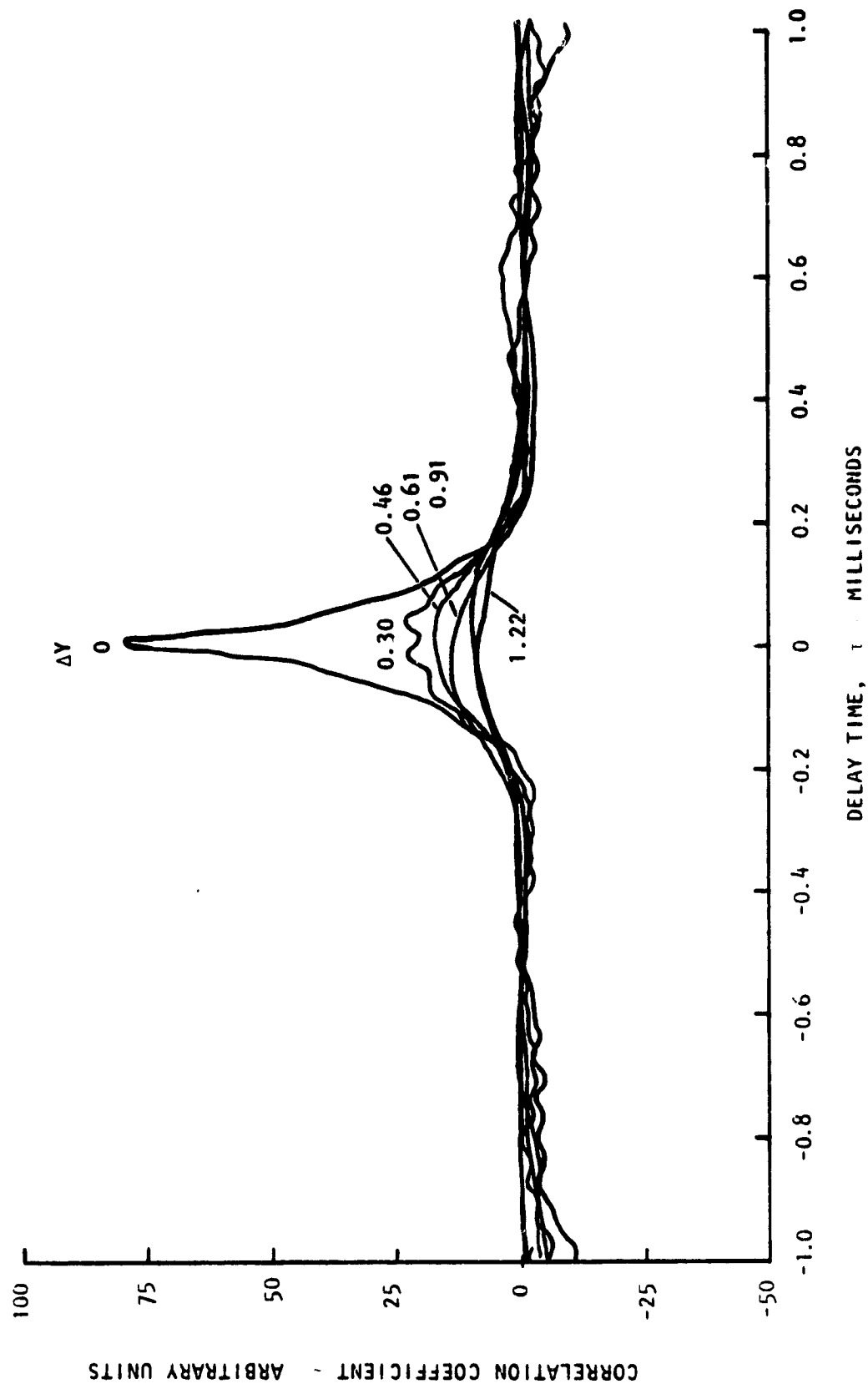


Figure B-5. Space-Time Correlation Function
(C) Nozzle Exit Screen

VEL. COMP.	U_J m/s	INIT. TURB.	θ_f	X' cm	$\Delta X'$ cm	Y cm	ΔY cm	Z' cm	$\Delta Z'$ cm
W	180.	SCREEN	30°	1.91	0	0	NOTED	0	0

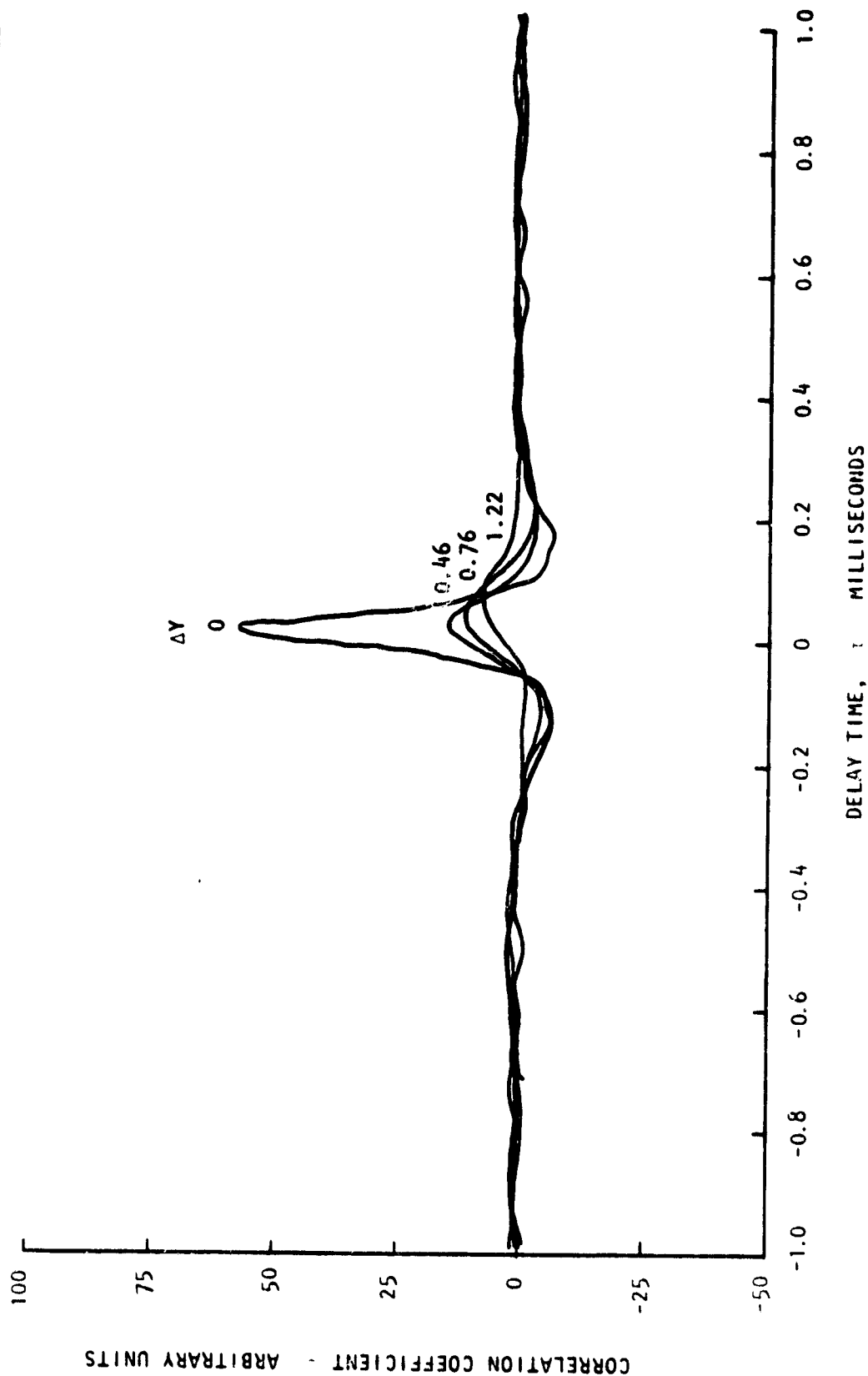


Figure B-5. Space-Time Correlation Function
(D) Nozzle Exit Screen

VEL. COMP.	U_j m/s	INIT. TURB.	θ_f	X' - cm	$\Delta X'$ - cm	Y - cm	ΔY - cm	Z' - cm	$\Delta Z'$ - cm
W	180.	SCREEN	30°	1.91	0	0	0	0	NOTED

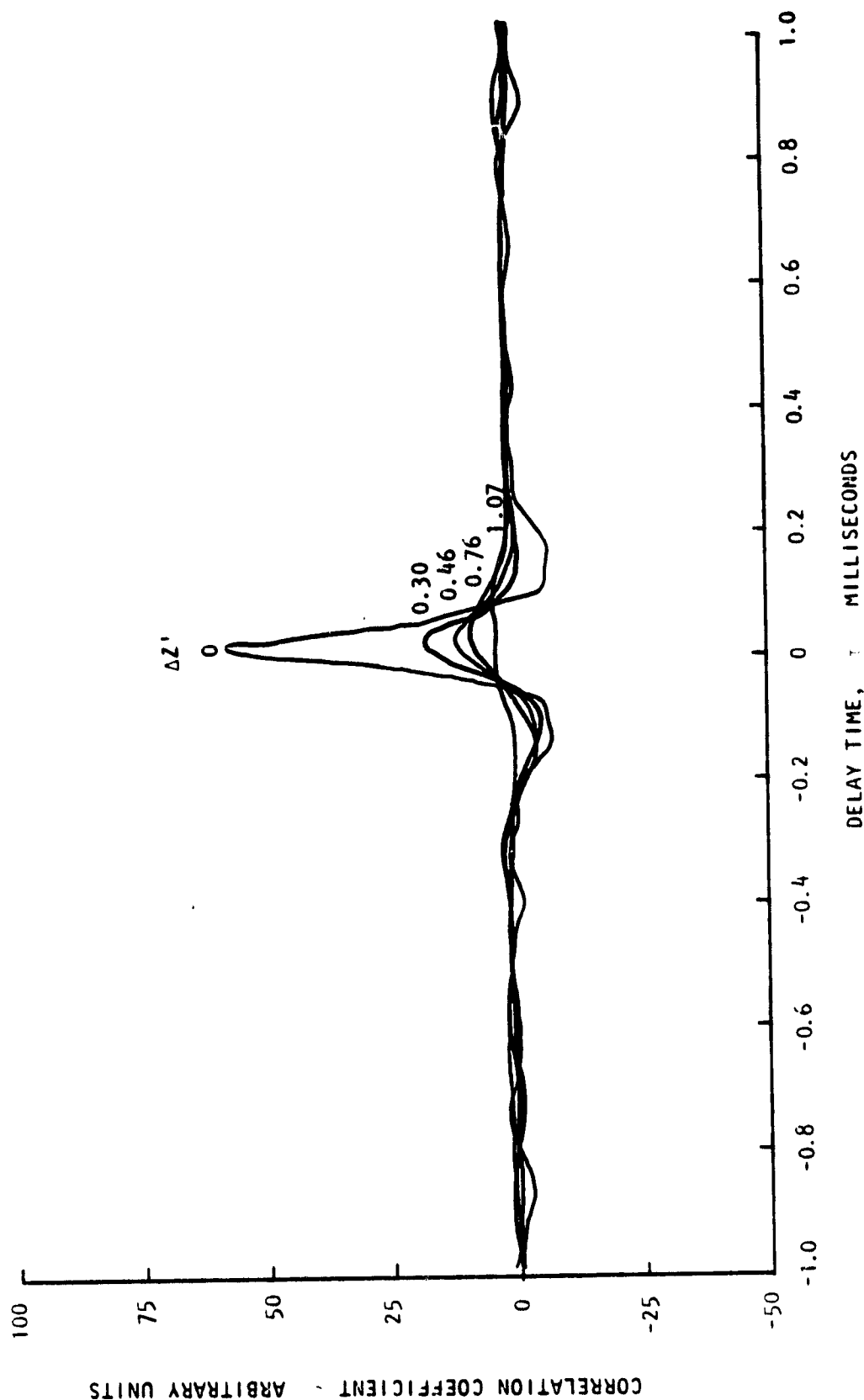


Figure B-5. Space-Time Correlation Function
(E) Nozzle Exit Screen

VEL. COMP.	U_J m/s	INIT. TURB.	τ_f	X' cm	$\Delta X'$ cm	Y cm	ΔY cm	Z' cm	$\Delta Z'$ cm
U	180.	SCREEN	30'	1.91	0	0	0	NOTED	0

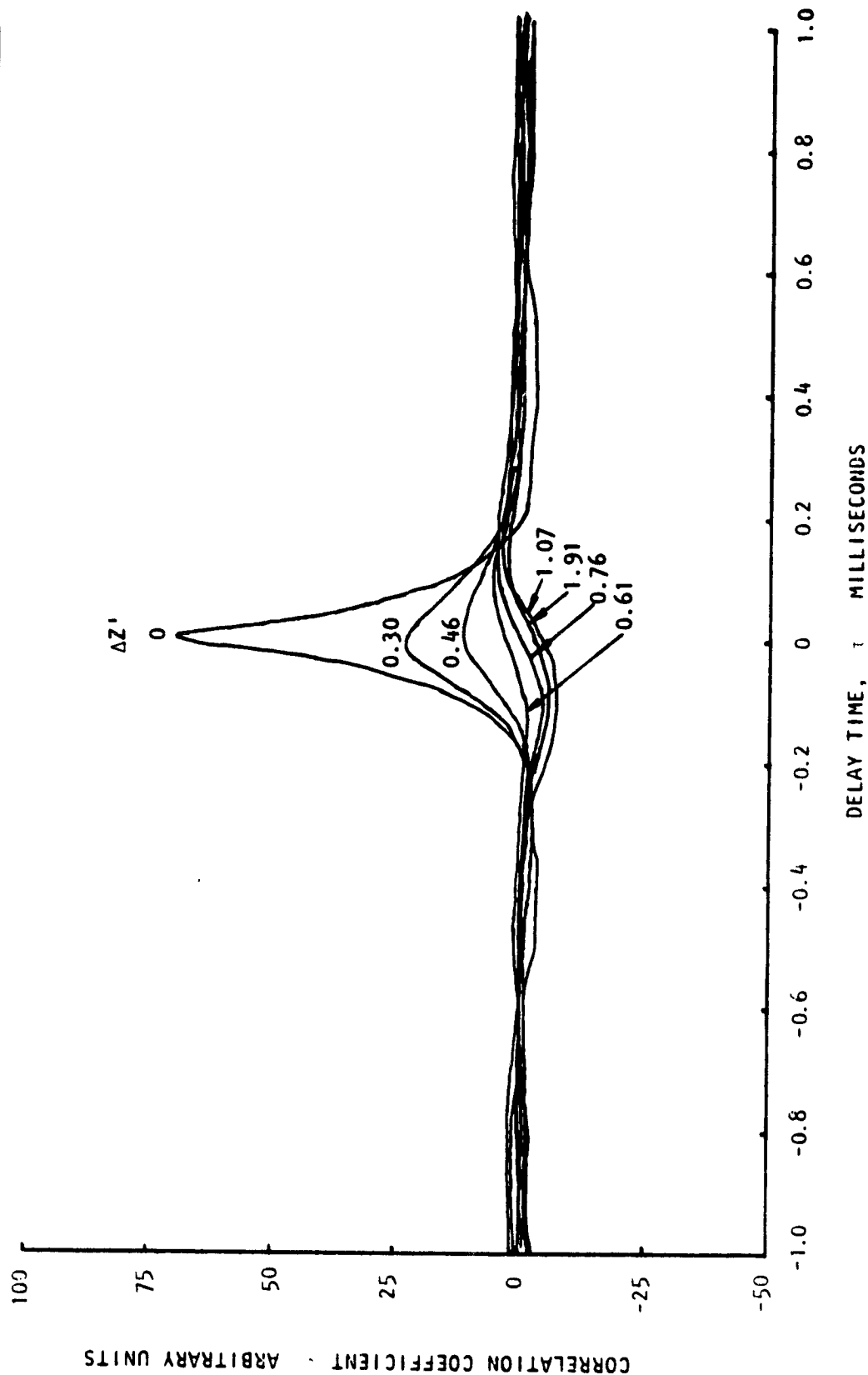


Figure B-5. Space-Time Correlation Function
(F) Nozzle Exit Screen

APPENDIX C WAKE FLOW CROSS POWER SPECTRA

This appendix contains a plot of the cross-power spectrum and the phase angle for each cross-correlation curve in Appendix B. Therefore, data are presented for separations in the X' , Y , and Z' directions, and flap angle and initial turbulence were varied. All variations are made from the following condition:

$$U_j = 180 \text{ m/s}$$

No Screen

$$\delta_f = 30^\circ$$

$$X' = 1.91 \text{ cm}$$

$$Y = 0$$

The data are arranged as shown in Table C-1, where each line represents a number of plots for both U and W components with all U 's first.

TABLE C-1 DATA CONTENTS

Figure	Initial Turbulence	δ_f	$X' \sim \text{cm}$	$Y \sim \text{cm}$	$Z' \sim \text{cm}$	Separation
C-1 ↓	No Screen ↓	30° ↓	1.91 3.81	0 ↓	0	$\Delta X' = 0.32$ to 2.54 ↓
C-2	No Screen	30°	1.91	0	0	$\Delta Y = 0.30$ to 1.22
C-3 ↓	No Screen ↓	30° ↓	1.91 ↓	0 ↓	0 0.64 1.27 1.91 2.54	$\Delta Z' = 0.30$ to 1.37 $\Delta Z' = 0.30$ to 1.22 $\Delta Z' = 0.30$ to 0.91 ↓
C-4	No Screen	60°	1.91	0	0	$\Delta X' = 0.32$ to 2.54
C-5	Screen	30°	1.91	0	0	$\Delta X' = 0.32$ to 2.54

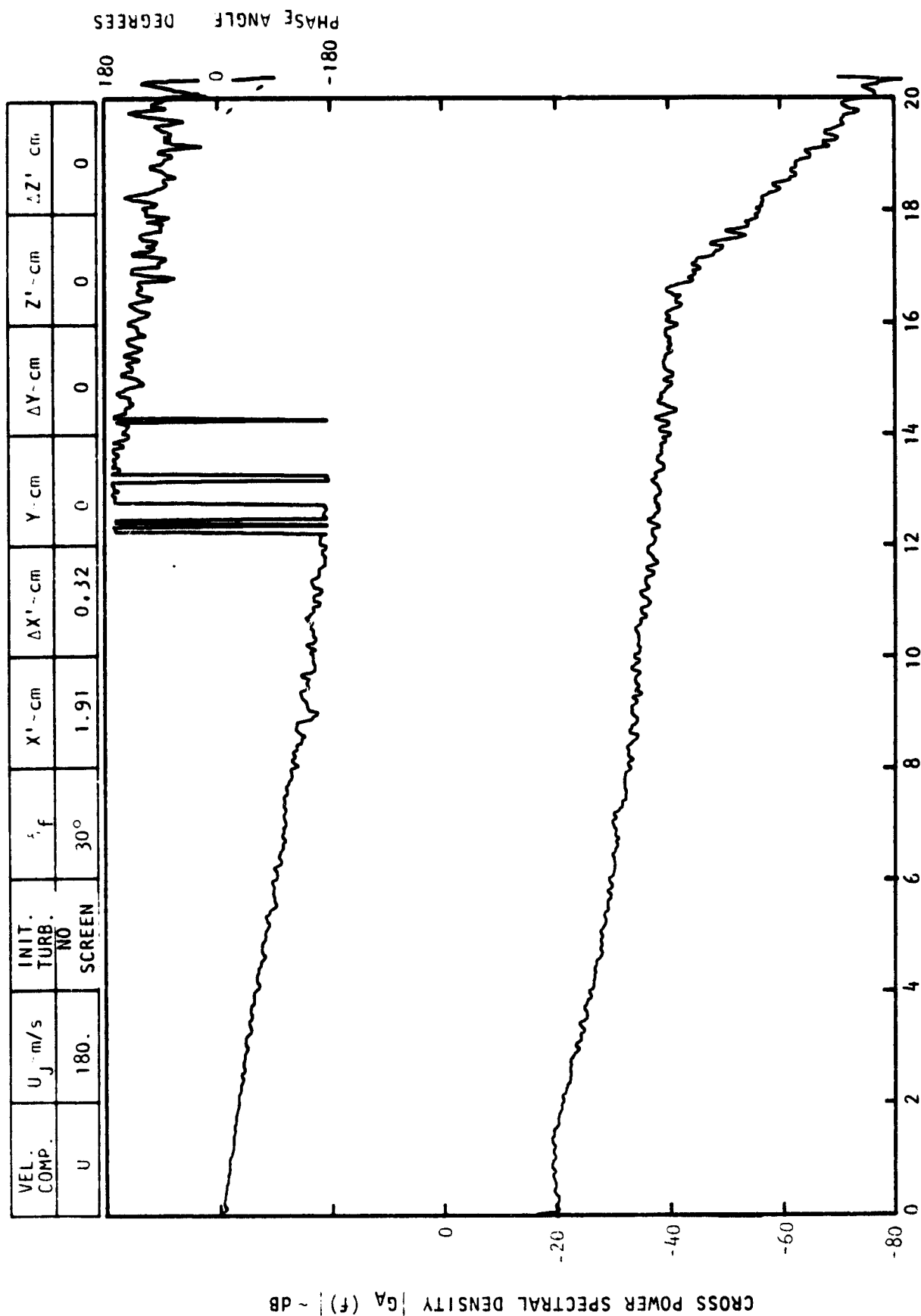


Figure C-1. Velocity-Velocity Cross Power Spectrum and Phase;

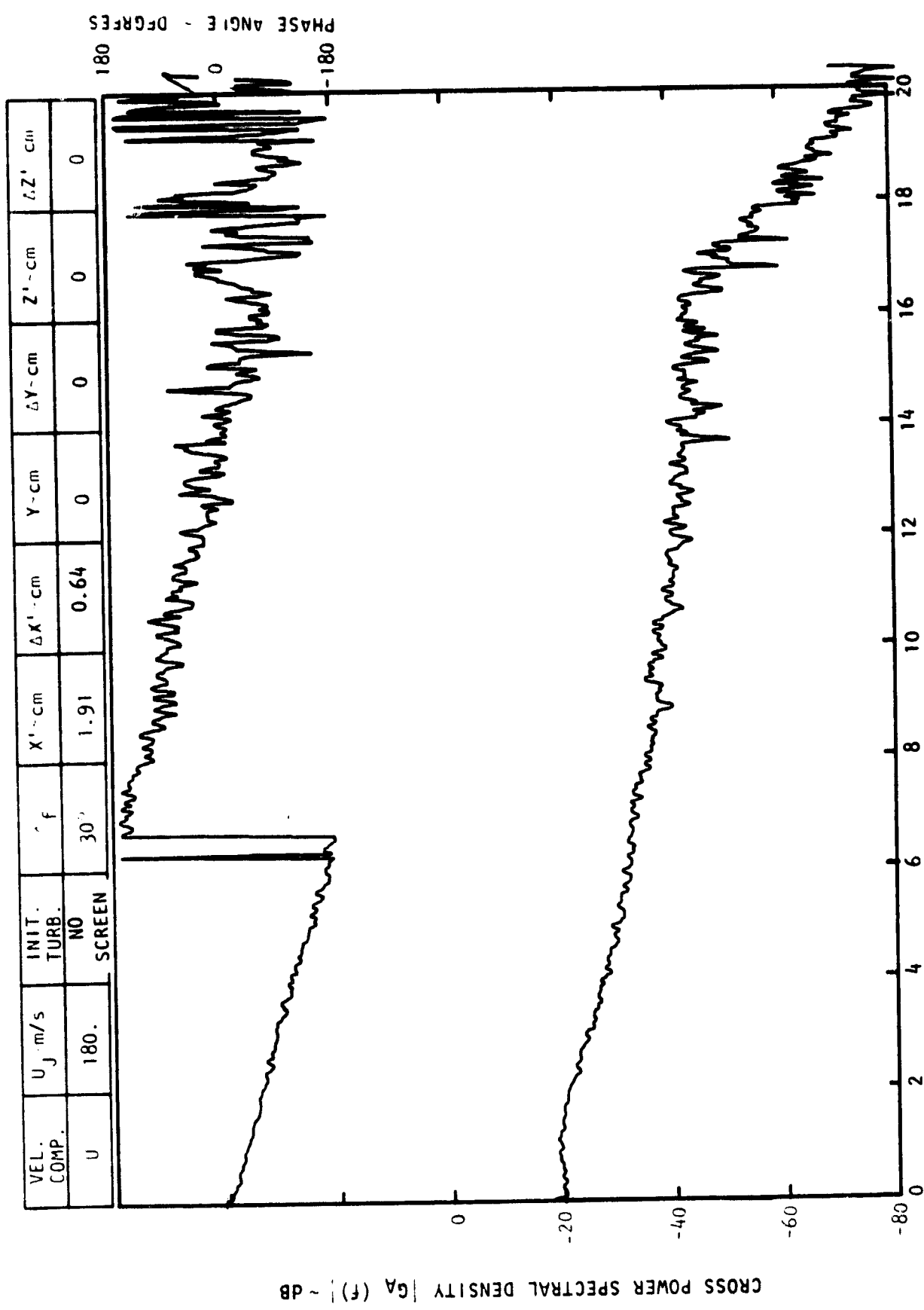
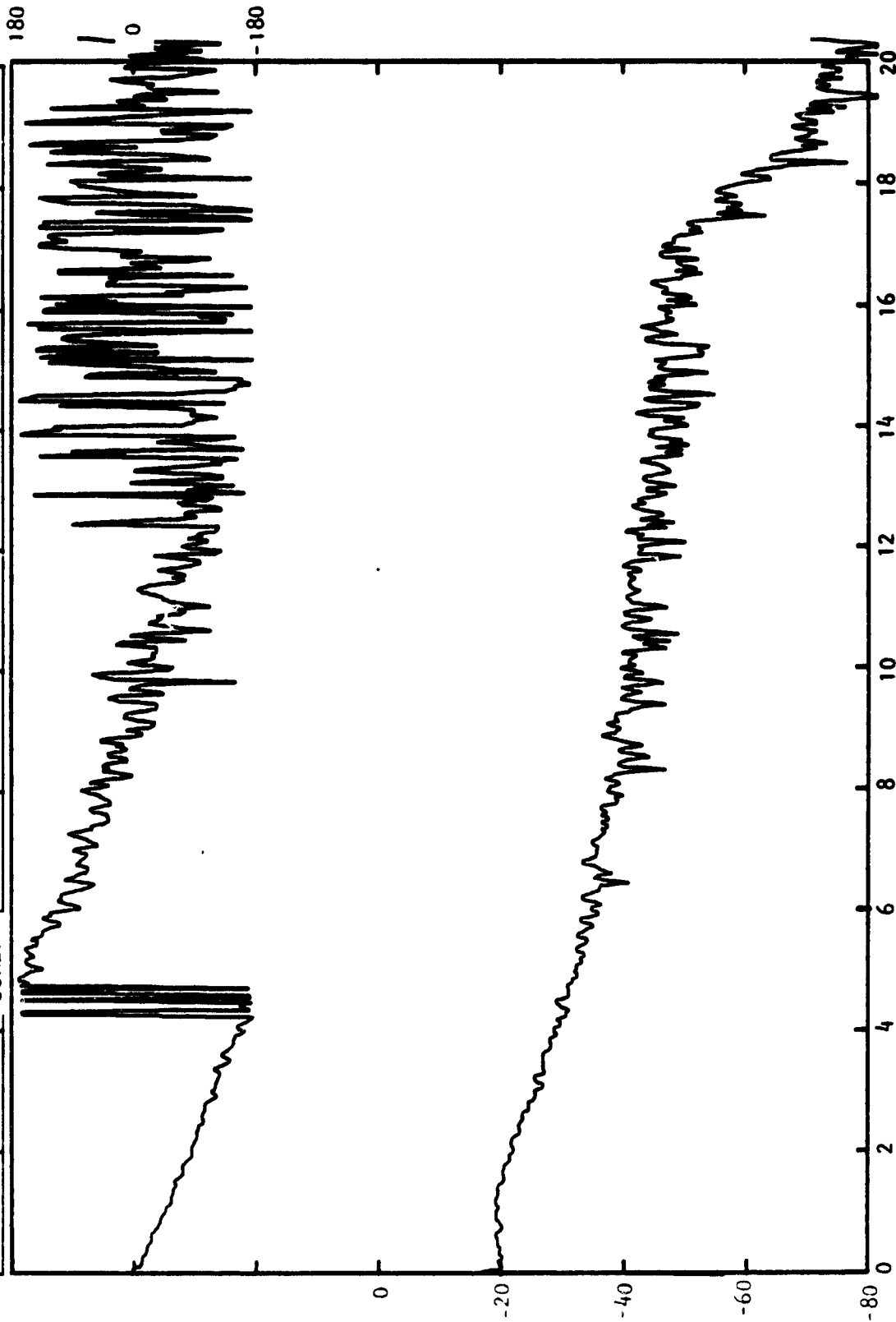


Figure C-1. Continued.

VEL. COMP.	U_j - m/s	INIT. TURB.	δ_f	$X' - \text{cm}$	$\Delta X' - \text{cm}$	$Y - \text{cm}$	$\Delta Y - \text{cm}$	$Z' - \text{cm}$	$\Delta Z' - \text{cm}$
U	180.	NO SCREEN	30°	1.91	0.95	0	0	0	0

PHASE ANGLE - DEGREES



FREQUENCY ~ KHZ

FIGURE C-4 Continued

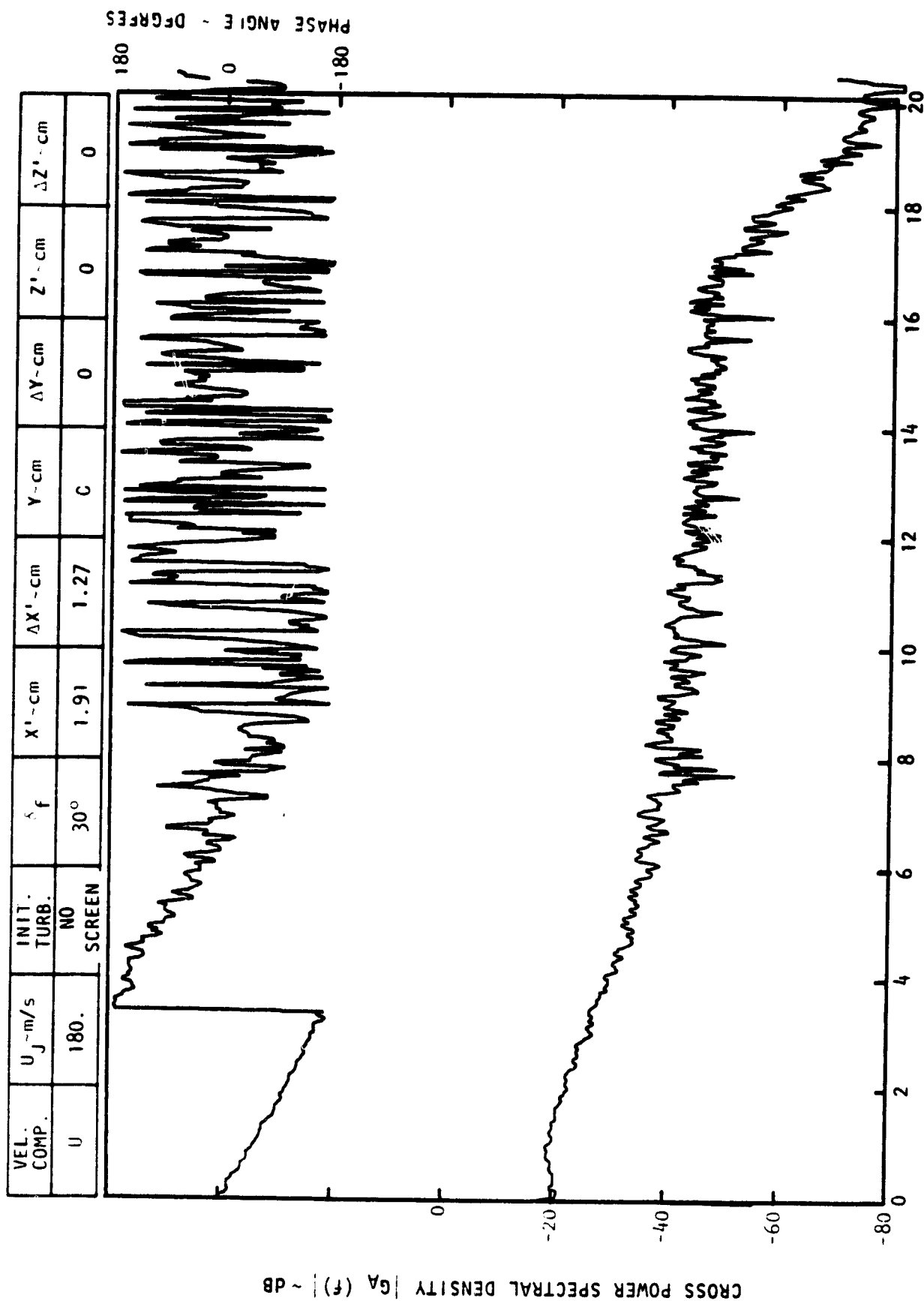
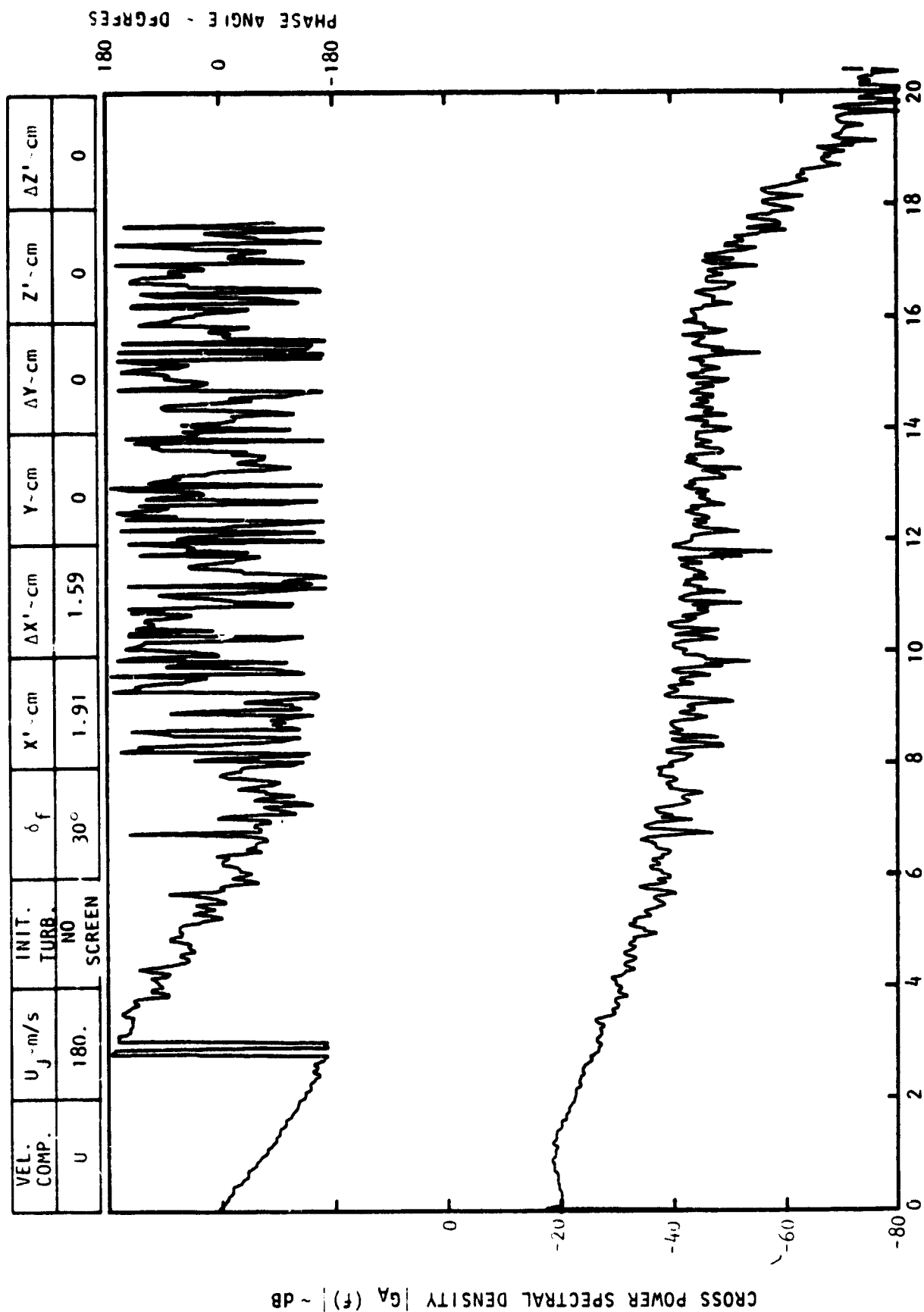


Figure C-1. Continued.



FREQUENCY ~ KHz
Figure C-1. Continued.

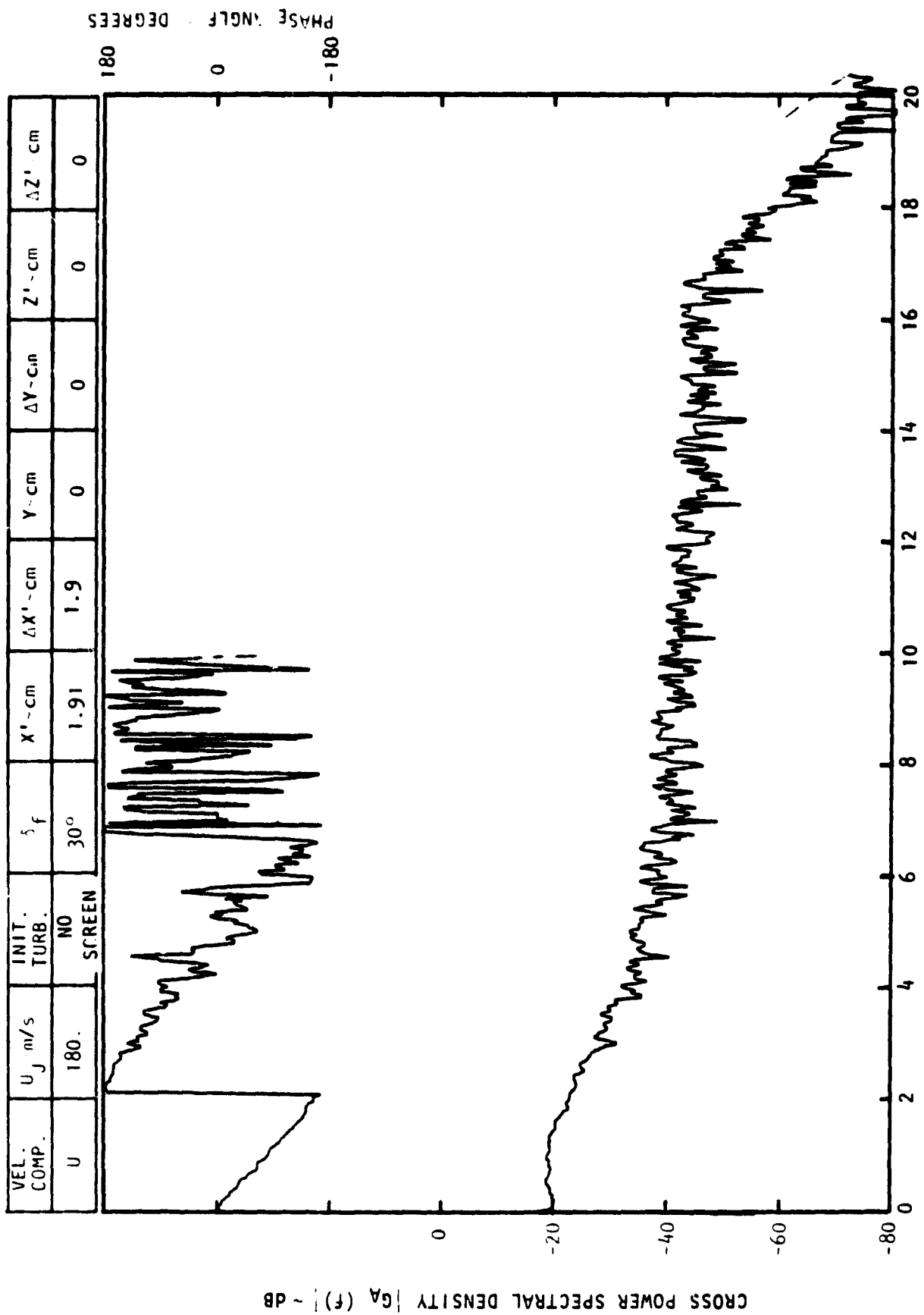
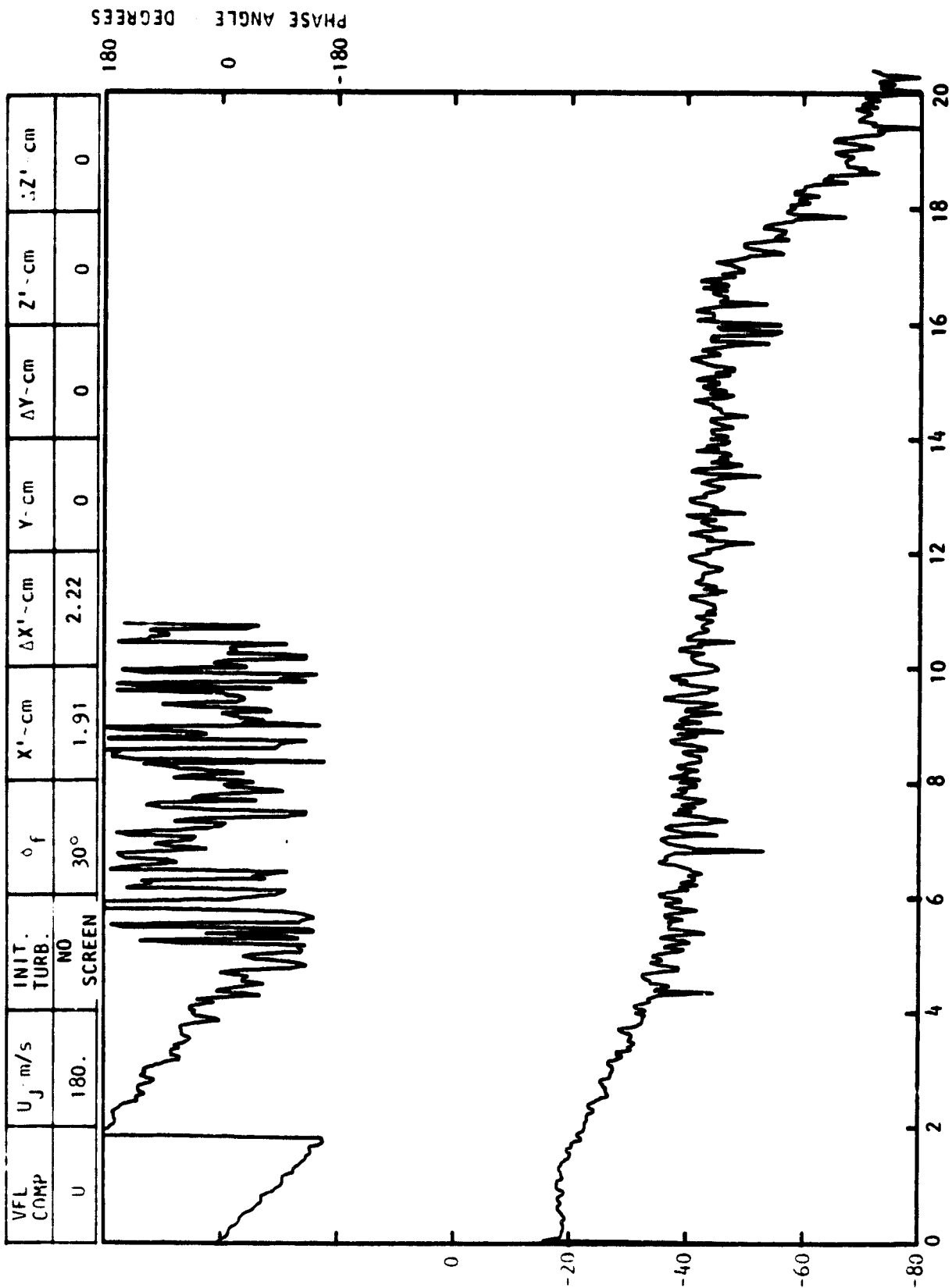
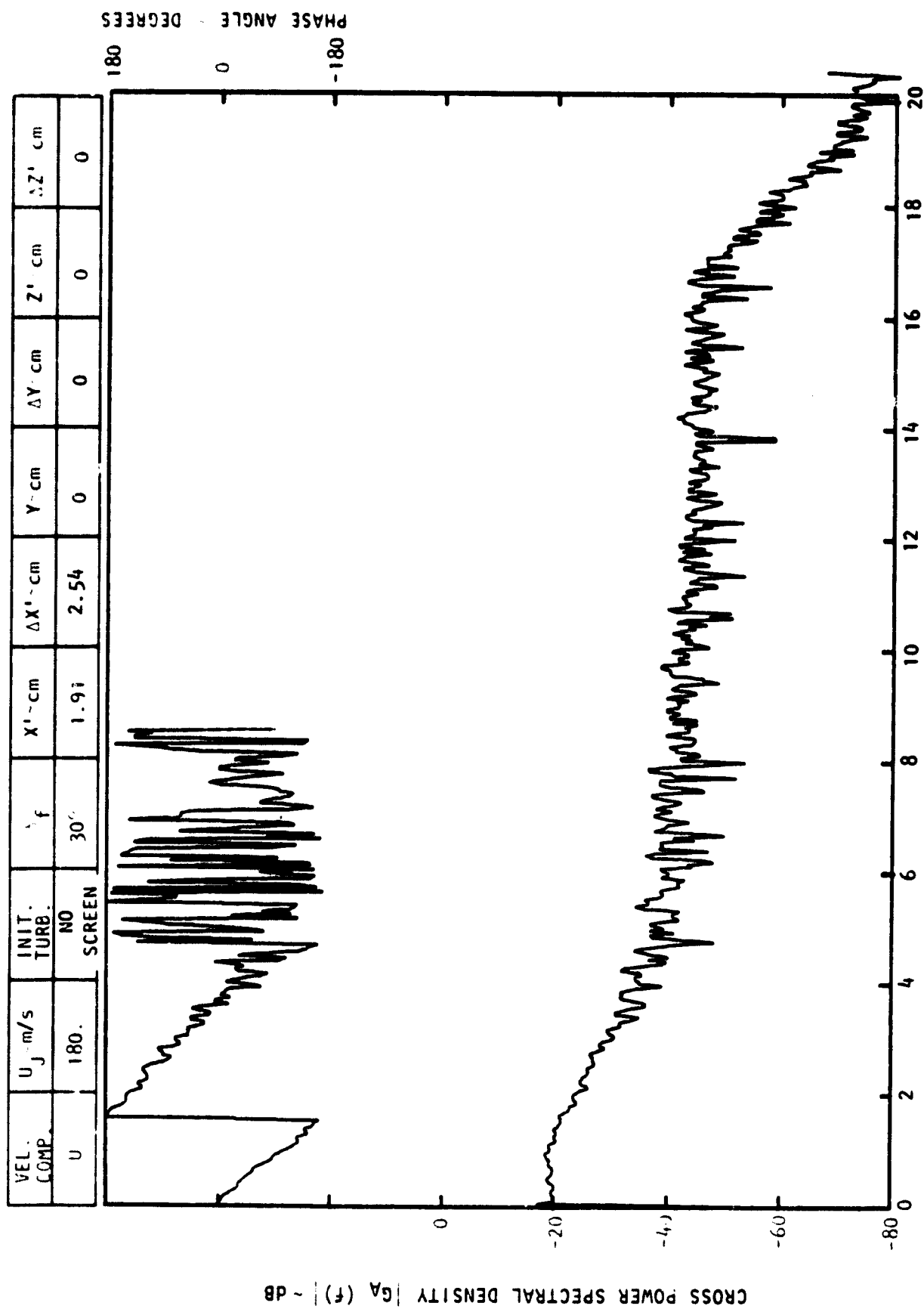
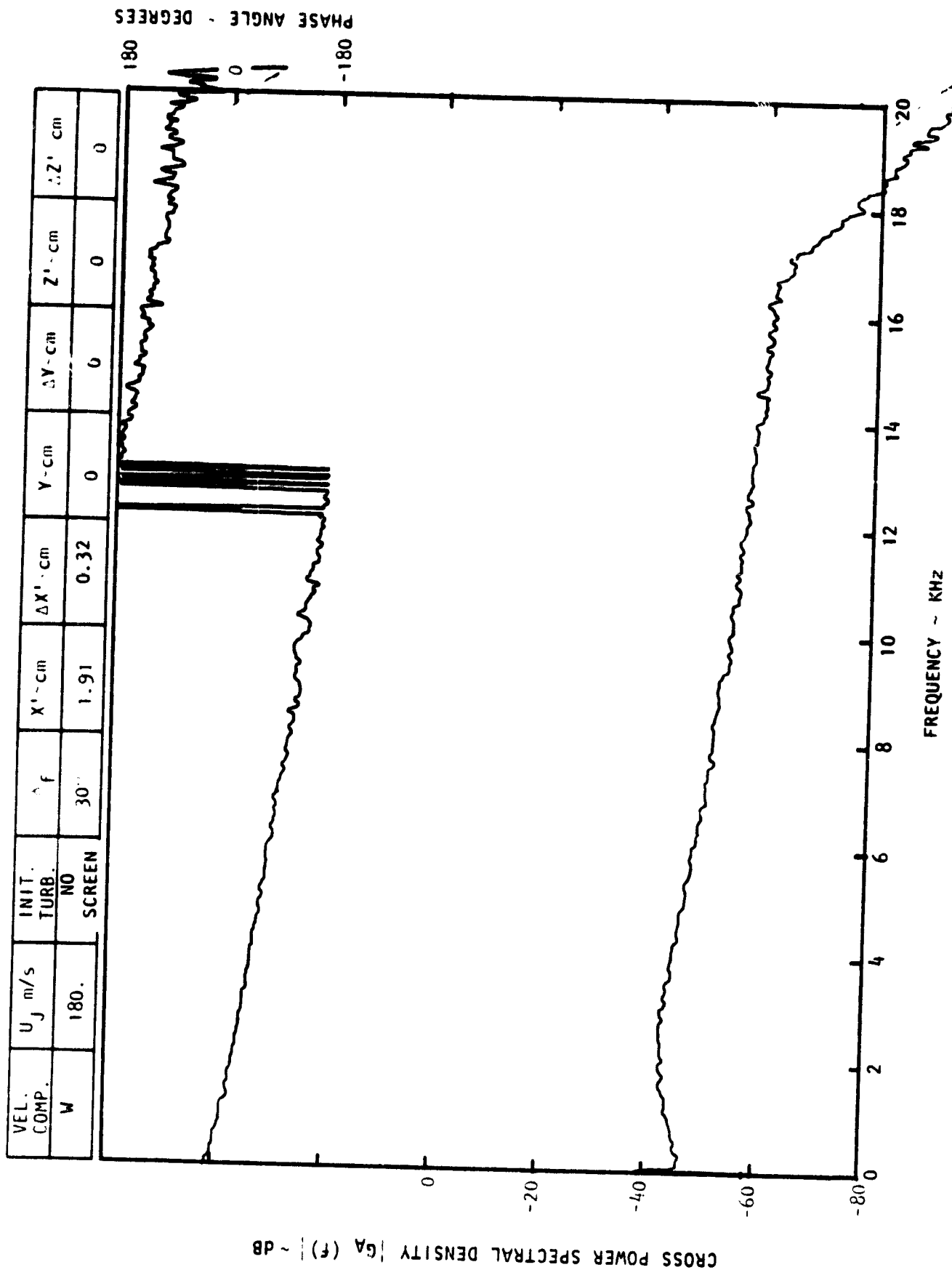


Figure C-1. Continued.

CROSS POWER SPECTRAL DENSITY $G_A(f)$ ~ dB

FREQUENCY ~ KHZ
Figure 8-1 Continued





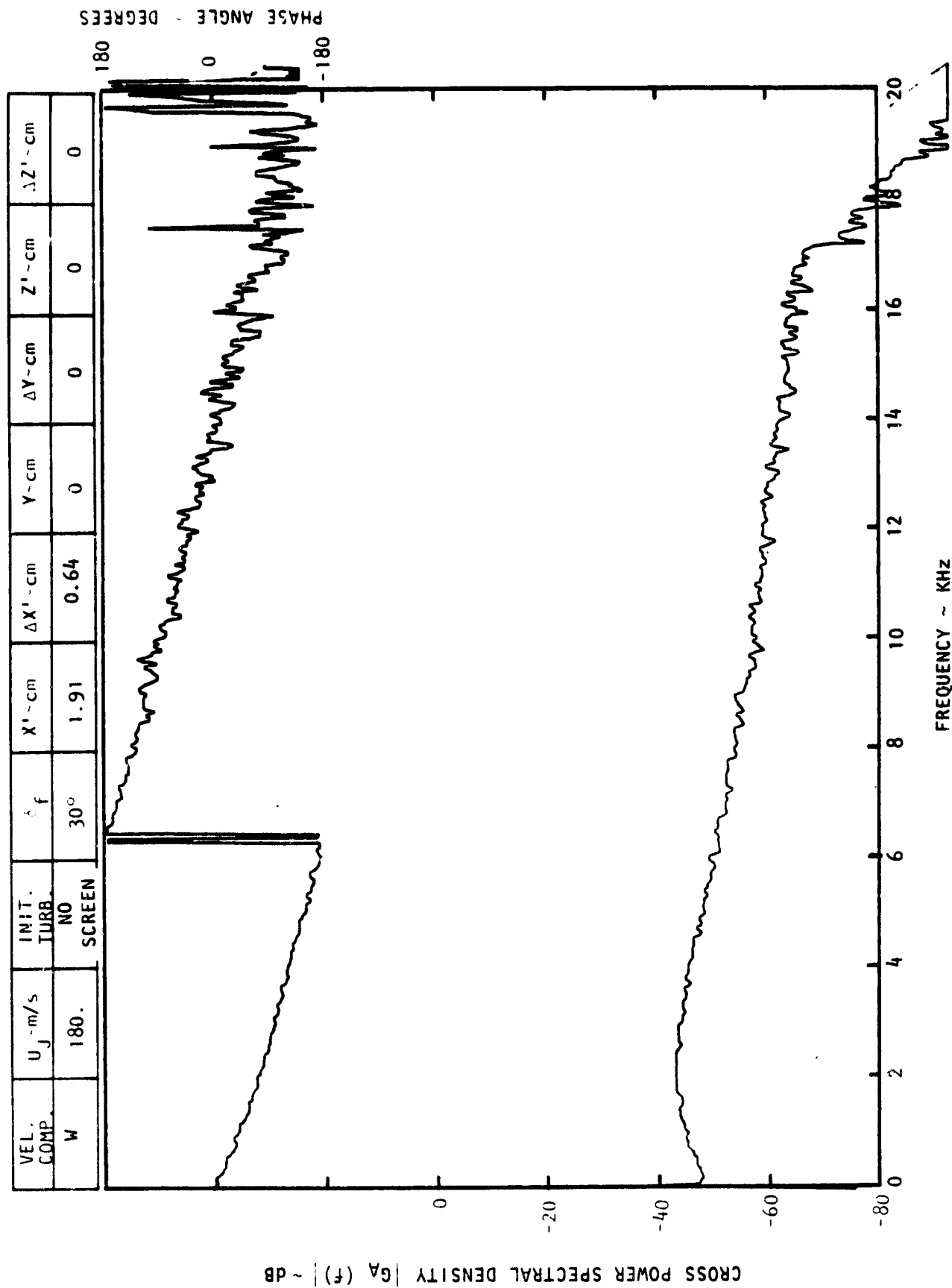
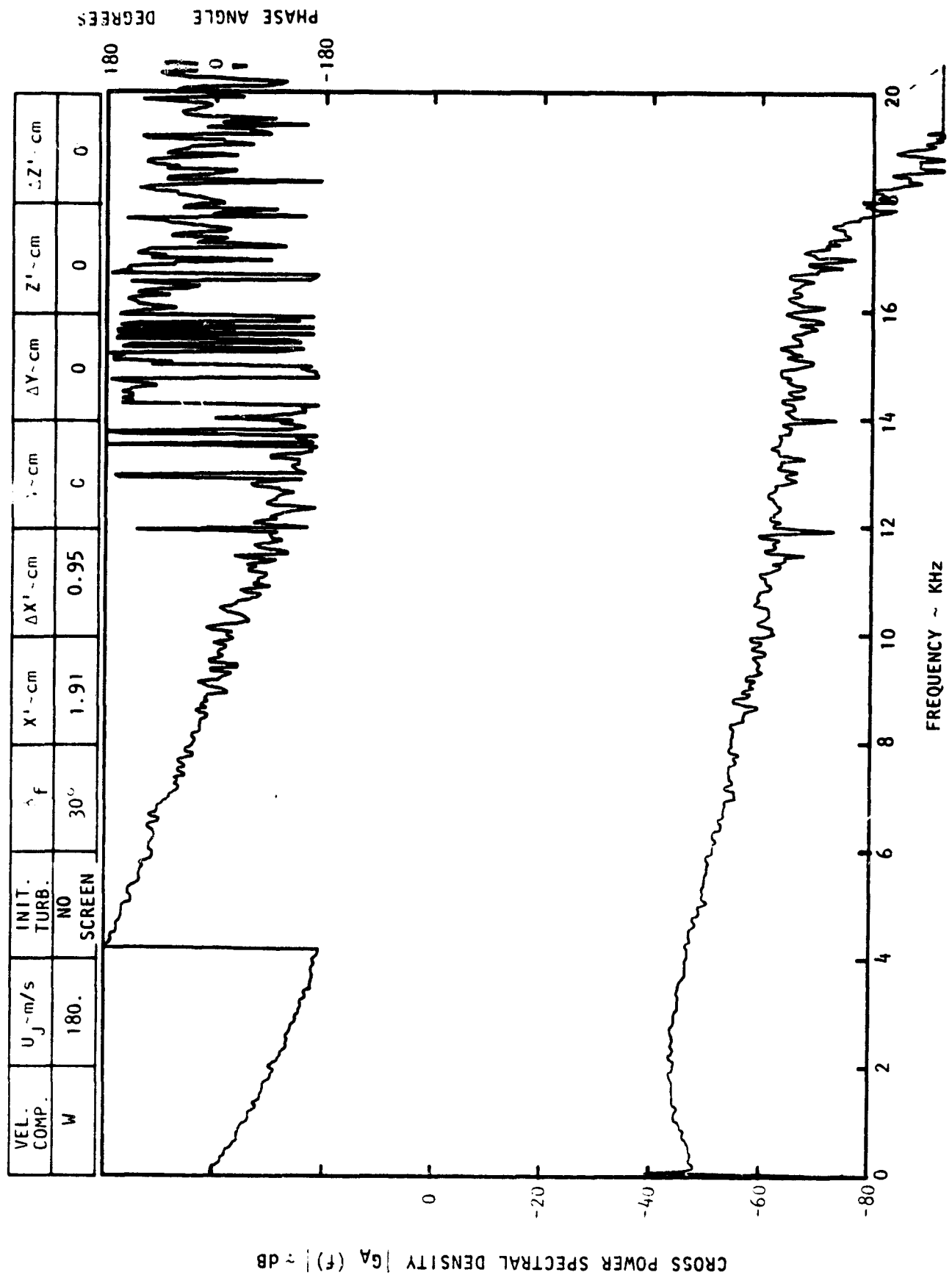


Figure C-1. Continued.



VEL. COMP.	U_j - m/s	INIT. TURB.	ϕ_f	$X' - \text{cm}$	$\Delta X' - \text{cm}$	$Y - \text{cm}$	$\Delta Y - \text{cm}$	$Z' - \text{cm}$	$\Delta Z' - \text{cm}$
W	180.	NO SCREEN	30°	1.91	1.27	0	0	0	0

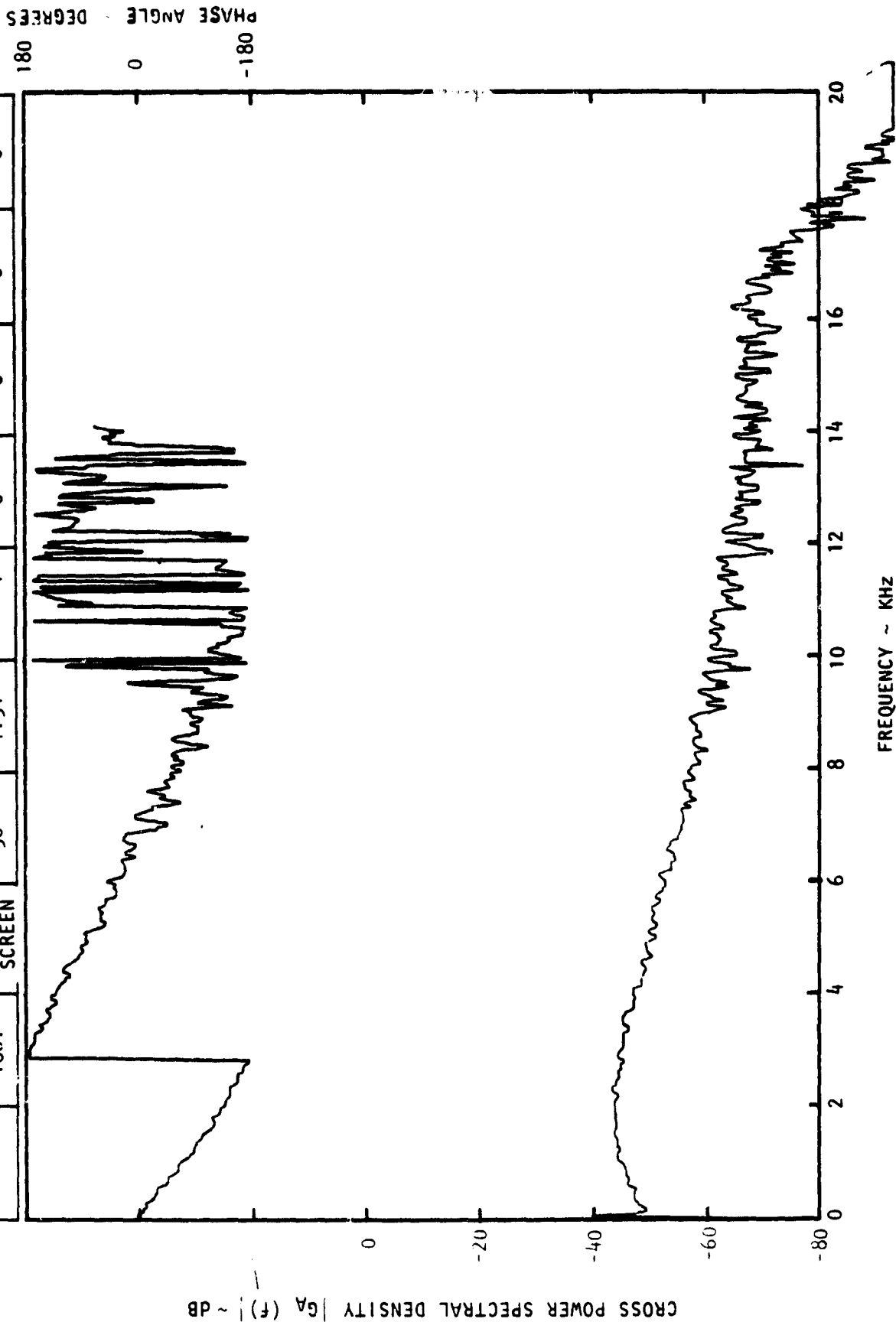
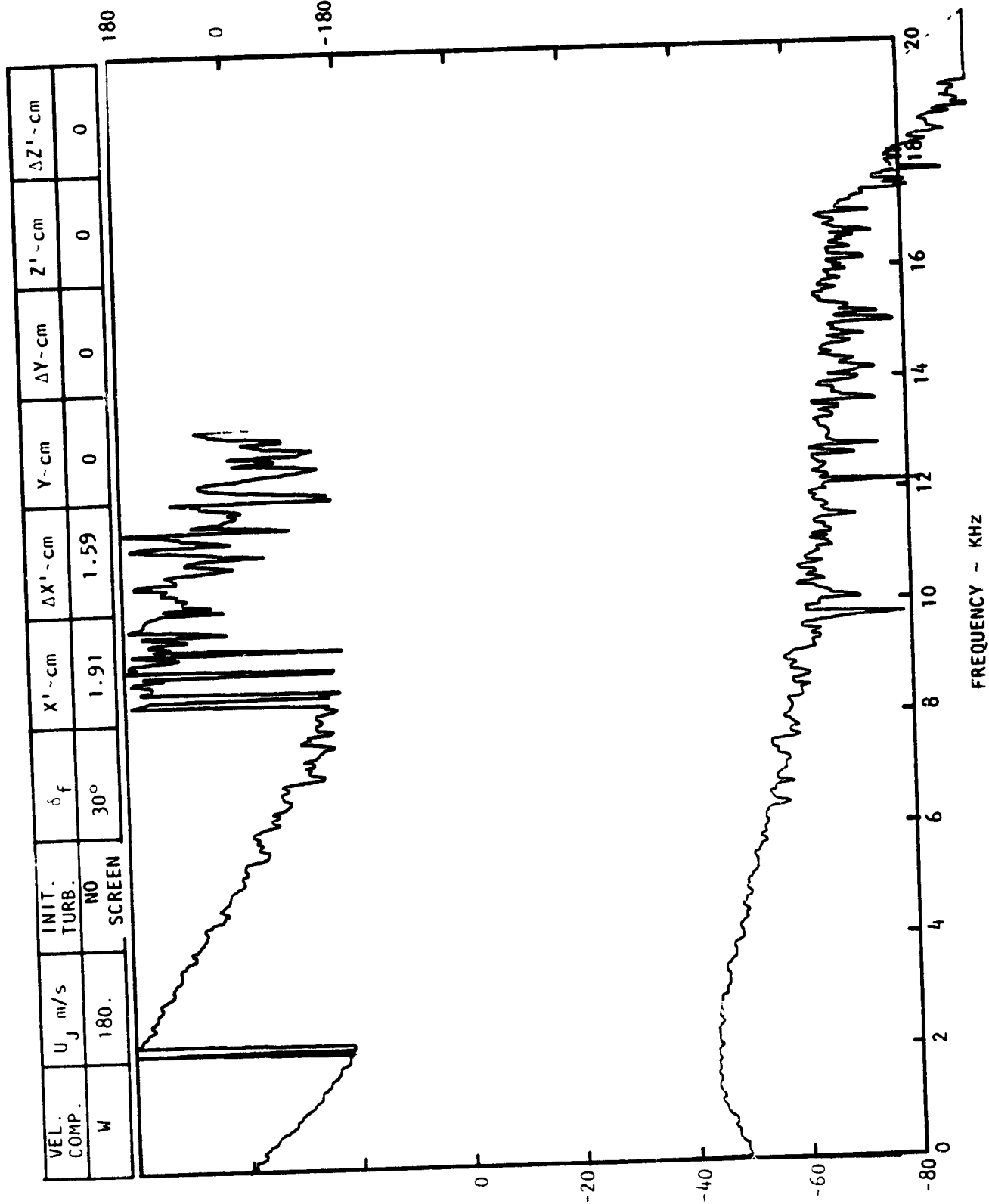


Figure C-1. Continued.

CROSS POWER SPECTRAL DENSITY $G_A(f)$ ~ dB

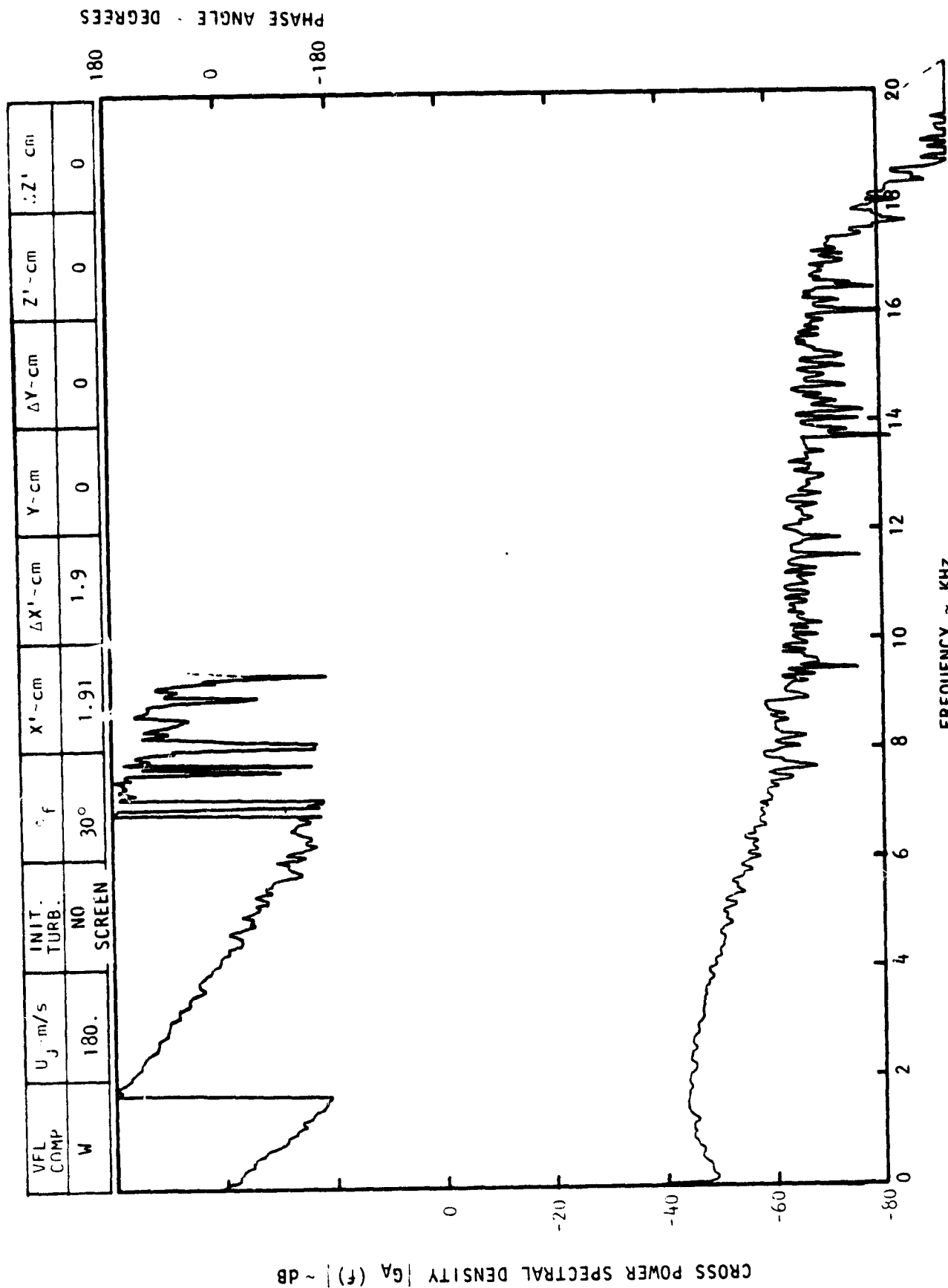
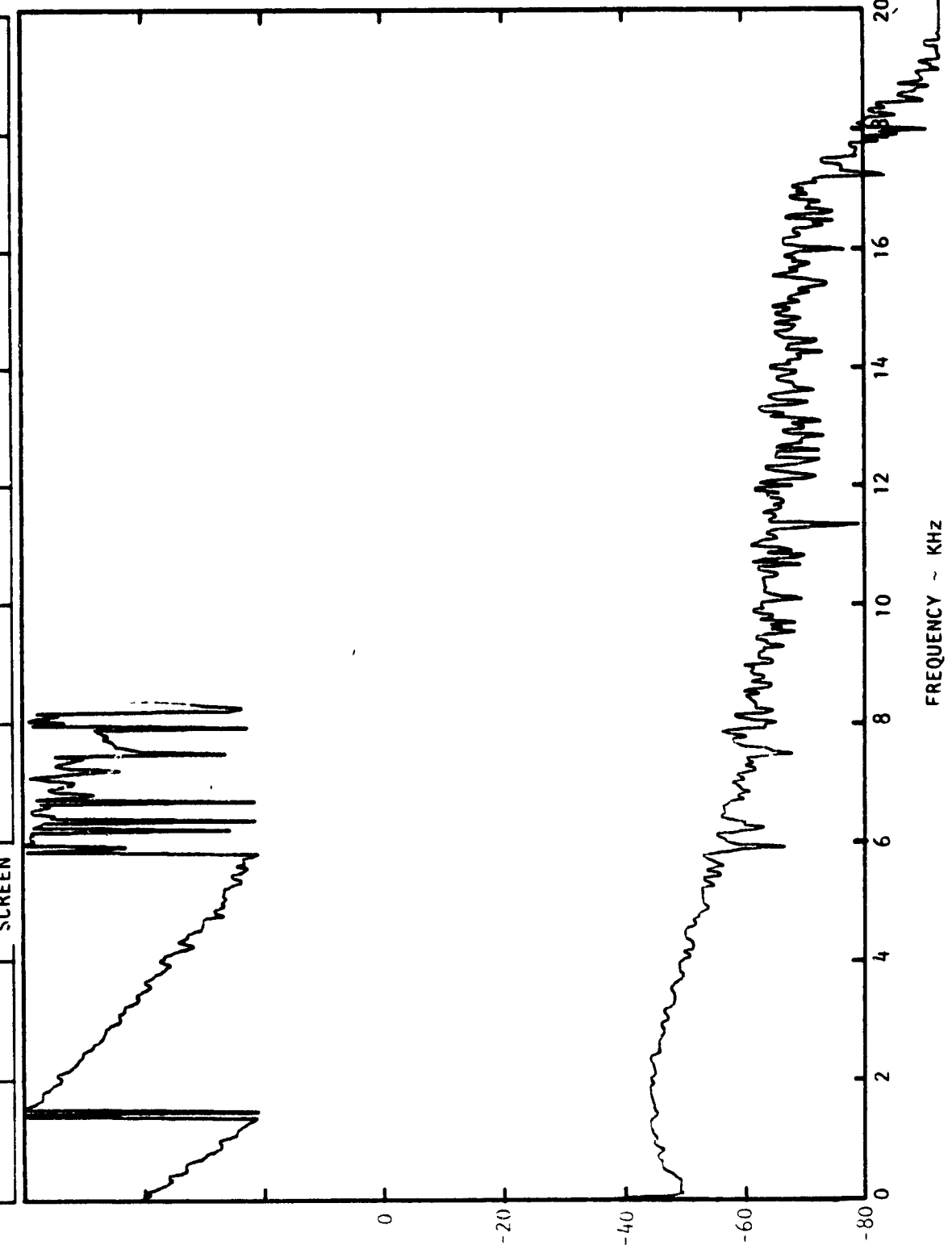


Figure C-1. Continued.

CROSS POWER SPECTRAL DENSITY $G_A(f)$ ~ DB

VEL. COMP.	U_j m/s	INIT. TURB.	β_f	X^1 - cm	ΔX^1 - cm	Y^1 - cm	ΔY^1 - cm	Z^1 - cm	ΔZ^1 - cm
W	180.	NO SCREEN	30°	1.91	2.22	0	0	0	0

PHASE ANGLE - DEGREES



FREQUENCY ~ KHZ

Figure 6-1 continued

VEL. COMP.	U_j - m/s	INIT. TURB.	δf	$X' - \text{cm}$	$\Delta X' - \text{cm}$	$Y - \text{cm}$	$\Delta Y - \text{cm}$	$Z' - \text{cm}$	$\Delta Z' - \text{cm}$
W	180.	NO SCREEN	30°	1.91	2.54	0	0	0	0

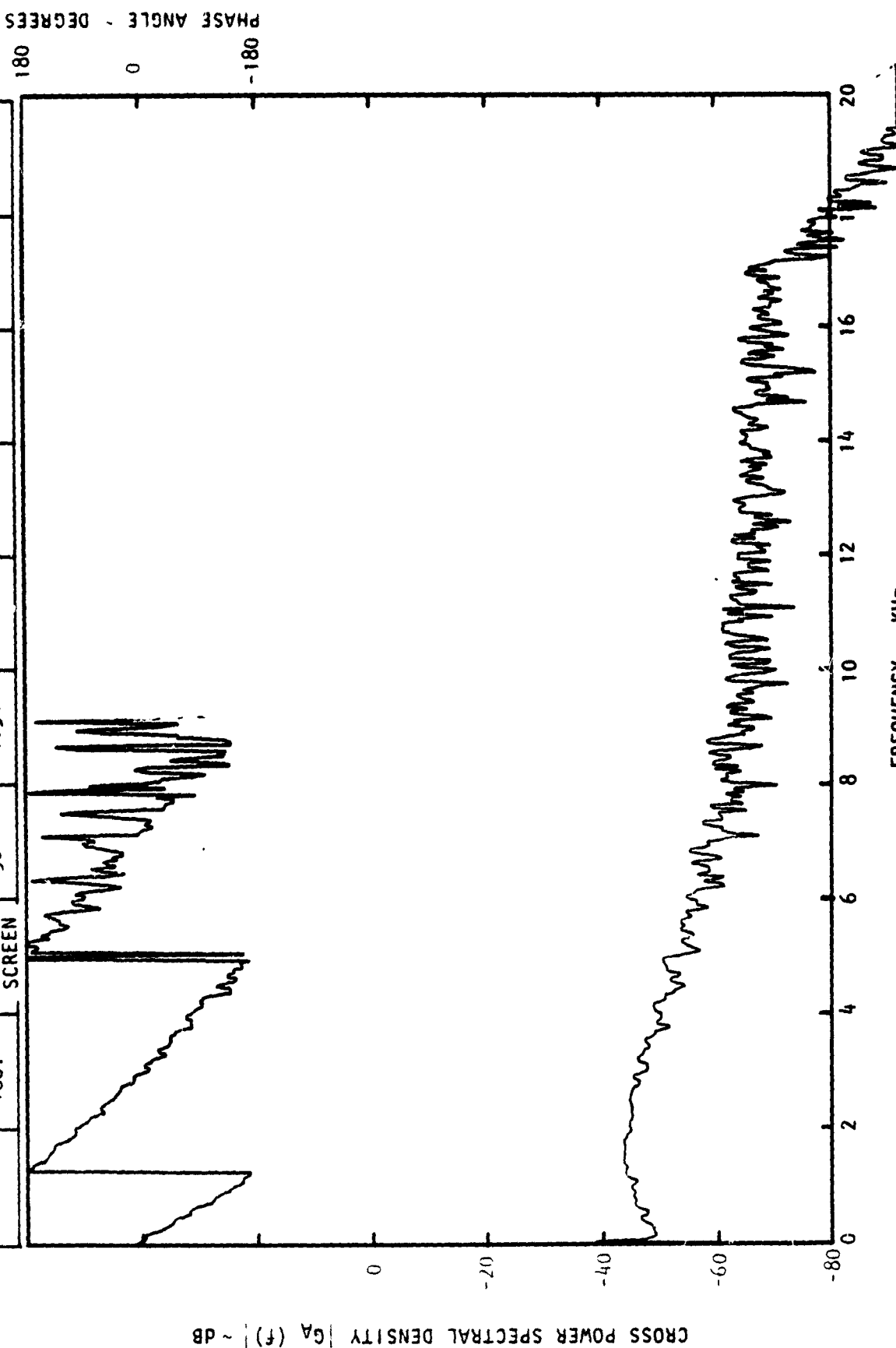
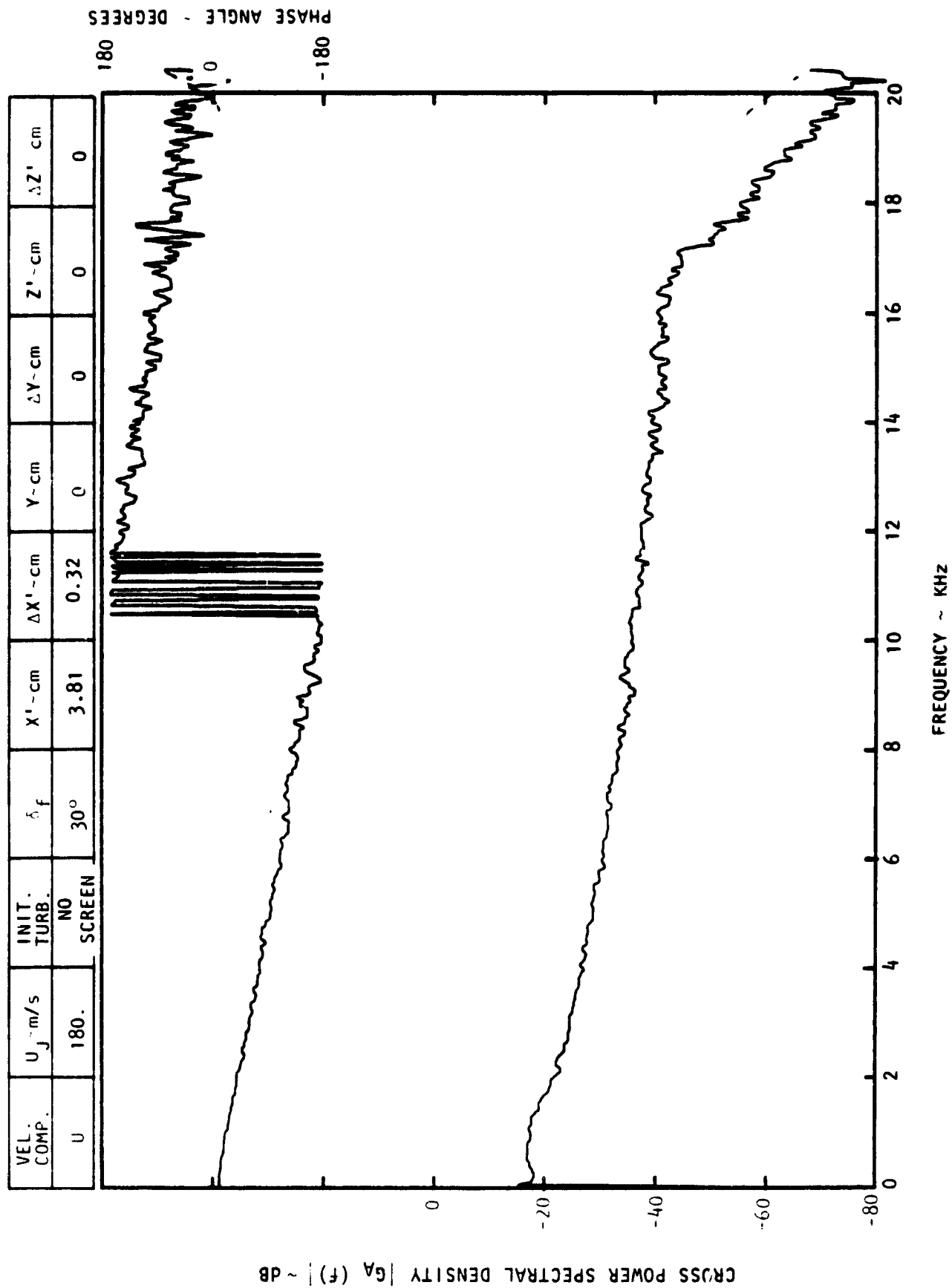
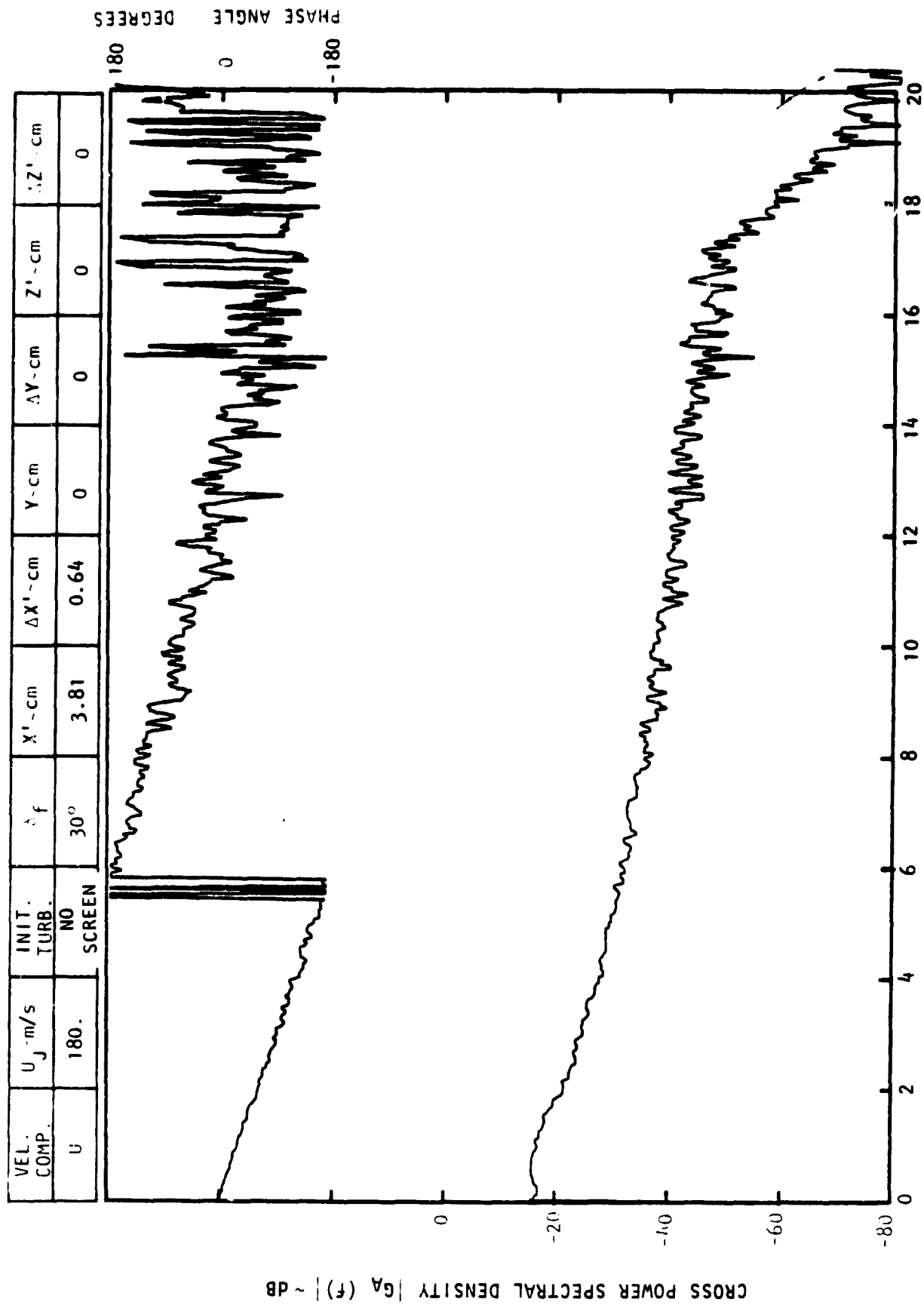


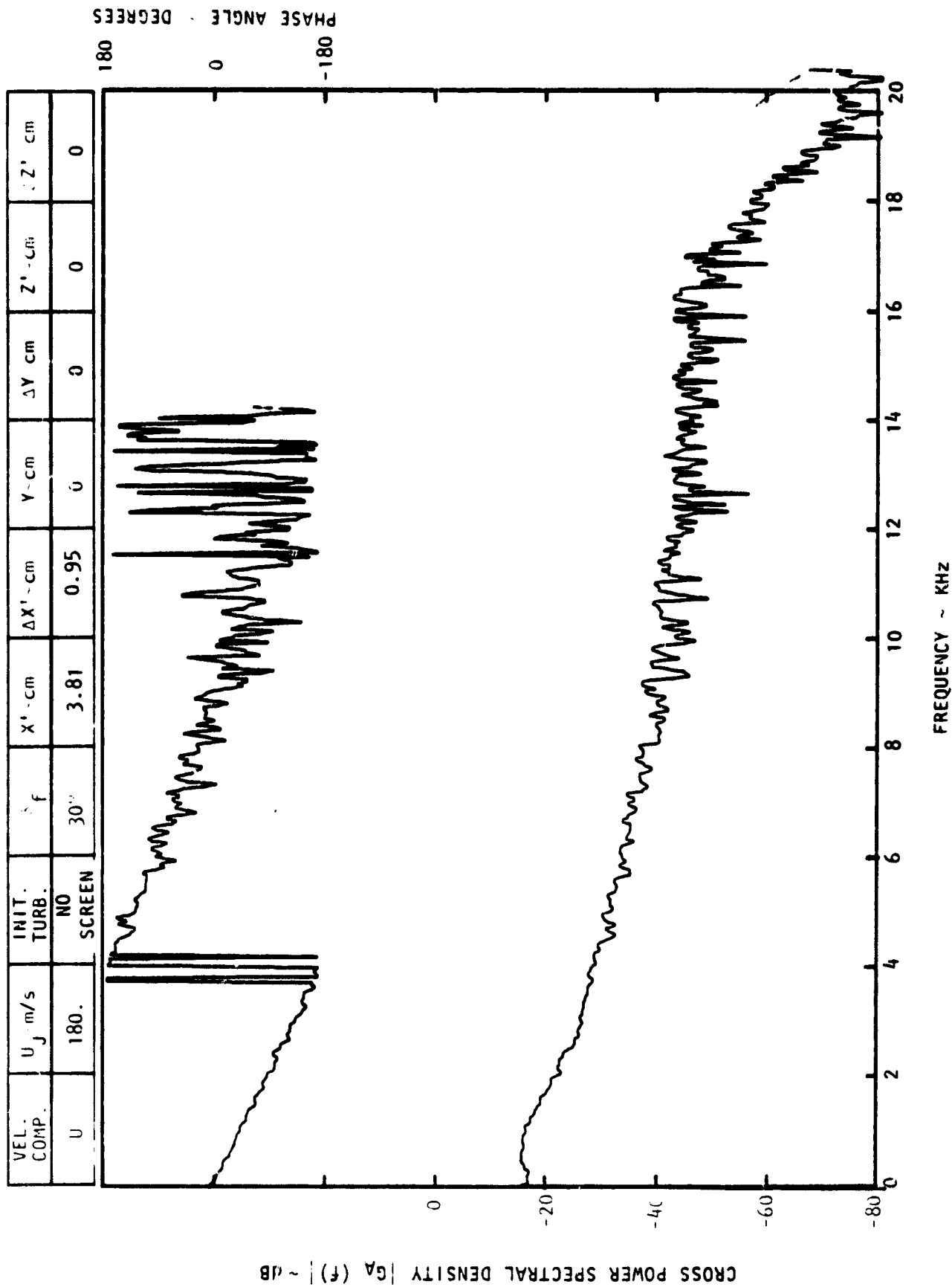
Figure C-1. Continued.

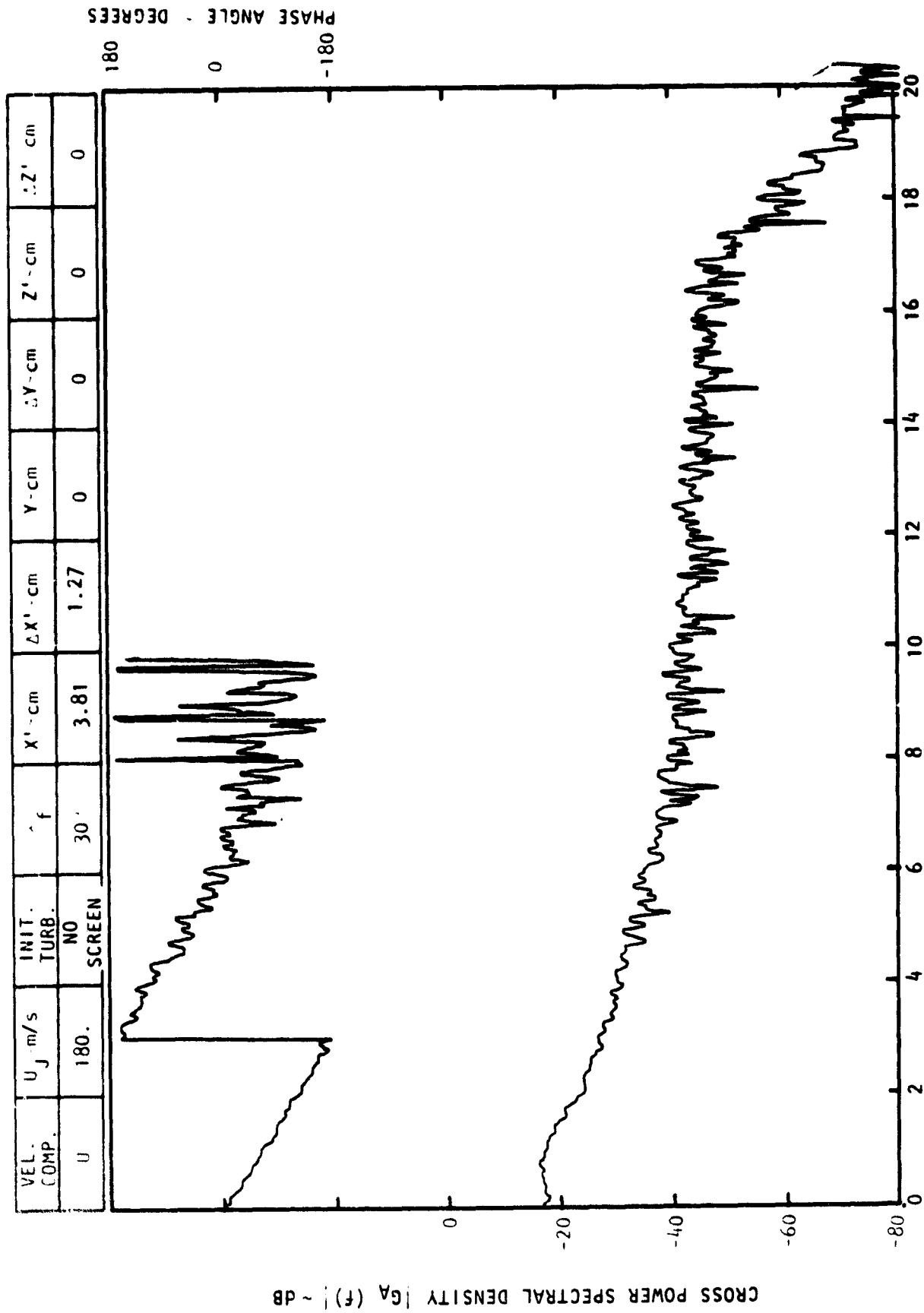




FREQUENCY ~ KHz

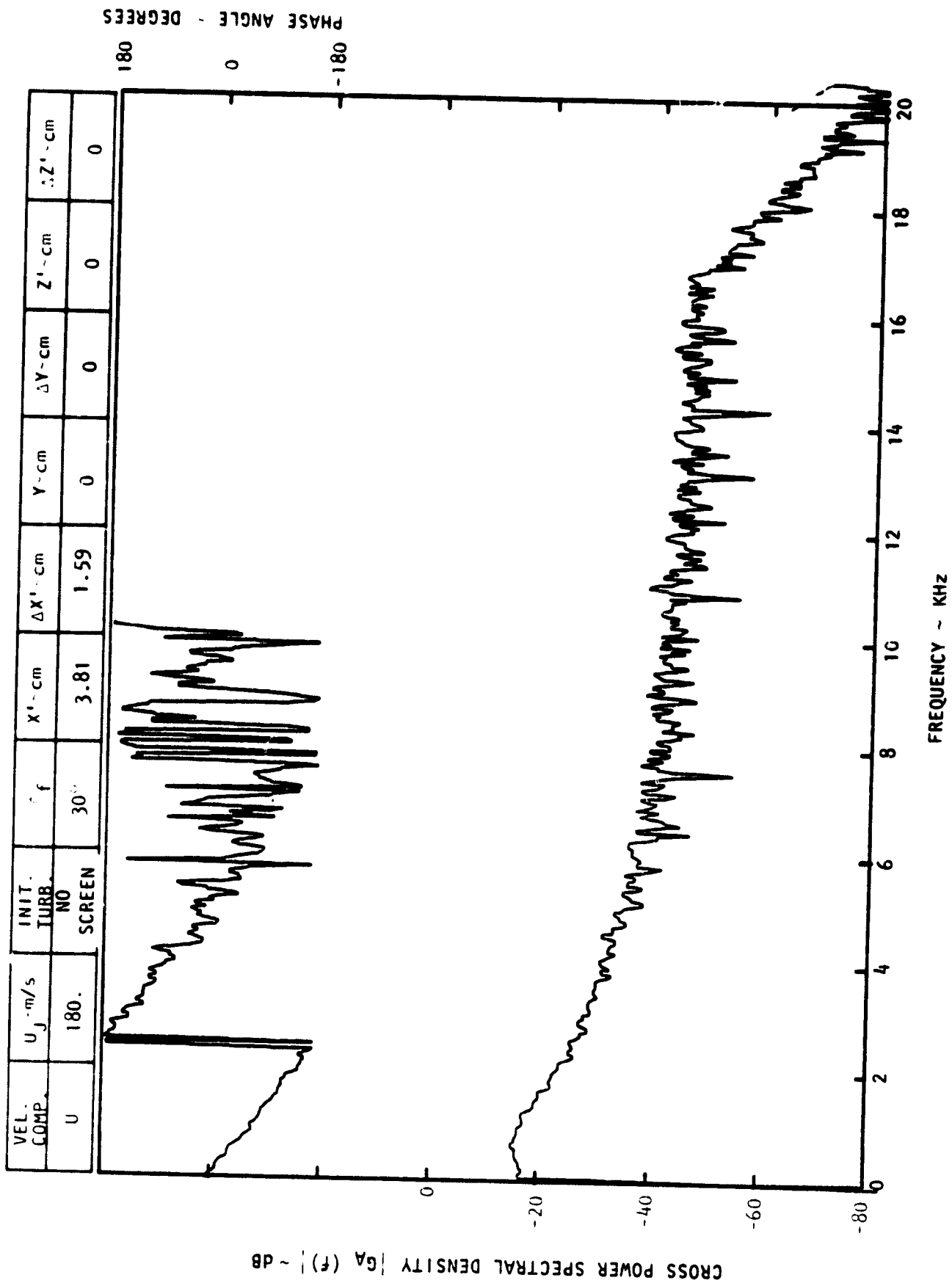
Figure C-1. Continued.

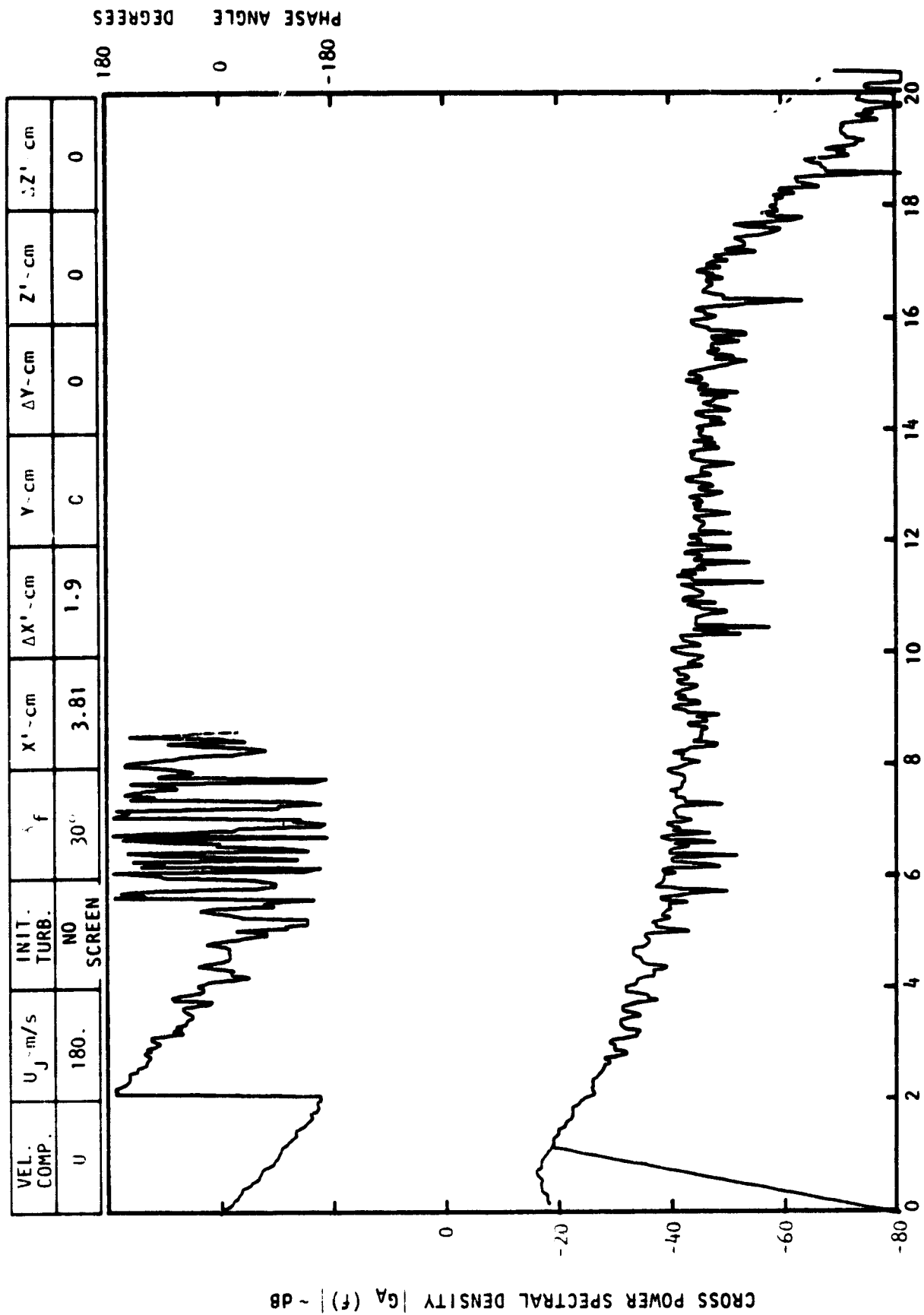




FREQUENCY ~ KHz

Figure C-1. Continued.



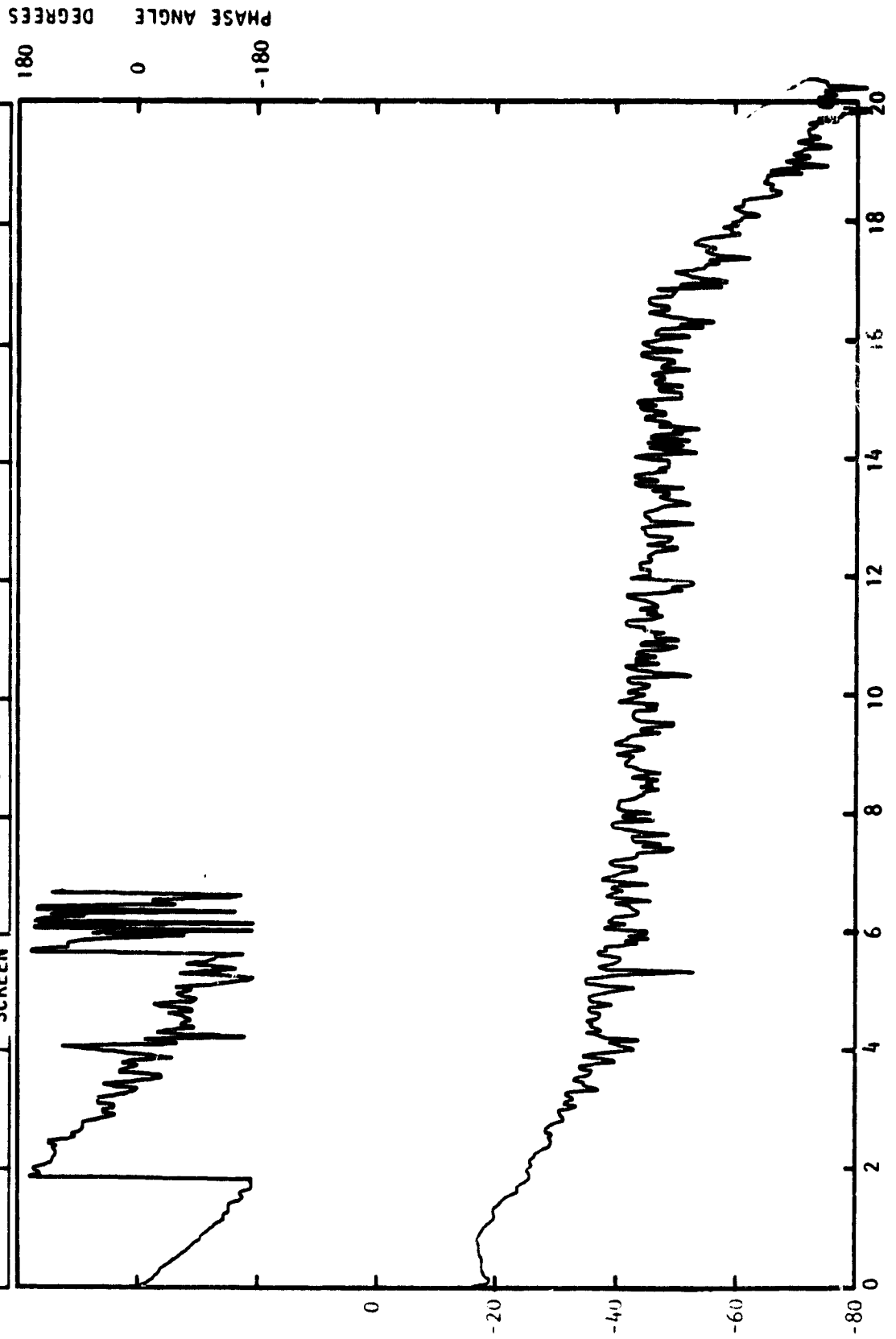


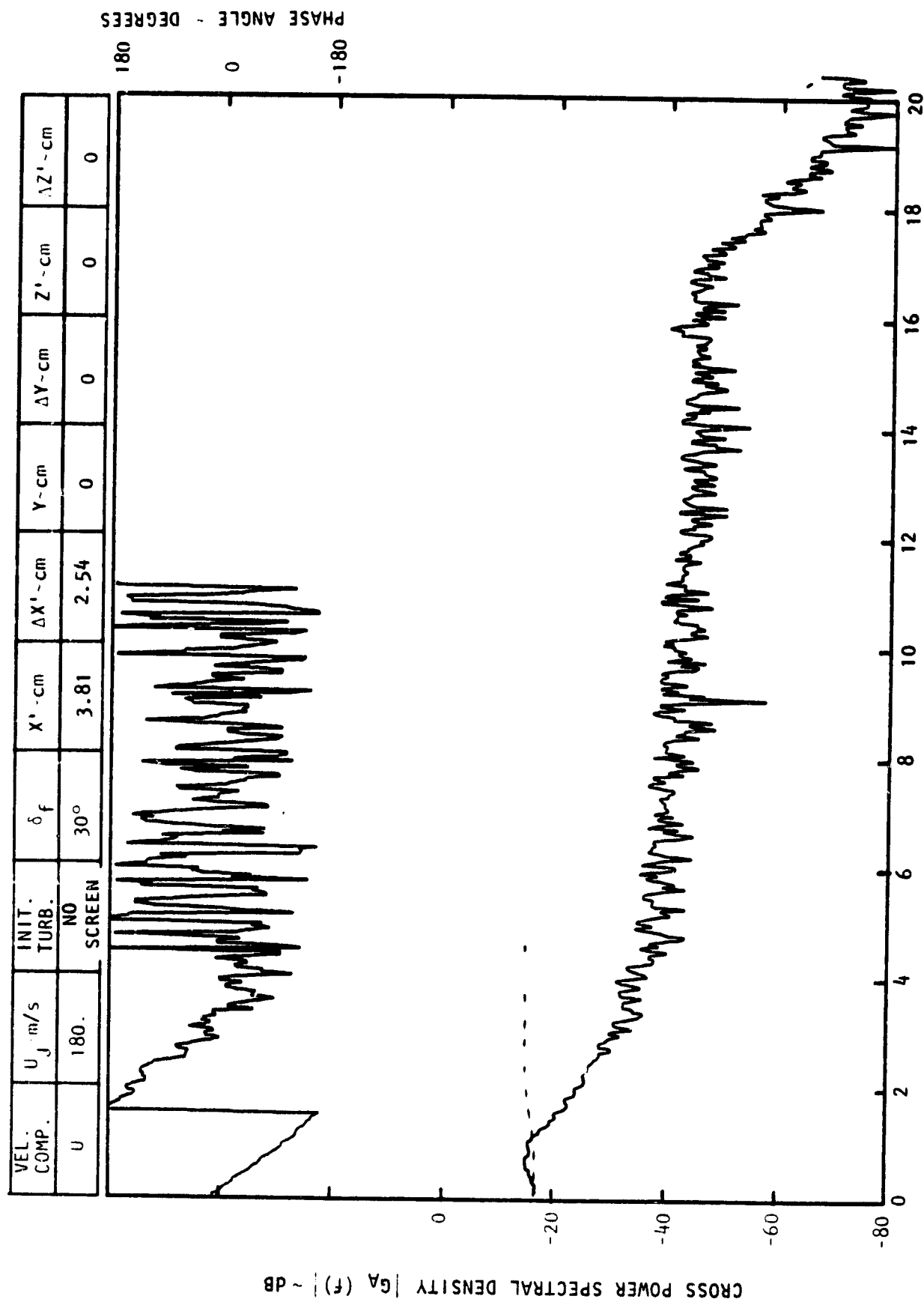
FREQUENCY ~ KHz

Figure C-1. Continued.

CROSS POWER SPECTRAL DENSITY $G_A(f)$ ~ DB

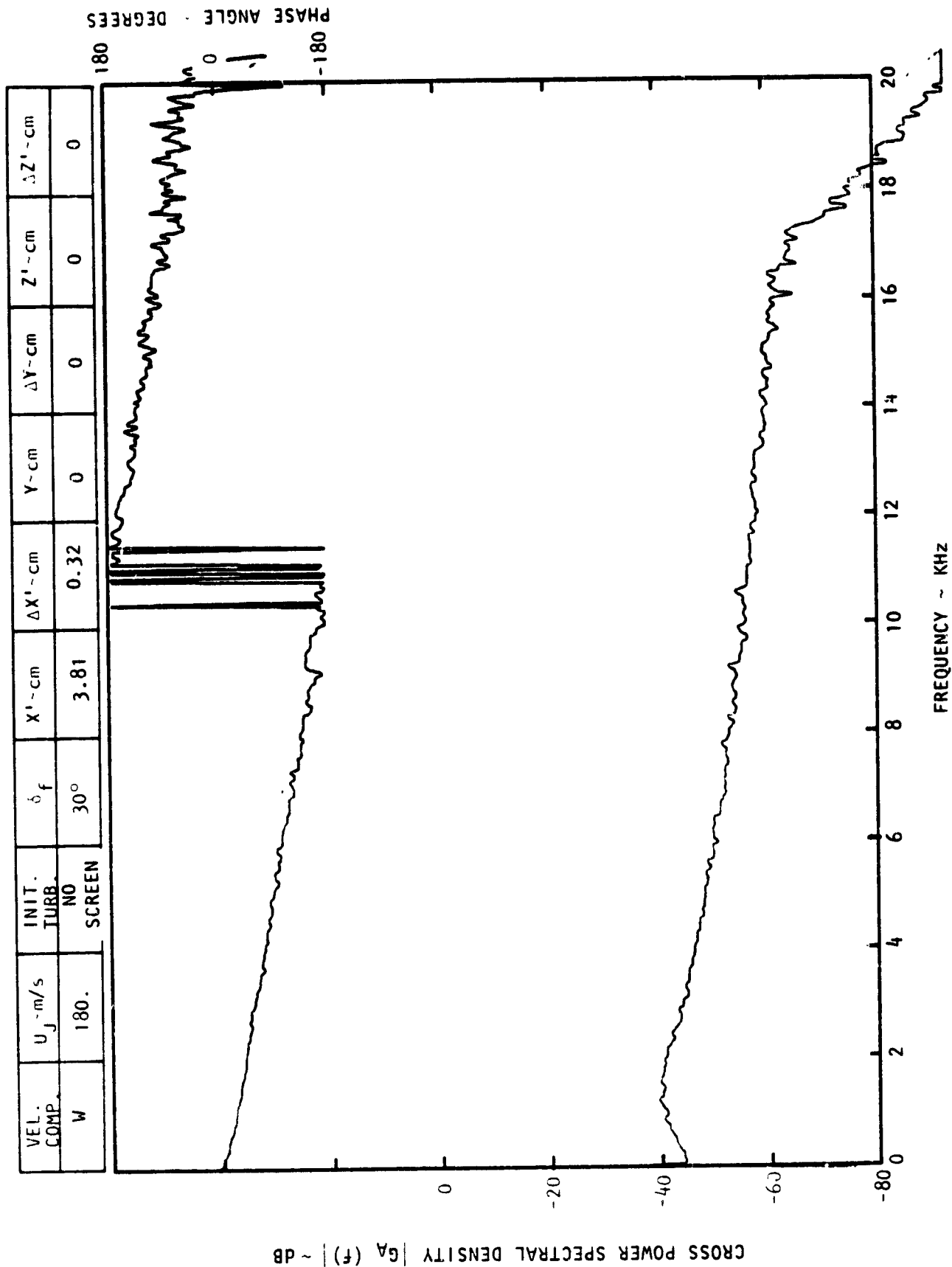
VEL. COMP.	U_j - m/s	INIT. TURB.	δ_f	X' - cm	$\Delta X'$ - cm	Y - cm	ΔY - cm	Z' - cm	$\Delta Z'$ - cm
U	180.	NO SCREEN	30°	3.81	2.22	0	0	0	0





FREQUENCY ~ KHz

Figure C-1. Continued.



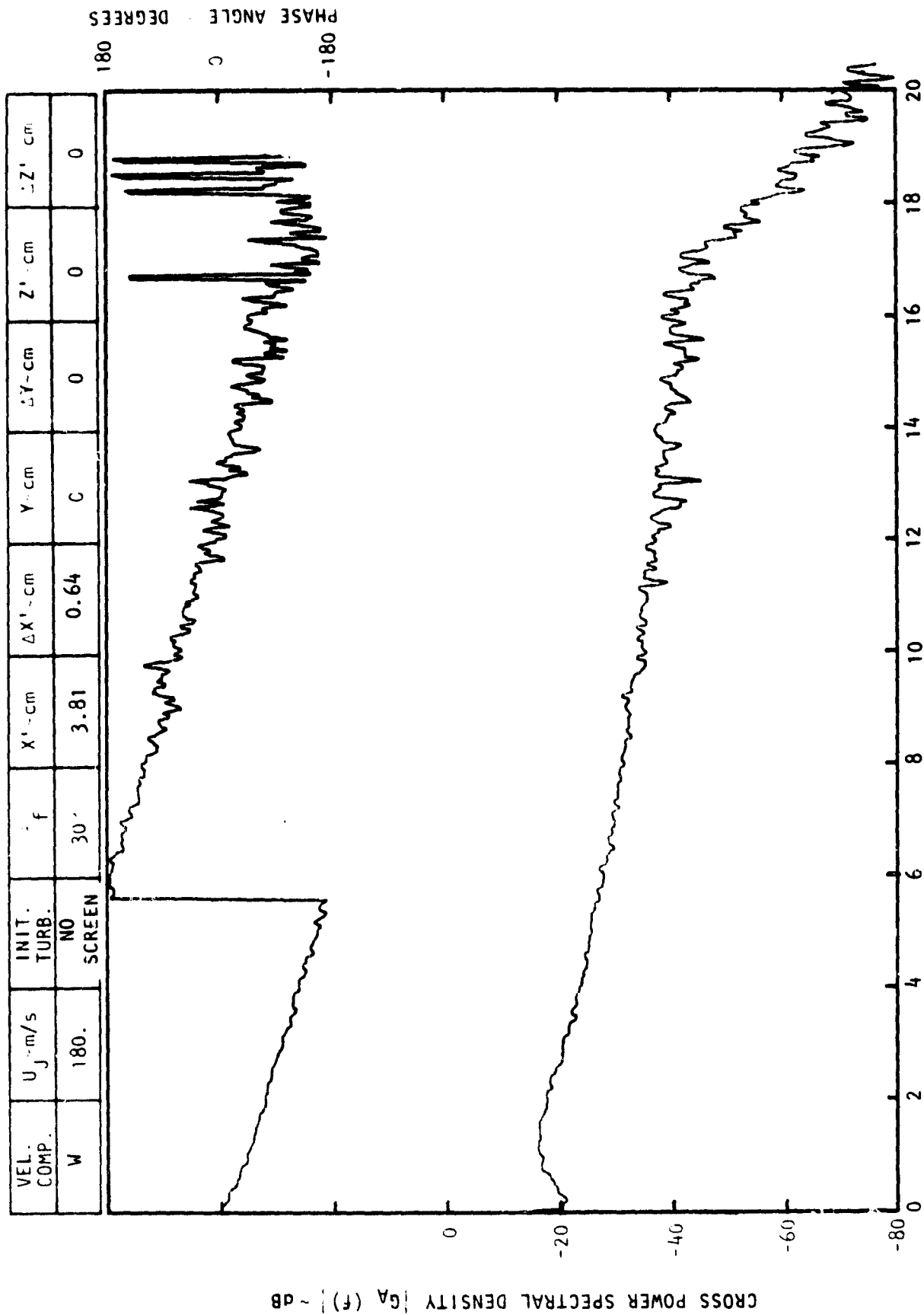
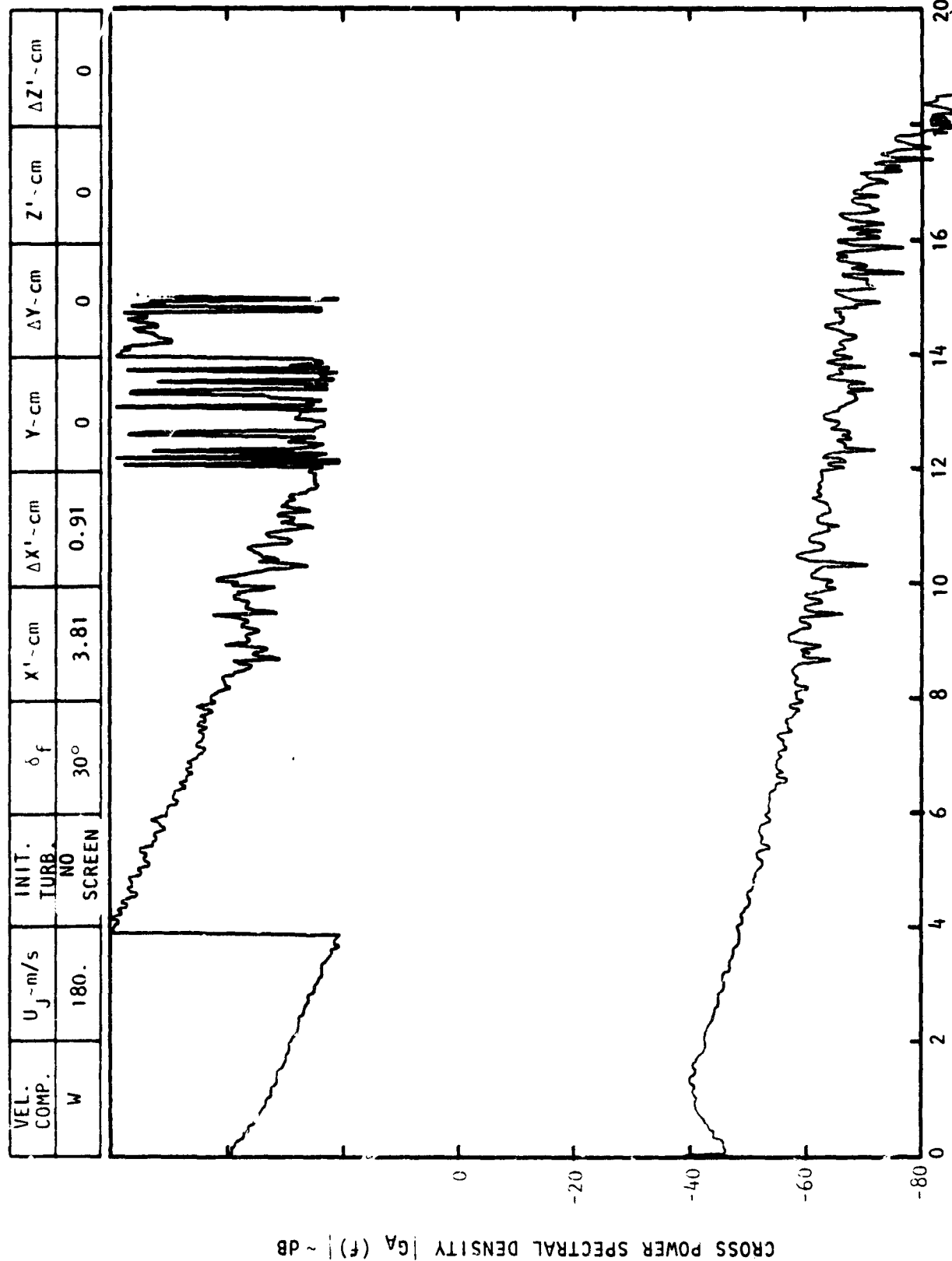


Figure C-1. Continued.



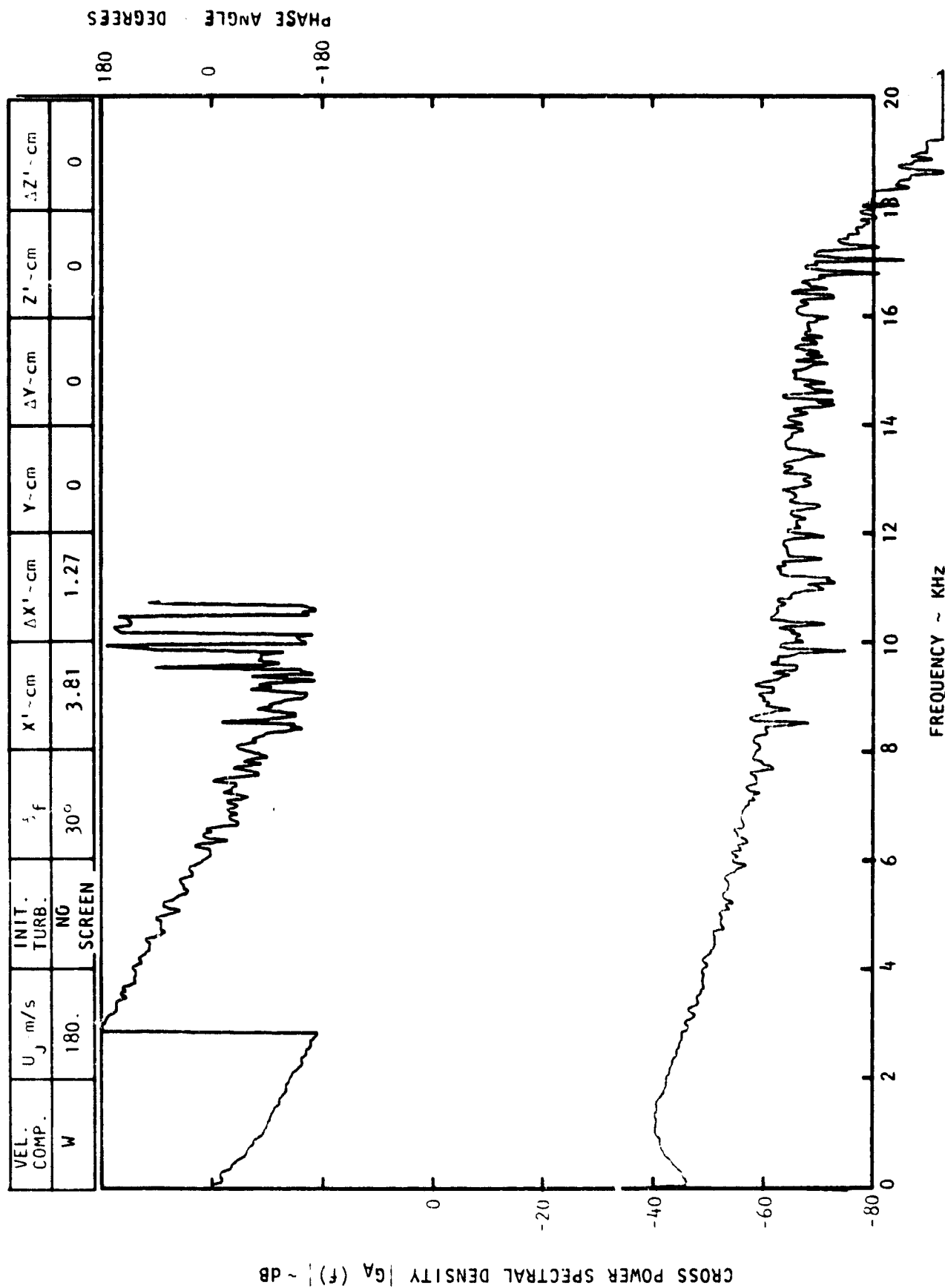
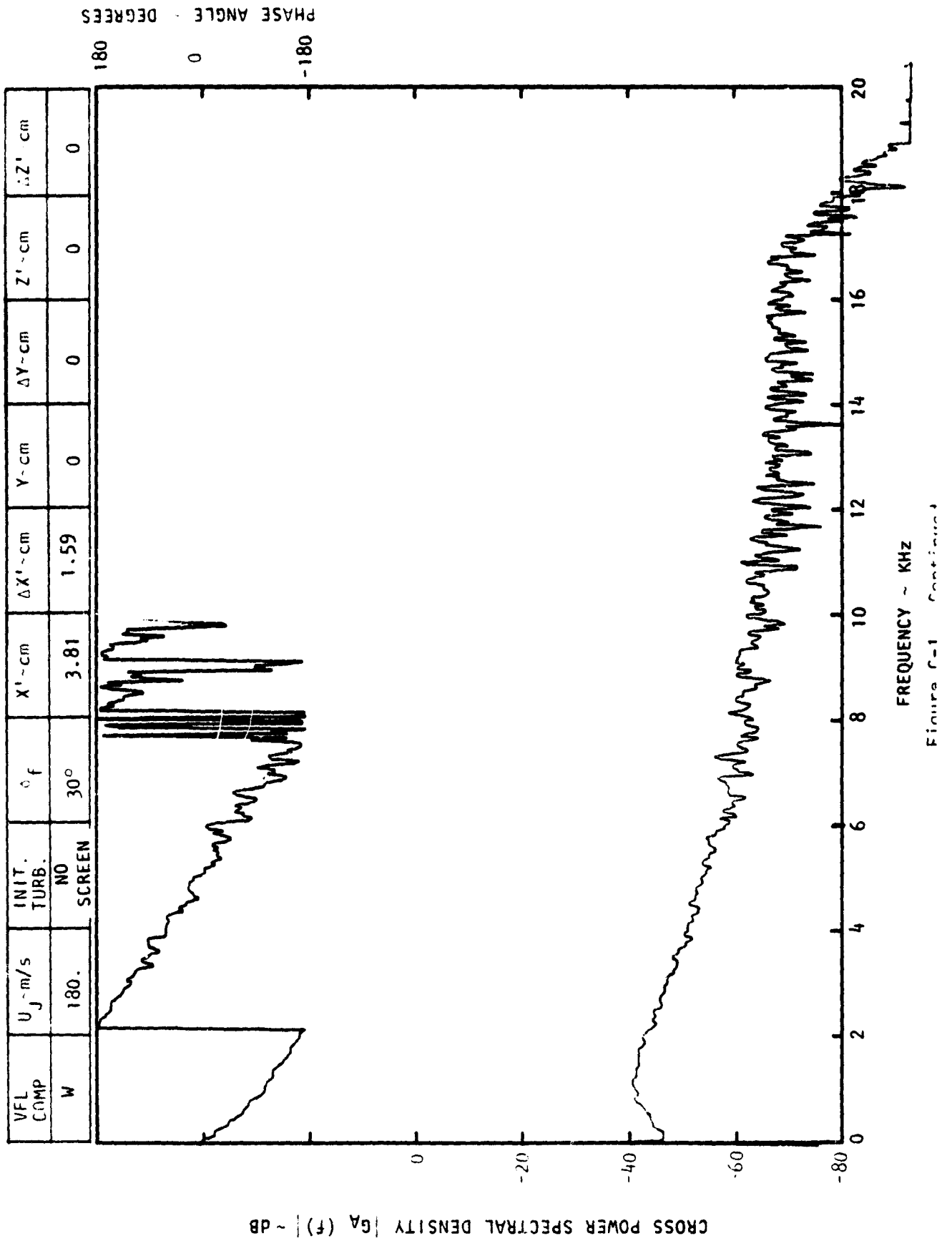


Figure C-1. Continued.



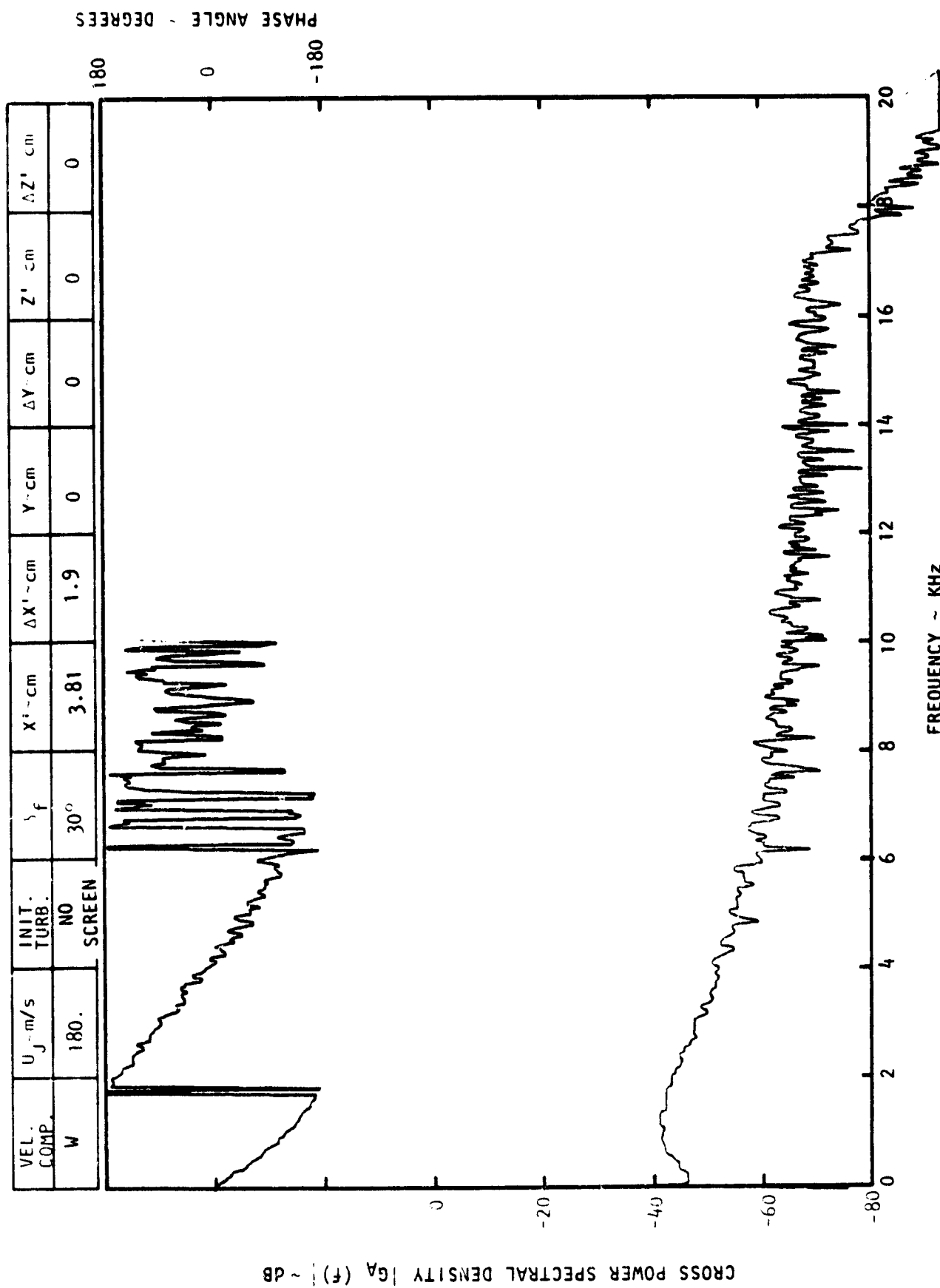
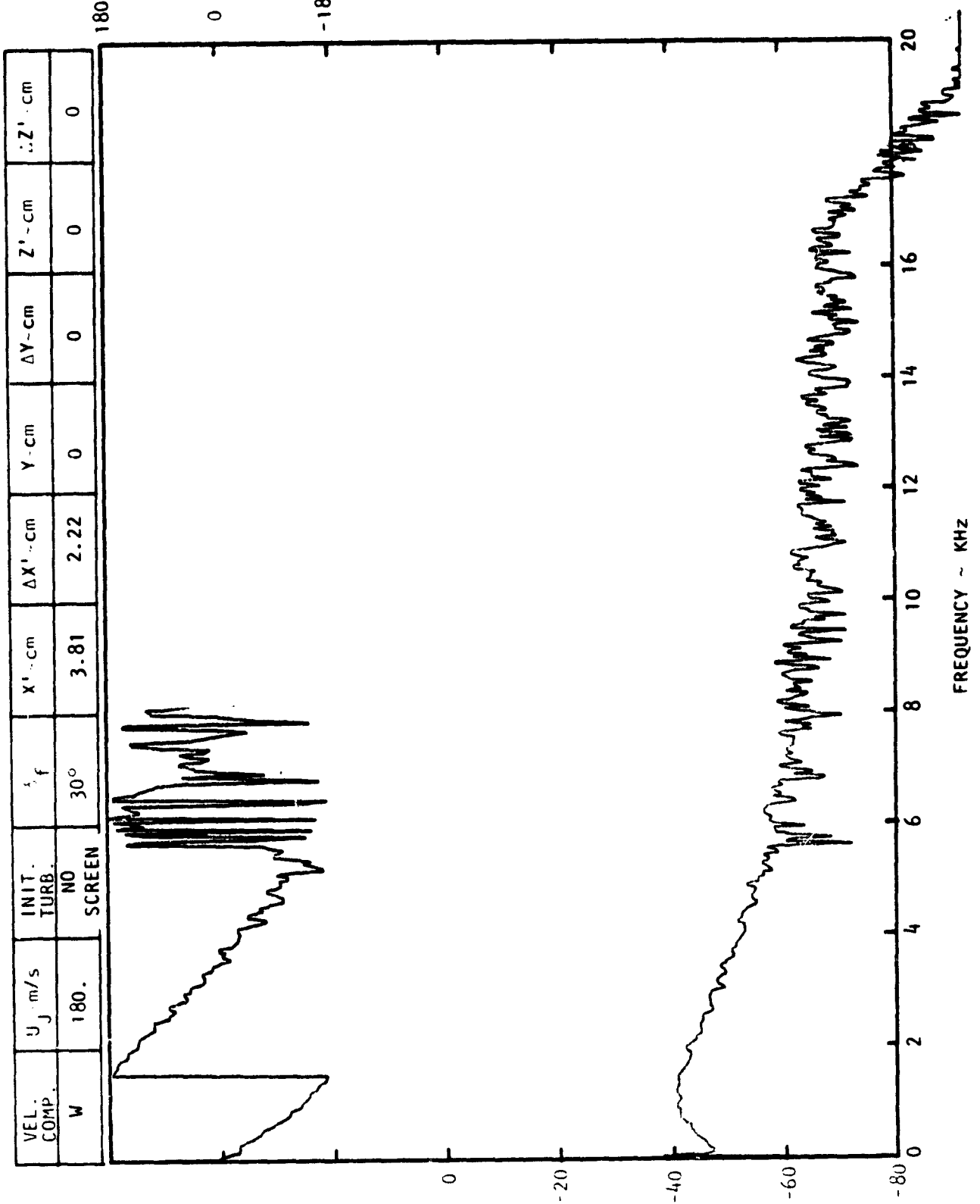


Figure C-1. Continued.

GROSS POWER SPECTRAL DENSITY $G_A(f)$ ~ dB



PHASE ANGLE - DEGREES

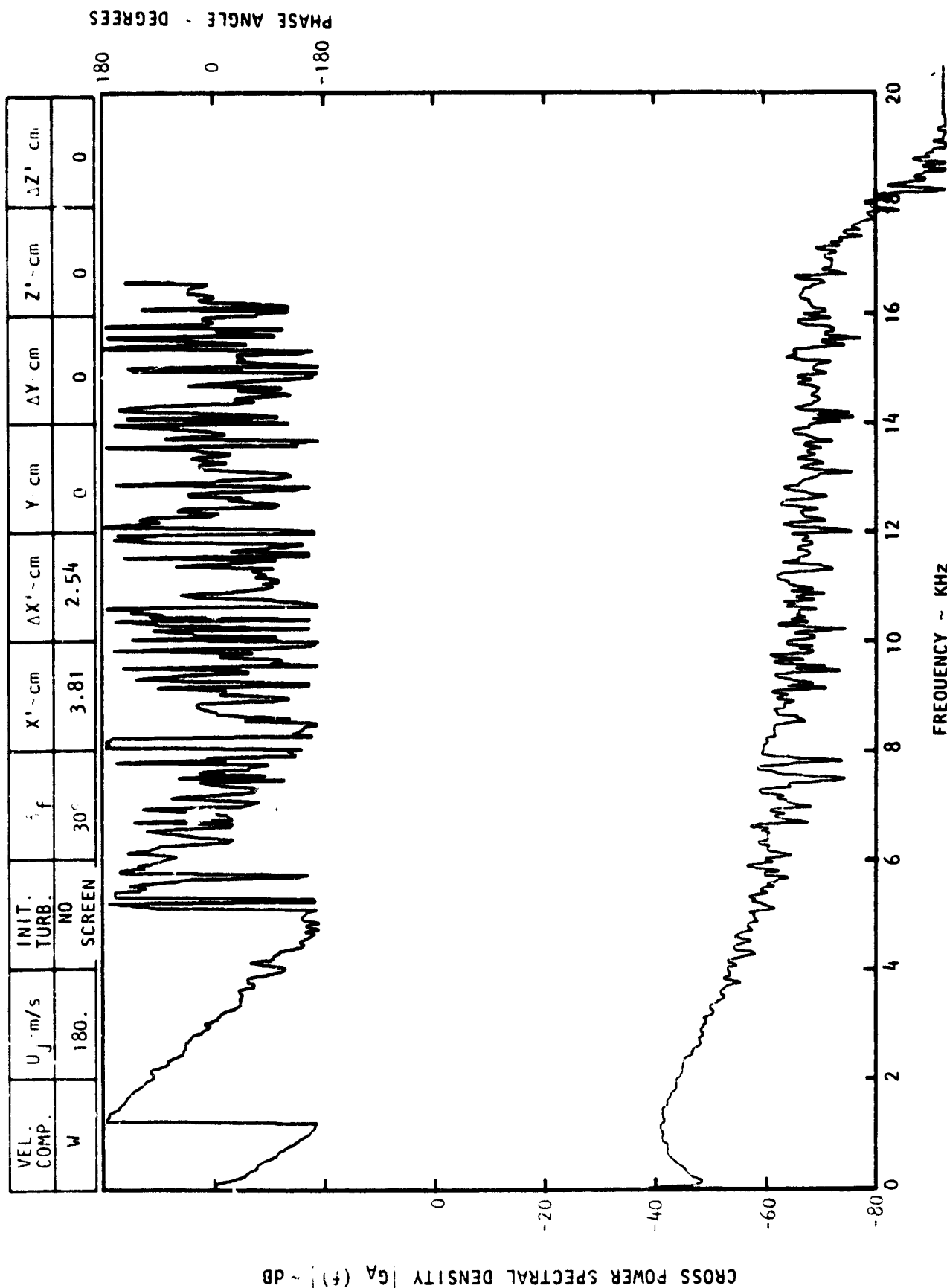
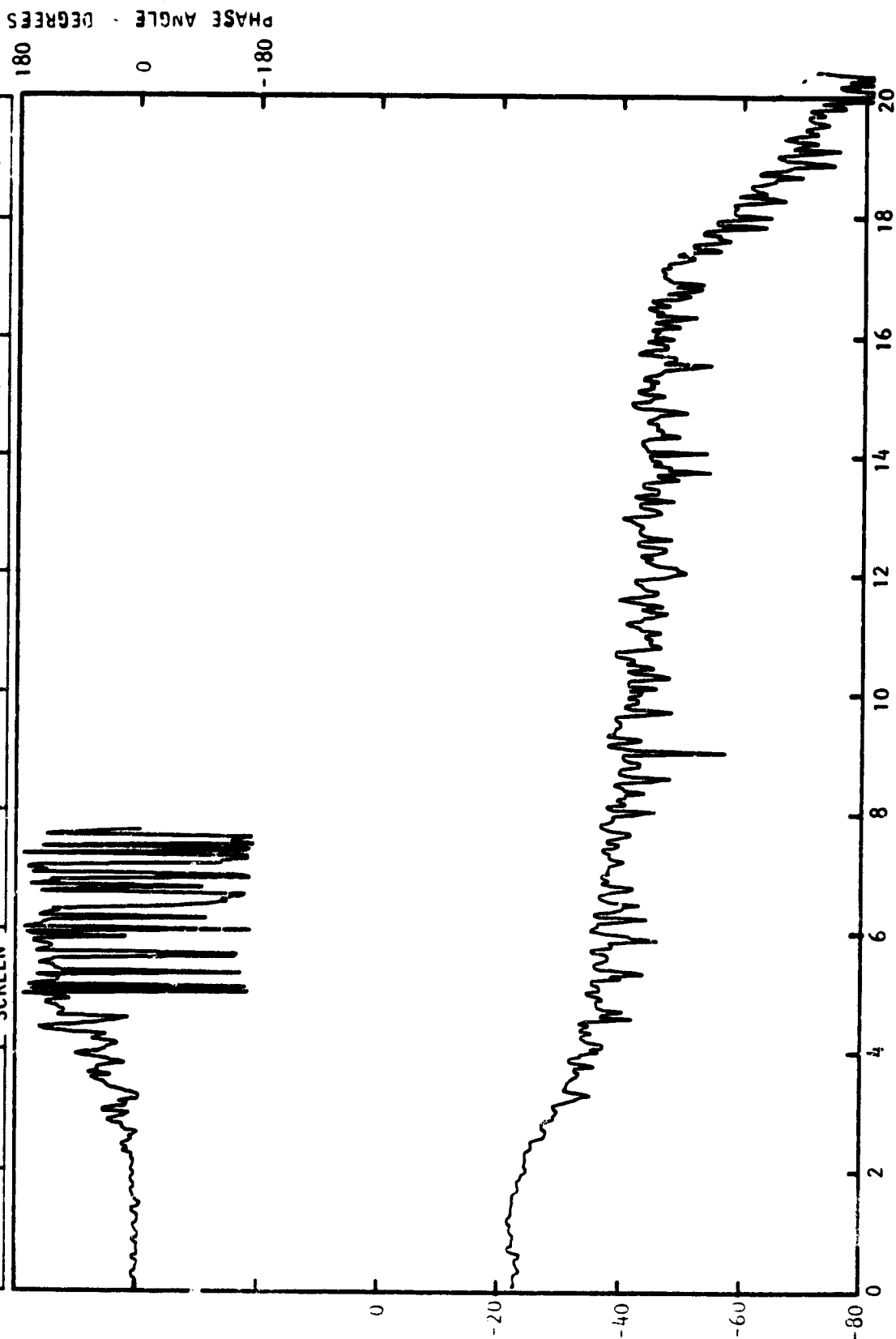


Figure C-1. Concluded.

CROSS POWER SPECTRAL DENSITY $G_{\alpha}(f)$ ~ dB

VFL COMP	U_j m/s	INIT. TURB.	ϕ_f	X' -cm	$\Delta X'$ -cm	Y -cm	ΔY -cm	Z' -cm	$\Delta Z'$ -cm
U	180.	NO SCREEN	30°	1.91	0	0	0.30	0	0



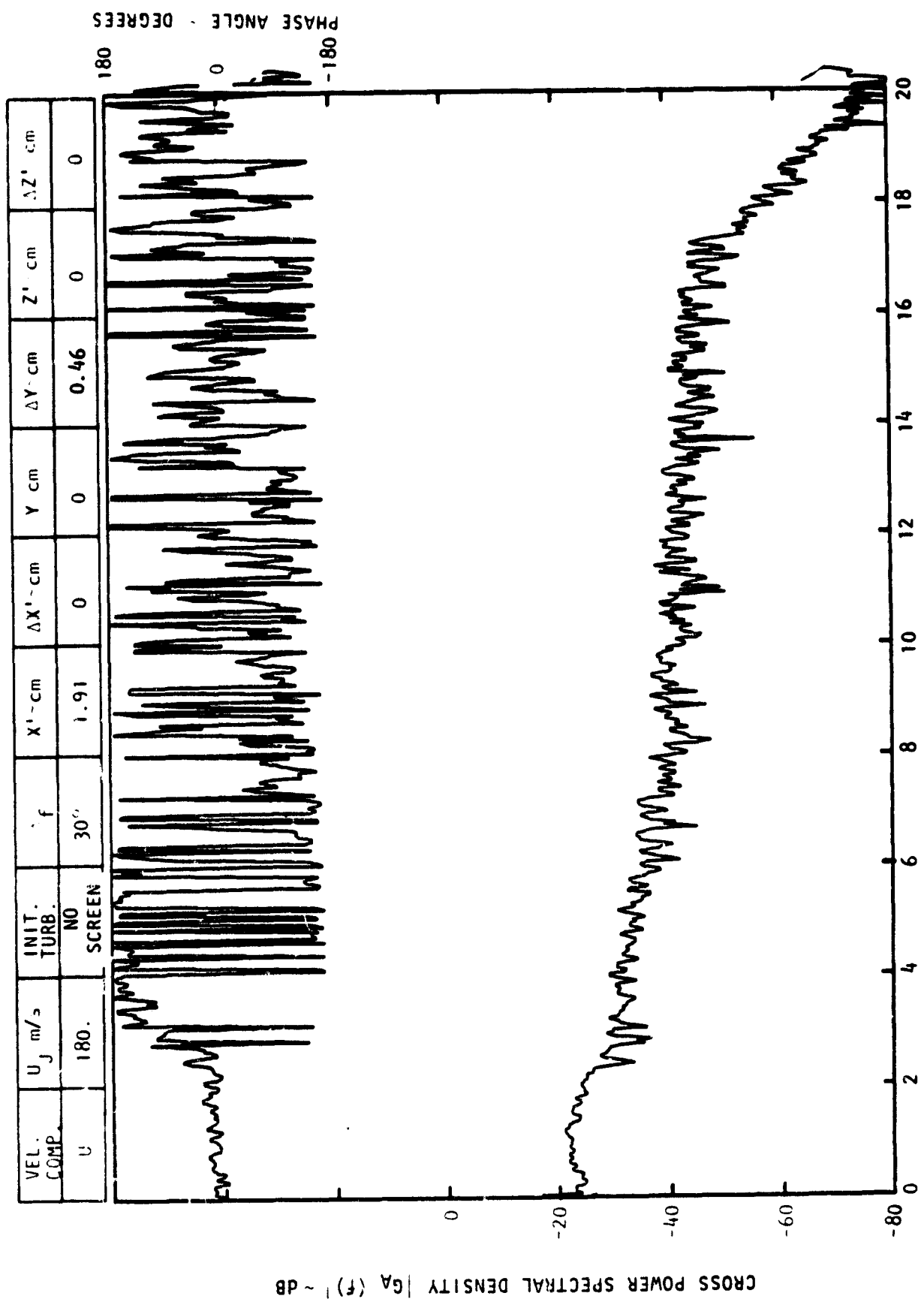
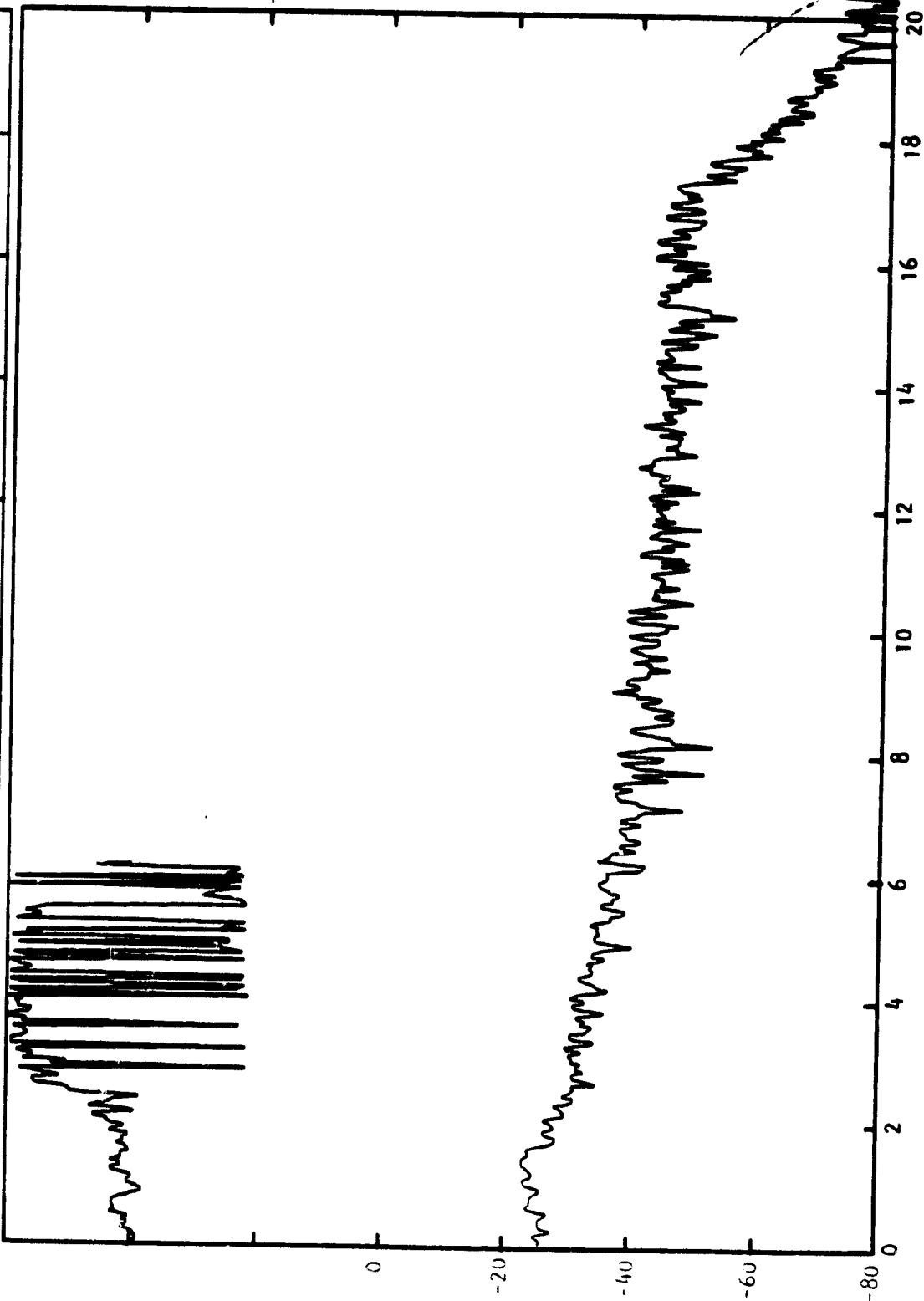


Figure C-2. Continued.

CROSS POWER SPECTRAL DENSITY $|G_A(f)|^2 \sim \text{dB}$

PHASE ANGLE DEGREES

VEL. COMP.	U_j - m/s	INIT. TURB.	ϕ_f	$X' - \text{cm}$	$\Delta X' - \text{cm}$	$Y - \text{cm}$	$\Delta Y - \text{cm}$	$Z' - \text{cm}$	$\Delta Z' - \text{cm}$
U	180.	NO SCREEN	30°	1.91	0	0	0.61	0	0



FREQUENCY ~ KHz

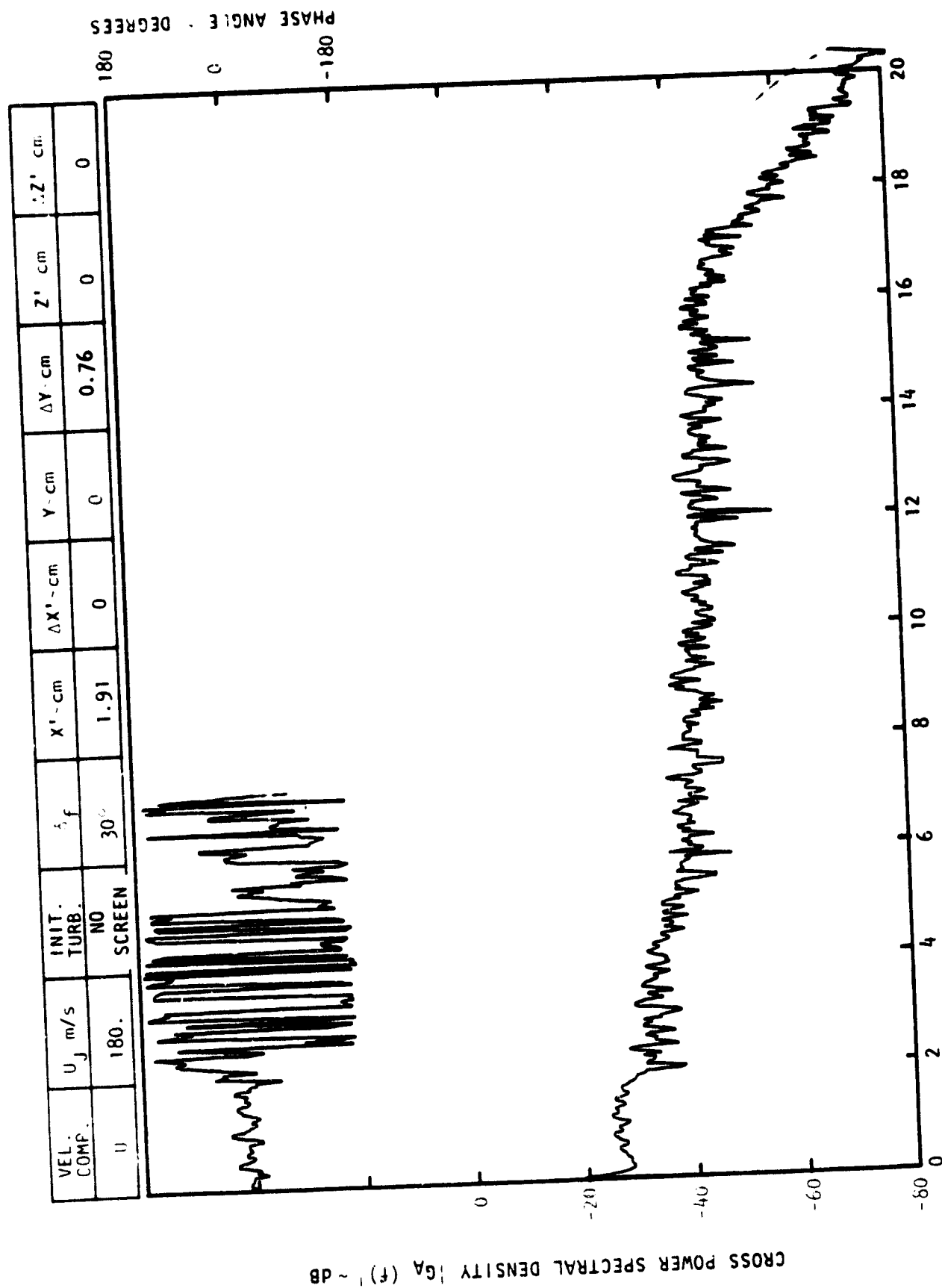
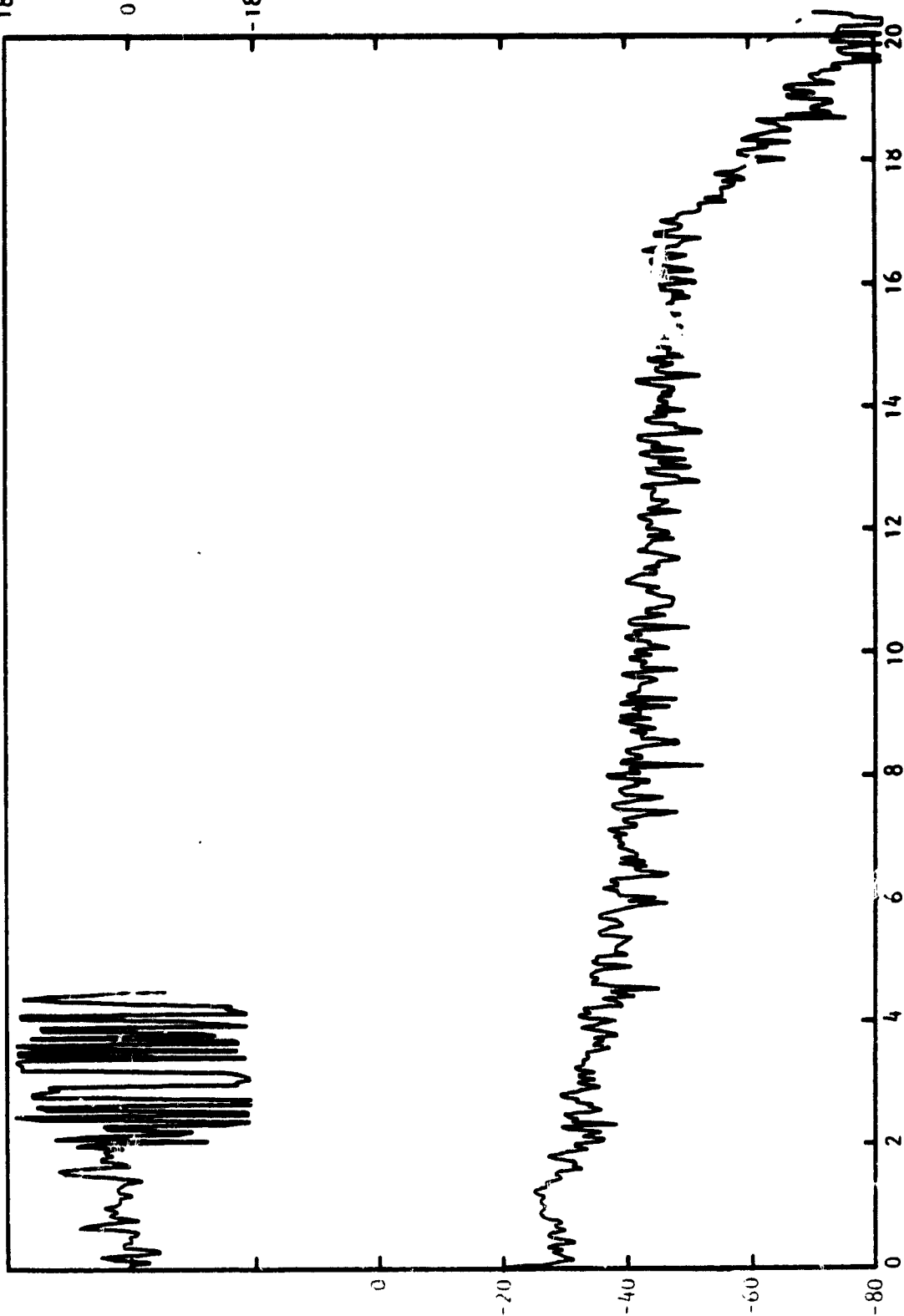


Figure C-2. Continued.

CROSS POWER SPECTRAL DENSITY $G_A(f)$ ~ DB

VEL. COMP.	U_j m/s	INIT. TURB.	θ_f	X^1 - cm	ΔX^1 - cm	Y - cm	ΔY - cm	Z^1 - cm	ΔZ^1 - cm
U	180.	NO SCREEN	30°	1.91	0	0	0.91	0	0

PHASE ANGLE - DEGREES



FREQUENCY ~ KHZ

C-4

VEL. COMP.	U_j - m/s	INIT. TURB.	δ_f	X^1 - cm	ΔX^1 - cm	Y - cm	ΔY - cm	Z^1 - cm	ΔZ^1 - cm
U	180.	NO SCREEN	30°	1.91	0	0	1.07	0	0

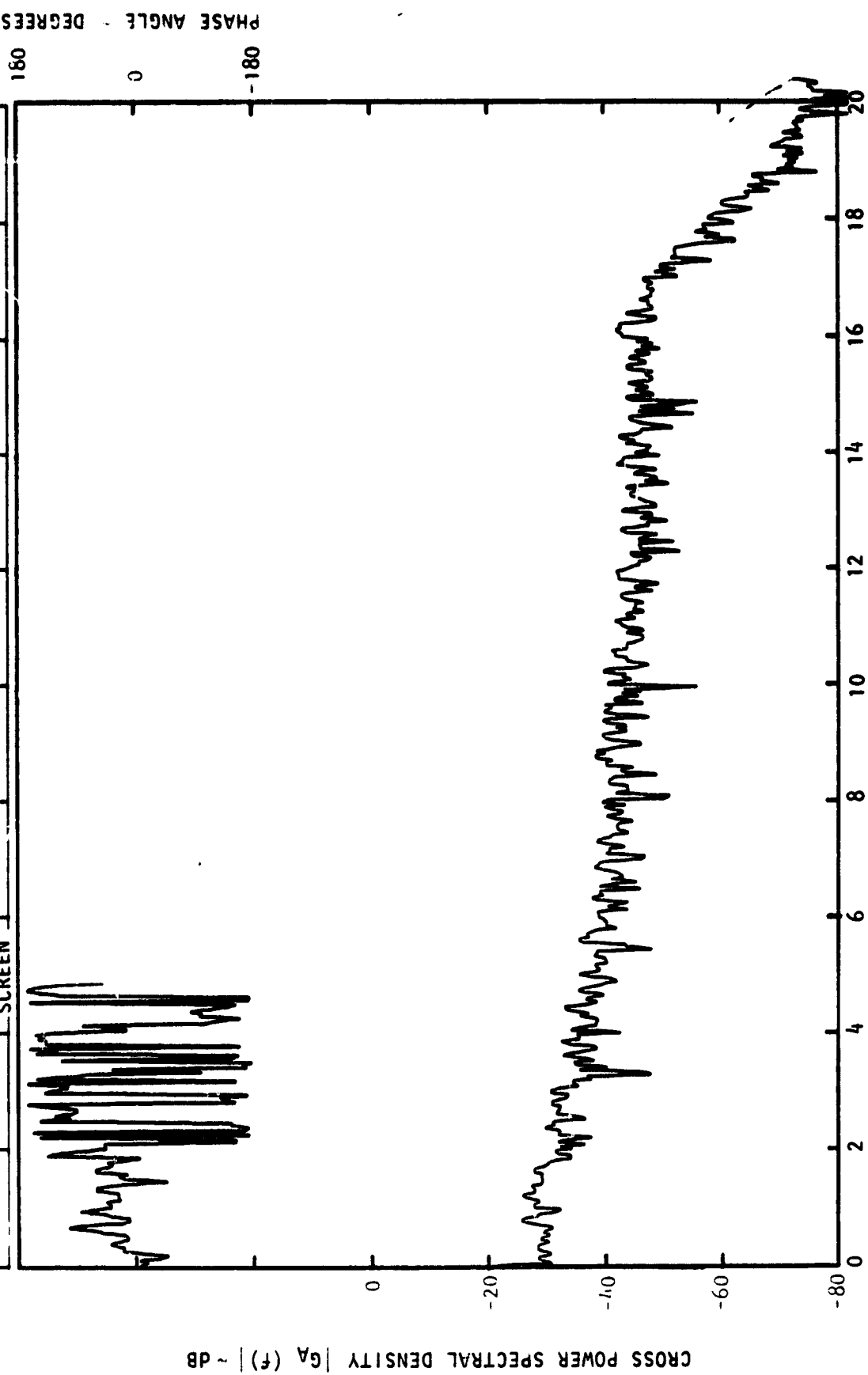


Figure C-2. Continued.

PHASE ANGLE - DEGREES

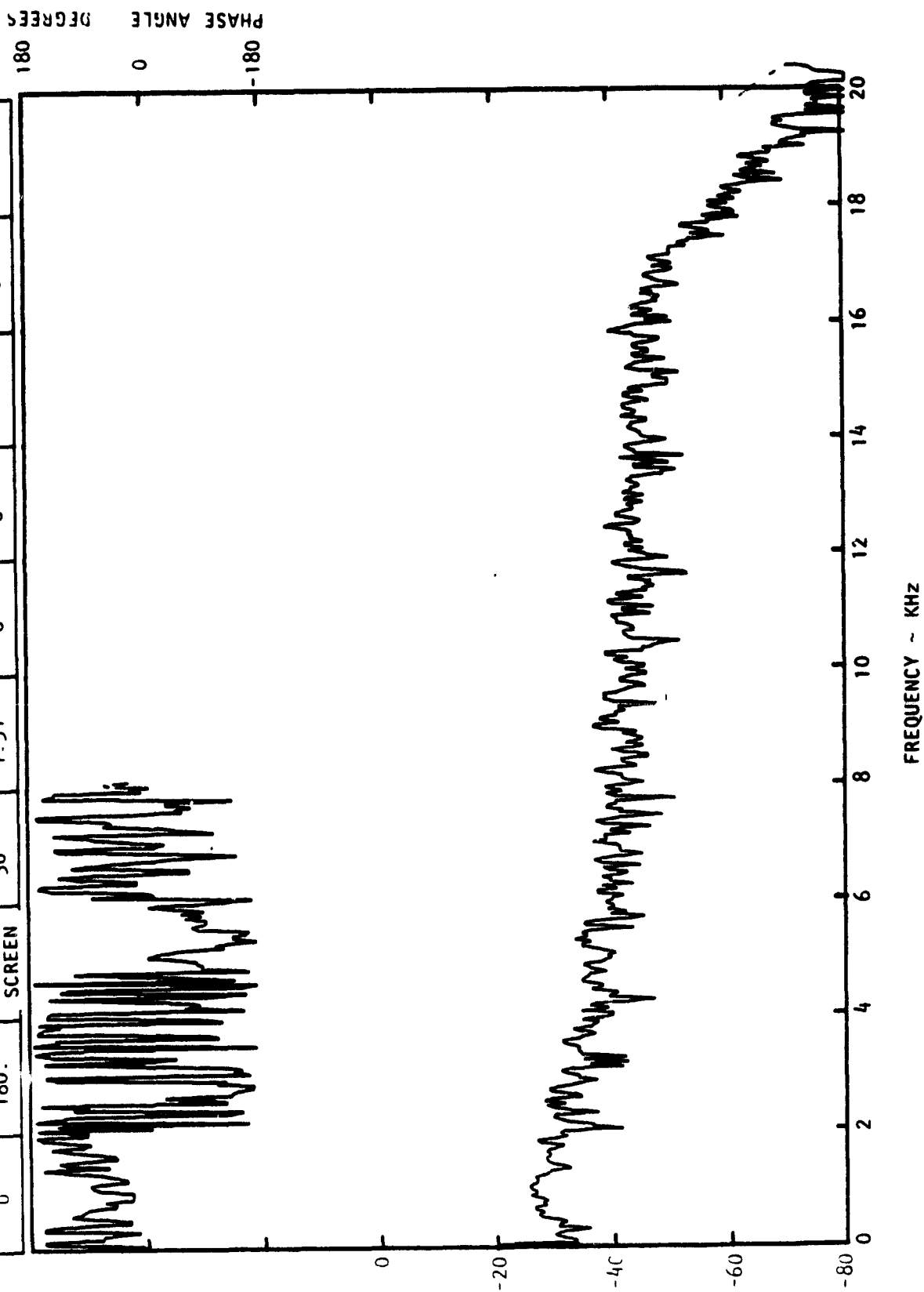
180

0

-180

CROSS POWER SPECTRAL DENSITY $G_A(f)$ ~ dB

VEL. COMP.	U_j - m/s	INIT. TURB.	δf	X^1 - cm	ΔX^1 - cm	Y - cm	ΔY - cm	Z^1 - cm	ΔZ^1 - cm
U	180.	NO SCREEN	30°	1.91	0	0	1.22	0	0



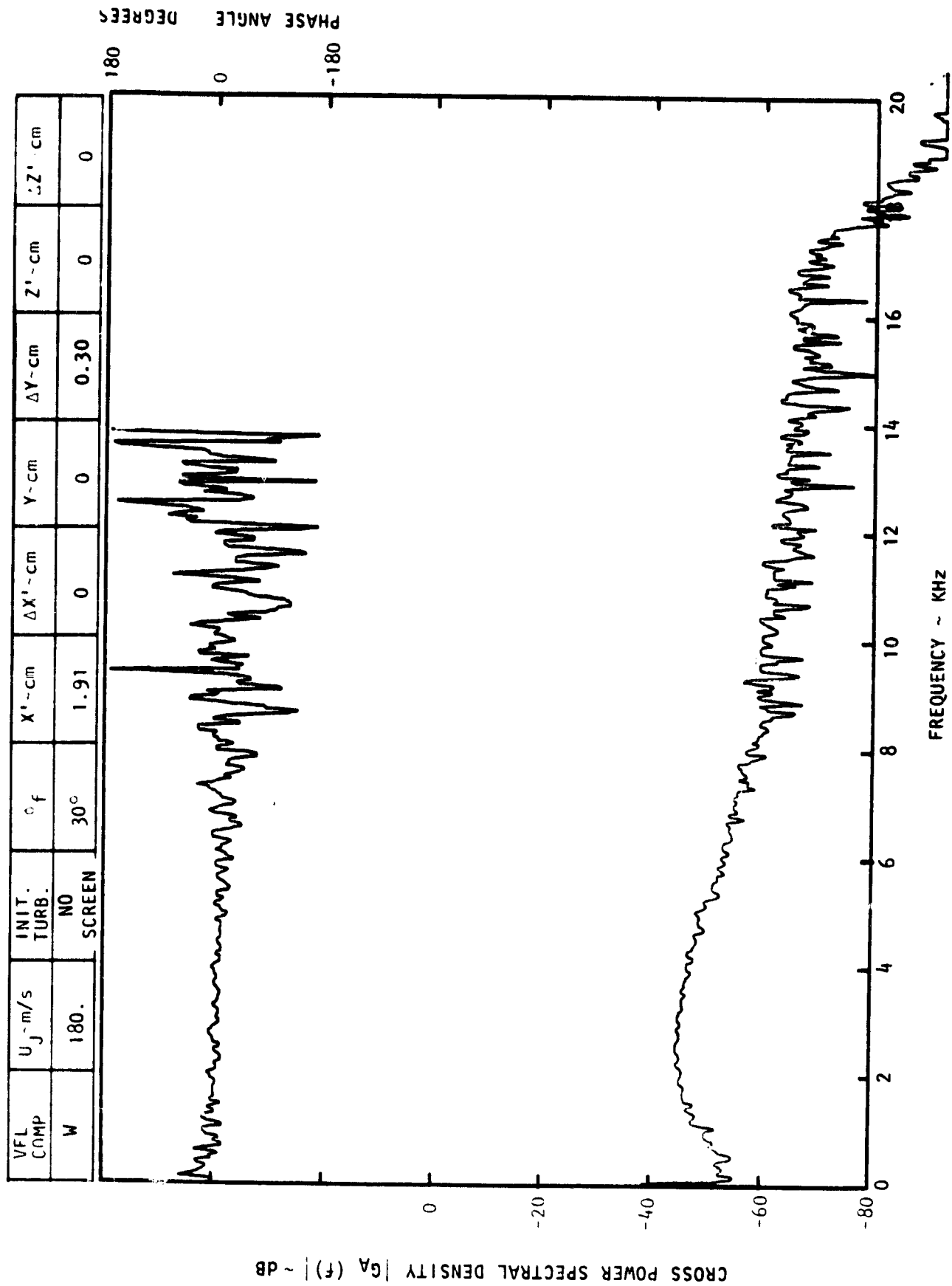
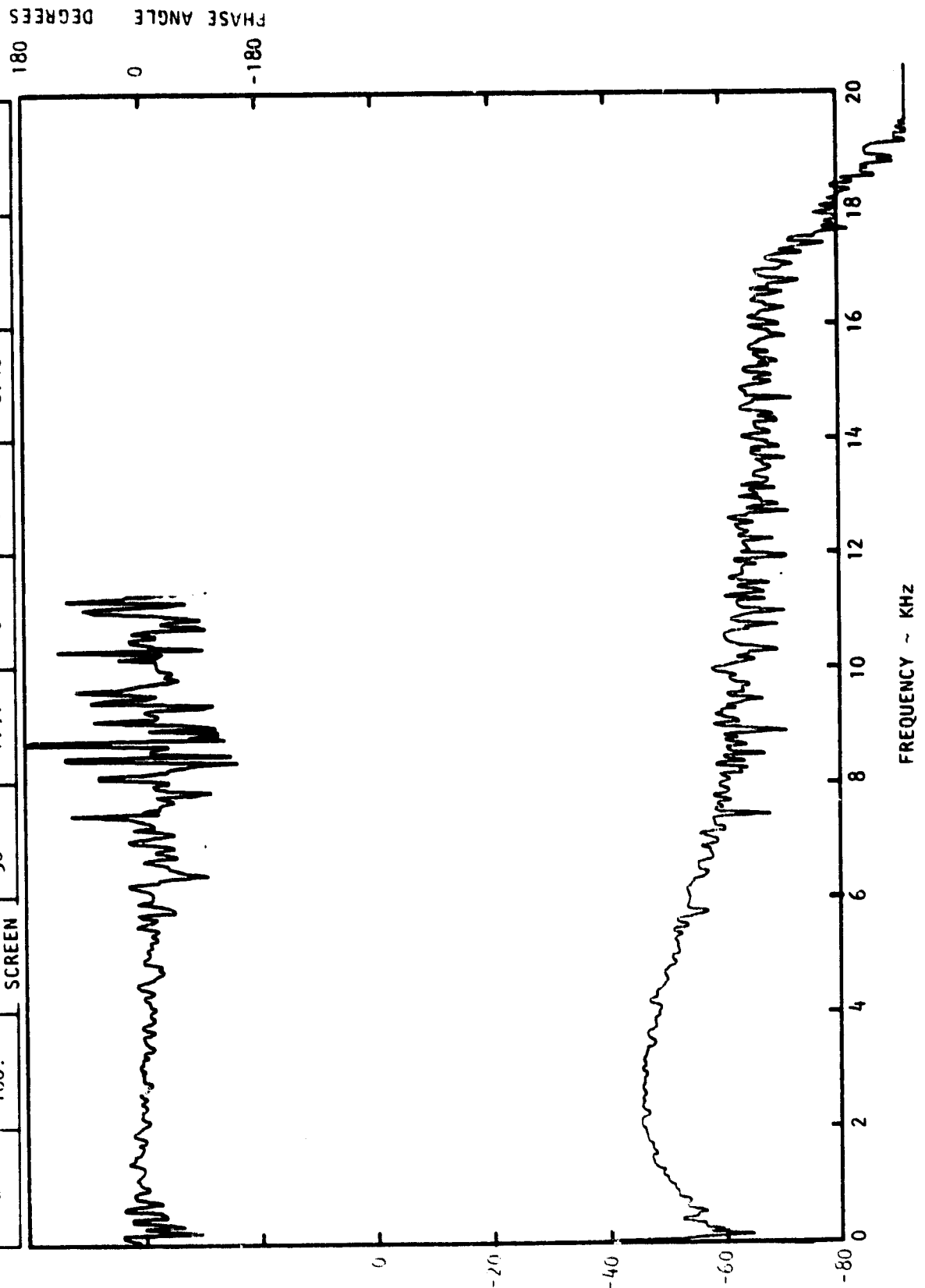
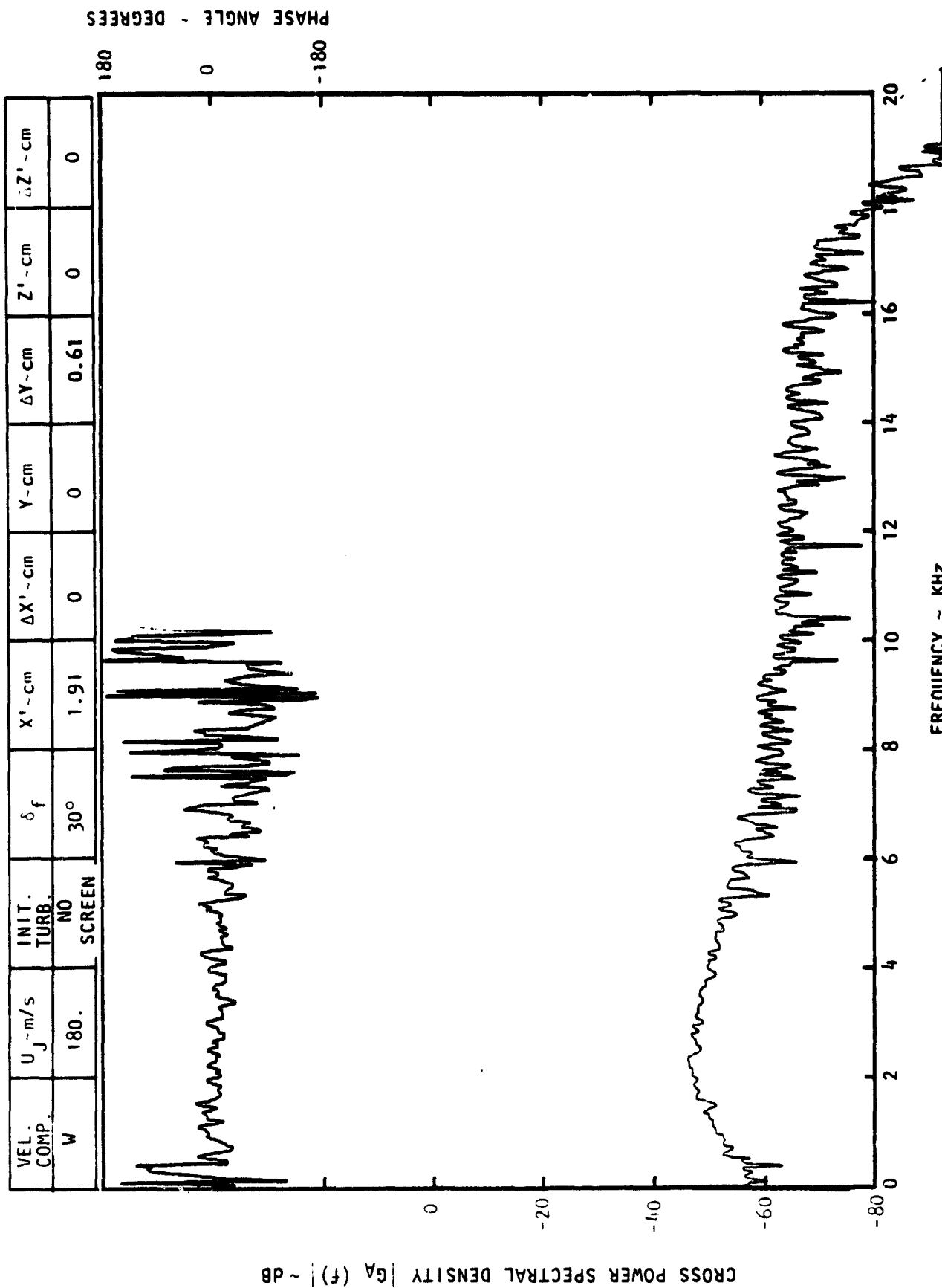
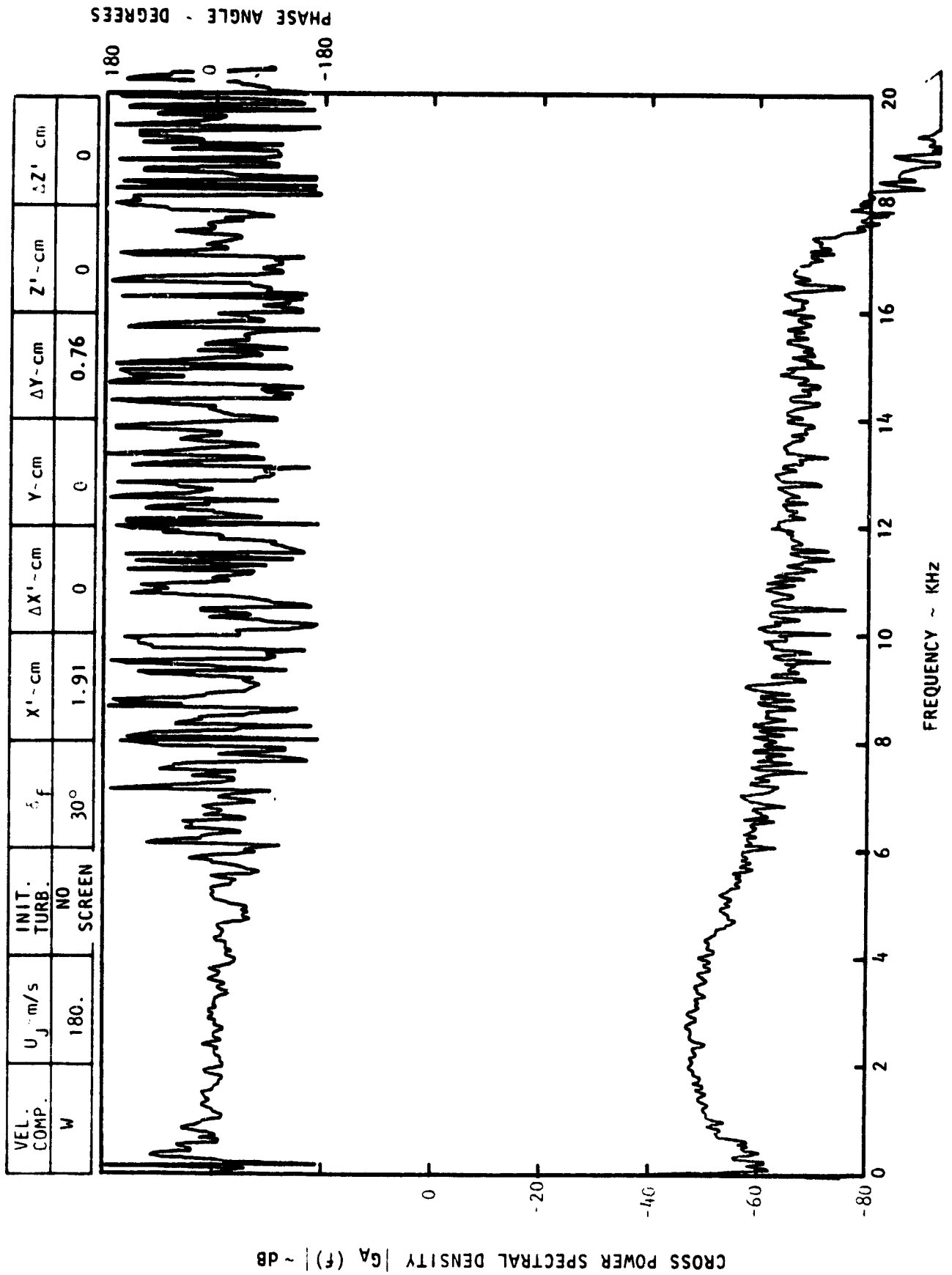


Figure C-2. Continued.

CROSS POWER SPECTRAL DENSITY $G_A(f)$ ~ dB

VEL. COMP.	U_j m/s	INIT. TURB.	θ_f	$X' - \text{cm}$	$\Delta X' - \text{cm}$	$Y - \text{cm}$	$\Delta Y - \text{cm}$	$Z' - \text{cm}$	$\Delta Z' - \text{cm}$
W	180.	NO SCREEN	30°	1.91	0	0	0.46	0	0





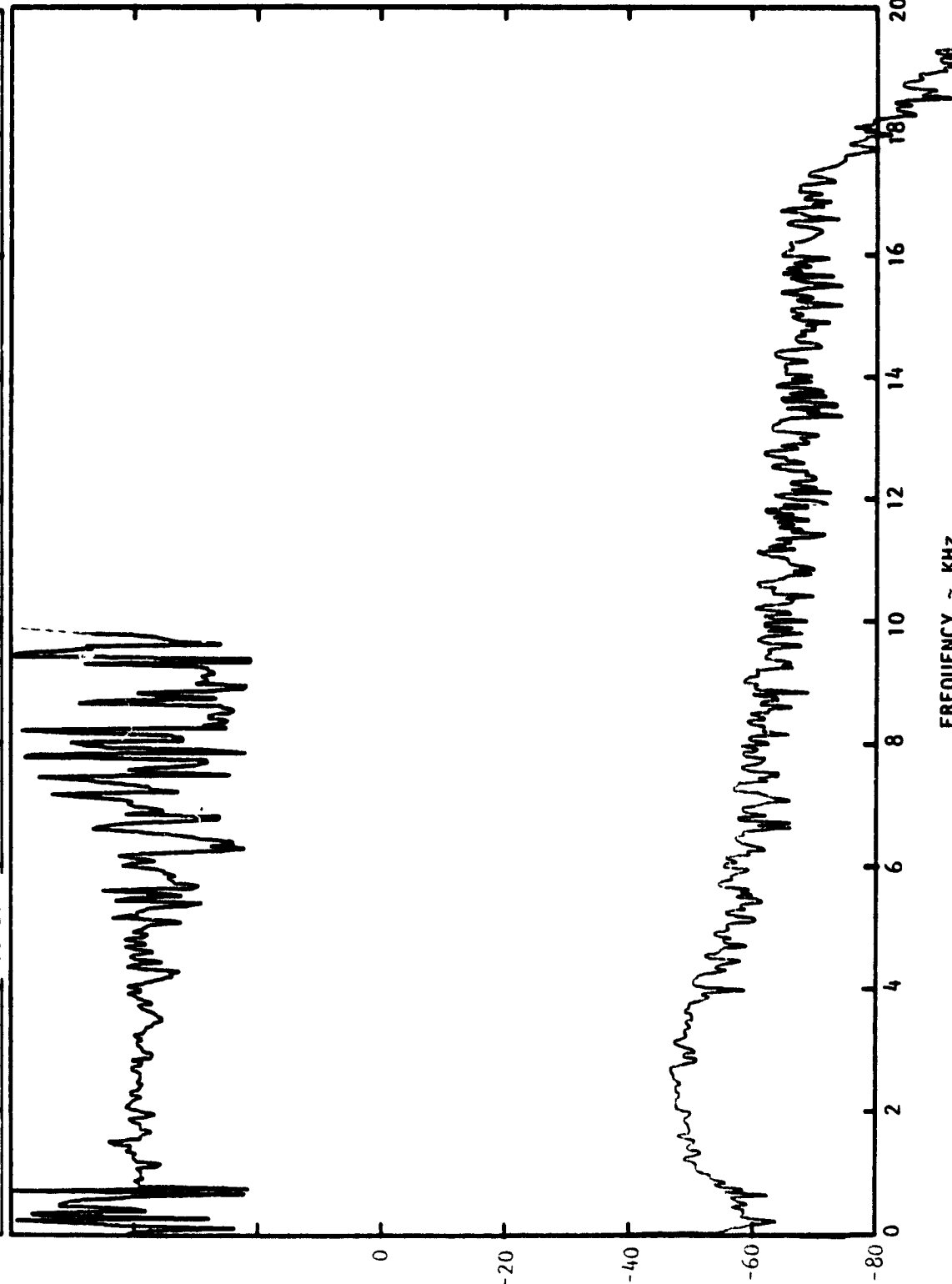
VEL. COMP.	U_j - m/s	INIT. TURB.	ϕ_f	$X' - \text{cm}$	$\Delta X' - \text{cm}$	$Y - \text{cm}$	$\Delta Y - \text{cm}$	$Z' - \text{cm}$	$\Delta Z' - \text{cm}$
W	180.	NO SCREEN	30°	1.91	0	0	0.91	0	0

PHASE ANGLE - DEGREES

180

0

-180



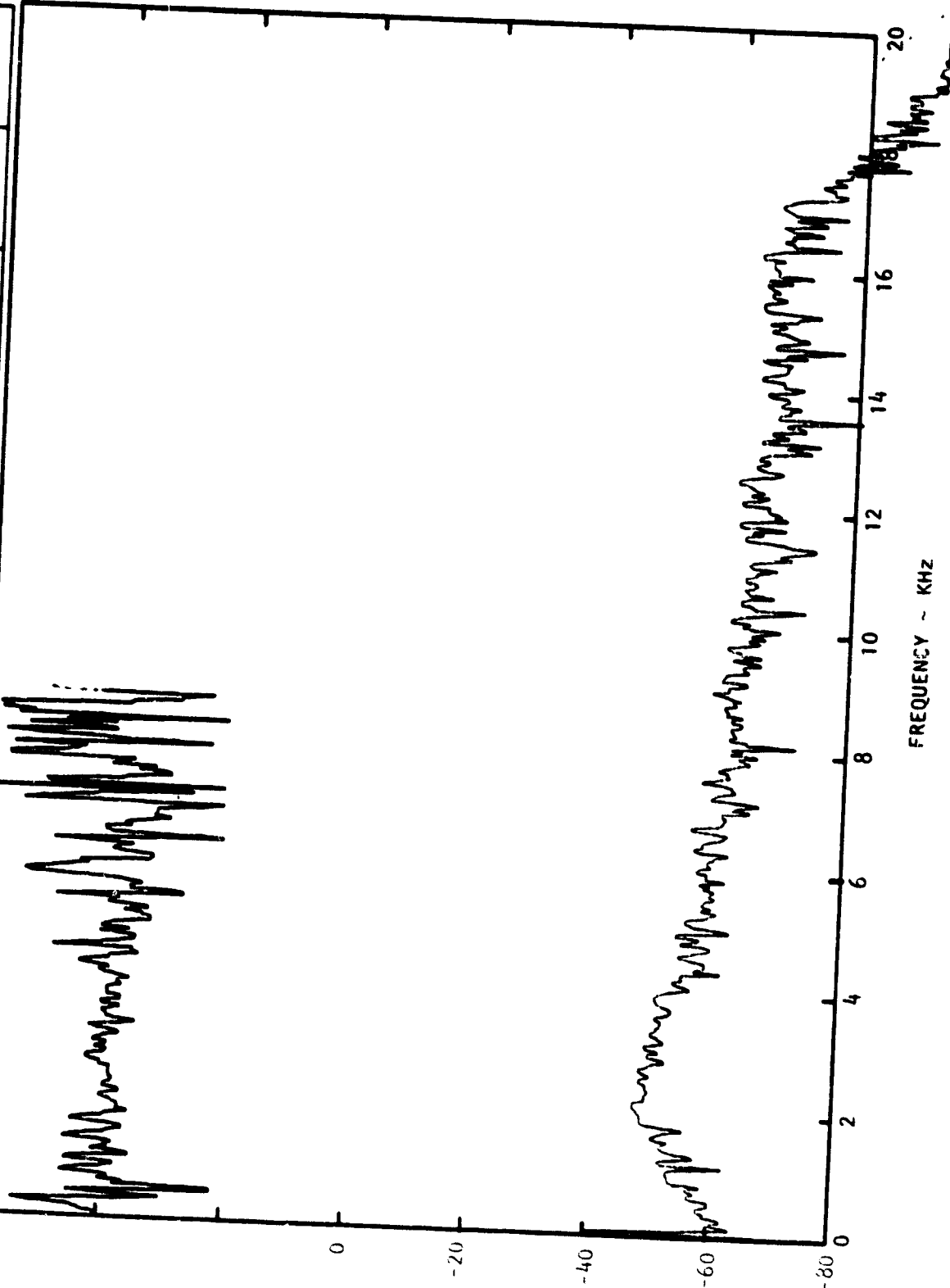
FREQUENCY ~ KHZ

Figure C-2. Continued.

CROSS POWER SPECTRAL DENSITY $G_A(f)$ - dB

PHASE ANGLE - DEGREES

VEL. COMP.	U_j m/s	INIT. TURB.	f	$X' - \text{cm}$	$\Delta X' - \text{cm}$	$Y - \text{cm}$	$\Delta Y - \text{cm}$	$Z' - \text{cm}$	$Z' - \text{cm}$
W	180.	NO SCREEN	30°	1.91	0	0	1.07	0	0



VEL. COMP.	U_j - m/s	INIT. TURB.	α - F	$X' - \text{cm}$	$\Delta X' - \text{cm}$	$Y - \text{cm}$	$\Delta Y - \text{cm}$	$Z' - \text{cm}$	$\Delta Z' - \text{cm}$
W	180.	NO SCREEN	30"	1.91	0	0	1.22	0	0

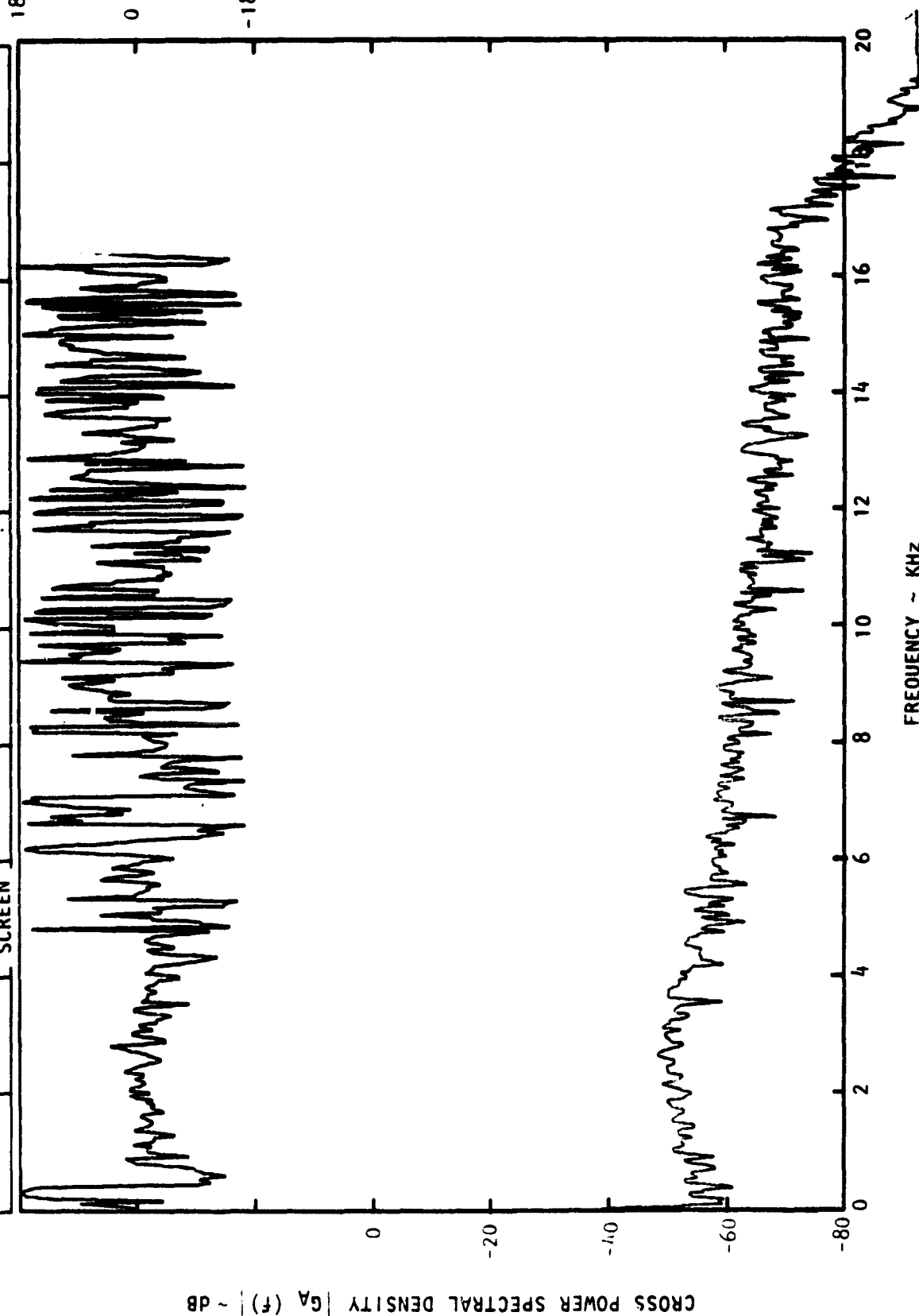
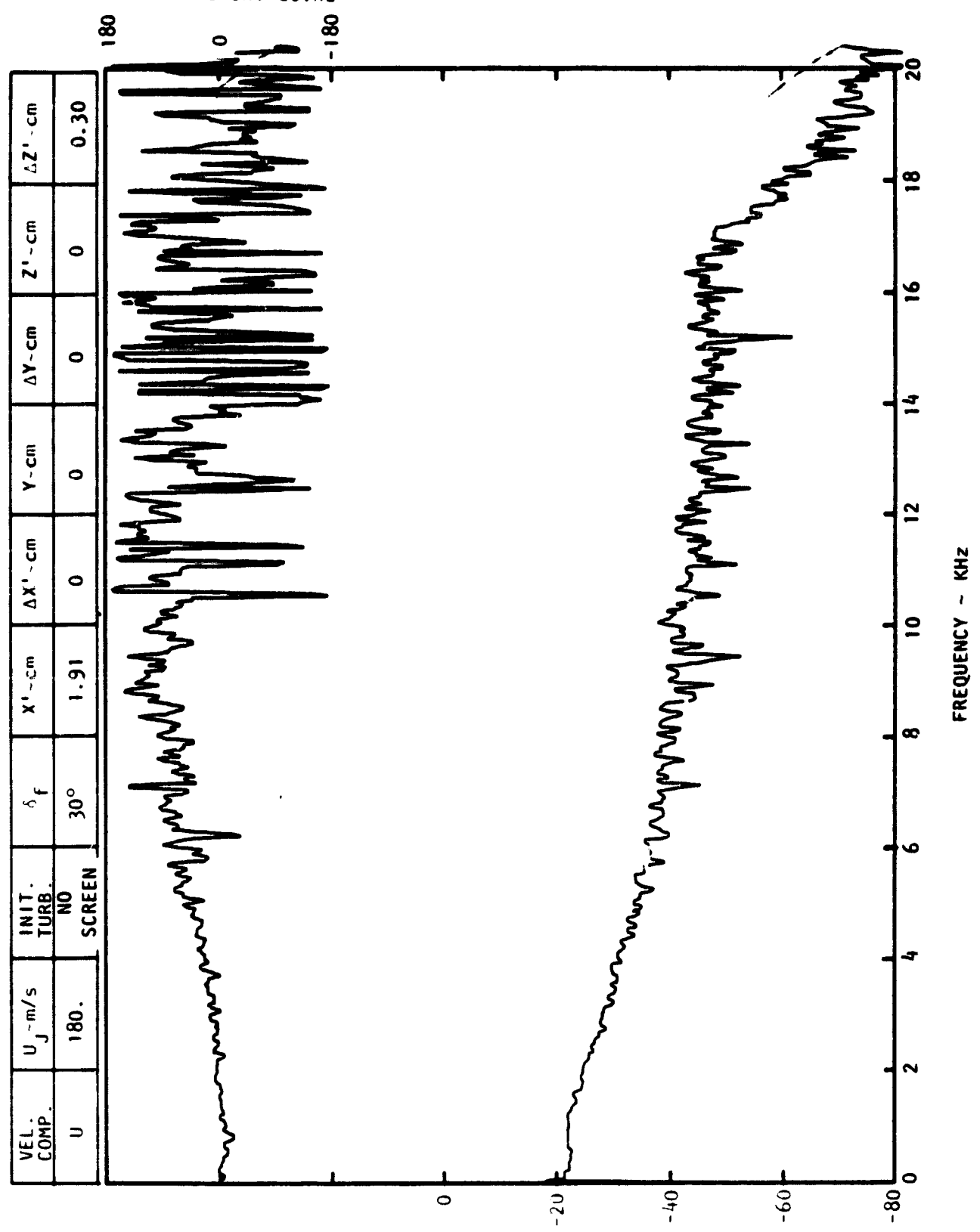


Figure C-2. Concluded.

CROSS POWER SPECTRAL DENSITY $|G_A(f)| \sim \text{dB}$



VEL. COMP.	$U_j \sim \text{m/s}$	INIT. TURB.	δf	$X^1 \sim \text{cm}$	$\Delta X^1 \sim \text{cm}$	$Y \sim \text{cm}$	$\Delta Y \sim \text{cm}$	$Z^1 \sim \text{cm}$	$\Delta Z^1 \sim \text{cm}$
U	180.	NO SCREEN	30°	1.91	0	0	0	0	0.30

VEL. COMP.	U_j - m/s	INIT. TURB.	Δf	$X' - \text{cm}$	$\Delta X' - \text{cm}$	$Y - \text{cm}$	$\Delta Y - \text{cm}$	$Z' - \text{cm}$	$\Delta Z' - \text{cm}$
U	180.	NO SCREEN	30°	1.91	0	0	0	0	0.46

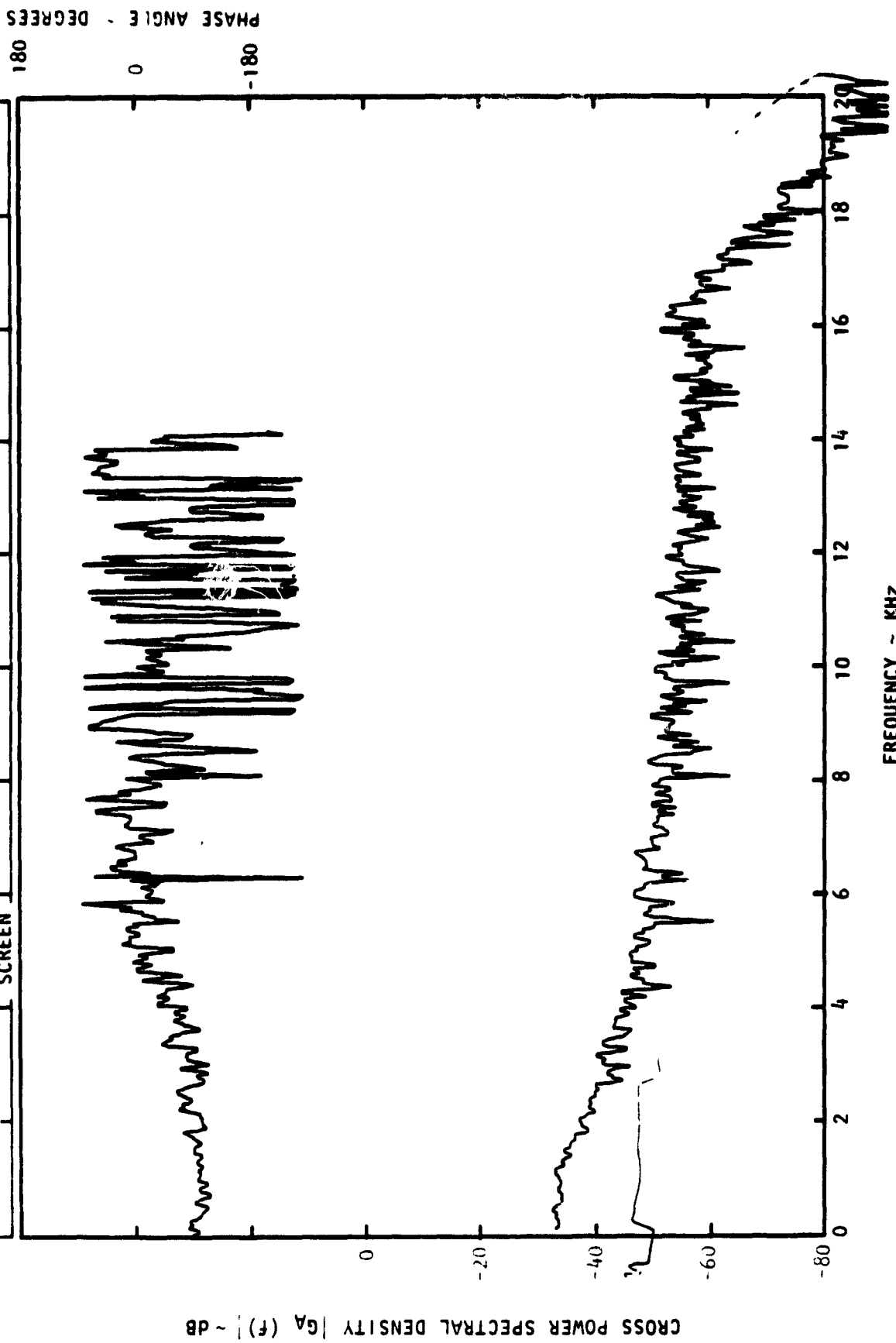
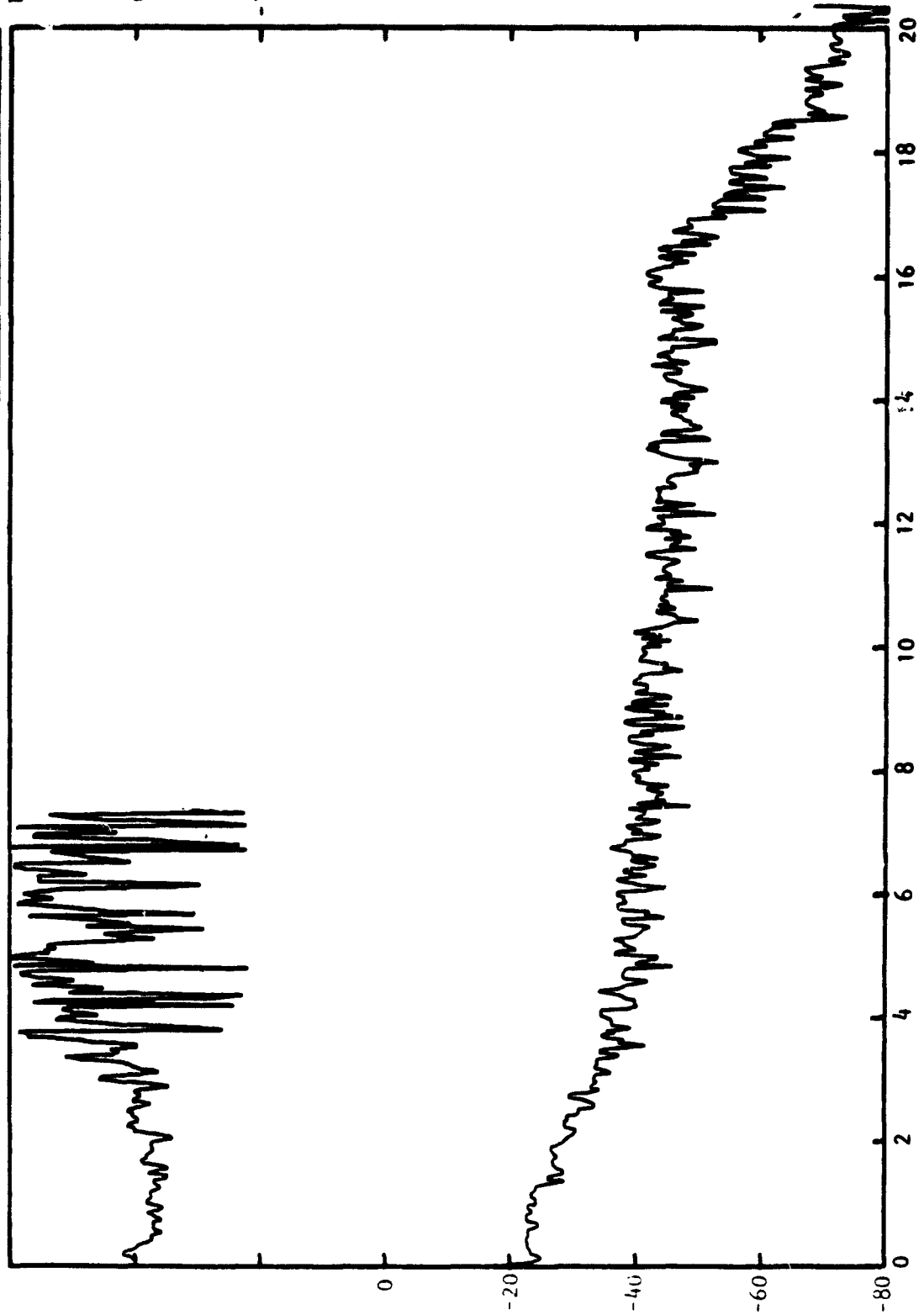


Figure C-3. Continued.

CROSS POWER SPECTRAL DENSITY $G_A(f)$ ~ dB

PHASE ANGLE - DEGREES

VEL. COMP.	U_j - m/s	INIT. TURB.	Δf	$X' - \text{cm}$	$\Delta X' - \text{cm}$	$Y - \text{cm}$	$\Delta Y - \text{cm}$	$Z' - \text{cm}$	$\Delta Z' - \text{cm}$
U	180.	NO SCREEN	30°	1.91	0	0	0	0	0.61



FREQUENCY ~ KHz

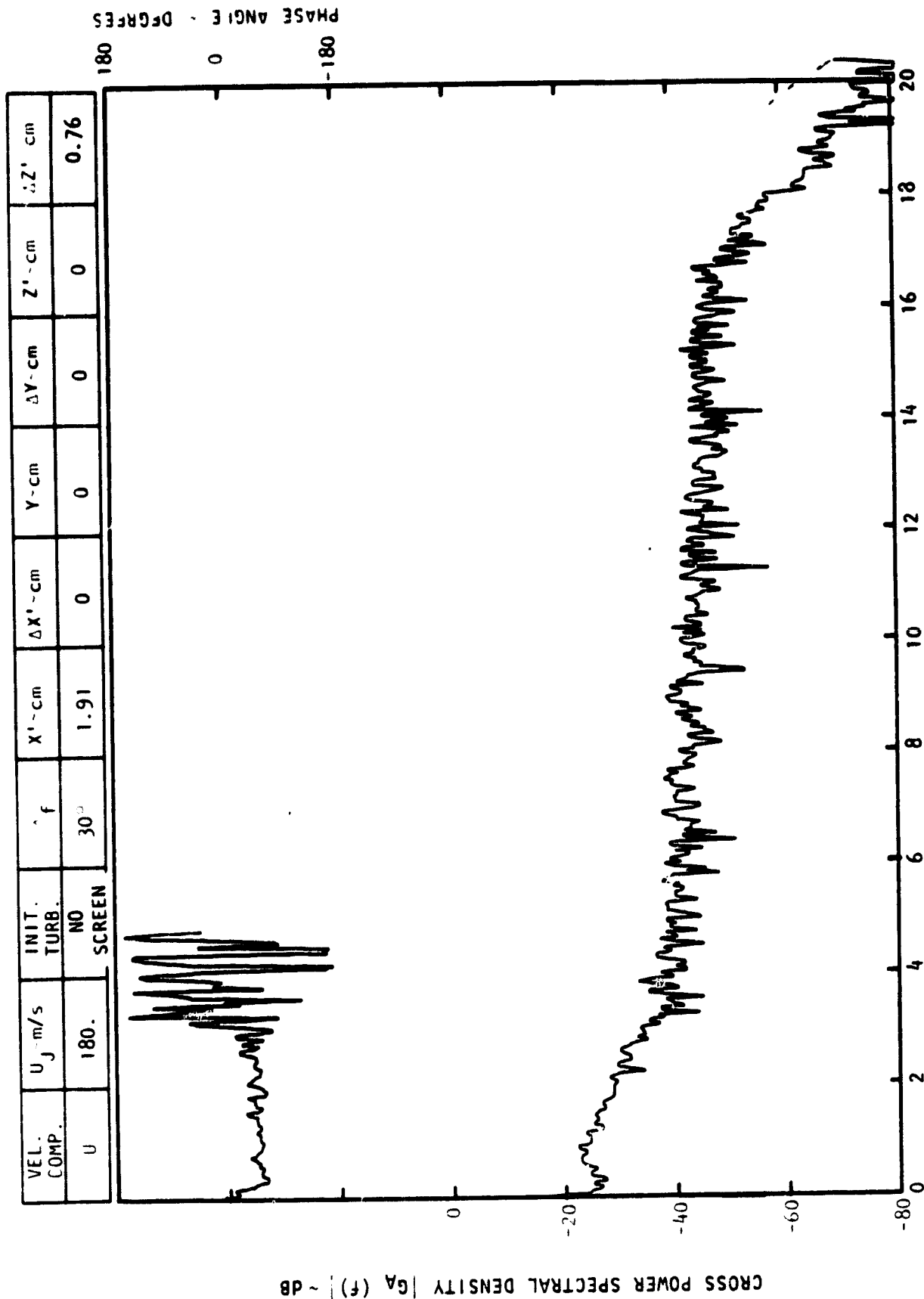
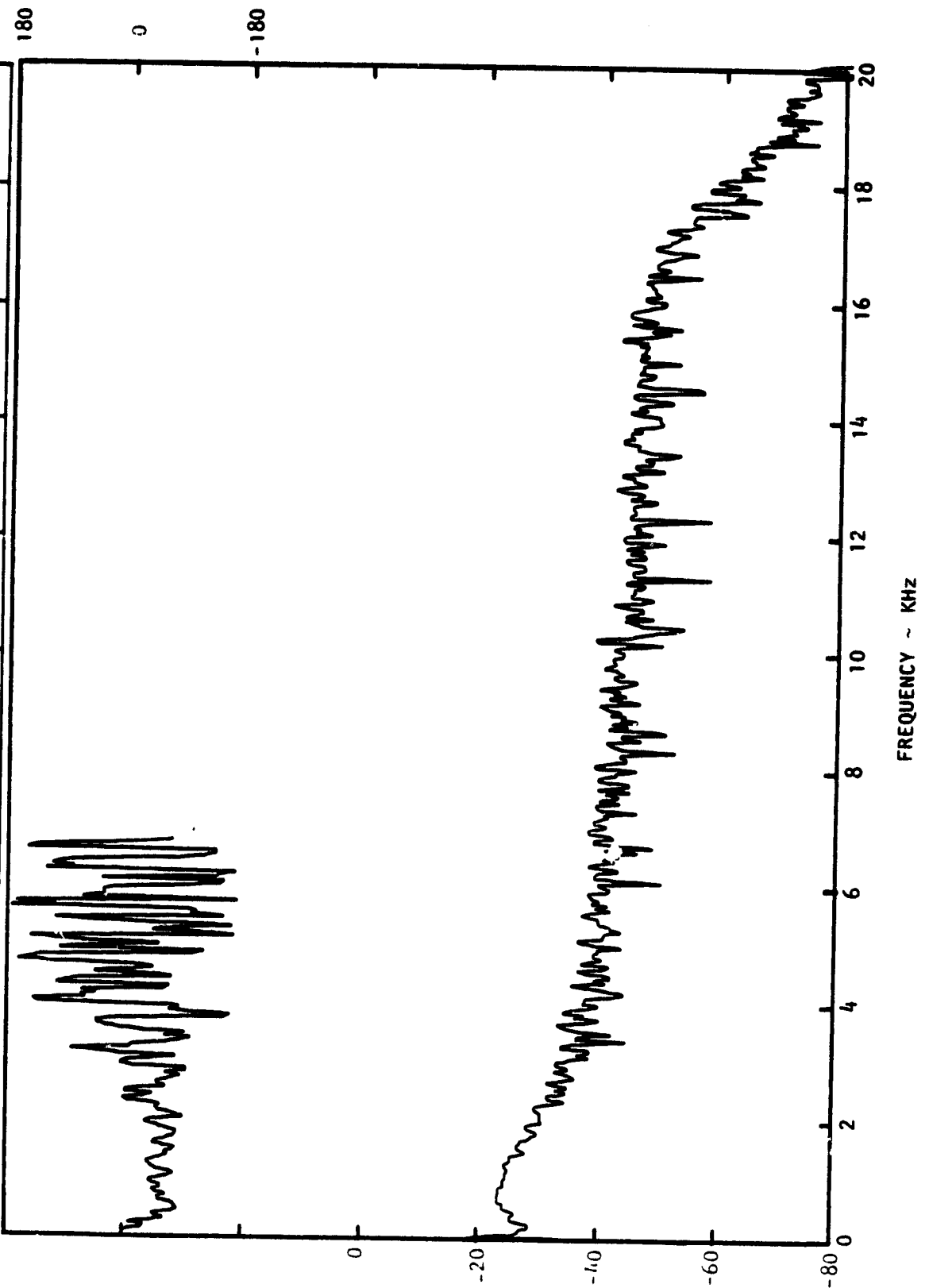
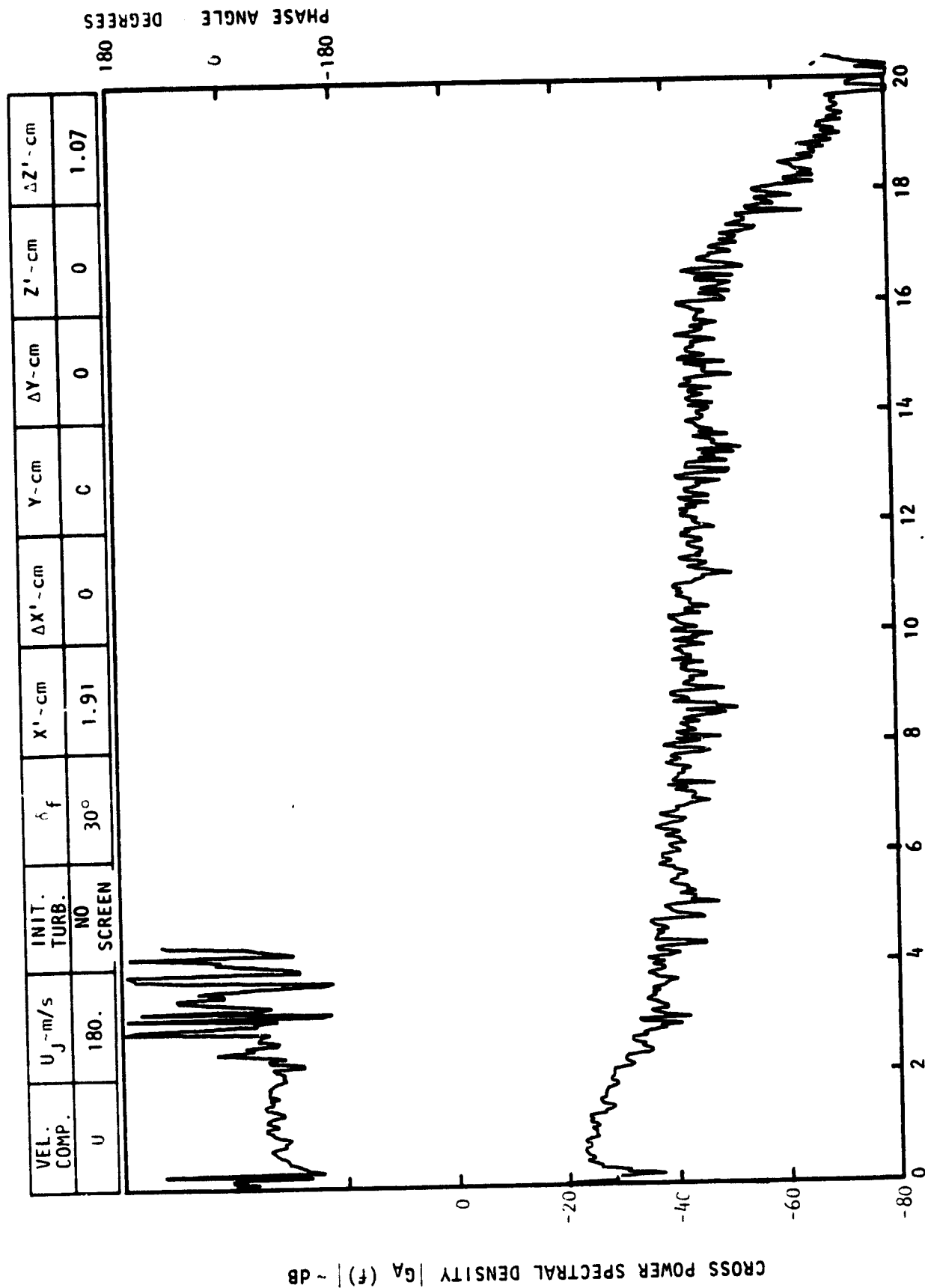


Figure C-3. Continued.

CROSS POWER SPECTRAL DENSITY $|G_A(f)| \sim \text{dB}$



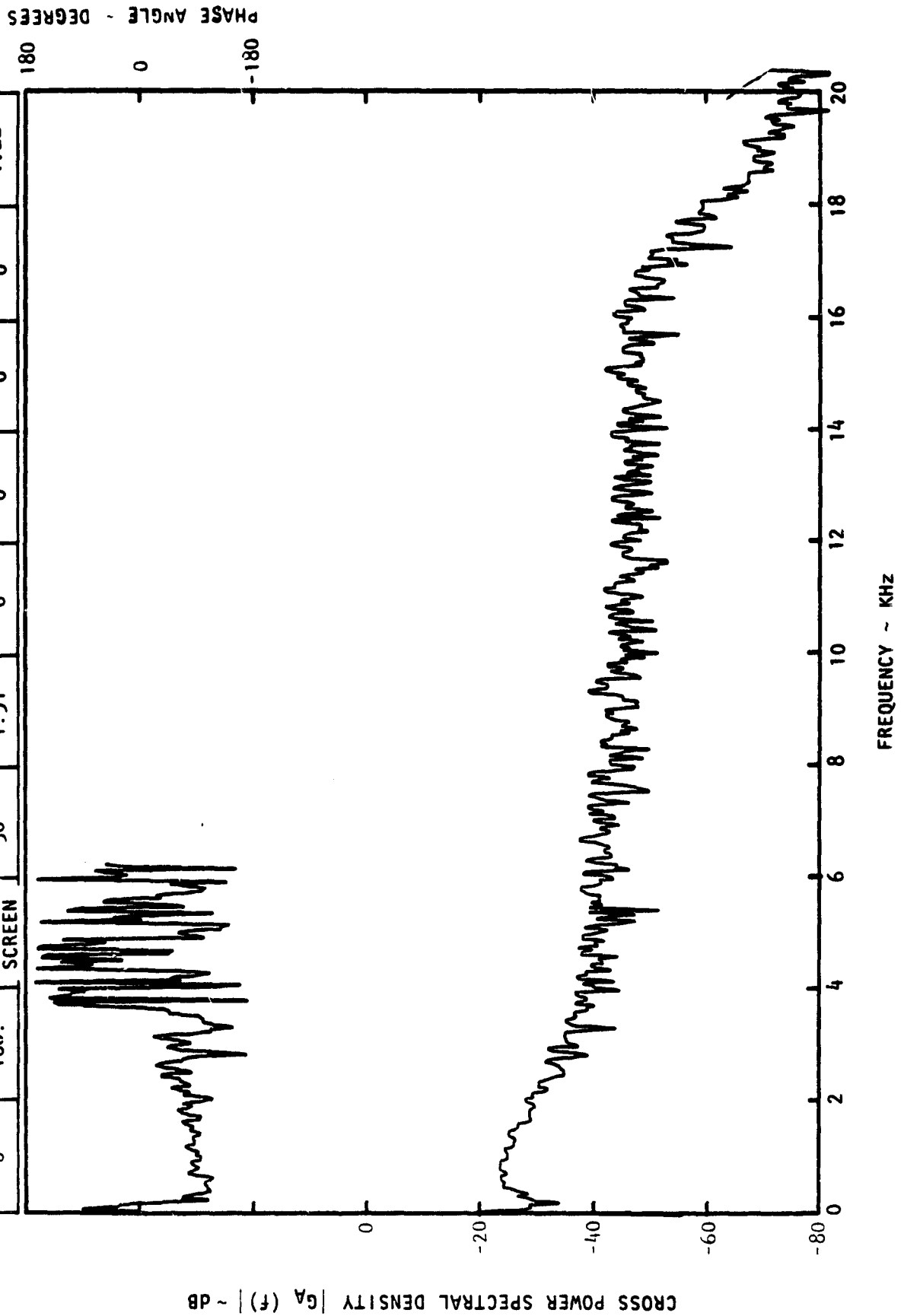
VEL. COMP.	U_j - m/s	INIT. TURB.	δ_f	$X' - \text{cm}$	$\Delta X' - \text{cm}$	$Y - \text{cm}$	$\Delta Y - \text{cm}$	$Z' - \text{cm}$	$\Delta Z' - \text{cm}$
U	180.	NO SCREEN	30''	1.91	0	0	0	0	0.91



FREQUENCY ~ KHz

Figure C-3. Continued.

VEL. COMP.	U_j - m/s	INIT. TURB.	δ_f	$X' - \text{cm}$	$\Delta X' - \text{cm}$	$Y - \text{cm}$	$\Delta Y - \text{cm}$	$Z' - \text{cm}$	$\Delta Z' - \text{cm}$
U	180.	NO SCREEN	30°	1.91	0	0	0	0	1.22



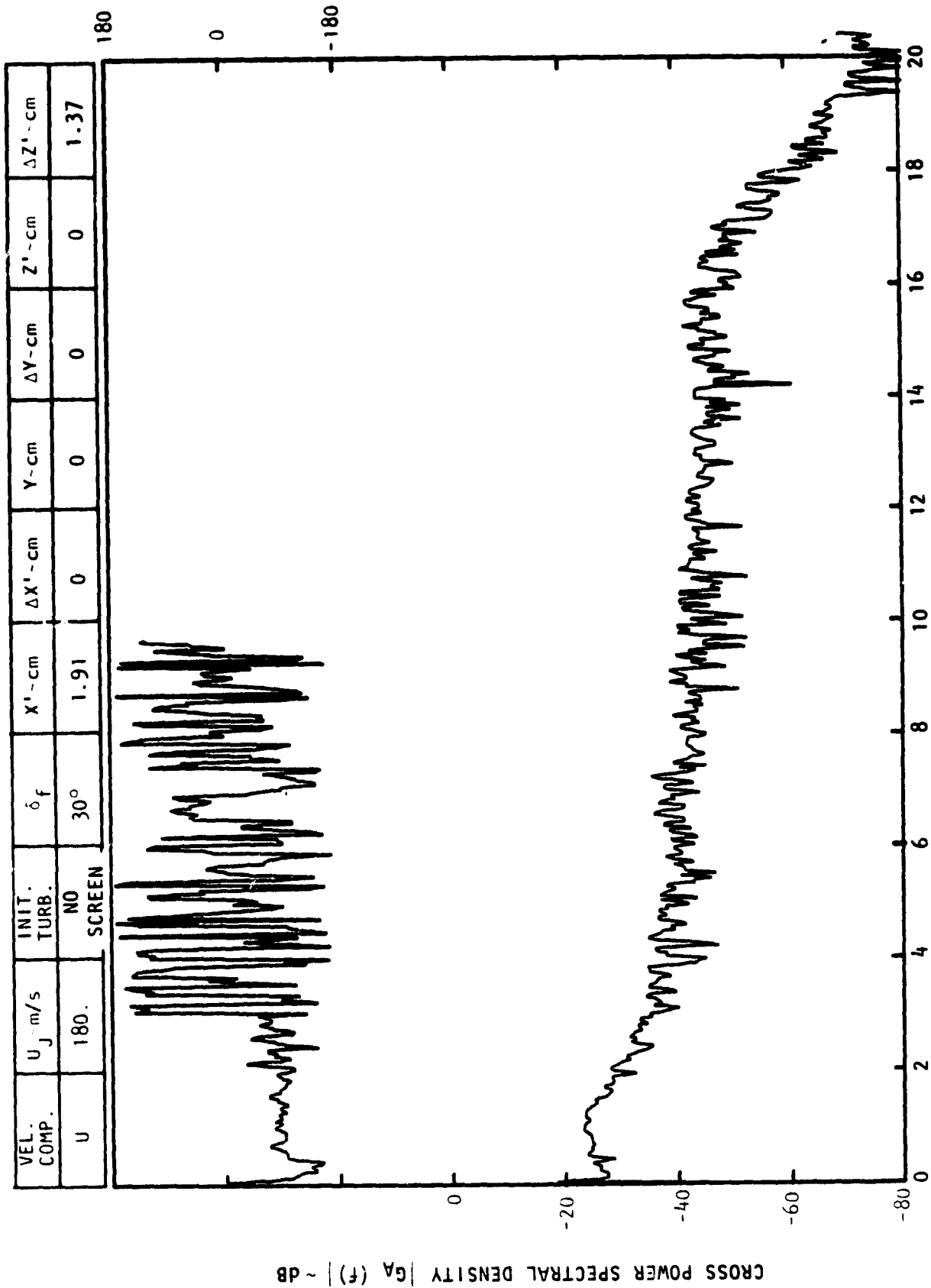
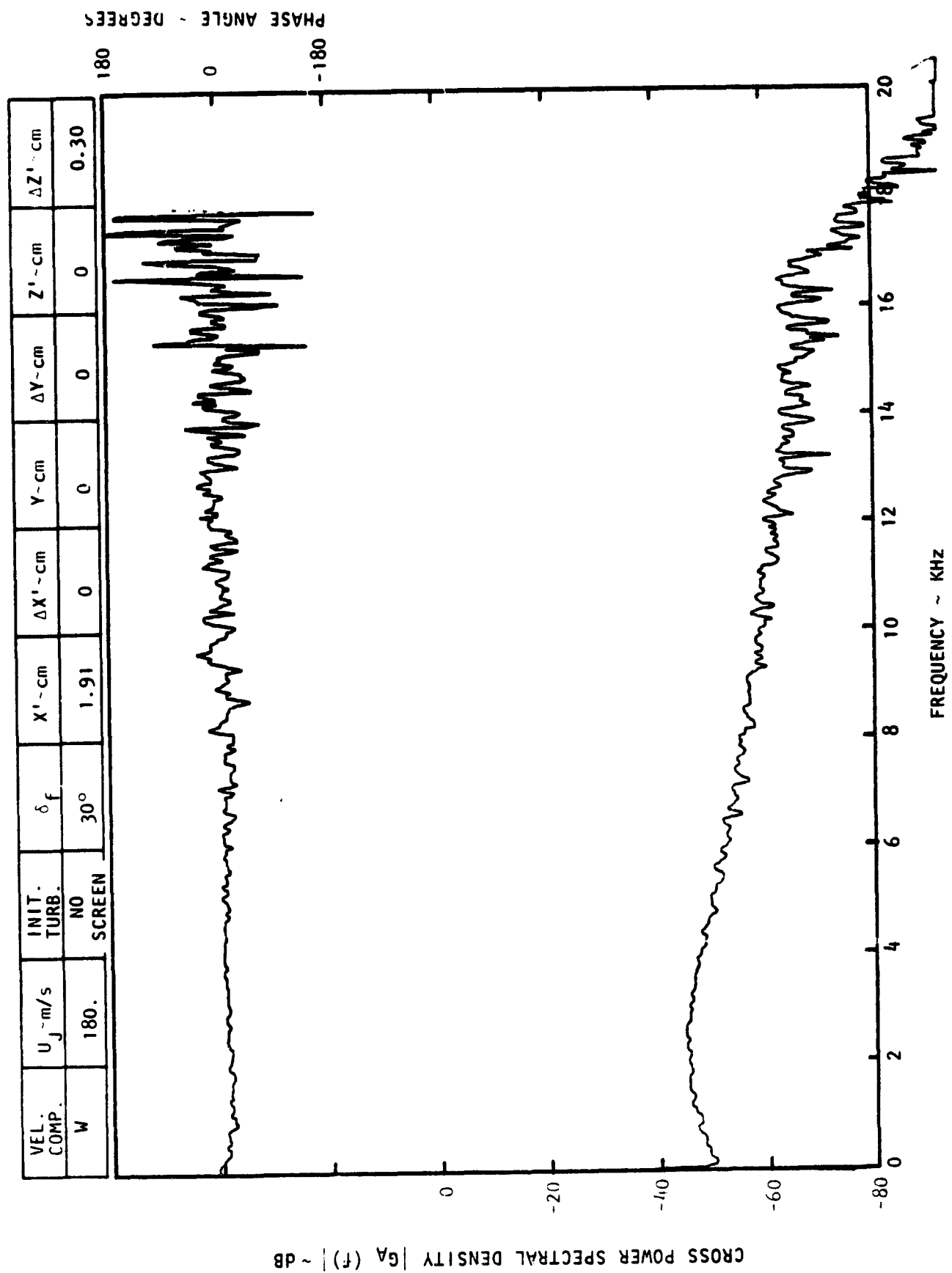


Figure C-3. Continued.



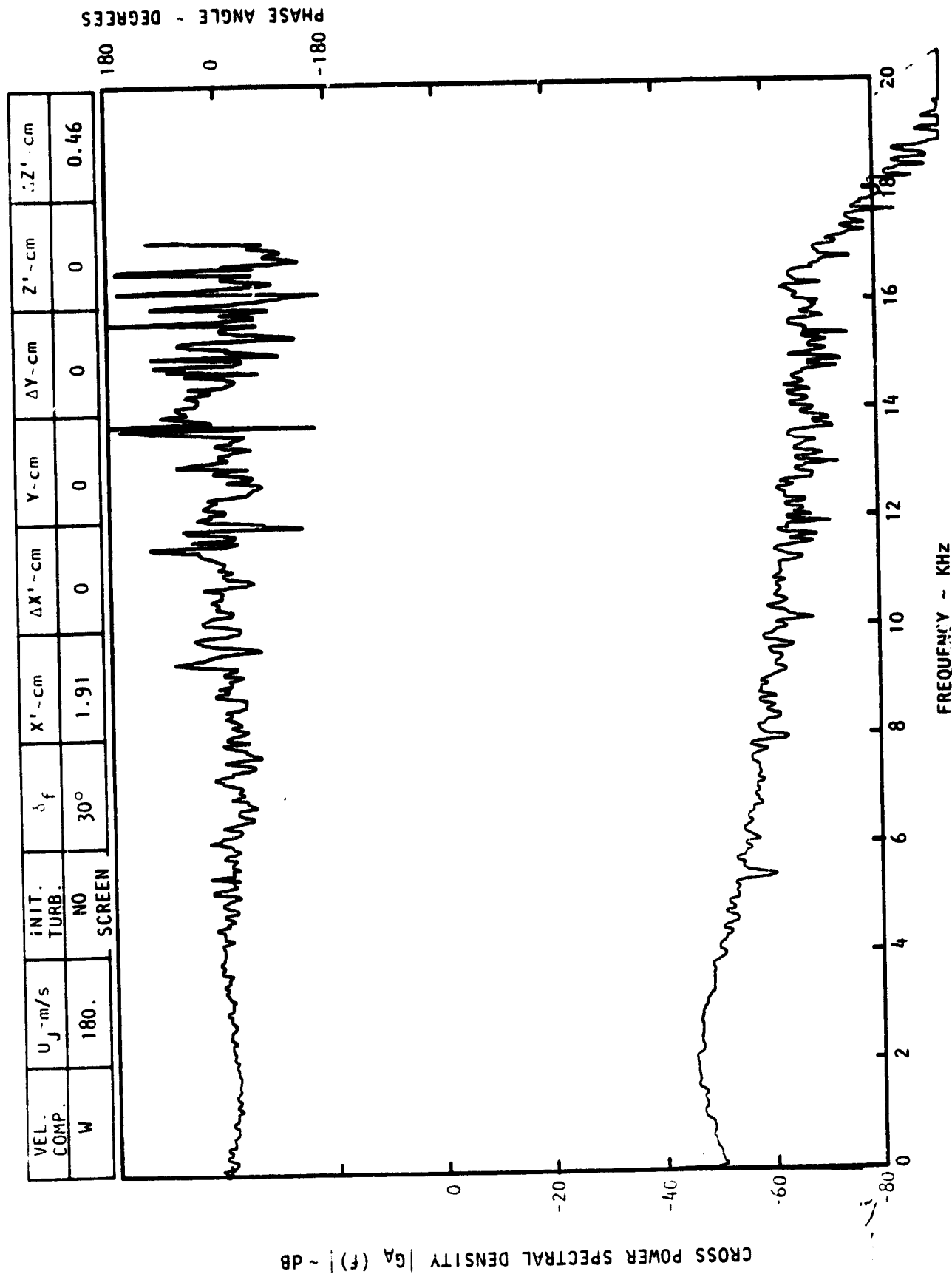
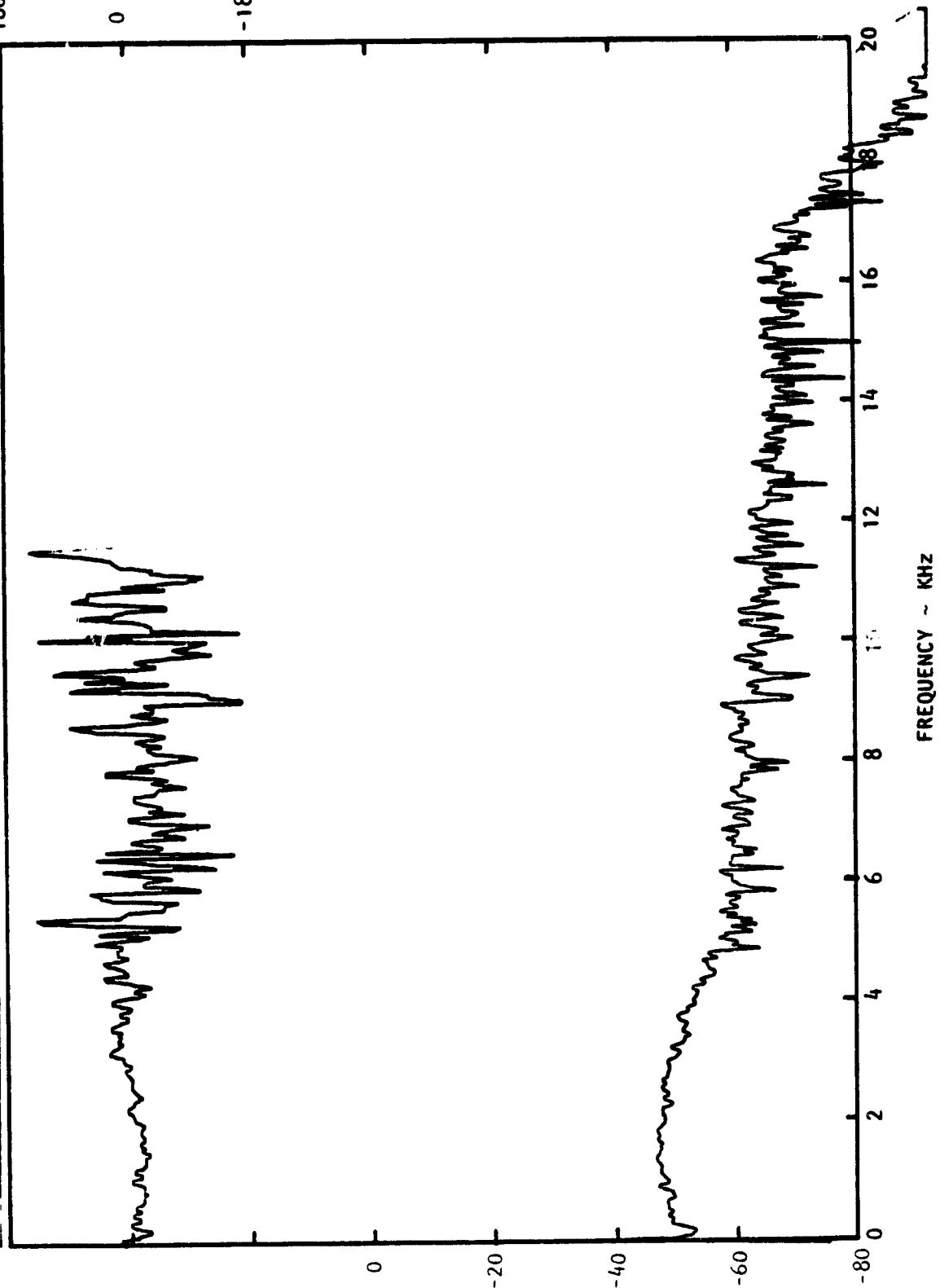


Figure C-3. Continued.

CROSS POWER SPECTRAL DENSITY |G_A(f)| ~ dB

PHASE ANGLE - DEGREES

VEL. COMP.	U _J - m/s	INIT. TURB.	δ_f	X' - cm	$\Delta X'$ - cm	Y - cm	ΔY - cm	Z' - cm	$\Delta Z'$ - cm
W	180.	NO SCREEN	30°	1.91	0	0	0	0	0.61



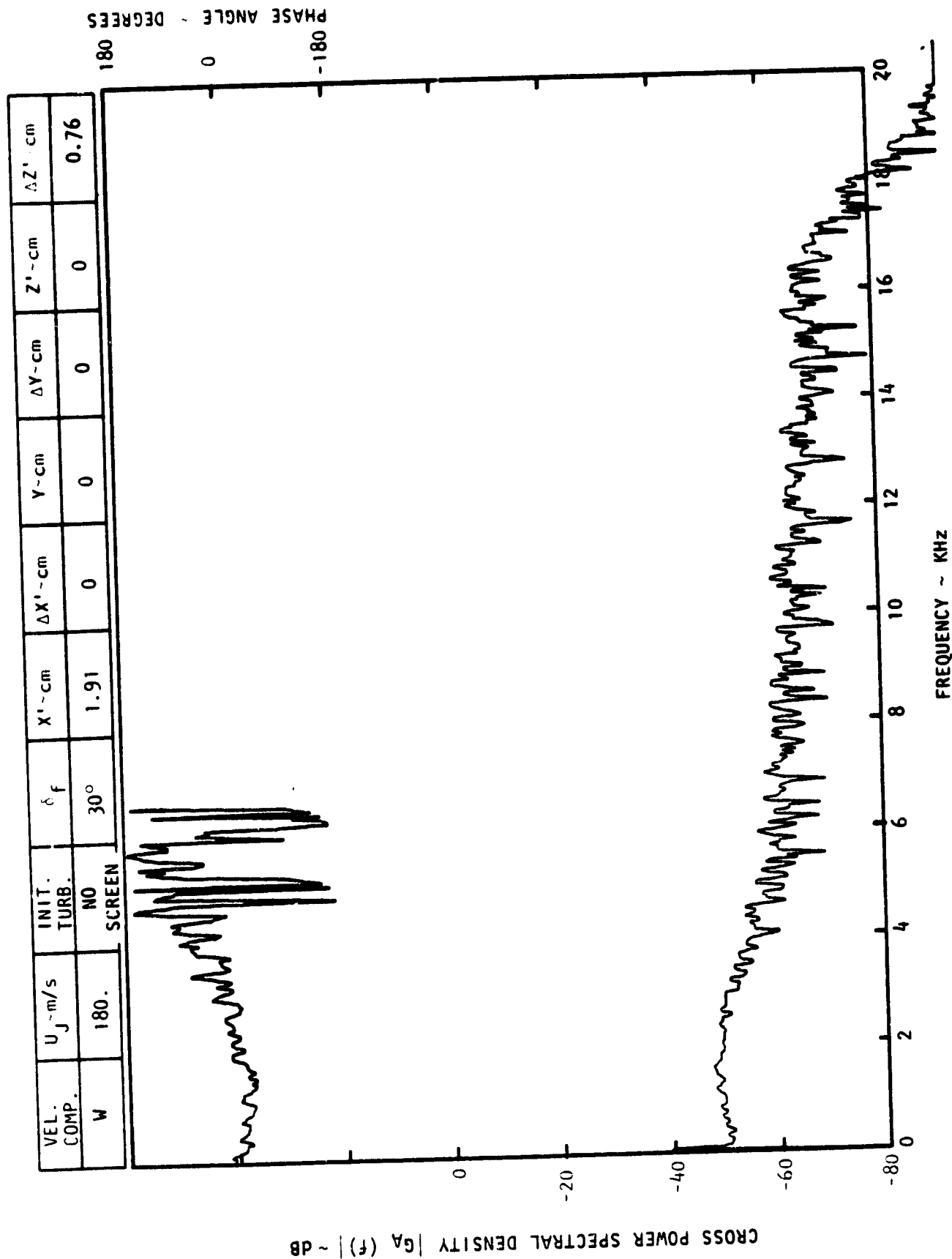
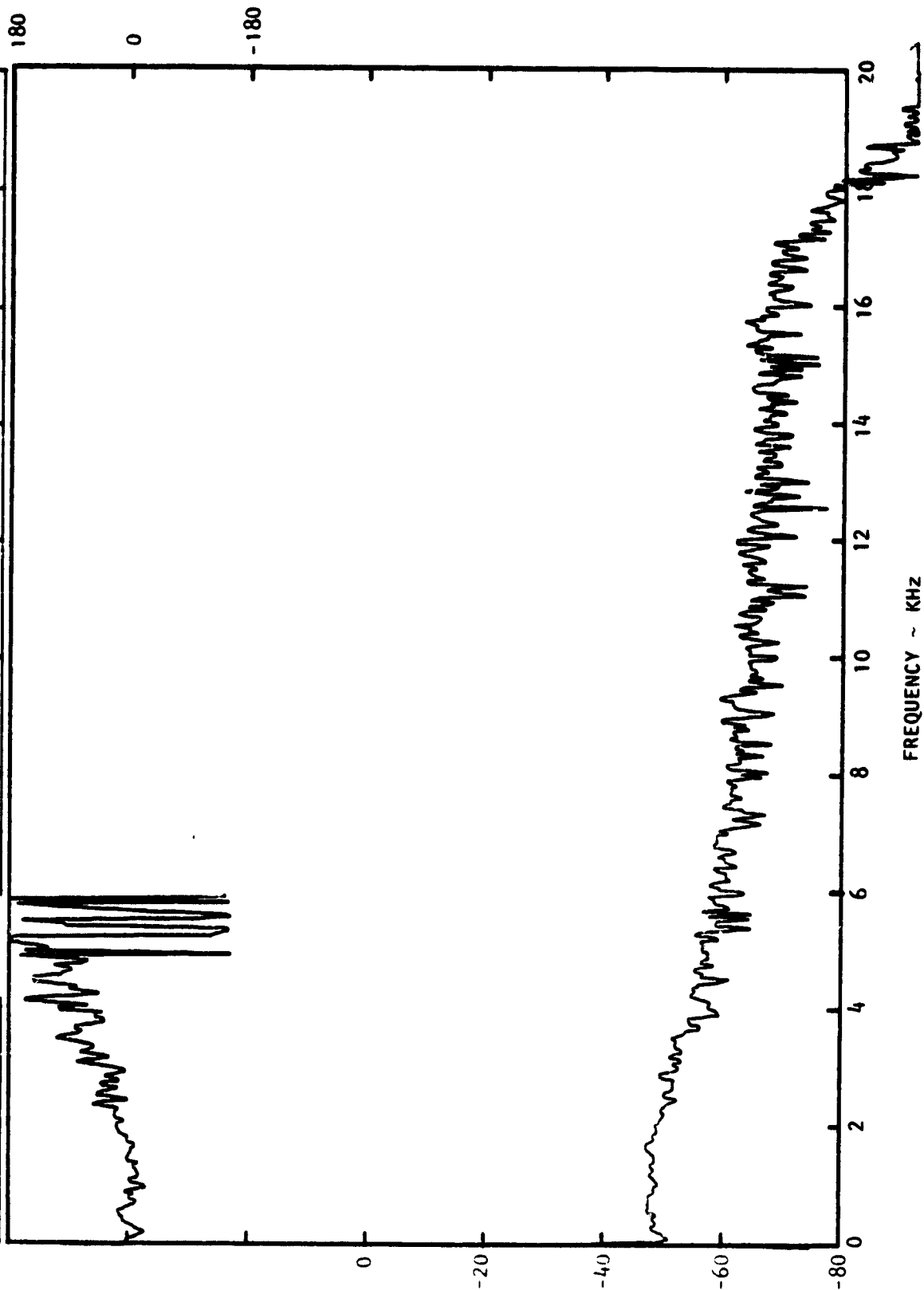


Figure C-3. Continued.

CROSS POWER SPECTRAL DENSITY $|G_A(f)|^2 \sim \text{dB}$

VEL. COMP.	U_j - m/s	INIT. TURB.	δ_f	X' - cm	$\Delta X'$ - cm	Y - cm	ΔY - cm	Z' - cm	$\Delta Z'$ - cm
W	180.	NO SCREEN	30°	1.91	0	0	0	0	0.91



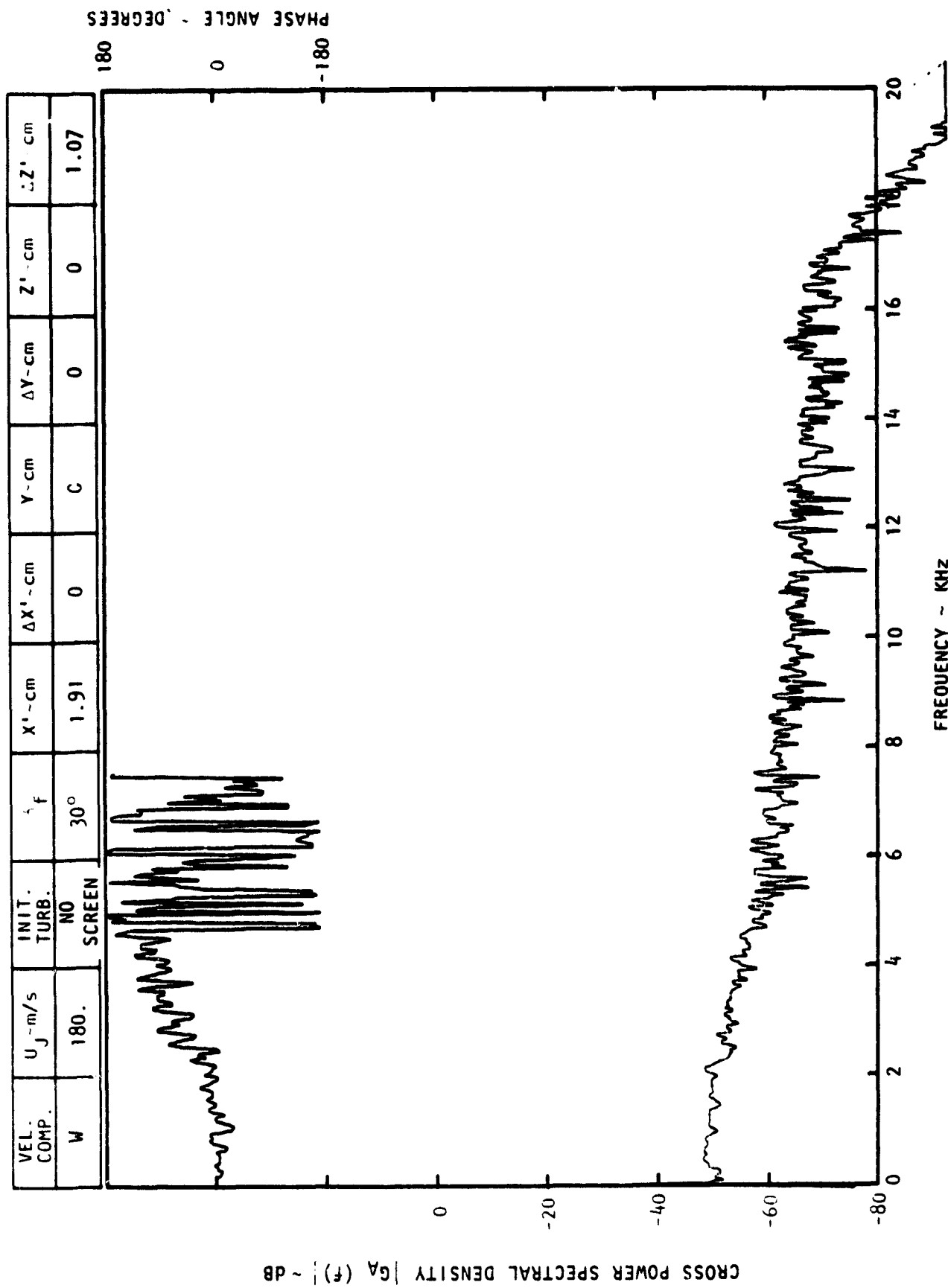
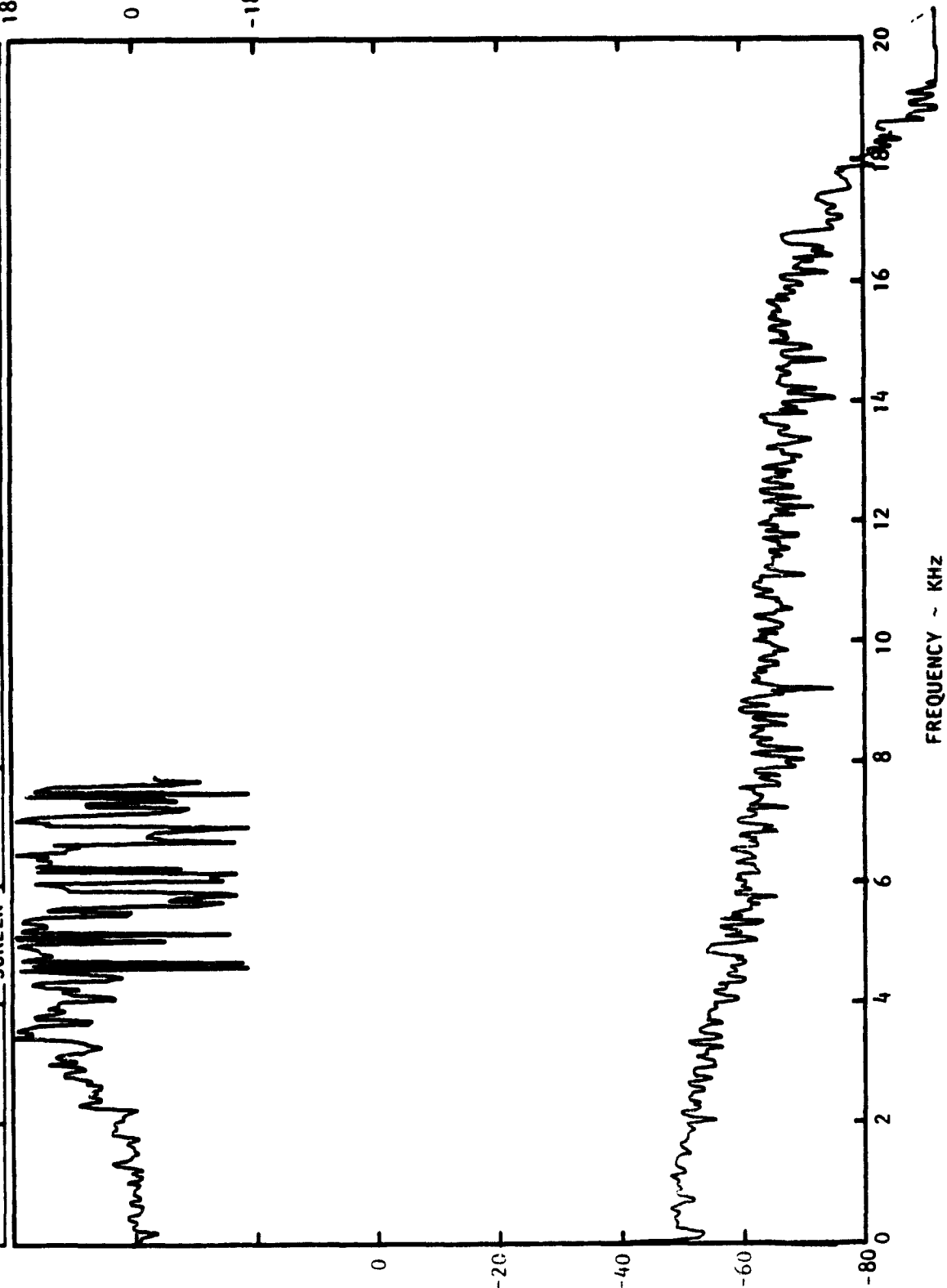


Figure C-3. Continued.

CROSS POWER SPECTRAL DENSITY $|G_A(f)|^2 \sim \text{dB}$

PHASE ANGLE - DEGREES

VEL. COMP.	U_j - m/s	INIT. TURB.	ϕ_f	$X' - \text{cm}$	$\Delta X' - \text{cm}$	$Y - \text{cm}$	$\Delta Y - \text{cm}$	$Z' - \text{cm}$	$\Delta Z' - \text{cm}$
W	180.	NO SCREEN	30°	1.91	0	0	0	0	1.22



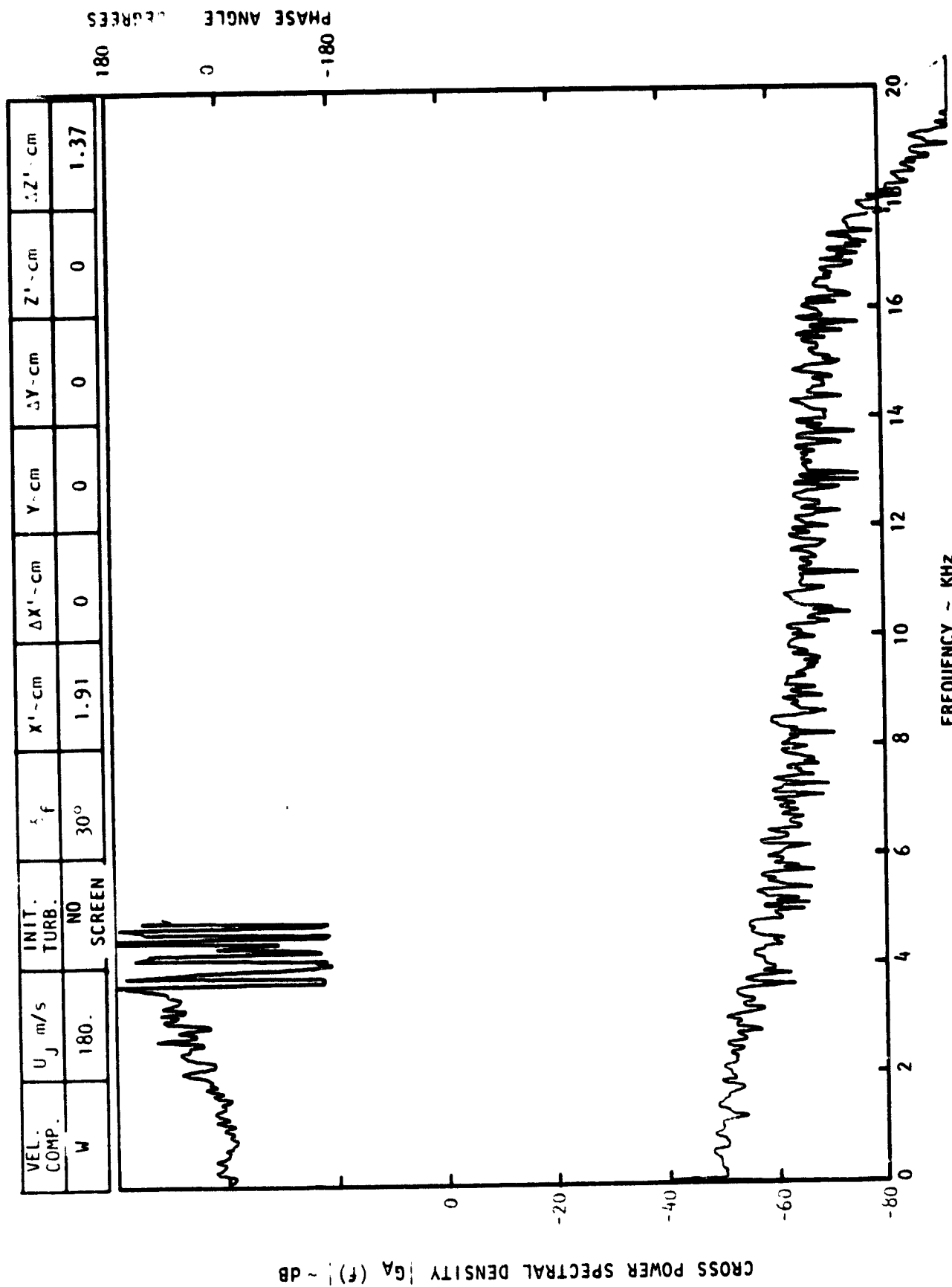
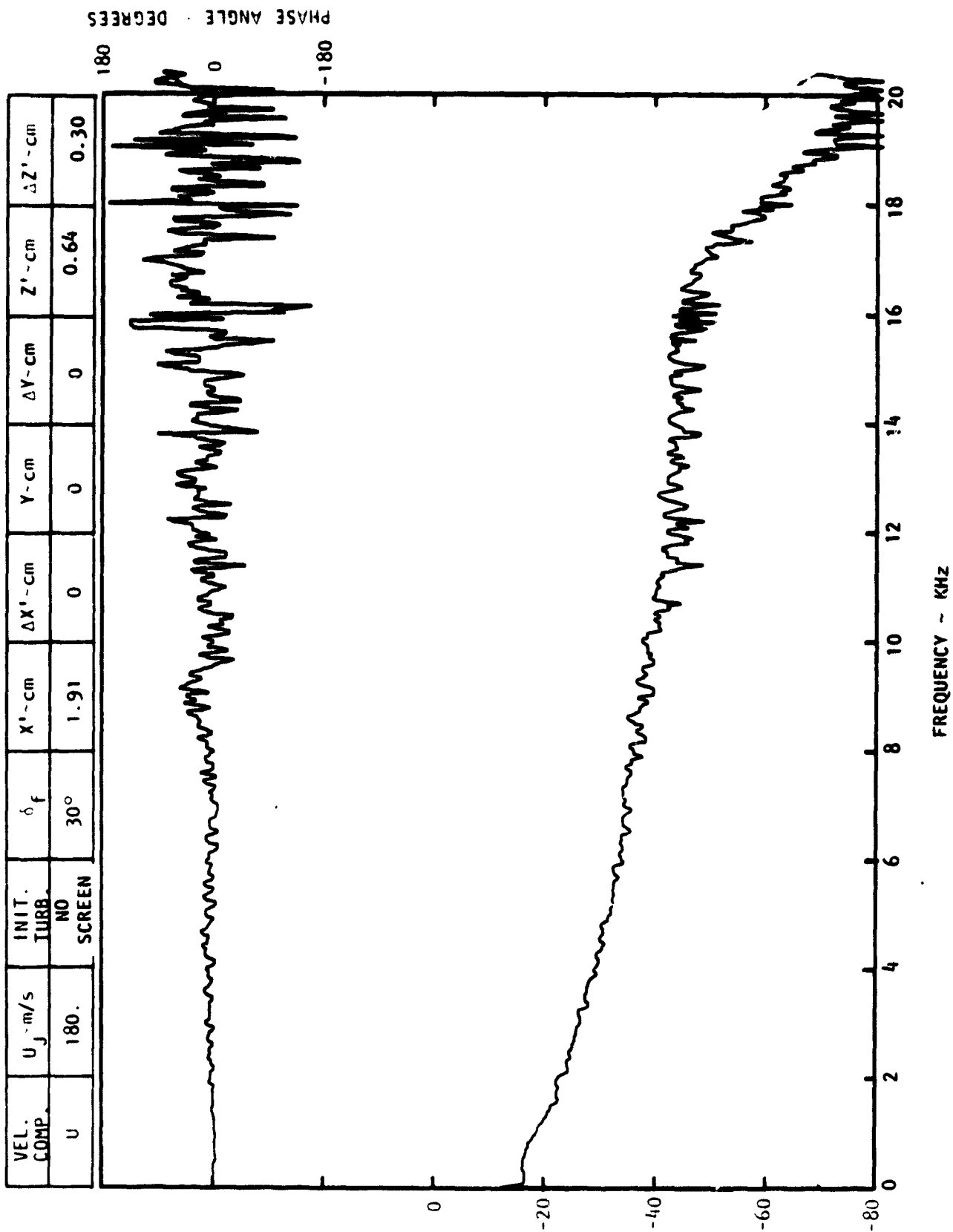
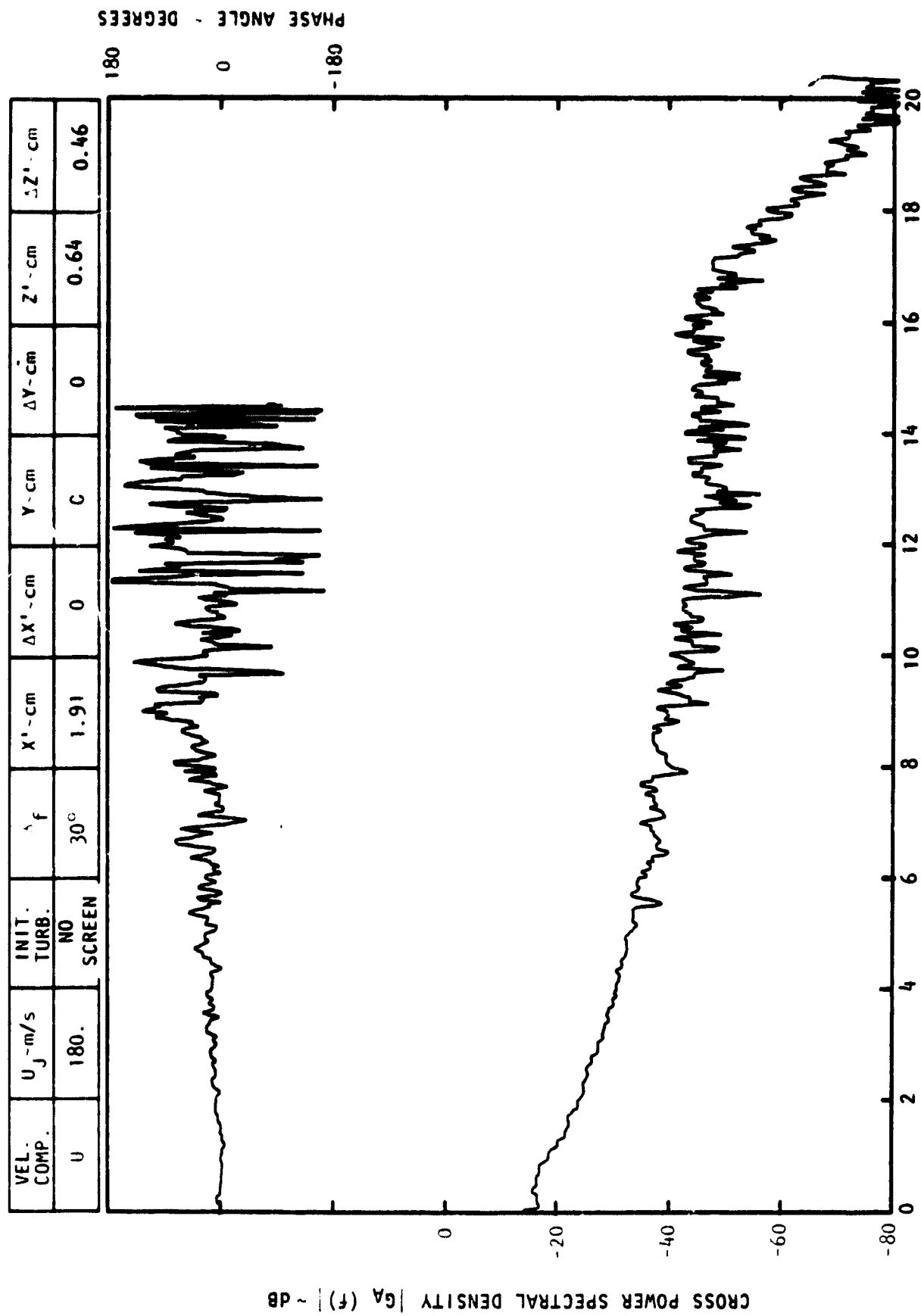


Figure C-3. Continued.

CROSS POWER SPECTRAL DENSITY $G_A(f)$ ~ dB

PHASE ANGLE - DEGREES



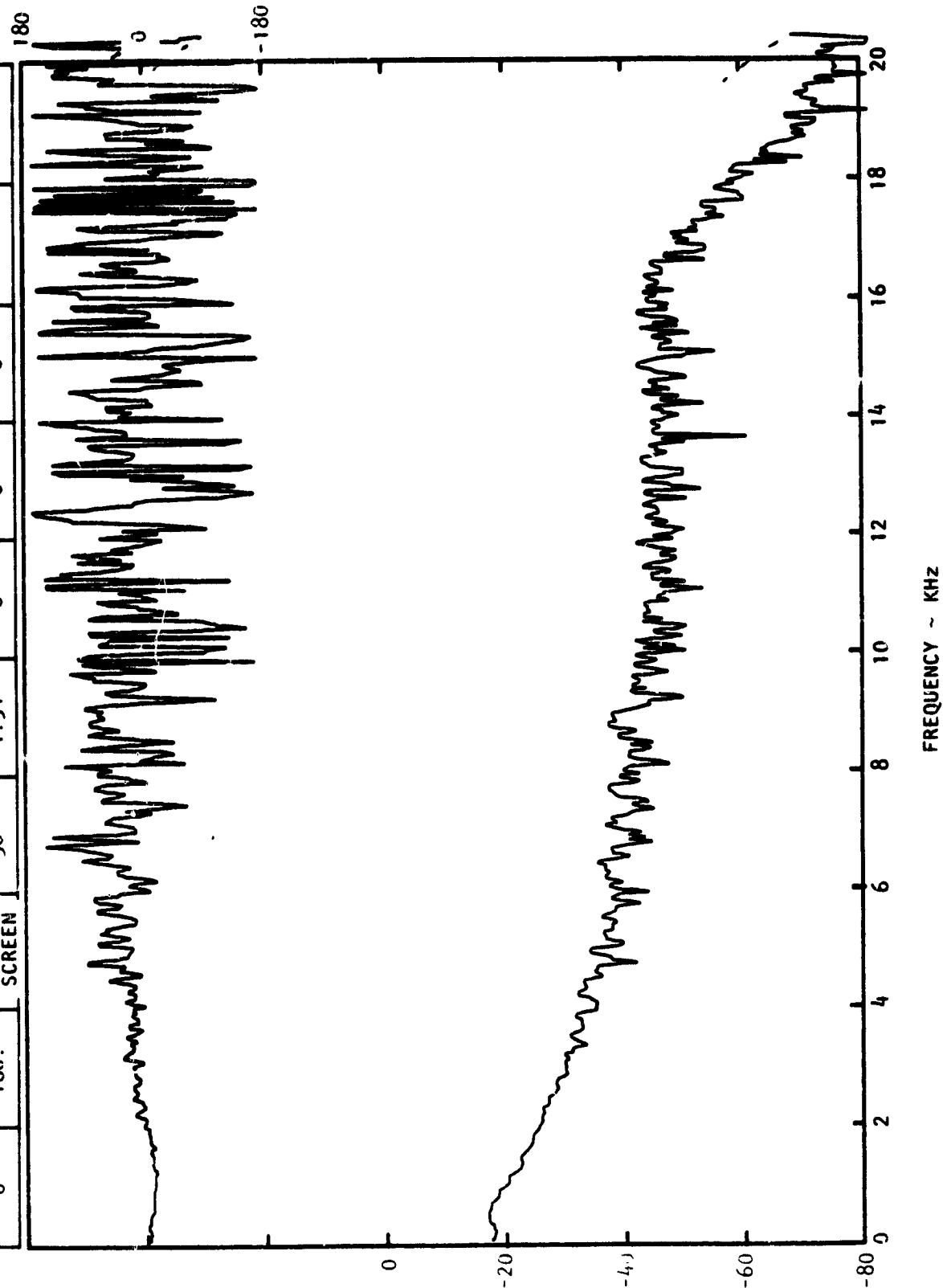
FREQUENCY ~ KHz

Figure C-3. Continued.

CROSS POWER SPECTRAL DENSITY $G_A(f)$ ~ dB

VEL. COMP.	U_j - m/s	INIT. TURB.	δ_f	$X' - \text{cm}$	$\Delta X' - \text{cm}$	$Y - \text{cm}$	$\Delta Y - \text{cm}$	$Z' - \text{cm}$	$\Delta Z' - \text{cm}$
U	180.	NO SCREEN	30°	1.91	0	0	0	0.64	0.61

PHASE ANGLE - DEGREES



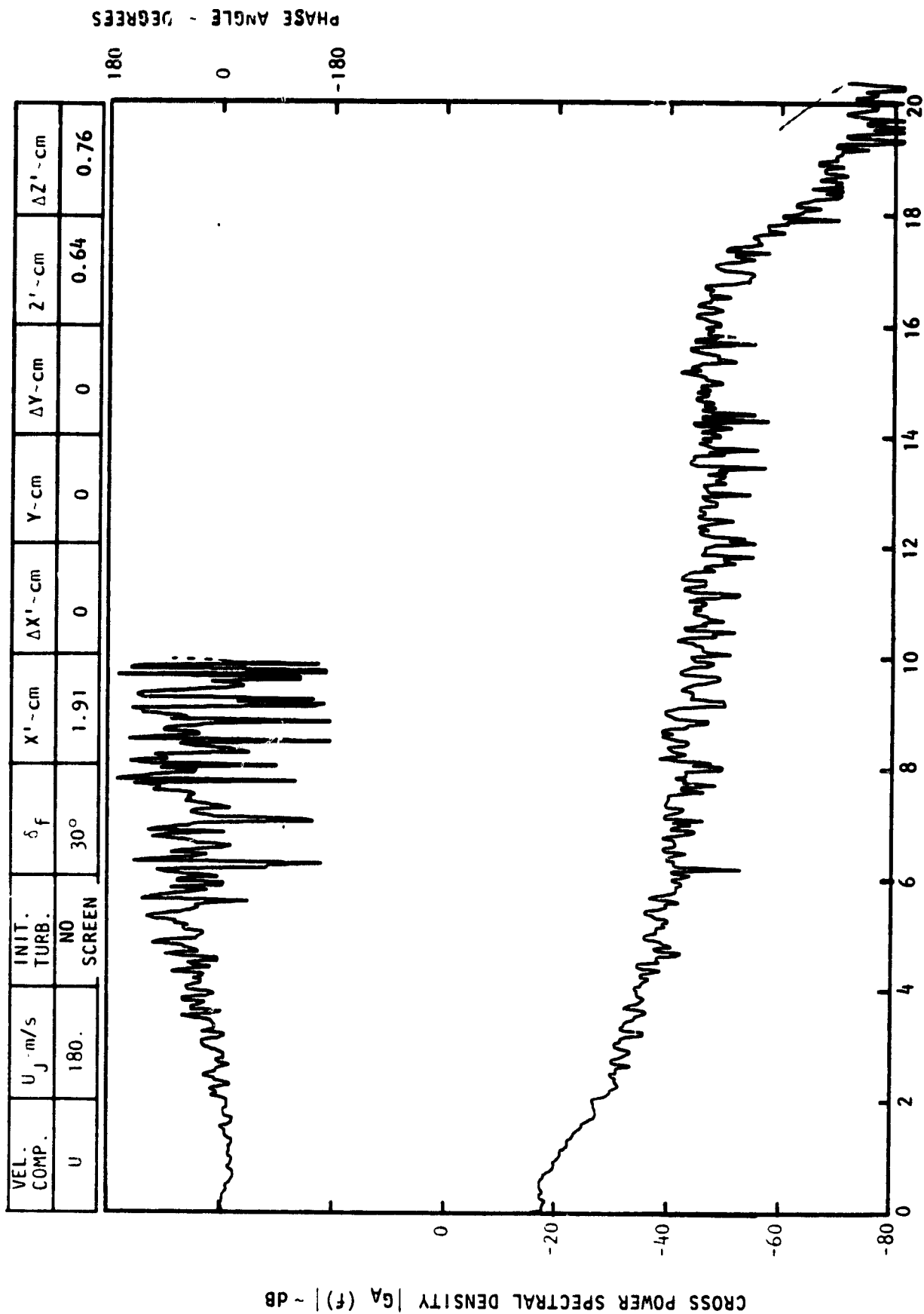
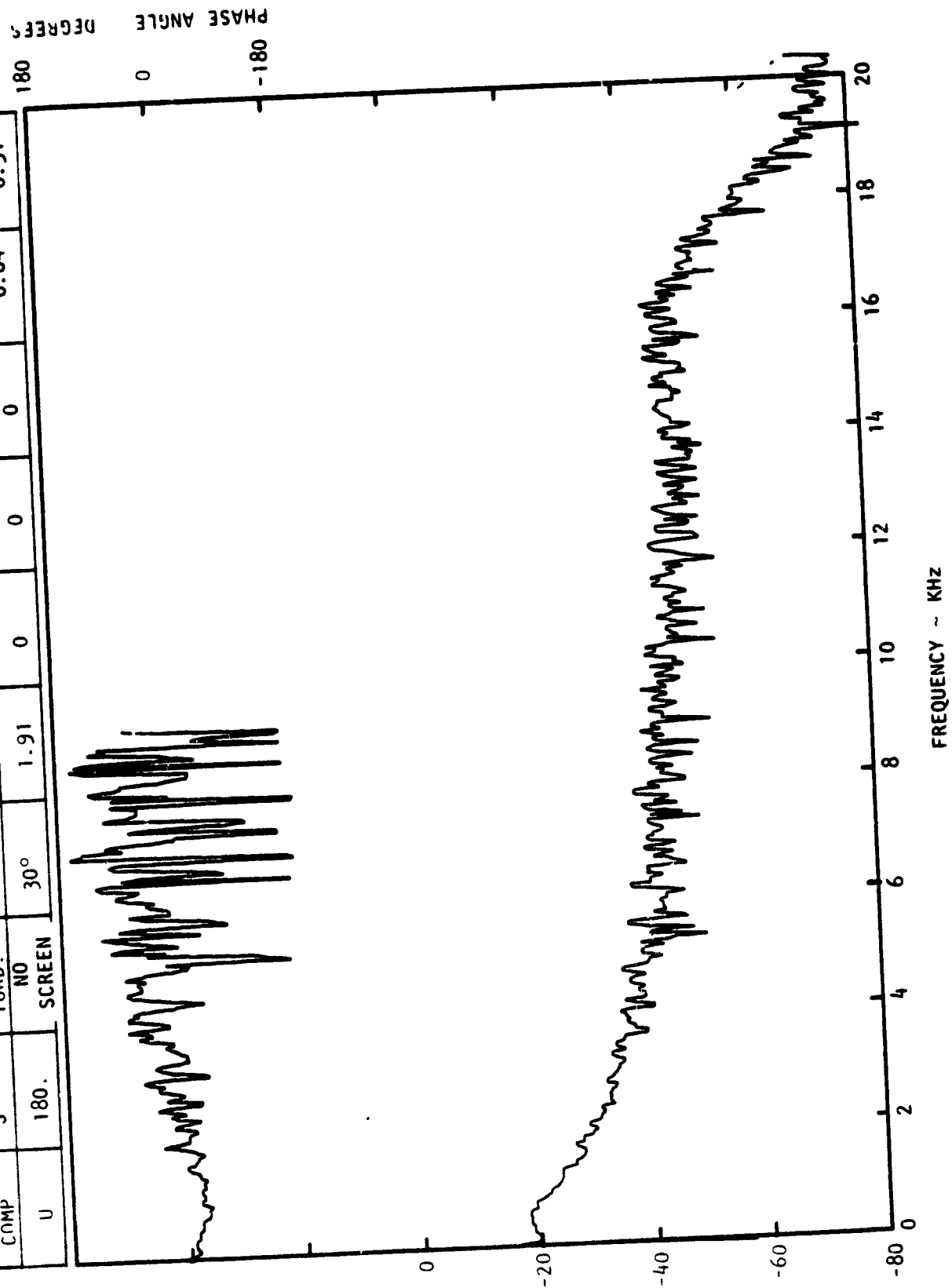


Figure C-3. Continued.

VCL COMP	U_j - m/s	INIT. TURB.	δ f	X^1 - cm	ΔX^1 - cm	Y - cm	ΔY - cm	Z^1 - cm	ΔZ^1 - cm
U	180.	NO SCREEN	30°	1.91	0	0	0	0.64	0.91



VEL. COMP.	U	U_j m/s	INIT. TURB.	Δf	X^1 - cm	ΔX^1 - cm	Y - cm	ΔY - cm	Z^1 - cm	ΔZ^1 - cm
		180.	NO SCREEN	30°	1.91	0	0	0	0.64	1.07

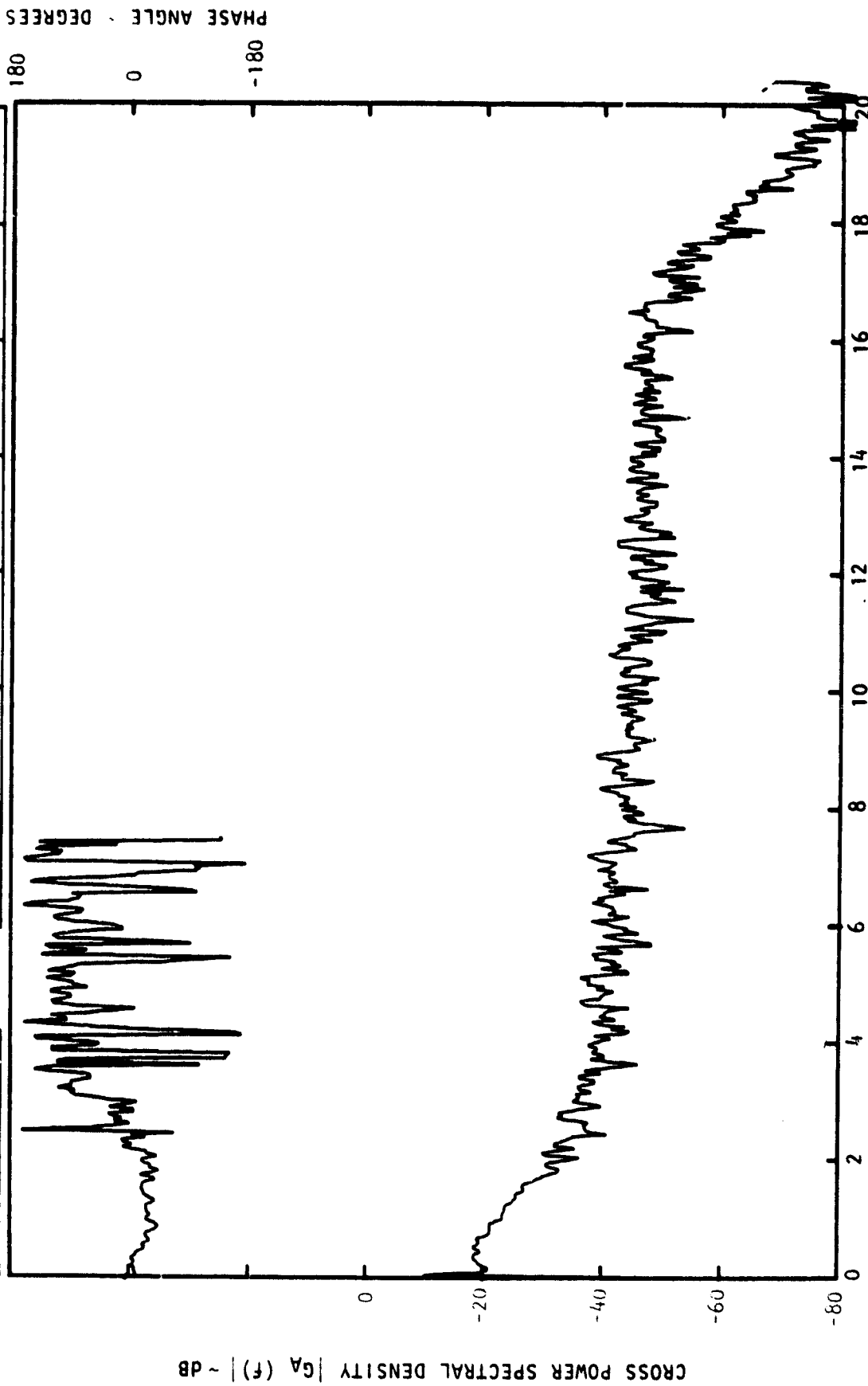
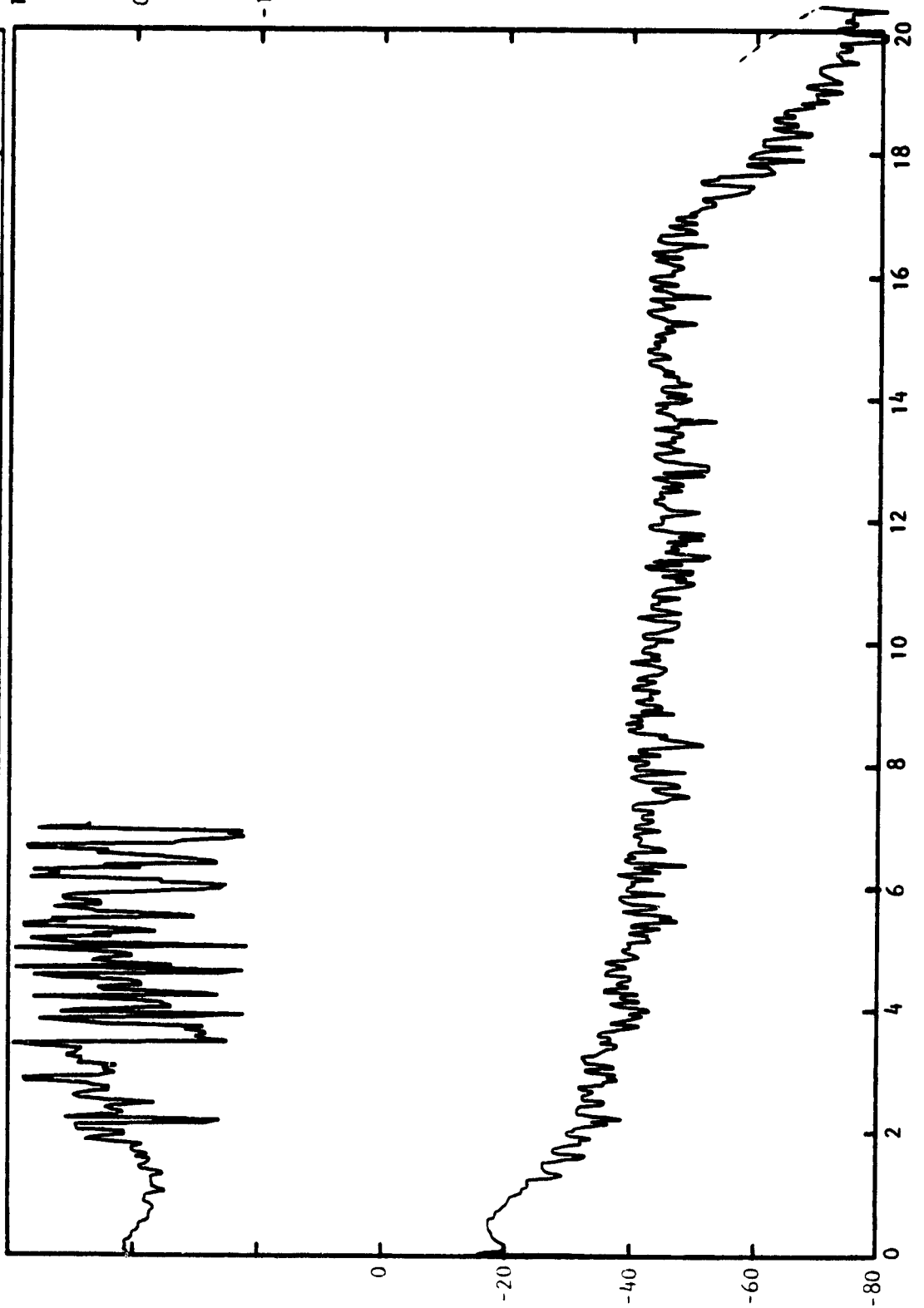


Figure C-3. Continued.

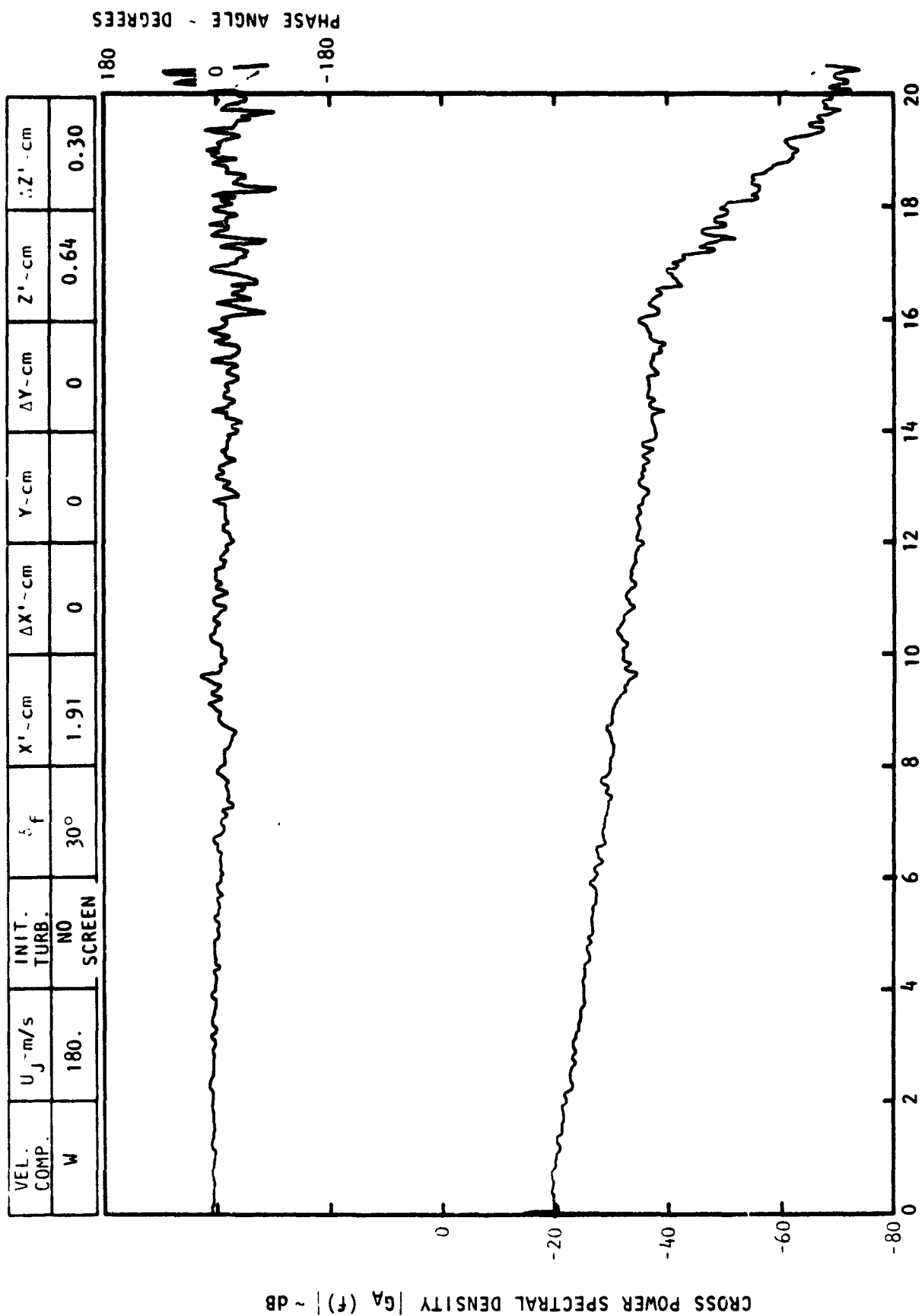
CROSS POWER SPECTRAL DENSITY $G_A(f)$ ~ DB

PHASE ANGLE - DEGREES

VEL. COMP.	U_j - m/s	INIT. TURB.	δ_f	$X' - \text{cm}$	$\Delta X' - \text{cm}$	$Y - \text{cm}$	$\Delta Y - \text{cm}$	$Z' - \text{cm}$	$\Delta Z' - \text{cm}$
U	180.	NO SCREEN	30°	1.91	0	0	0	0.64	1.22



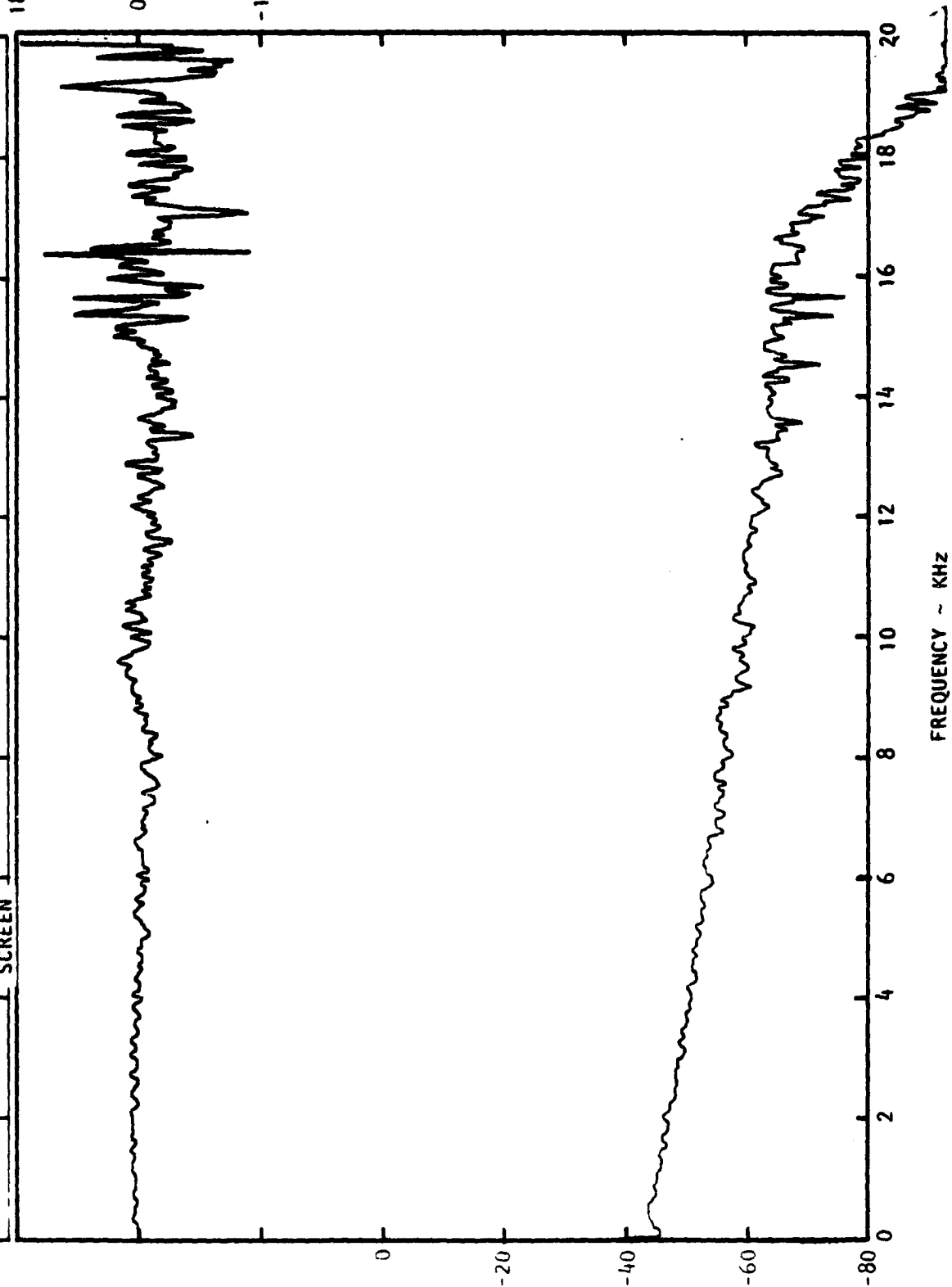
FREQUENCY ~ KHz



FREQUENCY ~ KHz
Figure C-3. Continued.

CROSS POWER SPECTRAL DENSITY |G_A(f)| ~ dB

VEL. COMP.	U _J - m/s	INIT. TURB.	δ _f	X' - cm	ΔX' - cm	Y - cm	ΔY - cm	Z' - cm	ΔZ' - cm
W	180.	NO SCREEN	30°	1.91	0	0	0	0.64	0.46



PHASE ANGLE - DEGREES

180
0
-180

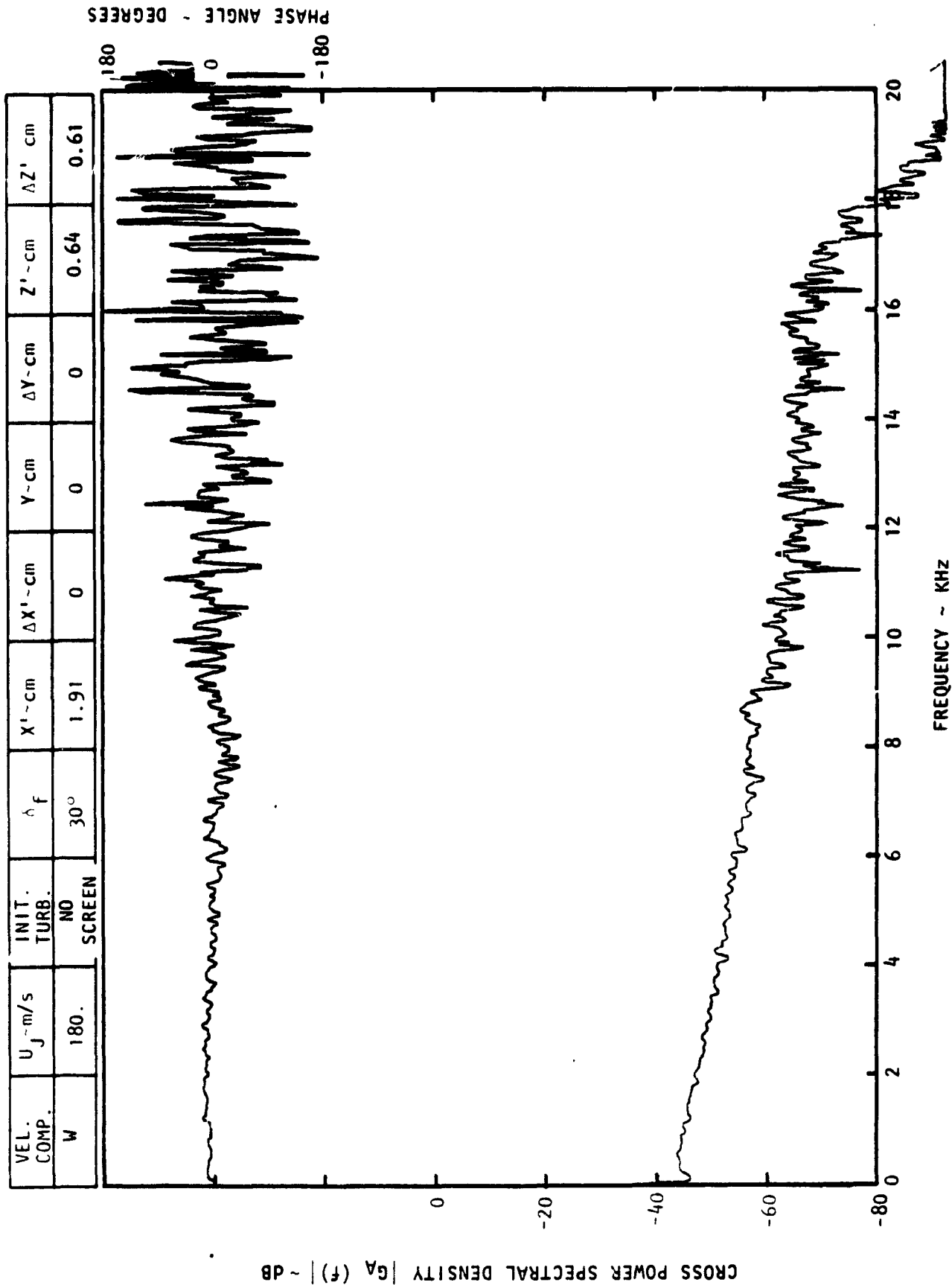
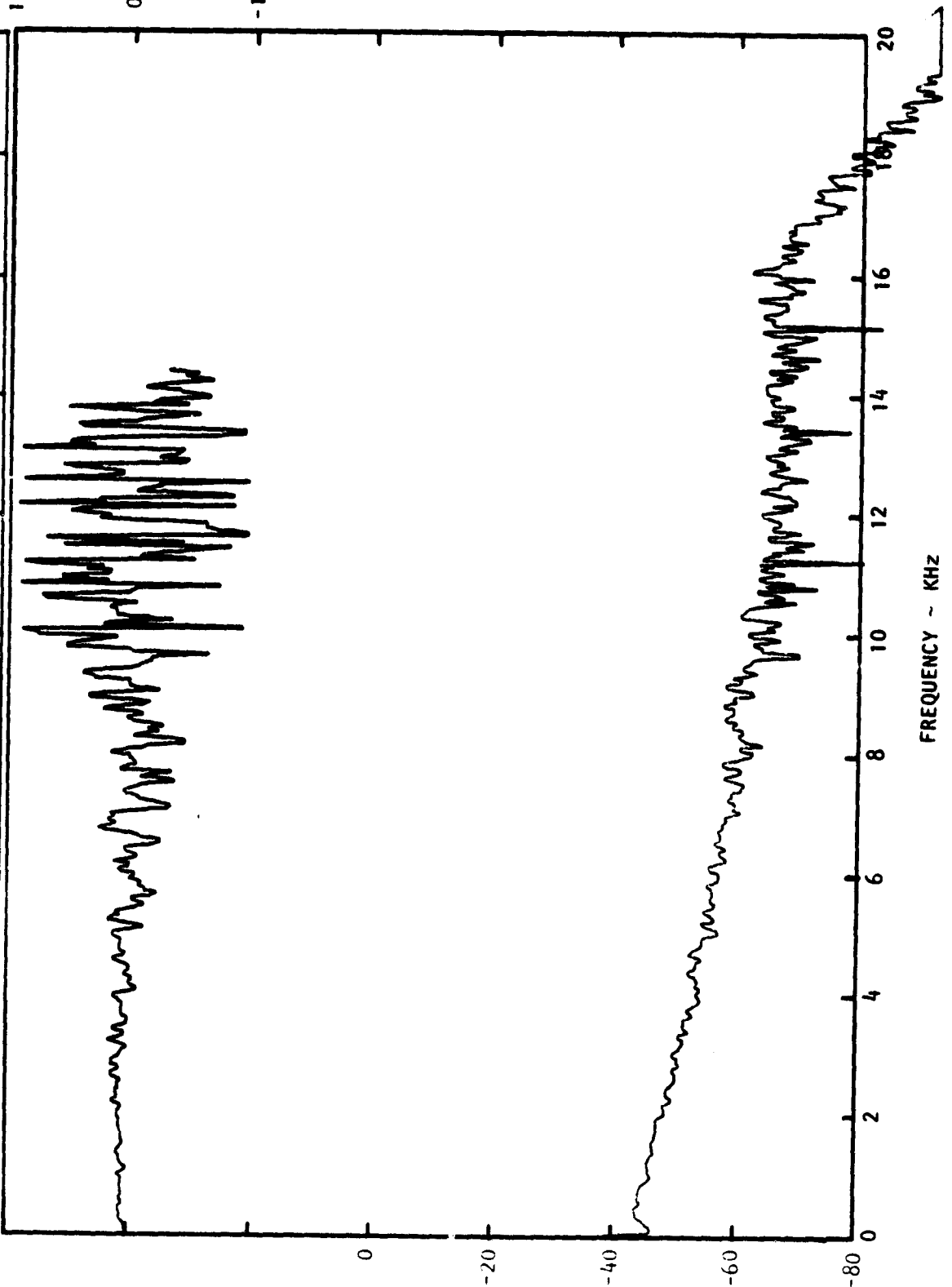


Figure C-3. Continued.

CROSS POWER SPECTRAL DENSITY $G_A(f)$ ~ DB

PHASE ANGLE - DEGREES

VEL. COMP.	U_j - m/s	INIT. TURB.	δf	$X' - \text{cm}$	$\Delta X' - \text{cm}$	$Y - \text{cm}$	$\Delta Y - \text{cm}$	$Z' - \text{cm}$	$\Delta Z' - \text{cm}$
W	180.	NO SCREEN	30°	1.91	0	0	0	0.64	0.76



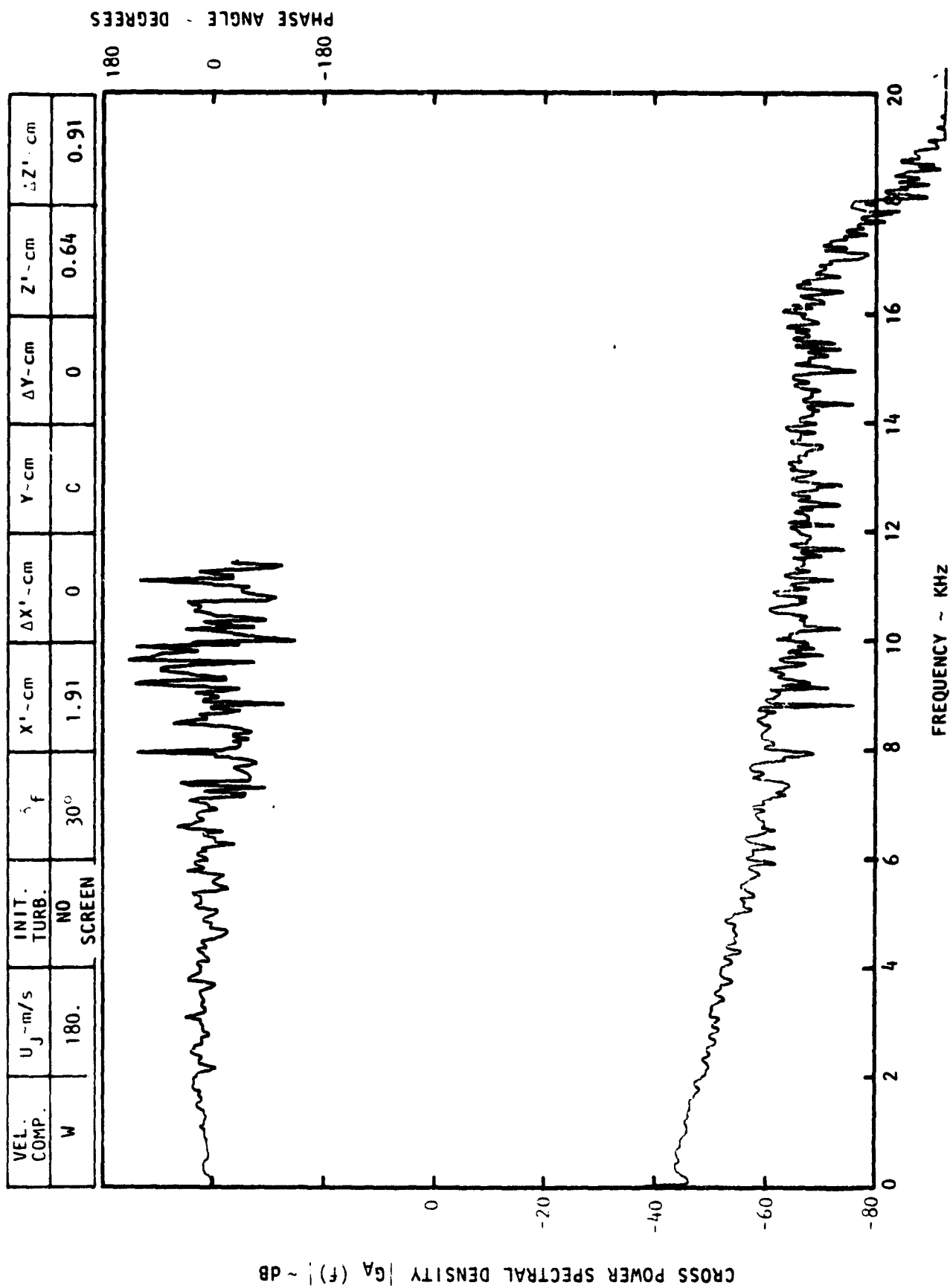
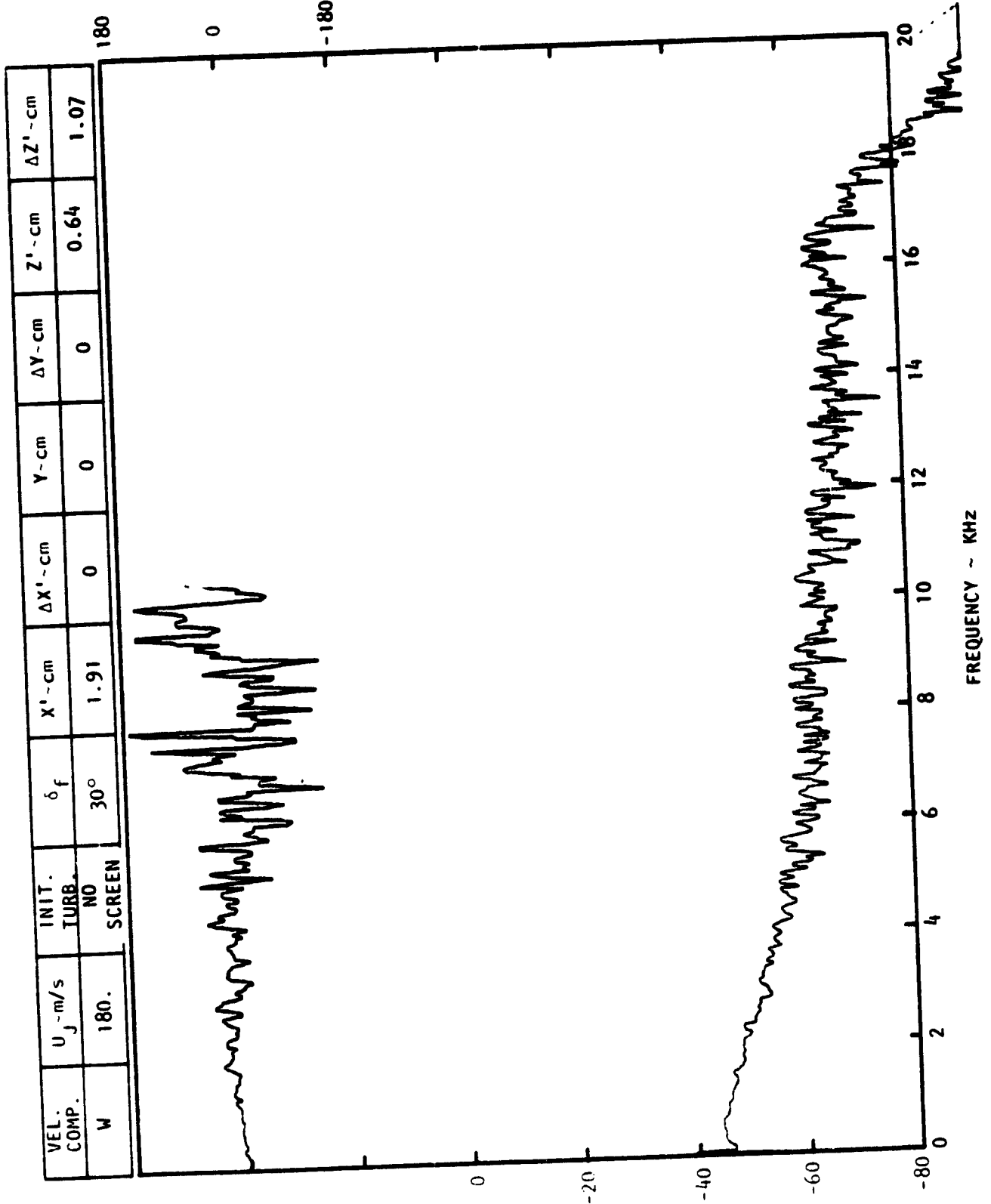


Figure C-3. Continued.

CROSS POWER SPECTRAL DENSITY $|G_A(f)| \sim \text{dB}$

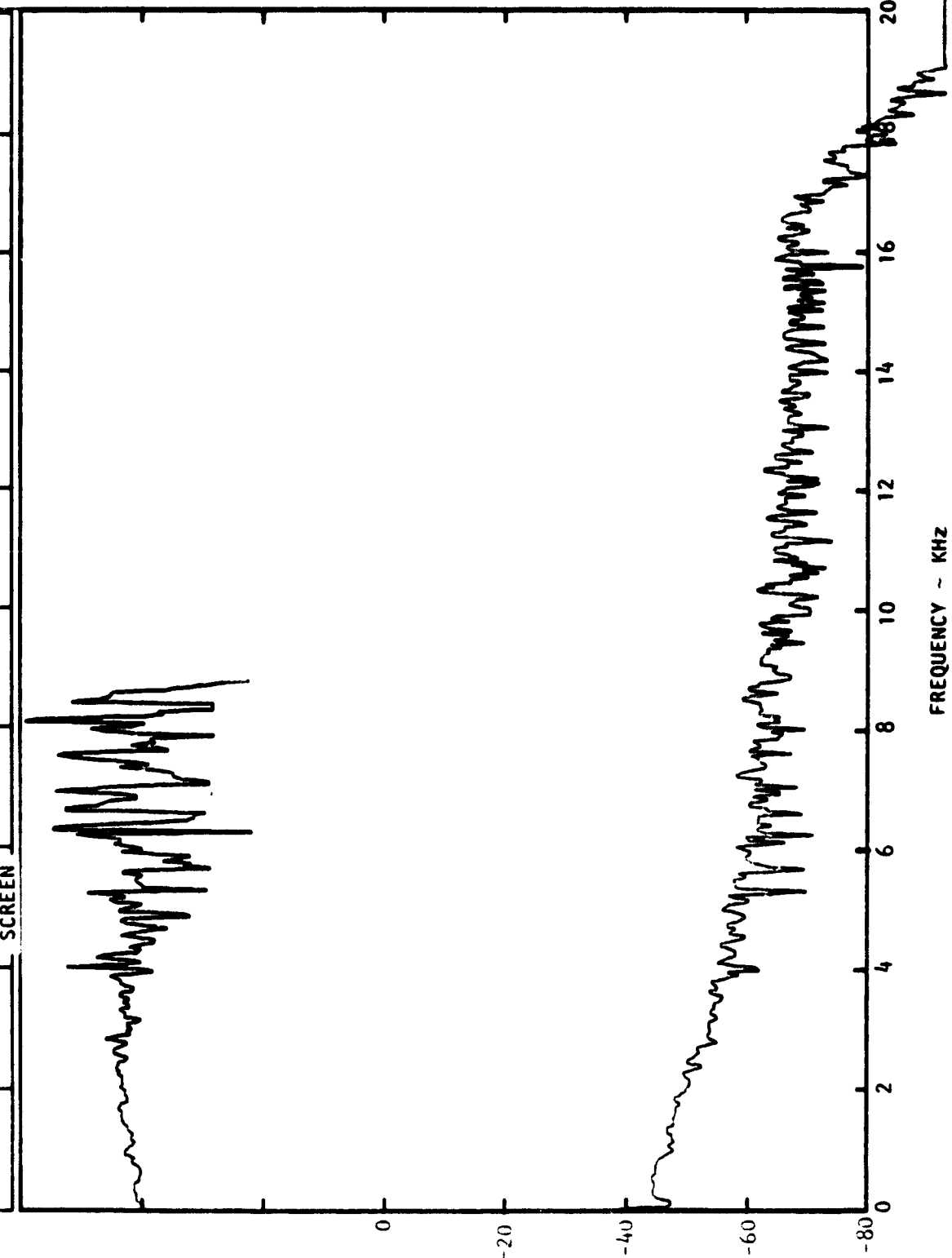
PHASE ANGLE - DEGREES



CROSS POWER SPECTRAL DENSITY $G_A(f)$ - dB

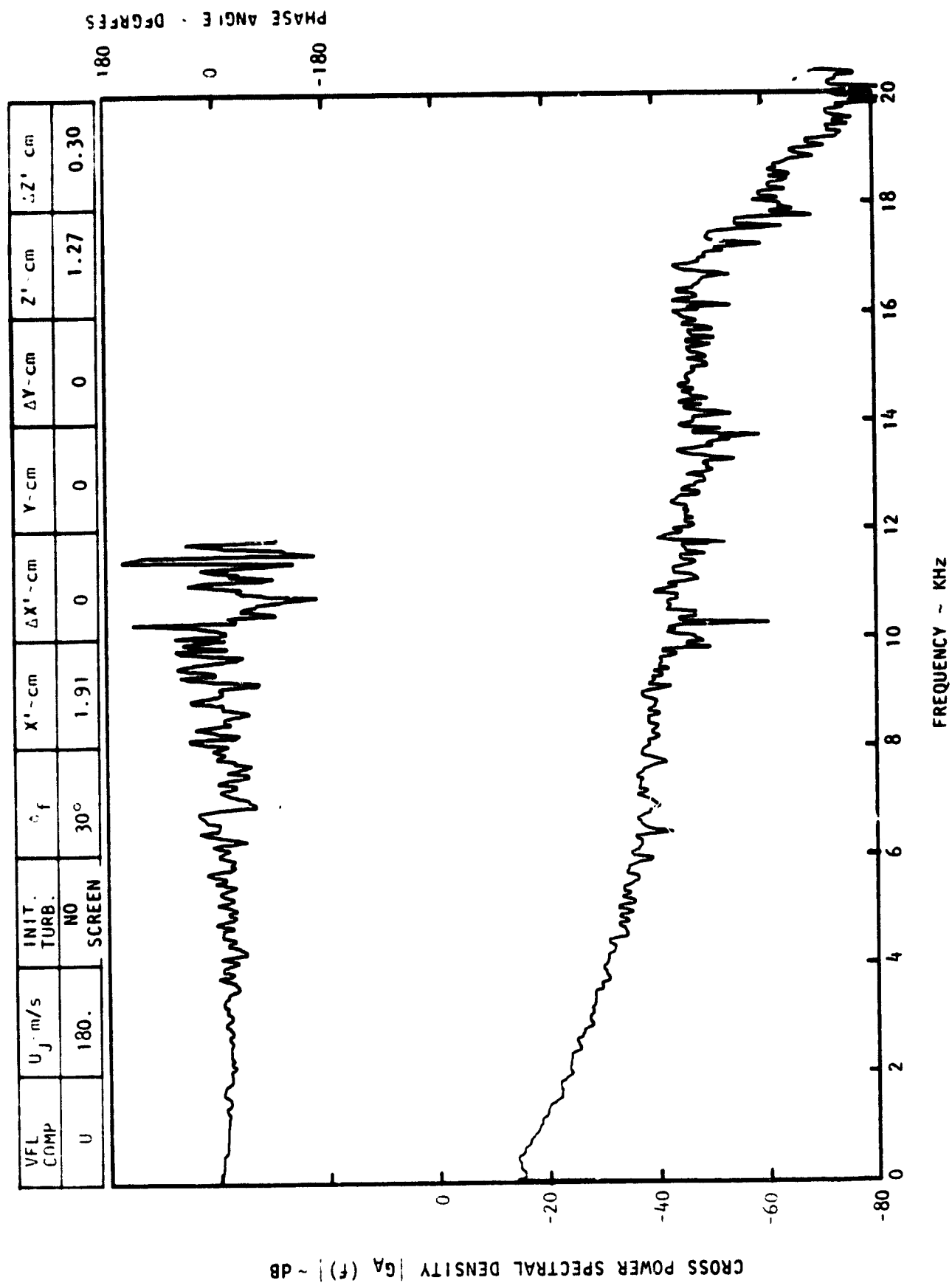
VEL. COMP.	U_j m/s	INIT. TURB.	ξ_f	$X' - \text{cm}$	$\Delta X' - \text{cm}$	$Y - \text{cm}$	$\Delta Y - \text{cm}$	$Z' - \text{cm}$	$\Delta Z' - \text{cm}$
W	180.	NO SCREEN	30°	1.91	0	0	0	0.64	1.22

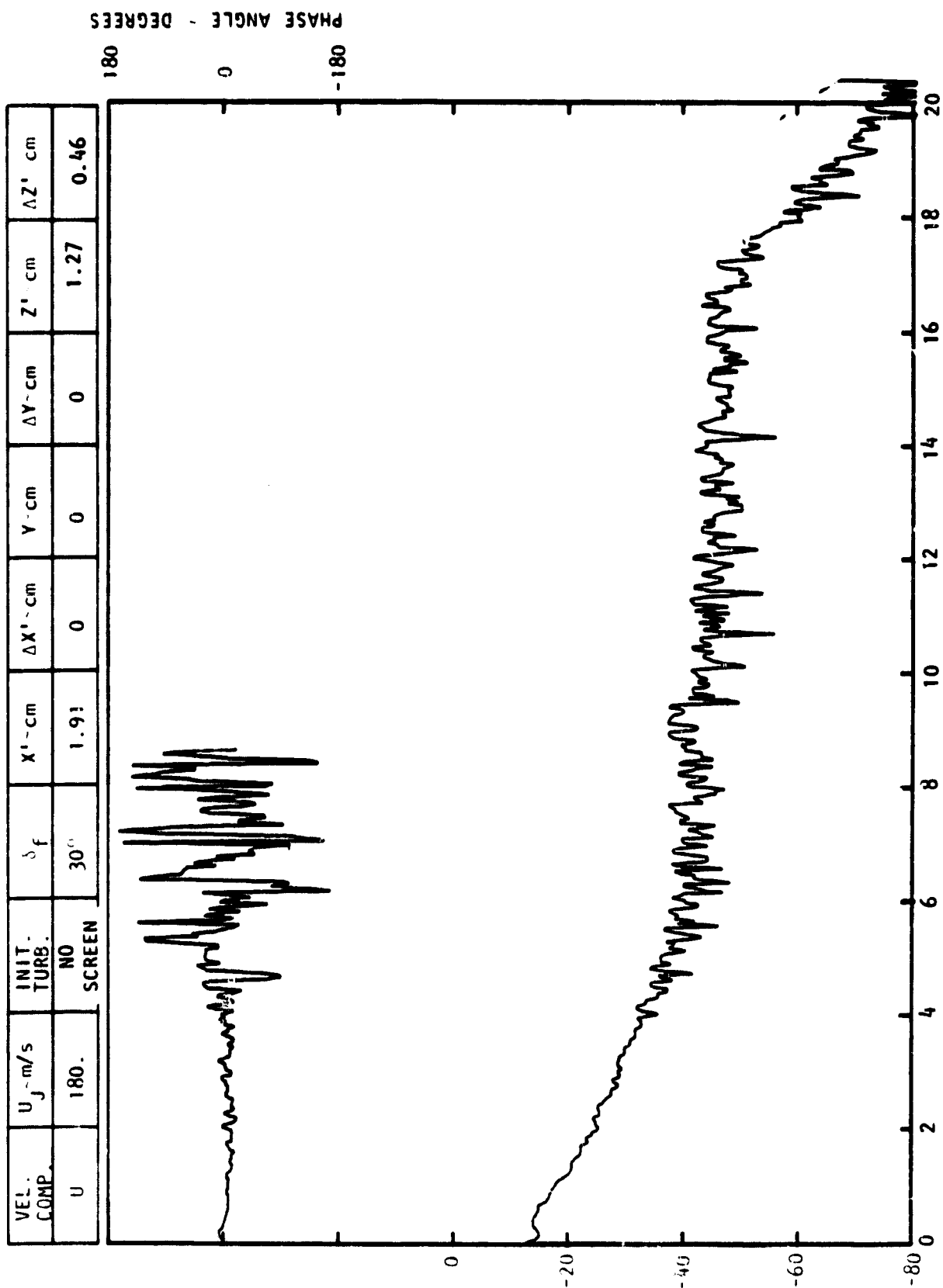
PHASE ANGLE - DEGREES



FREQUENCY - KHz

Figure C-3. Continued.



CROSS POWER SPECTRAL DENSITY $|G_A(f)|^2$ - DB

FREQUENCY ~ KHz

Figure C-3. Continued.

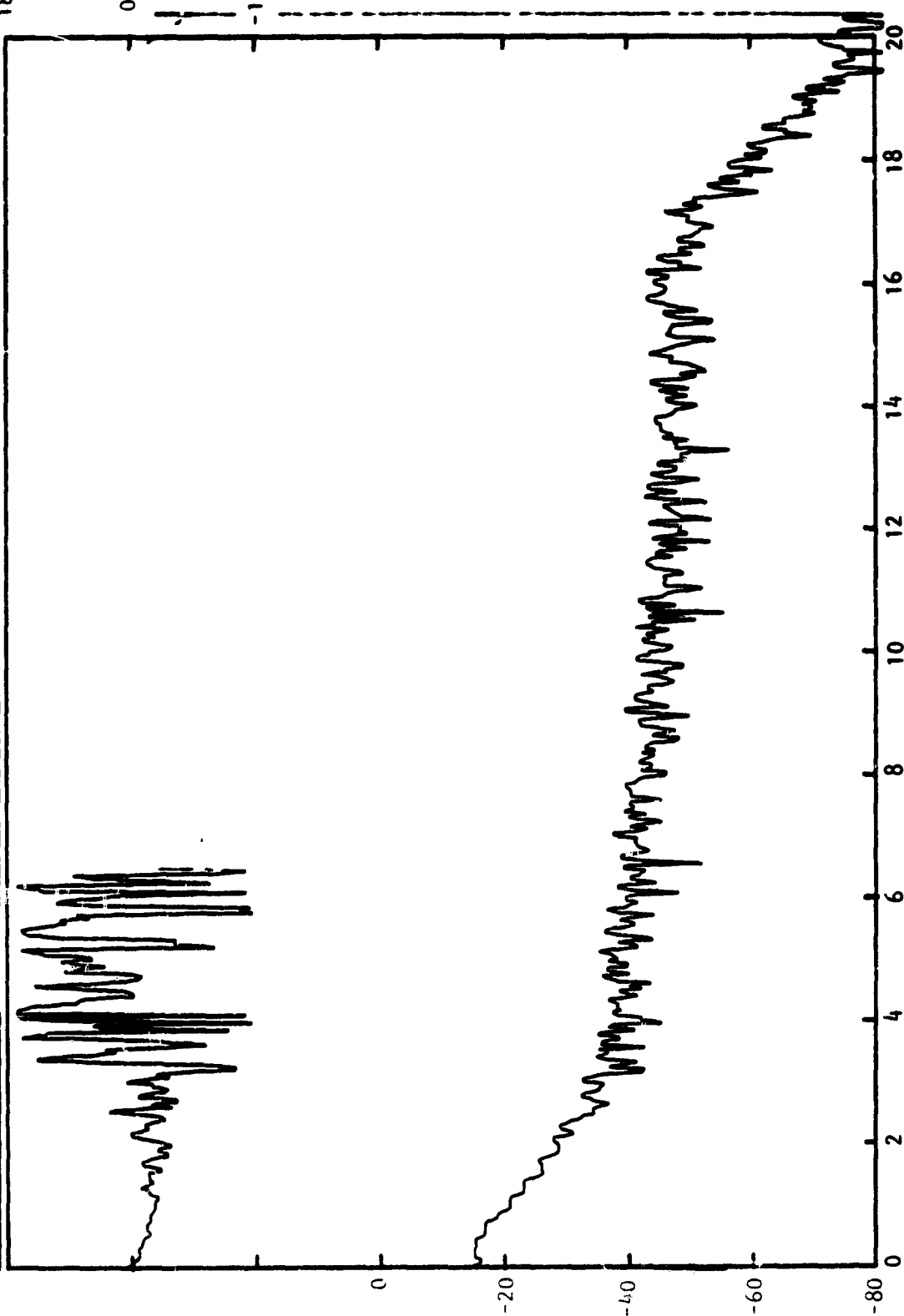
VEL. COMP.	U_j - m/s	INIT. TURB.	δ_f	X^1 - cm	ΔX^1 - cm	Y - cm	ΔY - cm	Z^1 - cm	ΔZ^1 - cm
U	180.	NO SCREEN	36°	1.91	0	0	0	1.27	0.76

PHASE ANGLE - DEGREES

180

0

-180

CROSS POWER SPECTRAL DENSITY $|C_A(f)|$ - dB

FREQUENCY - KHZ

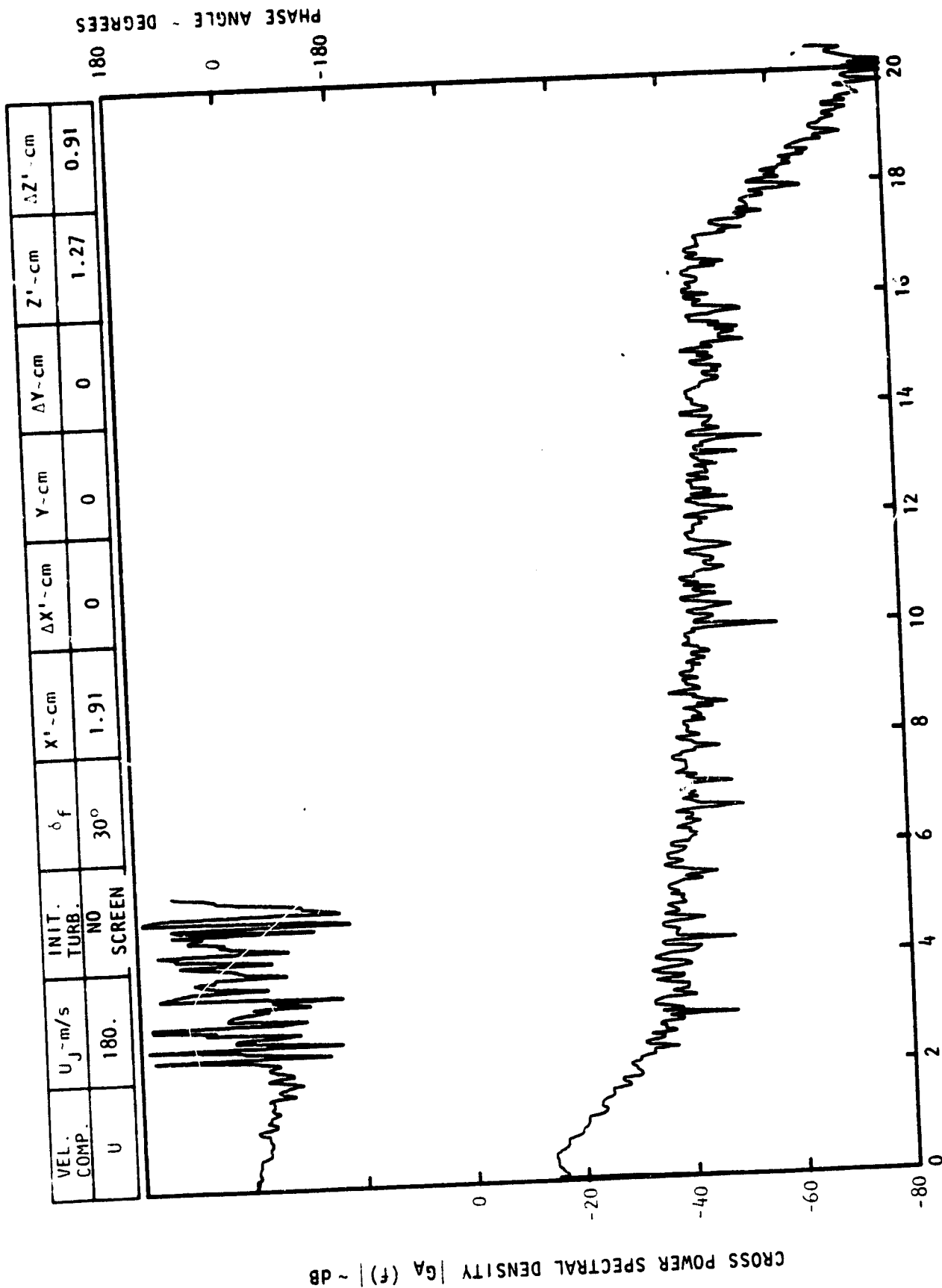
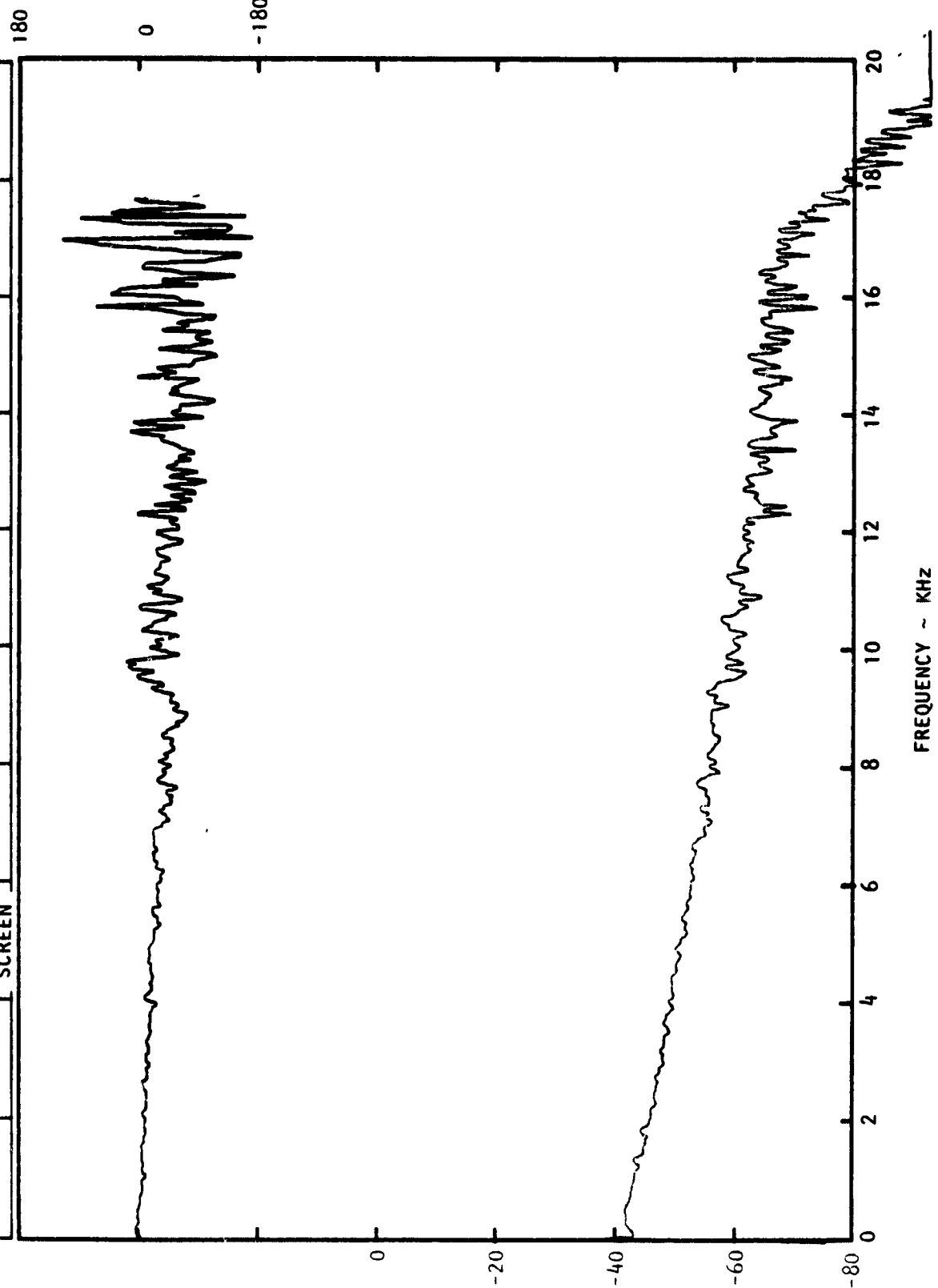


Figure C-3. Continued.

CROSS POWER SPECTRAL DENSITY $|G_A(f)| \sim \text{dB}$

VEL. COMP.	$U_j \sim \text{m/s}$	INIT. TURB.	δ_f	$X^1 \sim \text{cm}$	$\Delta X^1 \sim \text{cm}$	$Y \sim \text{cm}$	$\Delta Y \sim \text{cm}$	$Z^1 \sim \text{cm}$	$\Delta Z^1 \sim \text{cm}$
W	180.	NO SCREEN	30°	1.91	0	0	0	1.27	0.30

PHASE ANGLE - DEGREES



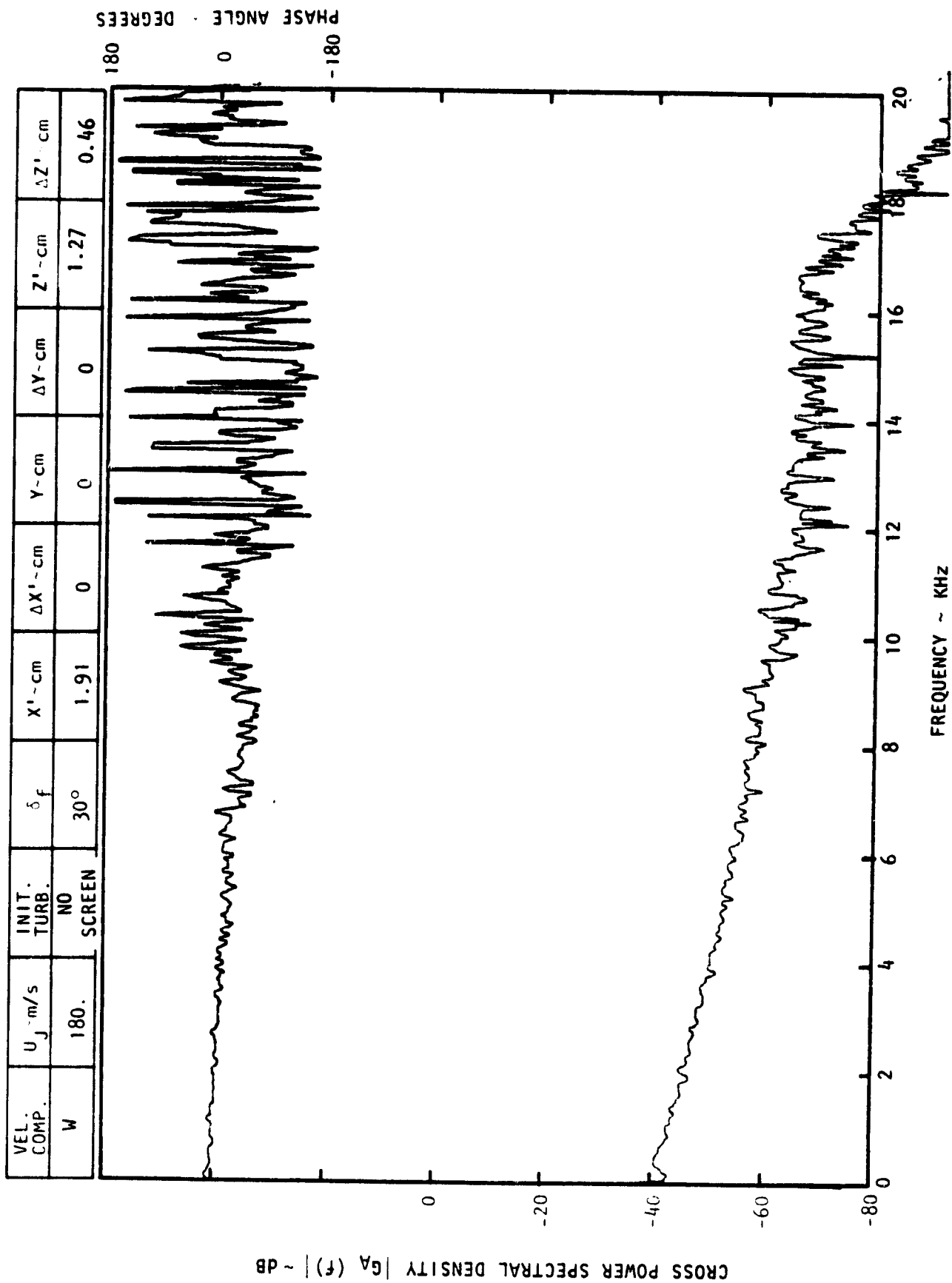
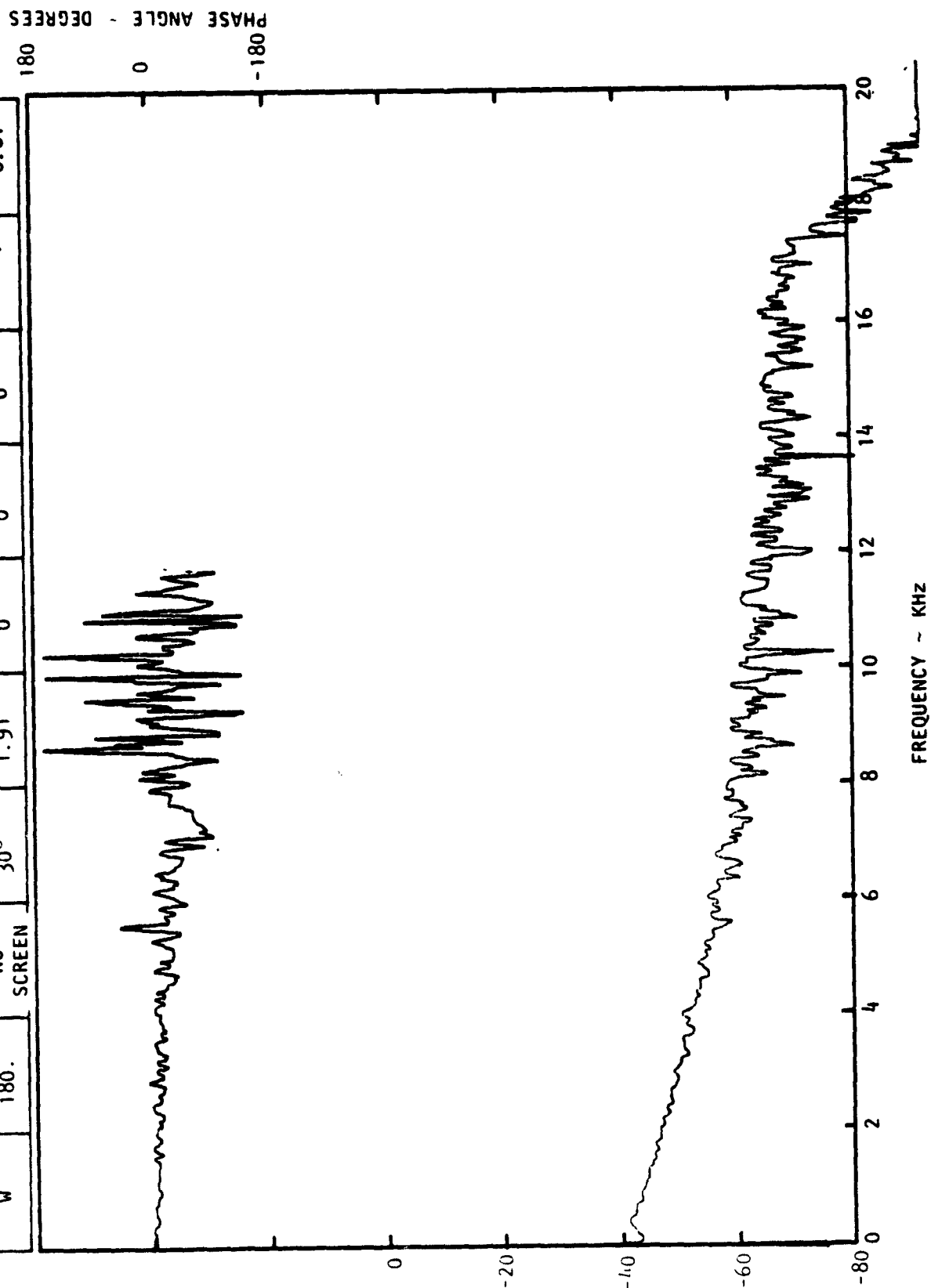


Figure C-3. Continued.

CROSS POWER SPECTRAL DENSITY $G_A(f)$ ~ dB

VEL. COMP.	U_j - m/s	INIT. TURB.	ϕ_f	$X' - \text{cm}$	$\Delta X' - \text{cm}$	$Y - \text{cm}$	$\Delta Y - \text{cm}$	$Z' - \text{cm}$	$\Delta Z' - \text{cm}$
W	180.	NO SCREEN	30°	1.91	0	0	0	1.27	0.61



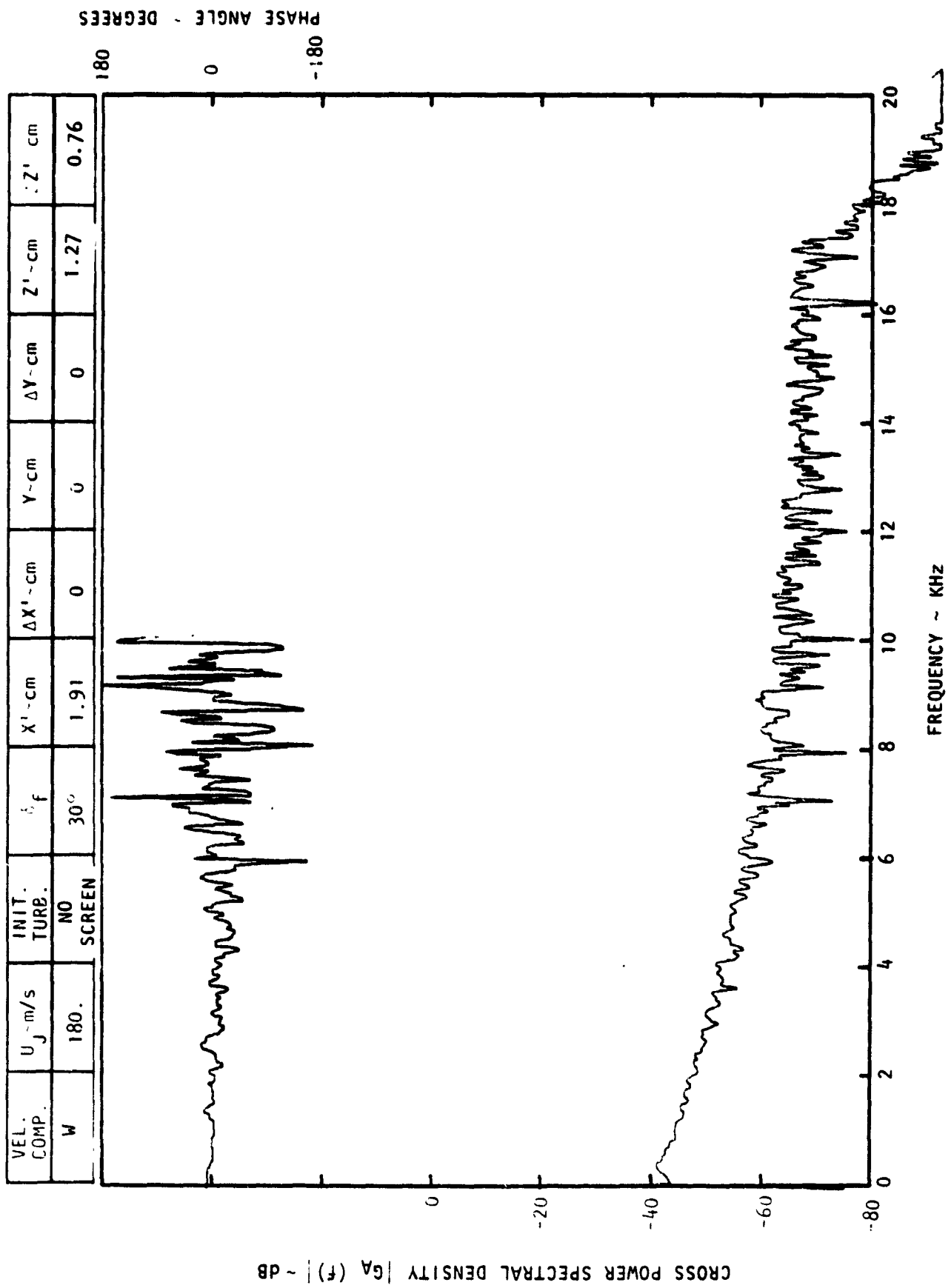
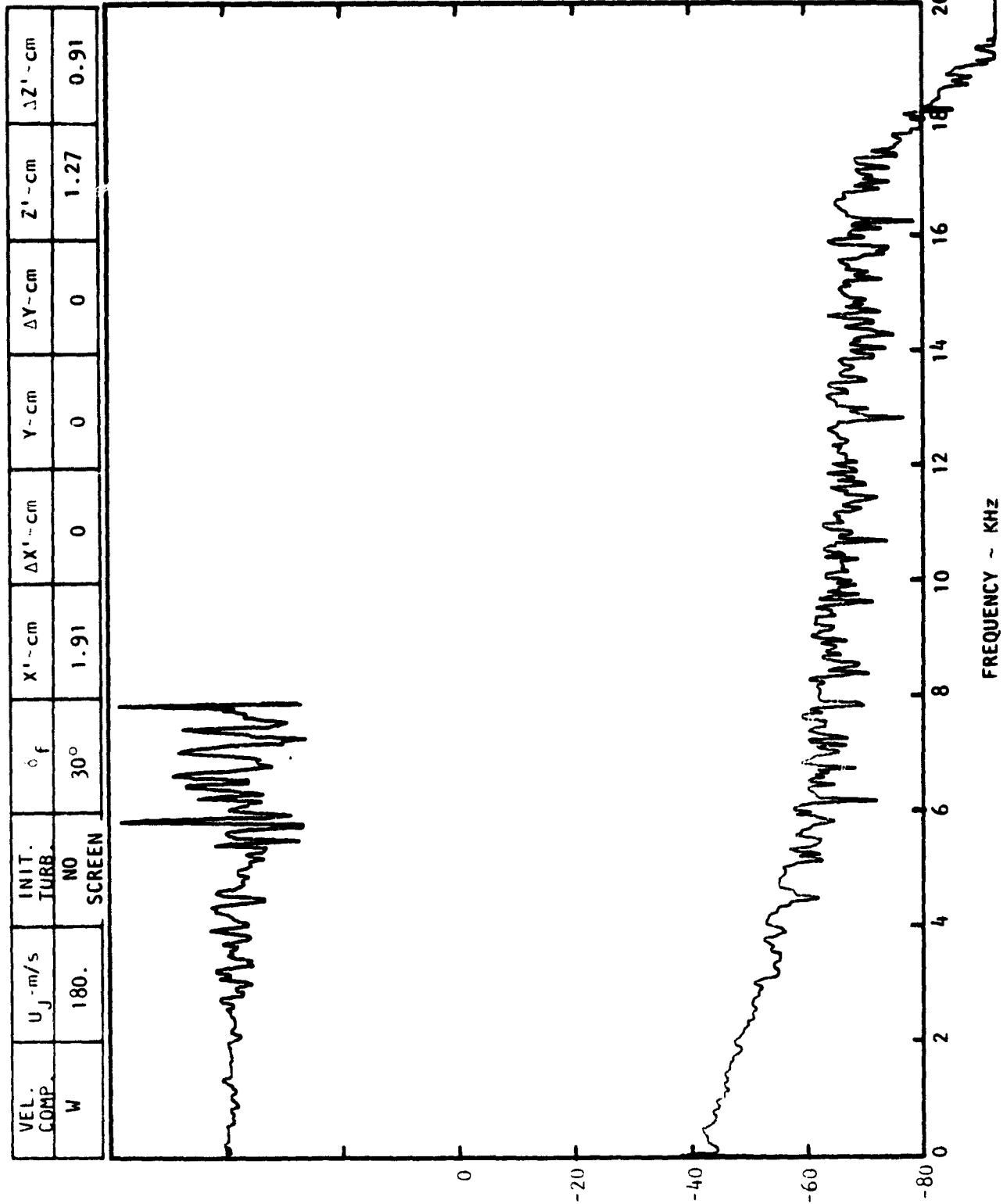
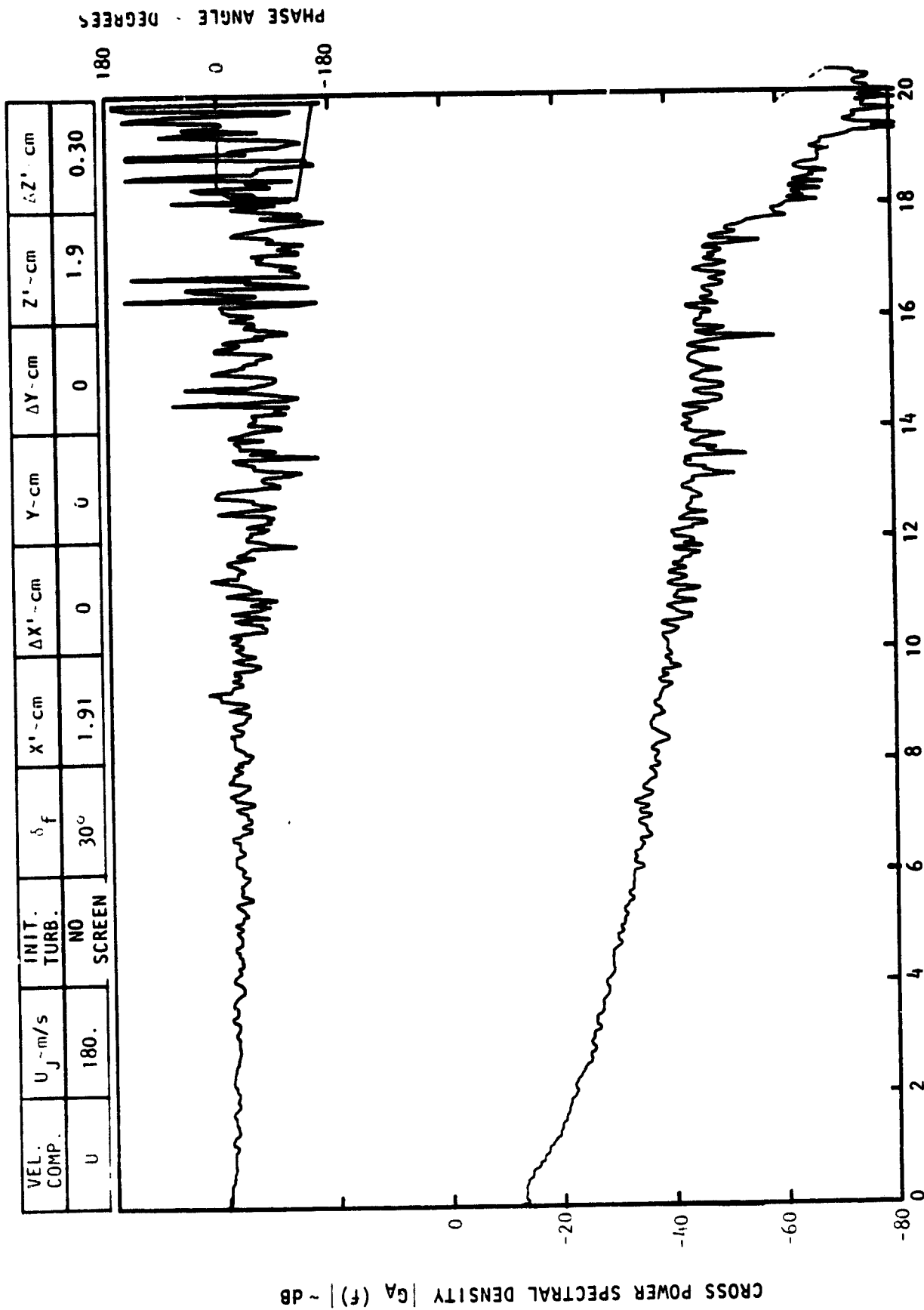


Figure C-3. Continued.

CROSS POWER SPECTRAL DENSITY $|G_A(f)| \sim \text{dB}$ 

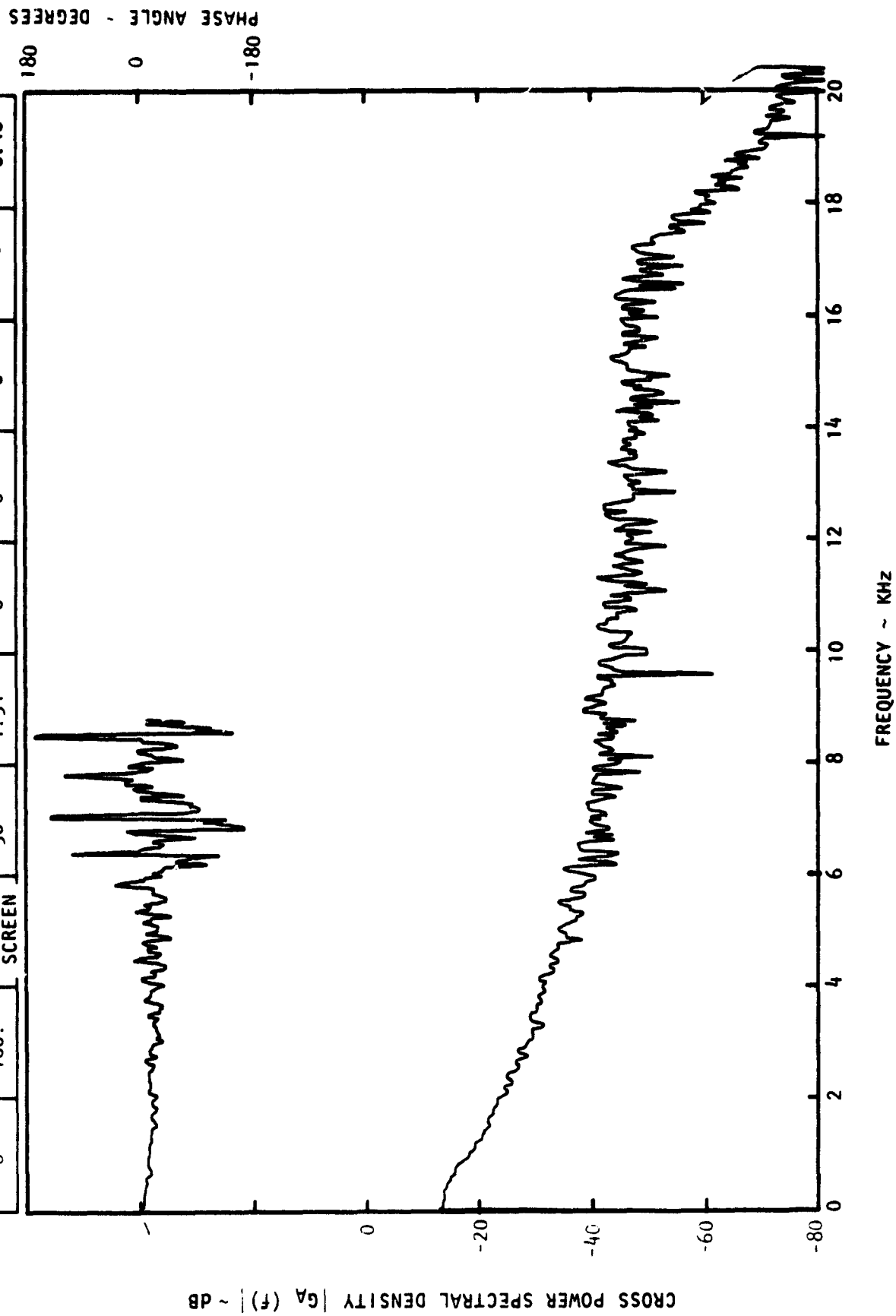


VEL. COMP.	U_j ~ m/s	INIT. TURB.	δ_f	X^1 ~ cm	ΔX^1 ~ cm	Y ~ cm	ΔY ~ cm	Z^1 ~ cm	ΔZ^1 ~ cm
U	180.	NO SCREEN	30°	1.91	0	0	0	1.9	0.30

FREQUENCY ~ KHz

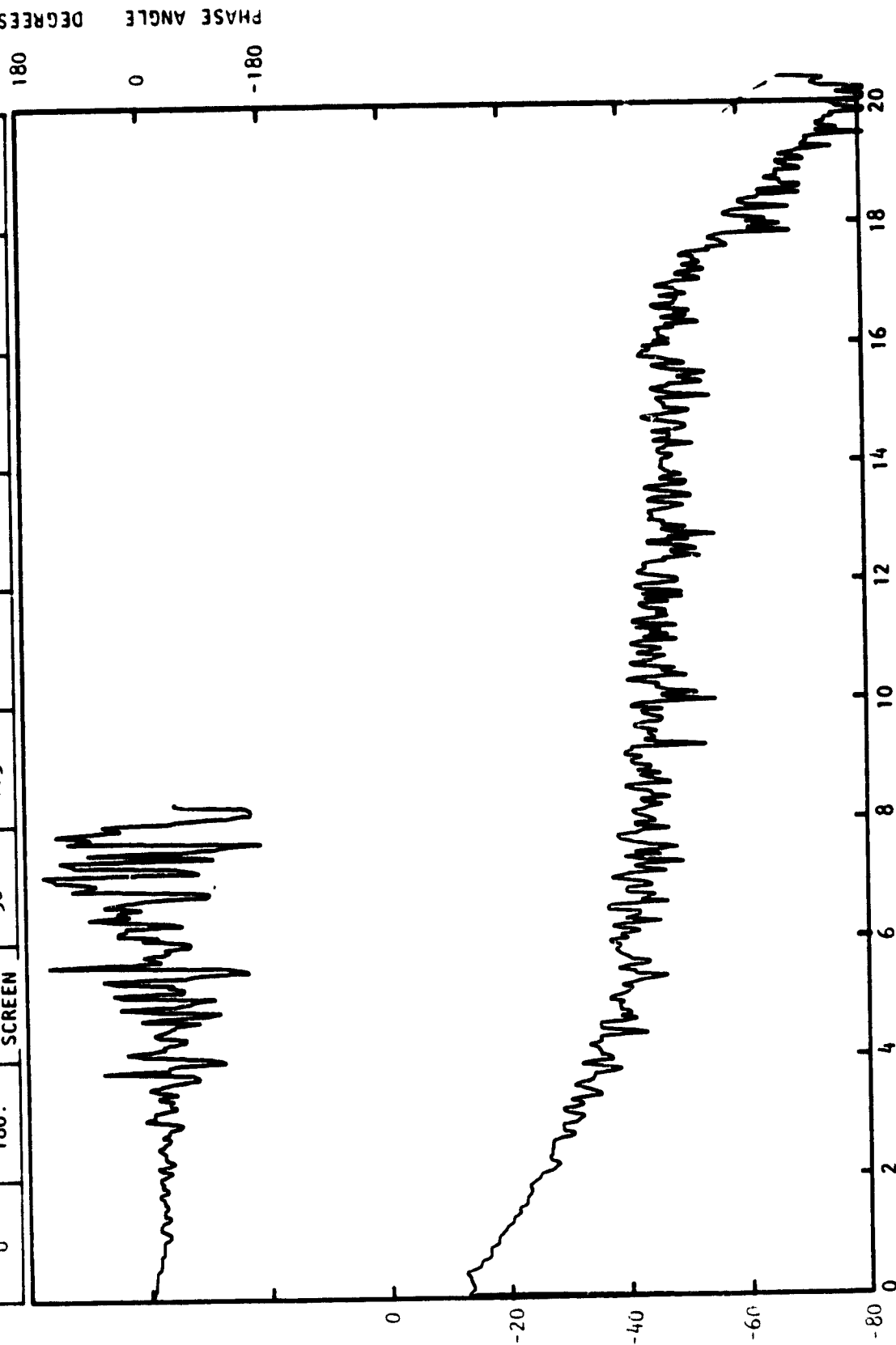
Figure C-3. Continued.

VEL. COMP.	U_j - m/s	INIT. TURB.	δ_f	X^1 - cm	ΔX^1 - cm	Y - cm	ΔY - cm	Z^1 - cm	ΔZ^1 - cm
U	180.	NO SCREEN	30°	1.91	0	0	0	1.9	0.46



CROSS POWER SPECTRAL DENSITY $|G_A(f)| \sim \text{dB}$

VEL. COMP.	U_j - m/s	INIT. TURB.	ϕ_f	$X' - \text{cm}$	$\Delta X' - \text{cm}$	$Y - \text{cm}$	$\Delta Y - \text{cm}$	$Z' - \text{cm}$	$\Delta Z' - \text{cm}$
U	180.	NO SCREEN	30°	1.91	0	0	0	1.9	0.61



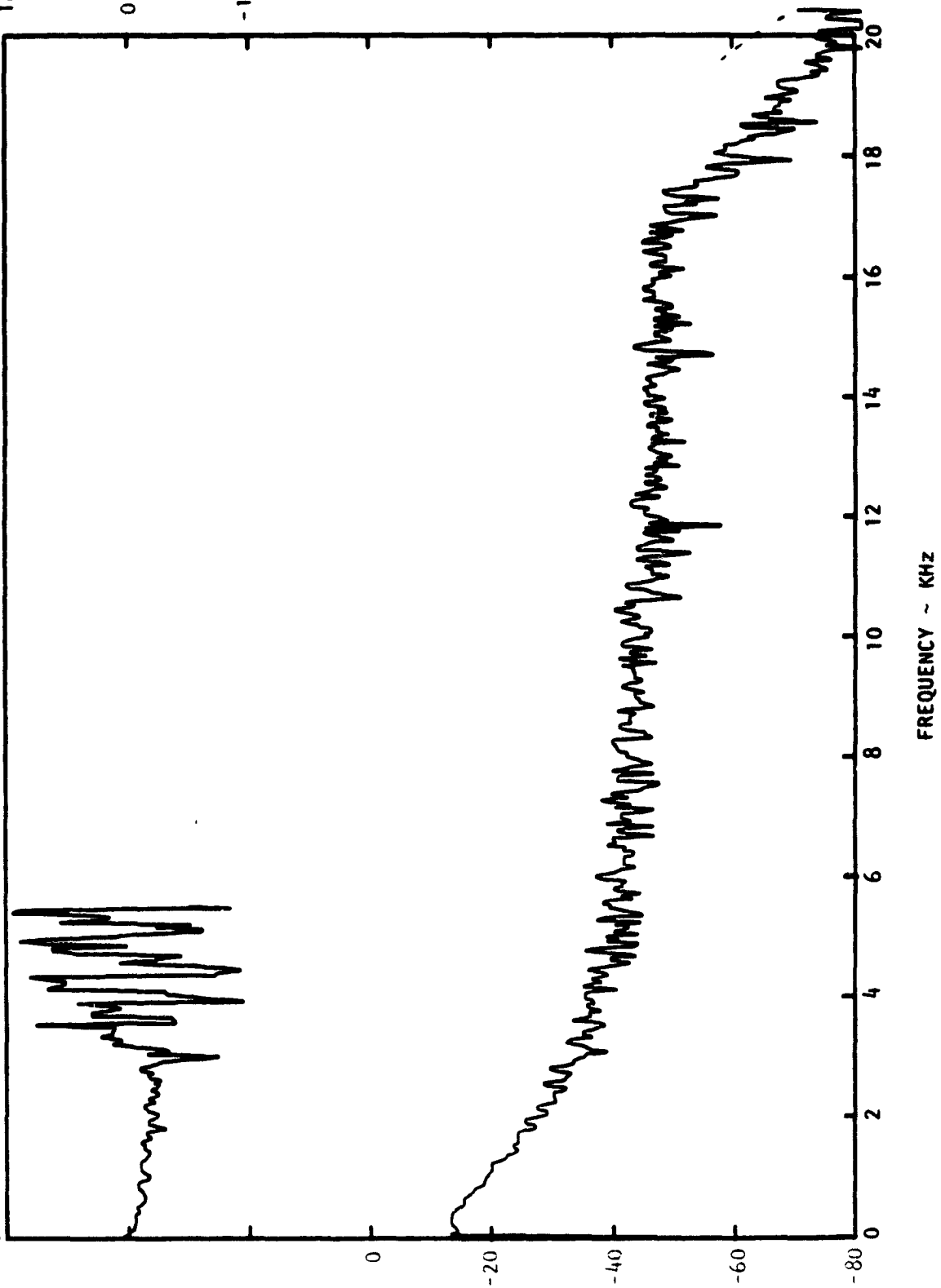
FREQUENCY ~ KHz

Figure C-3. Continued.

CROSS POWER SPECTRAL DENSITY $|G_A(f)| \sim \text{dB}$

PHASE ANGLE - DEGREES

VEL. COMP.	U_j - m/s	INIT. TURB.	α_f	X^1 - cm	ΔX^1 - cm	Y - cm	ΔY - cm	Z^1 - cm	ΔZ^1 - cm
U	180.	NO SCREEN	30°	1.91	0	0	0	1.9	0.76



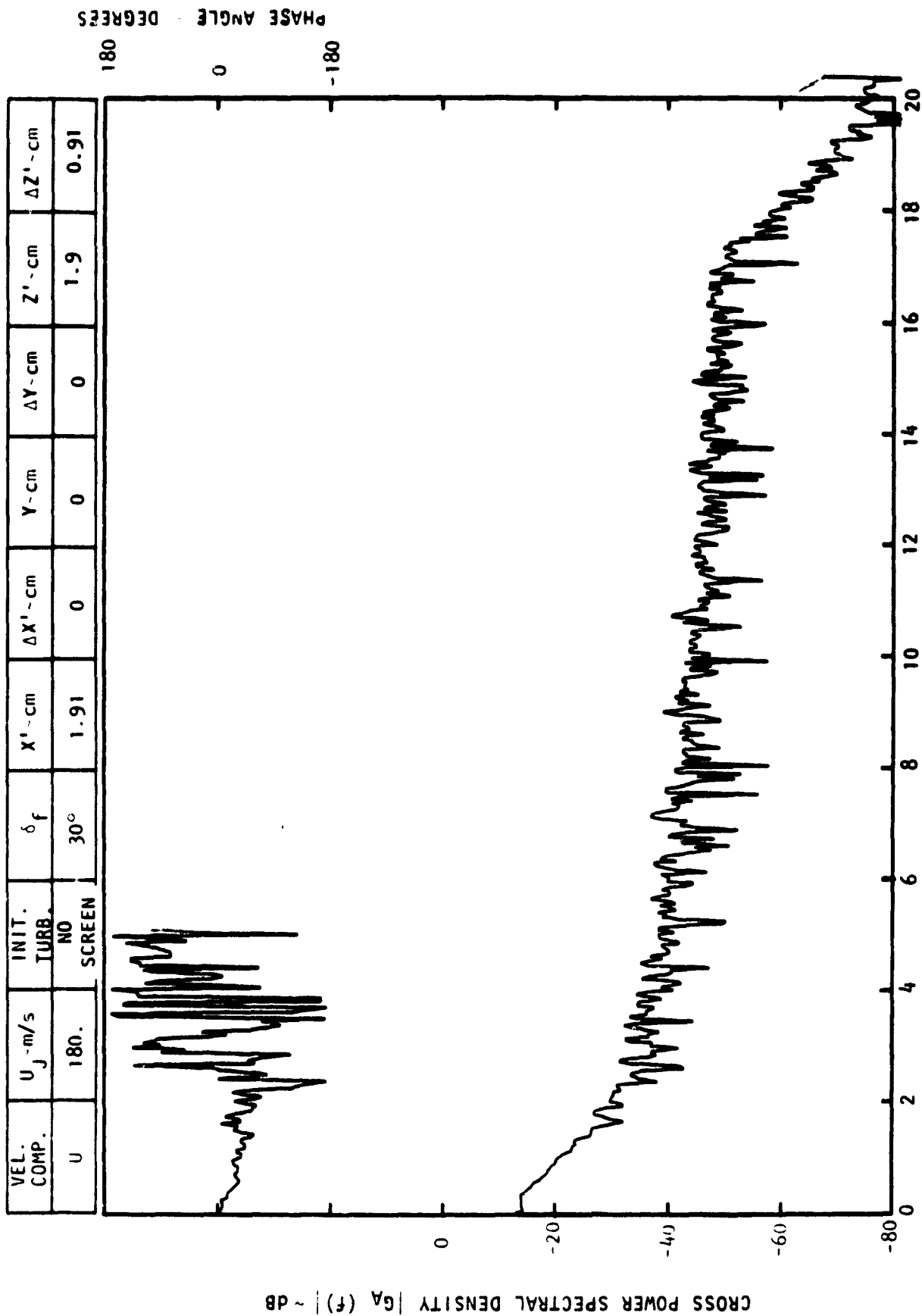
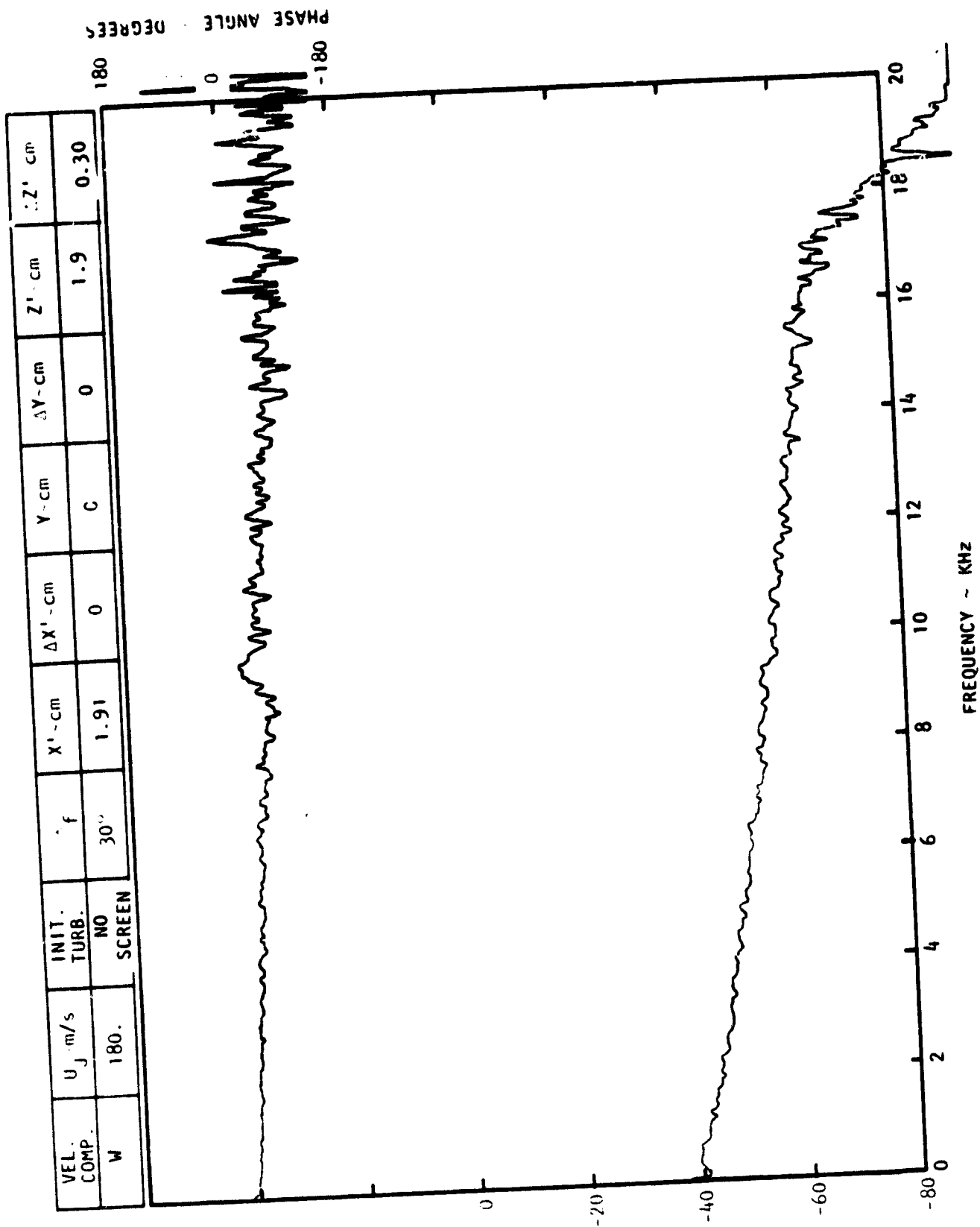


Figure C-3. Continued.

CROSS POWER SPECTRAL DENSITY $G_A(f)$ ~ dB

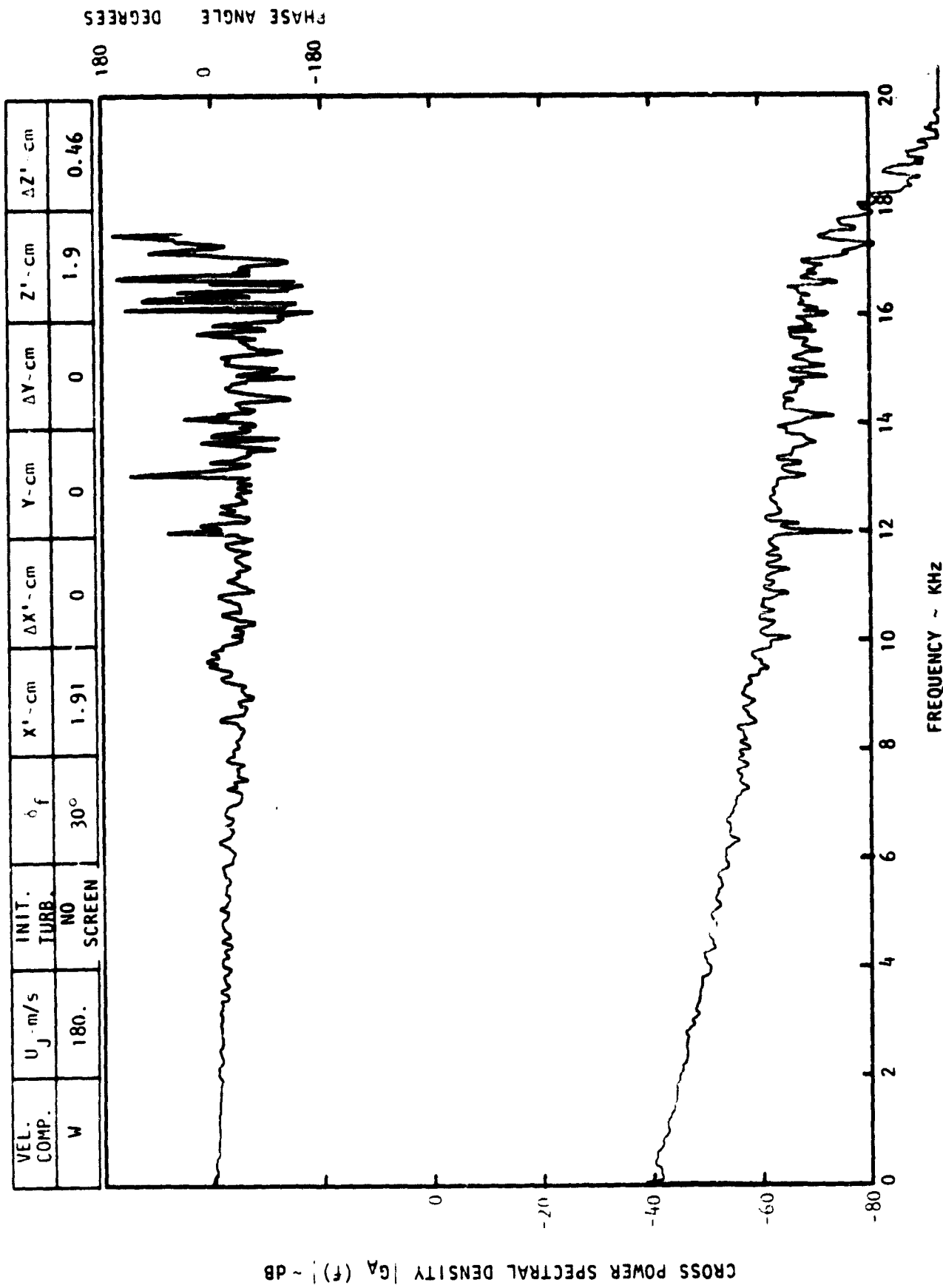
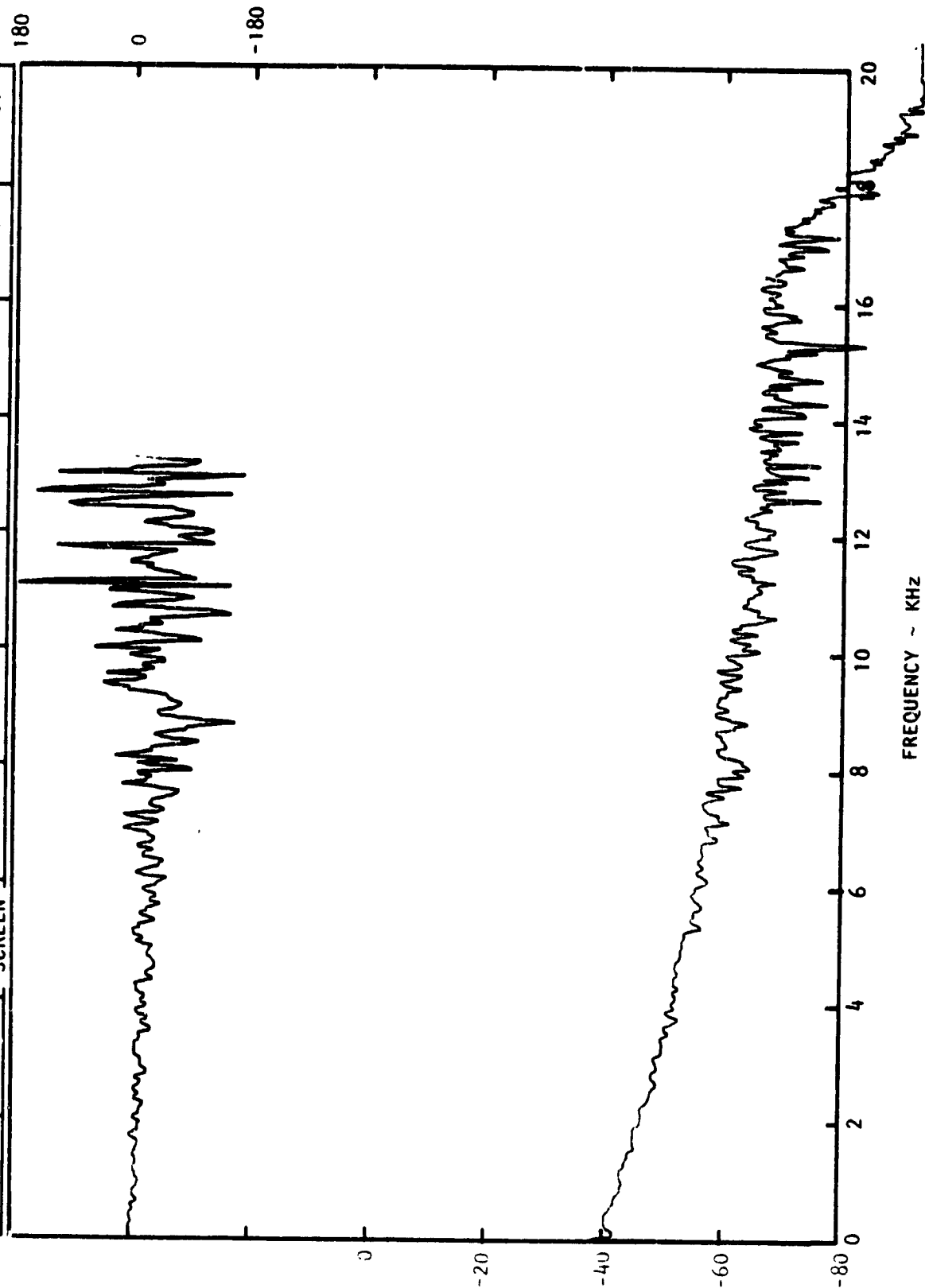
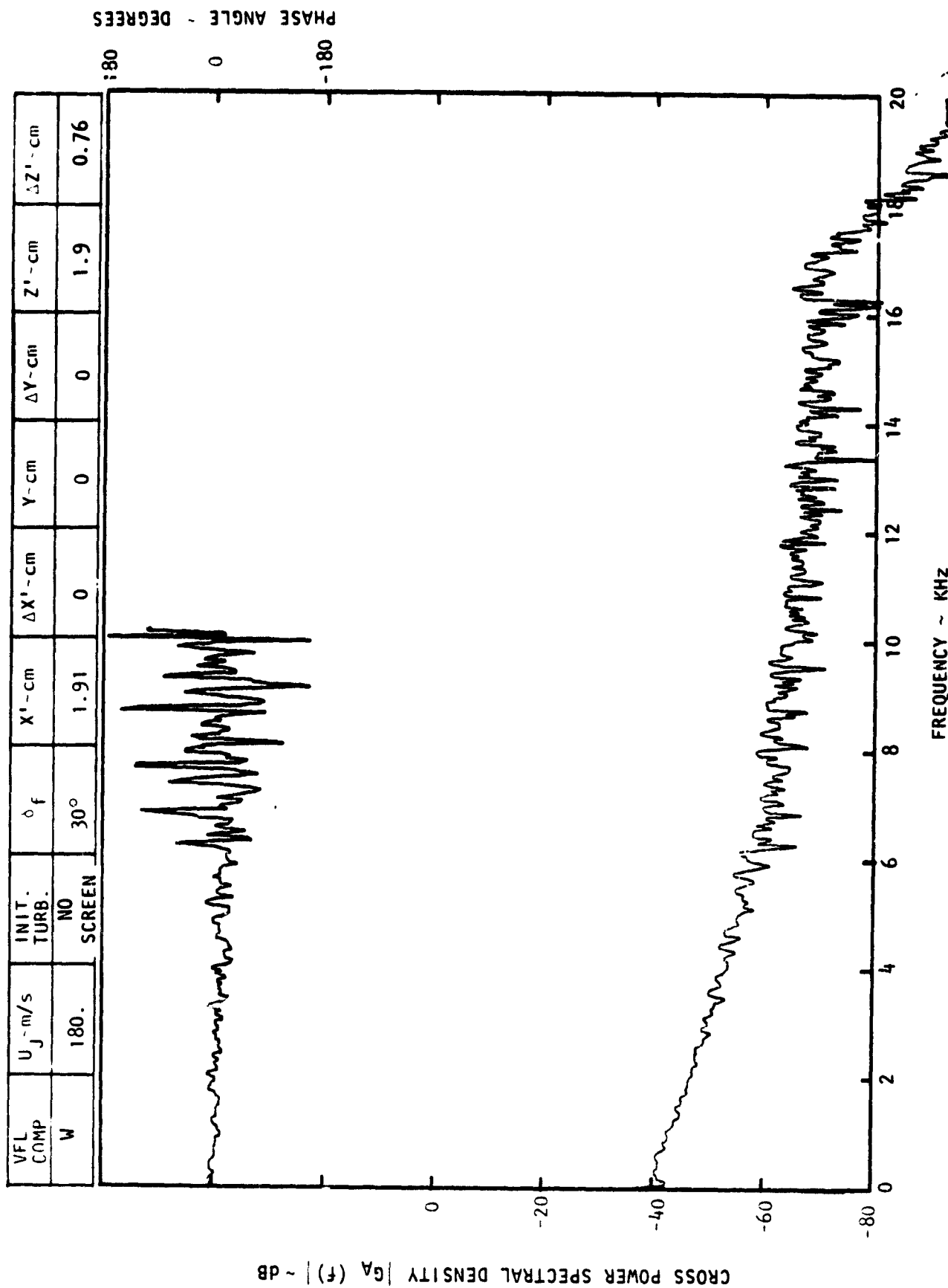


Figure C-3. Continued.

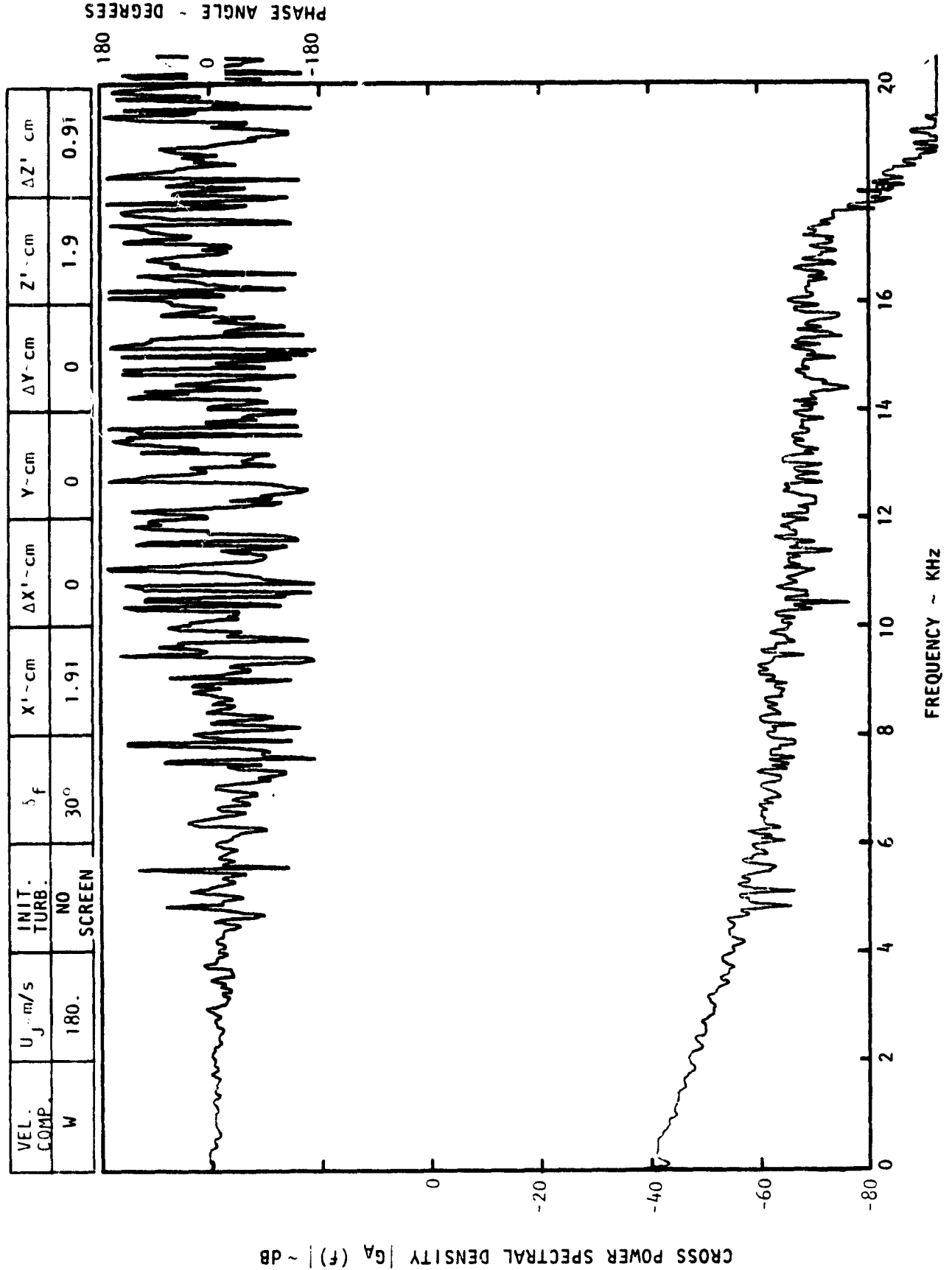
CROSS POWER SPECTRAL DENSITY $|G_A(f)| \sim \text{dB}$ 

VEL. COMP.	U_j - m/s	INIT. TURB.	δ_f	$X' - \text{cm}$	$\Delta X' - \text{cm}$	$Y - \text{cm}$	$\Delta Y - \text{cm}$	$Z' - \text{cm}$	$\Delta Z' - \text{cm}$
W	180.	NO SCREEN	30°	1.91	0	0	0	1.9	0.61



FREQUENCY ~ KHz

Figure C-3. Continued.



VEL. COMP.	U_j m/s	INIT. TURB.	δ_f	$X' \sim \text{cm}$	$\Delta X' \sim \text{cm}$	$Y \sim \text{cm}$	$\Delta Y \sim \text{cm}$	$Z' \sim \text{cm}$	$\Delta Z' \sim \text{cm}$
U	180.	NO SCREEN	30°	1.91	0	0	0	2.54	0.30

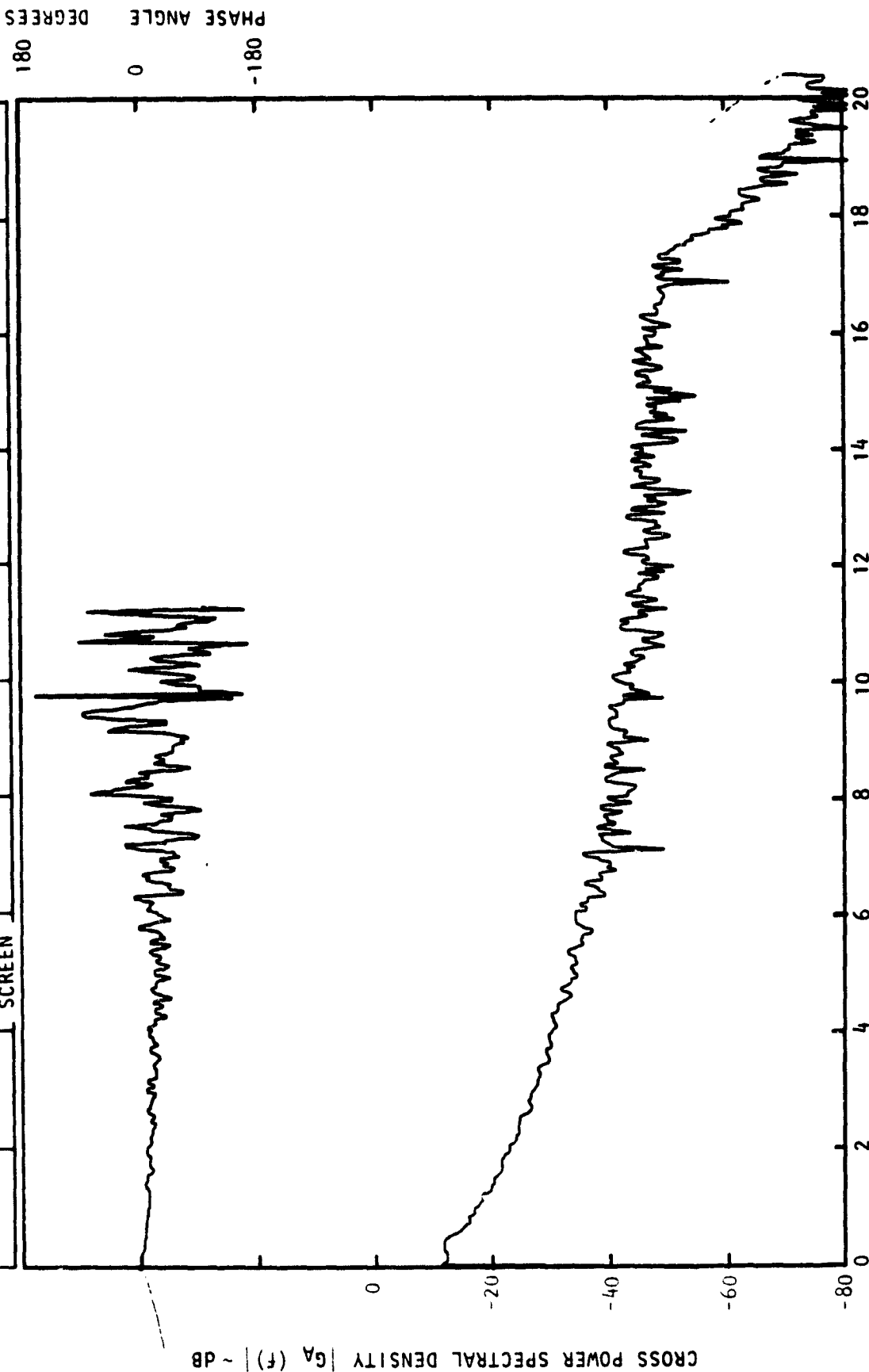
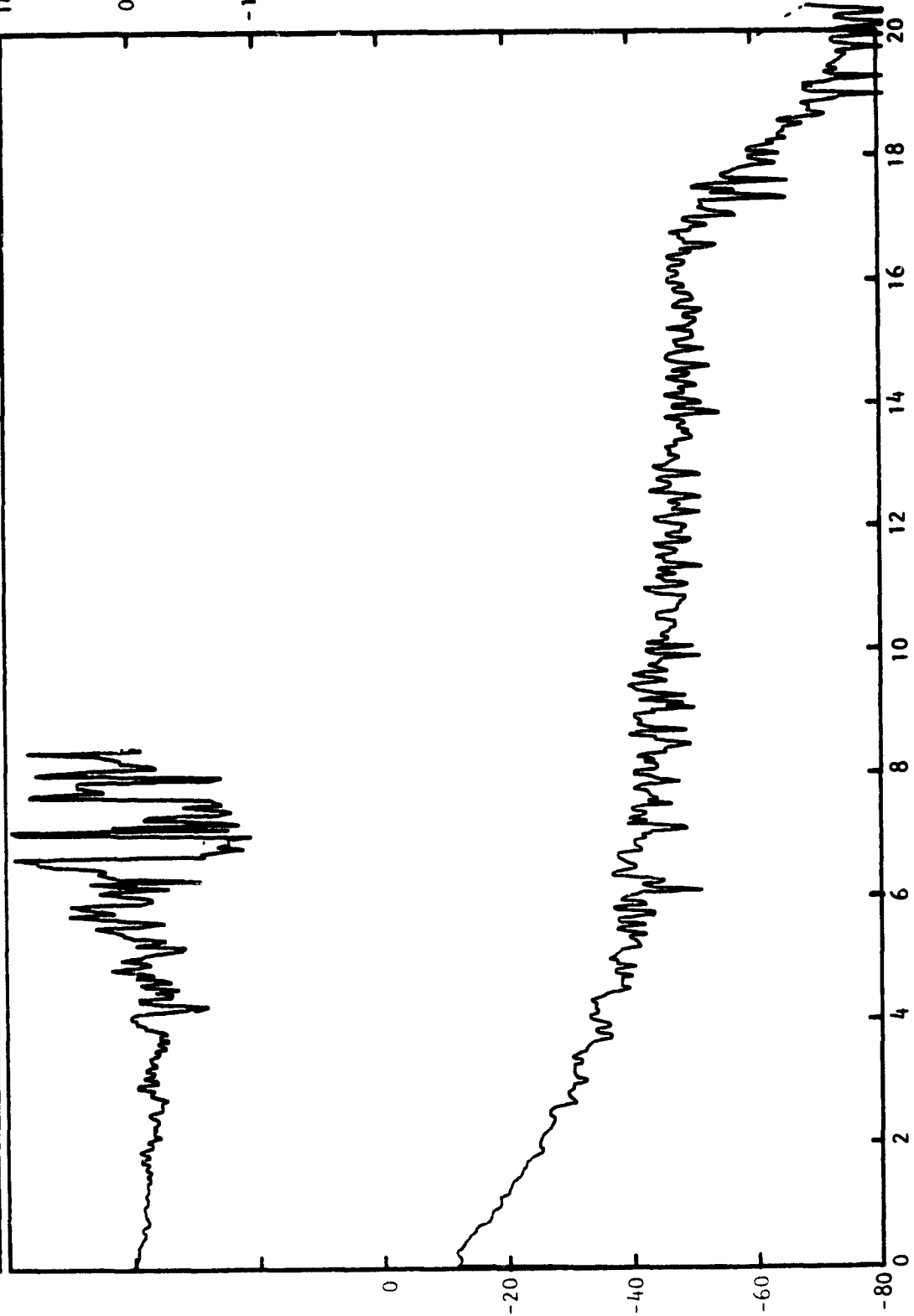


Figure C-3. Continued.

CROSS POWER SPECTRAL DENSITY $|G_A(f)|^2 \sim \text{dB}$

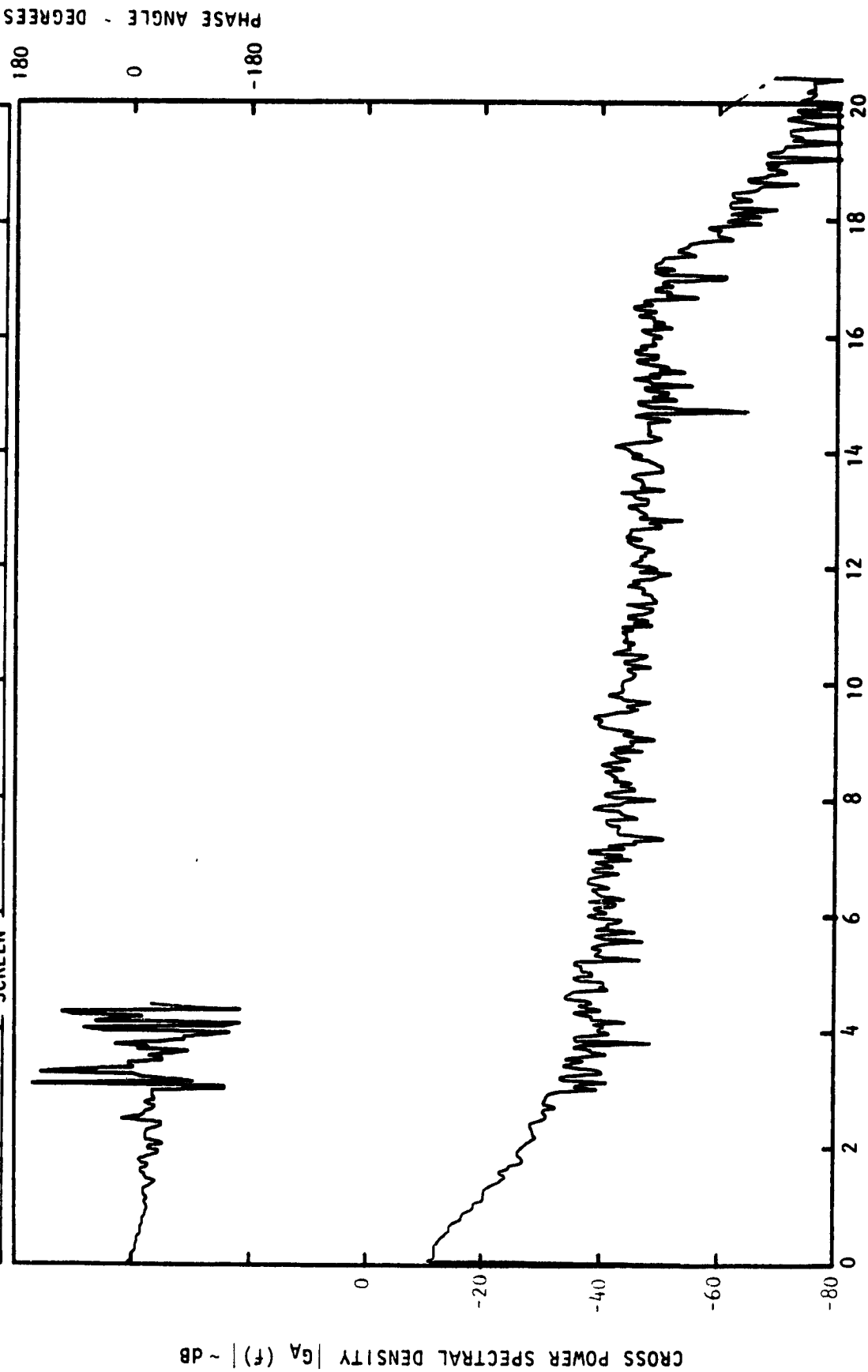
PHASE ANGLE - DEGREES

VFL COMP	U_j - m/s	INIT. TURB.	ϕ_f	X^1 - cm	ΔX^1 - cm	Y - cm	ΔY - cm	Z^1 - cm	ΔZ^1 - cm
U	180.	NO SCREEN	30°	1.91	0	0	0	2.54	0.46



FREQUENCY - KHz

VEL. COMP.	U_j - m/s	INIT. TURB.	δf	$X' - \text{cm}$	$\Delta X' - \text{cm}$	$Y - \text{cm}$	$\Delta Y - \text{cm}$	$Z' - \text{cm}$	$\Delta Z' - \text{cm}$
U	180.	NO SCREEN	30°	1.91	0	0	0	2.54	0.61



PHASE ANGLE - DEGREES

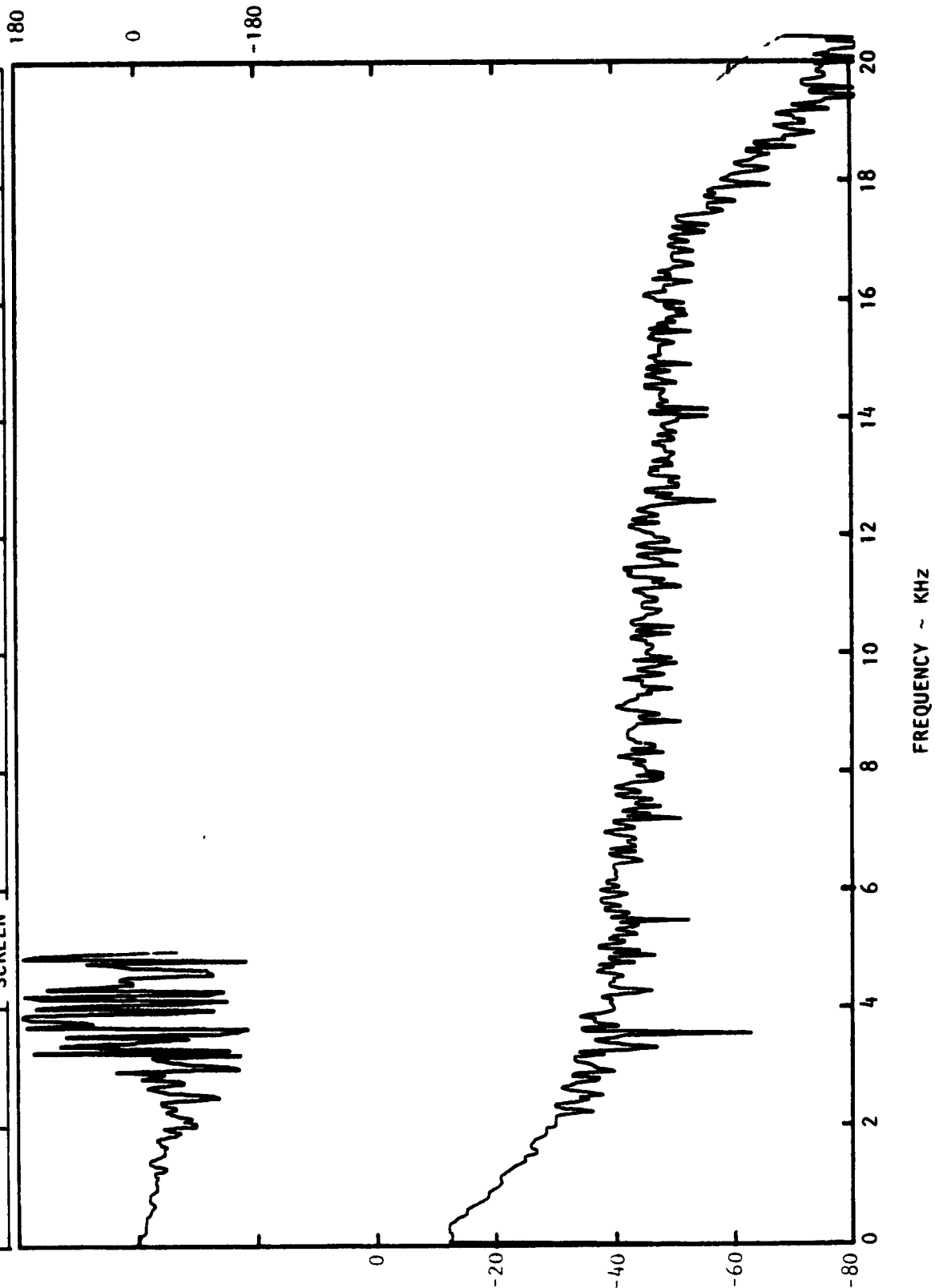
FREQUENCY ~ KHz

Figure C-3. Continued.

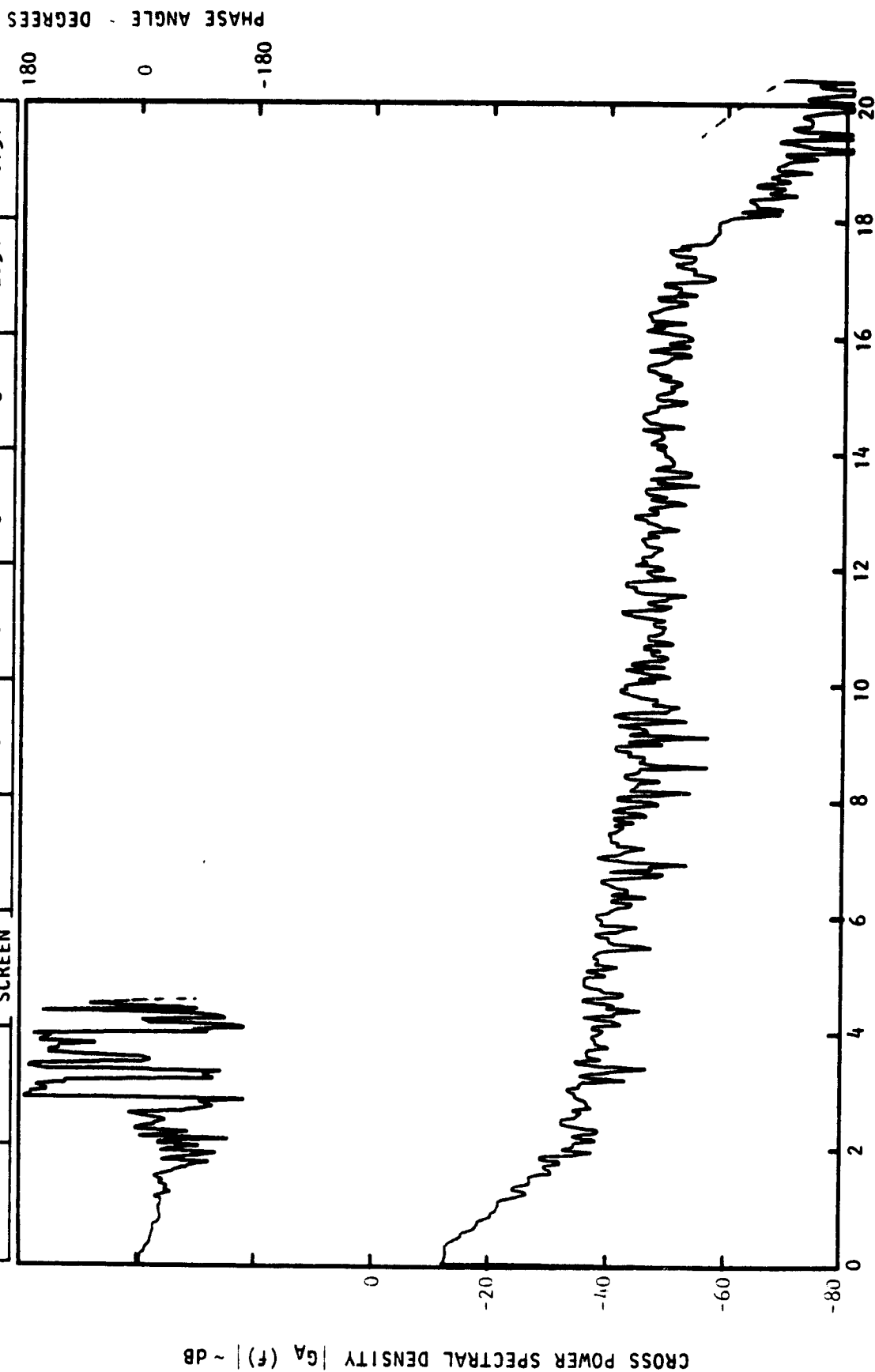
CROSS POWER SPECTRAL DENSITY $|G_A(f)|^2 \sim \text{dB}$

PHASE ANGLE - DEGREES

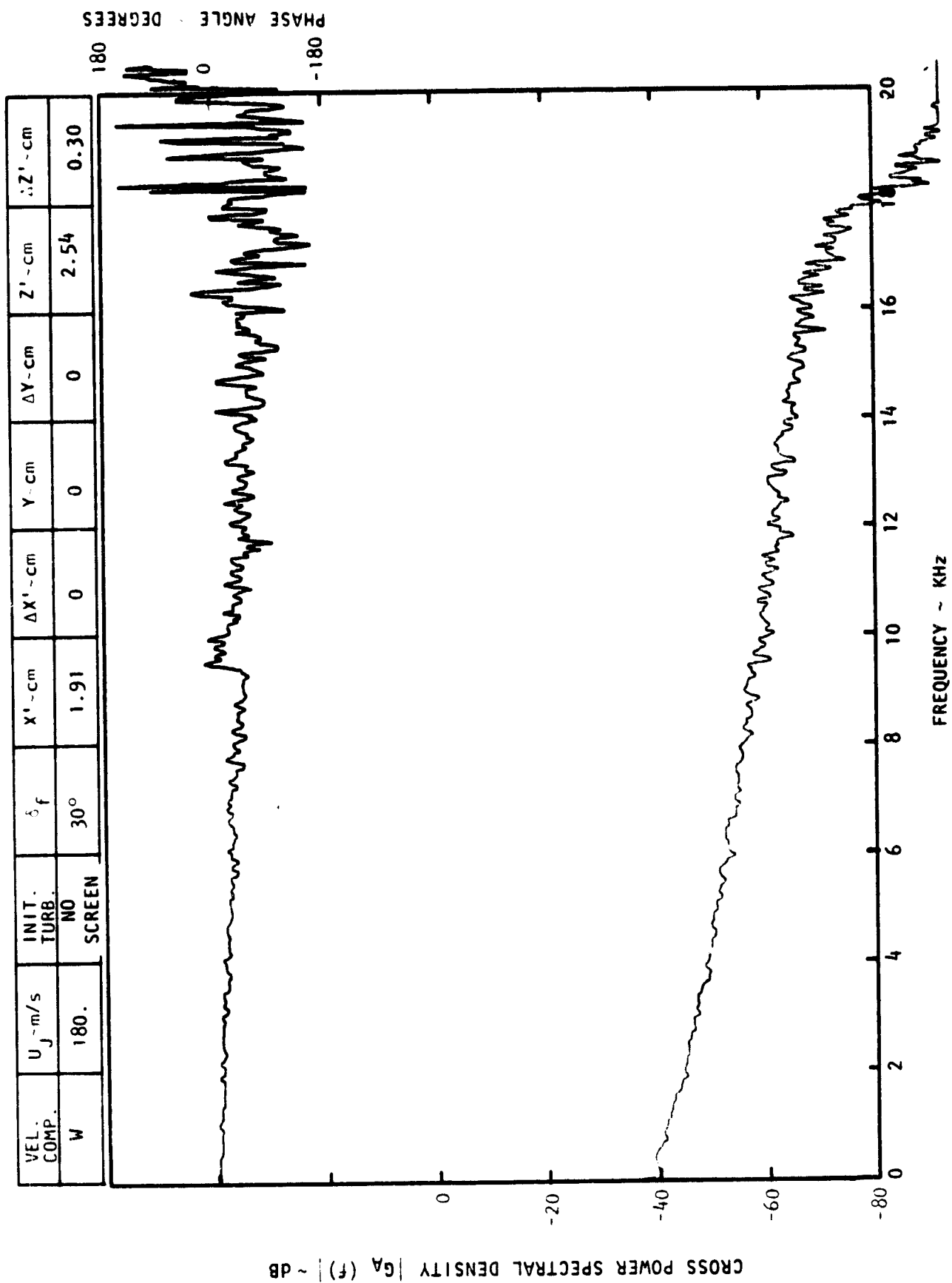
VEL. COMP.	U_j - m/s	INIT. TURB.	δ_f	$X' - \text{cm}$	$\Delta X' - \text{cm}$	$Y - \text{cm}$	$\Delta Y - \text{cm}$	$Z' - \text{cm}$	$\Delta Z' - \text{cm}$
U	180.	NO SCREEN	30°	1.91	0	0	0	2.54	0.76



VEL. COMP.	U_j - m/s	INIT. TURB.	δf	$X' - \text{cm}$	$\Delta X' - \text{cm}$	$Y - \text{cm}$	$\Delta Y - \text{cm}$	$Z' - \text{cm}$	$\Delta Z' - \text{cm}$
U	180.	NO SCREEN	30°	1.91	0	0	0	2.54	0.91



FREQUENCY ~ KHZ
Figure C-3. Continued.



VEL. COMP.	U_j - m/s	INIT. TURB.	δ_f	X' - cm	$\Delta X'$ - cm	Y - cm	ΔY - cm	Z' - cm	$\Delta Z'$ - cm
W	180.	NO SCREEN	30°	1.91	0	0	0	2.54	0.46

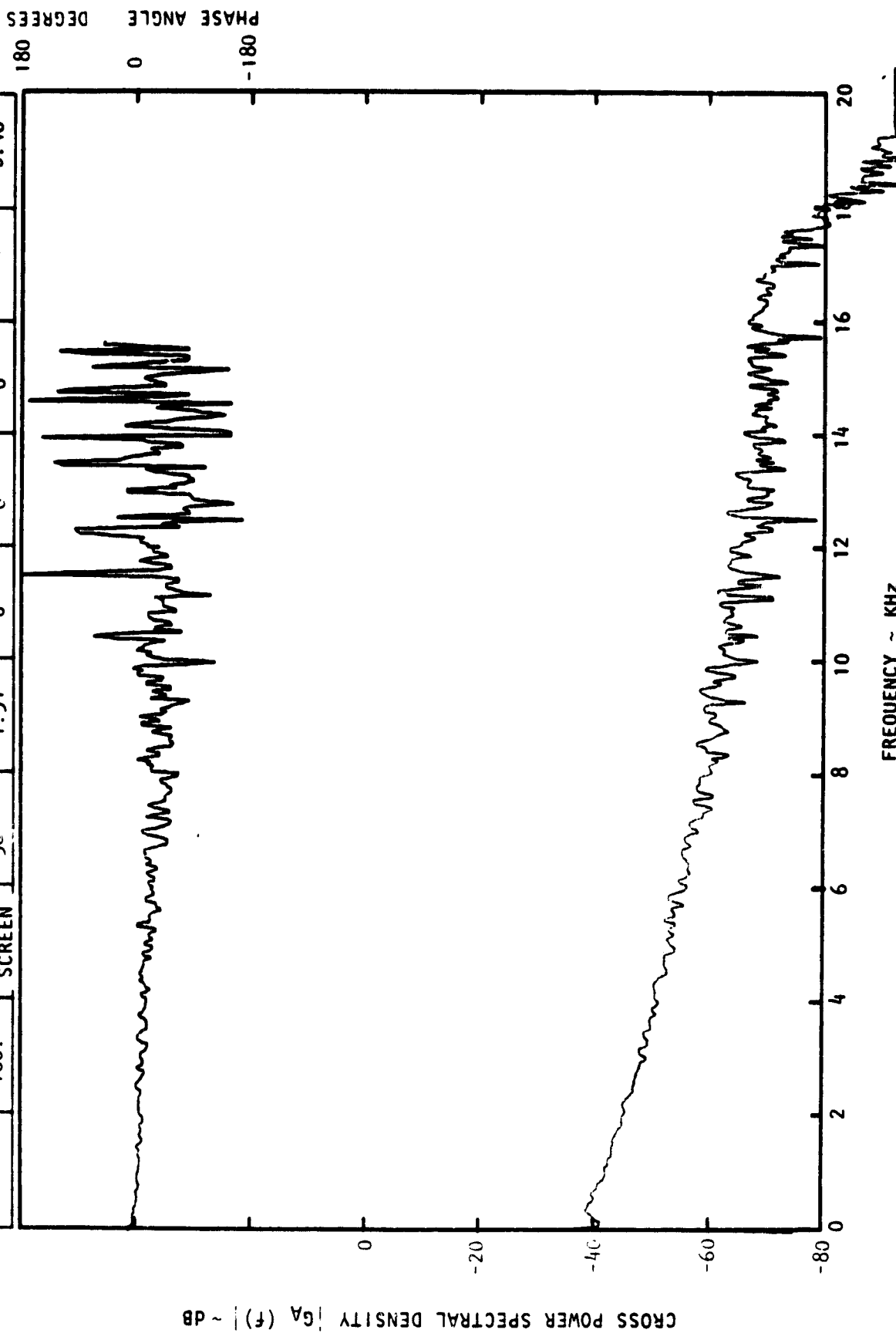
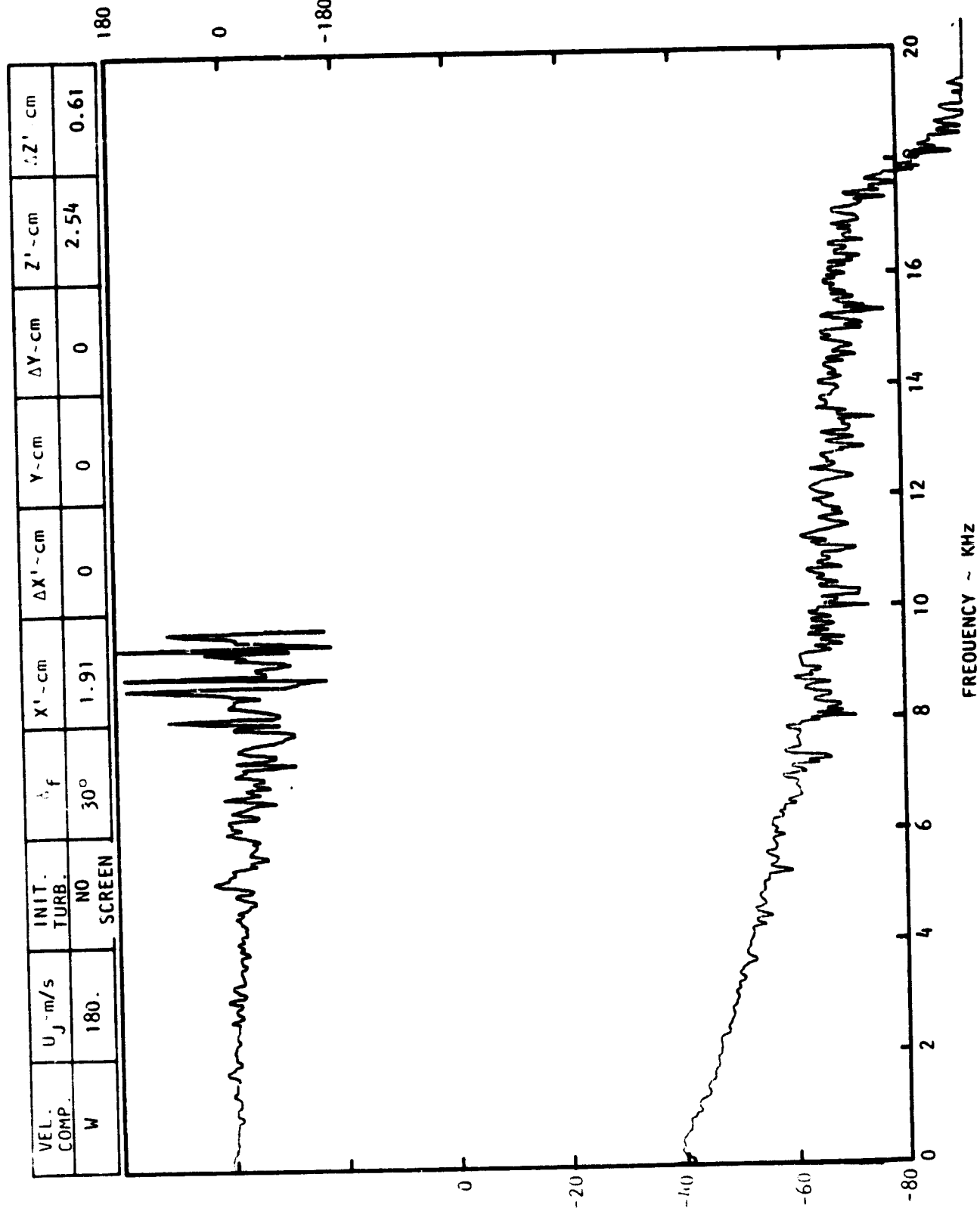


Figure C-3. Continued.

CROSS POWER SPECTRAL DENSITY $G_A(f)$ ~ dB

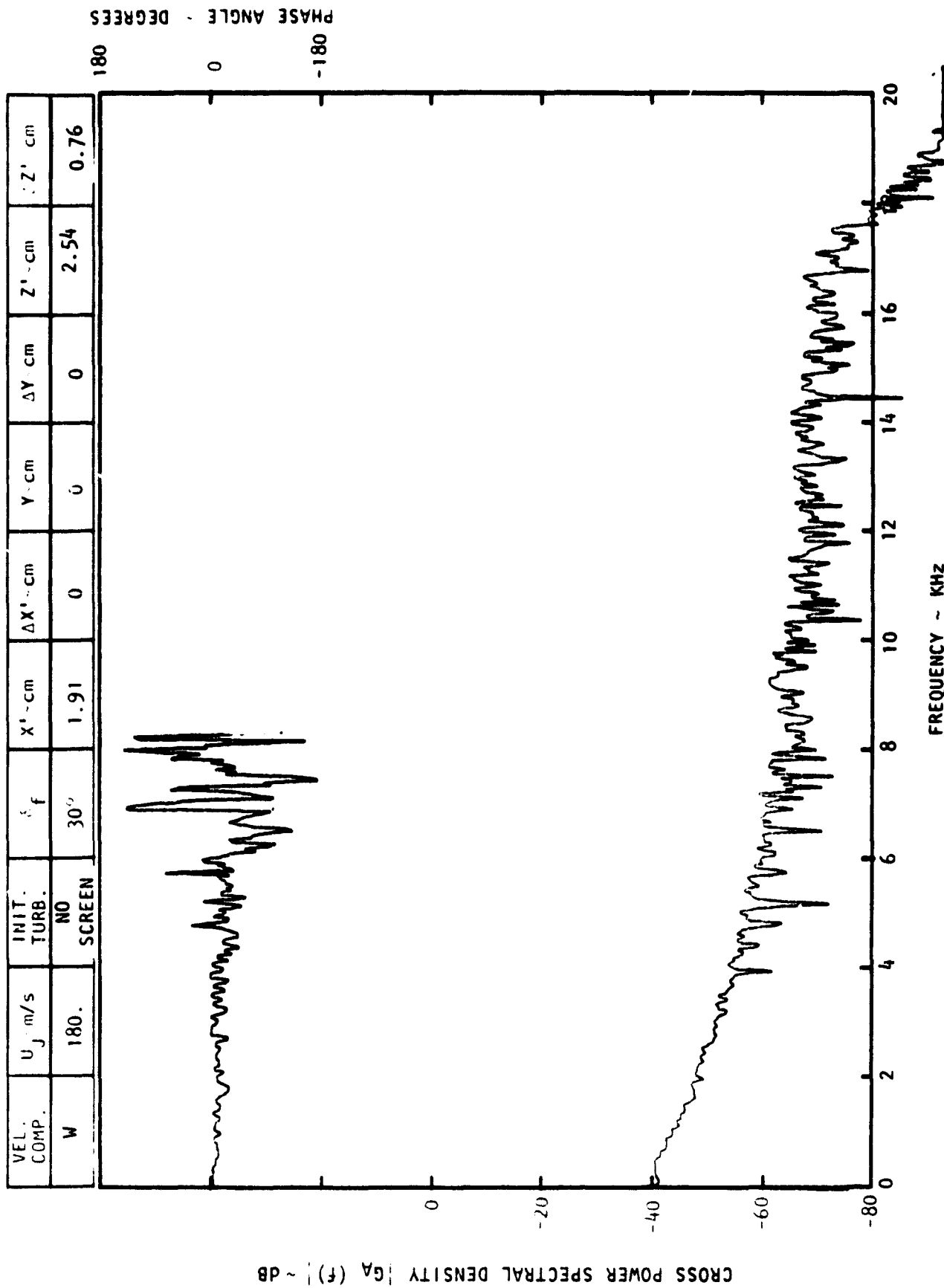
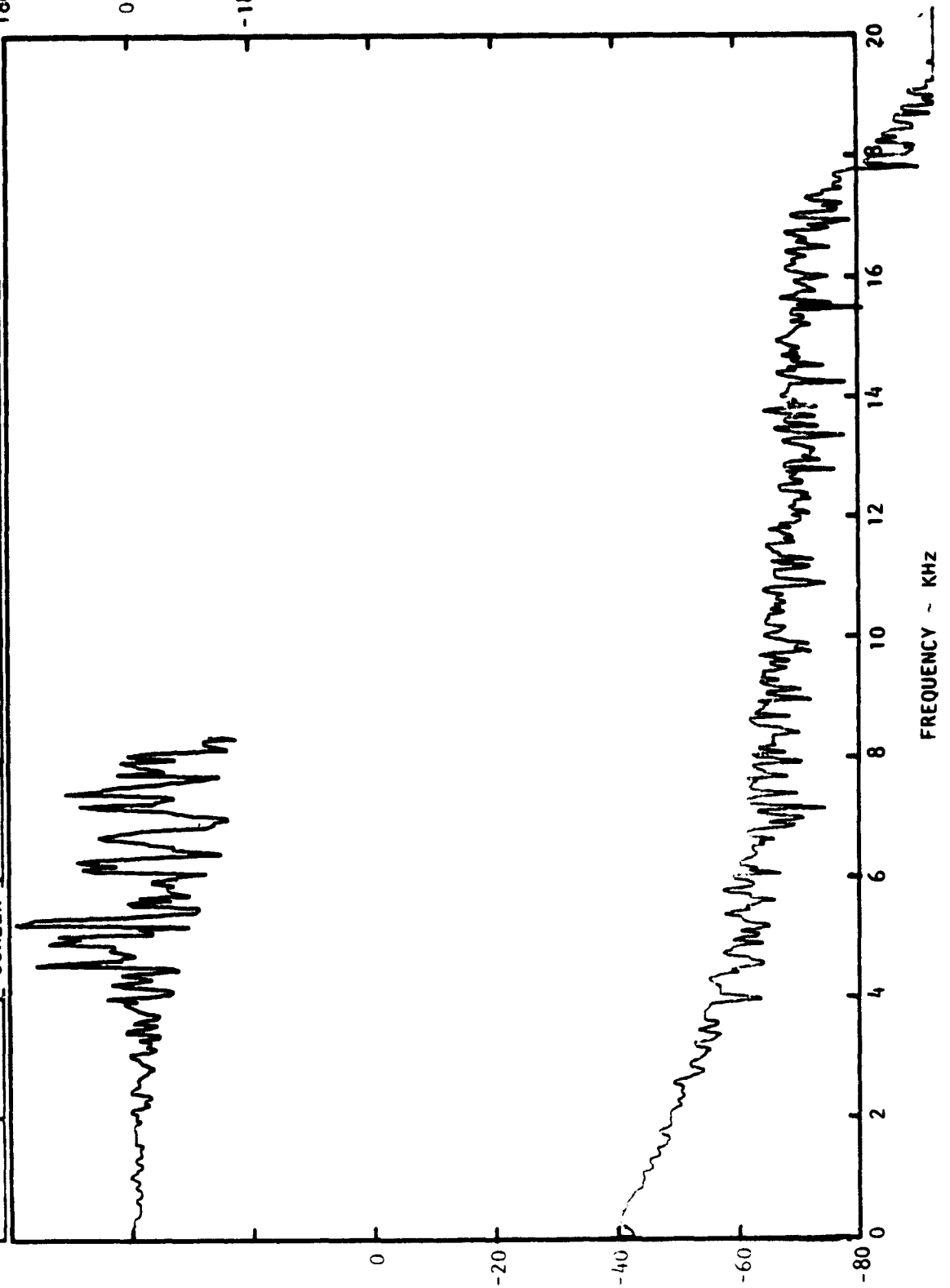


Figure C-3. Continued.

CROSS POWER SPECTRAL DENSITY $|G_A(f)| \sim \text{dB}$

PHASE ANGLE - DEGREES

VEL. COMP.	U_j m/s	INIT. TURB.	α_f	$X' - \text{cm}$	$\Delta X' - \text{cm}$	$Y - \text{cm}$	$\Delta Y - \text{cm}$	$Z' - \text{cm}$	$\Delta Z' - \text{cm}$
W	180.	NO SCREEN	30°	1.91	0	0	0	2.54	0.91



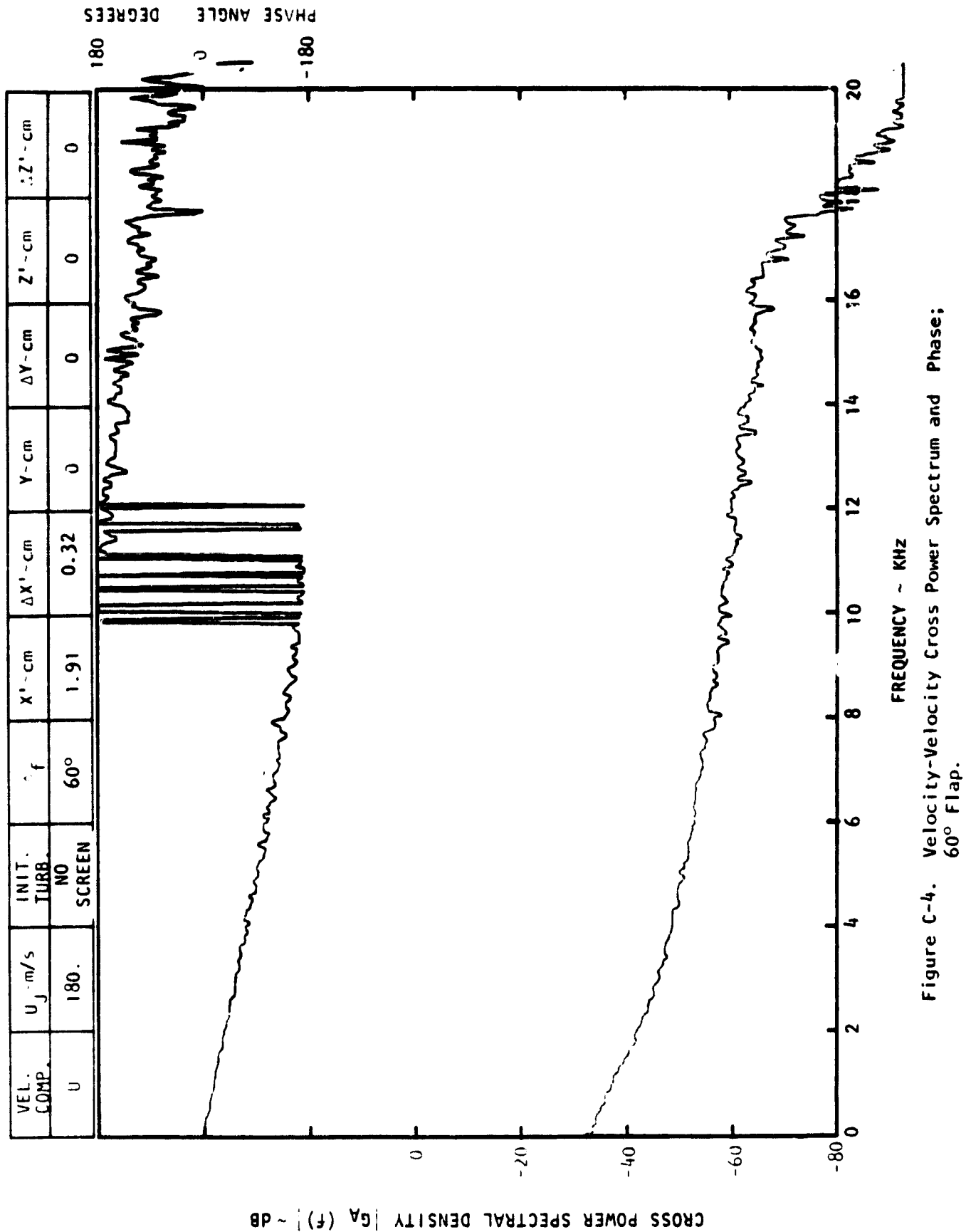
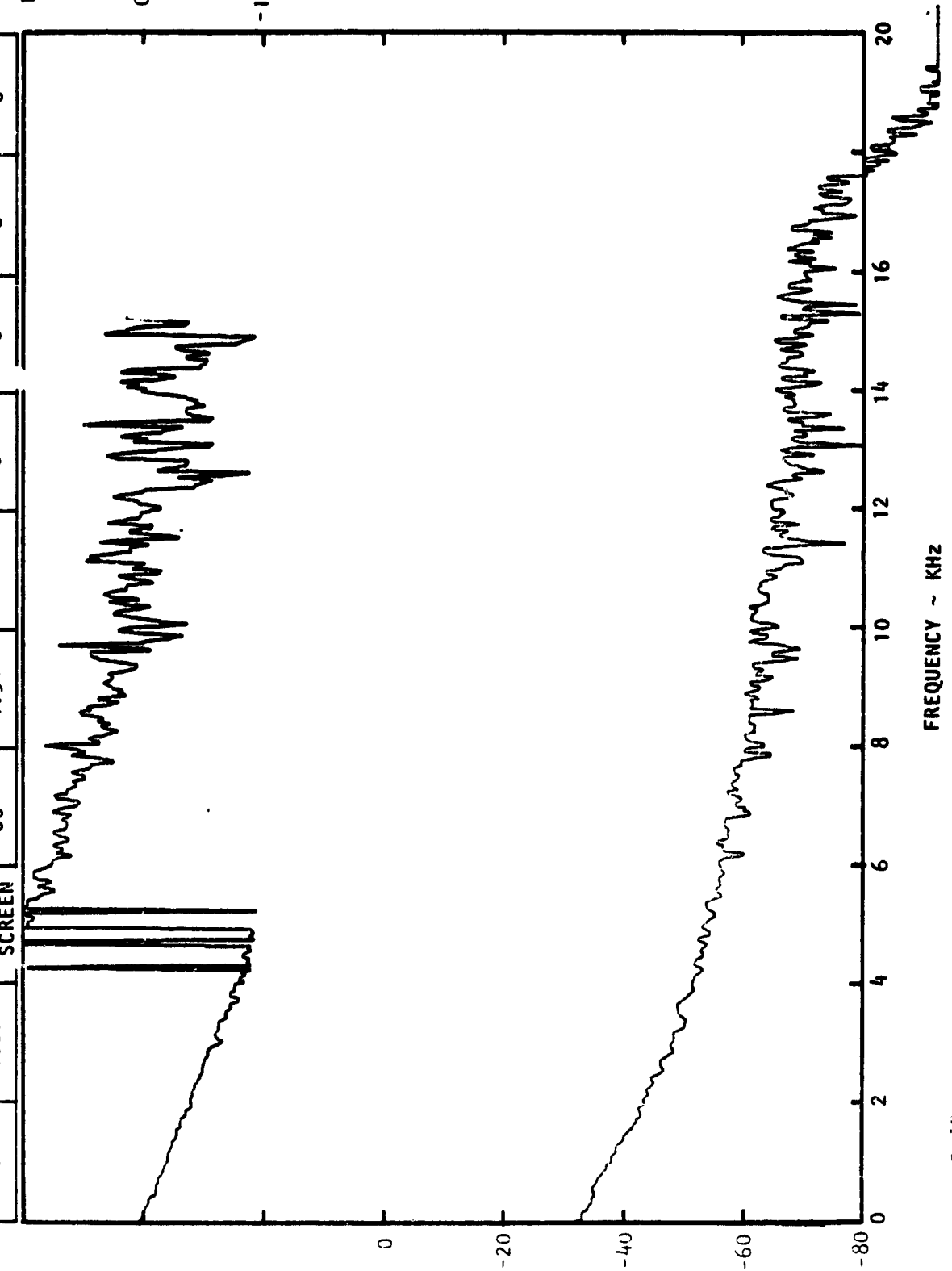


Figure C-4. Velocity-Velocity Cross Power Spectrum and Phase;
60° Flap.

CROSS POWER SPECTRAL DENSITY $|G_A(f)| \sim \text{dB}$ 

PHASE ANGLE - DEGREES

VEL. COMP.	$U_j \sim \text{m/s}$	INIT. TURB.	δ_f	$X' \sim \text{cm}$	$\Delta X' \sim \text{cm}$	$Y \sim \text{cm}$	$\Delta Y \sim \text{cm}$	$Z' \sim \text{cm}$	$\Delta Z' \sim \text{cm}$
U	180.	NO SCREEN	60°	1.91	0.64	C	0	0	0

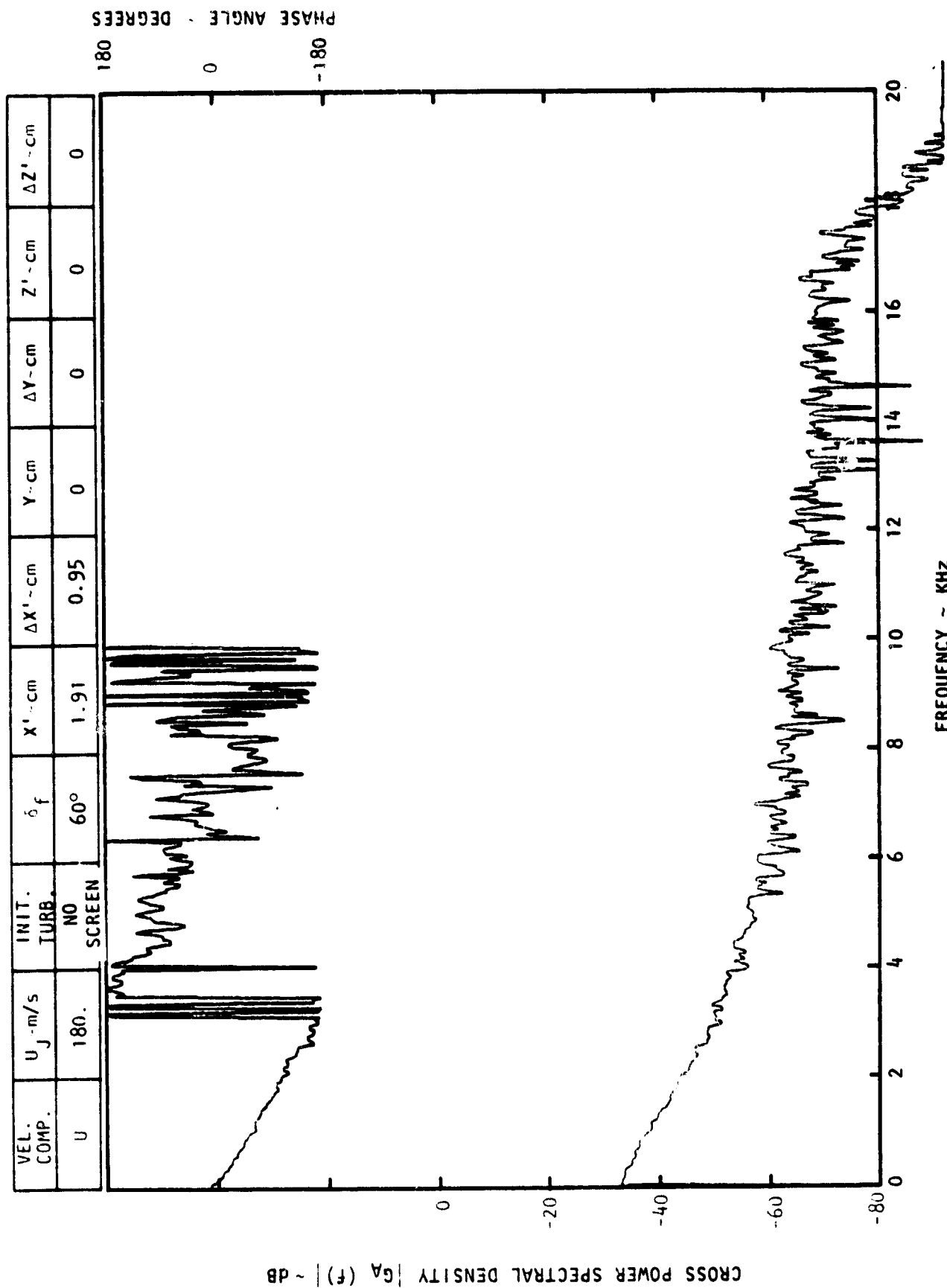
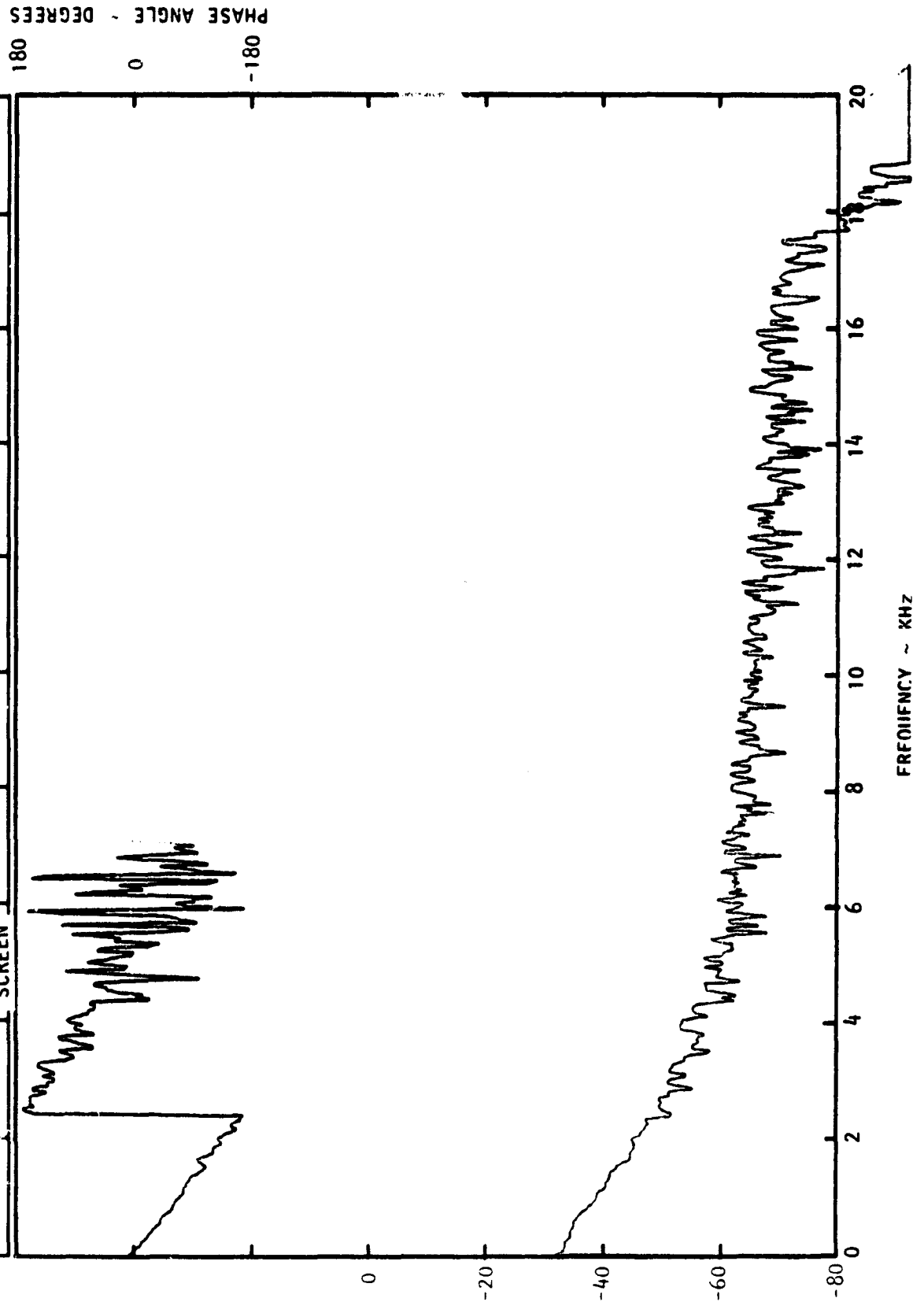
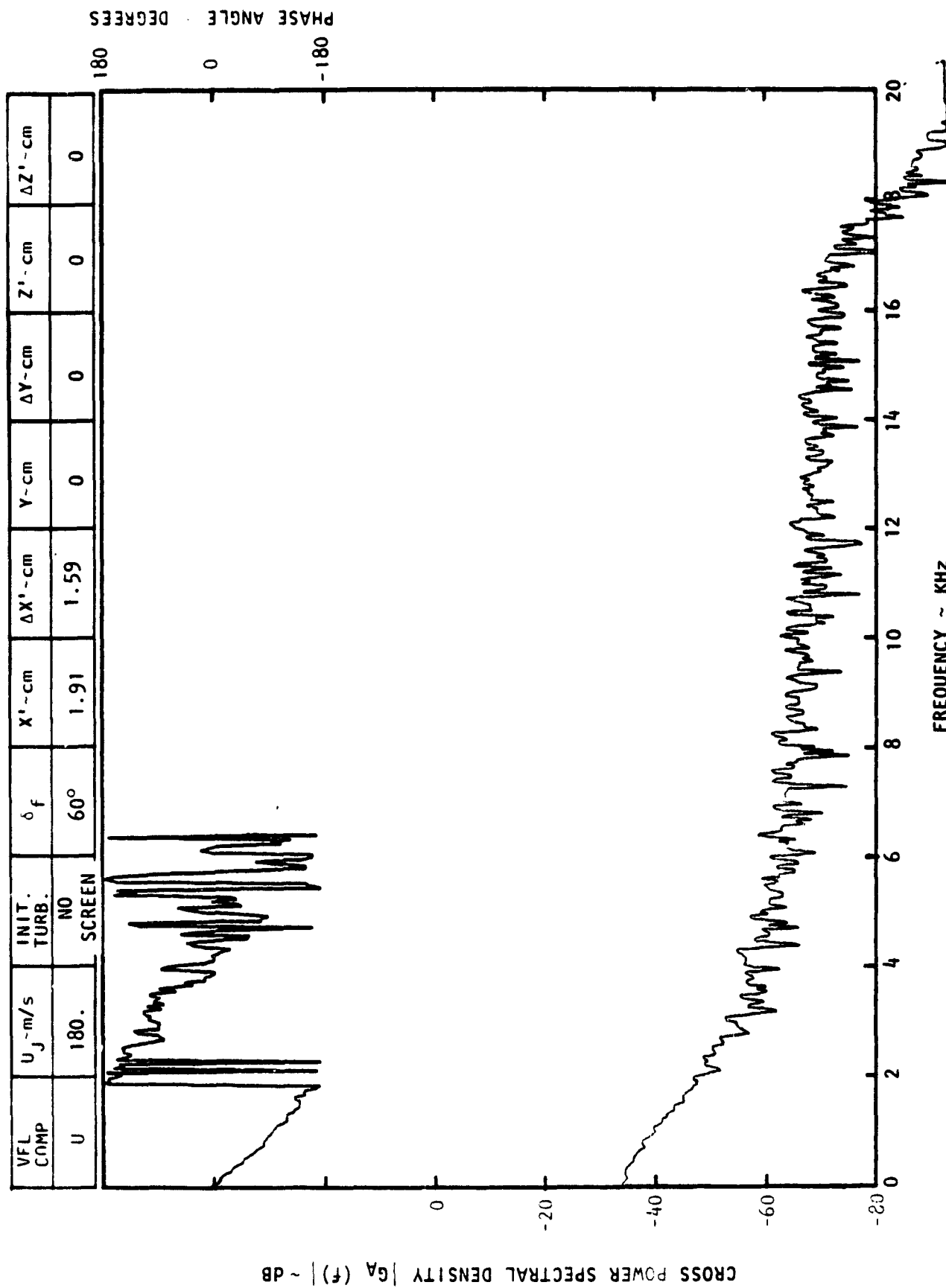


Figure C-4. Continued.

CROSS POWER SPECTRAL DENSITY $|G_A(f)| \sim \text{dB}$

VEL. COMP.	$U_j \sim \text{m/s}$	INIT. TURB.	δ_f	$X^1 \sim \text{cm}$	$\Delta X^1 \sim \text{cm}$	$Y \sim \text{cm}$	$\Delta Y \sim \text{cm}$	$Z^1 \sim \text{cm}$	$\Delta Z^1 \sim \text{cm}$
U	180.	NO SCREEN	60°	1.91	1.27	0	0	0	0

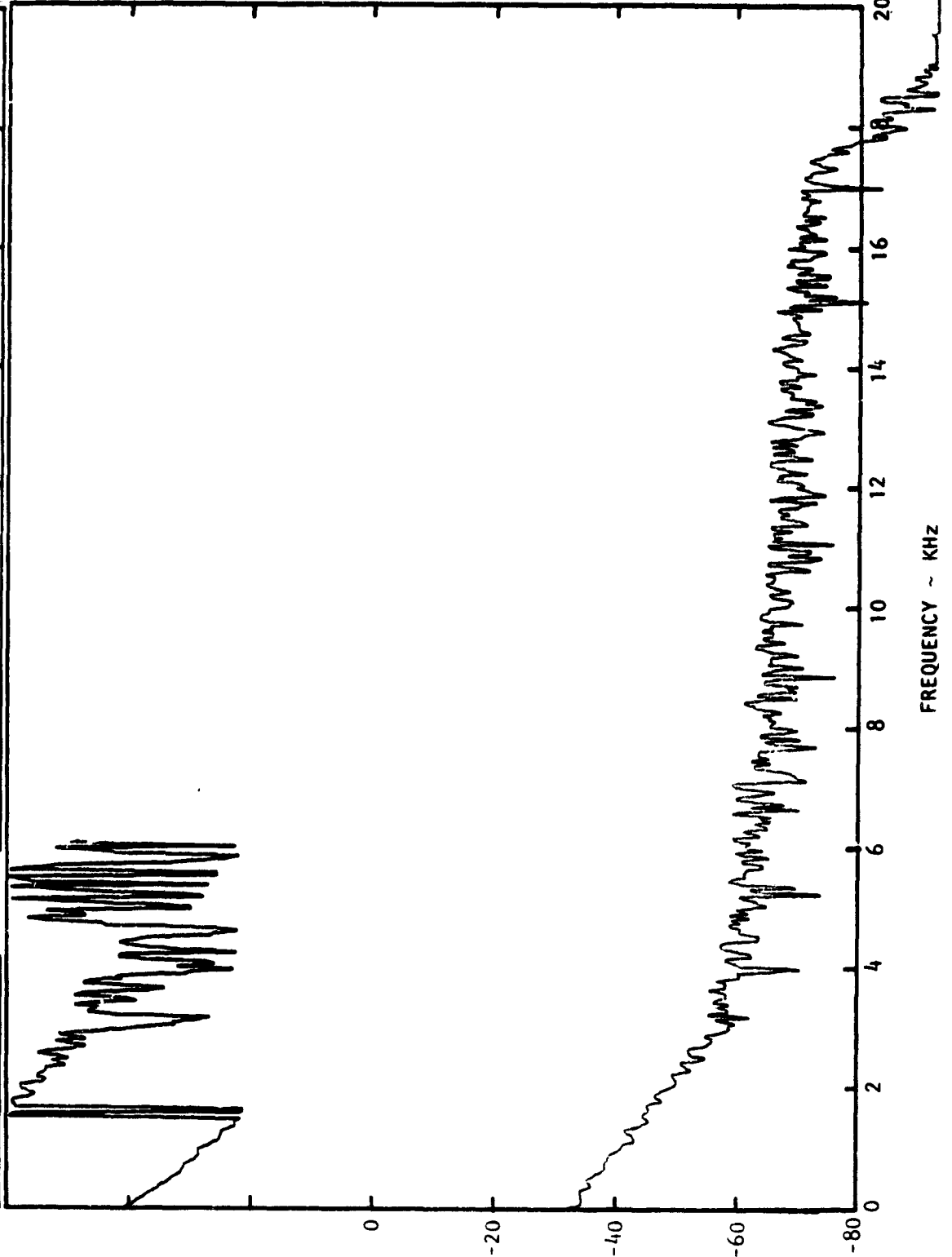




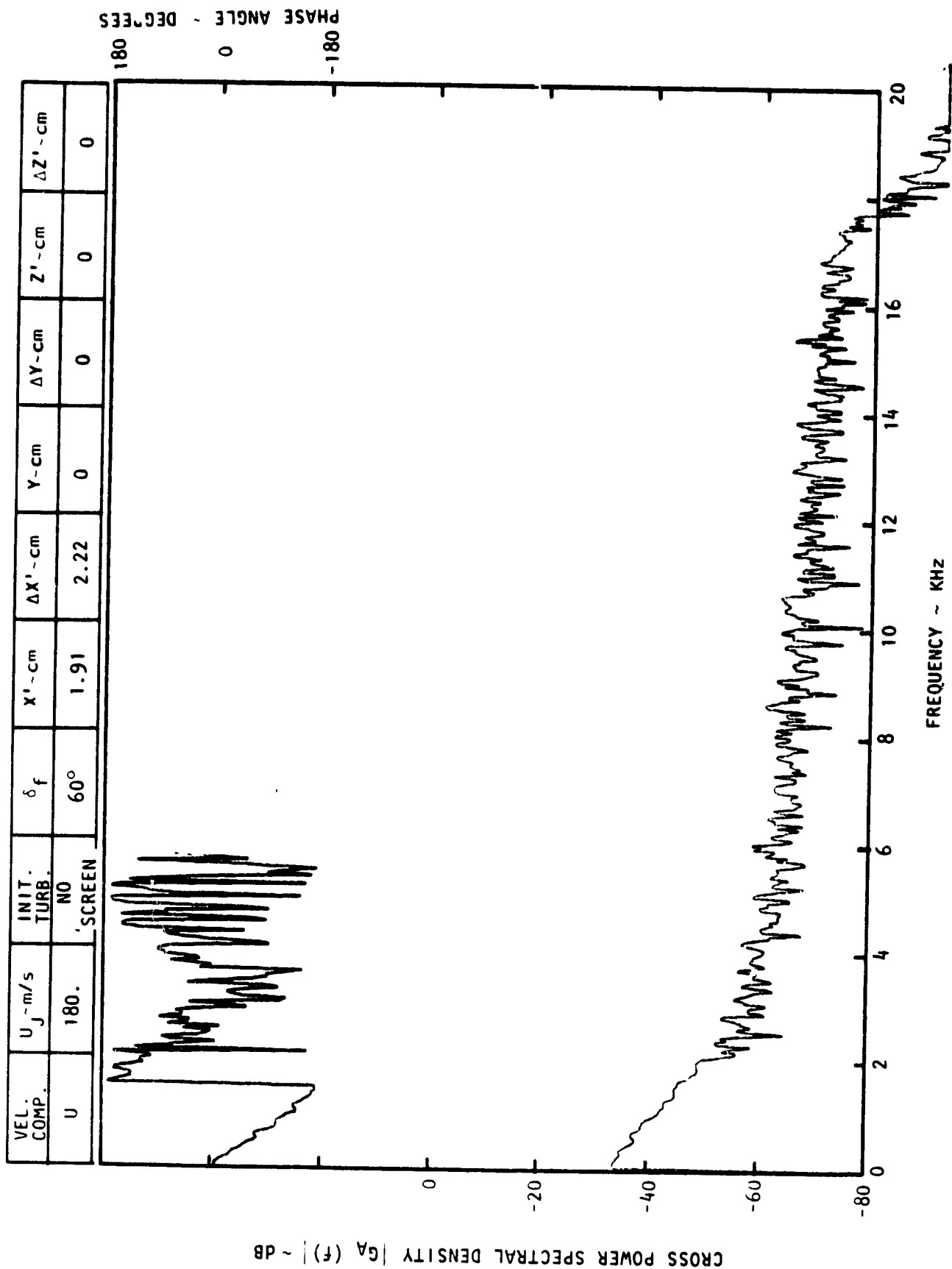
CROSS POWER SPECTRAL DENSITY $G_A(f)$ ~ DB

PHASE ANGLE - DEGREES
180
0
-180

VEL. COMP.	U_j - m/s	INIT. TURB.	δ_f	$X' - \text{cm}$	$\Delta X' - \text{cm}$	$Y - \text{cm}$	$\Delta Y - \text{cm}$	$Z' - \text{cm}$	$\Delta Z' - \text{cm}$
U	180.	NO SCREEN	60°	1.91	1.9	0	0	0	0

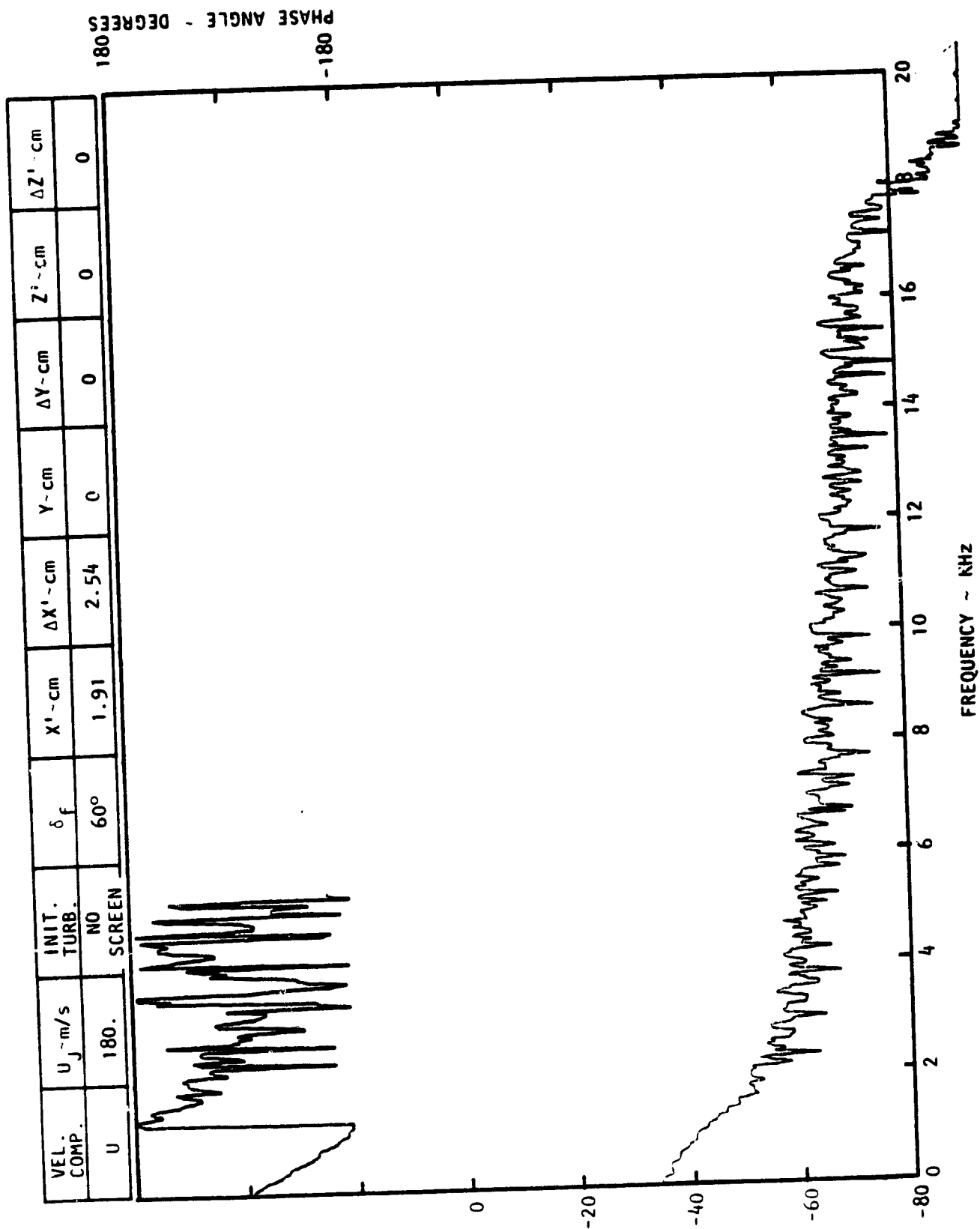


FREQUENCY ~ KHz



FREQUENCY ~ KHZ

Figure C-4. Continued.

CROSS POWER SPECTRAL DENSITY $G_A(f)$ ~ dB

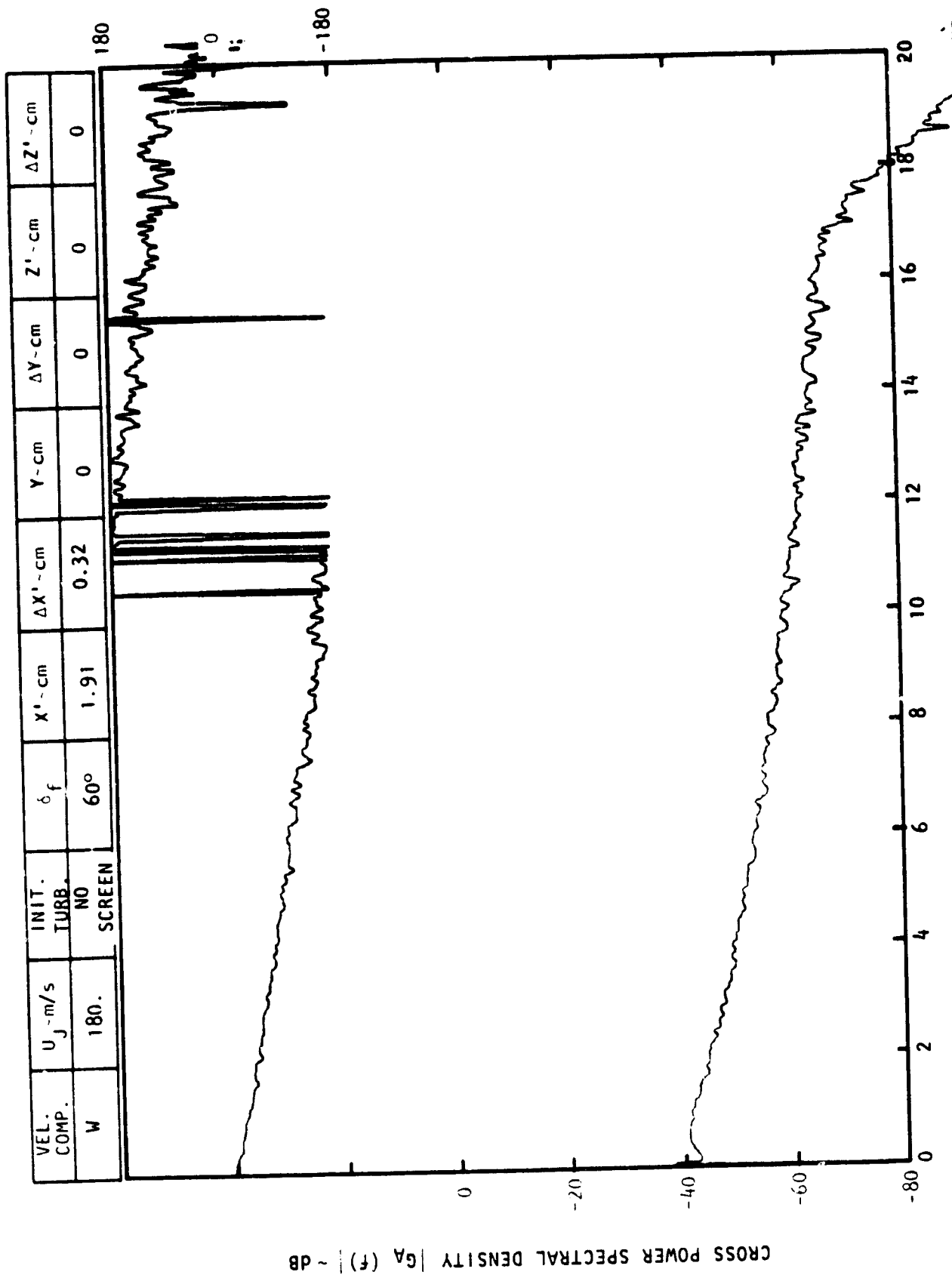
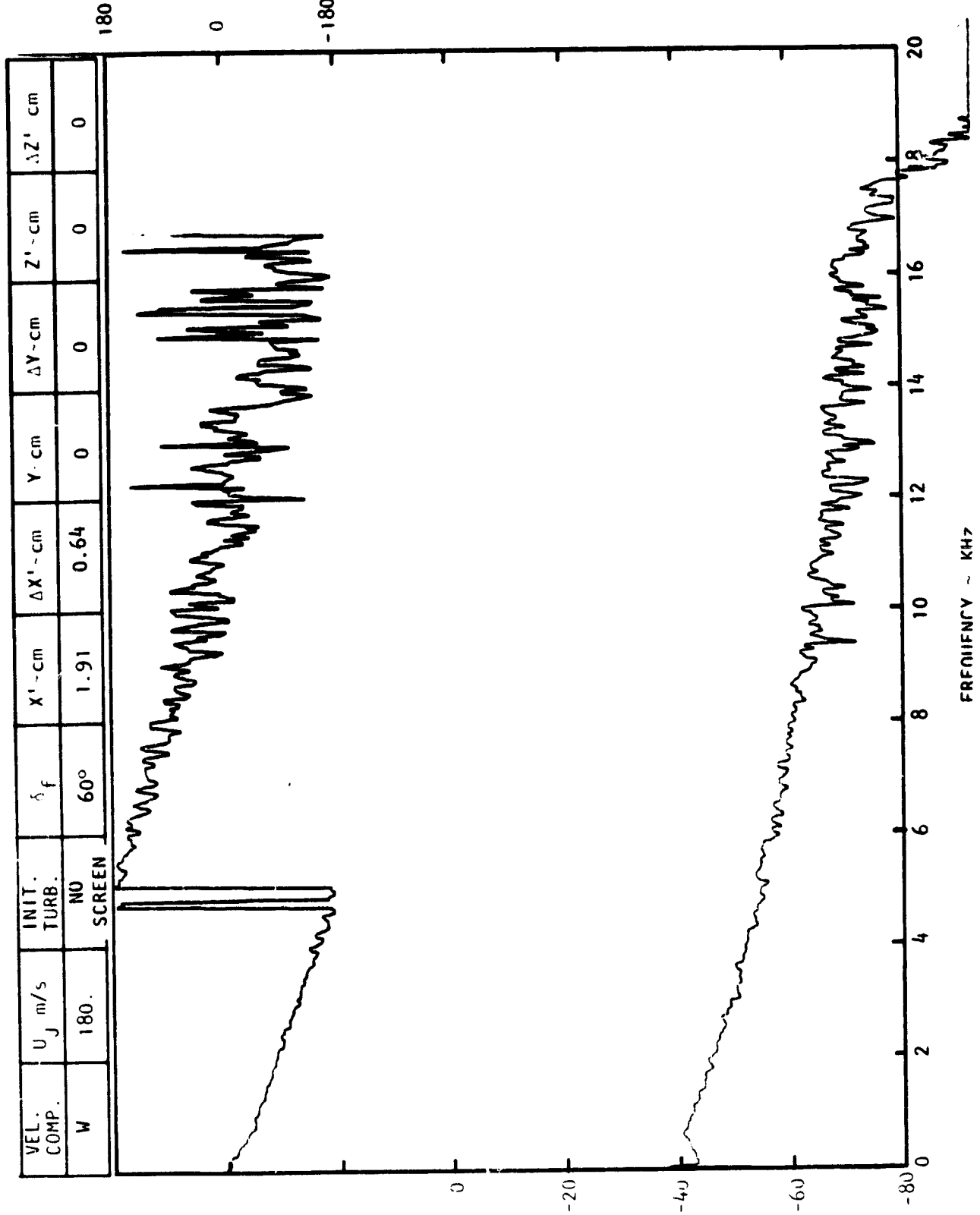
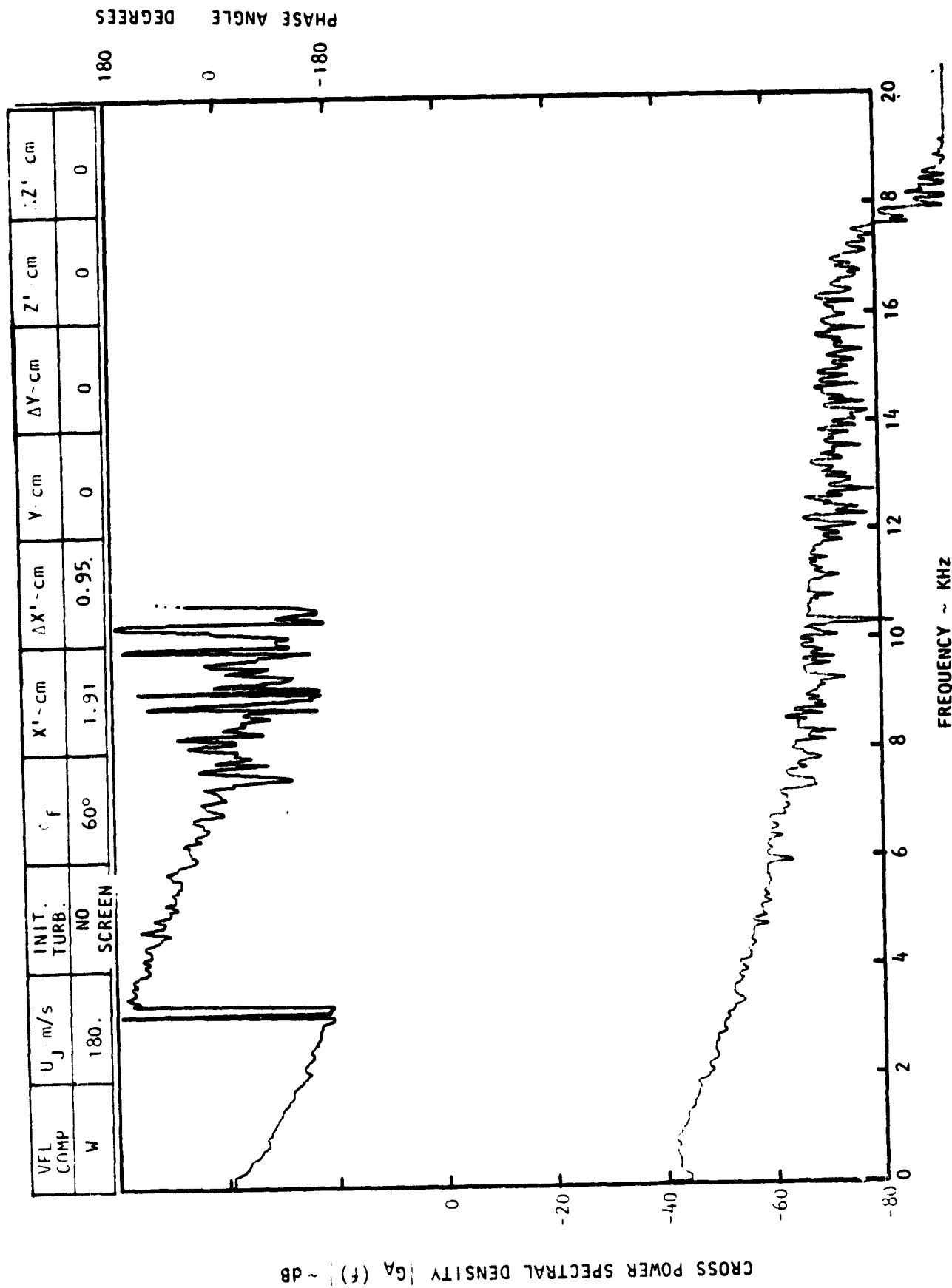


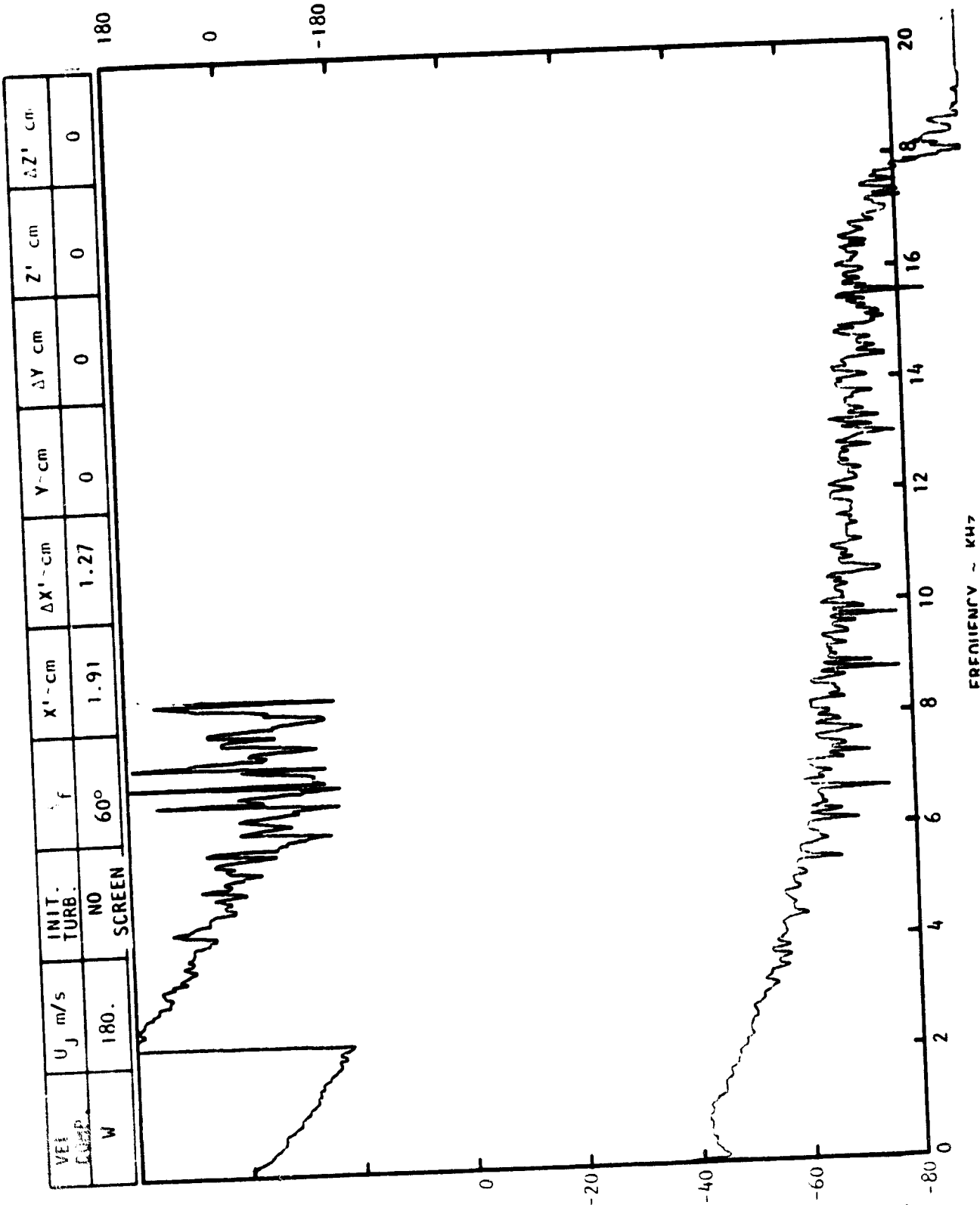
Figure C-4. Continued.

CROSS POWER SPECTRAL DENSITY $G_A(f)$ ~ dB

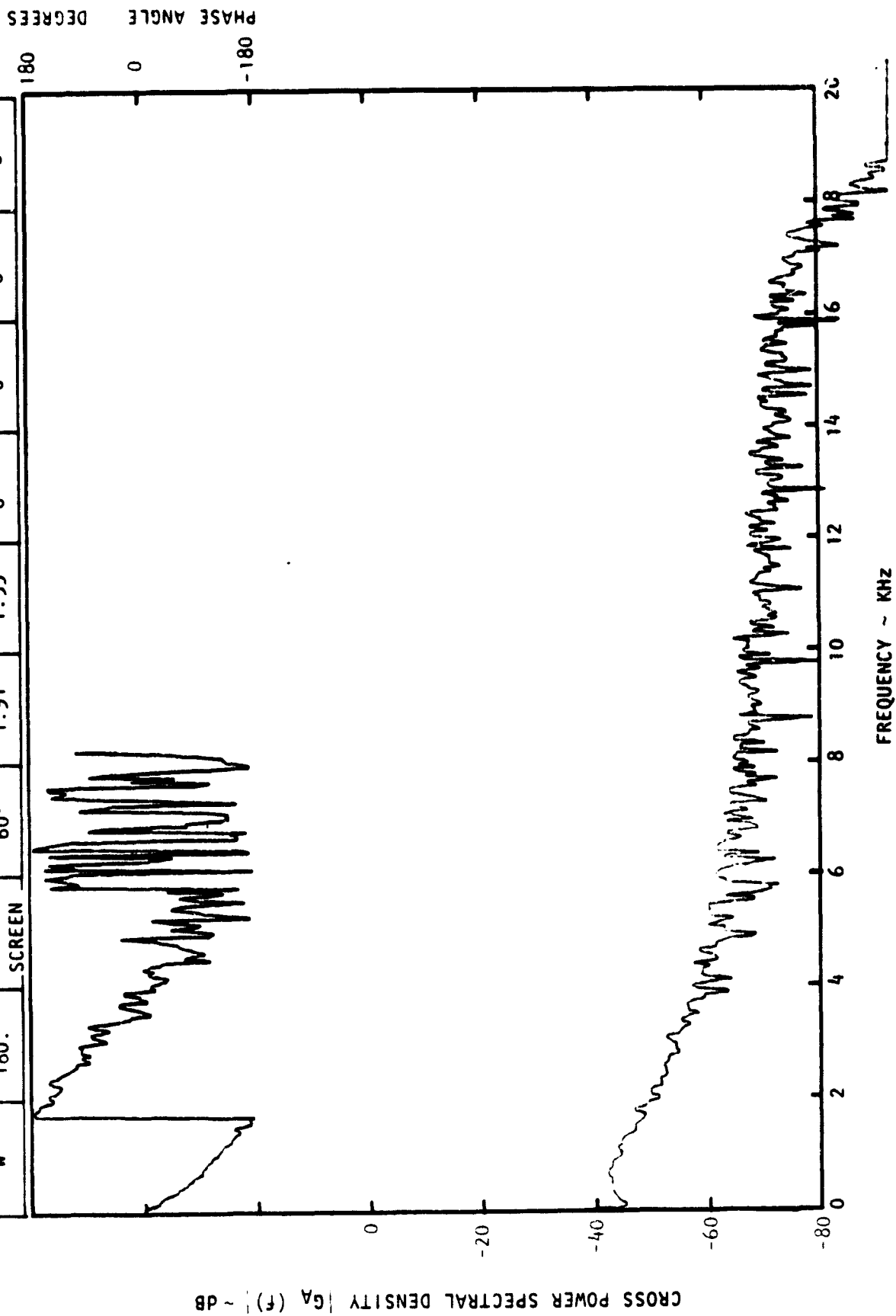


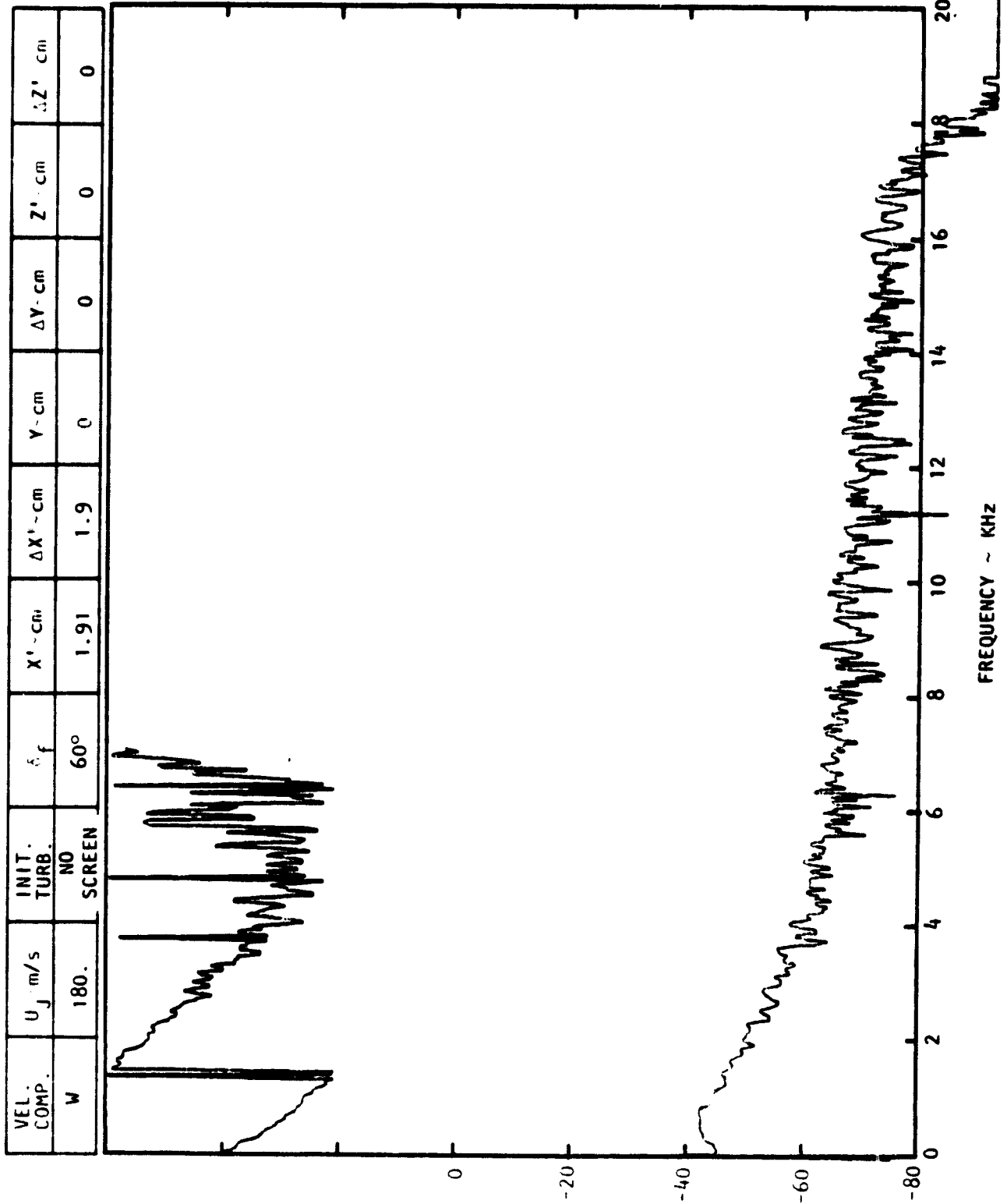
PHASE ANGLE - DEGREES



CROSS POWER SPECTRAL DENSITY $|G_A(f)|^2 \sim \text{dB}$ 

VEL. COMP.	U_j - m/s	INIT. TURB.	δ_f	X^1 - cm	ΔX^1 - cm	Y - cm	ΔY - cm	Z^1 - cm	ΔZ^1 - cm
W	180.	NO SCREEN	60°	1.91	1.59	0	0	0	0



CROSS POWER SPECTRAL DENSITY $G_A(f)$ ~ DB

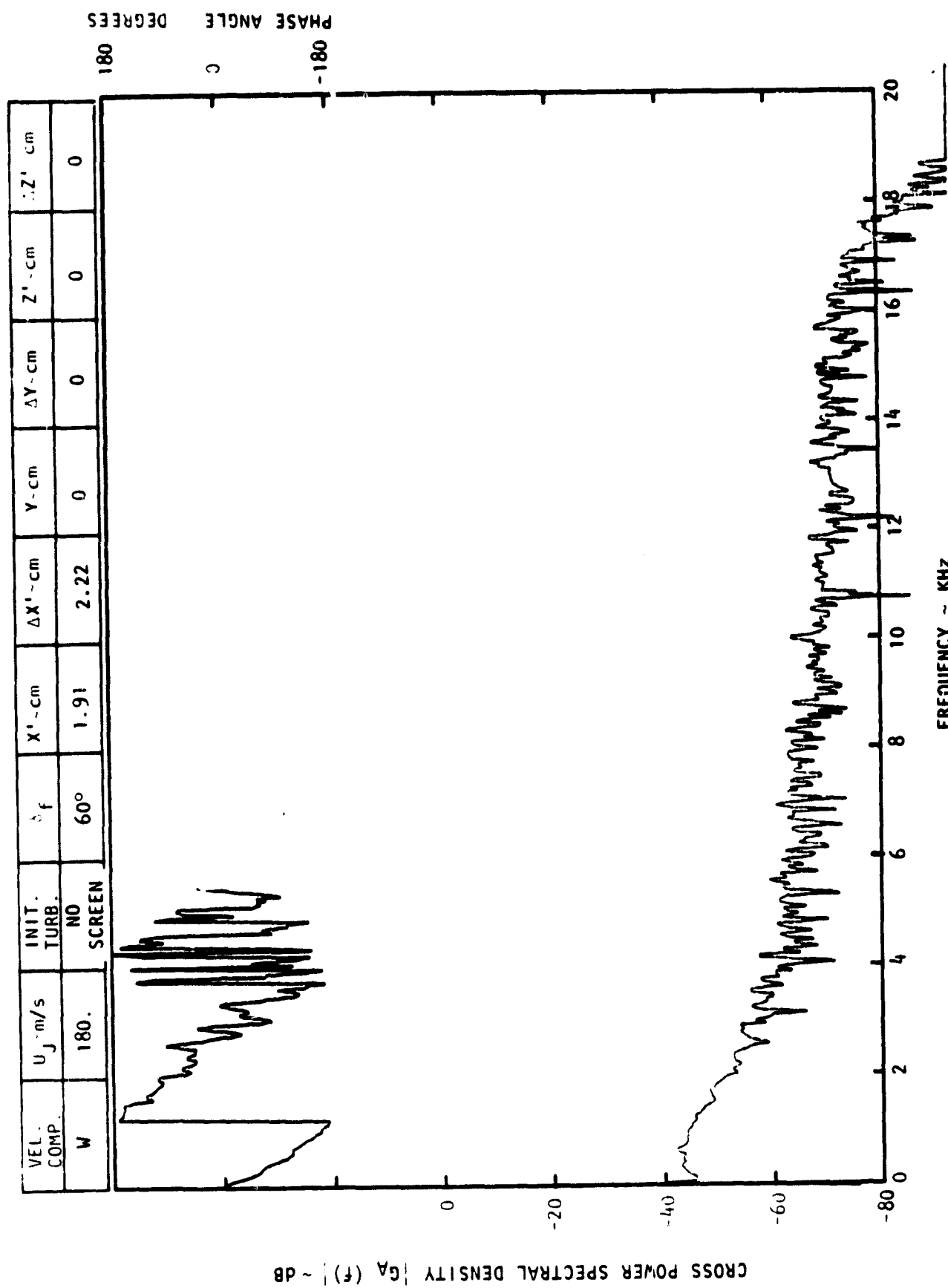
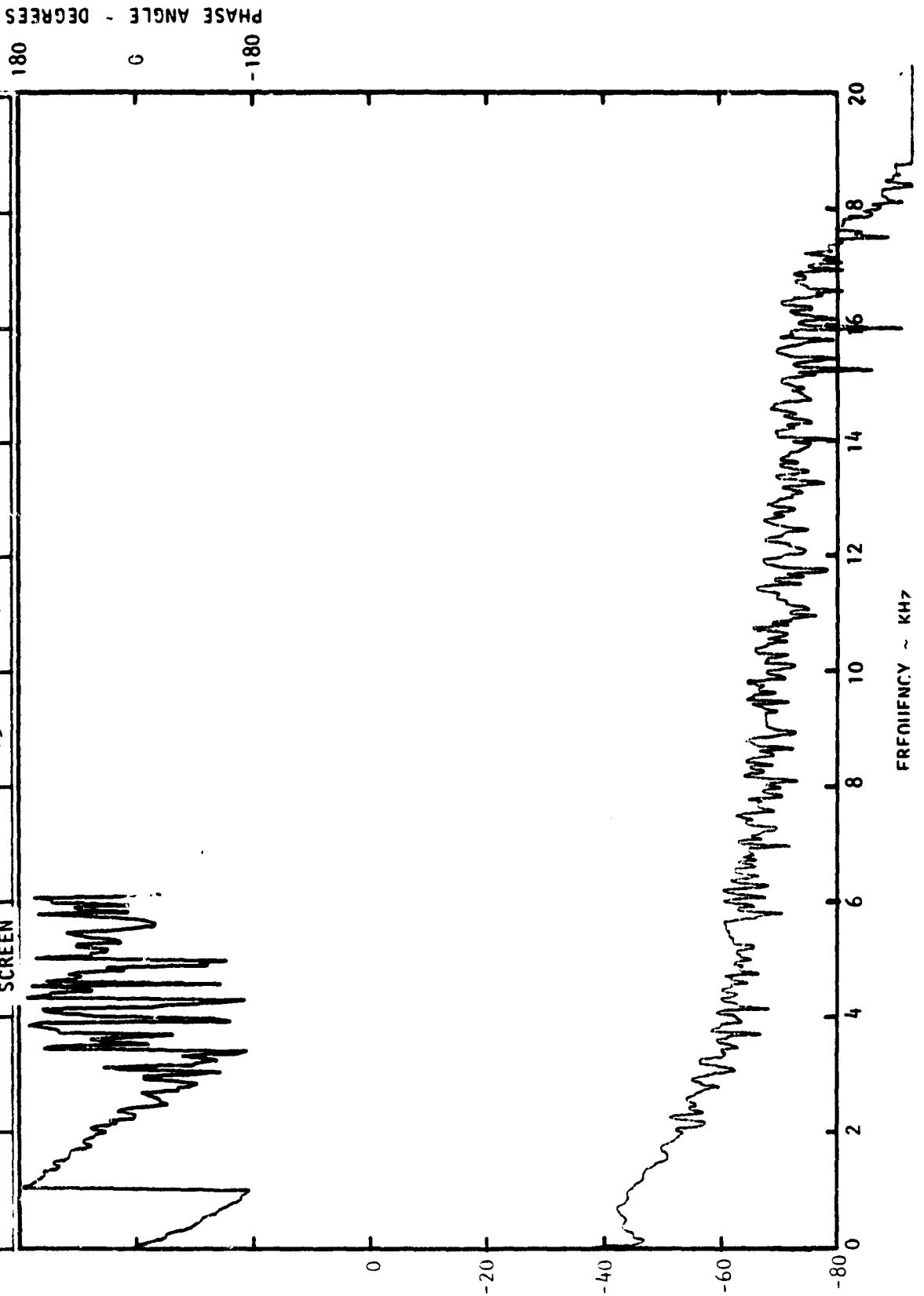


Figure C-4. Continued.

CROSS POWER SPECTRAL DENSITY $|G_A(f)| \sim \text{dB}$ 

VEL. COMP.	U_j - m/s	INIT. TURB.	δ_f	$X' - \text{cm}$	$\Delta X' - \text{cm}$	$Y - \text{cm}$	$\Delta Y - \text{cm}$	$Z' - \text{cm}$	$\Delta Z' - \text{cm}$
W	180.	NO SCREEN	60°	1.91	2.54	0	0	0	0

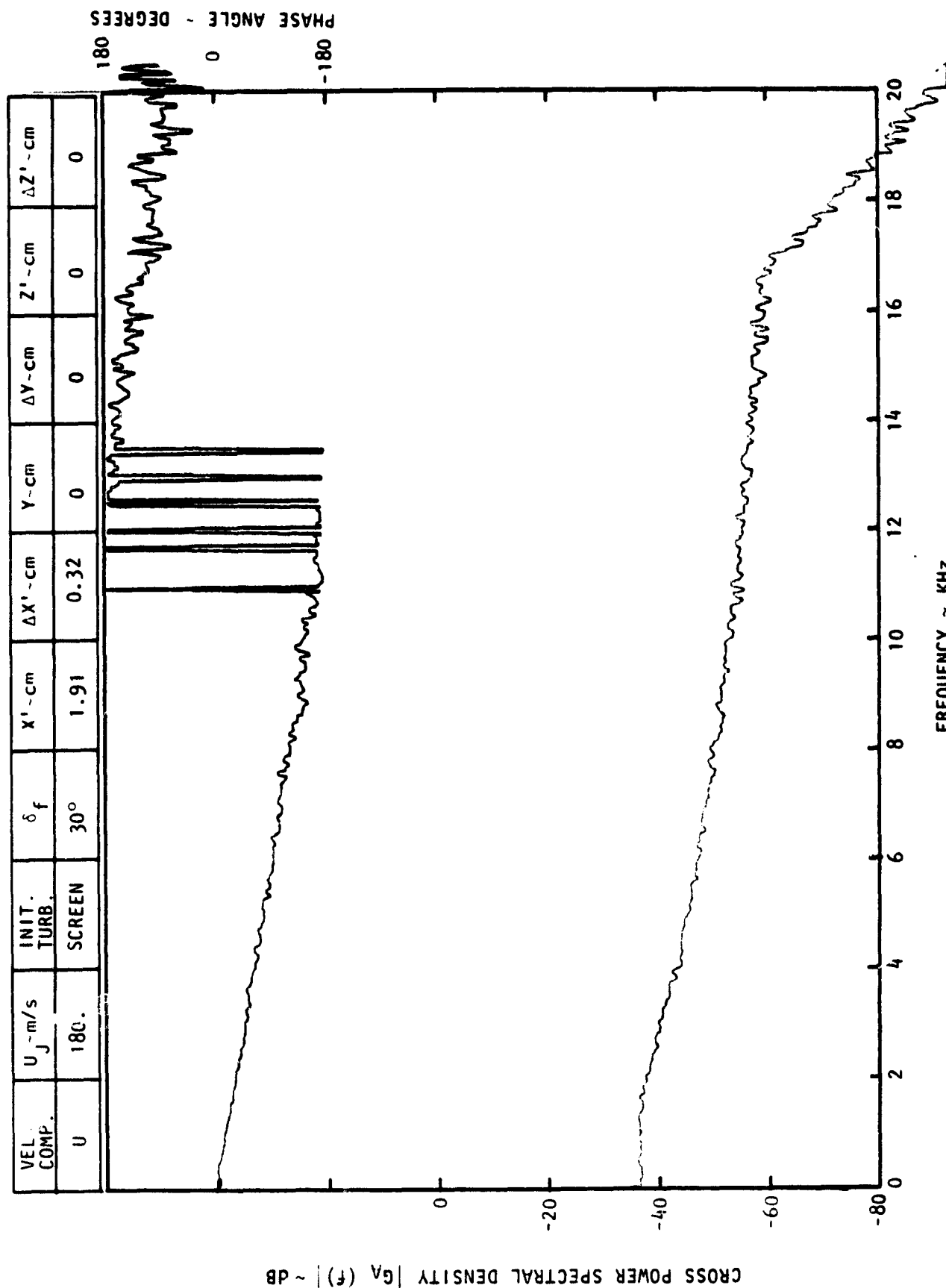
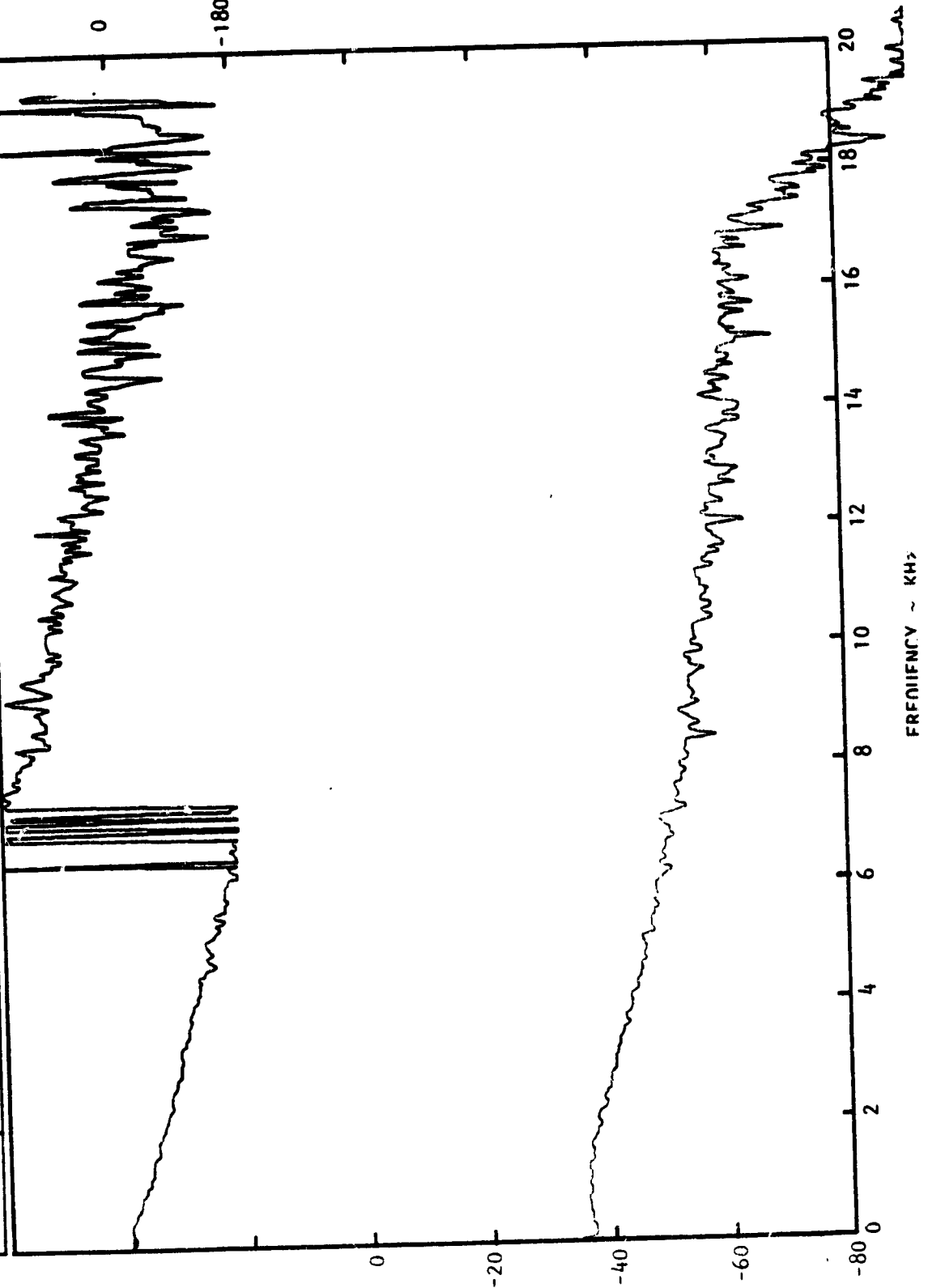


Figure C-5. Velocity-Velocity Cross Power Spectrum and Phase;
Nozzle Exit Screen.

CROSS POWER SPECTRAL DENSITY $|G_A(f)| \sim \text{dB}$

PHASE ANGLE - DEGREES

VEL. COMP.	$U_j \sim \text{m/s}$	INIT. TURB.	δ_f	$X' \sim \text{cm}$	$\Delta X' \sim \text{cm}$	$Y \sim \text{cm}$	$\Delta Y \sim \text{cm}$	$Z' \sim \text{cm}$	$\Delta Z' \sim \text{cm}$
U	180.	SCREEN	30°	1.91	0.64	0	0	0	0



FREQUENCY ~ KHz

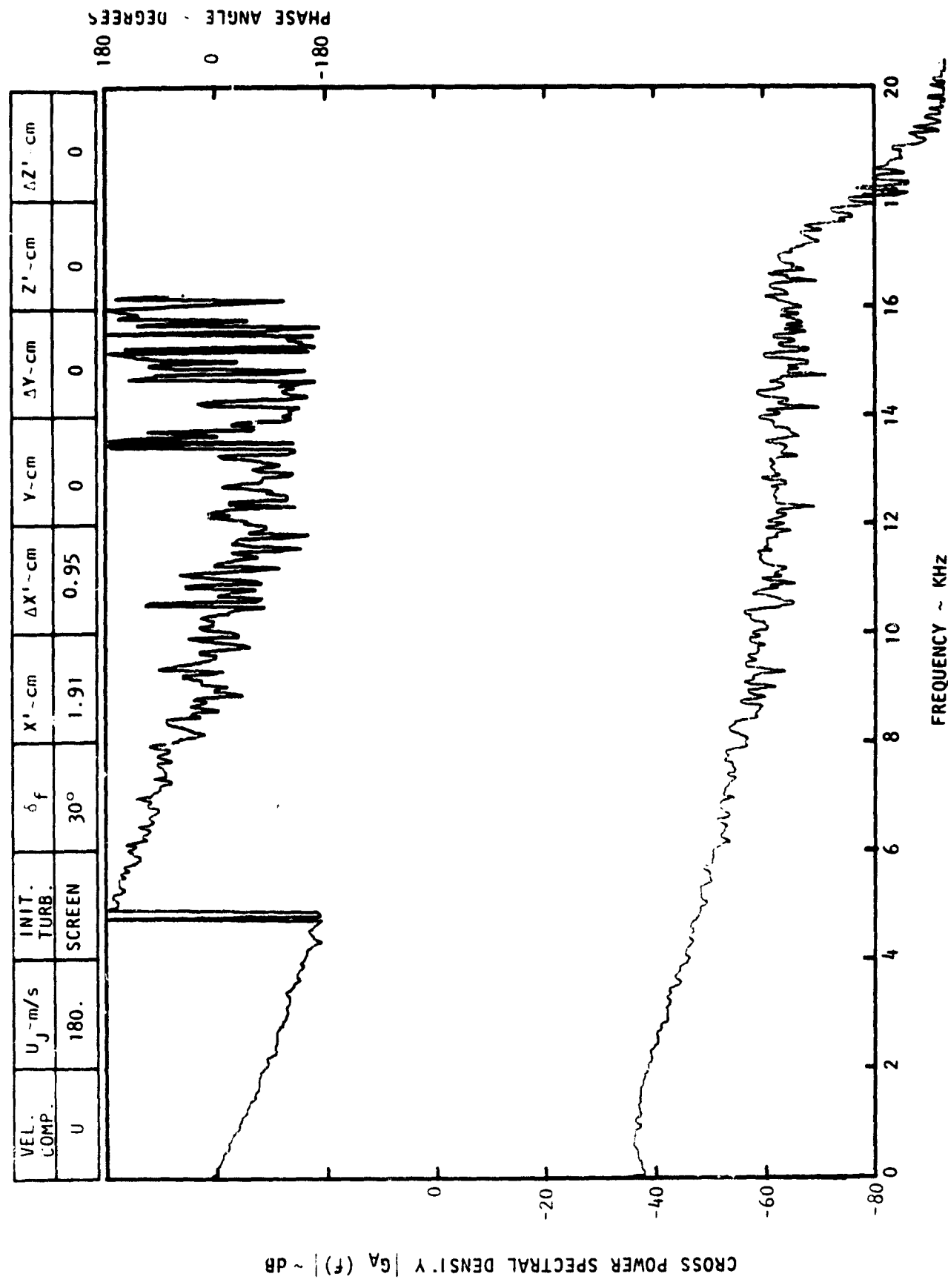
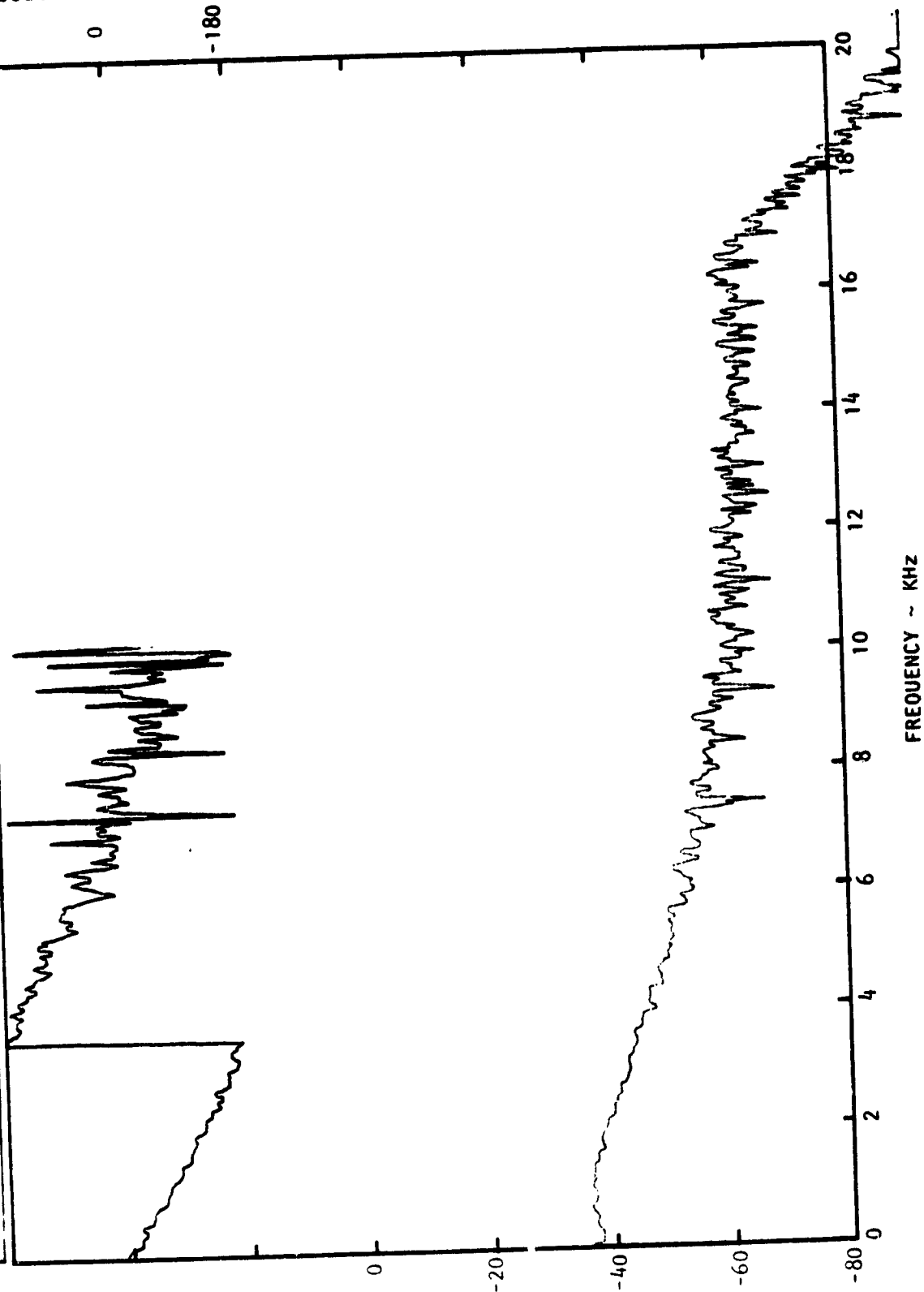


Figure C-5. Continued.

CROSS POWER SPECTRAL DENSITY $|G_A(f)| \sim \text{dB}$ PHASE ANGLE DEGREES
180
0
-180

VEL. COMP.	U_j - m/s	INIT. TURB.	δ_f	X^1 - cm	ΔX^1 - cm	Y - cm	ΔY - cm	Z^1 - cm	ΔZ^1 - cm
U	180.	SCREEN	30°	1.91	1.22	0	0	0	0



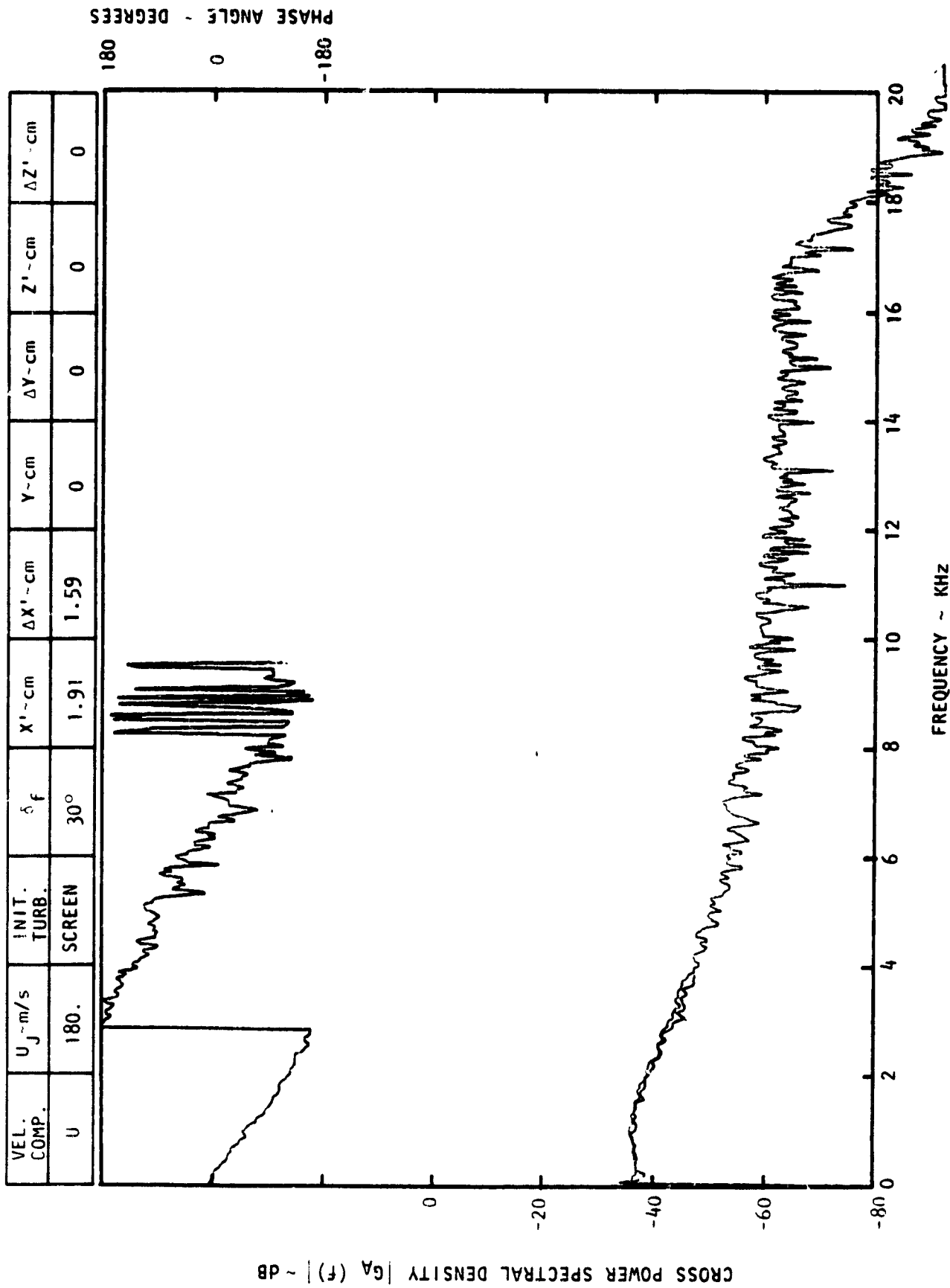
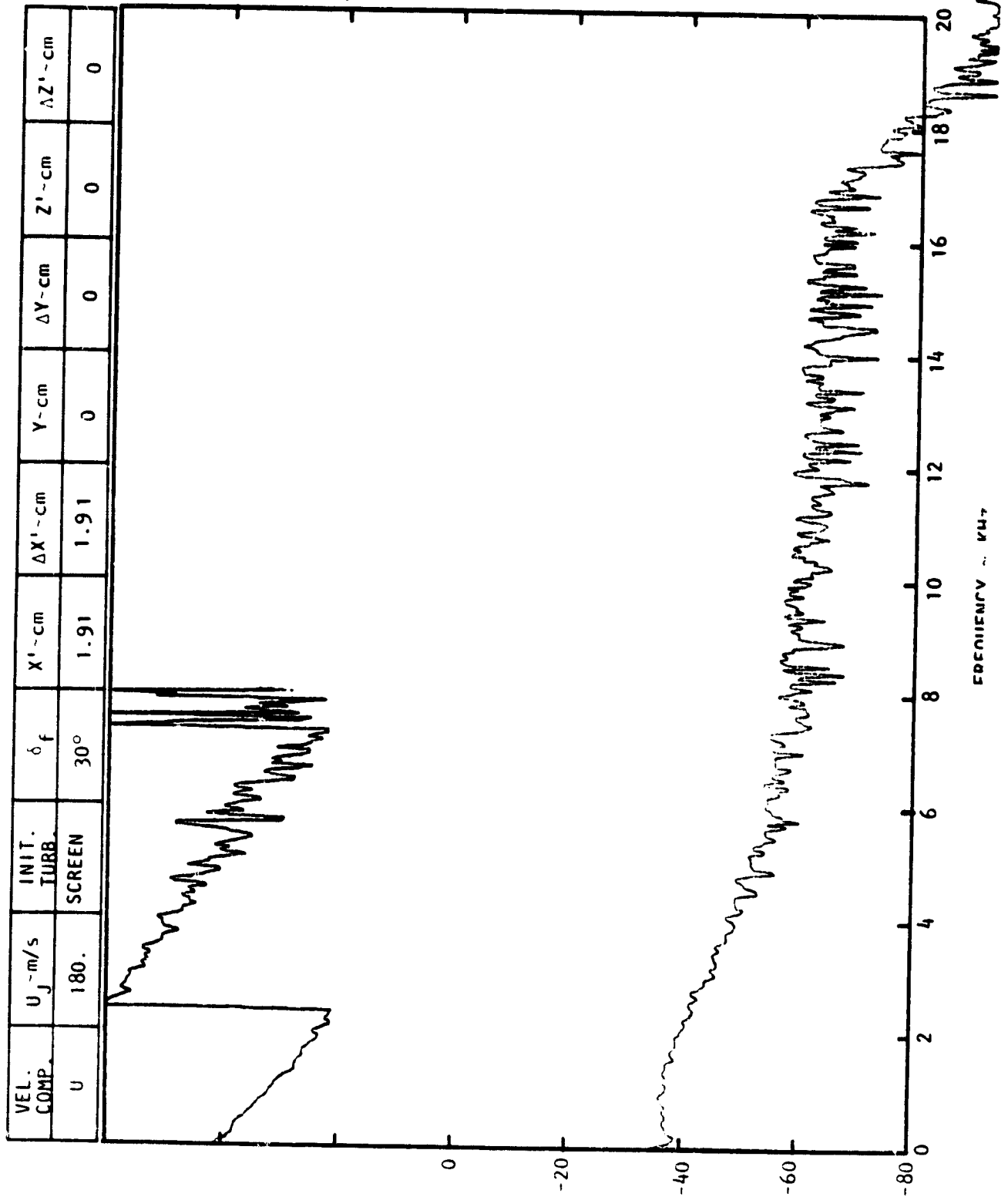


Figure C-5. Continued.

CROSS POWER SPECTRAL DENSITY $|G_A(f)|^2$ - DB

PHASE ANGLE - DEGREES



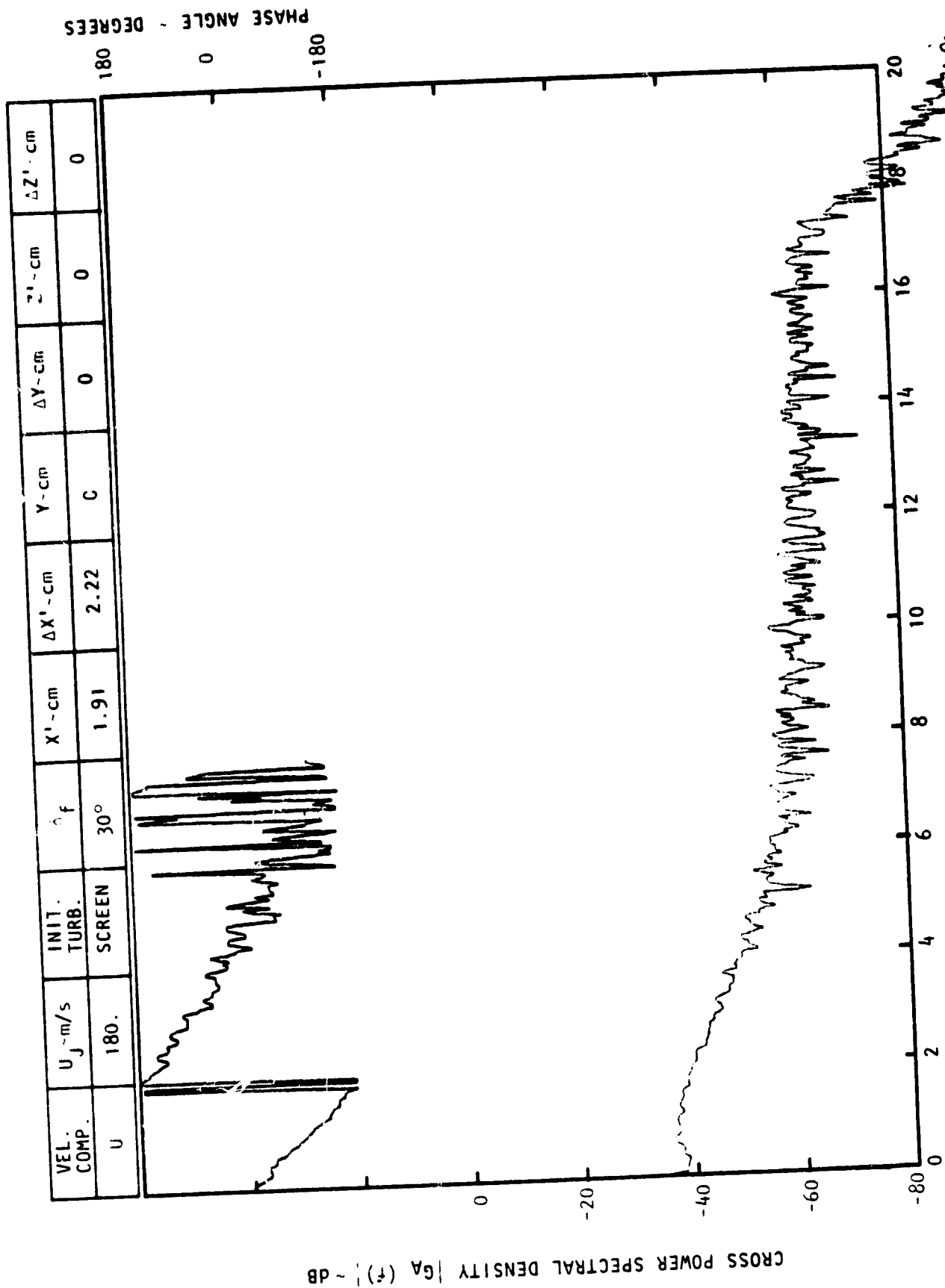
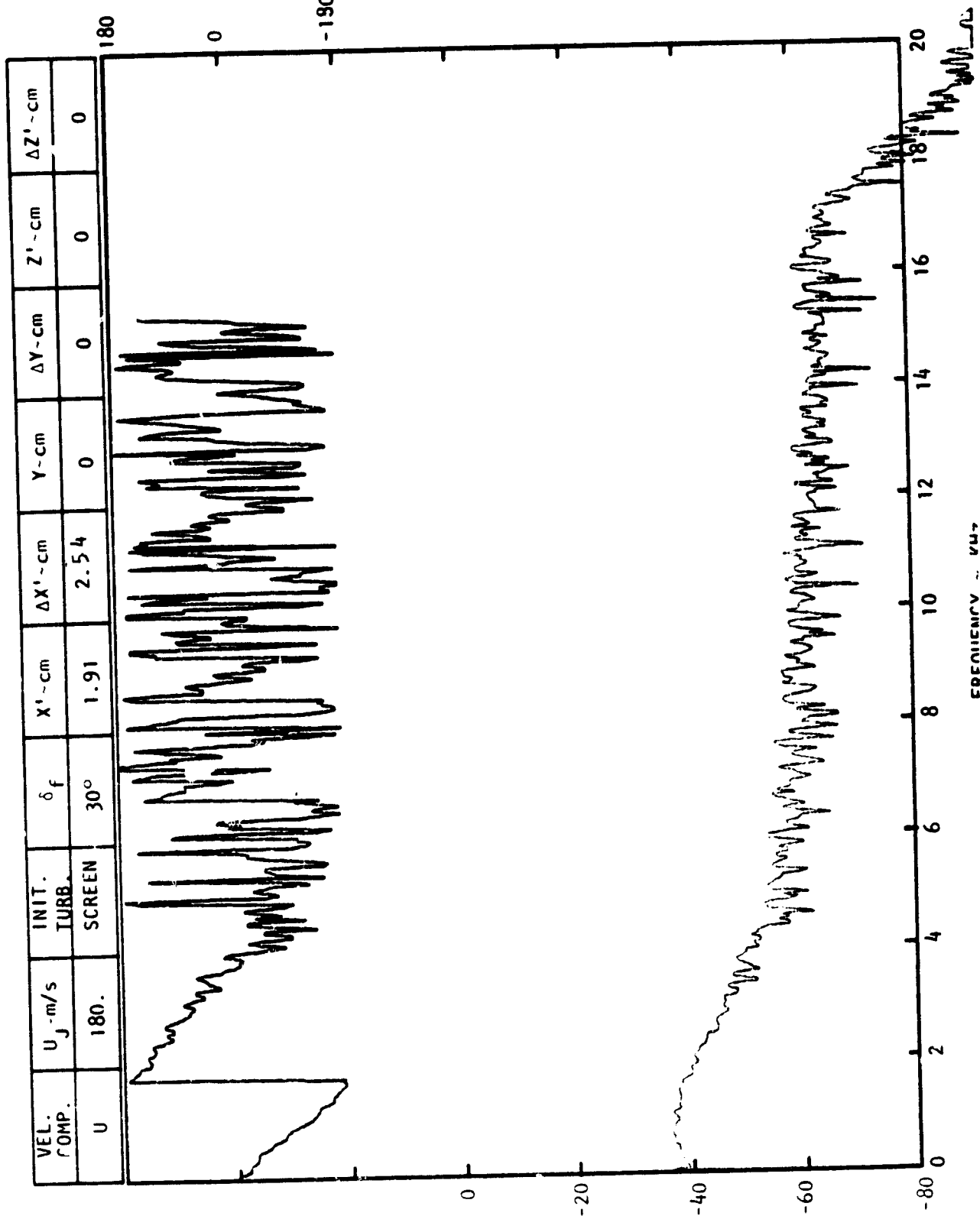


Figure C-5. Continued.

CROSS POWER SPECTRAL DENSITY $|G_A(f)|^2$ - dB



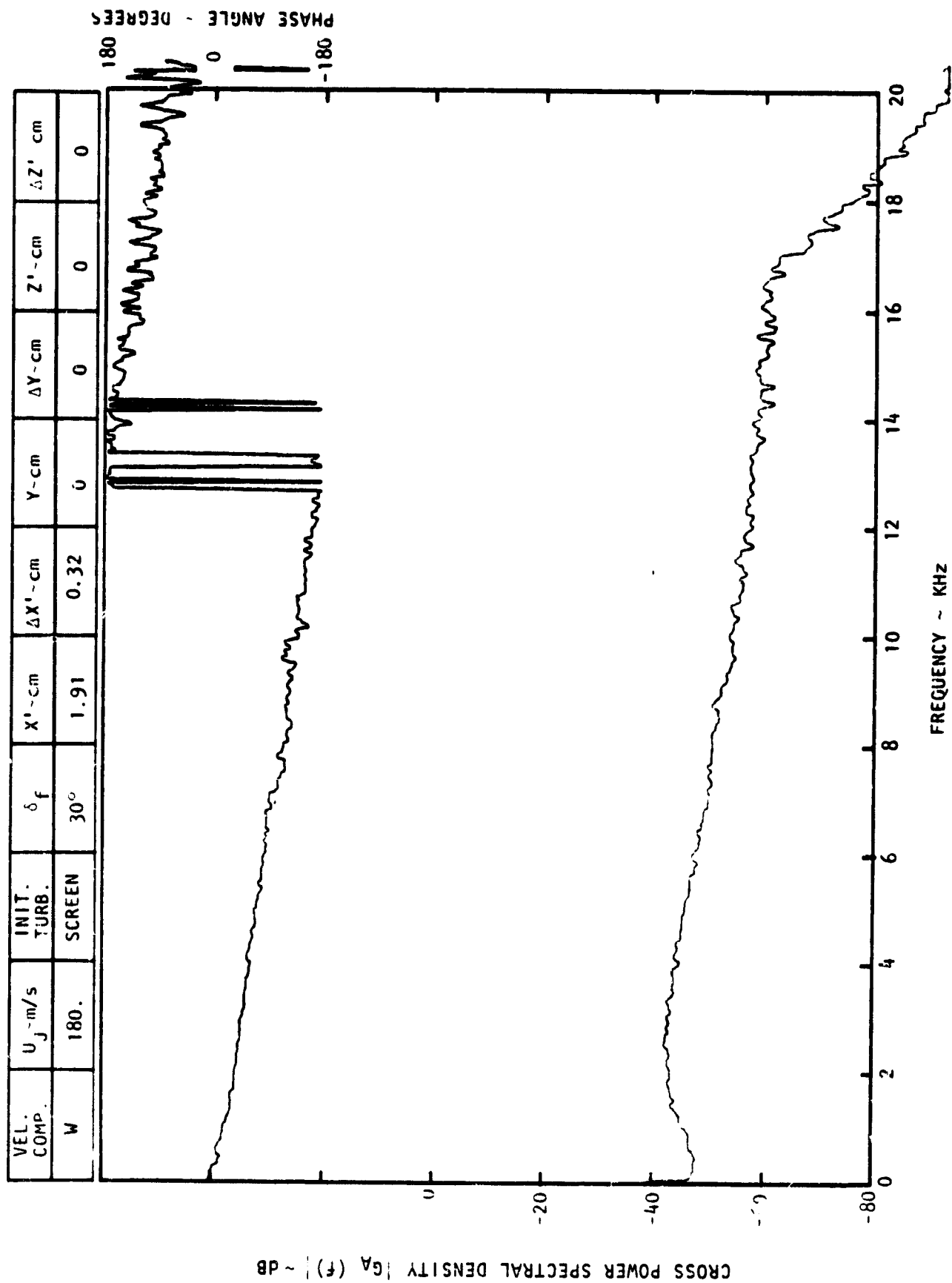
PHASE ANGLE - DEGREES

180

0

-180

EDENIENCV - VU7

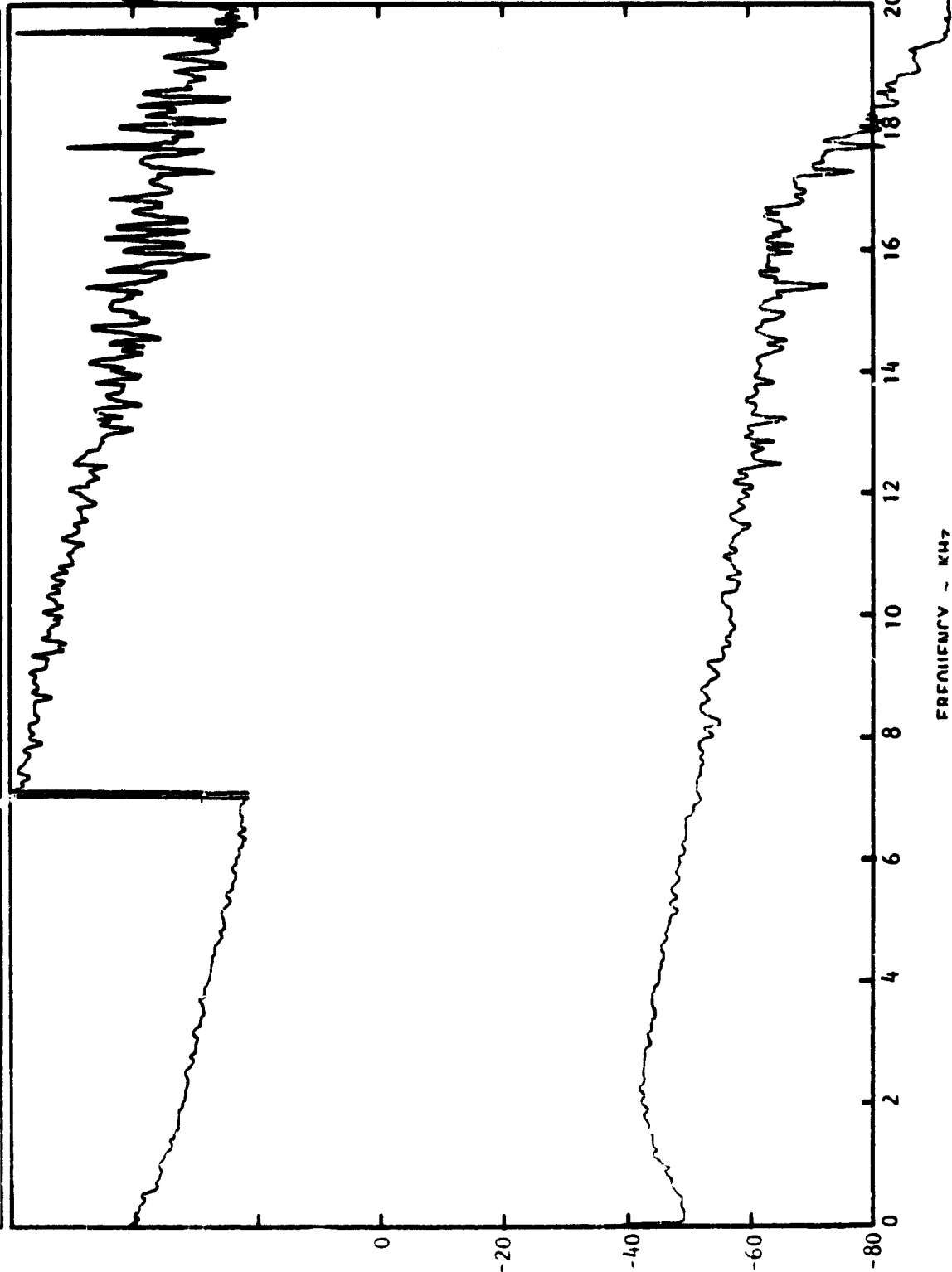


FREQUENCY ~ KHz
Figure C-5. Continued.

VEL. COMP.	U_j - m/s	INIT. TURB.	δ_f	$X' - \text{cm}$	$\Delta X' - \text{cm}$	$Y - \text{cm}$	$\Delta Y - \text{cm}$	$Z' - \text{cm}$	$\Delta Z' - \text{cm}$
W	180.	SCREEN	30°	1.91	0.64	0	0	0	0

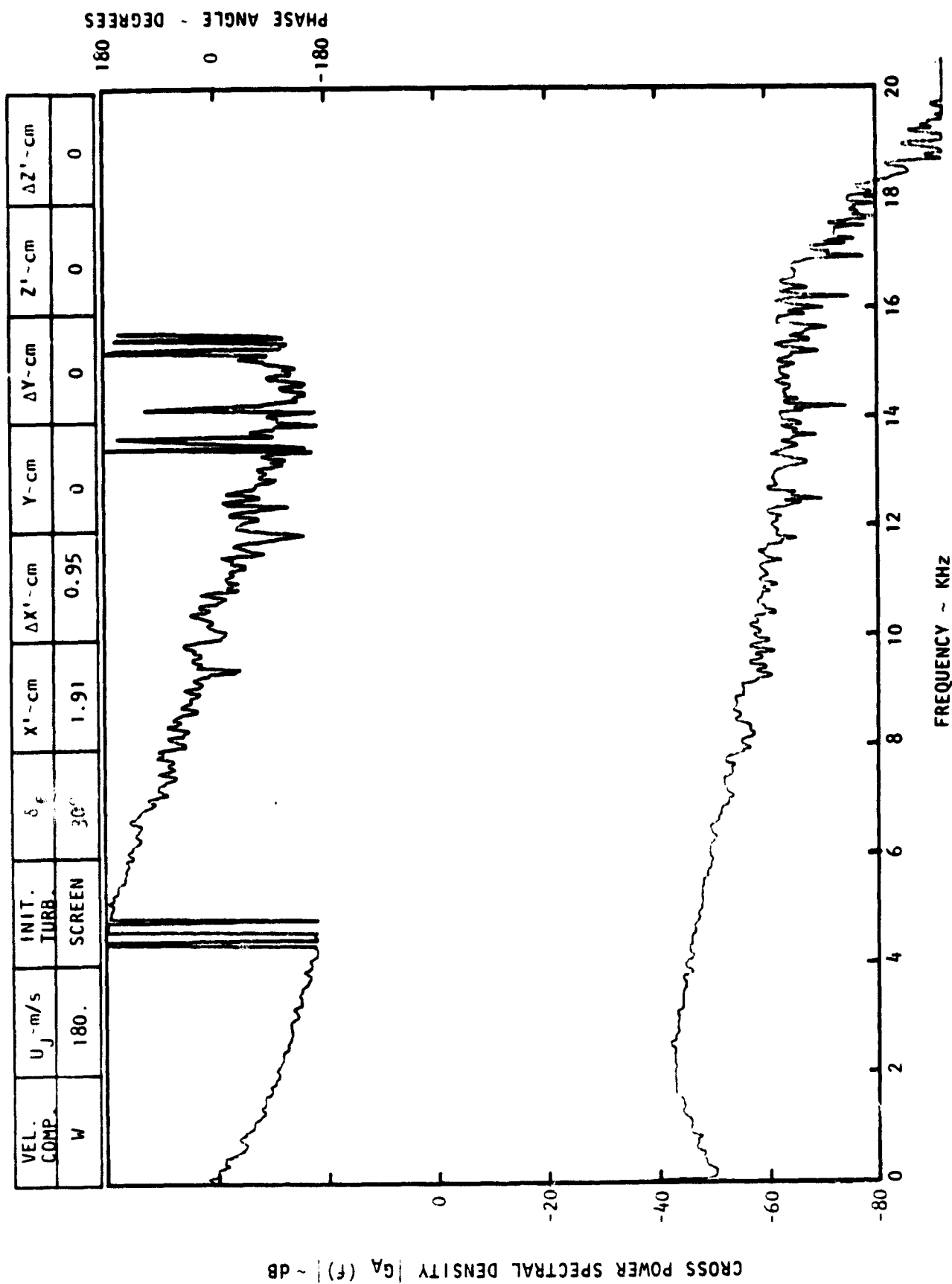
PHASE ANGLE - DEGREES

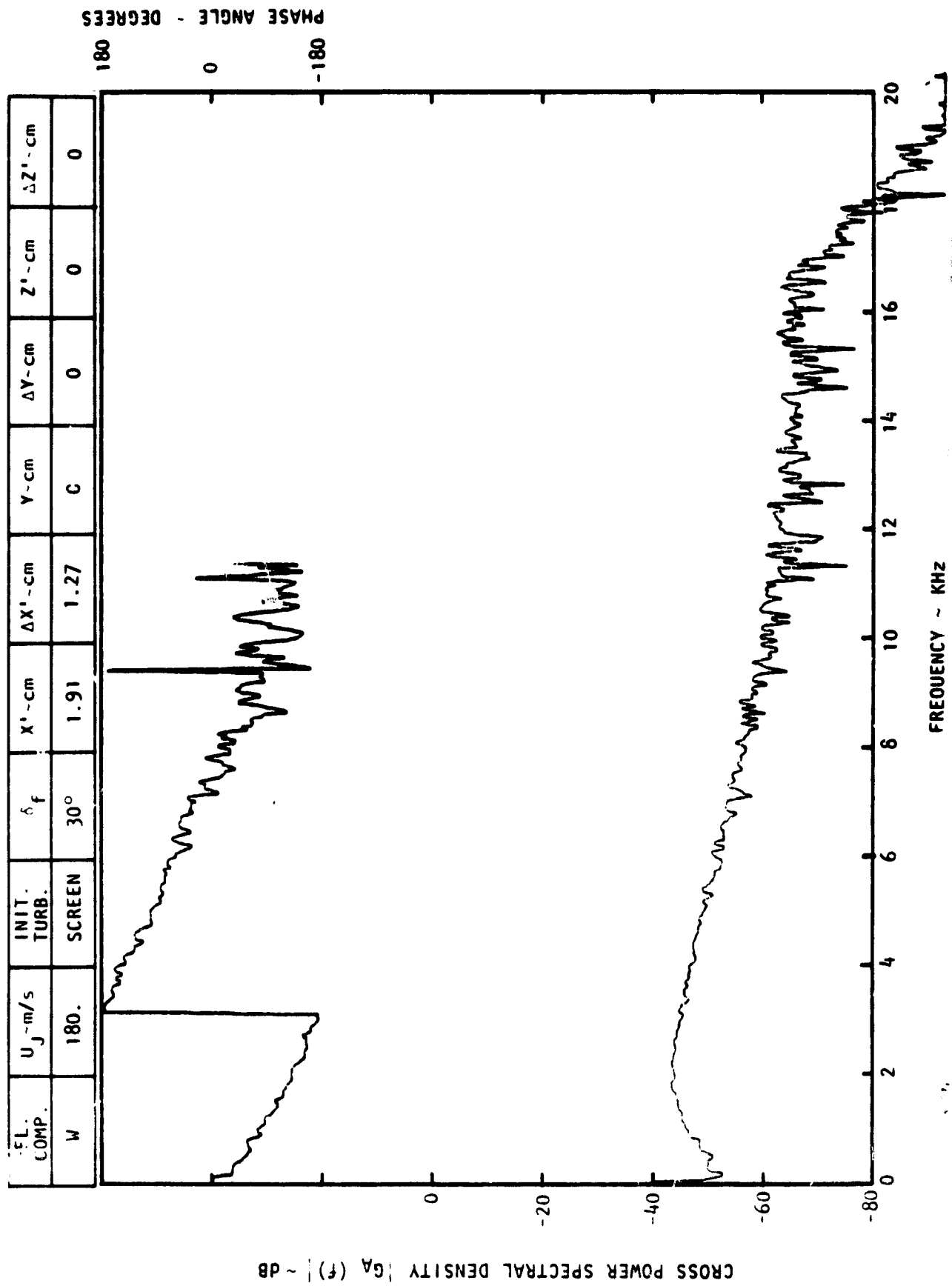
180
0
-180



CROSS POWER SPECTRAL DENSITY $|G_A(f)|$ - dB

FREQUENCY - KHZ





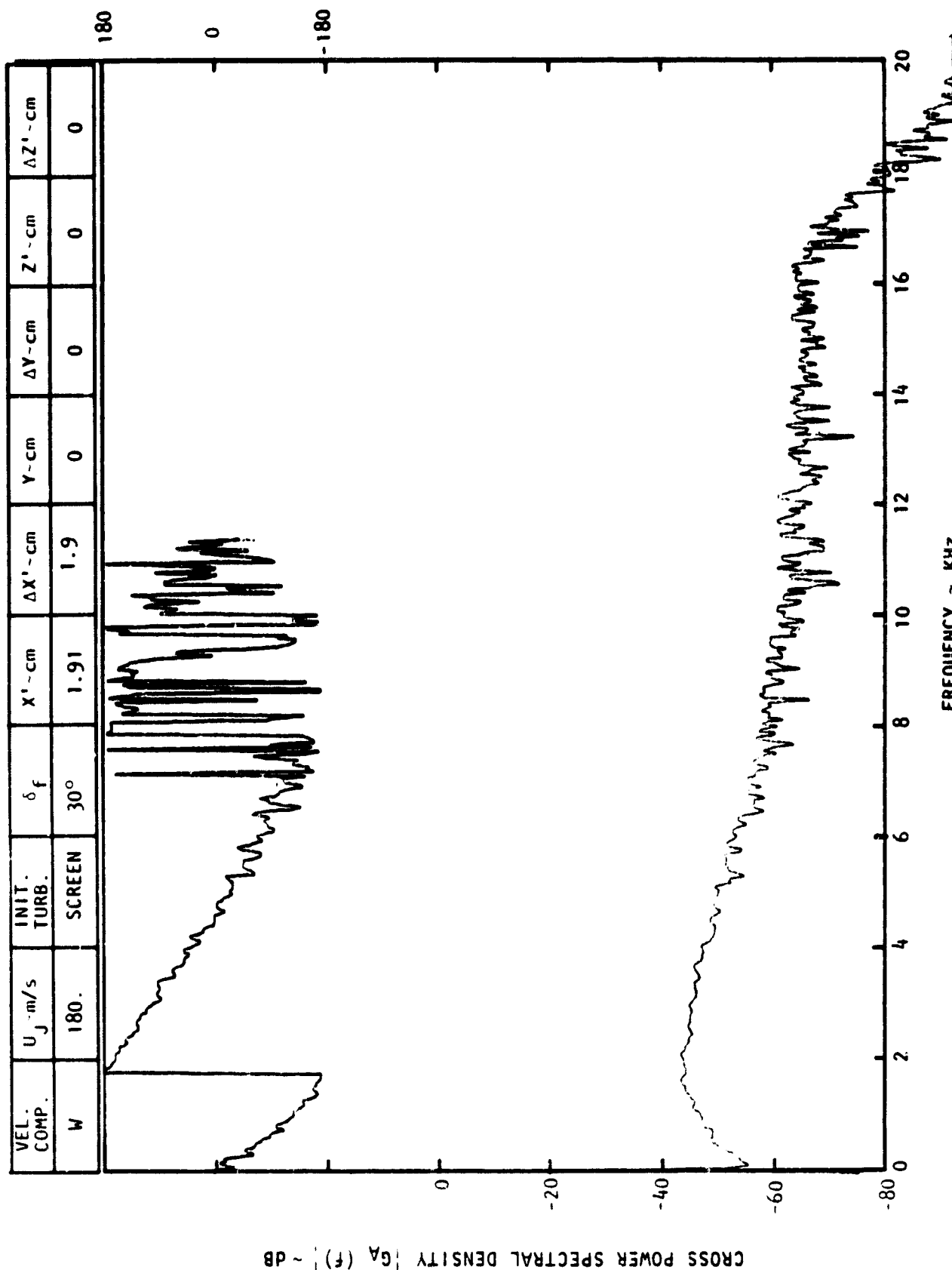
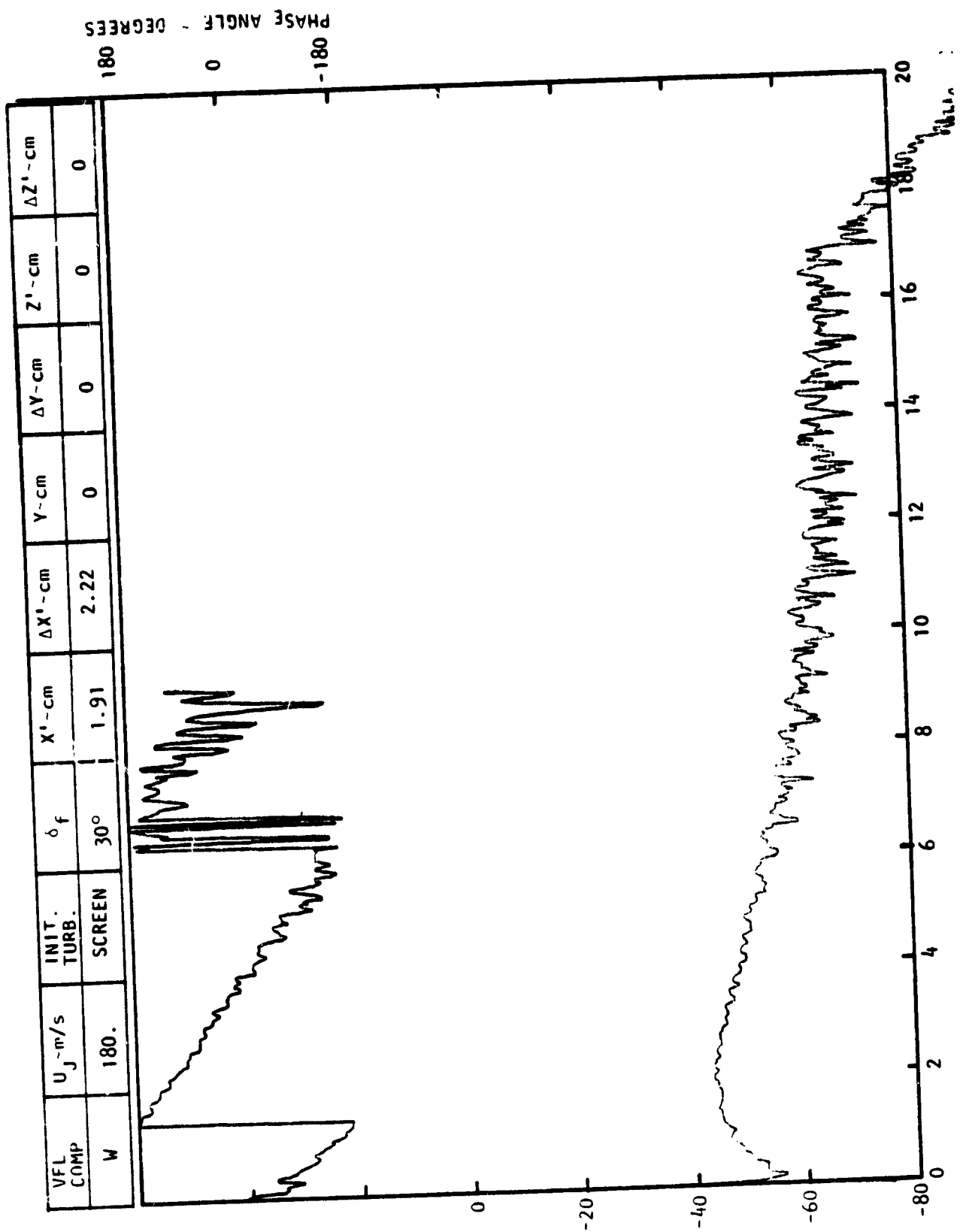


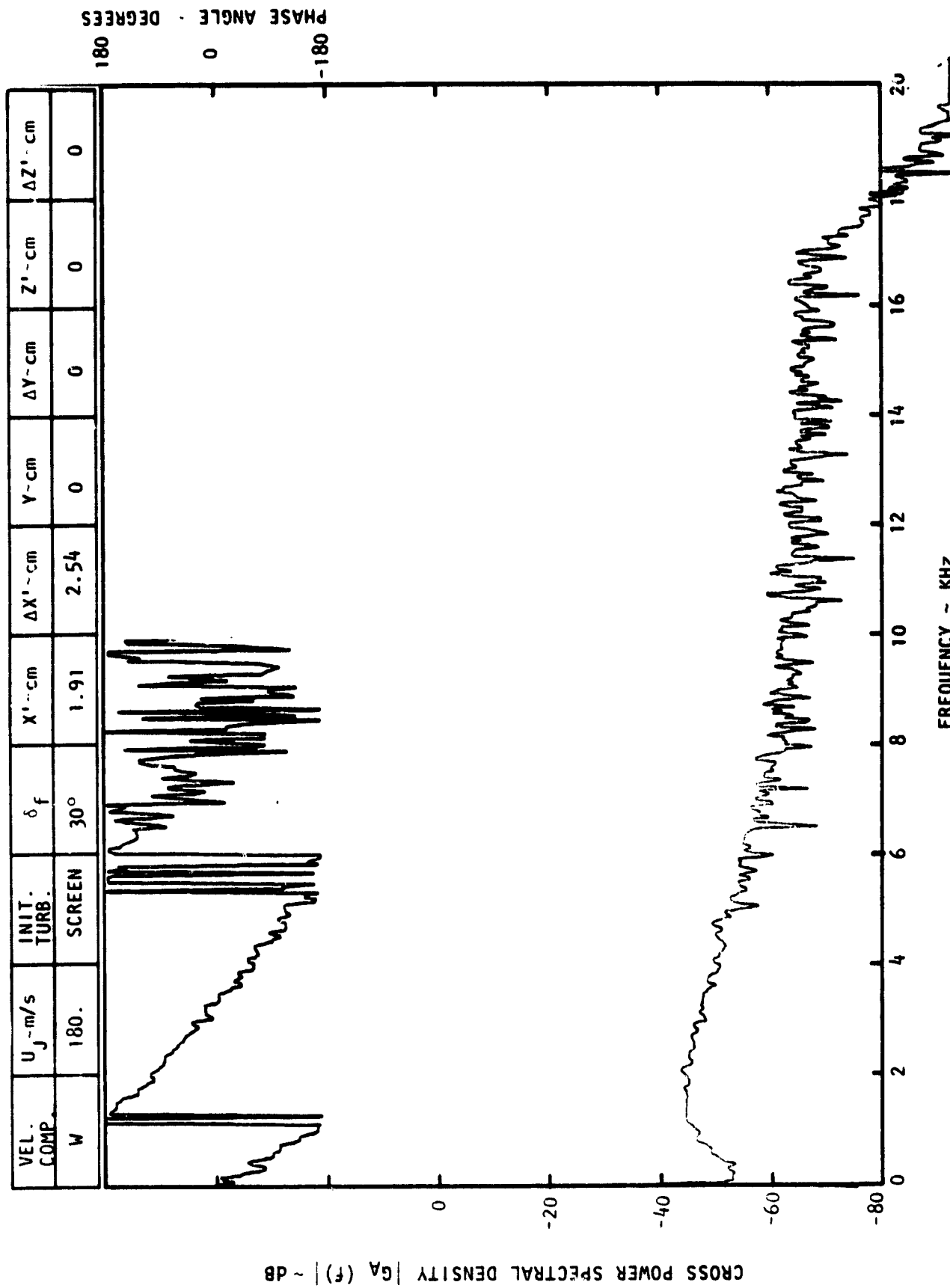
Figure C-5. Continued.

5-7

CROSS POWER SPECTRAL DENSITY $G_A(f)$ ~ dB



PHASE ANGLE - DEGREES



FREQUENCY - KHz

Figure C-5. Concluded.

APPENDIX D

NEAR-FIELD NOISE THIRD OCTAVE BAND SPECTRA

This appendix contains one-third octave-band spectra of near-field pressures measured in the mid-span plane of the model. Parameters varied were U_j , initial turbulence, and δ_f .

The data are divided into three parts:

- o Figure D-1; $\delta_f = 30^\circ$, No Screen
- o Figure D-2; $\delta_f = 60^\circ$, No Screen
- o Figure D-3; $\delta_f = 30^\circ$, Screen

Each figure includes an SPL plot for each of twelve or more microphone locations which are shown in Table D-1. At each location spectra are plotted for $U_j = 180, 215, 250$, and 285 m/s.

TABLE D-1 MICROPHONE LOCATIONS FOR NEAR-FIELD
PRESSURE SPECTRA MEASUREMENTS

Figure	δf	Initial Turbulence	Microphone	X'	Z'
D-1 ↓	30 ↓	No Screen ↓	1	NOZ.	2.54*
			2	-15.24	6.35*
			3	- 1.27	8.89
			4	1.91	10.00
			5	7.62	11.43
			6	11.43	12.70
			7	- 7.62	- 2.54**
			8	- 1.27	- 2.54
			9	1.91	- 2.06
			10	7.62	- 5.24
			11	15.24	- 7.30
			12	- 7.62	7.14
D-3 ↓	30 ↓	Screen ↓	1	NOZ.	2.54*
			2	-15.24	6.35*
			3	- 1.26	7.78
			4	1.91	10.00
			5	7.62	11.43
			6	11.43	12.70
			7	- 7.62	- 2.54*
			8	- 1.27	- 2.54
			9	1.91	- 2.06
			10	7.62	- 5.24
			11	15.24	- 7.30
			12	- 7.62	7.14
D-2 ↓	60 ↓	No Screen ↓	1	NOZ.	2.54*
			2	-13.72	5.08**
			3	- 1.27	8.26
			4	1.91	13.34
			5	7.62	16.19
			6	11.43	18.42
			7	- 7.62	- 2.54**
			8	- 1.27	- 2.54**
			9	1.91	- 2.54
			10	7.62	- 5.56
			11	11.43	- 7.30
			12	- 6.48	8.41
			1A	30.48	28.73
			2A	15.24	20.00
			6A	22.86	22.70
			7A	30.48	-17.78
			10A	15.24	-10.32
			11A	22.86	-13.34

*Measured from the nozzle lip. **Measured normal to the surface.

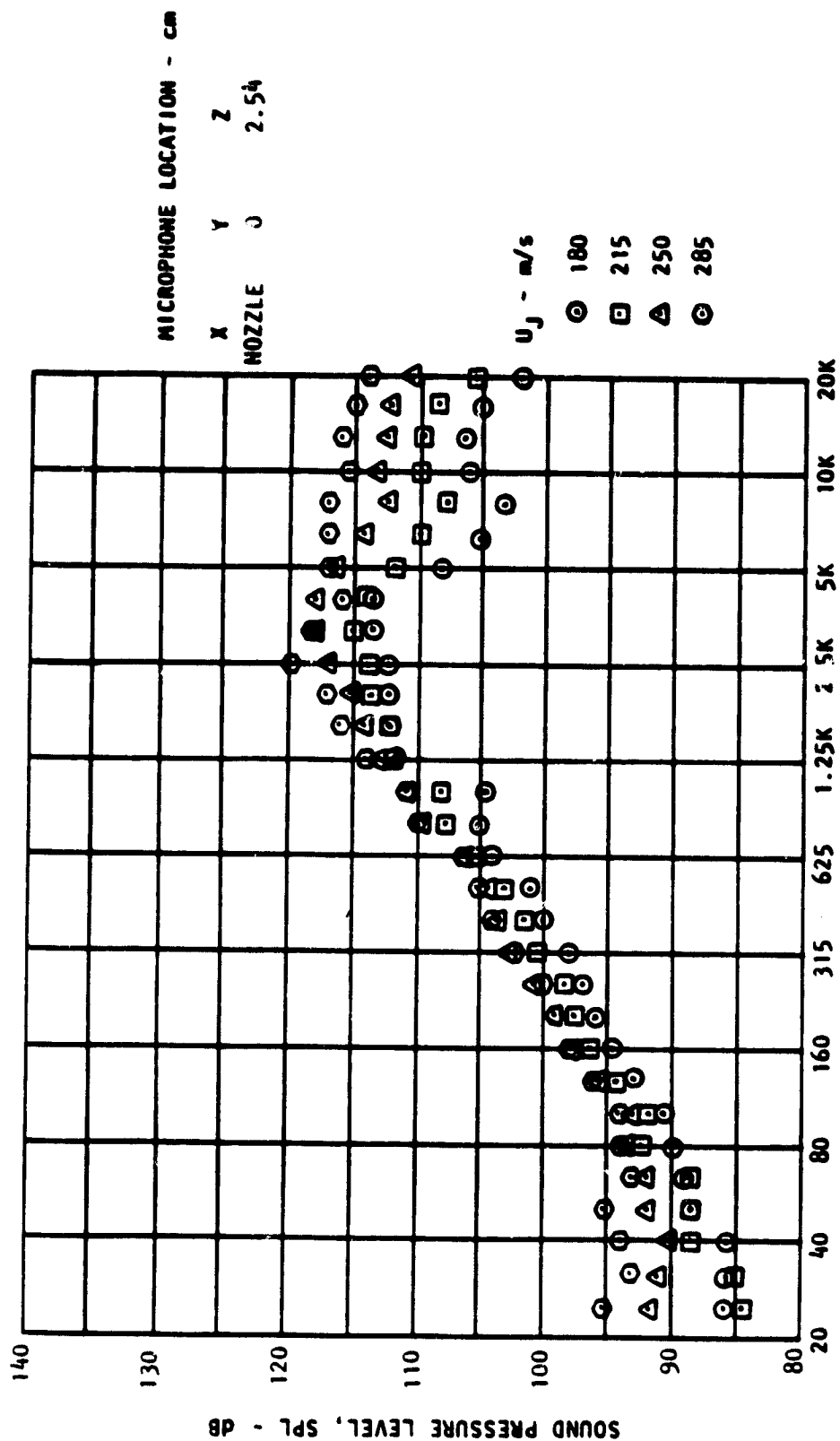


Figure D-1. Near-Field Spectra; $\delta f = 30^\circ$, No Screen
(A) Microphone 1.

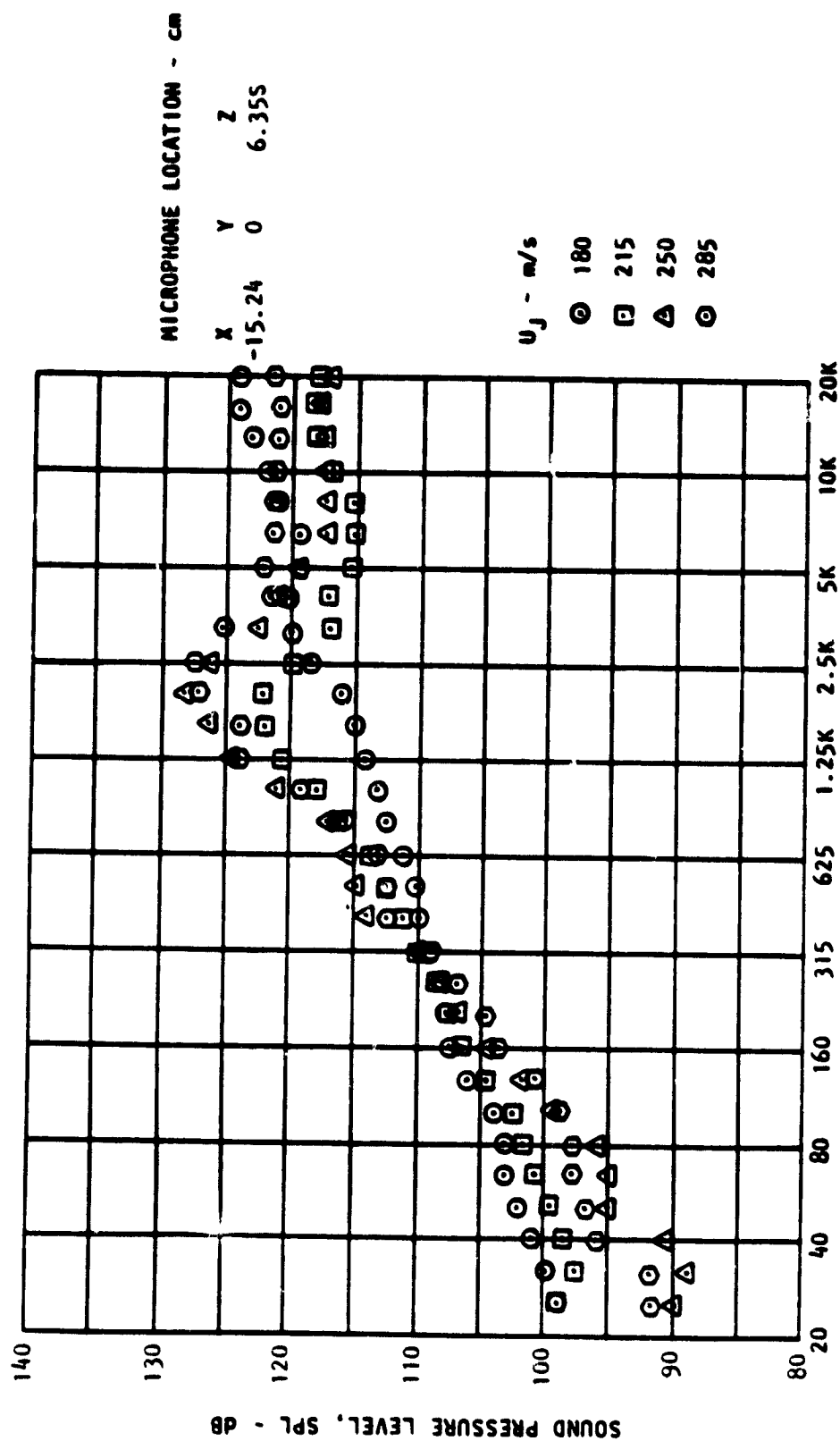


Figure D-1. Continued.

(B) Microphone 2

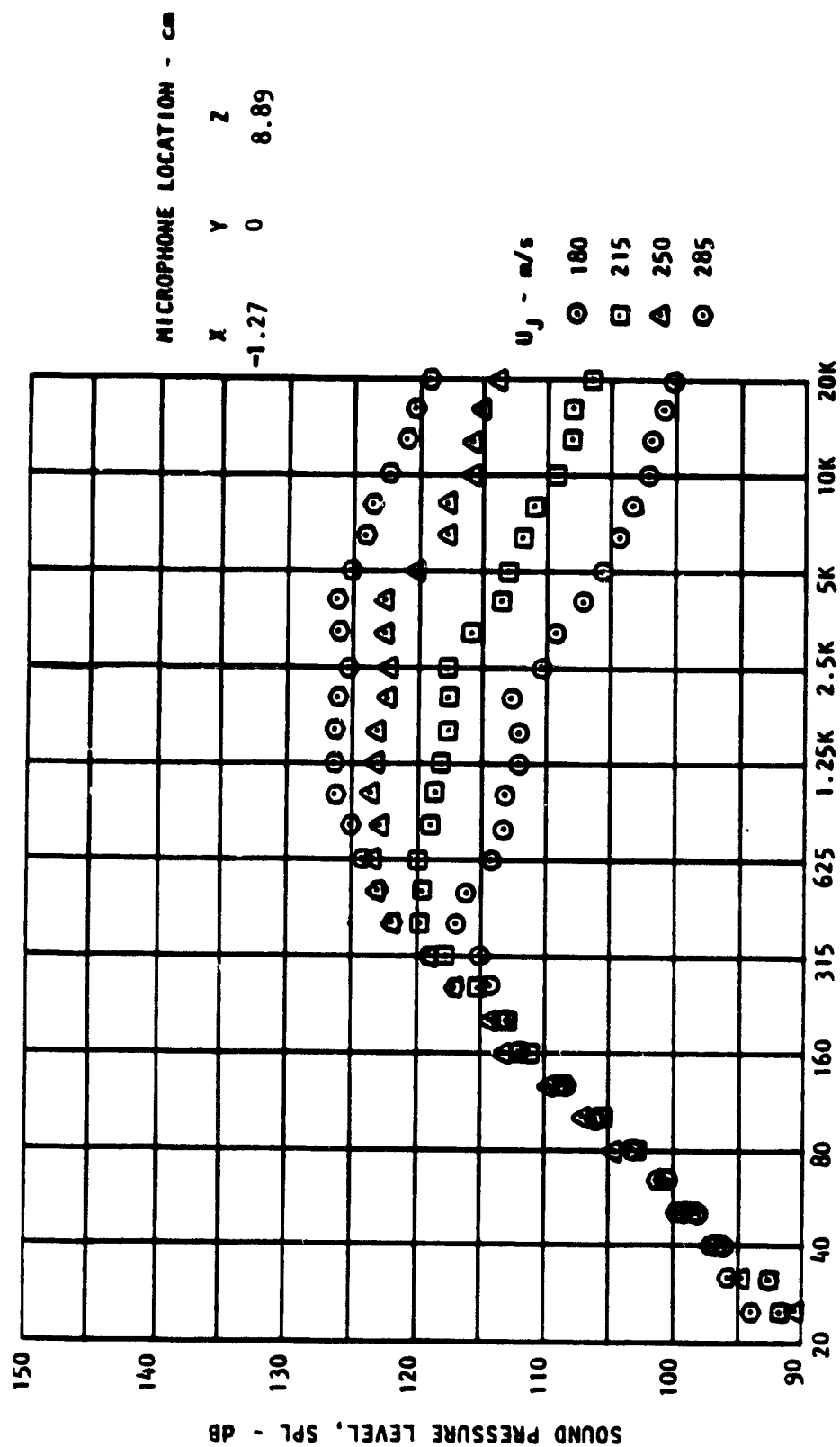


Figure D-1. Continued.
(C) Microphone 3.

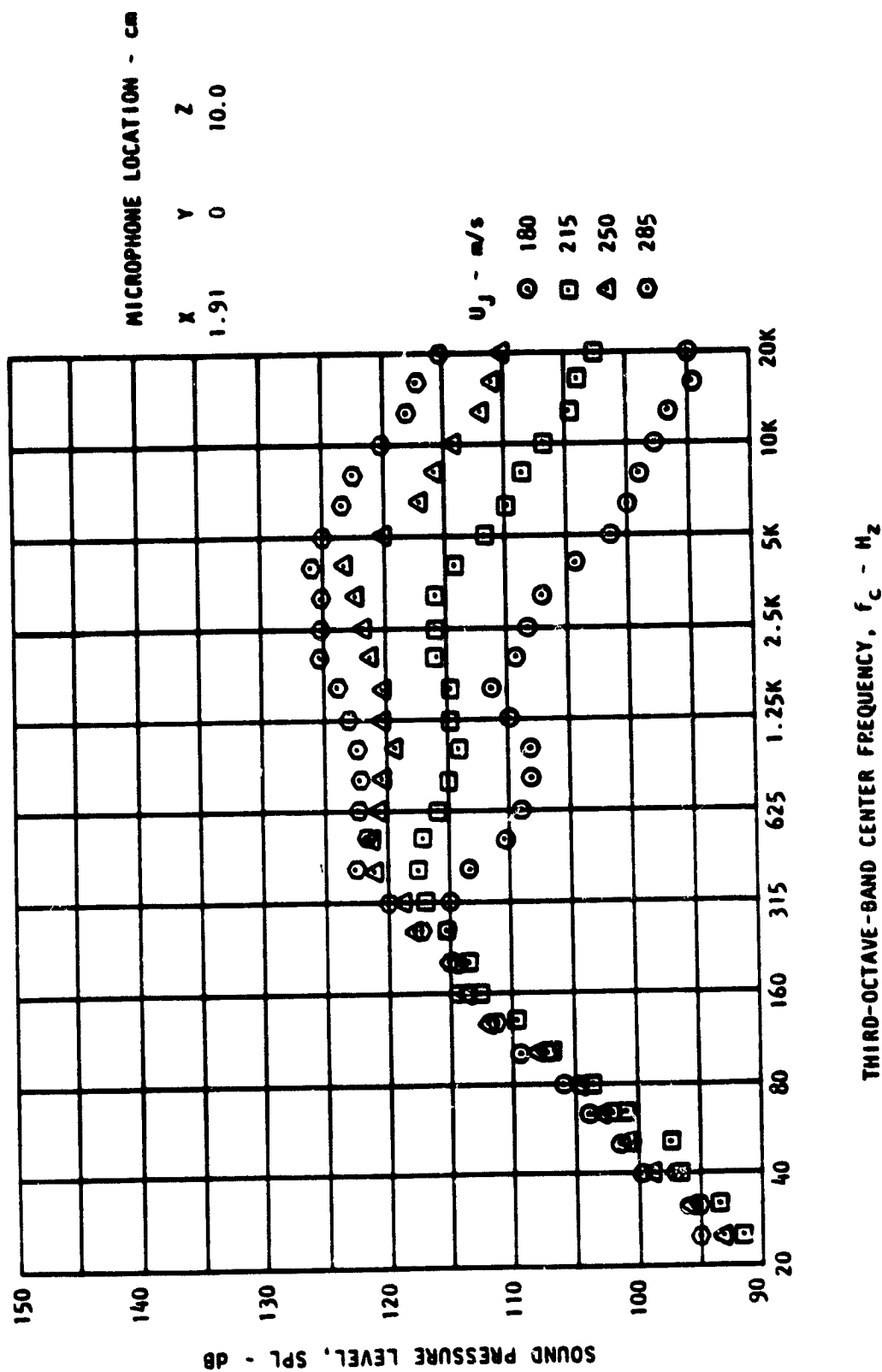


Figure D-1. Continued.

(D) Microphone 4.

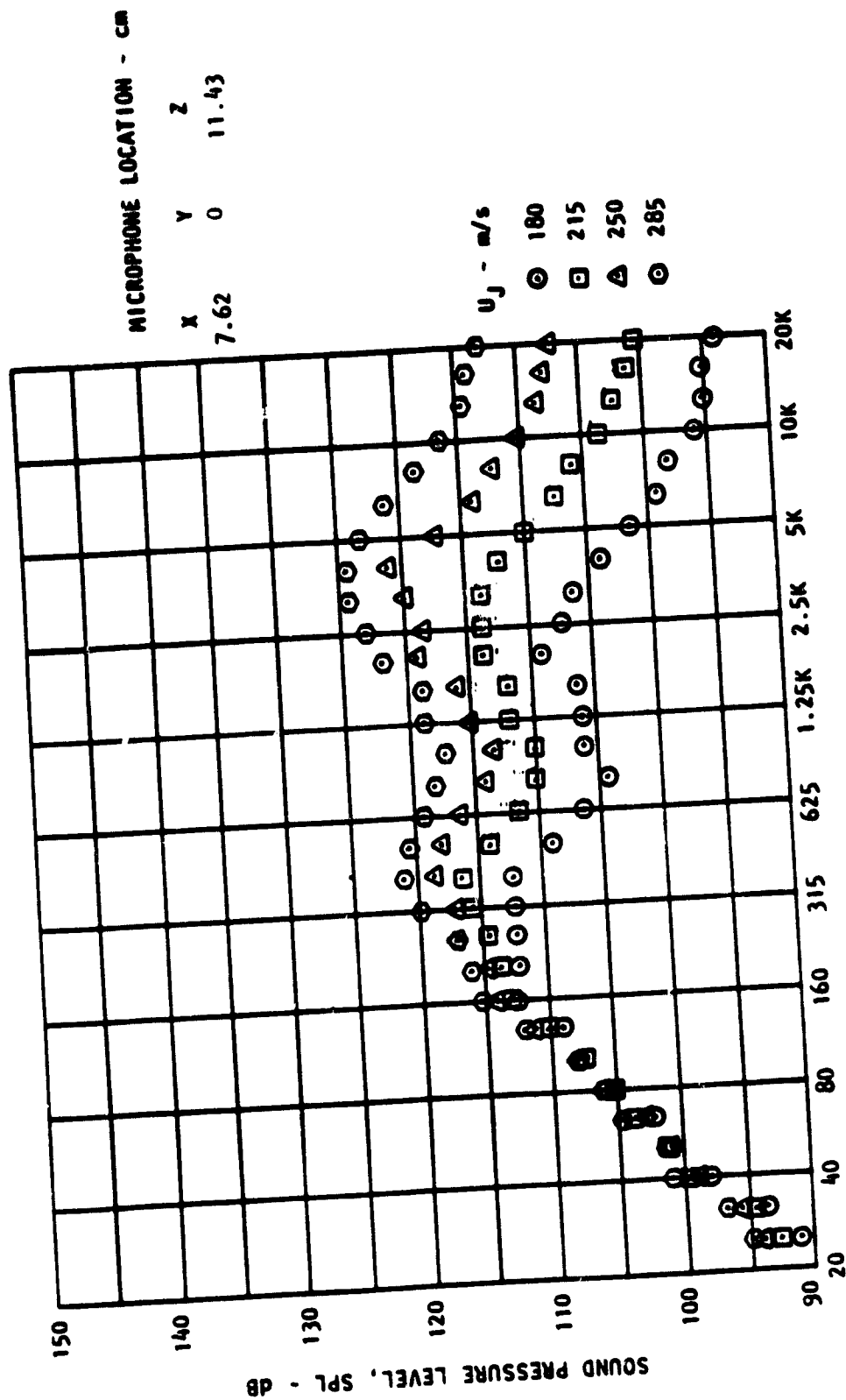


Figure D-1. Continued.
(E) Microphone 5.

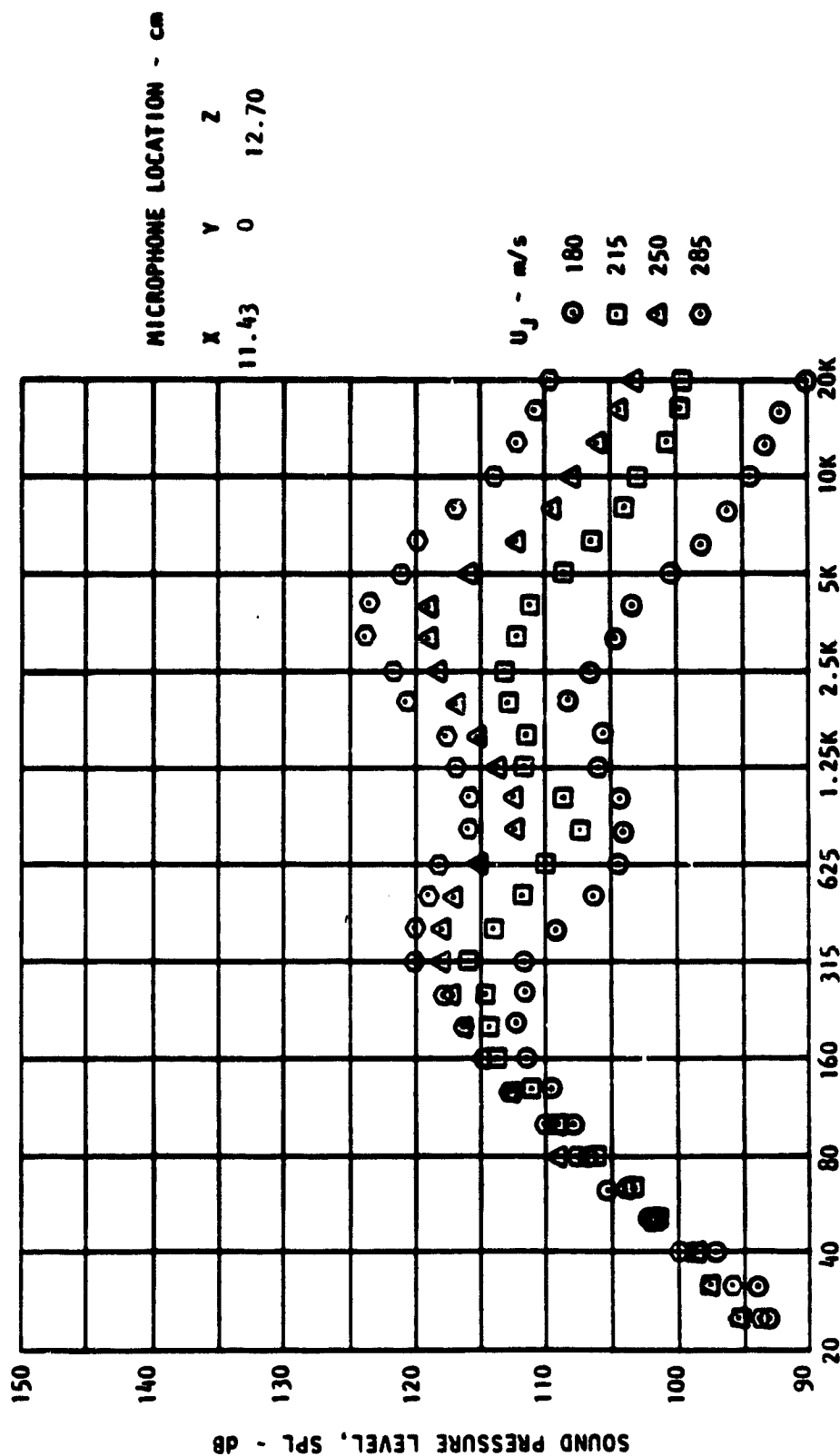


Figure D-1. Continued.

(F) Microphone 6.

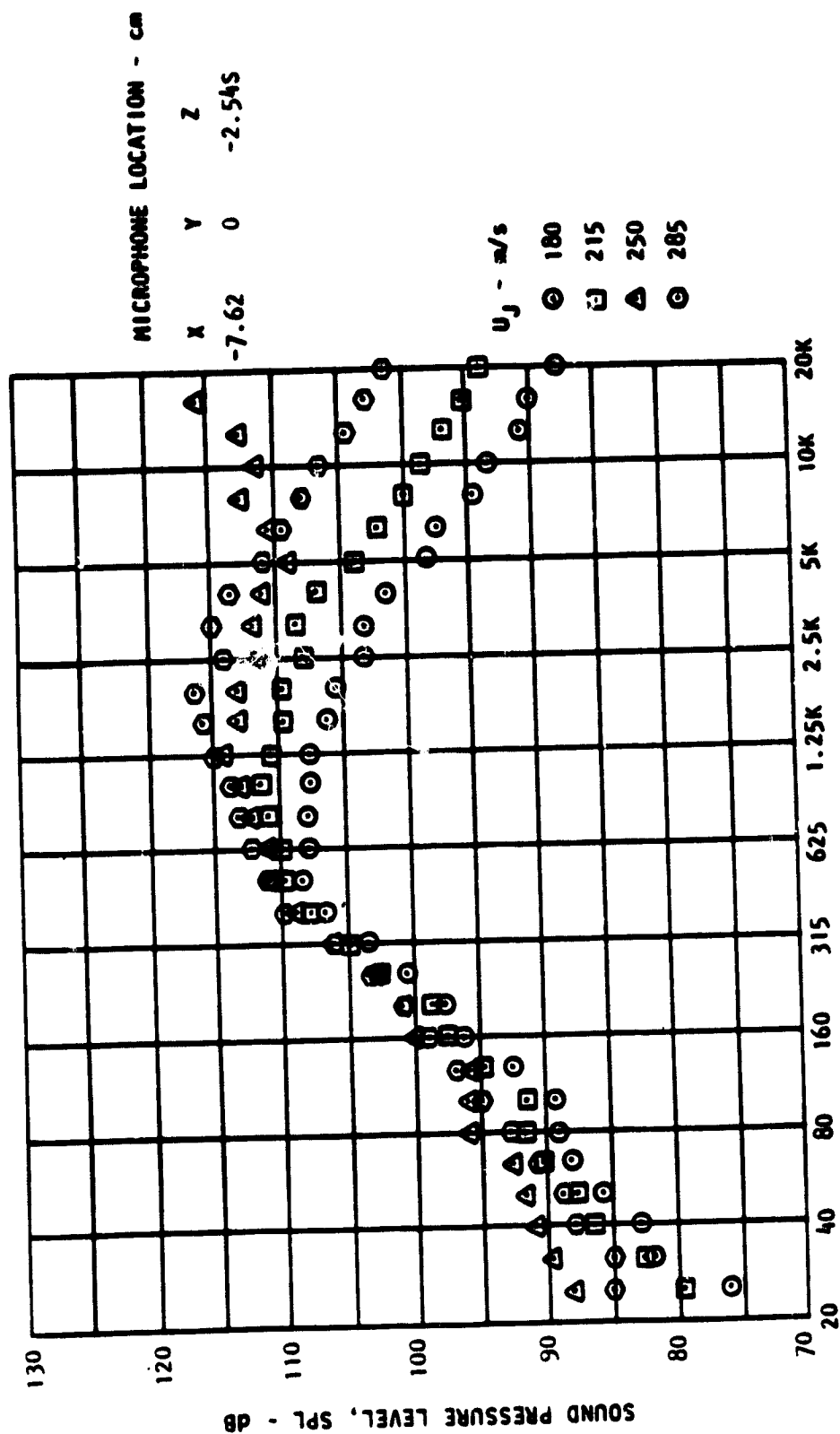


Figure D-1, Continued.

(G) Microphone 7.

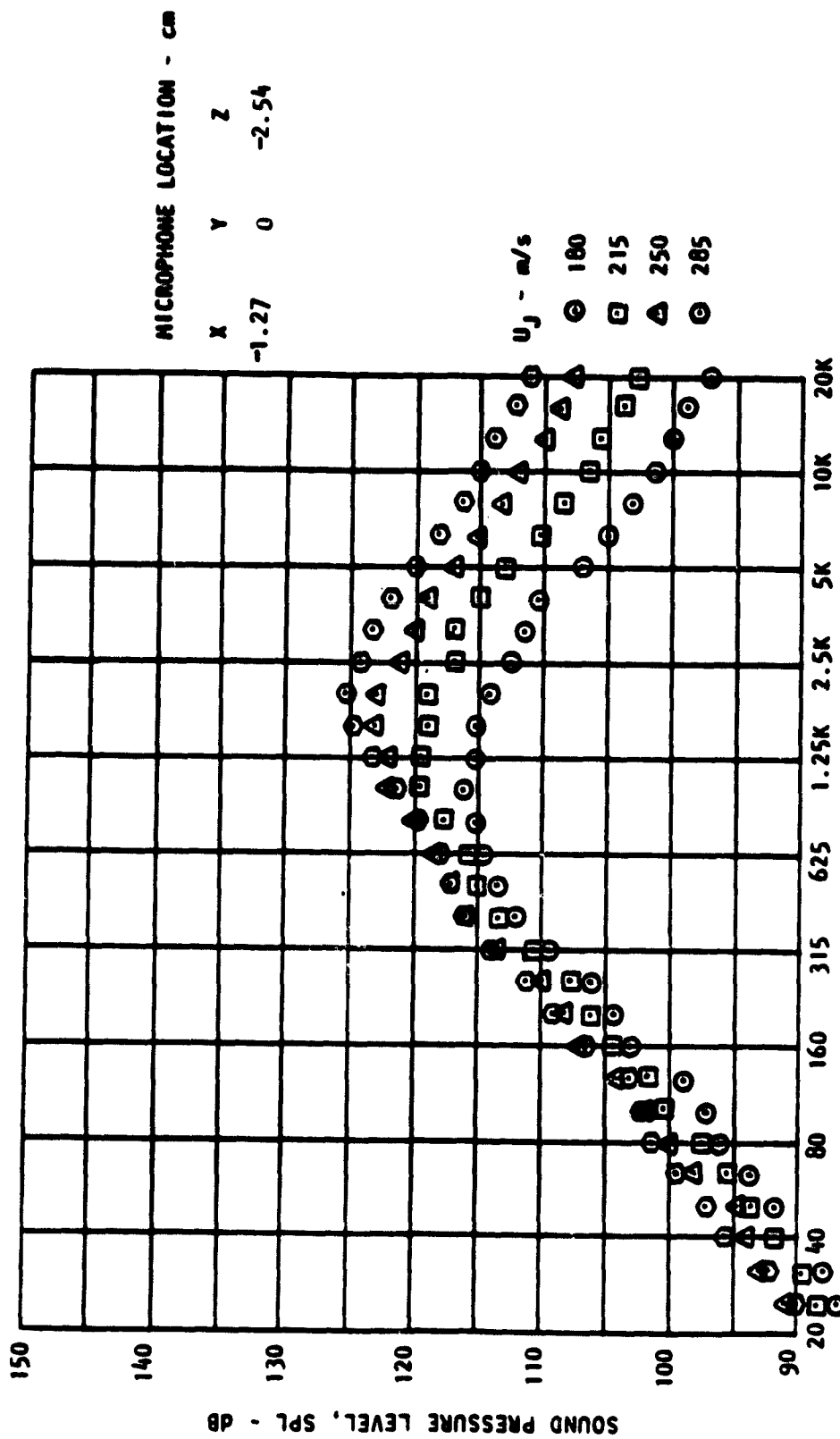


Figure D-1. Continued.
(H) Microphone 8.

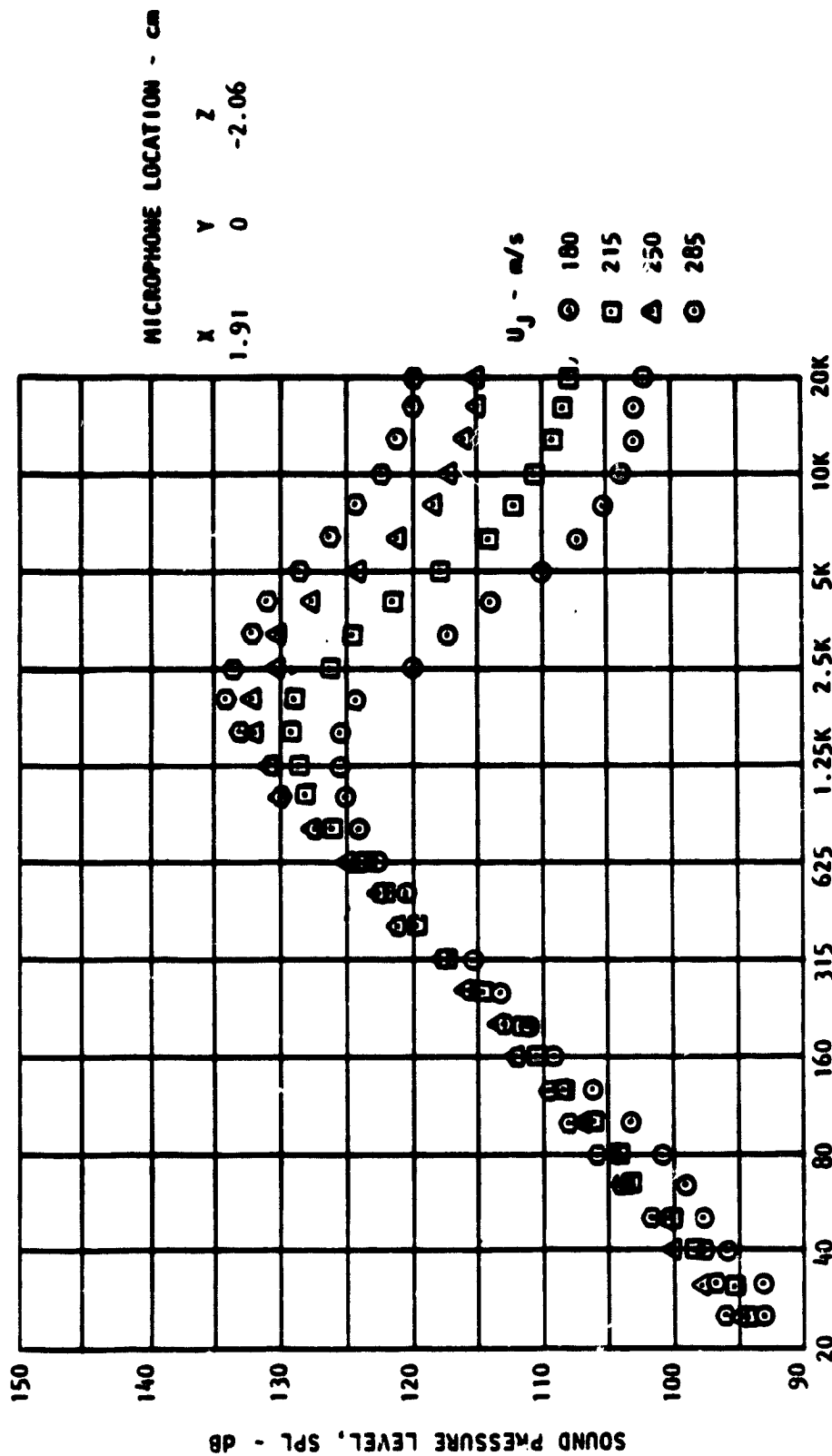


Figure D-1, Continued.
(1) Microphone 9.

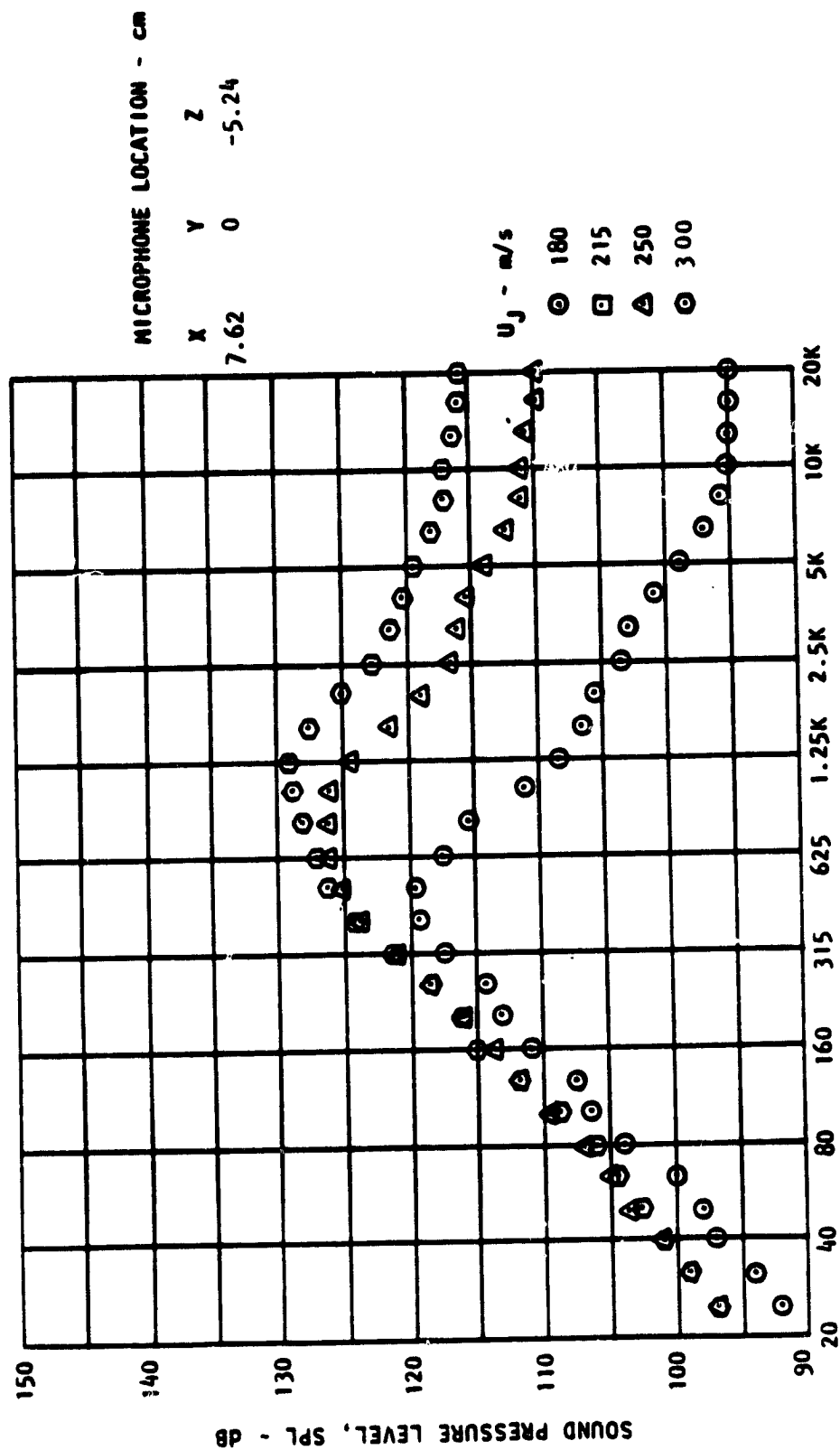


Figure D-1, Continued.
(J) Microphone 10.

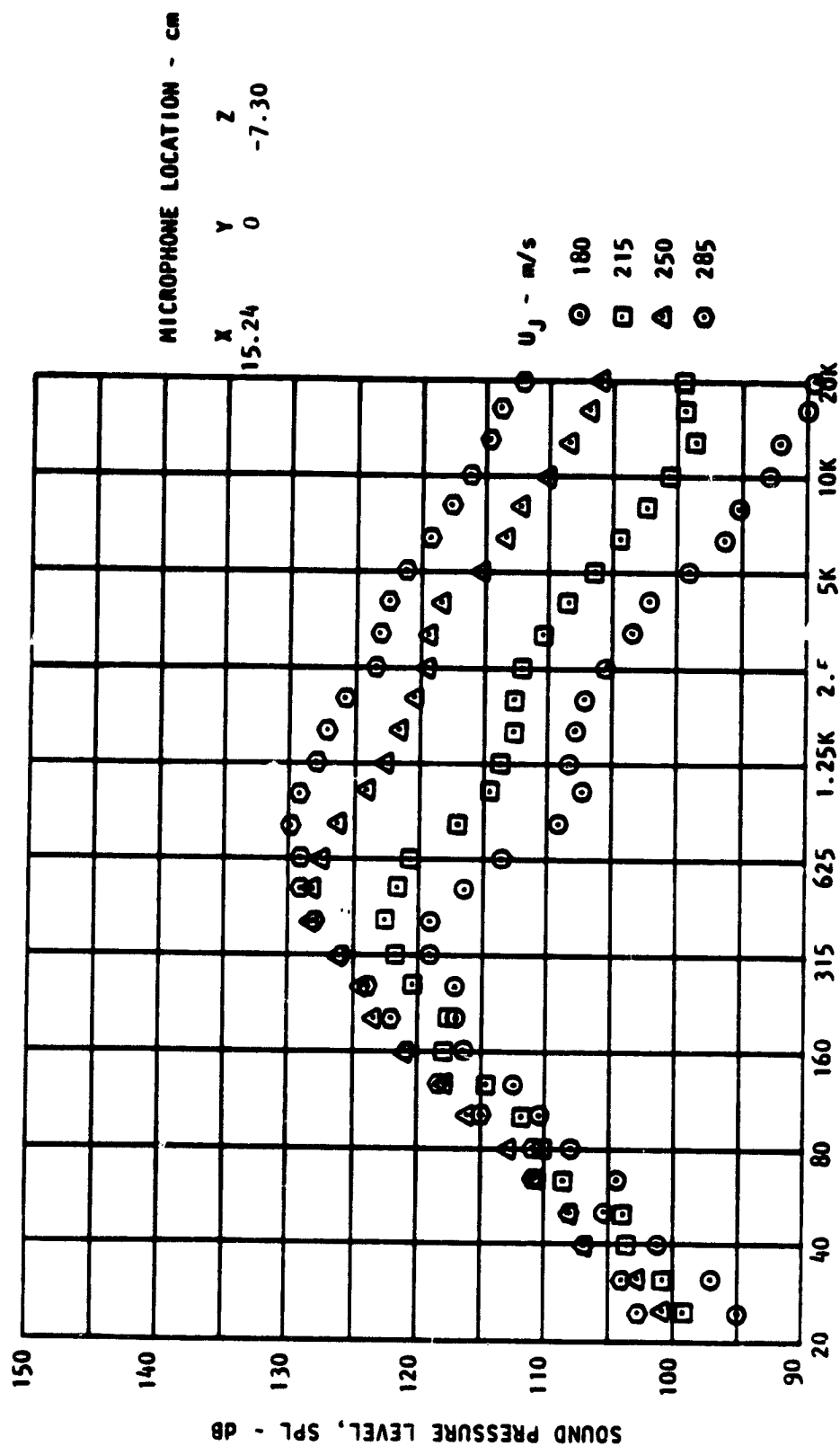


Figure D-1. Continued.

(K) Microphone 11.

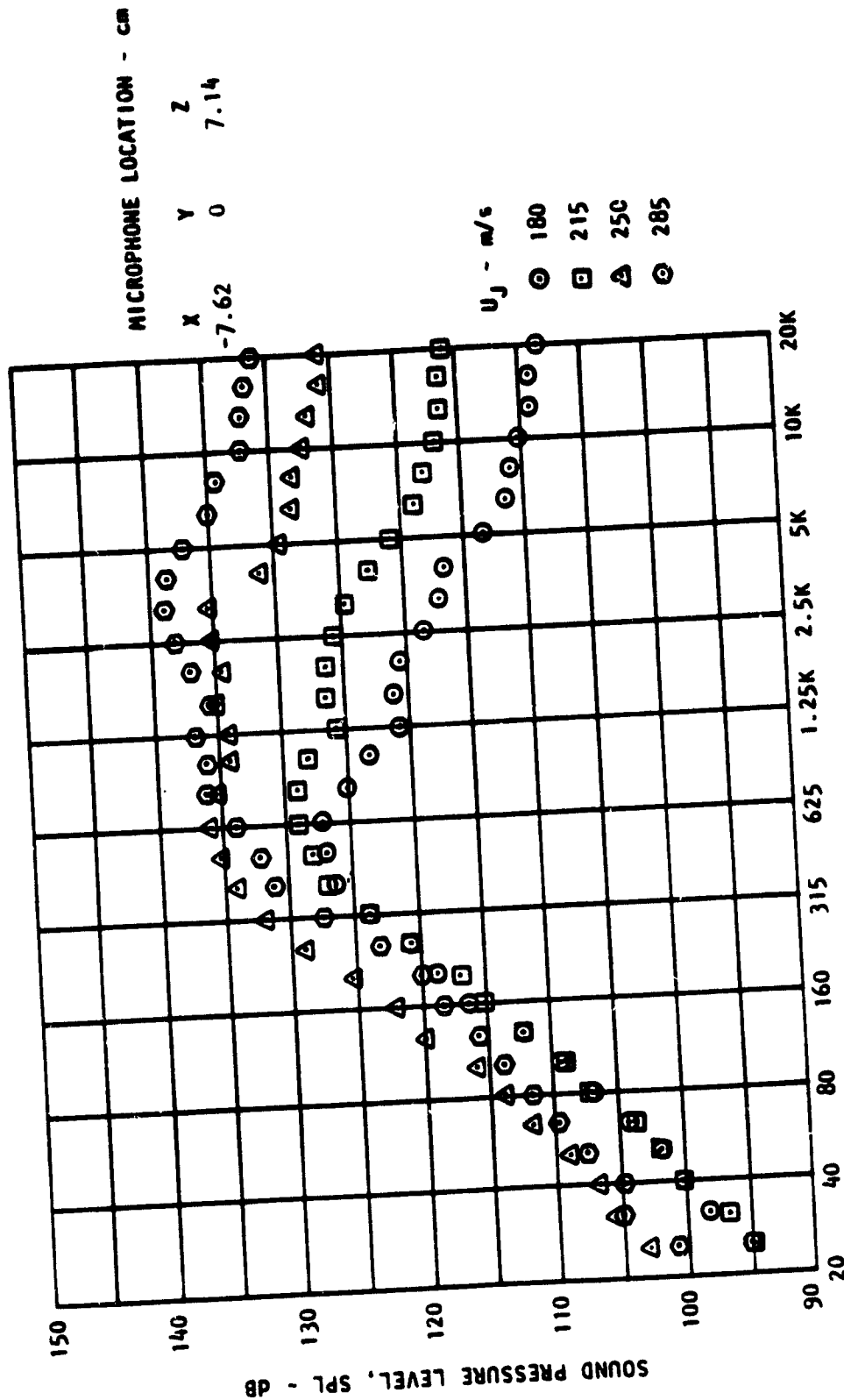


Figure D-1. Concluded.
(L) Microphone 12.

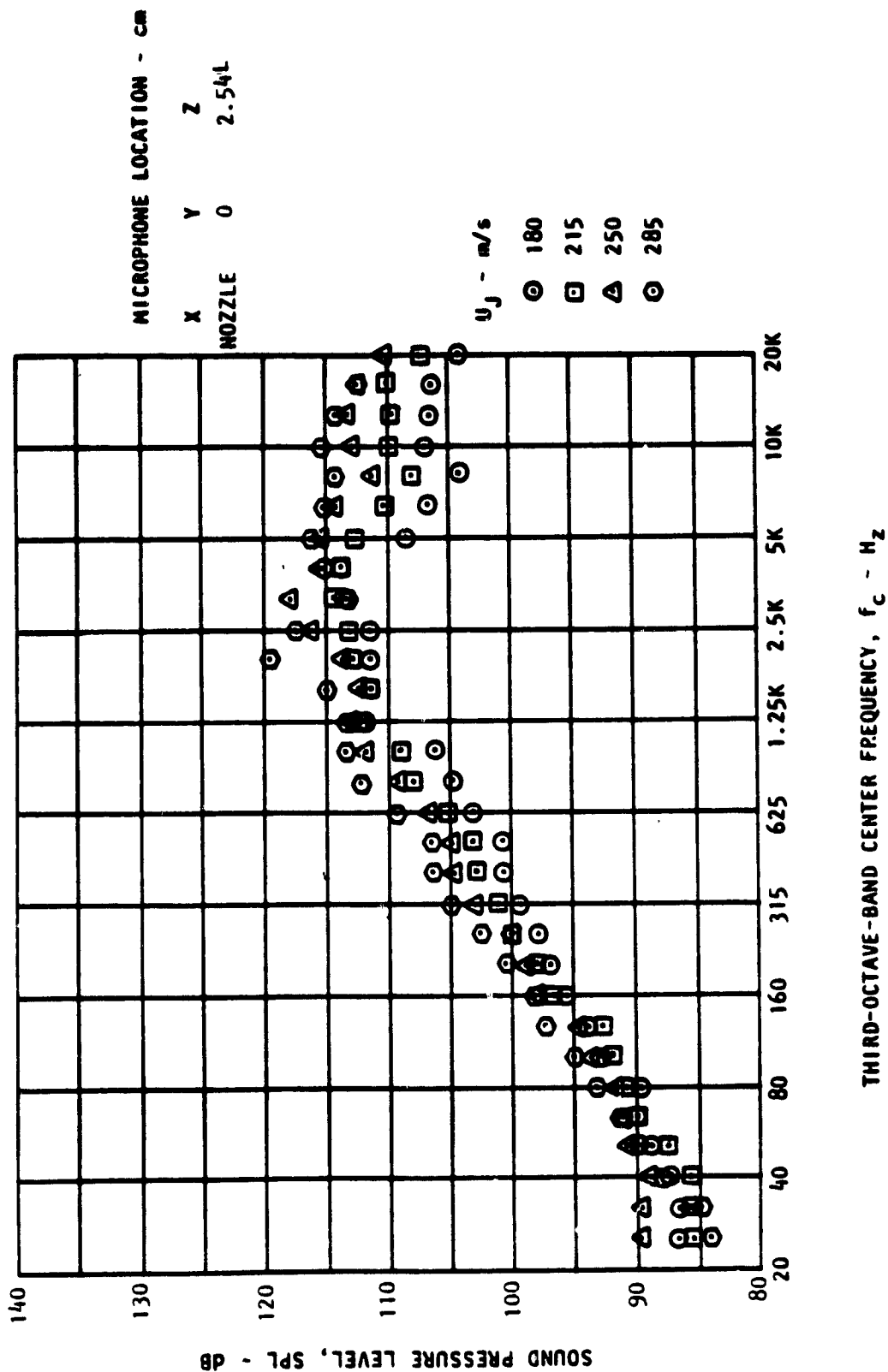


Figure D-2. Near-Field Spectra; $\delta f = 60^\circ$, No Screen
(A) Microphone 1.

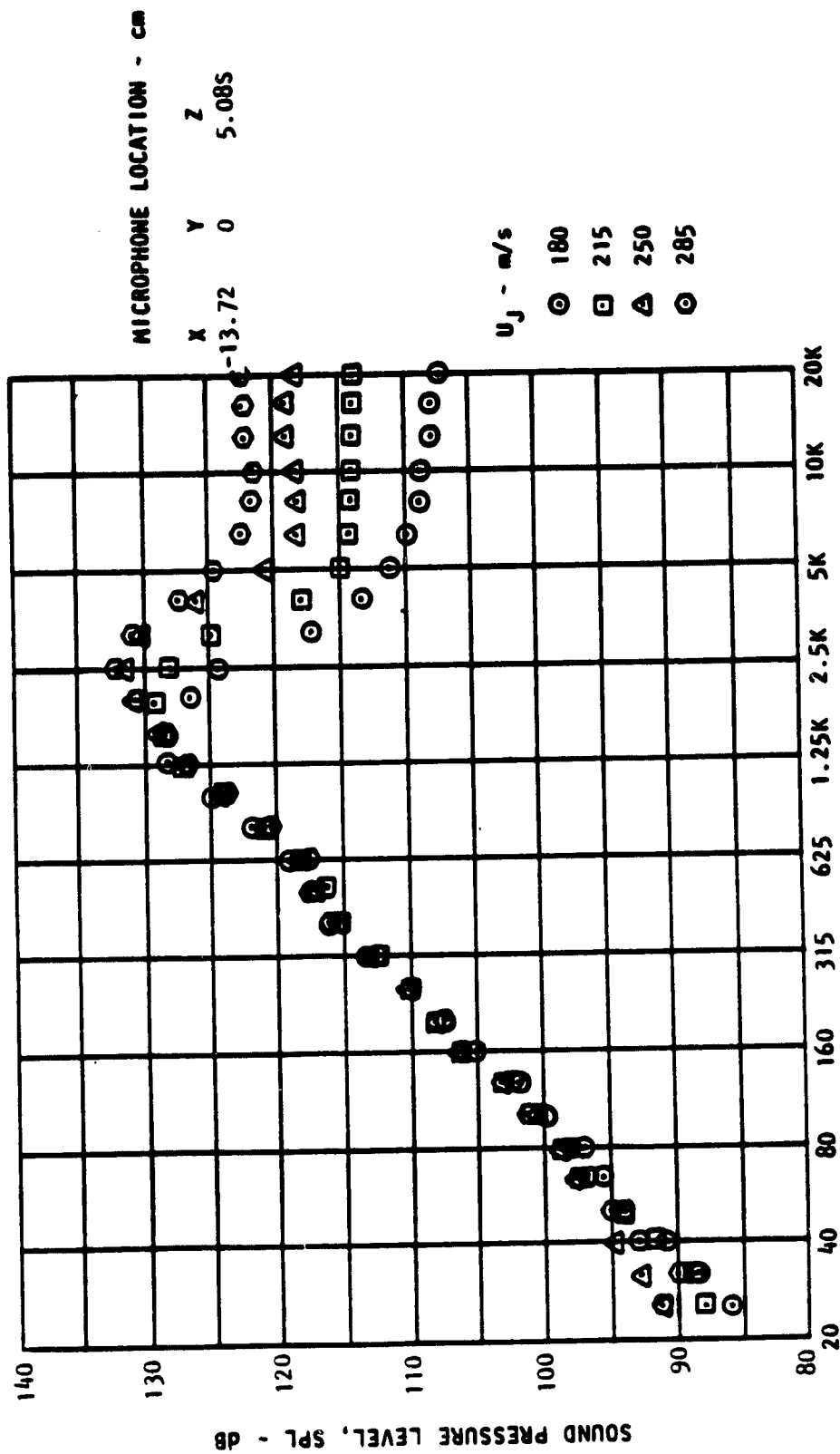


Figure D-2. Continued.

(B) Microphone 2.

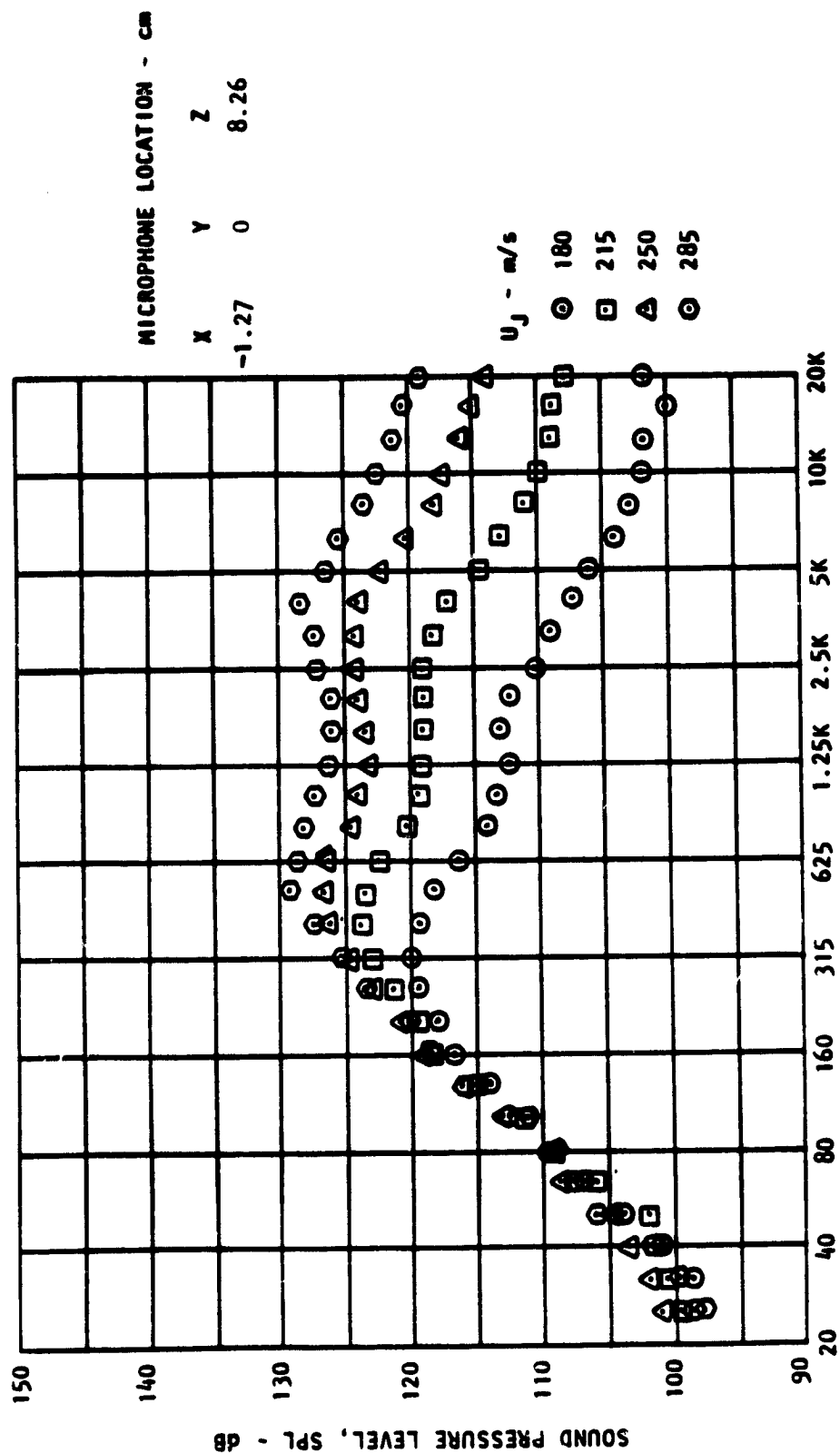


Figure D-2. Continued.
(C) Microphone 3.

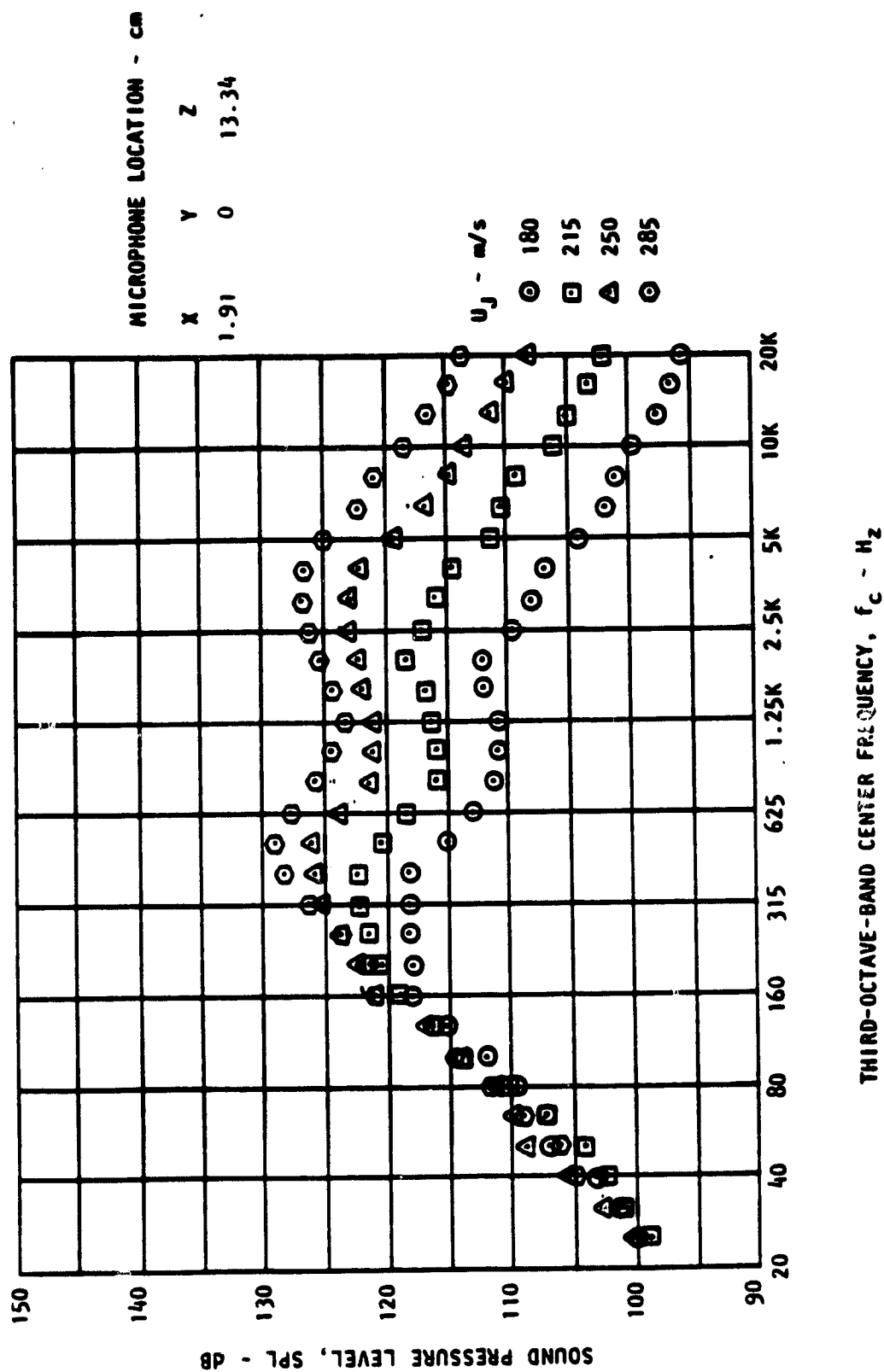


Figure D-2. Continued.
(D) Microphone 4.

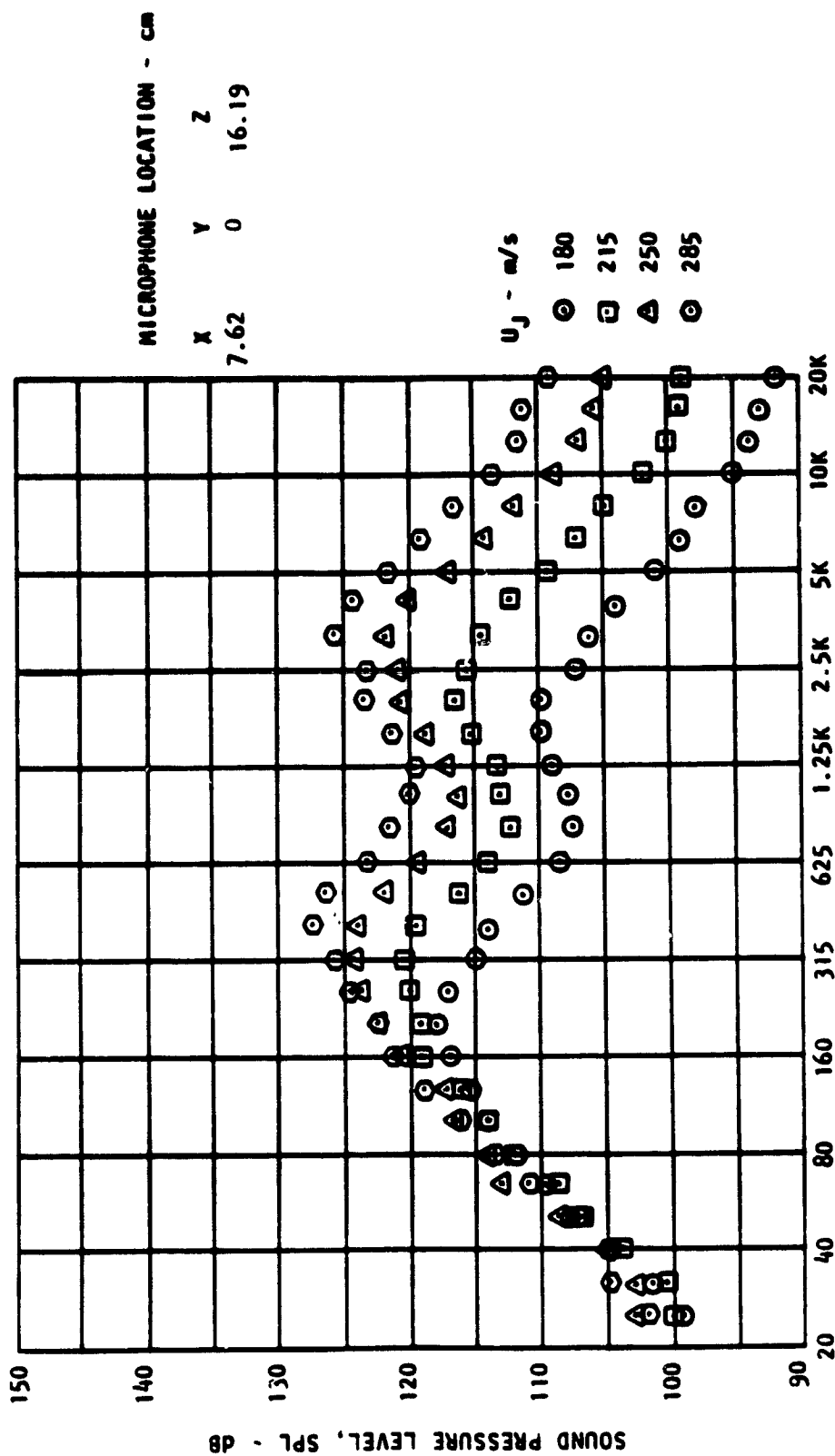


Figure D-2, Continued.
(E) Microphone 5.

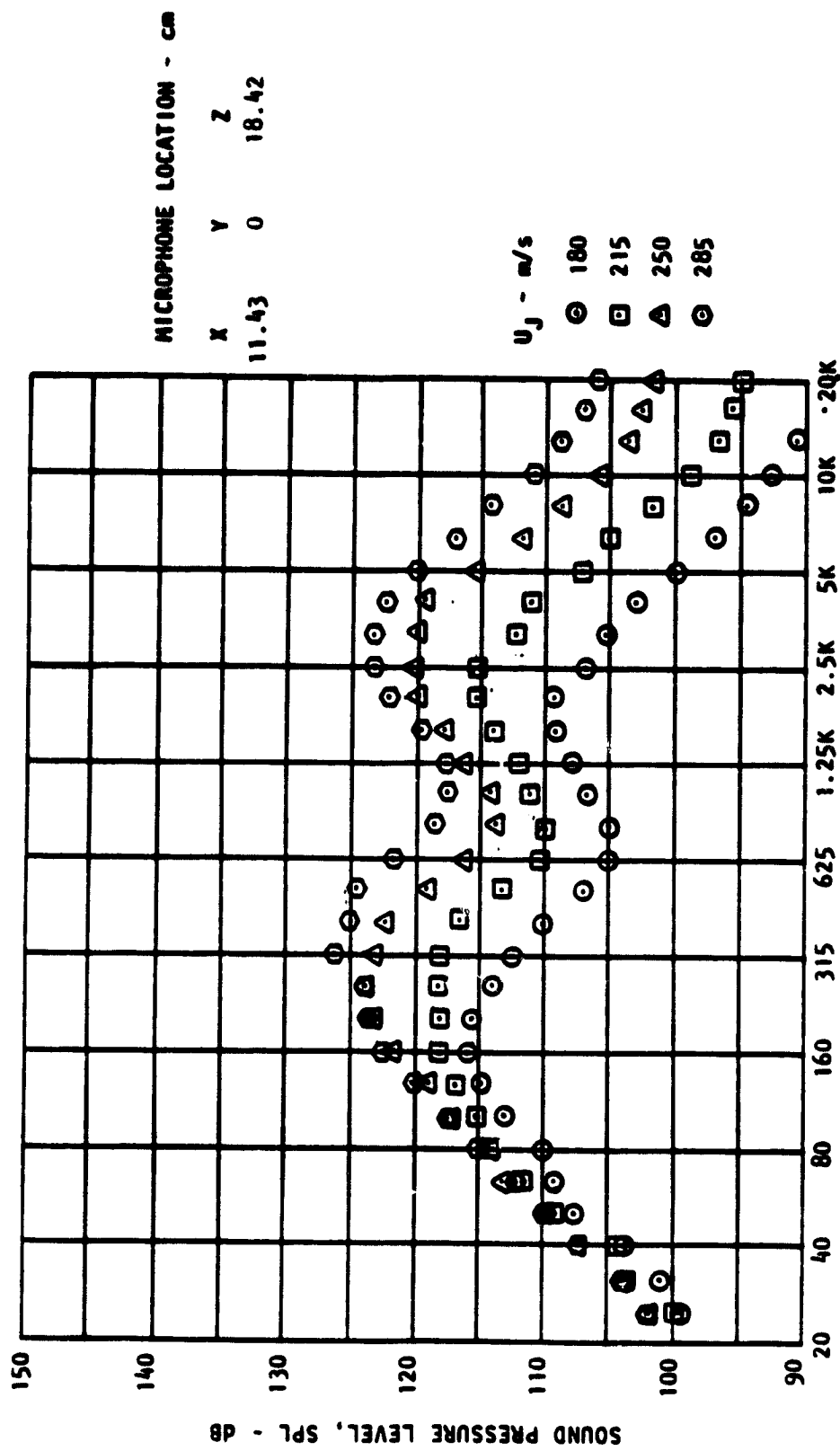


Figure D-2. Continued.
(F) Microphone 6.

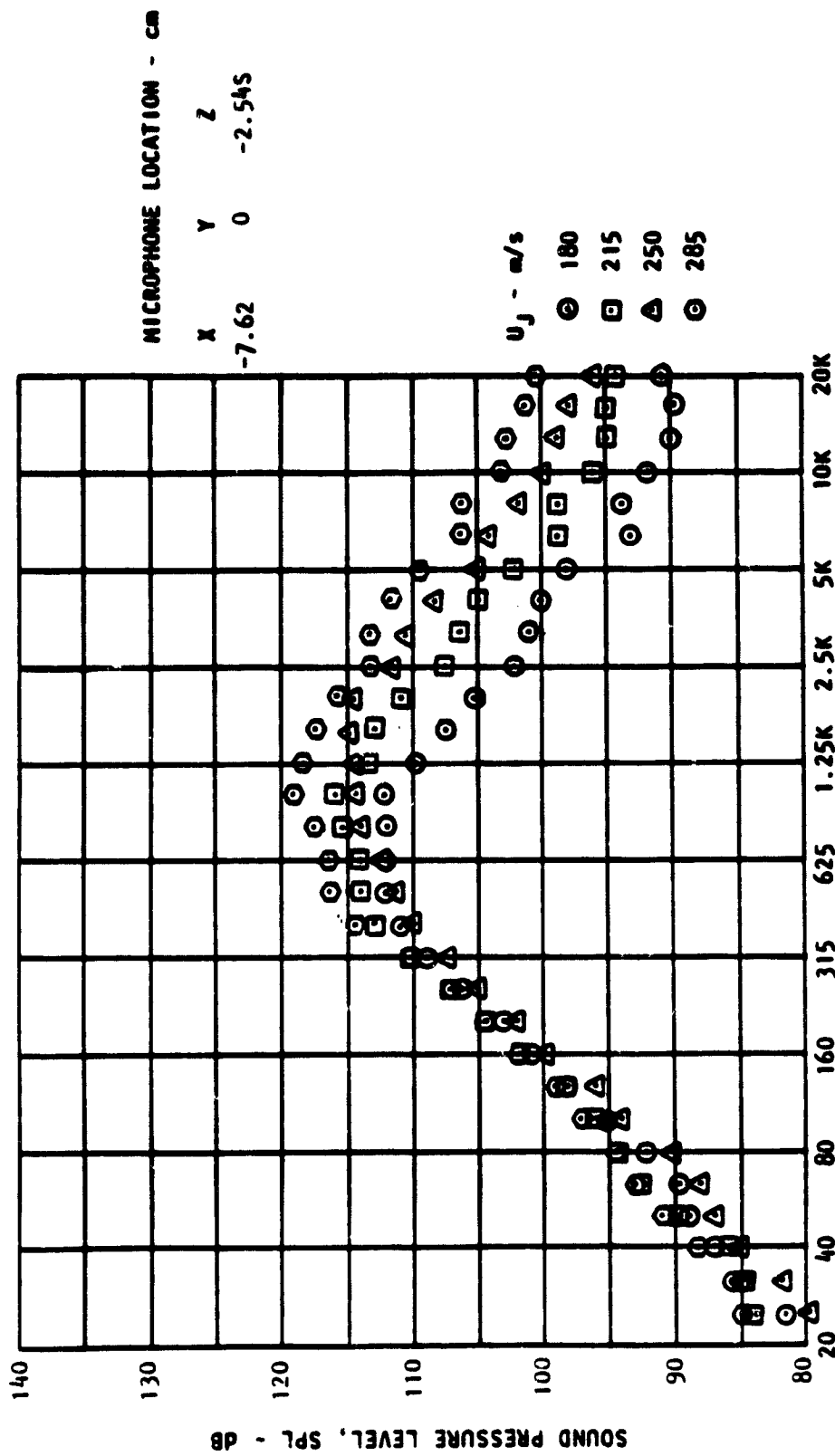


Figure D-2, Continued.
(G) Microphone 7.

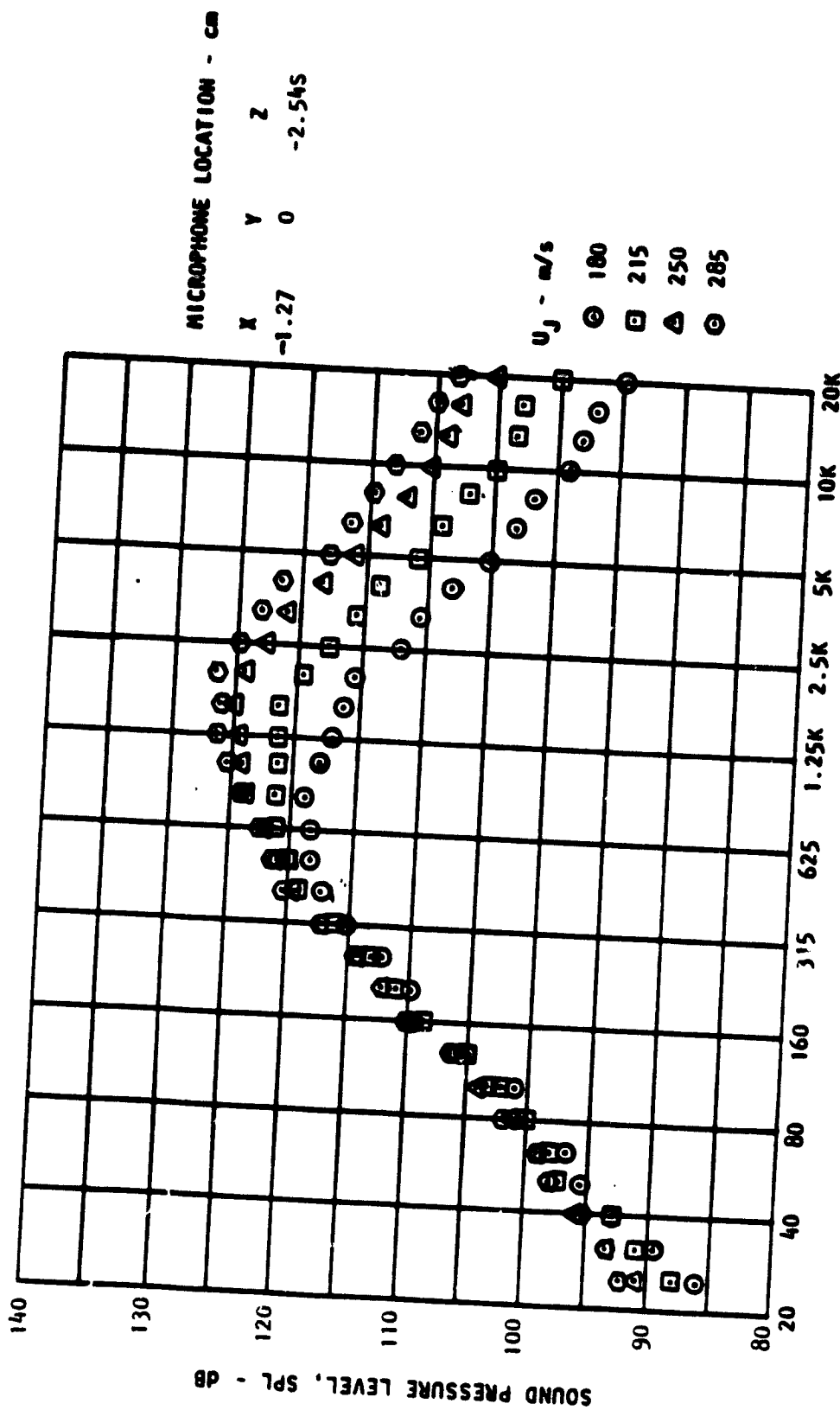


Figure D-2, Continued.

(H) Microphone 8.

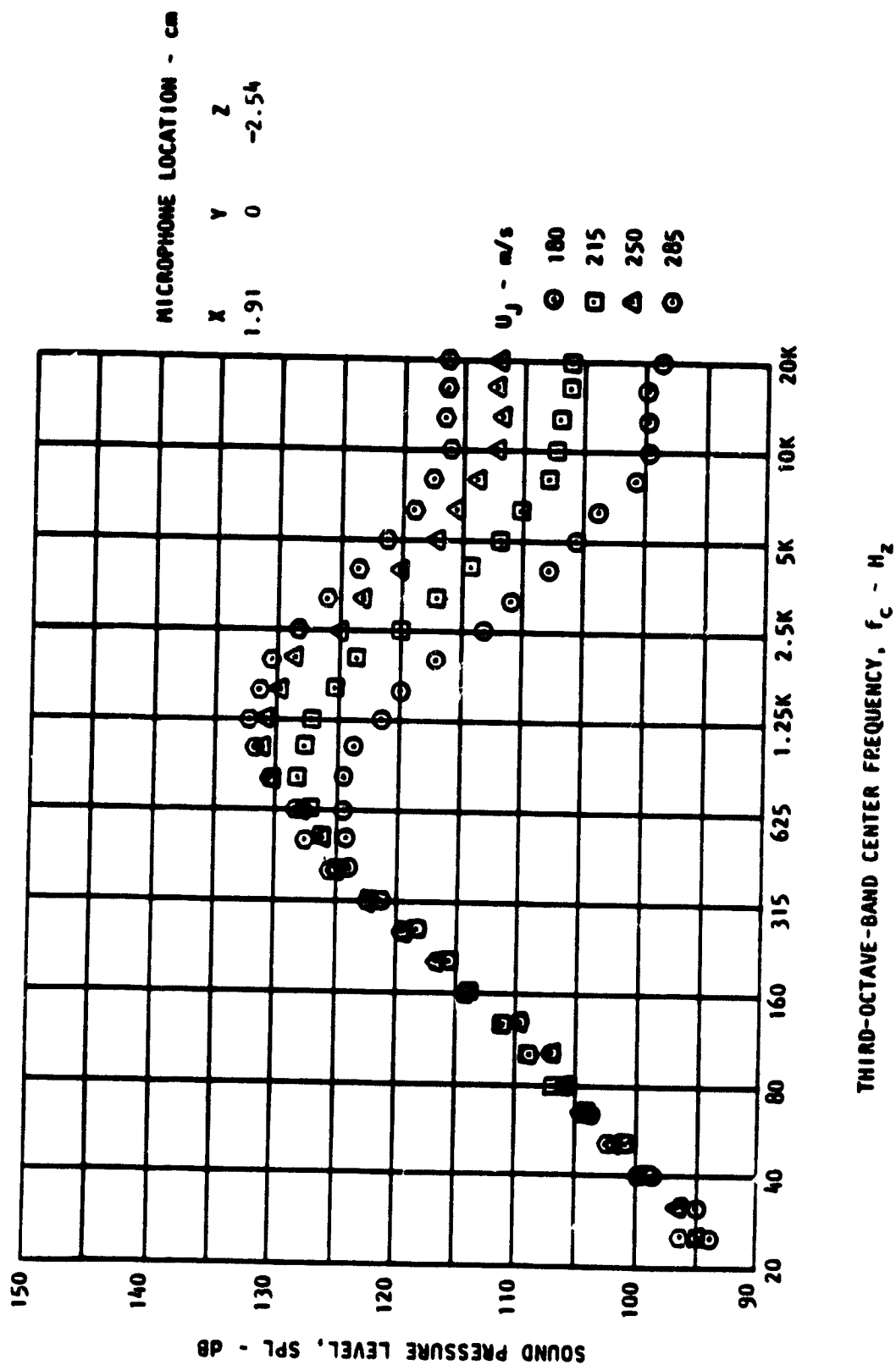


Figure D-2. Continued.

(1) Microphone 9.

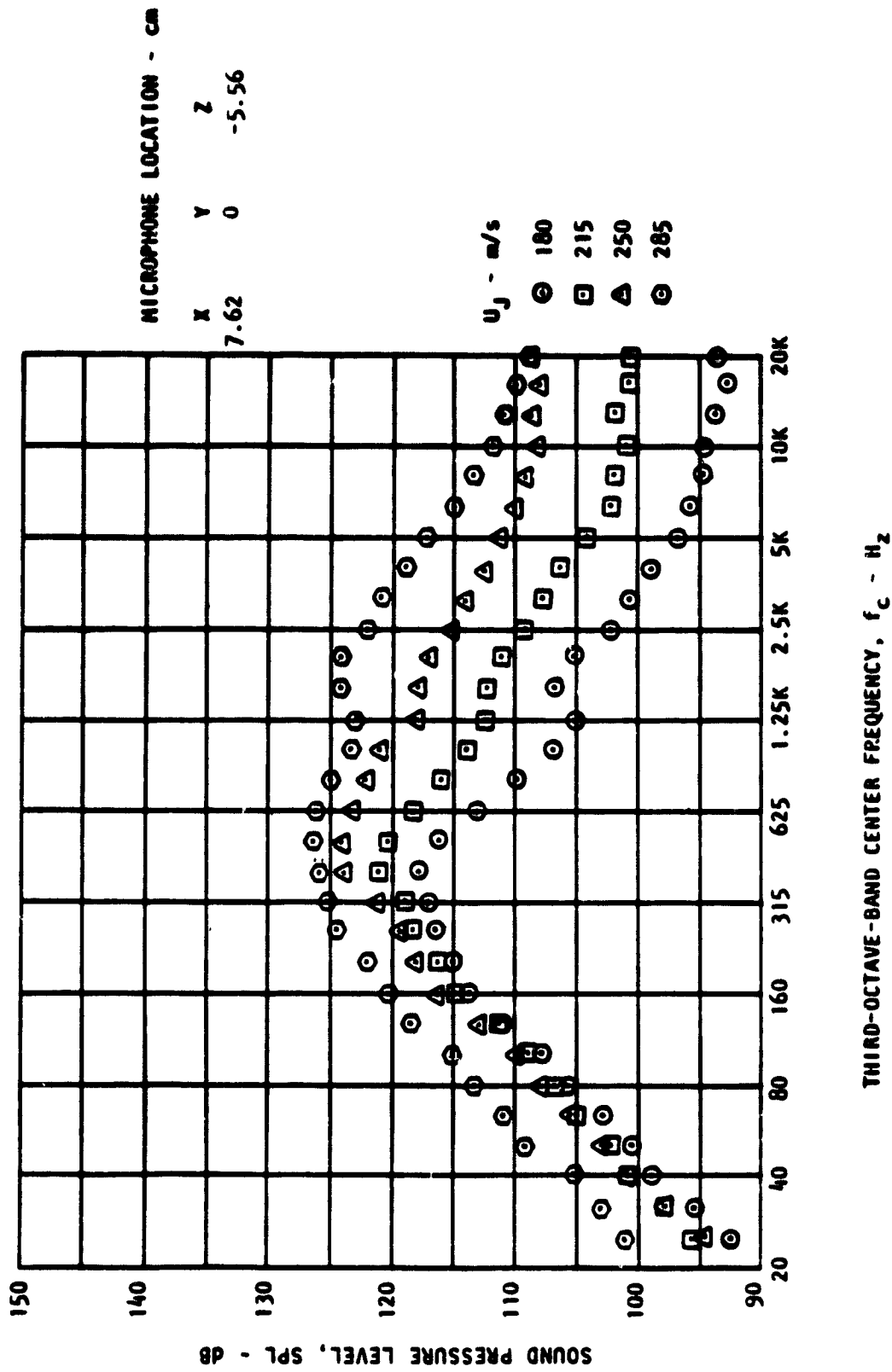


Figure D-2. Continued.
(J) Microphone 10.

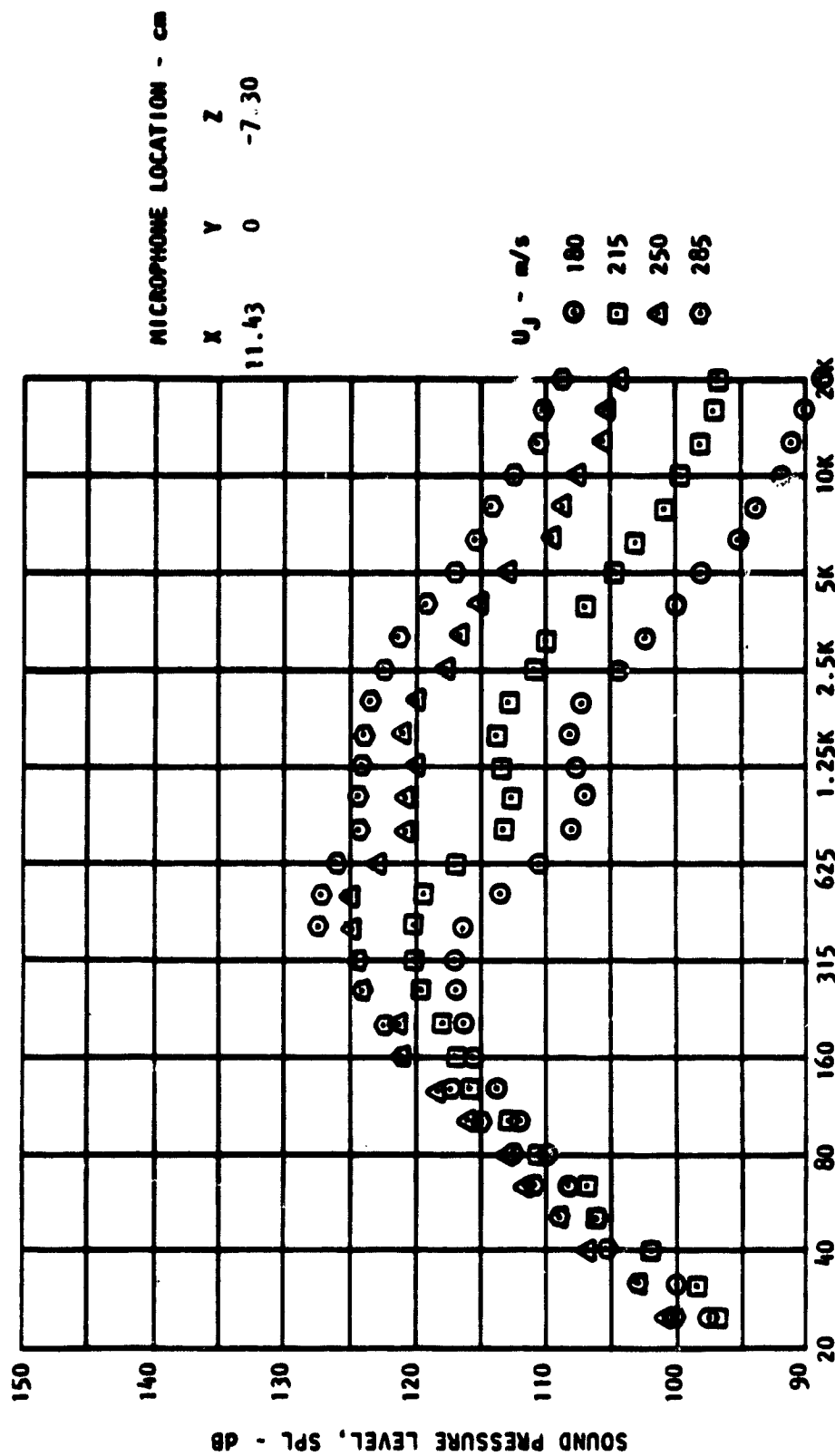


Figure D-2, Continued.

(K) Microphone 11.

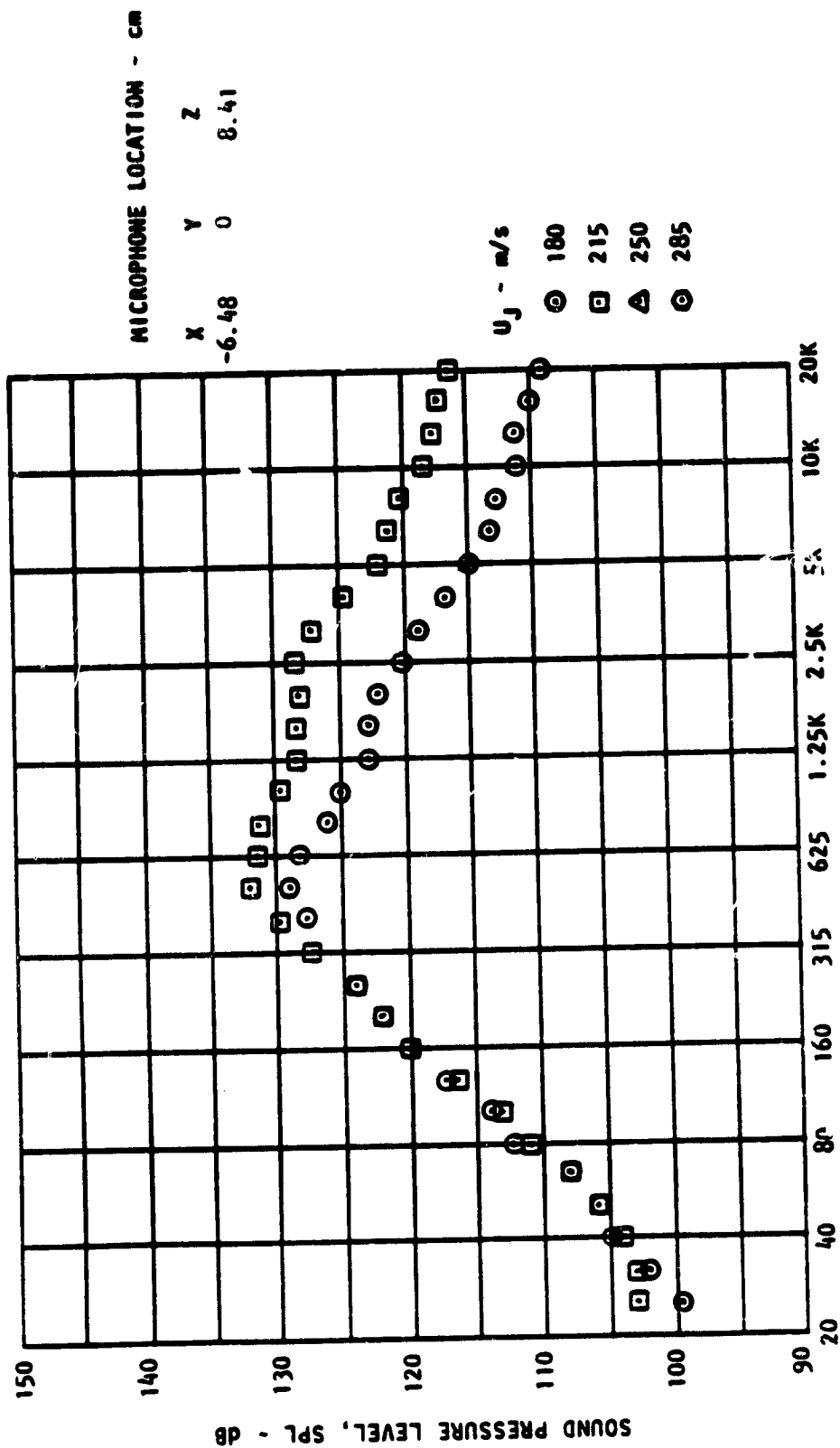


Figure D-2. Continued.
(L) Microphone 12.

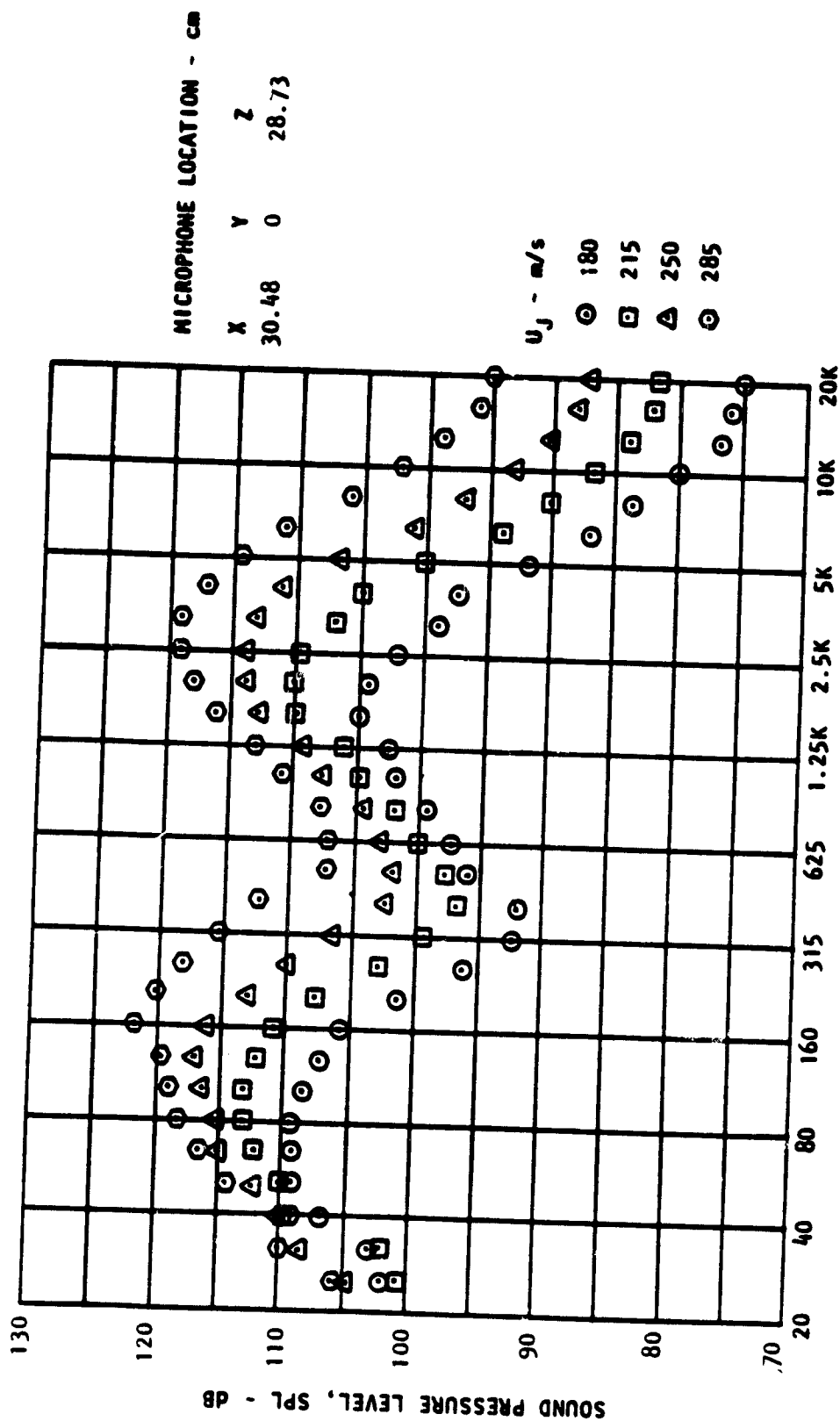


Figure D-2, Continued.
(M) Microphone 1A.

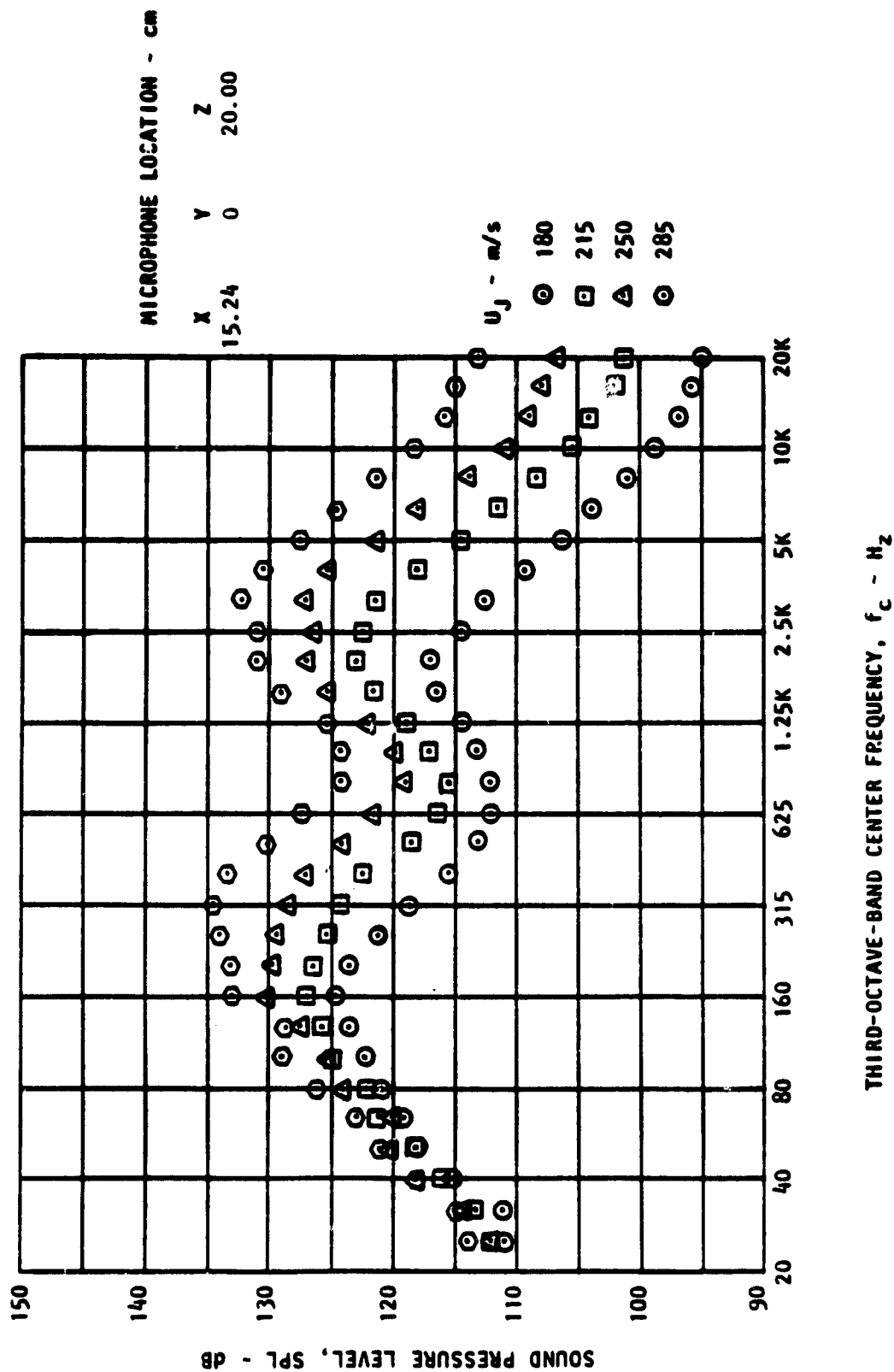


Figure D-2. Continued.
(N) Microphone 2A.

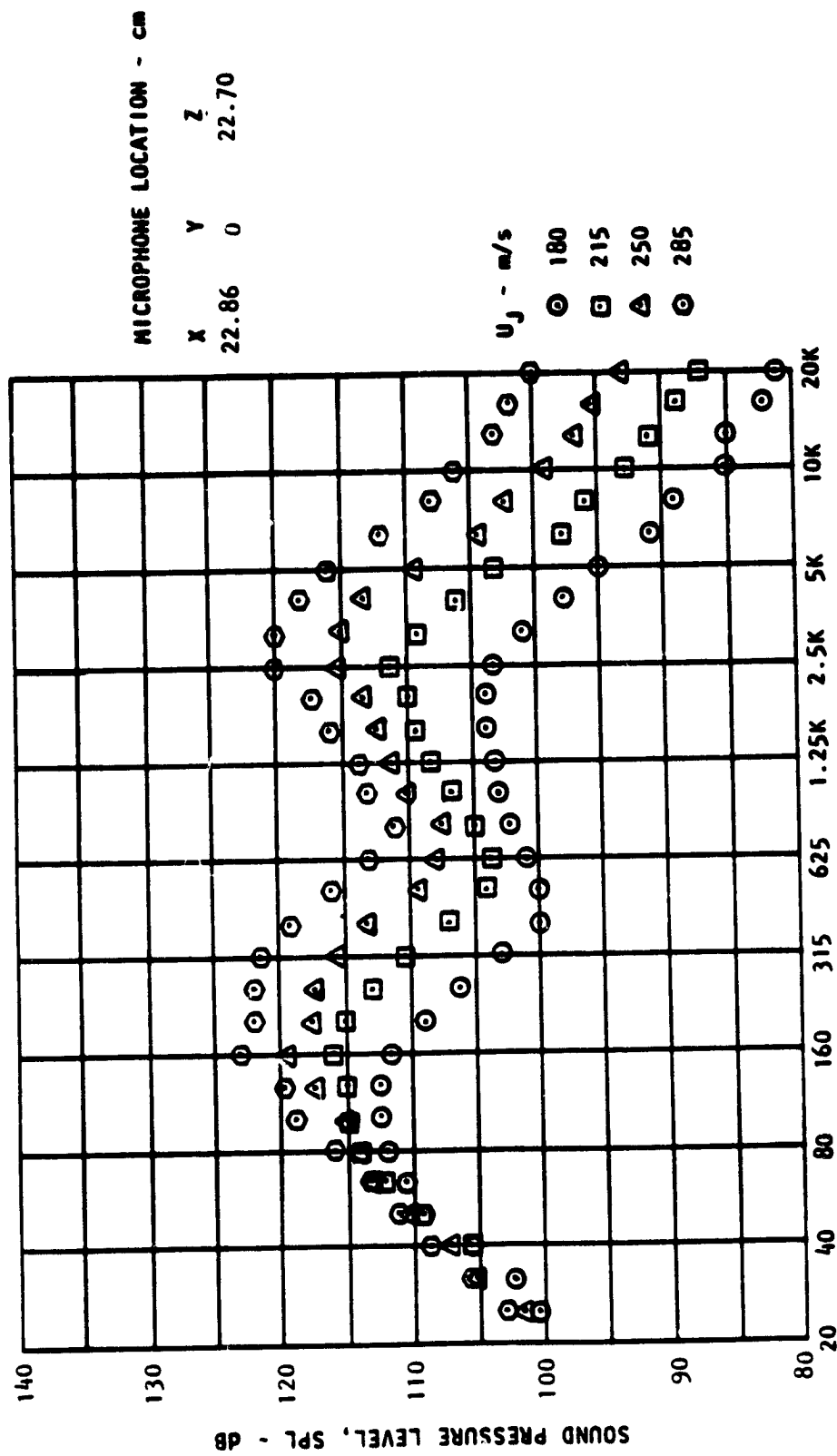


Figure D-2. Continued.
(O) Microphone 6A.

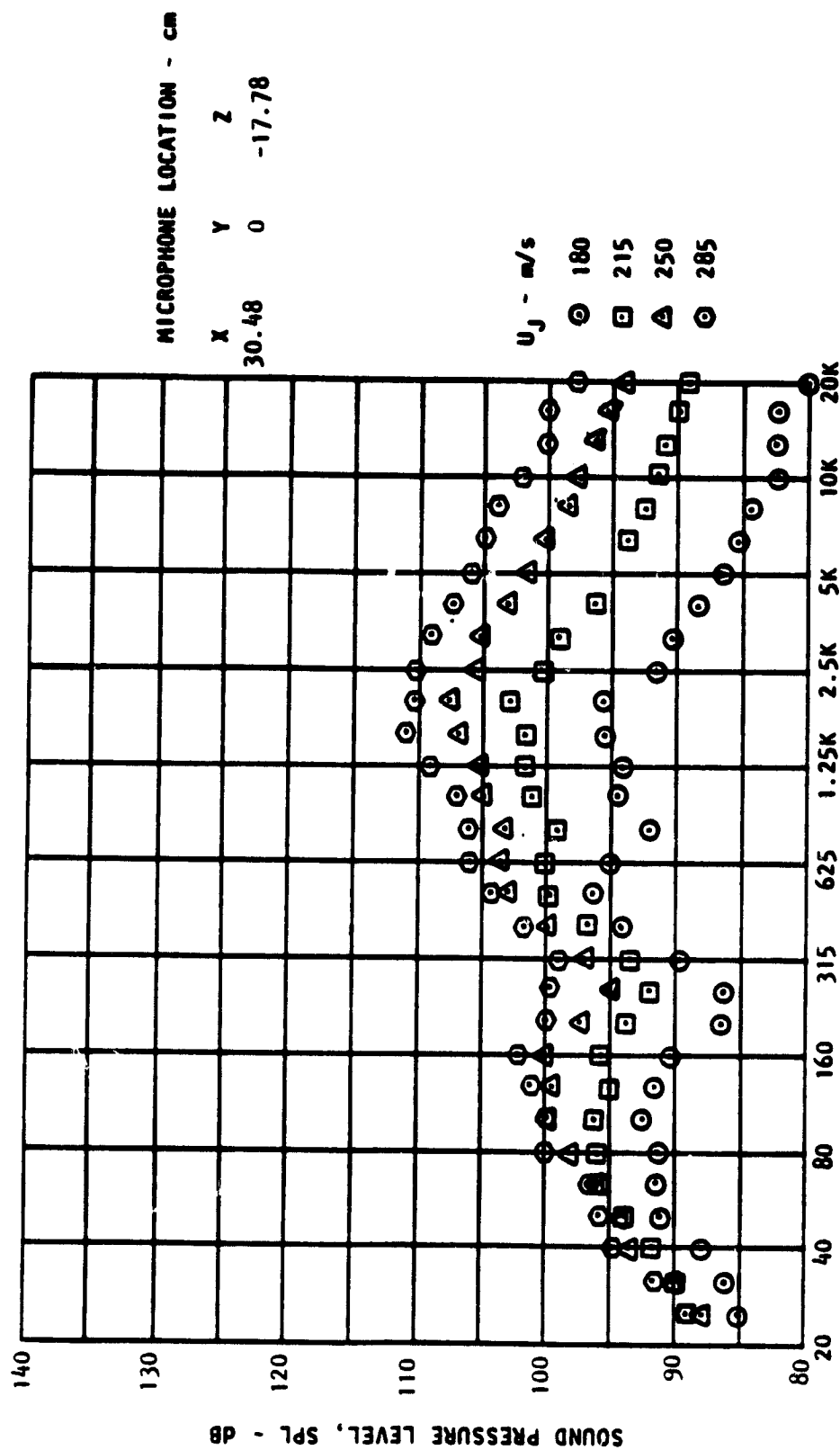


Figure D-2. Continued.
(P) Microphone 7A.

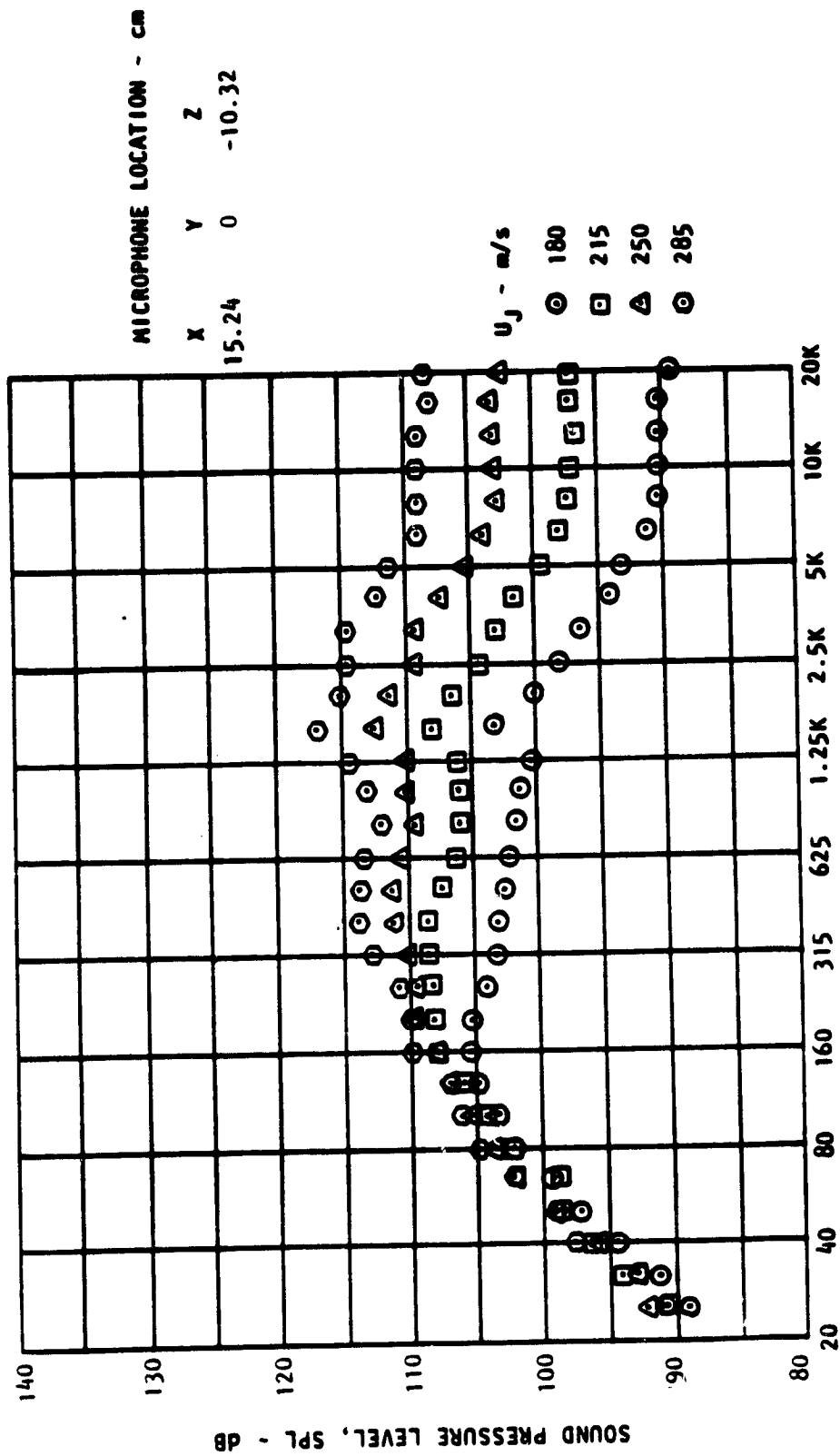
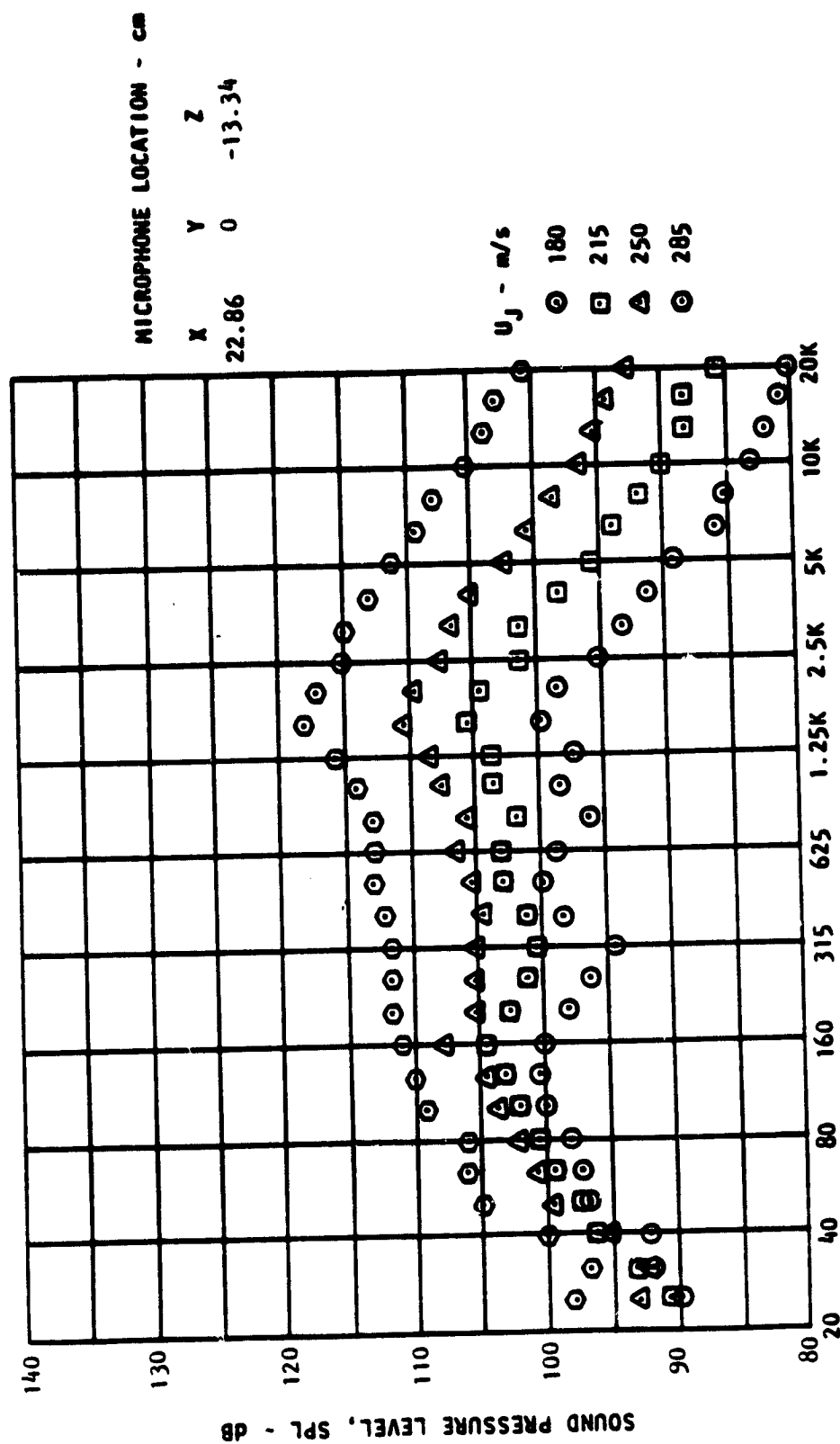


Figure D-2. Continued.
(Q) Microphone 10A.



THIRD-OCTAVE-BAND CENTER FREQUENCY, f_c - Hz

Figure D-2. Concluded.

(R) Microphone 11A.

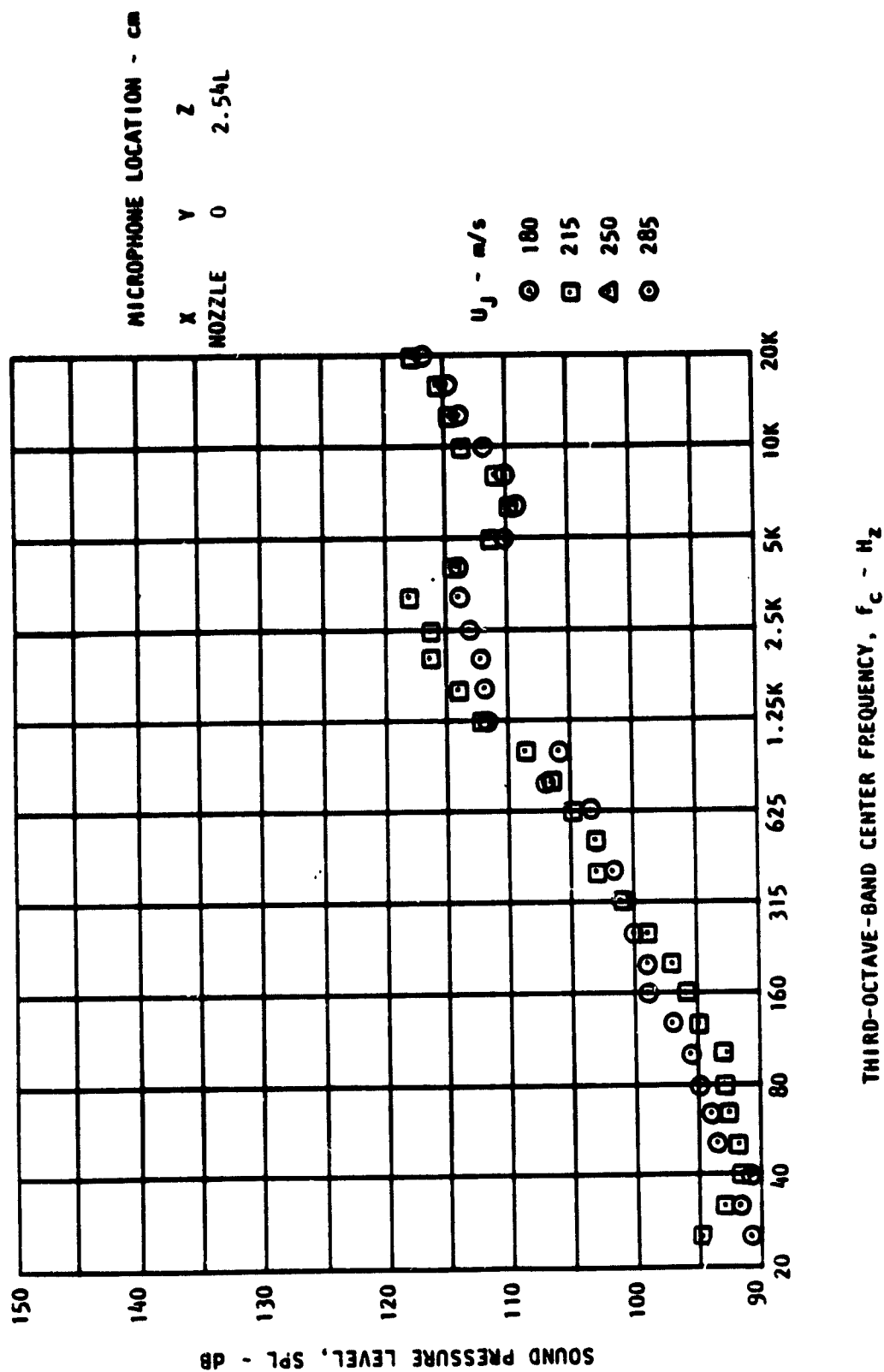


Figure D-3. Near-Field Spectra; $\delta_f = 30^\circ$, Screen
(A) Microphone 1.

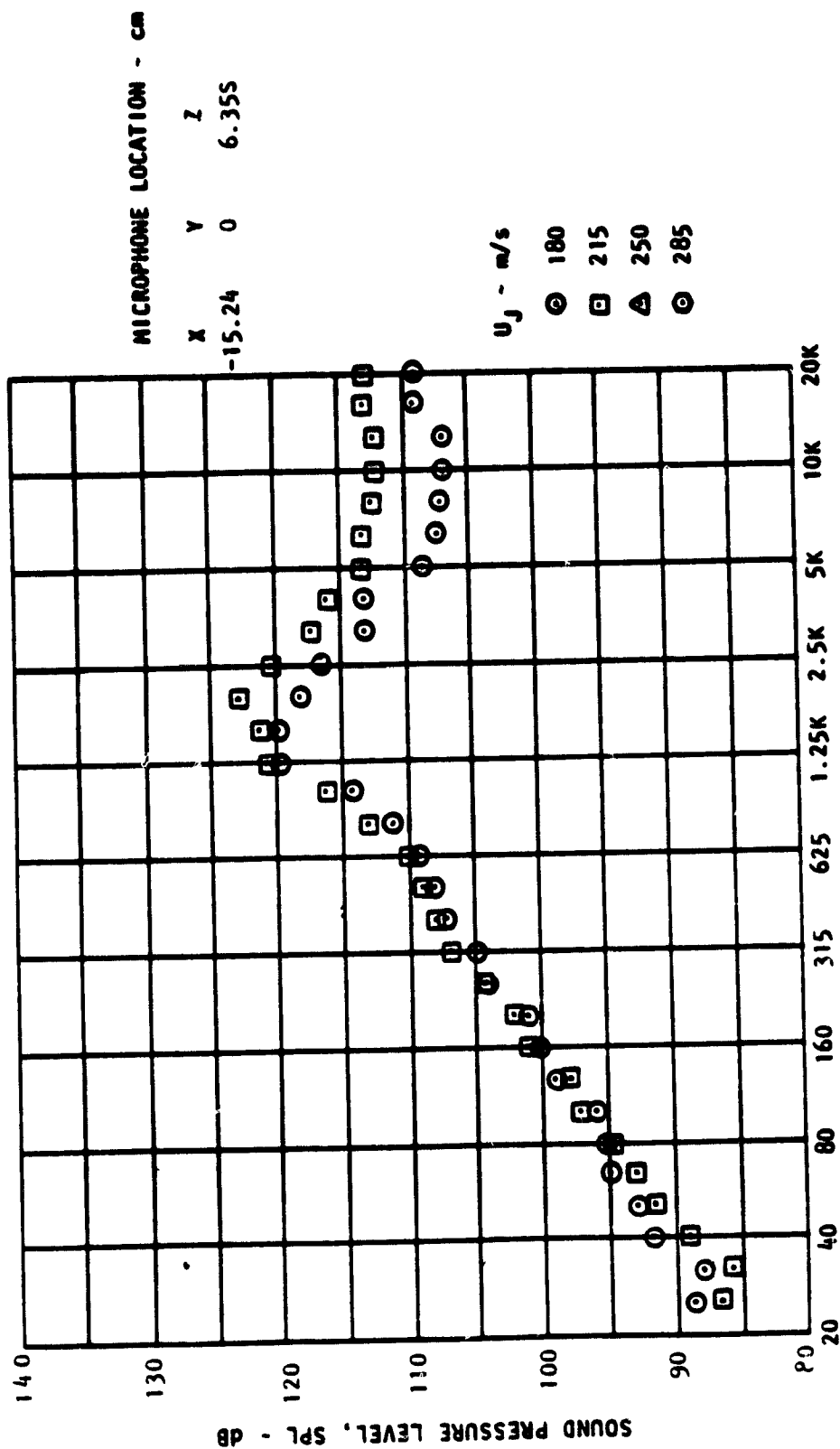


Figure D-3. Continued.

(B) Microphone 2.

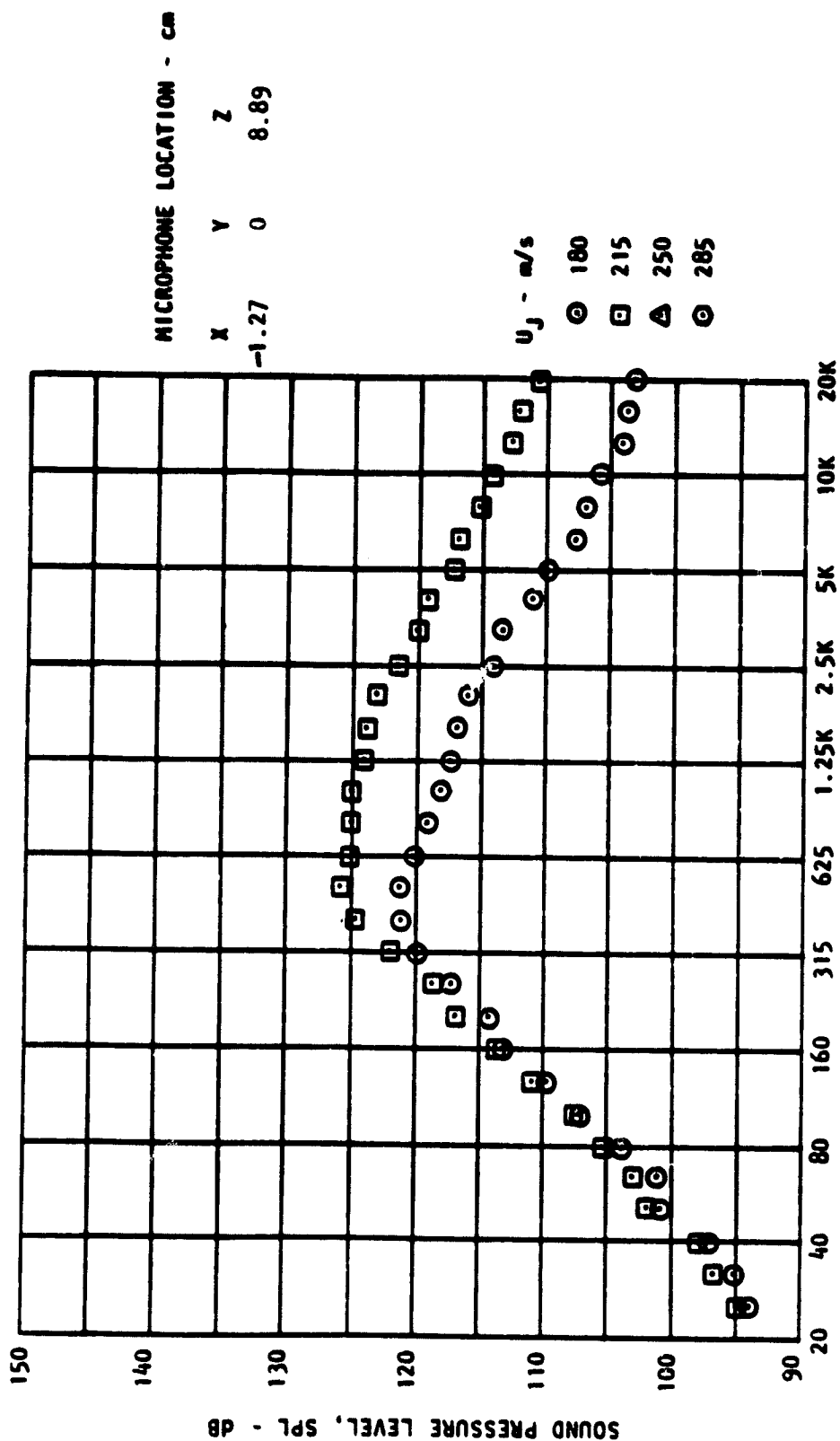


Figure D-3. Continued.
(C) Microphone 3.

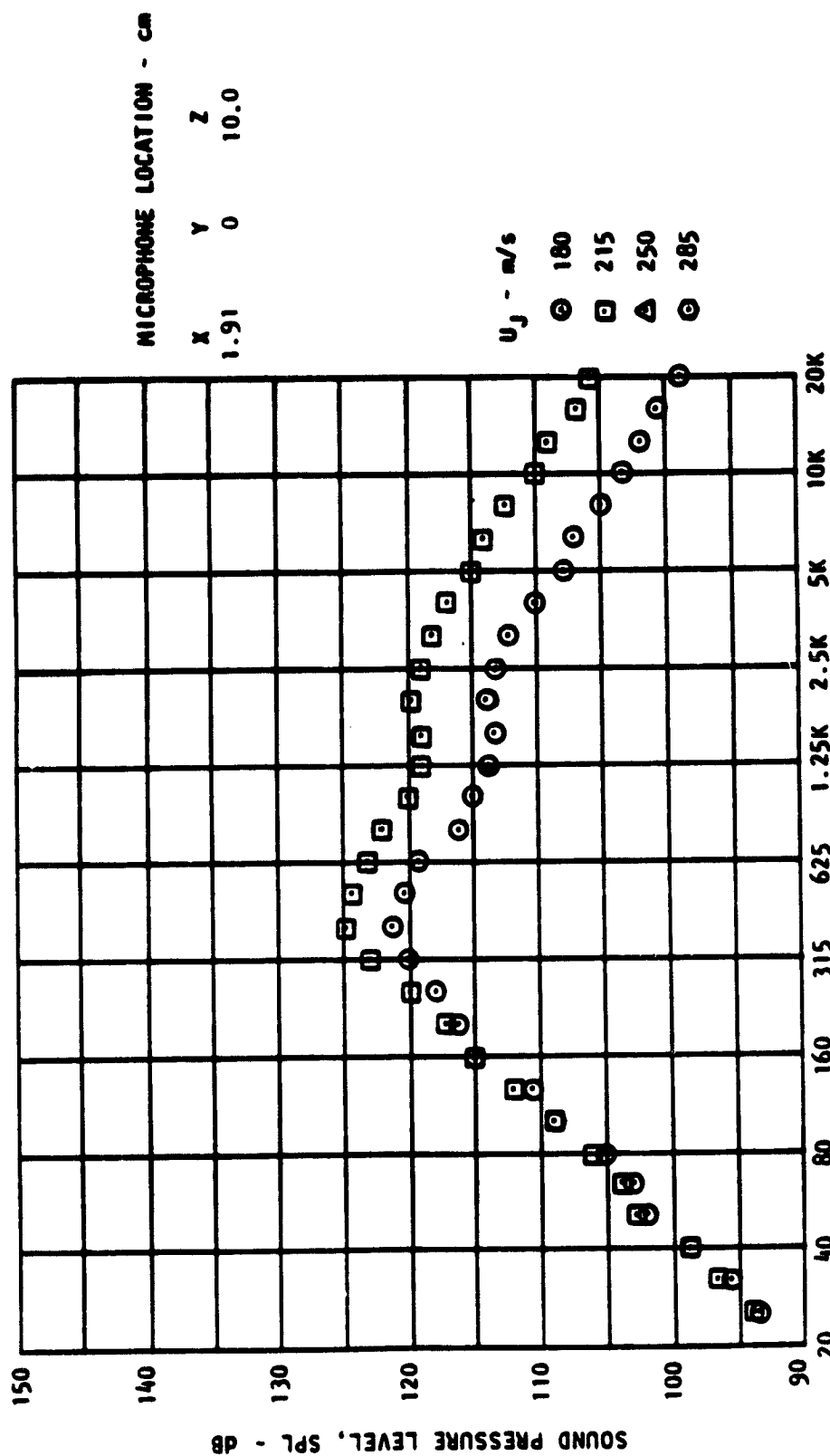


Figure D-3. Continued.

(D) Microphone 4.

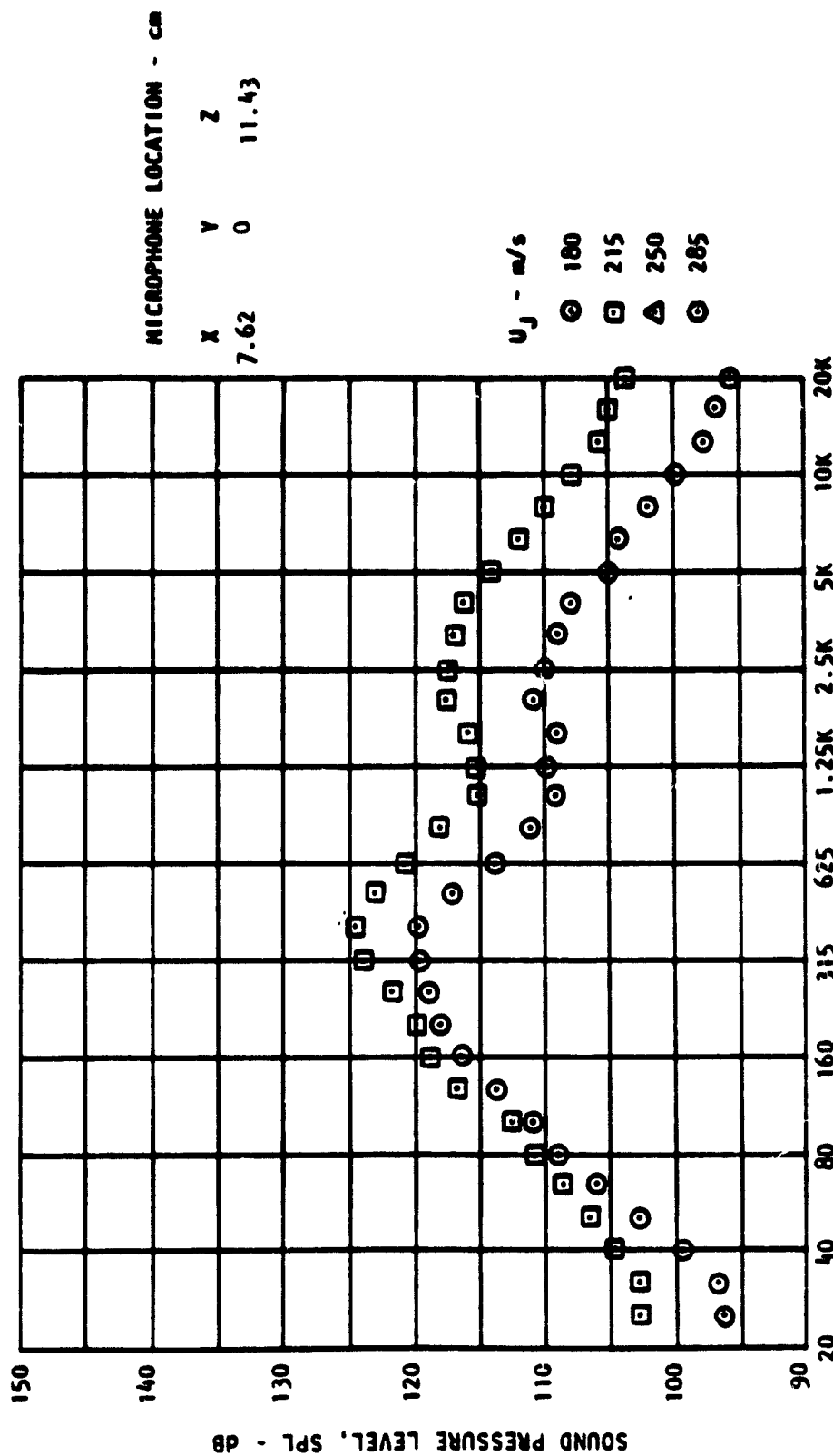


Figure D-3. Continued.

(E) Microphone 5.

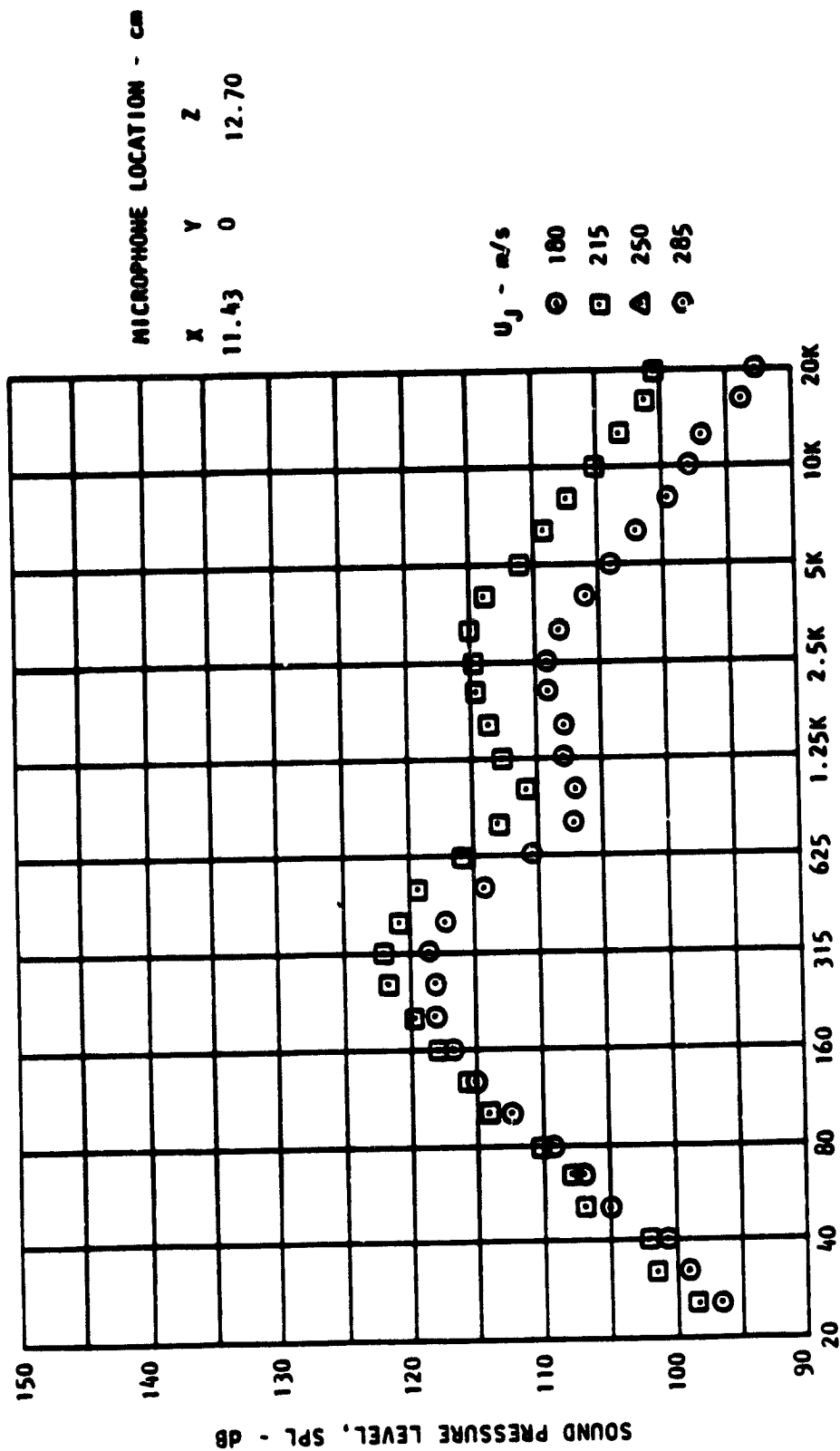


Figure D-3. Continued.
(F) Microphone 6.

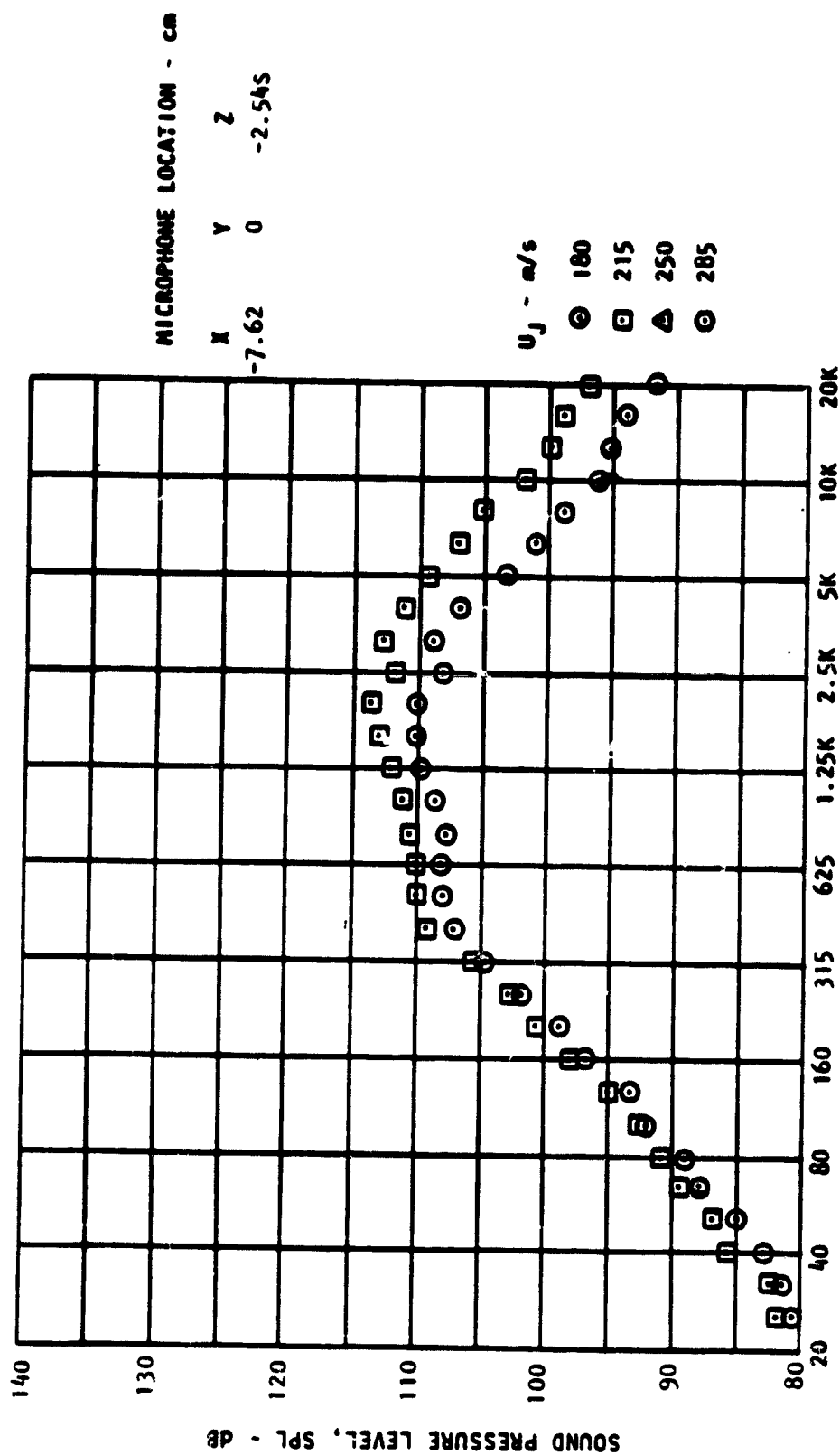


Figure D-3. Continued.

(G) Microphone 7)

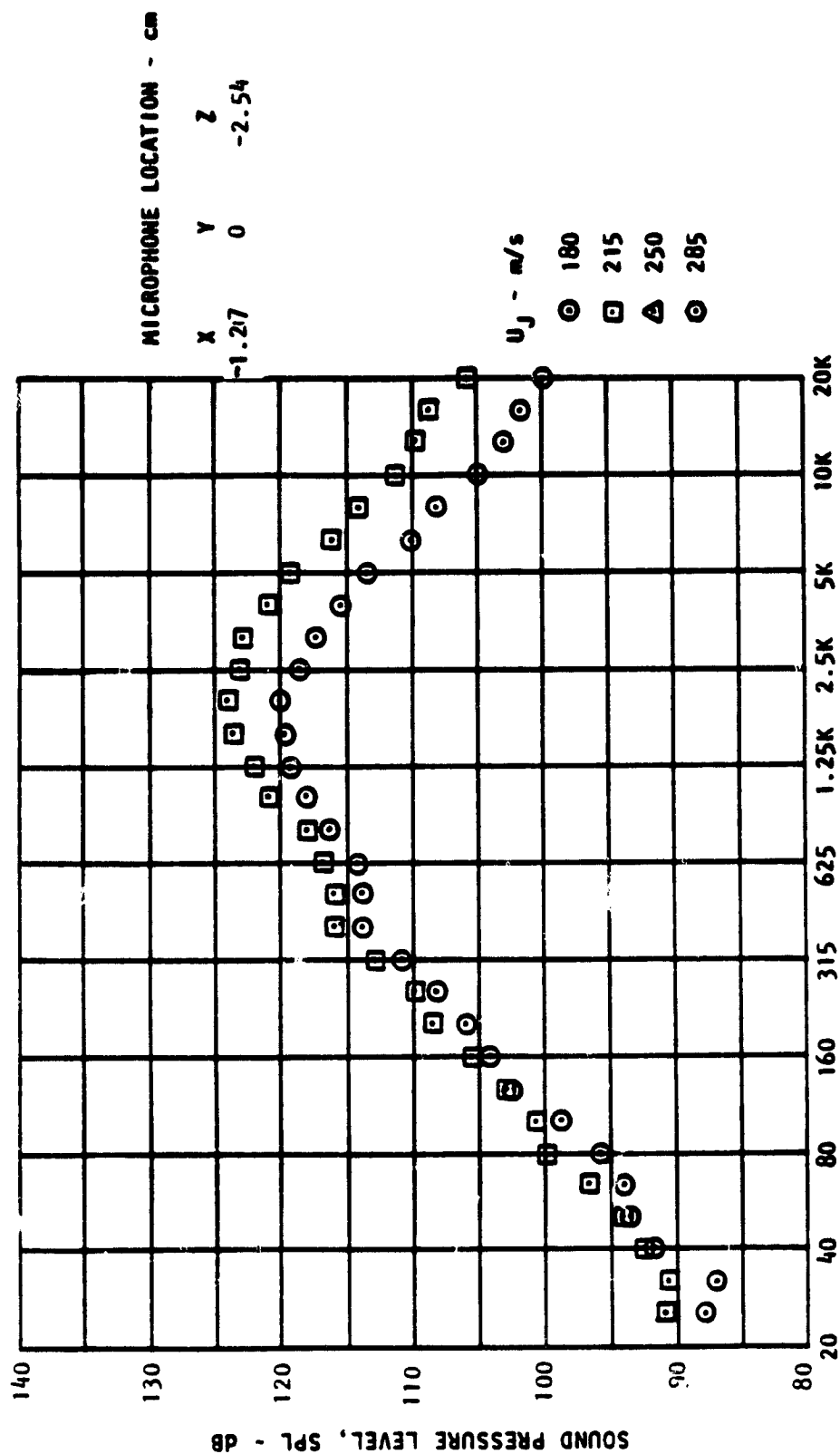


Figure D-3. Continued.

(H) Microphone 8.

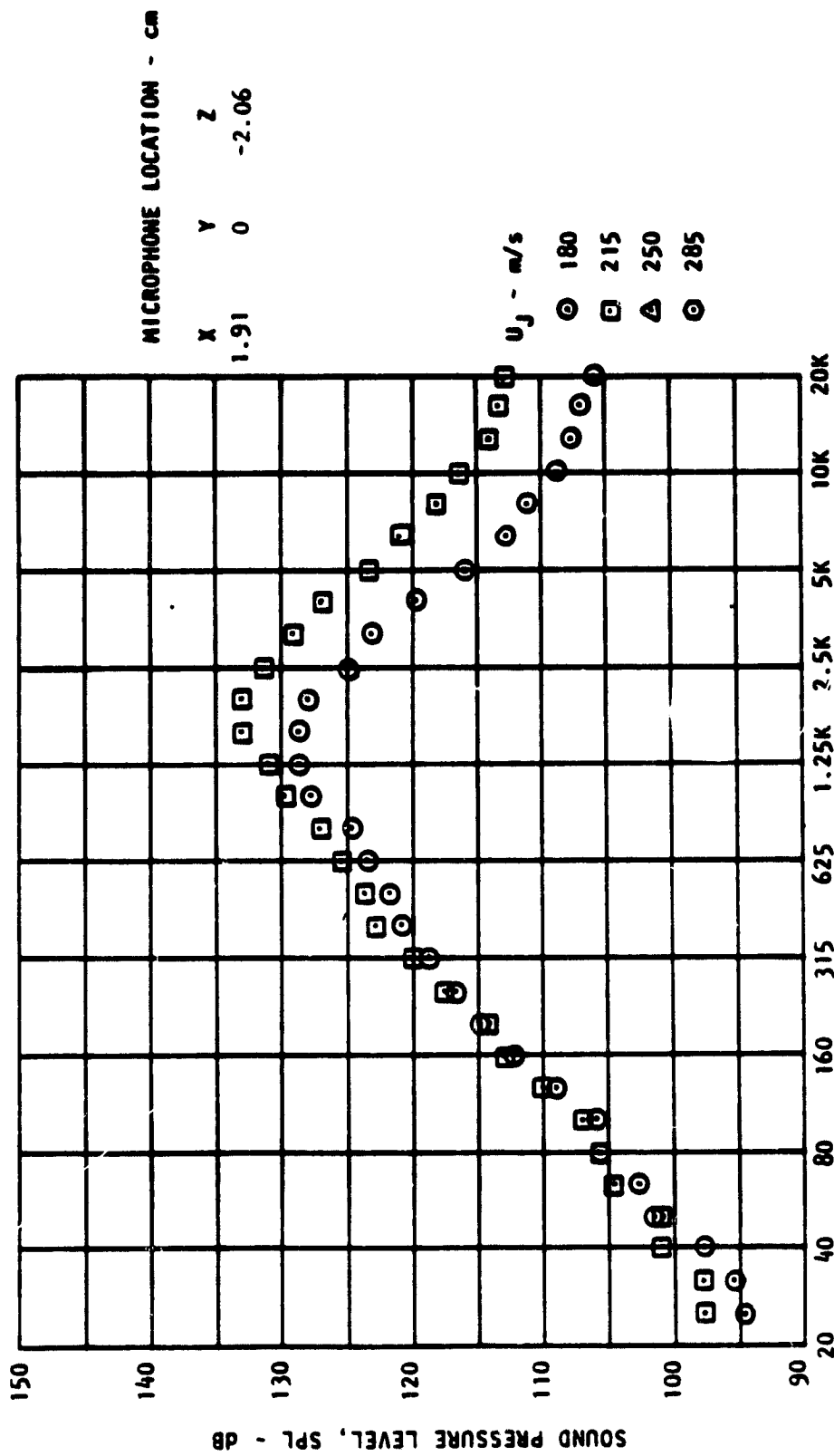


Figure D-3. Continued.

(1) Microphone 9.

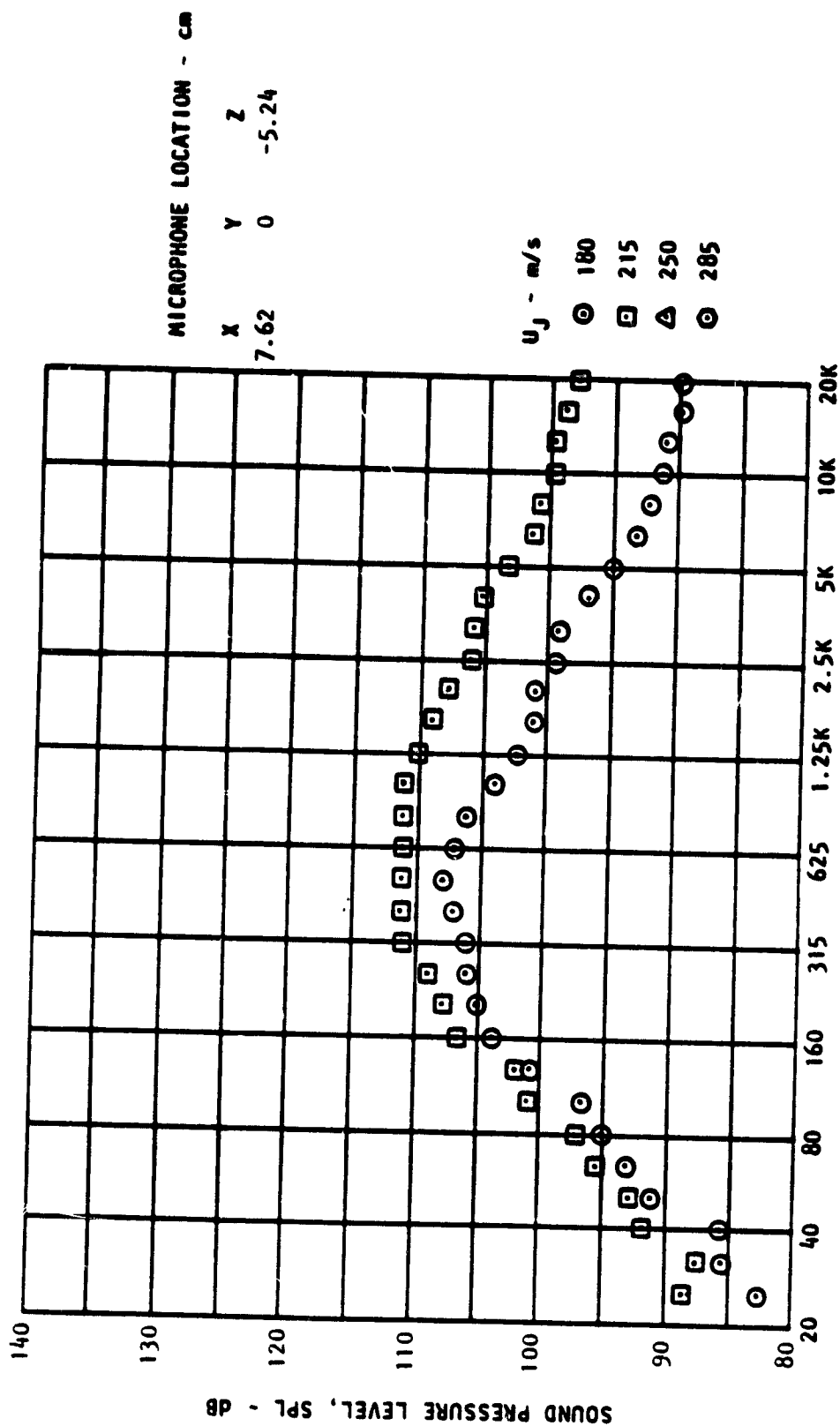


Figure D-3. Continued.

(J) Microphone 10.

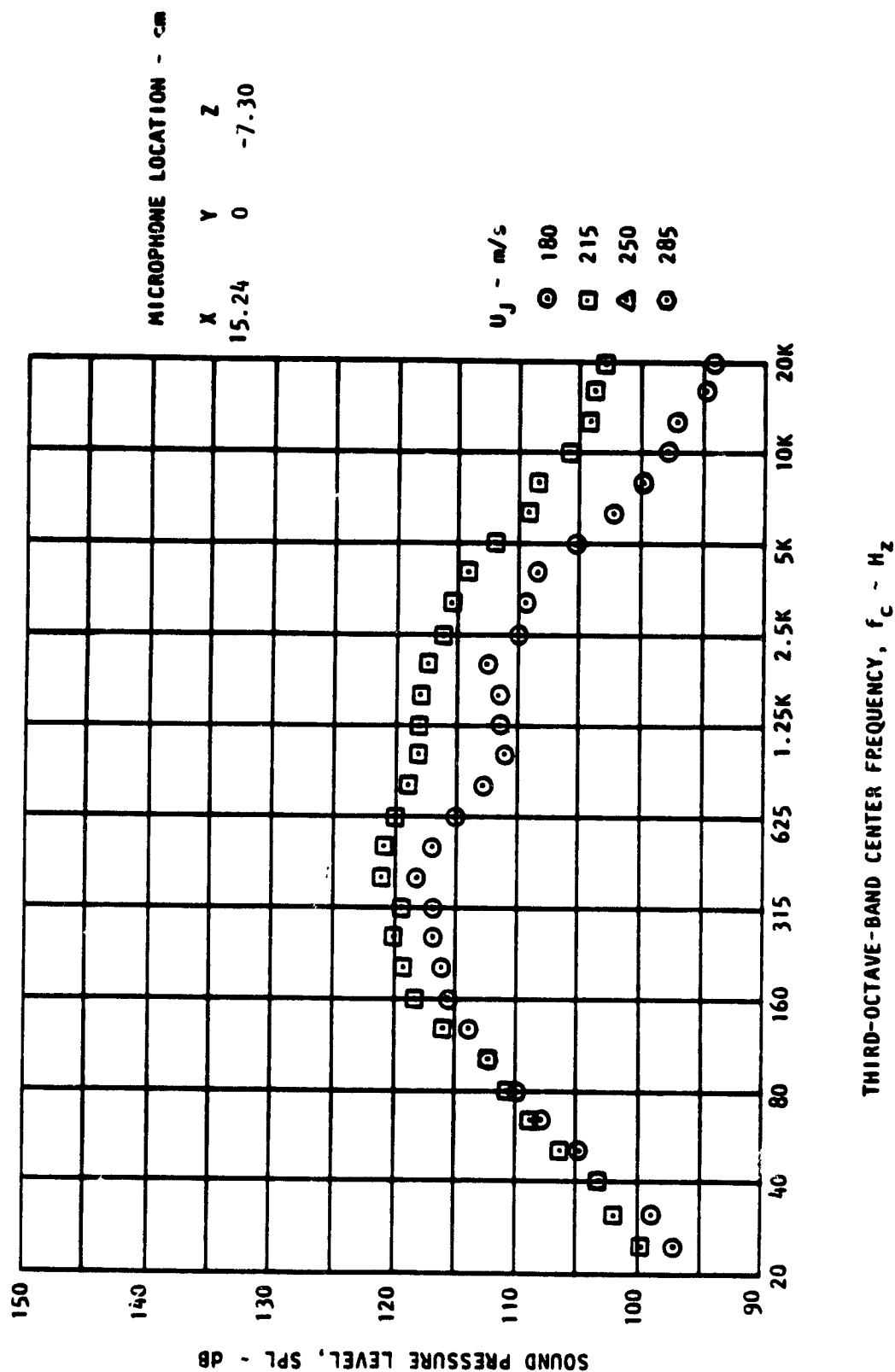


Figure D-3. Continued.

(K) Microphone 11.

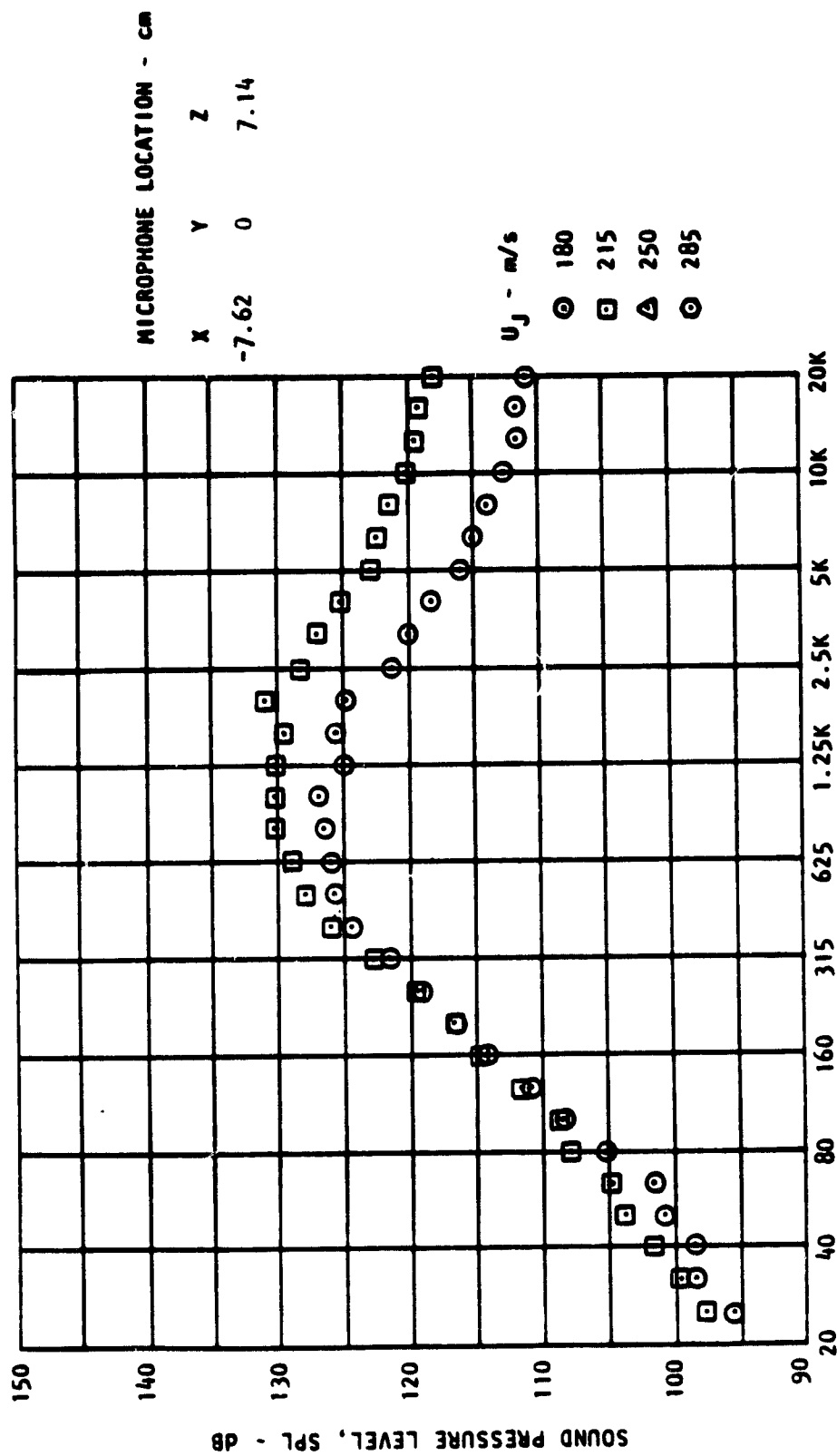


Figure D-3. Concluded.

(L) Microphone 12.